Investigations into the Radiochemistry of Gallium- and Fluorine-Containing Compounds for Molecular Imaging Applications

Sarpaki, Sophia

Award date:
2019

Awarding institution:
University of Bath
University of Bath

Investigations into the Radiochemistry of Gallium- and Fluorine-Containing Compounds for Molecular Imaging Applications

Sophia Sarpaki

A thesis submitted for the degree of Doctor of Philosophy

University of Bath

Department of Chemistry

March 2018

"I am among those who think that science has great beauty. A scientist in his laboratory is not only a technician: he is also a child placed before natural phenomena which impress him like a fairy tale. We should not allow it to be believed that all scientific progress can be reduced to mechanisms, machines, gearings, even though such machinery has its own beauty."

Marie Curie (1867-1934)

Contents

Acknowledgements

The writing of the acknowledgements section is a hard task for me since I believe that we often forget that there are more people behind the ones mentioned that contributed the most to our PhD experience. There is also a plethora of people that made us who we are, and that moulded our personalities in order to be in this position. Despite not having listed everyone, firstly I would like to acknowledge every single person that came through my life and in his/her way influenced my personality. I shall not forget all my teachers, professors and role models through the past years, because without their important role it is highly probable that I would not have been the scientist I am today. My passion for chemistry might not have been as strong without them, because they made me understand how great this science is. In addition, I wouldn't have been the strong, motivated and hard-working person I am today if I hadn't been influenced by them. So, THANK YOU all for being there and contributing in your way to be able to finish this thesis.

Moreover, I would like to acknowledge Prof. Sofia I. Pascu both for giving me the opportunity to work on such an exciting research project and for her guidance during these years, as well as ERC for grading this work through the O2Sense grand awarded to my supervisor. In addition, I would also like to thank University of Bath and Imperial College London for hosting my research and I would like to acknowledge my second supervisor Dr. Ian Eggleston who was always willing to help and find some time for me. His support has been decisive on finalizing this thesis. Further, Prof. Eric Aboagye and Prof. Jon Dilworth that with their guidance, help and knowledge helped me to get through different problems during my research. I would also like to express my gratitude to Dr. Laurence Carroll. Not only his guidance, patience and the help he provided through most of my radiolabelling experiments were very important for my thesis, but also he was there to listen to me, care for me and cheer me up at some darker moments of my PhD life. Additionally, I would like to thank Chris Barnes for his company and guidance during the fluorine-18 experiments, Jerry (Ruisni) Fu not only for his help during the cell uptake experiments but also for his flexibility to change his schedule to my convenience, as well as Frazer T. who first introduced me to Gallium-68 experiments. Furthermore, I am also grateful to Dr. David Gonzalez Calatayud for his support in an out of the lab despite having left Prof. Pascu's group two years ago. He has always been a helping hand when needed. Our discussions about metal complexes as well as his help in solving numerous

of the crystal structures enclosed to this report have been very important through the beginning of my PhD. I shouldn't forget Dr. Vincenzo Mirabello and Dr. Fernando Cortezon for their help during this thesis, for our NMR and fluorescence discussions which were very enlightening in order to successfully troubleshoot synthetic problems and titration procedures accordingly. I am also thankful to Dr. Haobo Ge for all the effort he put into assisting me with my *in vitro* experiments and Dr. Gabriele Kociok-Köhn for her crystallographic analysis as well as the Swansea mass spec centre for all the mass spectrometry results.

Additionally, I would like to thank the rest of the Prof. Pascu's group (Marina, Giuseppe, Federico and Sam) for all the nice moments we had together at uni and outside uni, my flatmates (Angelliki and Nota) because we've gone through some tuff situations together and all my friends from Bath (particularly to Rosa and Simone) and from Greece (Artemis, Aris, Dimitris, Dionysia, Eirini, Nikos, Iris etc) being my support system during these years. Most importantly to my friends Christina who have helped me a lot while I was writing my thesis, Georgia who has done a lot more than helping me or supporting me and she is always there no matter what and Christos who came in my life to make it a lit bit more difficult but also more joyful. To my colleagues from my new job that have been patient with me writing and working in parallel, but also for being very encouraging (specially to Afrodith, staying late at night at Demokritos and accompany me while I was writing). Some very special thanks are dedicated to my family in London (Maria, Mpampis and Eleni) for their encouragement and their hospitality every time I have been in London for experiments. I really believe that this thesis would not have been the same without their support. I would really like to express my gratitude for knowing that I have so far away from home a family that I can count on. Finally, my warmest thanks go to my parents. If it wasn't for my inspiring father, I do not think that I would be triggered by science and medicinal studies and if it wasn't for my mother, I really do not consider that I would have been that persistent and indomitable. Thus, I would like to thank both of them alongside my sister for their unconditional love and support.

Abstract

Hypoxia is the condition characterised by lack of oxygen supplied to the body or a region of the body. It has been strongly related to cancer since the 1950's and it is still considered responsible for the malignant progression of tumours, therapy resistance and weak prognosis. Thus, tumour hypoxia has been widely investigated in the last decades as a potential target in oncology. However, despite years of research and a variety of information collected, yet there are still many unanswered questions on hypoxia mechanisms that haven't yet been addressed. The inhibition of hypoxia-inducible factor (HIF) has attracted the interest in drug developments. However, in recent years, inhibition of carbonic anhydrase IX (CAIX), which is also related to HIF, has attracted the attention of many research groups working on hypoxia worldwide.

It was hypothesised that targeting HIF and CAIX together by a small molecule attached to an imaging agent for positron emission tomography (PET) or single photon emission tomography (SPECT) would allow one to detect and inhibit hypoxia. The new family of compounds discussed through this thesis aimed to shed further light on these aspects, by inclusion of an unsymmetrical thiosemicarbazonate complex, a glycosyl coumarin unit and a fluorine-18 unit in the tracer design. Bis(thiosemicarbazonate) metal complexes have been extensively used as PET and SPECT imaging agents and they have also shown some *in vivo* hypoxia uptake while glycosyl coumarin has shown good CAIX inhibition. Several new compounds have been synthesised and fully characterised through different techniques such as 1D and 2D NMR and mass spectrometry. Labelling with gallium-68 has been also performed in order to evaluate the potential application of such complexes as PET imaging agents additionally to optical imaging agents. Significant progress has been made in the direction of the synthesis of these compounds, and further cellular uptake and behaviour.

Specifically, **Chapter 1** includes a literature review, where medical imaging is introduced along with some basic background on cancer and hypoxia. Examples are cited on how thiosemicarbazonato complexes have been related and used through the years as antitumour and potential imaging agents. In addition, the potential of glucosyl coumarin as hypoxia target molecule are quoted. The review concludes with the upcoming field of nanomedicine and the possibility of graphene oxides as nanocarriers of targeting molecules or imaging tracers.

In **Chapters 2,3** and **4** are discussed the results obtained through the thesis. **Chapter 2** describes and analyses the synthesis of three new mono(substituted) precursors and of a number of new non-radioactive and radioactive metal complexes that are relied on two identical mono(substituted) ligands. Moreover, **Chapter 3** describes the synthesis and characterisation of asymmetric acenaphthenoquinone bis(thiosemicarbazonate) metal complexes originated by the mono(substituted) ligands described in Chapter 2. The radiolabelling of these complexes with gallium-68 and fluorine-18 is also presented. In both chapters, it is examined the investigations of the behaviour of those compounds in the cellular environment through *in vitro* fluorescence imaging, cell viability and radioactive uptake assays. Moreover, in Chapter 3 the attempted attachment of a CAIX-selective inhibitor to these metal complexes is outlined. Specifically, the characterisation and functionalisation of a glucosyl coumarin derivative is described. On the other side, **Chapter 4** communicates the potentials of graphene oxides as nanocarriers of thiosemicarbazonate complexes and/or glucosyl coumarin. The non-covalent radiolabelling of the new nanohybrids with gallium-68 is presented in this chapter for the first time along with the cellular investigation of their toxicity and uptaking features.

An overview of this work and the conclusions drawn are discussed in **Chapter 5**. Certain possible future exploitations related to the results discussed are suggested in this chapter to fully optimise the potentials of those complexes in a hypoxic environment.

Lastly, **Chapter 6** contains the experimental procedures and protocols that were developed through this thesis. Additional supporting crystallographic data, figures and tables are presented in the supplementary information.

List of publications and conference proceedings resulting from this PhD

- *Synthesis, Radiolabelling and In Vitro Imaging of Multifunctional Nanoceramics*, Marina Lledos, Dr. Vincenzo Mirabello, Sophia Sarpaki, Dr. Haobo Ge, Dr. Hubert J. Smugowski, Dr. Laurence Carroll, Prof. Eric O. Aboagye, Prof. Franklin I. Aigbirhio, Prof. Stanley W. Botchway, Prof. Jonathan R. Dilworth, Dr. David G. Calatayud, Dr. Pawel K. Plucinski, Prof. Gareth J. Price, Prof. Sofia I. Pascu; *Chem.Nano.Mat.* **2018**, 4(4), 361-372

- *Applications of "Hot" and "Cold" Bis(thiosemicarbazonato) Metal Complexes in Multimodal Imaging*, Cortezon-Tamarit F, Sarpaki S, Calatayud DG, Mirabello V, Pascu SI; *Chem Rec*. **2016**, 16(3), 1380-97.

List of conference presentations resulting from this PhD

- Abstracts of the 24th international isotope society (UK group) symposium: synthesis and applications of labelled compounds 2015; *J. Labelled Comp. Radiopharm.* **2016**, 59(4), 175-86.

- Abstracts of the 25th international isotope society (UK group) symposium: synthesis and applications of labelled compounds 2016; *J. Labelled Comp. Radiopharm.* **2017**, doi.org/10.1002/jlcr.3523.

List of abbreviations

aq	Aqueous
AcGC	Methylumbelliferyl-tetraacetyl-D-mannopyranose
ADAM	A Disintegrin And Metalloproteinase
APCI	Atmospheric-pressure chemical ionisation
ARNT	Hydrocarbon nuclear translocator domain
ATSM	Diacetyl-bis (N4-methyl thiosemicarbazone)
BCA	Bicinchoninic acid
BrGC	Methylumbelliferyl-6-bromoethyl-D-mannopyranose
BRS-3	Bombesin like receptor 3
Boc	t-Butyl carbamate
Bq	Becquerel
BTSC	Bis(thiosemicarbazone)
CA	Carbonic Anhydrase
CDT	Carbamodithioate
Cu-ATSM	Copper(II) diacetyl bis(N(4)-methylthiosemicarbazonato)
COSY	Correlation spectroscopy
Covf	Covariance of fitting
CSC	Cancer stem cell
CSX4	Strata- X- C 33 μm polymeric strong cation
CT	Computer tomography
DBU	1,8-Diazabicyclo[5.4.0]undec-7-ene
DFO	2,2-Difluoro-3-hydrostatine
DIC	Differential interference contrast
DIPEA	N, N-Diisopropylethylamine
DMAP	4-(Dimethylamino)pyridine
DMF	Dimethylformamide
DMSO	Dimethylsulfoxide
DNA	Deoxyribonucleic acid

DOTA	1,4,7,10-Tetraazacyclododecane-1,4,7,10-tetraacetic acid/ tetraxetan
DOTATATE	DOTA-octreotate/ (DOTA-(Tyr)^3-Octreotate
DOTATOC	Edotreotide/ (DOTA^0-Phe^1-Tyr^3)octreotide
DTPA	Diethylenetriaminepentaacetic acid
EDC	1-ethyl-3- 3-dimethyl aminopropyl carbodiimide hydrochloride
EDX	Energy-dispersive X-ray
EDTA	Ethylenediaminetetraacetic acid
ET	Emitting tomography
Et	Ethyl
EtOH	Ethanol
EMT6	Mice cell line for mammary cell carcinoma
eq	Equivalence
ES	Electrospray
ESI	Electrospray ionization
ESI-TOF	Electrospray ionization time of flight
FCS	Fetal Calf Serum
GC	Glycosyl coumarin/ methylumbelliferyl-D-mannopyranose
GO	Graphene oxide
HCl	Hydrochloric acid
HeLa	The human cervix carcinoma epithelioid cell line
HIF	Hypoxia inducible factor
HOBt	1-Hydroxybenzotriazole hydrate
HPLC	High-performance liquid chromatography
MALDI	Matrix-assisted laser desorption/ ionisation
Me	Methyl
MeOH	Methanol
MeCN	Acetonitrile
MRI	Magnetic resonance imaging
MS	Mass spectrometry
MTT	2-(4,5-Dimethyl-2-thiazolyl)-3,5-diphenyl-2H-tetrazolium bromide

μW	Microwave
NADH	Nicotinamide adenine dinucleotide
NADPH	Nicotinamide adenine dinucleotide phosphate
NMR	Nuclear magnetic resonance
NOE	Nuclear Overhauser Effect
NOESY	Nuclear Overhauser effect spectroscopy
NOTA	1,4,7-Triazacyclononane- 1,4,7-triacetic acid
NP	Nanoparticle
ODD	oxygen-dependent degradation doma
p53	Tumour protein
PAH	polycyclic aromatic hydrocarbon
PBS	Phosphate buffered saline
PC3	Human prostate cancer cell line
PET	Positron emission tomography
Ph	Phenyl
PSMA	Prostate specific membrane antigen
Py-BOP	Benzotriazol-1-yl-oxytripyrrolidinophosphonium hexafluorophosphate
rGO	Reduced graphene oxide
ROS	Reactive oxygen species
ROI	Radiochemical incorporation
RPMI	Roswell Park Memorial Institute
SE	Standard error
S_N	Substitution reaction
SPECT	Single-photon emission computed tomography
SPPS	Solid-phase peptide synthesis
TAME Hex	tris(aminomethyl) (ethane-N,N,N′,N′,N″,N″-hexaacetic acid)
tC18	Sep-Pak Light tC18 cartridges
TCC	Trichloroisocyanuric acid
TEM	transmission electron microscopy
TEMPO	2,2,6,6-Tetramethyl-1-piperidinyloxy

TFA	Trifluoroacetic acid
THF	Tetrahydrofuran
TLC	Thin layer chromatography
TOF-MS	Time-of-flight mass spectrometry
TSC	Thiosemicarbazone scaffold
TSCA	Thiosemicarbazone acenaphthenequinone scaffold
UV-Vis	Ultraviolet–visible
X-Ray	X-Radiation
3D	Three dimensional

Numbering of Compounds

Chapter 2:

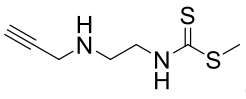

(2d)

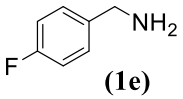

(1e)

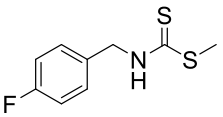

Fbnz-MeCDT **(2e)**

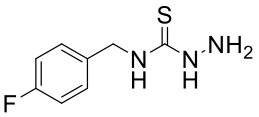

Fbnz-TSC **(3e)**

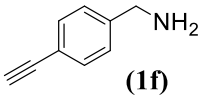

(1f)

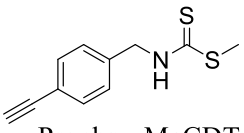

Propbnz-MeCDT **(2f)**

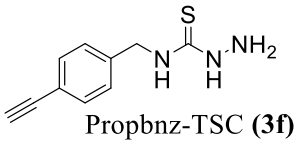

Propbnz-TSC **(3f)**

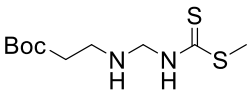

(2g)

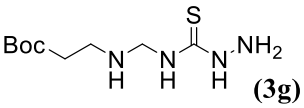

(3g)

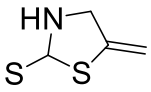

(4)

PhTSCA **(5a)**

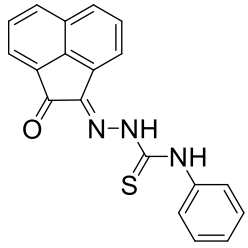

AllylTSCA **(5b)**

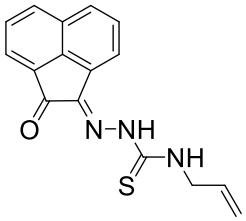

EtTSCA **(5c)**

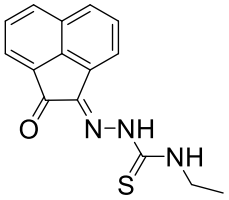

FbnzTSCA **(5e)**

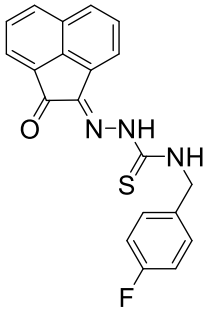

propbnzTSCA **(5f)**

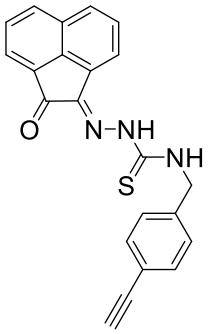

NH_2free-TSCA **(5h)**

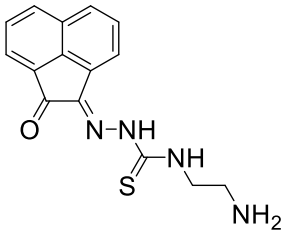

$Zn(PhTSCA)_2$ **(6a)**

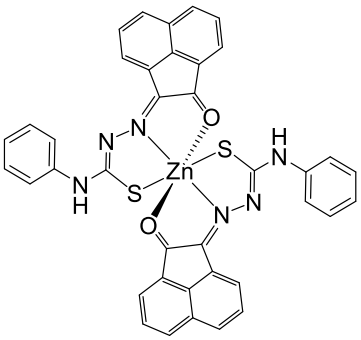

$Zn(AllylTSCA)_2$ **(6b)**

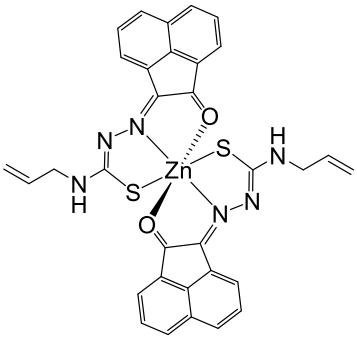

$Zn(EtTSCA)_2$ **(6b)**

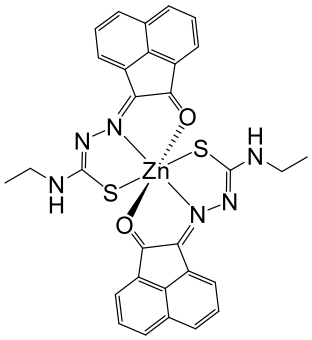

$Zn(FbnzTSCA)_2$ **(6e)**

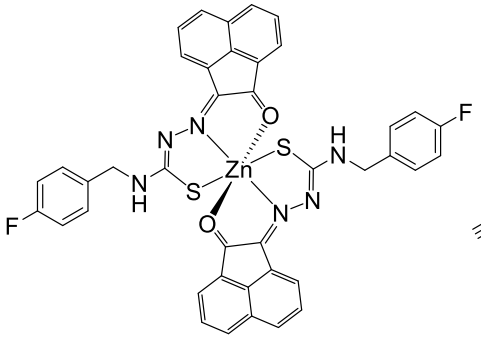

$Zn(propbnzTSCA)_2$ **(6f)**

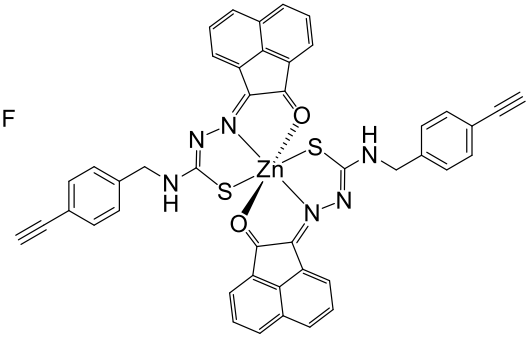

[^{68}Ga]Ga(PhTSCA)$_2$ **(7a)**

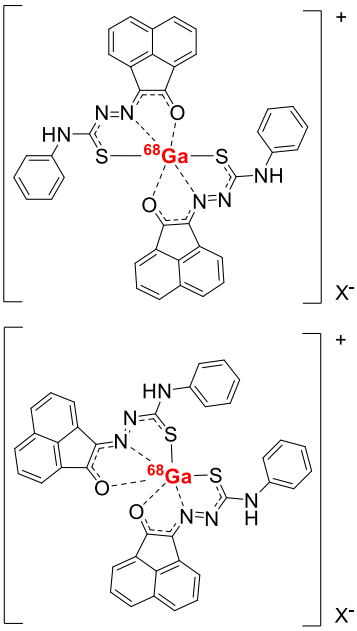

[^{68}Ga]Ga(AllylTSCA)$_2$ **(7b)**

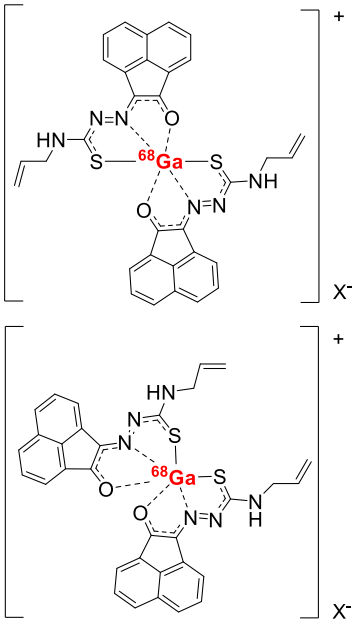

[^{68}Ga]Ga(EtTSCA)$_2$ **(7c)**

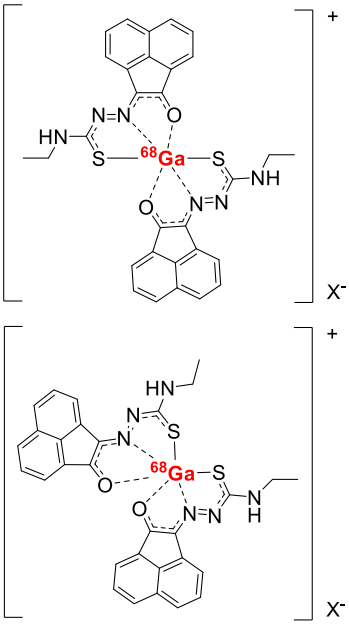

X: Cl, OH

[^{68}Ga]Ga(FbnzTSCA)$_2$ **(7e)**

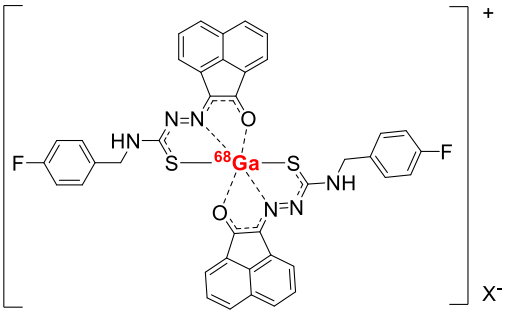

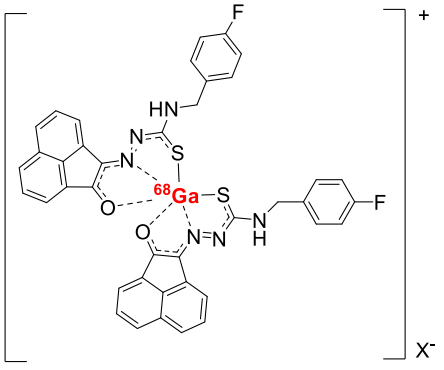

[^{68}Ga]Ga(propbnzTSCA)$_2$ **(7e)**

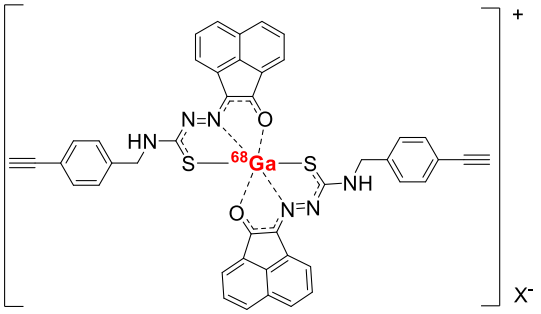

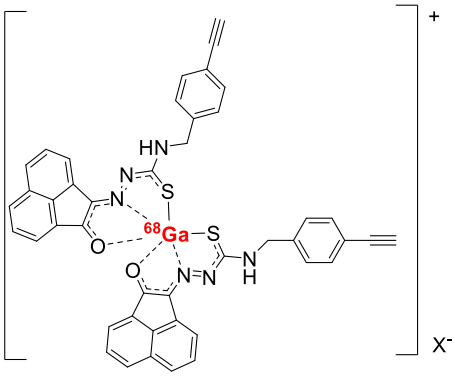

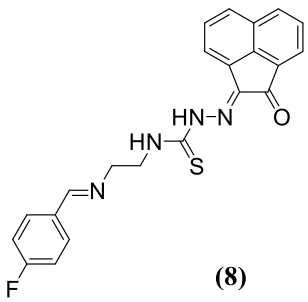

(8)

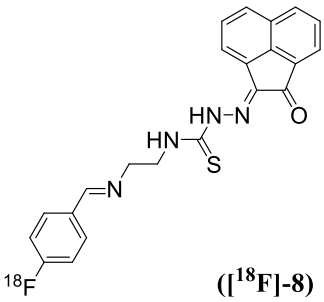

([^{18}F]-8)

Known compounds synthesised by adopted methodologies: **2d**, **5a-5c**, **5g**, **6b**

New compounds: **1e**, **1f**, **2e**, **2f**, **3e**, **3f**, **4**, **5e**, **5f**, **6a**, **6c-6f**, **[^{68}Ga]-7a-7f**, **8**, **[^{18}F]-8**

Chapter 3:

PhZnTSCA **(9a)**

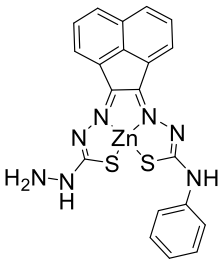

AllylZnTSCA **(9b)**

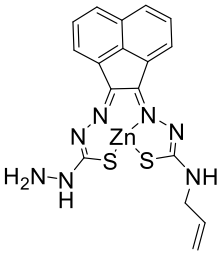

EtZnTSCA **(9c)**

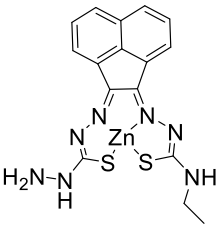

FbnzZnTSCAc **(9e)**

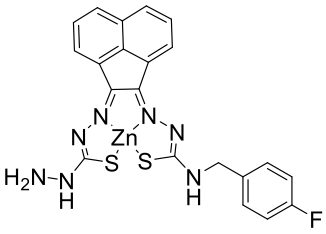

PropbnzZnTSCAc **(9f)**

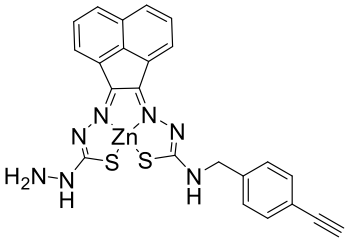

PhGaTSCAc **(10a)**

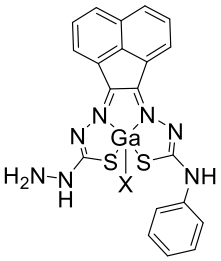

AllylGaTSCAc **(10b)**

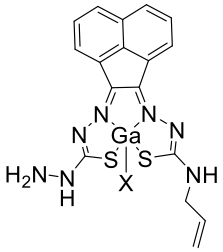

EtGaTSCA **(10c)**

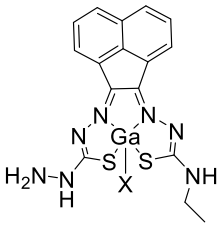

FbnzGaTSCAc **(10e)**

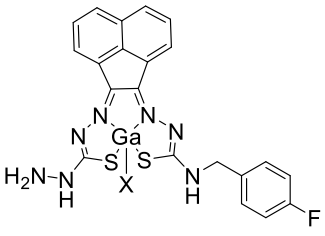

PropbnzGaTSCAc **(10f)**

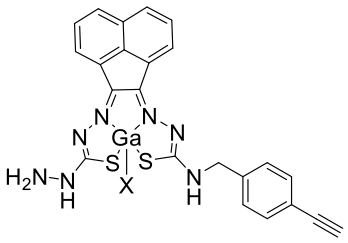

[^{68}Ga]PhGaTSCA

([^{68}Ga]-11a)

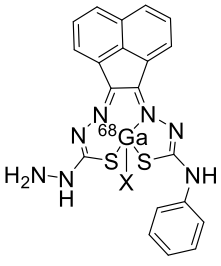

X: Cl^-, OH^- or CH_3COO^-

Known compounds synthesised by adopted methodologies: **9a-9c**, **9b**, **9c**,

New compounds: **9e**, **9f**, **10a**, **10e**, **10f**, **[^{68}Ga]-11a**

[^{18}F]Ph-Fbnz-ZnTSC (**[^{18}F]-12**)

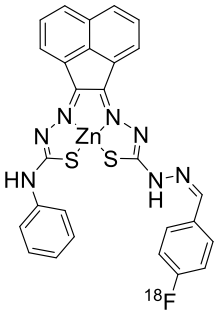

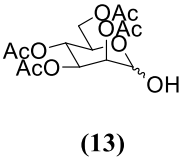

(13)

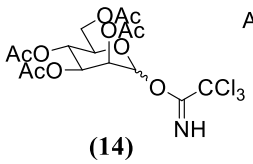

(14)

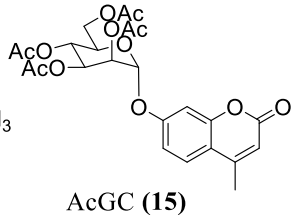

AcGC **(15)**

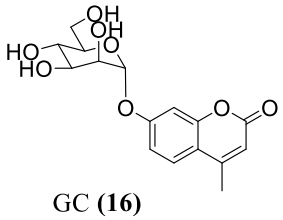

GC **(16)**

Ph-GC-ZnTSCA **(17)**

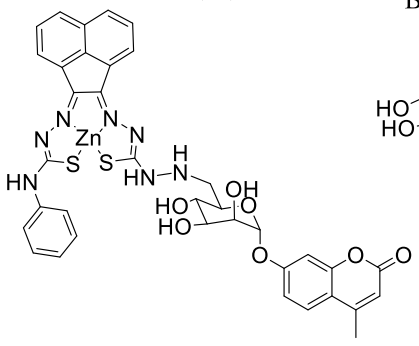

BrGC **(19)**

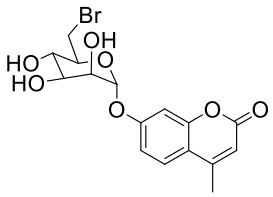

Known compounds synthesised by adopted methodologies: **13-16**,

New compounds: **12**, **17, 19**

Chapter 4:

Graphene oxide based nanohybrids (schematic representation)

(20)

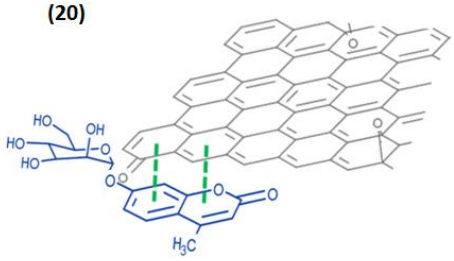

(21)

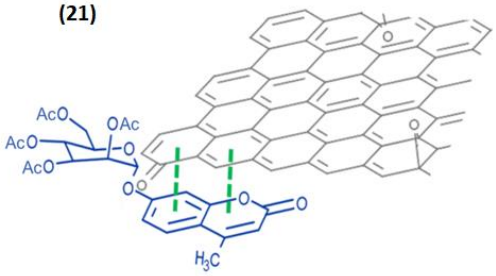

(23)

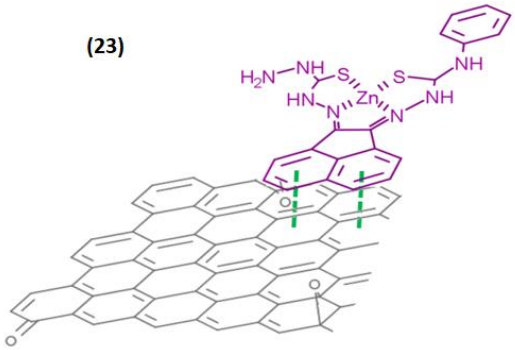

(24)

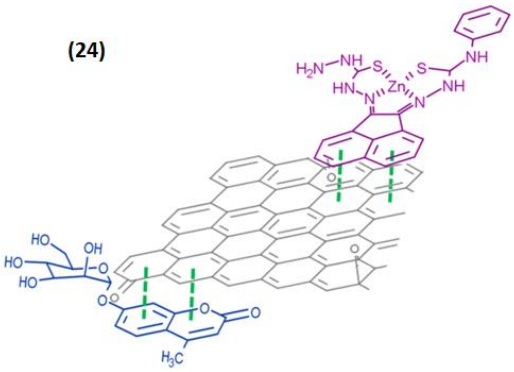

([^{68}Ga]-25)

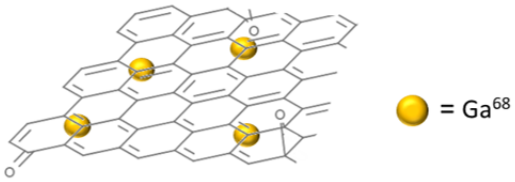

([^{68}Ga]-26)

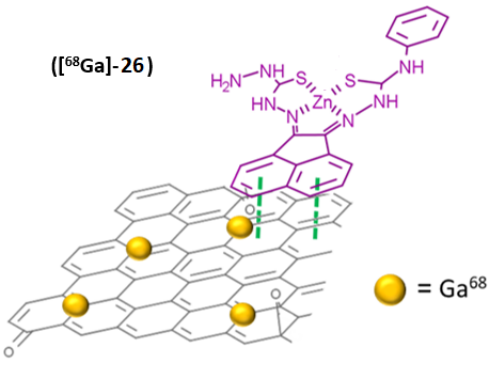

([^{68}Ga]-27)

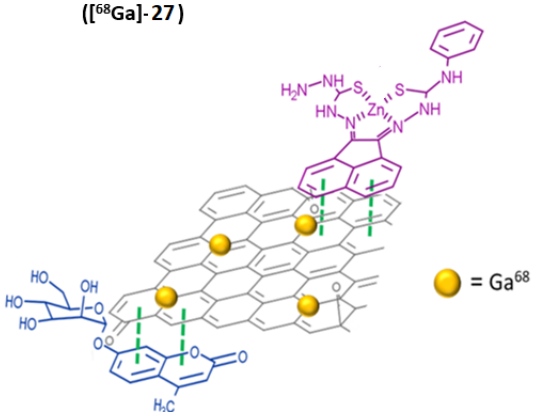

New compounds: all

Introduction to medical imaging and oncology

1.1. General considerations of molecular imaging

Medical imaging is a promising approach applied extensively for a wide range of diagnostical purposes particularly due to its non-invasive character, as through different techniques can accomplish distant visualisation of the interior of a body.[1] The chronicle of medical imaging starts at the late 1890's with the discovery of the X-Ray by Wilhelm Conrad Roentgen.[2] The development of this technology has flourished until the First World War when radiography was employed not only for imaging skeleton trauma but also for the visualisation of diseases such as tuberculosis or other lung lesions. By the 1950's, nuclear medicine was introduced to the field of medical imaging. This, alongside the introduction of computing technologies by the 1970's and the development of other imaging modalities not only revolutionised the field but also created an explosive growth of diagnostic imaging techniques that nowadays can detect a variety of pathogenic diseases.[1, 3] Since 2008, more than 5 billion medical imaging studies have been conducted for the early diagnosis of neurological, cardiovascular diseases and tumours allowing for more efficient treatments.[4-7]

A plethora of anatomical imaging techniques has facilitated the detection of intra-tumour heterogeneity or the tumour staging whilst providing quantitative information. Optical imaging, emission tomography (PET and SPECT), magnetic resonance, CT and ultrasound are the most robust imaging techniques. The advantages and drawbacks of each are listed in Figure 1.[5-8]

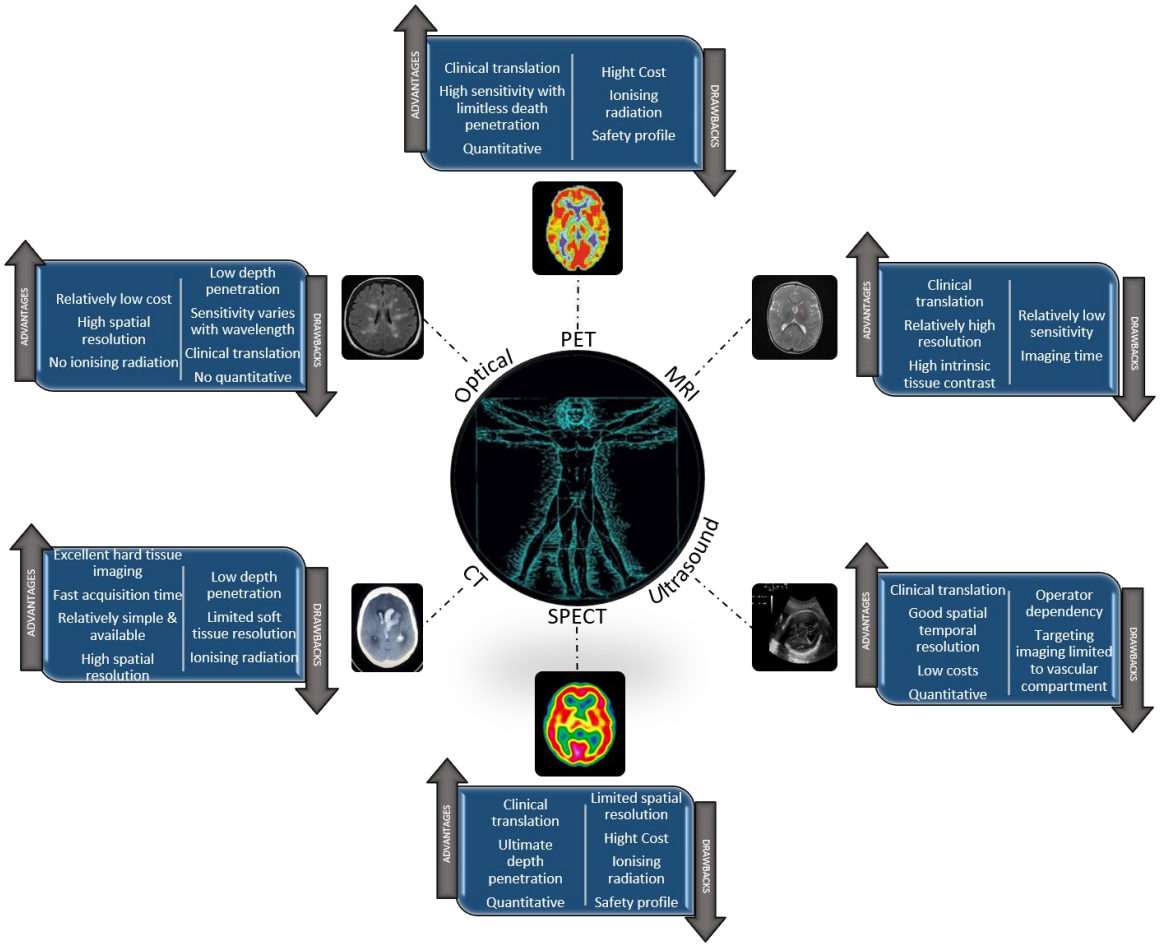

Figure 1: Advantages and drawbacks of different molecular imaging techniques. [7-9]

1.1.1. Emission tomography (ET)

One of the most frequently applied medical imaging techniques is emission tomography (ET). ET utilises radioactive elements (radiotracers) to permit the visualisation of the body's physiology and can depict the spatial distribution of different biological processes, such as glucose metabolism thus facilitating the detection of relevant diseases (tumours, etc.). [6, 7, 10, 11] The cornerstones of ET are:

1. *Tracer principle*, based on the principle that both radioactive and non-radioactive elements can mutually participate in biological processes, therefore the radioisotope can

be used to indicate the biodistribution of the non-radioactive analogues (George de Hevesy, Nobel Prize 1943).[12] In addition, radioactive species are used in the minimum possible amount in order to improve the accuracy and sensitivity of the analysis but without perturbing the biological system in question. [13]

2. *Tomography*, which relies on the principle that γ-ray energy is emitted by radionuclides, facilitating the visualisation as an image which can be acquired as a cross-sectional slice of the body.[10]

SPECT and PET are both emitting tomography imaging techniques. However, they can be easily distinguished due to the type of the radioisotope employed each time. As indicated by their names, PET's labelling isotope is a positron emitter, whereas SPECT uses a single photon emitter.[11]

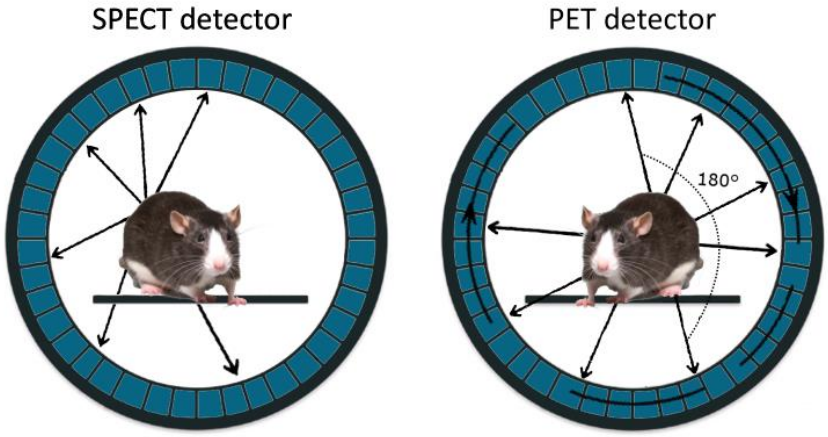

Figure 2: Typical configuration of a SPECT (left) and a PET (right) scanner.

Single-photon emission computed tomography (SPECT)

SPECT study is initiated by the injection of the radiotracer and its locomotion in the surrounding medium. This radiotracer decays during the process and one or more γ-ray segments are released in a different direction. The scanning procedure in SPECT's case is based on the detection and the recording of one resulting γ-ray segment. In order to point out the origin of the signal, the detector moves cyclically to acquire projection image data from different views around the patient (**Figure 2**). [10, 14-19] There are a variety of different metals

that are used as SPECT radionuclides such as Gallium-67 and Indium-111. However, approximately around 80% of nuclear medicine procedures in clinical practice involve Technetium-99m scans.[17, 20-22]

Positron emission tomography (PET)

An injection of the radiotracer marks the initiation of a PET study. A positron is ejected from the positron-emitting isotope's nucleus and the imaging procedure follows. The positron is transmitted to an average distance (depending on its energy) before it annihilates with an electron from the surrounding medium, resulting in the release of two antiparallel 511-keV photons *(decay event)* (**Figure 3**).[4-7, 18, 19, 23, 24] The patient is surrounded by a stationary ring γ-ray detector. An instantaneous detection of two γ-ray photons is interpreted as a consequence of the same decay event. Therefore, the detection of the spot where the decay event occurred can be determined by tracing their line segment (**Figure 2**).[4-6, 10, 18, 19, 21, 24] There are different PET radionuclides available for use, the most commonly used is fluorine-18 ($t_{1/2}$= 109.77 min, E_{max}= 634 keV) due to its relatively short half-life and cost.[19, 21-25]

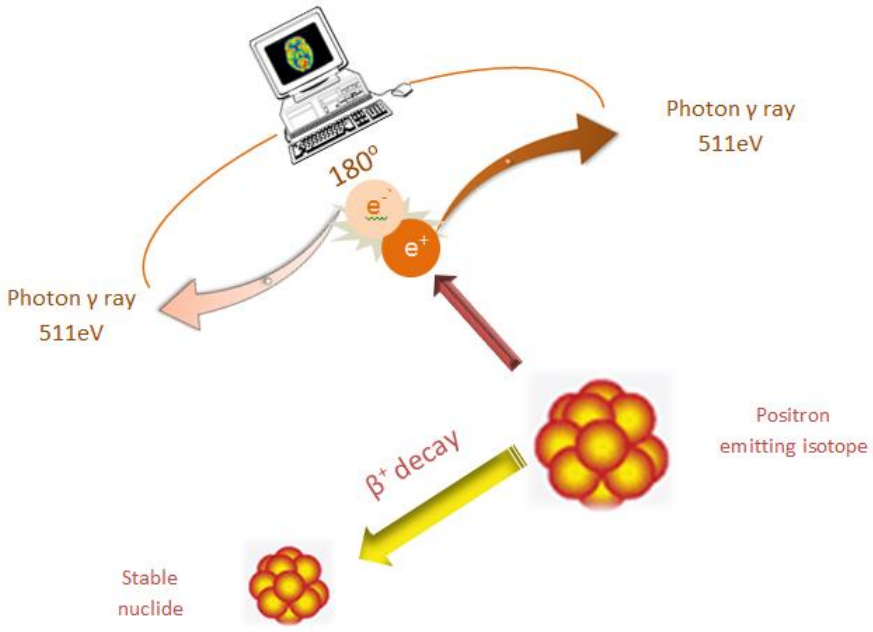

Figure 3: Schematic illustration of PET imaging principle operation[23].

1.1.2. Design and synthesis of radiotracers

The artificial nature of the emitting isotopes implies the production of radionuclides before their use. There are three different principles for the production of radioisotopes.[23] The first one involves the separation of the by-product after fission. In the second, high power electric and magnetic fields are employed to accelerate charged particles to high energies, which then bombard stable atoms and targets to give rise to radioactive isotopes.[6, 23, 26] Finally, the third involves the production of the radioisotope from neutron irradiation in a reactor (cyclotron).[6, 15, 23, 26] There is a variety of different radioisotopes, non-metallic (carbon-11, fluorine-18) and metallic (gallium-68, copper-64 and zirconium-89), which can be integrated in diverse compounds of biological interest to produce radiotracers suited for each study's subject (type of biological target, affinity and specificity of the radiotracer's target, capacity of the compound to be synthesised, pharmacokinetics and metabolism of the radiotracer and physical-chemical properties).[6, 23] Some of the most widely used PET tracers in clinical applications are [^{18}F]-Fluorodeoxyglucose ([^{18}F]FDG), elucidating a patient's glucose metabolism and the copper(II) diacetyl bis(N(4)-methylthiosemicarbazonato) (Cu-ATSM) tracer that has been applied for the detection of pancreatic tumours and hypoxia.[5, 23, 25] More recently, [^{68}Ga]Ga-PSMA (prostate specific membrane antigen) has gained importance as a prostate cancer imaging tool (**Figure 4**).[27-31]

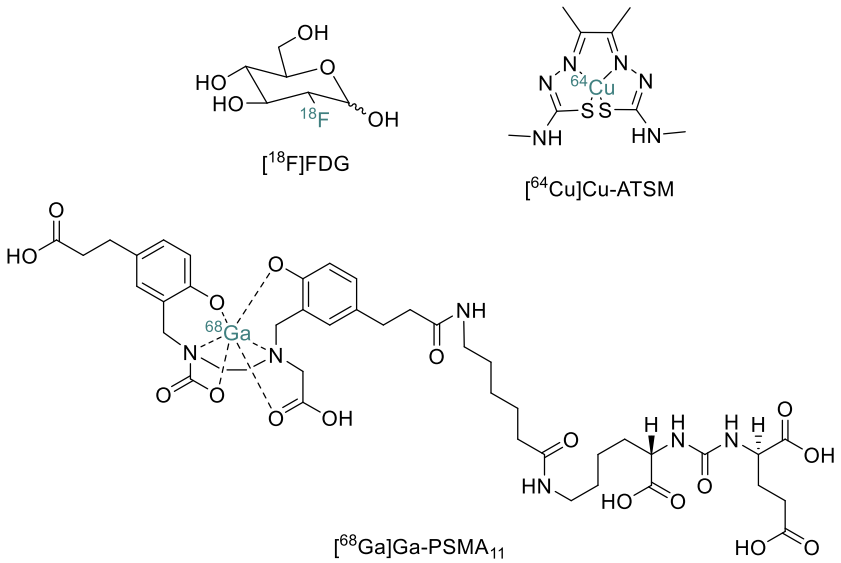

Figure 4: Radiotracers of PET imaging (emitting isotopes represented in blue colour).

Table 1: Common radionuclides used for PET and SPECT.[10, 15, 27, 32, 33]

Nuclide	*Decay mode*	*Maximum energy (MeV)*	*Half-life $t_{1/2}$*	*Method of production*	*Type of radionuclide*
^{11}C	99.8% β^+	0.96	20.38 min	Cyclotron	PET
^{13}N	99.8% β^+	1.19	9.96 min	Cyclotron	PET
^{15}O	99.9% β^+	1.72	122 sec	Cyclotron	PET
^{18}F	96.9% β^+	0.64	109.77 min	Cyclotron	PET
^{64}Cu	17.5% β^+	0.65	12.7 h	Cyclotron	PET
^{67}Ga	EC, γ	0.19	78.3 h	Cyclotron	SPECT
^{68}Ga	87.7% β^+	1.90	67.8 min	$^{68}Ge/^{68}Ga$ generator	PET
^{89}Zr	22.7% β^+	0.91	78.41 h	Cyclotron	PET
^{99m}Tc	EC,γ	0.14	6 h	$^{90}Mo/^{99m}Tc$ generator	SPECT
^{111}In	EC,γ	0.28	67.32 h	Cyclotron	SPECT
^{124}I	11.7% β^+	1.54	100.2 h	Cyclotron	PET

The use of radioactive elements results in higher safety requirements compared to other imaging modalities, and the use of emitting species is minimized. Therefore, a significant trait of each radiotracer is the specific activity or molar activity. The first one referred to the measured activity per total amount in gram of compound whilst the latter in mole of compound. Low specific or molar activity results in low signal-to-noise ratio and therefore saturation of the target by non-radioactive products.[5, 10, 26] Another major impact on exploitation ET radioisotopes is the amount of time required for the activity of the nuclide to be reduced by half (*half-life; $t_{1/2}$).* For example, most of the non-metallic isotopes such as oxygen-15 ($t_{1/2}$= 122 sec), carbon-11 ($t_{1/2}$= 20.4 min) and nitrogen-13 ($t_{1/2}$= 9.96 min) have significantly shorter half-lives than the inorganic ones (copper-64 ($t_{1/2}$= 12.7 h), zirconium-89 ($t_{1/2}$= 6.02 h) and gallium-68 ($t_{1/2}$= 67.8 min)). Table 1 presents some of the most commonly used radionuclides in both PET and SPECT imaging and their main

characteristics (half-life, maximum energy, production). Finally, a highly important characteristic is the purity of the radioisotope, as often the radionuclide is being produced along with an unwanted isotope which will be delivered through the patient's body without providing useful information. For that reason, the half-life of the contaminant isotope, if any, is crucial.[26]

1.1.3. Radiolabelling with gallium-68

Gallium-68 has been applied in clinical medicine since the 1960's.[34] It has a half-life of 67.8 minutes and one of its major advantages is that it can be prepared using a $^{68}Ge/^{68}Ga$ generator.[35] Generally, gallium is a non-physiological metal of group 13 of the Periodic Table and is frequently represented by a +III oxidation state as the Ga(III) cation. Due to its high charge density and small ionic radius (0.62 Å), it can be considered as a hard or intermediate Lewis acid. Subsequently, Ga(III) cation is usually chelated through strong, highly ionic bonds with nonpolarizable hard Lewis bases (eg. nitrogen, oxygen) or with softer donor atoms such as phenolate and thiol groups. The Ga(III) cation can form four-, five- and six-coordinated complexes but is usually chelated up to its maximum coordination number in a distorted octahedral geometry.[36, 37]

Due to the tendency of the unsaturated complexes towards metal hydrolysis or ligand exchange, the full engagement of the coordinate positions of Ga(III) complexes is favoured. Consequently, polydentate ligands with hard donor groups are more preferred for gallium labelled biomolecules. Two main ligand categories can be employed for $[^{68}Ga]Ga^{+3}$ coordination; linear chain and macrocyclic ligands, the most prominent ligands of which are shown in **Figure 5**. Nevertheless, it is important to note that four- and five-coordinate gallium complexes have also displayed an adequate stability *in vivo.*[35-38]

Gallium-68 has shown promising results for the radiolabelling of peptides and antibodies of relevance towards targeted imaging. The chelation systems used for gallium-68 coordination in water are the same as indium-111, so it could also potentially replace this SPECT radiotracer.[25, 35, 39, 40] There are several bifunctional chelators that have been developed for ^{68}Ga complexation but the most widely used is tetraxetan (1,4,7,10-

tetraazacyclododecane-1,4,7,10-tetraacetic acid, DOTA) with the analogues of [^{68}Ga]Ga-DOTA-TOC, [^{68}Ga]Ga-DOTA-TATE and [^{68}Ga]Ga-DOTA-NOC to be already available in ^{68}Ga-based clinical trials (**Figure 6**).[35, 41, 42]

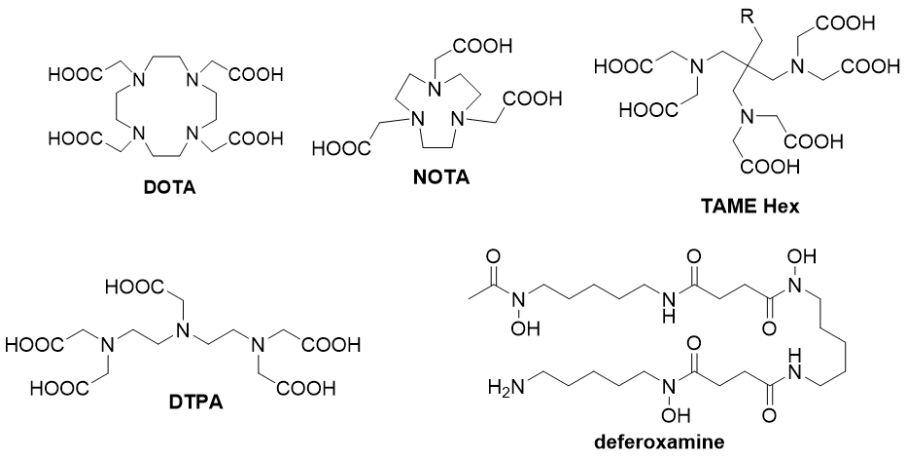

Figure 5: Schematic representations of the ligands DOTA (1,4,7,10-tetraazacyclododecane-1,4,7,10-tetraacetic acid), NOTA (1,4,7-triazacyclononane- 1,4,7-triacetic acid), DTPA (diethylenetriaminepentaacetic acid), TAME Hex (tris(aminomethyl) (ethane-N,N,N′,N′,N″,N″-hexaacetic acid), and deferoxamine.

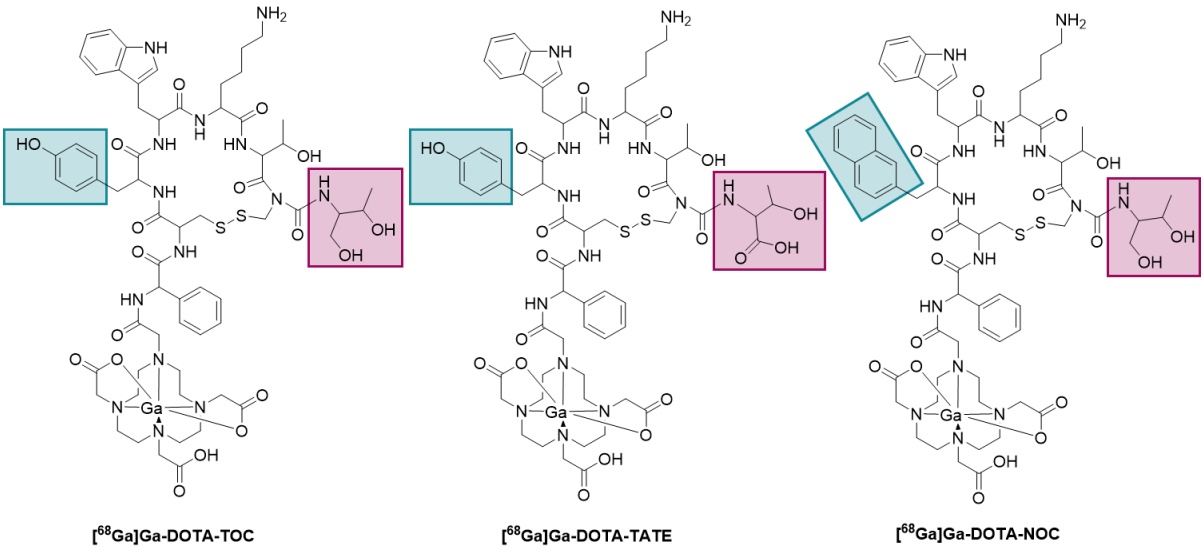

Figure 6: Schematic illustration of the structures of [^{68}Ga]Ga-DOTA-TOC, [^{68}Ga]Ga-DOTA-TATE and [^{68}Ga]Ga-DOTA-NOC.[41]

1.1.4. Radiolabelling with fluorine-18

As mentioned above fluorine-18 is the most popular amongst all available PET radionuclides. The combination of its relatively small half-life of 109.77 minutes (long enough to allow scans up to 12 hours), with its clean decay profile (97% positron emission) and its low positron energy resulting in better spatial resolution for imaging physical characteristics, make fluorine-18 the predominant radioisotope in PET.[43-48] Fluorine-18 can be produced through different nuclear reactions but most commonly it is produced through a cyclotron via proton irradiation of ^{18}O.[45-49] The main synthetic strategies for fluorine-18 labelling may be divided into two main distinct methods. The first one involves a late-stage radio-fluorination. Where fluorine-18 is introduced in the last step of PET tracer synthesis by direct labelling of the precursor with [^{18}F] fluoride. The second one includes a modular build-up approach. During this method, the fast and efficient introduction of fluorine-18 into the building block by radiolabelling with [^{18}F] fluoride occurs prior to the arrival of one or more additional reaction steps to arrive at the actual PET tracer.[45-48] [^{18}F]-Fluorodeoxyglucose ([^{18}F]FDG) constitutes as the most common PET tracer in clinical practice (**Figure 4)** and allows the profiling of the glucose metabolic activity both in tumours and neurodegenerative diseases.[50-54]

1.1.5. Fluorescence microscopy

Optical imaging has enabled the expansion of knowledge regarding cellular biology at a molecular level either *in vitro* or, more recently, *in vivo*. This allowed the real-time tracking of cellular movement, growth or functions. The optical imaging is based on the emission of photons from the excitation of a molecule (fluorophore) that has absorbed photons. This is a consequence of a three-stage procedure, in which the fluorophore undergoes: excitation, internal conversion, and emission processes.

Confocal fluorescence microscopy techniques

Confocal fluorescence microscopy is an optical imaging technique that uses the excitation point of fluorescent molecules to image specific biological systems. It was first

conceived in the mid-1950's by Minsky in an effort to image neural networks for his studies.[55] This achievement was followed by the production of microscopes for imaging unstained brain[56] and nerve cells.[56, 57] By the end of the 1980's, the confocal microscopy technology had already started growing and spreading. In the late 1990's, the incorporation of advances in optics consolidated the current design and improved the speed and the quality of the images acquired, leading to a fundamental extension in a number of applications of its technology.[58, 59]

The main principle of confocal fluorescence microscopy is still based on Minsky's pattern, however instead of using a zirconium arc lamp as a light source, a variety of lasers are used because of their high intensity and the range of wavelengths that could possibly be employed. Initially, the laser emits at a given wavelength which activates the target's fluorescence. Then, both laser-emitted and fluorescent light passes through mirrors, redirecting them to face a pinhole which will only allow the fluorescent light to pass from the focused plane (thus excluding the laser-emitted one). Finally, the fluorescent light is measured by a detector to be analysed by an associated computer (**Figure 7**). This technique yields in an improved image with less haze of the laser-emitted light.[59, 60]

Two-photon fluorescence microscopy techniques

Since the 1990's, two-photon absorption has been employed for the development of fluorescence imaging allowing for the selection of individual cells for imaging. Recent advances have resulted in the design of two-photon fluorescence lifetime imaging microscopy (FLIM), which has been used for better understanding of cellular processes. More specifically, FLIM can measure the duration of the excited state (decay time) of a fluorophore within the living cell.[61] Different fluorophores will not have the same lifetime, but also the same fluorophore might have different lifetimes depending on the microenvironment. In addition, the decay time does not depend on the concentration or the photobleaching of the probe which makes it advantageous compared to other techniques such as confocal or epifluorescence.[61] This sensitivity of the fluorescence lifetime to the environment surrounding the probe has found different applications, such as the measurement of the pH[61-63] or the concentration[61-63] and the monitoring of the presence of

cations (e.g. Ca^{2+}, Mg^{2+}, K^{+}) or oxygen.[61-63] Lastly, when combined with other techniques, it can even provide evidence for the interaction of the fluorophore with proteins.[64]

The main principle of a two-photon excitation fluorescence microscopy involves the excitation of a fluorophore from its ground state by two combined low energy photons which arrived almost simultaneously to the molecule. The one-photon excites the fluorophore to an intermediate state limited by an objective, whilst the second photon further excites the fluorophore to the excited state (**Figure 7**).[65-67] The main advantage of this technique is that the laser light does not produce any excitation along its path through the specimen and the excitation takes place only in the focal spot of the microscope resulting in generating all of the photons in-focus.[67, 68]

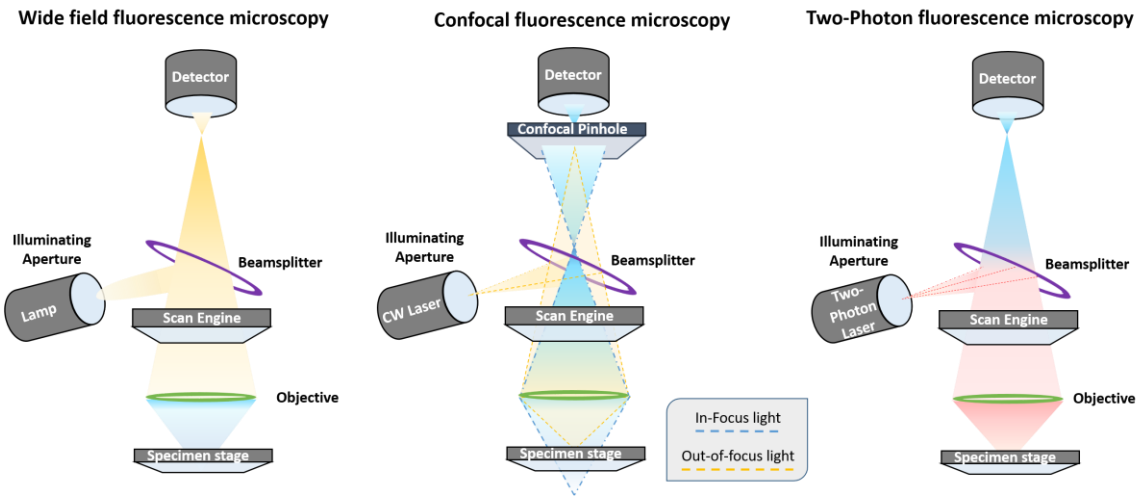

Figure 7: Schematic illustration of different techniques of fluorescence microscopy.[60]

1.2. Considerations in cancer diagnosis with medicinal imaging

Cancer (med: malignand neoplasm) is the second leading cause of deaths worldwide accounting for 8.8 million deaths in 2015 (13% of total deaths). [69, 70] Despite the fact that the word cancer was first reported by Hippocrates (460-370 BC), a Greek physician, who used the term 'karkinos' to describe both non-nuclear forming and unclear forming tumours, some of the earliest evidence of cancer is dated centuries earlier in Egypt. Since Hippocrates, a plethora of theories were developed regarding the causes of cancer but it was not until the

middle of the 20th Century that the current theories became shaped. Cancer is a heterogeneous disease involving the accumulation of multiple mutations in a multi-step process. Tumours are not just a group of cells that are unregulated and are growing uncontrollably, but a complex tissue with different cell types all of which function together. To date, researchers have distinguished at least 200 different cancer types that can affect humans with lung cancer being the most predominant (1.69 million deaths in 2015). Liver, colorectal, stomach and breast cancer follow in prevalence.[23, 71-73]

Through the last decades, the research community has shown a particular interest in the chemical and the biological aspects of cancer metabolism, focusing on its onset and prevention. As a result, highly distinctive functional capabilities were suggested as hallmarks of cancer.[71, 73-75] Those hallmarks are the result of the numerous different cancer cell types (**Figure 8**). More specifically: [71, 74, 75]

a. *Sustaining proliferative signalling*: where the abnormal function of growth signalling results in the false activation of the proliferative signals.
b. *Evading growth suppressors*: where cell proliferation is not an entirely cell-autonomous process resulting in the moderated growth of normal cells.
c. *Resisting cell death:* when instinct mechanisms induce programmed cell death by altering normal autophagy, apoptosis and necrosis.
d. *Enabling replicative immortality:* cancer cells overcome the replicative ability by overexpressing telomerase.
e. *Induction of angiogenesis:* caused by the ability of cancer cells to develop new blood vessels.
f. *Enabling replicative immortality:* concerns the triggering of invasiveness either in the surrounding tissue or vessels and the formation and growth of metastatic foci.
g. *Deregulating cellular energetics and metabolism*: unlike normal cells, cancer cells favour glycolysis and the increased application of this process results in the activation of oncogenes.
h. *Avoiding immune destruction*: cancer cells have also the ability to evade the control mechanisms of the immune system which would eliminate the proliferating pre-malignant cells.

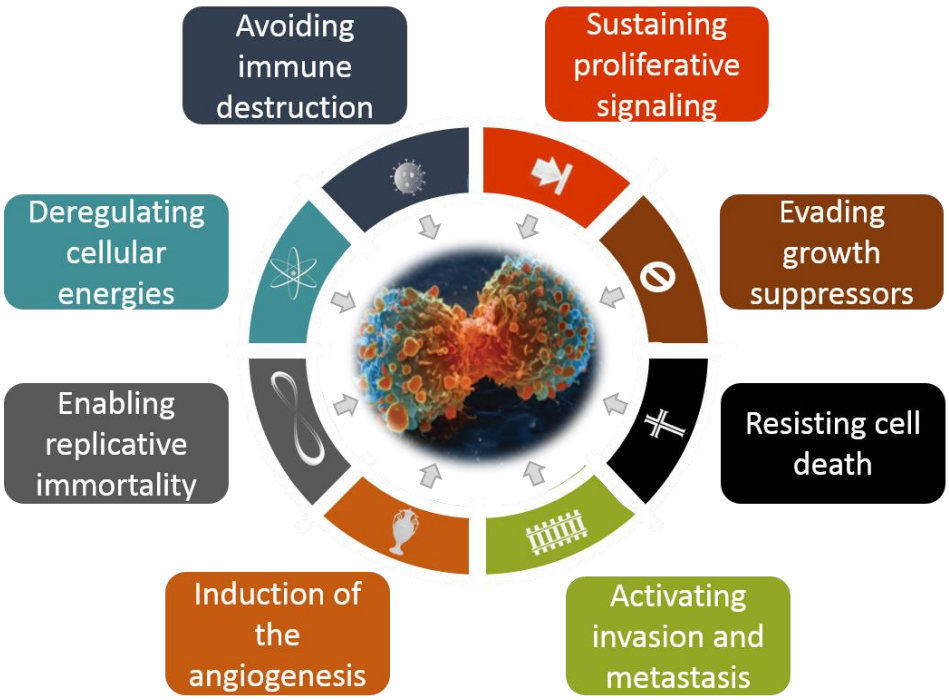

Figure 8: The eight commonly accepted hallmarks of cancer.[74, 75]

1.3. Hypoxia and Cancer

1.3.1. An introduction to hypoxia

Adequate oxygen supply constitutes the key element of the normal life cycle of aerobic organisms. In case of absence of oxygen, an active defence mechanism is adopted to address any potentially damaging situation. An imbalance between oxygen supply and oxygen consumption can cause a variety of conditions, such as pulmonary diseases, cardiovascular diseases and cancer. The condition that is characterised by low oxygen supply in blood is called *hypoxemia* whilst a reduction in oxygen supplies is termed *hypoxia* [Anc Greek υπό/hypo (=under, sub-) + oxygen [Anc Greek οξύς/oxys(=sharp)]. This two terms should be distinguished even though most of the time hypoxemia frequently induces hypoxia in humans. From the other side, the condition where the oxygen supply is normal (complete absence of hypoxia) is named normoxia [Latin normal + oxygen [Anc Greek οξύς/oxys(=sharp)]. In tissue, lack of oxygen can occur due to numerous reasons, but the

terms of hypoxia and hypoxemia shouldn't be confused. Extreme conditions, such as high altitude or diving, can cause generalised hypoxia in healthy humans, but the oxygen levels usually normalise after a period of time, without permanent damage to healthy tissues. Hypoxia can result in a failure of tissue oxygenation at any stage of its delivery to the cells. This often lead to a decrease in the partial pressure of oxygen, failure of the lungs to diffuse oxygen, insufficient levels of available haemoglobin and alterations of blood circulation to the tissue or of breathing rhythm. There are five different types of hypoxia:

1. *Affinity hypoxia*, resulting from impairment of oxygen release in tissues by haemoglobin, producing a left-shifted oxyhaemoglobin dissociation curve;
2. *Anemic hypoxia*, is caused when there is a reduction of the oxygen-carrying capacity of the blood. This can be the result of a decrease in the total haemoglobin or a factor alteration in the haemoglobin itself;
3. *Circulatory hypoxia* or *histotoxic hypoxia*. In this case even though the affinity of the haemoglobin is not disturbed, not the carrying capacity of blood oxygen, the tissues do not receive sufficient oxygen e.g. in cyanide poisoning);
4. *Hypoxemic hypoxia* (or hypoxic hypoxia), which is due to insufficient levels/quantity of oxygen reaching the blood, as in lung diseases or decreased barometric pressures at high altitudes.
5. *Stagnant hypoxia*, a condition resulting in failure in the circulatory system which leads to insufficient transport of oxygen to tissues. This is usually caused due to inadequate blood flow due to tissue blocking from a variety of reason such as heart failure.

Concomitantly, physiological compensation of hypoxia is divided into *acute* and *chronic hypoxia*. In the first case, a sudden or rapid depletion of available oxygen takes place at the tissue level; whereas the latter is attributed to a usually slow, unregulated reduction of oxygen delivery in tissue which gradually results in heart disorders, lung diseases such as chronic obstructive pulmonary disease, or chronic blood loss.[11, 76]

1.3.2. How hypoxia is related to cancer

In the 1950s, Gray *et al.* identified for the first time the presence of low oxygen tensions in human tumours[77] and their possible influence on radiation results.[77, 78] Consequently, the cancer research community focused their research towards studying hypoxic cells and their sensitivity. This was achieved by using either hyperbaric oxygen chambers[79] (before the early 1970s) or small molecules which could mimic the effect of oxygen[80, 81] (after the1980s). By the 1990s, the heterogeneity of oxygen supplies in human tumours had been identified.[82, 83] Nowadays, the importance of tumour hypoxia has been confirmed by a plethora of studies which further underlined its detrimental role in tumour progression and therapy resistance. Therefore, the pathology of hypoxic conditions is an open research field in the literature and there are a wide range of studies that attempt to identify and comprehend hypoxia and finally lead to the development of next generation therapeutics.

Hypoxia in a tissue is characterised by the lack of oxygen supply. In tumours, the oxygen supplied to neoplastic cells is often less than the oxygen they consume, resulting in tissue areas with reduced oxygen level. Hypoxia in cancer can be caused by:

- Limitations in perfusion of oxygen delivery due to structural and functional abnormalities of tumour microvessels (*acute hypoxia*)
- Limitation in the diffusion of oxygen delivery generated by the increased distance between the cell and the blood vessel (*chronic hypoxia*) or,
- Reduction of the oxygen capacity in the blood caused by therapy-induced and/or tumour-associated anaemia (*anemic hypoxia*).[84-86]

The prolonged exposure to hypoxic conditions often results in diversification of cell cycle distribution. On the contrary, the reduction of protein synthesis that occurs in hypoxic cells results in restrained proliferation and cell death. As a result, tumour cells often establish mechanisms to evade this hostile environment and generate tumour progression (**Figure 9**). It is very important to highlight that hypoxia is not selective against inducing apoptosis of neoplastic cells or normal cells.[86-88]

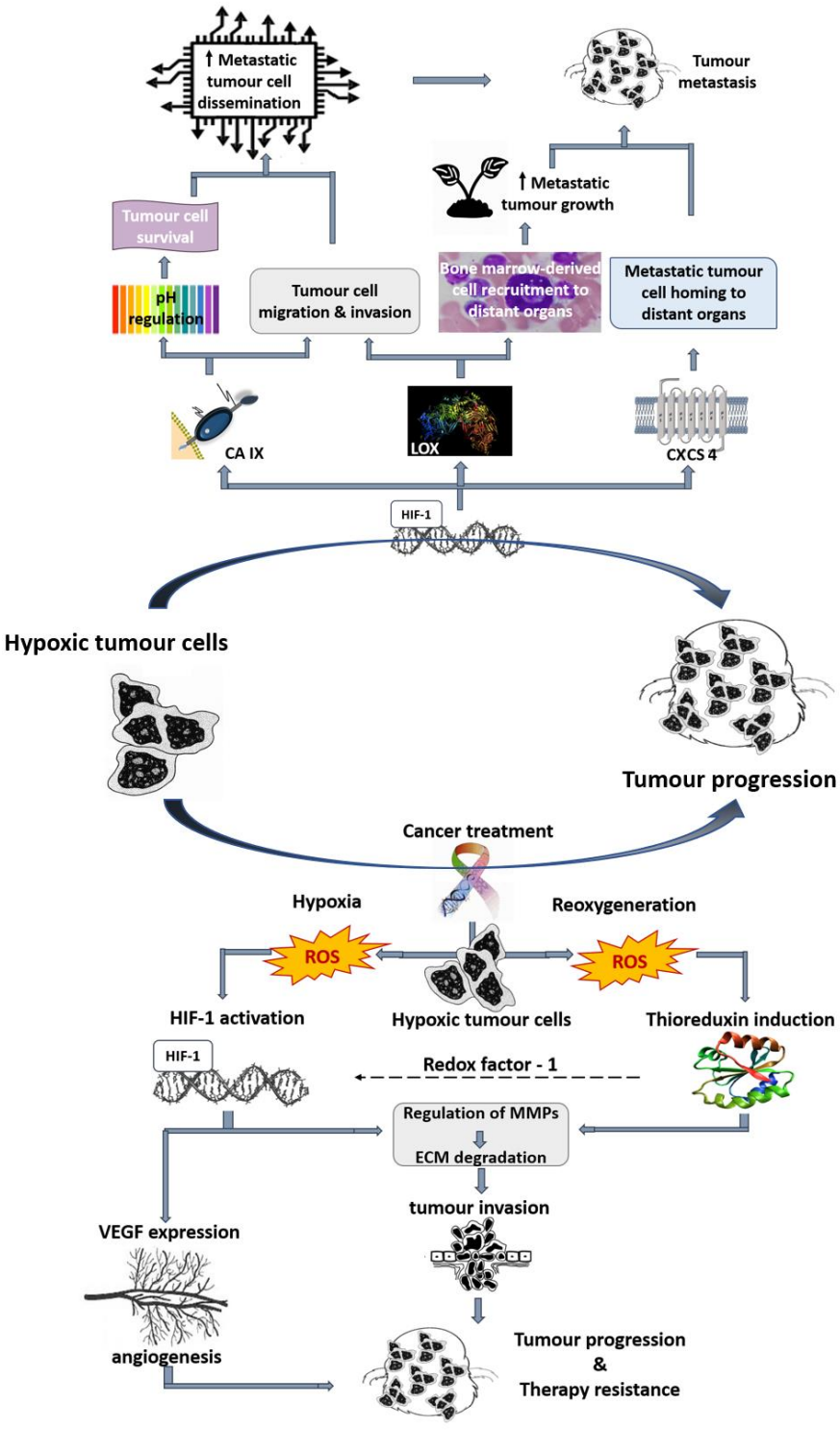

Figure 9: Schematic diagram explaining some of the features of hypoxia to tumour metastasis (top) and to therapy resistance (bottom). CA: carbonic anhydrate; LOX: lysyl oxidase; CXCS4: chemokine receptor type 4; ROS: reactive oxygen species; MMP: matrix metalloproteinase; ECM: extracellular matrix; VEGF: vascular endothelial growth factor.[89,90]

Additionally, hypoxia conditions intercept cancer therapy through various mechanisms, such as:

(i) potential p53 mediated senseless cell selection[87, 88]

(ii) progression of chronic hypoxia which results in an inadequate exposure to chemotherapy and radiation therapy[91]

(iii) via the upregulation of drug-resistant genes and "encoding genes" (such as p-glycoprotein and ADAM metallopeptidase domain 17).[92-95]

The alterations in gene expression with subsequent changes in the proteome and/or the genome[87] and cell selection[87, 88, 95-97] are some of the underlying mechanism by which hypoxia prevent tumour malignancy. Considering tumour hypoxia's role in determining progression to malignancy, linked with its relationship to resistance development to cancer therapies, it has been noted as a valuable indicator in tumour prognosis. As a result, a variety of detection techniques have been advanced to distinguish hypoxia in tumours. Detection of low oxygen areas,[98-102] targeting of endogenous markers such as hypoxia-inducible factor 1 (HIF-1) and carbonic anhydrase IX (CAIX) ,[102-106] use of exogenous hypoxia markers, such as 2-nitroimidazoles,[107] and imaging of hypoxia environment through non-invasive techniques such as PET/SPECT imaging and MRI[108-111] are among them.

1.3.3. Hypoxia-inducible factors (HIF)

Hypoxia-inducible factors (HIFs) are a family of transcription factors that are particularly sensitive to oxygen adequacy as they are capable of activating the expression of complex gene models which can adapt the low oxygen conditions. All the 3 different members of the HIF family (HIF-1, HIF-2 and HIF-3, **Figure 10**) are composed of two subunits (α and β). The alpha (α) subunit which contains an oxygen-dependent degradation domain (ODD) and results from the uniqueness of each gene. On the other hand, the beta (β) subunit is a hydrocarbon nuclear translocator domain (ARNT) which is expressed ubiquitously.[112, 113] Thus, the α-subunit leads the regulation of the hypoxia-inducible behaviour. HIFs are considered as crucial mediators of the cellular adaption to hypoxia since they have been detected in a variety of both hypoxic or hypoxemia pathogenic conditions such as pulmonary diseases, cardiovascular diseases and cancer.[105, 114-118]

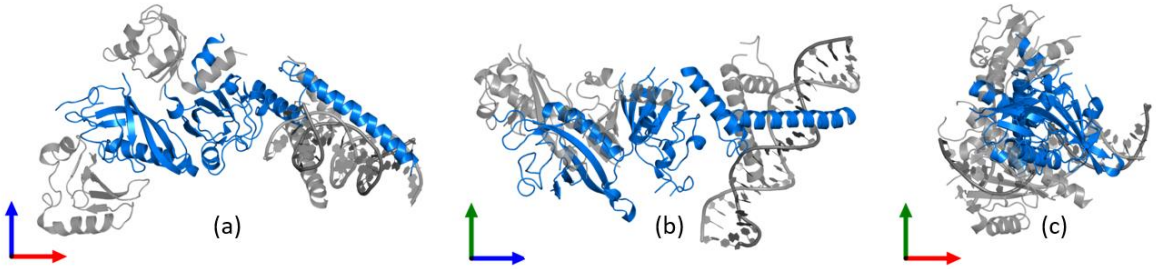

Figure 10: Hypoxia-inducible factor in 1-alpha (1α) in assembly. This protein is highlighted and viewed from (a) front (b) side (c) top. (PDB 4ZPR).[119]

Tumour hypoxia is mainly related to HIF-1α and HIF-2α factors that are the most studied genes as opposed to HIF-3α, a negative regulator of hypoxia-inducible gene expression.[112] Alterations in gene regulations have been suggested with regards to HIF-1α and HIF-2α, , although they activate the gene transcription triggered by hypoxia in a similar fashion. In prolonged hypoxic conditions the HIF-2α is the one which is mainly active, whereas in acute hypoxic conditions the HIF-1α is activated (**Figure 11**).[113, 120]

Under normoxia, HIF-α usually remains unnoticeable, but in hypoxic conditions, prolyl and asparaginyl hydroxylation reactions are catalysed by Fe(II) and 2-oxoglutarate dependent dioxygenases superfamily.[121, 122] These reactions regulate both transcriptional activity and protein abundance of cancer cells[123]. However, since 1993, it has been shown that iron chelators induce HIF-1α.[124] Later evidence have demonstrated that a plethora of metal ions (Cu(II), Co(II), Ni(II),Zn(II)) may be able to mimic iron's ability to stabilise HIF-1α.[125-128] Subsequently, development of appropriate metal chelators could potentially allow the reduction of HIF's expression.

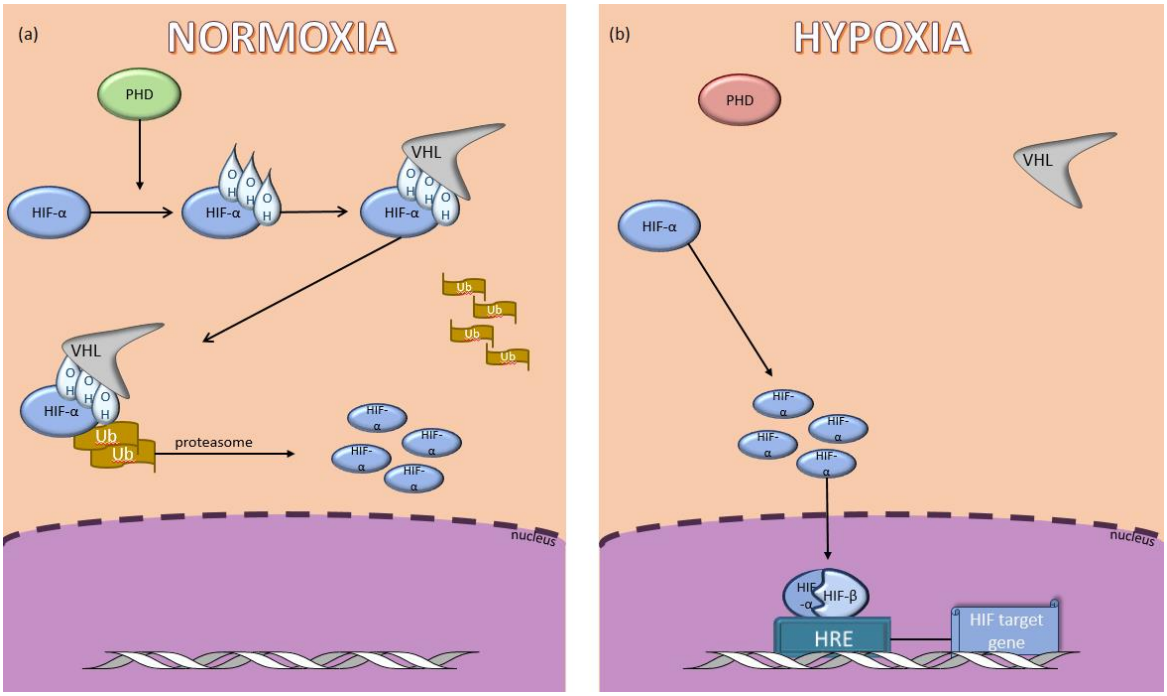

Figure 11: Mechanism of targeted genes activation by HIF. (a) HIF-α pathway in normoxia: in the presence of oxygen, propyl hydroxylases (PHD) hydroxylates HIF-α at the conserved proline-residues, leading to binding of the gene by the Von Hippel Lindau (VHL) tumour suppressor protein and consequent ubiquitylation of HIF-α followed by its degradation in the proteasome. (b) HIF-α pathway in hypoxia: the lack of oxygen prevents HIF-a hydroxylation by PHD giving rise to the stabilization of HIF-α which allows its escape from the VHL and further drift to the nucleus where it dimerizes with the HIF-β to form an active transcription complex. The HIF complex then induces the transcription of genes containing a hypoxia-responsive element (HRE) which then leads to activation of HIF target gene.[11, 129]

1.3.4. Carbonic anhydrase

Carbonic anhydrase was isolated from haemoglobin in 1933 and fully characterised biologically to show that is a Zn(II)-centered metalloenzyme.[130] Prior to 1944, the importance of this enzyme in plants was well established, as it seemed to be present in most key cellular processes, resulting in the purification of five different types of carbonic anhydrases (CA).[131, 132] Their greater role in pathological processes in prokaryotic species was only highlighted towards the middle 1990's.[133-136] Soon after confirming the existence of CA in mammals, the study of the catalytic mechanism begun.[137, 138]

To date, it has been fully established that CAs are zinc metalloenzymes that catalyse the reversible hydration reaction of cell-generated CO_2

$$(CO_2 + H_2O \rightleftarrows HCO_3^- + H^+),$$

an essential and ubiquitous reaction in nature, as various, both cellular and physiological processes depend on it.[130, 133, 134, 136, 139] As mentioned above, CA is present in all plants, prokaryotic and eukaryotic species. Each of them is related to a different family of CA enzymes, arising from diverse pathways and classified as α-CA, β-CA and γ-CA respectively.[130, 133, 134, 136, 139] After years of kinetic studies, it has been specified that all three species share the same mechanism of action, which consists of two steps: initially a nucleophilic attack of a hydroxide ion on the zinc-bounded CO_2, followed by the ionisation of the zinc-bounded water molecule and a proton removal from its active site.[137, 140]

Through the years, 16 different α-CA isoenzymes have been described and characterised in mammals. The catalytic activity, the cellular localisation (cytosolic, membrane-bound or mitochondrial) and the distribution within the tissues are not the same for all of them.[141-149] Because of their specific character, the CA isoenzymes participate in different biological processes leading to different applications in clinical research.[150-156] Only two of them are associated with hypoxia *via* the HIF1α and HIF2α pathways, the CAIX and the CAXII. Notably, CAIX is the only one expressed mainly in tumour tissues but not in the majority of the corresponding normal tissues.[157-161]

Carbonic anhydrase IX

Membrane antigen (MN) protein, as CAIX was originally named, was first detected in the human cervix carcinoma epithelioid cell line (HeLa) in 1993[162] and was further characterised as a plasma membrane antigen regulated by cell density and correlated with an oncogenesis phenotype.[163] Furthermore, it has been revealed that the human genome contains only a single copy of MN, coding for a 466 amino acid transcript crossing the plasma membrane. This protein contains four distinct regions: a large extracellular part with an N-terminal domain proteoglycan-related (PG); a central carbonic anhydrase domain (CA); a hydrophobic signal peptide with a hydrophobic transmembrane section (TM); and a C-terminal region with a short intracellular tail (IC) *(***Figure 12**).[129, 164]

The active site of the CAIX enzyme is enclosed in the *CA* region which is found on the exterior side of the plasma membrane facing the extracellular environment. This implies that the reversible hydration reaction is carried out extracellularly but through a specific cooperation of the CAIX with bicarbonate transporters, acquiring the ability to control the pH both intracellularly and extracellularly.[165-167] This ability links CAIX with numerous functional aspects of tumour growth under hypoxic conditions and with drug resistance.[167-169] Thus, CAIX is considered as a viable prognostic hypoxia marker in cancer research.

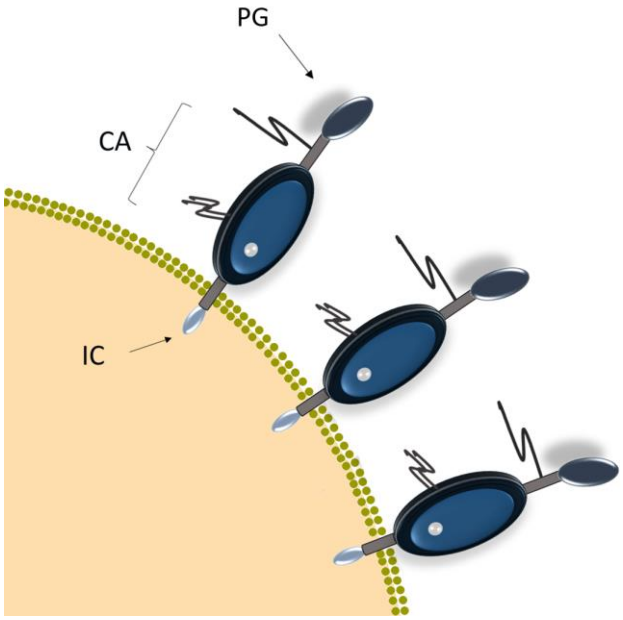

Figure 12: Schematic representation of the CAIX protein composition (IC: C-terminal region, CA: central carbonic anhydrase domain, PG: N-terminal domain).

CAIX as a therapeutic target

There are two main approaches to target CAIX for hypoxia prognosis and tumour therapy. The first involves the use of monoclonal antibodies (immunotherapy) and the second, the inhibition of CAIX by small molecules, blocking its activity and catalytic role. The first strategy represents an extensively studied therapeutic intervention and encouraging outcomes resulting from ongoing third phase clinical trials have been published.[170] Meanwhile, the second way refers to an expanding class which can be exploited not only for tumour prognosis but also for the production of molecularly targeted antineoplastic drugs.[158]

Both sulphonamides and sulphur-related compound (sultiame[171], sulfatase steroids[172]) have already illustrated an efficient inhibition against CAIX *in vitro* already, as well as an anti-metastatic activity in animal models *in vivo.* [171, 173, 174] In addition, fluorescent sulphonamide compounds have yielded promising results in the selective inhibition of CAIX, enabling hypoxia imaging to be conducted.[165, 175, 176] Furthermore, some coumarin derivatives have demonstrated a significant inhibition of CAIX and CAXII isoenzymes upon their incorporation with hydroxyl-, chloro-, chloromethyl- thioxy- or sugar moieties.[177-181] Lastly, an interesting inhibitor was recently developed by Dubois and his group:[182] a nitroimidazole-based sulphonamide molecule acting through reduction of tumour growth and increasing tumour sensitivity to irradiation.

1.4. Thiosemicarbazonato complexes as molecular probes and imaging agents

The broad pharmacological utilities of the thiosemicarbazone (TSC) scaffold has been well established by medicinal chemists. Through the years, thiosemicarbazones have been proposed as antibacterial[183, 184], antifugal[185, 186] and antiviral[187, 188] probes. The first clinically approved drug of this family, which is actually still in use for the treatment of multidrug-resistant tuberculosis is commercially called thioacetazone, (**Figure 13**).[189] Also, a plethora of other drugs have been developed and clinically tested against various infections (smallpox) or malaria.[190, 191]

Even though the motif of the thiosemicarbazone family as potential derivatisation agents for ketones and aldehydes has been known since the 1900's, their antineoplastic activity was not recognised until the mid-1950's when E.Skipper and his group observed the antileukemic activity of different compounds from this family.[192-195] Later on, the ability of thiosemicarbazone compounds to inhibit ribonucleotide reductase, a mammalian enzyme involved in the DNA synthesis, was highlighted[196-198] alongside with their ability to chelate a variety of metal ions (Cu(II), Fe(II/III), Zn(II), Ga(III)) through different coordination modes.[199] A great interest has developed from different research groups in the last decades in thiosemicarbazone derivatives due to their ability to form reactive oxygen species (*ROS*)

[194, 200-203] and to block hypoxia by the stabilization of HIF-1α.[125-128] Even though through the years it was suggested that their plasma half-life is very short for drug delivery and resistance to these drugs is often developed, they still are the focus of interest and currently two new α-N-heterocyclic thiosemicarbazones (COTI-2 and DpC, **Figure 13**) are under clinical evaluation. [204-206]

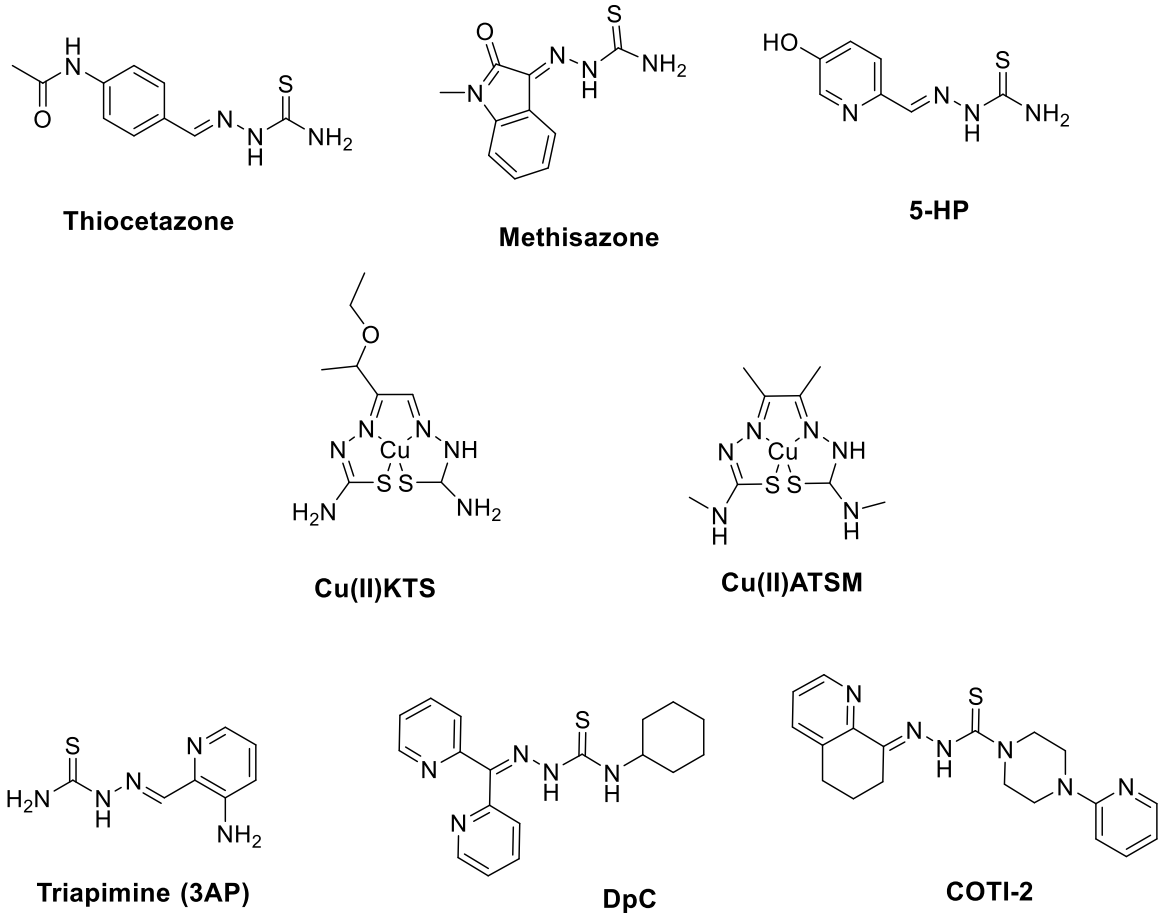

Figure 13: Schematic illustration of different TSC compounds which have been used in clinical trials or have been proposed as important anti-tumour agents[189-192, 204, 207-211]

The synthesis of bis(thiosemicarbazone) ligands was first reported in 1902[212] and although a variety of different procedures have been proposed since then,[213-215] the majority of the reported ligands derive from 1,2-diketones.[11, 216] Specifically, a 1,2-diketone is functionalised with a thiosemicarbazide (**Scheme 1**). This results in the formation of an iminic bond when both components are heated in a slightly acidic alcoholic solution.[11, 188] The syntheses are usually successful resulting in good yields although slight modifications

on the scaffold could lead to significant changes in molecules' activity and often lead to cyclisation products or dimers.[216-219] The synthesis of symmetrical variants has been cited more often, but also the synthesis of unsymmetrical derivatives has been reported, although it is considered to be a more challenging procedure.[11]

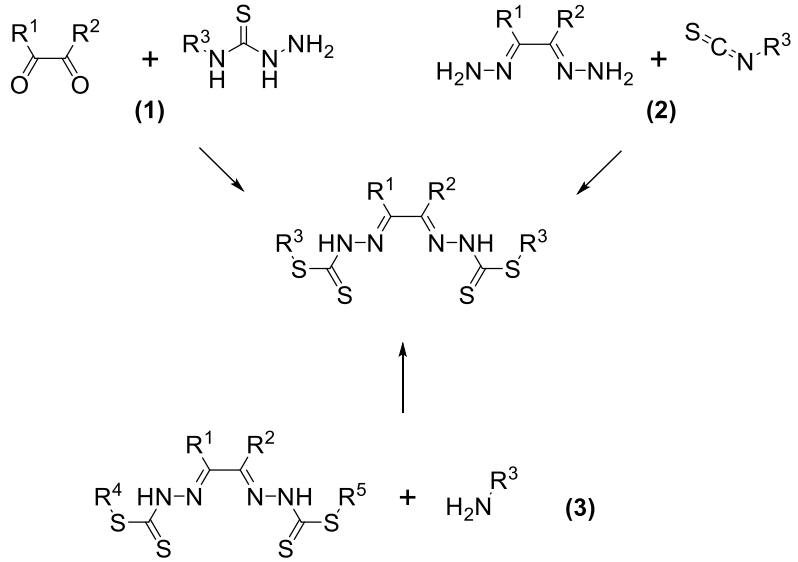

Scheme 1: Different synthetic routes to aliphatic bis(thiosemicarbazones)

The coordination of thiosemicarbazone compounds was first reported in the 1930's by Jensen *et al* [216] who suggested that a five-member ring may be formed via the sulphur and the azomethine nitrogen, yet a tetrahedral coordination was established later by Baehr *et al*.[216] Thiosemicarbazones are multifunctional ligands and they can coordinate to metal ions by a bidentate binding; mono(thiosemicarbazones), by tridentate binding; mono(thiosemicarbazones) if there is a donor atom at the substituent involved in the metal coordination, or by a tetradentate binding; bis(thiosemicarbazones). In general, thione and thiol form of TSCs are in a tautomeric equilibrium in solution, so their complexation with the metal can be either via a neutral nitrogen/sulphur (N, S) or anionic (N,S^-) donor set when the thiol proton is lost.[11, 220] The stability of the complexes can be increased in the presence of an additional coordinating component resulting in a (N, N, S) donor set.[11, 220] A wide variety of metals have been reported that thiosemicarbazones can chelate, including transition metals, main group metals or semi-metals.[184, 199, 207, 216, 221] Furthermore, unlike the

simple metals, radioactive metallic isotopes may be used allowing the use of PET and SPECT imaging for tumour detection.

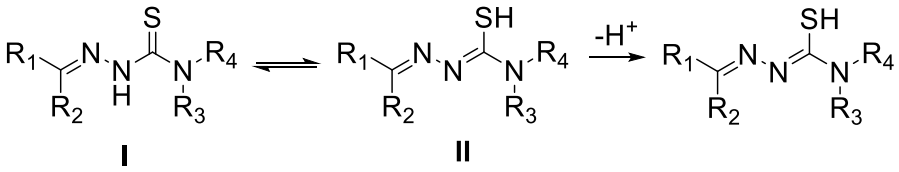

Scheme 2: Tautomeric equilibrium of thiosemicarbazone compounds in solution phase.[23]

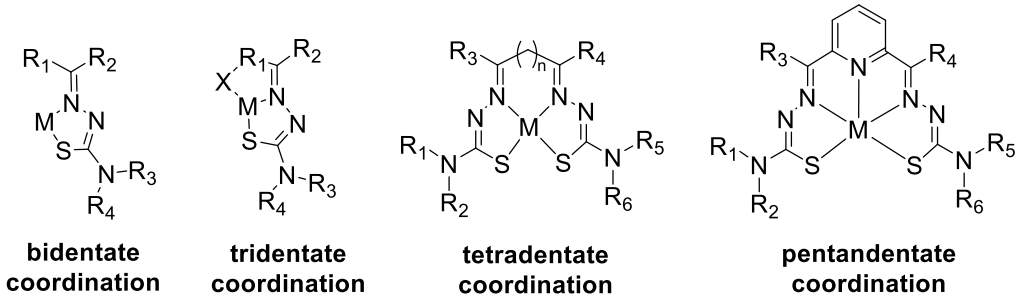

Scheme 3: Common mono and bis(thiosemicarbazone) ligands coordination arrangements to metals.[23] M = Ga(III), Cu(II), In(III)

The use of bis(thiosemicarbazonato) metal complexes in imaging has been limited to PET radionuclides. Unquestionably, one of the most well-known and most studied molecules of the subfamily of bis(thiosemicarbazonato) metal complexes is Cu-ATSM (**Figure 4**). Its efficacy as an imaging probe to delineate hypoxia in tumours and cardiac ischemia[11, 222-224] are established alongside its potential for Alzheimer's treatment.[225-227] Cu-ATSM has been exploited as a radiotracer by use of copper-64, although other radioisotopes of Cu have been used likewise.[216, 228-232] The exact mechanicm of action in hypoxia of the Cu-ATSM's is not yet fully understood, and it was suggested by Hueting et al that copper metabolism could be essential for the selectivity of Cu-ATSM complexes.[233] In addition, Cu-ATSM's potential in dual labelling with other radionuclides has been explored aiming to reveal the *in vivo* biological effects of these compounds.[234, 235]

Lack of a fluorescent moiety at the thiosemicarbazone substituents of aliphatic bis(thiosemicarbazonato) metal complexes render their use in optical imaging techniques

challenging. In 2005 Dilworth and his group introduced a new Zinc(II) diacetyl-bis(4-methylthiosemicarbazonato) (Zn-ATSM) derivative with modified side chains showing fluorescence emission in cells. Uptake studies performed in several cell lines by fluorescence microscopy suggested a strong cell-line dependence.[236] Since then, the addition of a fluorophore to the ATSM precursor has been explored by various groups in an attempt to study the *in vitro* properties of the complexes in different cell lines. [237-239] Use of aromatic and fluorescent groups in the bis(thiosemicarbazone) scaffold would increase the fluorescent character of the molecule, allowing visualisation through the incorporation of a luminescent sensor. Many examples have been found in literature since the very early discovery of the potential of thiosemicarbazones in pharmaceutical research. The first Zn(II) and Cu(II) complexes, based on acenaphthenequinone bis(thiosemicarbazone) ligands, were reported by Pascu *et al.* 2007.[240] Therefore, acenaphthenequinone bis(thiosemicarbazonato) metal complexes have been intensively studied under different optical techniques[11] and it was suggested that Zn(II) enables the transmetalation reaction in order for TSC compounds to chelate different metals of relevance to SPECT and PET.[241]

Moreover, Ga(III)-TSC complexes have been investigated as both anti-neoplastic drugs and imaging agents ([^{68}Ga]Ga(III))[216, 242-245] through the years and recently Pascu and co-workers reported the *in vitro* hypoxia selectivity of [^{68}Ga]Ga(III) bis(thiosemicarbazonato) complexes. *In vivo* tests by microPET in nude (athymic) mice was also reported in this study suggesting that [^{68}Ga]Ga(III) bis(thiosemicarbazonato) complexes can be excreted within 1 hour post-administration *in vivo*.[246]

1.5. Glycosyl coumarins as targeting molecules

1.5.1. Coumarins

Coumarins were used extensively in pharmaceutical research soon after their initial synthesis in 1868 by W.H. Perkin.[247] However, it was not until 2009 when A. Maresca *et al.*[181] pointed out for the first time their relation with hypoxia. In this publication, the authors reported X-ray crystallography along with mass spectrometry data and introduced coumarins as carbonic anhydrase suicide inhibitors suggesting a possible mechanism of action. Claudio

T. Supuran and his research group have carried out extensive research in the field of the inhibition of CA IX as a target for the design of anti-tumour agents.[248] Since 2009, they have reported the synthesis of coumarin-derivative compounds besides their X-ray crystallography data, and characterisation of coumarin binding sides in CA II inhibition.[181, 249] In addition, in 2010, they reported the potential of a group of coumarin-derivative compounds as CA inhibitors, revealing their greater efficiency against CA IX and CA XII in comparison with their efficacy against CA I and CA II. Accordingly, they suggested that the potential of those compounds to act as designed isoform-enzyme selective inhibitors.[180] In 2011 Dubois and colleagues published the results of *in vivo* experiments of coumarin compounds along with other promising inhibitors such as acetazolamide, confirming the Supuran group's suggestion.[250]

To date, a variety of laboratories have studied the labelling of coumarin compounds with different PET radioisotopes and in 2012 Wang and colleagues[251] reported the synthesis and the results of a fluoro-coumarin compound (3-(4-(dimethylamino)phenyl)-7-(3-fluoropropoxy)-2H-chromen-2-one, **Figure 14**) as a promising PET imaging probe.

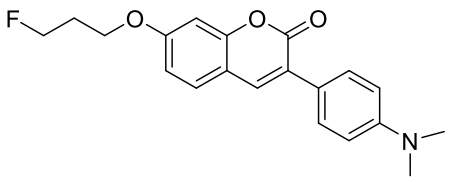

Figure 14: Schematic illustration of 3-(4-(dimethylamino)phenyl)-7-(3-fluoropropoxy)-2H-chromen-2-one.

1.5.2. Glycosyl coumarins

In early 2011, Y.Lou and colleagues reported for the first time hypoxia uptake results of two glycosyl coumarin (GC-204 and GC-205, **Figure 15**) indicating their potential as small molecule inhibitors against CA IX.[155] No further information was published regarding these compounds but in late 2011, Touisni and colleagues confirmed the efficiency of substituted coumarins incorporating glycosyl moieties against both CA IX and CA XII.[252] They state the significant inhibition of tumour growth by GC-204 in mice compared to vehicle controls which have arisen from flow experiments in 4T1 murine mammary adenocarcinoma cancer

cells. Later Lock and colleagues[158] reported that treatment of mice with GC-205 led to a reduction of cancer stem cell (CSC) population. In addition, numerous scientific publications, review papers and books have been published referring to this work without any further investigation on this kind of compounds.[253, 254]

Regardless of their clear effect on CA inhibition, there has been no reported attempt to label glycosyl coumarins with either PET or SPECT radioisotopes towards a combination of imaging with chemotherapy or radiation, to target hypoxic cells that typically demonstrate resistance to those therapies.[252, 253]

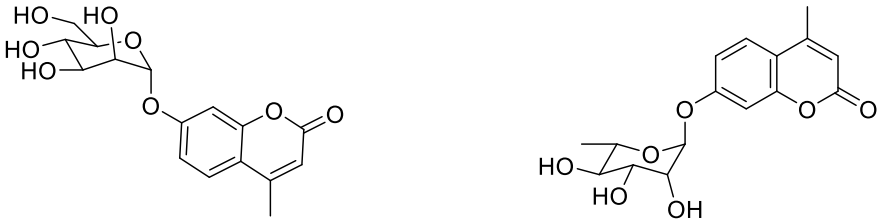

GC-204 GC-205

Figure 15: Schematic illustration of the two most promising compounds as small molecule inhibitors against CAIX.[255]

1.6. Introduction to nanomedicine and radiolabelling approaches

In 1959, the Nobel Laureate physicist, Richard Feynman first envisioned nanotechnology[256] and just decades later this was defined as the science which involves the technological engineering and applications of materials and assemblies in the nano-scale.[257] More specifically, synthetic nanomaterials have at least one dimension in the range of 1 to 100 nm,[257, 258] which is typically the size of biologically relevant molecules, and their shape differs according to their applications. Today, nanotechnology advances rapidly due to the unique physiochemical properties of nanostructures (increased surface and quantum effects) which could find applications in different scientific areas.[258, 259] An interest in the applications of nanotechnology in medicine has gradually grown in the last decades, resulting in the interdisciplinary field of nanomedicine. Furthermore, cancer research has adapted nanotechnology approaches and potential applications of nanomaterials aiming towards

cancer treatment and diagnosis[260] resulting in a variety of different drugs that are currently in clinical trials or even approved by the FDA.[261, 262]

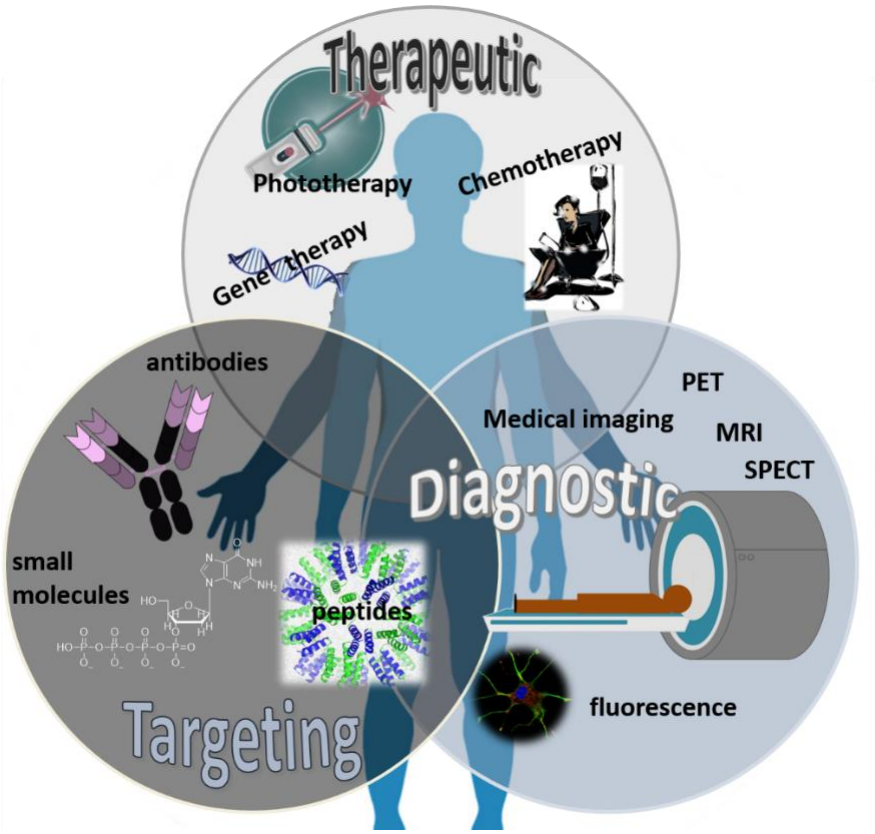

Figure 16: A schematic illustrated overview of the different applications of nanoparticles in theragnostics.

In clinical oncology, nanoparticles (NPs) are drug loaded and their overall size should not exceed the 100 nm limit, in order to be effective *in vivo*.[262] They enable improved solubility, excess in drug loading and the possibility of imaging modalities[262-265]. Due to their small size, they can deliver drugs in areas that are difficult to access, by crossing physiological barriers and by appropriate modification nanoparticles can mediate controlled drug release[262, 263, 266]. Since NPs localise in tumours, they evoke in cancer cells a cytotoxic response applying one or all three of the following modalities simultaneously:

- Drug release,
- Hyperthermia or thermal ablation, or
- Reactive oxygen species (ROS)-mediated killing.

Due to their high surface area to volume ratio and their boundless possibilities for chemical modification, nanoparticles could also have great potential as imaging agents.[267, 268] A variety of different NPs have been developed as potential MRI agents (Fe_2O_3-NPs, Gd-NPs),[269] as well as with enhanced CT or X-Ray image contrast (Au-NPs, TiO_2-NPs). Additionally, a plethora of nanoparticles has been radiolabelled with either PET or SPECT radioisotopes[270, 271]. The radiolabelling of the nanoparticles has been developed through three main different approaches. The first one involves the surface modification of the particles using either radioisotope-based prosthetic groups[272] or radiometal ion chelation[273, 274]. The second one is based on a modification to the particle coating.[275] In more detail, the nanoparticle coating is functionalised and the radioactive compound is attached to it *via* covalent binding. Lastly, modern approaches have been developed in order to limit the alteration of nanoparticle structure which often affect their pharmacokinetic properties and cytotoxicity. These could be achieved either by non-covalent binding of the radionuclide or the radiolabelled compound to the nanoparticle's surface, by addition of aliquots of radioactivity during particle construction, by the cavity encapsulation of the radioactivity, or reactor-based activation.[276-278]

Moreover, nanoparticles have been considered as key elements towards hybrid imaging. As mentioned earlier their large surface can be functionalised through various techniques and their versatile scaffolds render them potent multimodal agents through which to attempt to balance the benefits and drawbacks of the various imaging techniques. Magnetic resonance imaging, nuclear and optical imaging are the three imaging techniques which have been combined the most towards that purpose.[279] Through the years, research on magnetic nanoparticles and potential radiolabelling techniques has been well-developed offering many alternatives.[276, 280-282] In *in vitro* biological studies a combination of magnetic nanoparticles with fluorophore moieties is often used, but their *in vivo* use has remained limited.[279, 283]Additionally, merging nuclear imaging techniques with optical imaging approaches has been demonstrated already in small molecules for many years and it is now developing in nanoparticle research as well. This type of hybrid imaging is aimed primarily towards image-guided surgery. Undoubtedly the combination of all three techniques could overcome imaging limitations, but the chemistry behind nanoparticles with such scaffolds is very

challenging. Nevertheless, a number of research groups are involved in this research with the synthesis of tripodal ligands for medical imaging.[276, 279, 284]

1.6.1. Graphene Oxides as platforms for biosensing and imaging applications

Graphene was first isolated in the early 21st century by Novoselov and Geim earning them the Nobel Prize in Physics.[285] This new material consists of carbons bound in a honeycomb lattice constructing a 2D planar surface enriched in sp^2 layer orbitals. Since 2010, two graphene derivatives have been reported and studied, graphene oxide (GO) and reduced graphene oxide (rGO). Graphene oxide's surface contains uncharged epoxides (O) allowing the binding with chemotherapeutic drugs through hydrogen bonding or other interactions, and hydroxyl (OH) groups on the peripheral surface which increase the hydrophilicity of the molecule (**Figure 17**).[286-289] This is the most favourable one for applications such as drug delivery and bio-sensing.

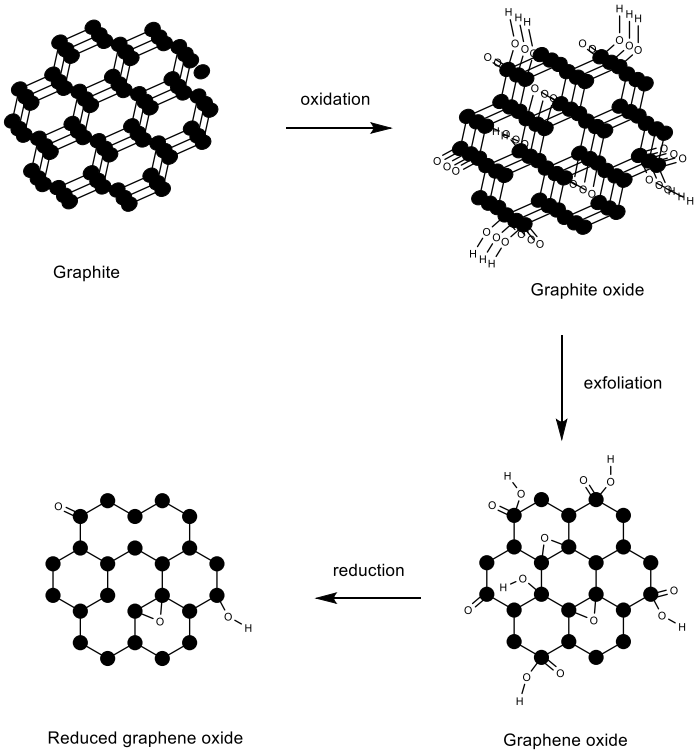

Figure 17: Schematic representation of the necessary procedures to obtain graphene and reduced graphene oxide.[290]

Graphene has presented potent opportunities for the development of a broad range of biomedical applications. Due to graphene's tuneable surface, its lower toxicity and to its superior biocompatibility in comparison with other nanoparticles, its use has been intensively explored as a nanocarrier for drug/gene delivery[291-294] or as biosensors[294-298] and theranostics.[299-301] Recent developments have shown that a variety of anticancer molecules (doxorubicin, camptothecin, nucleic acids etc) can be loaded onto the GO's surface.[302-304] At the same time, GO's potential to reduce reactive oxygen species in target cancer cells has been proposed in the literature.[305] Nevertheless, their toxicity may be affected by many parameters such as the number of layers, the size, the surface, the time of exposure or the cell type.[294, 295, 306] The main challenge of GOs nanocomposites, similarly to most nanoparticles is the selective drug delivery, but tumour-targeted GO drug carriers have been reported. This has been achieved by further functionalisation of the GO surface with folic acid, PEG, Herceptin or different antibodies that target a specific cancer type.[293, 307, 308] Furthermore, GO nanocomposites were tested as potential nanoplatforms for a variety of imaging techniques, such as MRI,[295, 309] fluorescence markers allowing intracellular imaging studies[295, 309-312] or PET techniques.[295, 313, 314] Last but not least, the combination of different imaging modalities on the same nanocomposite has also been explored.[295, 296, 315, 316]

1.7. Aims of this thesis

The overall objective of this project was the synthesis of aromatic thiosemicarbazonato complexes coordinated to the radioisotope [^{68}Ga]Ga(III) in order to be able to provide multimodal imaging modalities. The functionalisation of these Ga(III) complexes with specific targeting moieties can potentially lead to the development of promising imaging probes of interest in tumour hypoxia and prostate cancer imaging

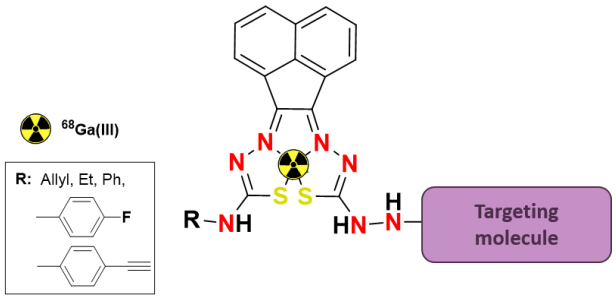

Figure 18: Schematic illustration of the design of unsymmetric aromatic BTSCs class. This class will be used as imaging probes synthetic scaffold towards the detection of hypoxic tumour cells via PET imaging.

Specific objectives are:

- The inclusion of an asymmetric acenaphthenoquinone thiosemicarbazonato (TSCA) complex as the core. As it has been previously commented, thiosemicarbasones (TSC) are flexible as ligands and at the same time their structure has important optical and biological properties. Thus, these properties of TSCA complexes will permit the use of both PET/SPECT imaging for *in vivo* experiments and confocal fluorescence microscopy for *in vitro* experiments.
- The possibility of including a fluorine-18 moiety to allow the use of PET imaging which will result in obtaining experiments with better image resolution.
- Synthesis and functionalisation of a glucosyl coumarin (GC) moiety, to be used as the target molecule, inhibiting CAIX and CAXI. GC also has high fluorescence intensity and it will probably enhance the fluorescence of our final molecule which is crucial for confocal fluorescence microscopy.
- Use of radiolabelled graphene oxide (GO) as a nanocarrier of metal unsymmetric bis(thiosemicarbazonato) complexes and GC for imaging of hypoxia.

1.8. References to Chapter 1

1. W. G. Bradley, *Proc. Am. Philos. Soc.*, 2008, **152**, 349-361.
2. M. Tubiana, *Bull Acad. Natl. Med.*, 1996, **180**, 97-108.
3. J. H. Scatliff and P. J. Morris, *N. C. Med. J.*, 2014, **75**, 111-113.
4. M. Rudin and R. Weissleder, *Nat. Rev. Drug Discov.*, 2003, **2**, 123-131.
5. F. Dollé, *Curr. Pharm. Des.*, 2005, **11**, 3221-3235.
6. E. O. Aboagye, in *Modern Biopharmaceuticals*, Wiley-VCH Verlag GmbH, 2008, ch51, pp. 1243-1270.
7. J. K. Willmann, N. van Bruggen, L. M. Dinkelborg and S. S. Gambhir, *Nat Rev Drug Discov.*, 2008, **7**, 591-607.
8. J. P. Holland, F. I. Aigbirhio, H. M. Betts, P. D. Bonnitcha, P. Burke, M. Christlieb, G. C. Churchill, A. R. Cowley, J. R. Dilworth, P. S. Donnelly, J. C. Green, J. M. Peach, S. R. Vasudevan and J. E. Warren, *Inorg. Chem.*, 2007, **46**, 465-485.
9. Z.-Y. Chen, Y.-X. Wang, Y. Lin, J.-S. Zhang, F. Yang, Q.-L. Zhou and Y.-Y. Liao, *BioMed Res.Int.*, 2014, **2014**, 12.
10. M. N. Wernick and J. N. Aarsvold, in *Emission Tomography*, ed. M. N. W. N. Aarsvold, Academic Press, San Diego, 2004, ch3, pp. 11-23.
11. F. Cortezon-Tamarit, S. Sarpaki, D. G. Calatayud, V. Mirabello and S. I. Pascu, *Chem Rec.*, 2016, **16**, 1380-1397.
12. H. W. Strauss, B. Zaret, P. Pieri and A. Lahiri, *J. Nucl. Cardiol.*, 2017, **24**, 1848-1849.
13. G. Hevesy, *Biochem. J.*, 1923, **17**, 439-445.
14. S. H. A. Alehyani, *J. King Saud Uni.- Sci.*, 2009, **21**, 109-117.
15. D. J. Brooks, *NeuroRx*, 2005, **2**, 226-236.
16. G. Porenta, J. Czernin and H. Schelbert, *Wien. Med. Wochenschr*, 1992, **142**, 358-366.
17. G. L. Zeng, J. R. Galt, M. N. Wernick, R. A. Mintzer and J. N. Aarsvold, in *Emission Tomography*, ed. M. N. W. N. Aarsvold, Academic Press, San Diego, 2004, ch7, pp. 127-152.

18. G.-L. Law and W.-T. Wong, in *The Chemistry of Molecular Imaging*, John Wiley & Sons, Inc, 2014,.ch1, pp. 1-24.
19. J. V. Frangioni, *J. Clin. Oncol.*, 2008, **26**, 4012-4021.
20. S. Liu, *Chem. Soc. Rev.*, 2004, **33**, 445-461.
21. K. H. Lieser, *Nuclear and radiochemistry: fundamentals and applications*, John Wiley & Sons, 2008.
22. W.-T. Wong, *The chemistry of molecular imaging*, John Wiley & Sons, 2014.
23. S. Sofia, MRes, Imperial College London, London, 2014.
24. S. I. Ziegler, *Nucl. Phys. A.*, 2005, **752**, 679-687.
25. L. Fass, *Mol. Oncol.*, 2008, **2**, 115-152.
26. H. P. Jadvar, J.A., *Clinical PET and PET/CT*, Springer, 2005.
27. G. Smith, L. Carroll and E. O. Aboagye, *Mol. Imaging Biol.*, 2012, **14**, 653-666.
28. I. Rauscher, T. Maurer, W. P. Fendler, W. H. Sommer, M. Schwaiger and M. Eiber, *Cancer Imaging*, 2016, **16**, 14.
29. H. Zacho, J. Nielsen, K. Dettmann, U. Haberkorn, N. Langkilde, J. Jensen and L. Petersen, *Eur. Urol. Suppl.*, 2018, **17**, e579-e580.
30. I. Rauscher, C. Düwel, B. Haller, C. Rischpler, M. M. Heck, J. E. Gschwend, M. Schwaiger, T. Maurer and M. Eiber, *Eur. Urol.*, 2018, **73**, 656-661.
31. A. Lambertini, P. Castellucci, A. Farolfi and S. Fanti, *Clin. Transl. Imaging*, 2018, DOI: 10.1007/s40336-018-0282-y.
32. J. Magill, J. Galy, C. Apostolidis, J. Somers and P. Jehenson, *Journal*, 2004.
33. M. Conti and L. Eriksson, *EJNMMI Physics*, 2016, **3**, 8.
34. H. O. Anger and A. Gottschalk, *J. Nucl. Med.*, 1963, **4**, 326-330.
35. S. R. Banerjee and M. G. Pomper, *Appl. Radiat. Isot.*, 2013, **0**, 2-13.
36. G. Bandoli, A. Dolmella, F. Tisato, M. Porchia and F. Refosco, *Coord. Chem. Rev.*, 2009, **253**, 56-77.
37. A. R. Jalilian, *Iran J. Nucl. Med.*, 2016, **24**, 1-10.
38. M. I. Prata, *Curr. Radiopharm.*, 2012, **5**, 142-149.
39. N. F. Schreiter, V. Prasad, M. H. Maurer and W. Brenner, *Eur. J. Nucl. Med. Mol. Imaging*, 2012, **39**, 725-726.

40. M. Gabriel, C. Decristoforo, D. Kendler, G. Dobrozemsky, D. Heute, C. Uprimny, P. Kovacs, E. Von Guggenberg, R. Bale and I. J. Virgolini, *J. Nucl. Med.*, 2007, **48**, 508-518.
41. I. Velikyan, *Theranostics*, 2014, **4**, 47.
42. W. A. P. Breeman, E. de Blois, H. Sze Chan, M. Konijnenberg, D. J. Kwekkeboom and E. P. Krenning, *Semin. Nucl. Med.*, 2011, **41**, 314-321.
43. P. W. Miller, N. J. Long, R. Vilar and A. D. Gee, *Angew. Chem. Int. Ed. Engl.*, 2008, **47**, 8998-9033.
44. M. Attiná, F. Cacace and A. Wolf, *J. Chem. Soc. Chem. Comm.*, 1983, 108-109.
45. O. Jacobson, D. O. Kiesewetter and X. Chen, *Bioconjugate Chem.*, 2015, **26**, 1-18.
46. E. L. Cole, M. N. Stewart, R. Littich, R. Hoareau and P. J. H. Scott, *Curr. Top. Med. Chem.*, 2014, **14**, 875-900.
47. D. van der Born, A. Pees, A. J. Poot, R. V. A. Orru, A. D. Windhorst and D. J. Vugts, *Chem. Soc. Rev.*, 2017, **46**, 4709-4773.
48. D. Roeda and F. Dollé, in *The Chemistry of Molecular Imaging*, John Wiley & Sons, Inc, 2014, ch3, pp. 55-77.
49. M. R. Kilbourn and J. R. Huizenga, *Fluorine-18 labeling of radiopharmaceuticals*, National Academy Press, 1990.
50. L. Teune, A. Bartels and K. Leenders, in *Functional Brain Mapping and the Endeavor to Understand the Working Brain*, InTech, 2013.
51. M. Bélanger, I. Allaman and Pierre J. Magistretti, *Cell Metab.*, 2011, **14**, 724-738.
52. P. Rigo, P. Paulus, B. J. Kaschten, R. Hustinx, T. Bury, G. Jerusalem, T. Benoit and J. Foidart-Willems, *Eur. J. Nucl. Med.*, 1996, **23**, 1641-1674.
53. Y.-x. He and Q.-y. Guo, *Postgrad. Med. J.*, 2008, **84**, 246-251.
54. A. Almuhaideb, N. Papathanasiou and J. Bomanji, *Ann. Saudi Med.*, 2011, **31**, 3-13.
55. M. Minsky, *Scanning*, 1988, **10**, 128-138.
56. M. D. Egger and M. Petran, *Science*, 1967, **157**, 305-307.
57. P. Davidovits and M. D. Egger, *Appl. Opt.*, 1971, **10**, 1615-1619.
58. http://www.olympusfluoview.com/theory/confocalintro.html, (accessed 29/06/2015, 2015).

59. D. Semwogerere and E. R. Weeks, *Encyclopedia of Biomaterials and Biomedical Engineering*, 2005, 1-10.
60. N. Rezai, *Retrieved*, 2004, **4**, 2008.
61. W. Becker, *J. Microsc.*, 2012, **247**, 119-136.
62. J. R. Lakowicz, H. Szmacinski, K. Nowaczyk and M. L. Johnson, *Proc. Natl. Acad. Sci. U.S.A.*, 1992, **89**, 1271-1275.
63. T. French, P. T. C. So, J. D. J. Weaver, T. Coelho-Sampaio, E. Gratton, J. E. W. Voss and J. Carrero, *J. Microsc.*, 1997, **185**, 339-353.
64. R. Yasuda, *Cold Spring Harb. Protoc.*, 2012, **2012**, pdb. top072090.
65. A. Esposito, F. Federici, C. Usai, F. Cannone, G. Chirico, M. Collini and A. Diaspro, *Microsc. Res. Tech.*, 2004, **63**, 12-17.
66. K. Svoboda and R. Yasuda, *Neuron*, 2006, **50**, 823-839.
67. M. Oheim, D. J. Michael, M. Geisbauer, D. Madsen and R. H. Chow, *Adv. Drug. Deliv. Rev.*, 2006, **58**, 788-808.
68. A. Ustione and D. W. Piston, *J. Microsc.*, 2011, **243**, 221-226.
69. W. B. Coleman and T. C. Rubinas, in *Essential Concepts in Molecular Pathology*, Academic Press, San Diego, 2010, ch9, pp. 45-61.
70. World Health Organisation, http://www.who.int/mediacentre/factsheets/fs297/en/).
71. D. H. a. R. A. Weinberg, *Chapter 1: The hallmarks of cancer*, OUP Oxford, Oxford, 3d edn., 2016.
72. B. Laxman, D. E. Hall, M. S. Bhojani, D. A. Hamstra, T. L. Chenevert, B. D. Ross and A. Rehemtulla, *Proc. Natl. Acad. Sci. U.S.A.*, 2002, **99**, 16551-16555.
73. A. Sudhakar, *J. Cancer Sci. Ther.*, 2009, **1**, 1-4.
74. D. Hanahan and R. A. Weinberg, *Cell*, 2000, **100**, 57-70.
75. D. Hanahan and R. A. Weinberg, *Cell*, 2011, **144**, 646-674.
76. J. K. Oliver Rácz, Rudolf Korec, František Ništiar, Anna Šipulová, and Z. T. Anna Šofranková, László Kovács, Eugen Kóňa, Peter Dombrovský, *Journal*, 1995, **2**, 123.
77. R. H. Thomlinson and L. H. Gray, *Br. J. Cancer*, 1955, **9**, 539-549.
78. L. H. Gray, A. D. Conger, M. Ebert, S. Hornsey and O. C. A. Scott, *Br. J. Radiol.*, 1953, **26**, 638-648.
79. P. J. Sheffield and J. C. Davis, *Aviat. Space Environ. Med.*, 1976, **47**, 759-762.

80. R. J. Hodgkiss, *Anti-cancer drug design*, 1998, **13**, 687-702.
81. J. M. Brown, *Int. J. Radiat. Oncol. Biol. Phys.*, 1984, **10**, 425-429.
82. F. Kallinowski, K. H. Schlenger, S. Runkel, M. Kloes, M. Stohrer, P. Okunieff and P. Vaupel, *Cancer Res.*, 1989, **49**, 3759-3764.
83. P. Vaupel, K. Schlenger, C. Knoop and M. Höckel, *Cancer Res.*, 1991, **51**, 3316-3322.
84. P. Vaupel and L. Harrison, *The oncologist*, 2004, **9 Suppl 5**, 4-9.
85. D. J. Pierson, *Respir. Care*, 2000, **45**, 39-51.
86. P. I. Papaioannou Vasilios, *Pneumon*, 2008, **21**, 10.
87. T. G. Graeber, C. Osmanian, T. Jacks, D. E. Housman, C. J. Koch, S. W. Lowe and A. J. Giaccia, *Nature*, 1996, **379**, 88-91.
88. C. Y. Kim, M. H. Tsai, C. Osmanian, T. G. Graeber, J. E. Lee, R. G. Giffard, J. A. DiPaolo, D. M. Peehl and A. J. Giaccia, *Cancer Res*, 1997, **57**, 4200-4204.
89. K. Bennewith and S. Dedhar, *BMC Cancer*, 2011, **11**, 1-6.
90. M. Bhatia, T. C. Karlenius, G. Di Trapani and K. F. Tonissen, *The interaction between redox and hypoxic signalling pathways in the dynamic oxygen environment of cancer cells*, InTech, 2013.
91. R. E. Durand, *In vivo (Athens, Greece)*, 1994, **8**, 691-702.
92. E. Tak, S. Lee, J. Lee, M. A. Rashid, Y. W. Kim, J. H. Park, W. S. Park, K. M. Shokat, J. Ha and S. S. Kim, *J. Hepatol.*, 2011, **54**, 328-339.
93. K. M. Comerford, T. J. Wallace, J. Karhausen, N. A. Louis, M. C. Montalto and S. P. Colgan, *Cancer Res.*, 2002, **62**, 3387-3394.
94. M. Wartenberg, E. Hoffmann, H. Schwindt, F. Grünheck, J. Petros, J. R. S. Arnold, J. Hescheler and H. Sauer, *FEBS Lett.*, 2005, **579**, 4541-4549.
95. X. J. Wang, C. W. Feng and M. Li, *Mol Cell Biochem*, 2013, **380**, 57-66.
96. A. Kondo, R. Safaei, M. Mishima, H. Niedner, X. Lin and S. B. Howell, *Cancer Res.*, 2001, **61**, 7603-7607.
97. S. Osinsky, M. Zavelevich and P. Vaupel, *Exp. Oncol.*, 2009, **31**, 80-86.
98. M. Hockel, C. Knoop, K. Schlenger, B. Vorndran, E. Baussmann, M. Mitze, P. G. Knapstein and P. Vaupel, *Radiother. Oncol.*, 1993, **26**, 45-50.

99. H. Lyng, K. Sundfor, C. Trope and E. K. Rofstad, *Clin. Cancer Res.*, 2000, **6**, 1104-1112.

100. T. H. Knocke, H. D. Weitmann, H. J. Feldmann, E. Selzer and R. Pötter, *Radiother. Oncol.*, 1999, **53**, 99-104.

101. M. Nordsmark, S. M. Bentzen, V. Rudat, D. Brizel, E. Lartigau, P. Stadler, A. Becker, M. Adam, M. Molls, J. Dunst, D. J. Terris and J. Overgaard, *Radiother. Oncol.*, 2005, **77**, 18-24.

102. G. Gruber, R. H. Greiner, R. Hlushchuk, D. M. Aebersold, H. J. Altermatt, G. Berclaz and V. Djonov, *Breast Cancer Res.*, 2004, **6**, R191-198.

103. P. Burri, V. Djonov, D. M. Aebersold, K. Lindel, U. Studer, H. J. Altermatt, L. Mazzucchelli, R. H. Greiner and G. Gruber, *Int. J. Radiat. Oncol. Biol. Phys.*, 2003, **56**, 494-501.

104. T. Onita, P. G. Ji, J. W. Xuan, H. Sakai, H. Kanetake, P. H. Maxwell, G. H. Fong, M. Y. Gabril, M. Moussa and J. L. Chin, *Clin. Cancer Res.*, 2002, **8**, 471-480.

105. M. Schindl, S. F. Schoppmann, H. Samonigg, H. Hausmaninger, W. Kwasny, M. Gnant, R. Jakesz, E. Kubista, P. Birner and G. Oberhuber, *Clin. Cancer Res.*, 2002, **8**, 1831-1837.

106. M. H. Bui, D. Seligson, K. R. Han, A. J. Pantuck, F. J. Dorey, Y. Huang, S. Horvath, B. C. Leibovich, S. Chopra, S. Y. Liao, E. Stanbridge, M. I. Lerman, A. Palotie, R. A. Figlin and A. S. Belldegrun, *Clin. Cancer Res.*, 2003, **9**, 802-811.

107. J. H. Kaanders, K. I. Wijffels, H. A. Marres, A. S. Ljungkvist, L. A. Pop, F. J. van den Hoogen, P. C. de Wilde, J. Bussink, J. A. Raleigh and A. J. van der Kogel, *Cancer Res.*, 2002, **62**, 7066-7074.

108. K. Lehtiö, O. Eskola, T. Viljanen, V. Oikonen, T. Grönroos, L. Sillanmäki, R. Grénman and H. Minn, *Int. J. Radiat. Oncol. Biol. Phys.*, 2004, **59**, 971-982.

109. F. Dehdashti, P. W. Grigsby, M. A. Mintun, J. S. Lewis, B. A. Siegel and M. J. Welch, *Int. J. Radiat. Oncol. Biol. Phys.*, 2003, **55**, 1233-1238.

110. J. A. Loncaster, B. M. Carrington, J. R. Sykes, A. P. Jones, S. M. Todd, R. Cooper, D. L. Buckley, S. E. Davidson, J. P. Logue, R. D. Hunter and C. M. West, *Int. J. Radiat. Oncol. Biol. Phys.*, 2002, **54**, 759-767.

111. J. M. Price, S. P. Robinson and D. M. Koh, *Q. J. Nucl. Med. Mol. Imaging*, 2013, **57**, 257-270.
112. M. A. Maynard, A. J. Evans, W. Shi, W. Y. Kim, F.-F. Liu and M. Ohh, *Cell Cycle*, 2007, **6**, 2810-2816.
113. M. C. Simon, *Diverse effects of hypoxia on tumor progression*, Springer Science & Business Media, 2010.
114. C. Brahimi-Horn and J. Pouyssegur, *Bull Cancer*, 2006, **93**, E73-80.
115. M. J. Calzada and L. del Peso, *Clin. Transl. Oncol.*, 2007, **9**, 278-289.
116. D. L. Ramirez-Bergeron and M. C. Simon, *Stem Cells*, 2001, **19**, 279-286.
117. G. L. Semenza, *Annu. Rev. Physiol.*, 2014, **76**, 39-56.
118. L. A. Shimoda and G. L. Semenza, *Am. J. Respir. Crit. Care Med.*, 2011, **183**, 152-156.
119. D. Wu, N. Potluri, J. Lu, Y. Kim and F. Rastinejad, *Nature*, 2015, **524**, 303-308.
120. L. Holmquist-Mengelbier, E. Fredlund, T. Lofstedt, R. Noguera, S. Navarro, H. Nilsson, A. Pietras, J. Vallon-Christersson, A. Borg, K. Gradin, L. Poellinger and S. Pahlman, *Cancer cell*, 2006, **10**, 413-423.
121. Q. Li, H. Chen, X. Huang and M. Costa, *Toxicol. Appl. Pharmacol.*, 2006, **213**, 245-255.
122. K. S. Hewitson, L. A. McNeill, J. M. Elkins and C. J. Schofield, *Biochem. Soc. Trans.*, 2003, **31**, 510-515.
123. N. Masson and P. J. Ratcliffe, *Cancer. Metab.*, 2014, **2**, 3-3.
124. G. L. Wang and G. L. Semenza, *Blood*, 1993, **82**, 3610-3615.
125. K. Salnikow, T. Davidson, Q. Zhang, L. C. Chen, W. Su and M. Costa, *Cancer Res.*, 2003, **63**, 3524-3530.
126. F. Martin, T. Linden, D. M. Katschinski, F. Oehme, I. Flamme, C. K. Mukhopadhyay, K. Eckhardt, J. Troger, S. Barth, G. Camenisch and R. H. Wenger, *Blood*, 2005, **105**, 4613-4619.
127. Y. S. Chun, E. Choi, G. T. Kim, M. J. Lee, M. J. Lee, S. E. Lee, M. S. Kim and J. W. Park, *Biochem. Biophys. Res. Commun.*, 2000, **268**, 652-656.
128. F. Grasselli, G. Basini, S. Bussolati and F. Bianco, *Reprod. Fertil. Dev.*, 2005, **17**, 715-720.

129. G. Melillo, *Hypoxia and Cancer: Biological Implications and Therapeutic Opportunities*, Springer Science & Business Media, 2013.
130. N. U. Meldrum and F. J. W. Roughton, *J. Physiol.*, 1933, **80**, 113-142.
131. J. R. G. BRADFIELD, *Nature*, 1947, **159**, 2.
132. M. R. Badger and G. D. Price, *Annu. Rev. Plant Biol.*, 1994, **45**, 369-392.
133. B. E. Alber and J. G. Ferry, *Proc. Natl. Acad. Sci. U.S.A.*, 1994, **91**, 6909-6913.
134. K. S. Smith, C. Jakubzick, T. S. Whittam and J. G. Ferry, *Proc. Natl. Acad. Sci. USA*, 1999, **96**, 15184-15189.
135. S. A. Braus-Stromeyer, G. Schnappauf, G. H. Braus, A. S. Gossner and H. L. Drake, *J. Bacteriol.*, 1997, **179**, 7197-7200.
136. B. E. Alber and J. G. Ferry, *J. Bacteriol.*, 1996, **178**, 3270-3274.
137. D. B. Northrop and F. B. Simpson, *Arch. Biochem. Biophys.*, 1998, **352**, 288-292.
138. S. Lindskog, *Pharmacol. Ther.*, 1997, **74**, 1-20.
139. R. P. Henry, *Annu. Rev. Physiol.*, 1996, **58**, 523-538.
140. D. N. Silverman and S. Lindskog, *Acc. Chem. Res.*, 1988, **21**, 30-36.
141. I. Nishimori, T. Minakuchi, S. Onishi, D. Vullo, A. Scozzafava and C. T. Supuran, *J. Med. Chem.*, 2007, **50**, 381-388.
142. M. Hilvo, M. Tolvanen, A. Clark, B. Shen, G. N. Shah, A. Waheed, P. Halmi, M. Hanninen, J. M. Hamalainen, M. Vihinen, W. S. Sly and S. Parkkila, *Biochem. J.*, 2005, **392**, 83-92.
143. I. Nishimori, T. Minakuchi, S. Onishi, D. Vullo, A. Cecchi, A. Scozzafava and C. T. Supuran, *J. Enzyme Inhib. Med. Chem.*, 2008, **24**, 70-76.
144. P. J. Wistrand, *Ups. J. Med. Sci.*, 2002, **107**, 77-88.
145. R. T. Fernley, R. D. Wright and J. P. Coghlan, *FEBS Lett*, 1979, **105**, 299-302.
146. P. Aldred, P. Fu, G. Barrett, J. D. Penschow, R. D. Wright, J. P. Coghlan and R. T. Fernley, *Biochemistry*, 1991, **30**, 569-575.
147. D. Vullo, M. Franchi, E. Gallori, J. Pastorek, A. Scozzafava, S. Pastorekova and C. T. Supuran, *Bioorg. Med. Chem. Lett.*, 2003, **13**, 1005-1009.
148. D. Vullo, A. Innocenti, I. Nishimori, J. Pastorek, A. Scozzafava, S. Pastorekova and C. T. Supuran, *Bioorg. Med. Chem. Lett.*, 2005, **15**, 963-969.

149. J. Lehtonen, B. Shen, M. Vihinen, A. Casini, A. Scozzafava, C. T. Supuran, A. K. Parkkila, J. Saarnio, A. J. Kivela, A. Waheed, W. S. Sly and S. Parkkila, *J. Biol. Chem.*, 2004, **279**, 2719-2727.

150. B. Becker, *Am. J. Ophthalmol.*, 1954, **37**, 13-15.

151. S. J. Dodgson, R. P. Shank and B. E. Maryanoff, *Epilepsia*, 2000, **41 Suppl 1**, S35-39.

152. D. Vullo, A. Innocenti, I. Nishimori, J. r. Pastorek, A. Scozzafava, S. Pastoreková and C. T. Supuran, *Bioorganic Med. Chem. Lett.*, 2005, **15**, 963-969.

153. C. T. Supuran, A. Scozzafava and J. Conway, *Carbonic anhydrase: its inhibitors and activators*, CRC Press, 2004.

154. F. Fabrizi, F. Mincione, T. Somma, G. Scozzafava, F. Galassi, E. Masini, F. Impagnatiello and C. T. Supuran, *J. Enzyme Inhib. Med. Chem.*, 2012, **27**, 138-147.

155. Y. Lou, P. C. McDonald, A. Oloumi, S. Chia, C. Ostlund, A. Ahmadi, A. Kyle, U. Auf dem Keller, S. Leung, D. Huntsman, B. Clarke, B. W. Sutherland, D. Waterhouse, M. Bally, C. Roskelley, C. M. Overall, A. Minchinton, F. Pacchiano, F. Carta, A. Scozzafava, N. Touisni, J. Y. Winum, C. T. Supuran and S. Dedhar, *Cancer Res.*, 2011, **71**, 3364-3376.

156. J. G. Millichap, D. M. Woodbury and L. S. Goodman, *J. Pharmacol. Exp. Ther.*, 1955, **115**, 251-258.

157. O. Sedlakova, E. Svastova, M. Takacova, J. Kopacek, J. Pastorek and S. Pastorekova, *Front. Physiol.*, 2014, **4**.

158. F. E. Lock, P. C. McDonald, Y. Lou, I. Serrano, S. C. Chafe, C. Ostlund, S. Aparicio, J. Y. Winum, C. T. Supuran and S. Dedhar, *Oncogene*, 2013, **32**, 5210-5219.

159. J. Chiche, K. Ilc, J. Laferriere, E. Trottier, F. Dayan, N. M. Mazure, M. C. Brahimi-Horn and J. Pouyssegur, *Cancer Res.*, 2009, **69**, 358-368.

160. J. Chiche, K. Ilc, J. Laferrière, E. Trottier, F. Dayan, N. M. Mazure, M. C. Brahimi-Horn and J. Pouysségur, *Cancer Res.*, 2009, **69**, 358-368.

161. M. A. Proescholdt, C. Mayer, M. Kubitza, T. Schubert, S.-Y. Liao, E. J. Stanbridge, S. Ivanov, E. H. Oldfield, A. Brawanski and M. J. Merrill, *Neuro-Oncol.*, 2005, **7**, 465-475.

162. S. Pastorekova, Z. Zavadova, M. Kostal, O. Babusikova and J. Zavada, *Virology*, 1992, **187**, 620-626.

163. J. Pastorek, S. Pastorekova, I. Callebaut, J. P. Mornon, V. Zelnik, R. Opavsky, M. Zat'ovicova, S. Liao, D. Portetelle, E. J. Stanbridge and et al., *Oncogene*, 1994, **9**, 2877-2888.

164. R. Opavsky, S. Pastorekova, V. Zelnik, A. Gibadulinova, E. J. Stanbridge, J. Zavada, R. Kettmann and J. Pastorek, *Genomics*, 1996, **33**, 480-487.

165. E. Svastova, A. Hulikova, M. Rafajova, M. Zat'ovicova, A. Gibadulinova, A. Casini, A. Cecchi, A. Scozzafava, C. T. Supuran, J. Pastorek and S. Pastorekova, *FEBS Lett.*, 2004, **577**, 439-445.

166. P. Swietach, S. Patiar, C. T. Supuran, A. L. Harris and R. D. Vaughan-Jones, *J. Biol. Chem.*, 2009, **284**, 20299-20310.

167. P. Swietach, R. D. Vaughan-Jones and A. L. Harris, *Cancer Metastasis Rev.*, 2007, **26**, 299-310.

168. J. W. Wojtkowiak, D. Verduzco, K. J. Schramm and R. J. Gillies, *Mol. Pharm.*, 2011, **8**, 2032-2038.

169. E. Svastova, W. Witarski, L. Csaderova, I. Kosik, L. Skvarkova, A. Hulikova, M. Zatovicova, M. Barathova, J. Kopacek, J. Pastorek and S. Pastorekova, *J. Biol. Chem.*, 2012, **287**, 3392-3402.

170. J. C. Oosterwijk-Wakka, O. Boerman, P. A. Mulders and E. Oosterwijk, in *Renal Cell Carcinoma*, eds. R. Bukowski, R. Figlin and R. Motzer, Humana Press, 2009, ch. 13, pp. 231-247.

171. C. Temperini, A. Innocenti, A. Mastrolorenzo, A. Scozzafava and C. T. Supuran, *Bioorg. Med. Chem. Lett.*, 2007, **17**, 4866-4872.

172. J.-Y. Winum, D. Vullo, A. Casini, J.-L. Montero, A. Scozzafava and C. T. Supuran, *J. Med. Chem.*, 2003, **46**, 2197-2204.

173. R. G. Gieling, M. Babur, L. Mamnani, N. Burrows, B. A. Telfer, F. Carta, J. Y. Winum, A. Scozzafava, C. T. Supuran and K. J. Williams, *J. Med. Chem.*, 2012, **55**, 5591-5600.

174. C. Supuran, S. Dedhar, P. C. Mcdonald and F. Carta, *Journal*, 2013.

175. A. Cecchi, A. Hulikova, J. Pastorek, S. Pastoreková, A. Scozzafava, J.-Y. Winum, J.-L. Montero and C. T. Supuran, *J. Med. Chem.*, 2005, **48**, 4834-4841.
176. L. Dubois, K. Douma, C. T. Supuran, R. K. Chiu, M. A. van Zandvoort, S. Pastoreková, A. Scozzafava, B. G. Wouters and P. Lambin, *Radiother. Oncol.*, 2007, **83**, 367-373.
177. F. Carta, A. Maresca, A. Scozzafava and C. T. Supuran, *Bioorg. Med. Chem.*, 2012, **20**, 2266-2273.
178. S. Durdagi, M. Senturk, D. Ekinci, H. T. Balaydin, S. Goksu, O. I. Kufrevioglu, A. Innocenti, A. Scozzafava and C. T. Supuran, *Bioorg. Med. Chem.*, 2011, **19**, 1381-1389.
179. A. Maresca, A. Scozzafava and C. T. Supuran, *Bioorganic Med. Chem. Lett.*, 2010, **20**, 7255-7258.
180. A. Maresca and C. T. Supuran, *Bioorganic Med. Chem. Lett.*, 2010, **20**, 4511-4514.
181. A. Maresca, C. Temperini, H. Vu, N. B. Pham, S.-A. Poulsen, A. Scozzafava, R. J. Quinn and C. T. Supuran, *J. Am. Chem. Soc.*, 2009, **131**, 3057-3062.
182. L. Dubois, S. G. J. A. Peeters, S. J. A. van Kuijk, A. Yaromina, N. G. Lieuwes, R. Saraya, R. Biemans, M. Rami, N. K. Parvathaneni, D. Vullo, M. Vooijs, C. T. Supuran, J.-Y. Winum and P. Lambin, *Radiother. Oncol.*, 2013, **108**, 523-528.
183. İ. Kizilcikli, Y. D. Kurt, B. Akkurt, A. Y. Genel, S. Birteksöz, G. Ötük and B. Ülküseven, *Folia Microbiol.*, 2007, **52**, 15-25.
184. K. S. Abou Melha, *J. Enzyme Inhib. Med. Chem.*, 2008, **23**, 493-503.
185. A. E. Liberta and D. X. West, *BioMetals*, 1992, **5**, 121-126.
186. M. A. Souza, S. Johann, L. A. R. d. S. Lima, F. F. Campos, I. C. Mendes, H. Beraldo, E. M. de Souza-Fagundes, P. S. Cisalpino, C. A. Rosa, T. M. d. A. Alves, N. P. de Sá and C. L. Zani, *Mem. Inst. Oswaldo Cruz*, 2013, **108**, 342-351.
187. D. J. Bauer, *Ann. N. Y. Acad. Sci.*, 1965, **130**, 110-117.
188. C. Shipman, S. H. Smith, J. C. Drach and D. L. Klayman, *Antimicrob. Agents Chemother.*, 1981, **19**, 682-685.
189. P. R. Donald and H. McIlleron, in *Tuberculosis*, W.B. Saunders, Edinburgh, 2009, ch7, pp. 608-617.

190. N. S. Moorthy, N. M. Cerqueira, M. J. Ramos and P. A. Fernandes, *Mini Rev. Med. Chem.*, 2013, **13**, 1862-1872.
191. F. R. Pavan, S. M. P. I. da, S. R. Leite, V. M. Deflon, A. A. Batista, D. N. Sato, S. G. Franzblau and C. Q. Leite, *Eur. J. Med. Chem.*, 2010, **45**, 1898-1905.
192. Y. Yu, D. S. Kalinowski, Z. Kovacevic, A. R. Siafakas, P. J. Jansson, C. Stefani, D. B. Lovejoy, P. C. Sharpe, P. V. Bernhardt and D. R. Richardson, *J. Med. Chem.*, 2009, **52**, 5271-5294.
193. K. Agrawal and A. Sartorelli, *Prog. Med. Chem*, 1978, **15**, 321-356.
194. D. S. Kalinowski and D. R. Richardson, *Pharmacol. Rev.*, 2005, **57**, 547-583.
195. R. W. Brockman, J. R. Thomson, M. J. Bell and H. E. Skipper, *Cancer Res.*, 1956, **16**, 167-170.
196. A. C. Sartorelli and B. A. Booth, *Cancer Res.*, 1967, **27**, 1614-1619.
197. A. C. Sartorelli, K. C. Agrawal and E. C. Moore, *Biochem. Pharm.*, 1971, **20**, 3119-3123.
198. A. C. Sartorelli, K. C. Agrawal, A. S. Tsiftsoglou and E. Colleen Moore, *Adv. Enzyme Regul.*, 1977, **15**, 117-139.
199. R. Pedrido, A. M. Gonzalez-Noya, M. J. Romero, M. Martinez-Calvo, M. Vazquez Lopez, E. Gomez-Forneas, G. Zaragoza and M. R. Bermejo, *Dalton Trans.*, 2008, **47**, 6776-6787.
200. D. S. Kalinowski and D. R. Richardson, *Chem. Res. Toxicol.*, 2007, **20**, 715-720.
201. D. R. Richardson, P. C. Sharpe, D. B. Lovejoy, D. Senaratne, D. S. Kalinowski, M. Islam and P. V. Bernhardt, *J. Med. Chem.*, 2006, **49**, 6510-6521.
202. D. S. Kalinowski, Y. Yu, P. C. Sharpe, M. Islam, Y. T. Liao, D. B. Lovejoy, N. Kumar, P. V. Bernhardt and D. R. Richardson, *J. Med. Chem.*, 2007, **50**, 3716-3729.
203. L. M. Bystrom, M. L. Guzman and S. Rivella, *Antioxid. Redox signal.*, 2014, **20**, 1917-1924.
204. Z. L. Guo, D. R. Richardson, D. S. Kalinowski, Z. Kovacevic, K. C. Tan-Un and G. C. Chan, *J. Hematol. Oncol.*, 2016, **9**, 98.
205. K. Y. Salim, S. Maleki Vareki, W. R. Danter and J. Koropatnick, *Oncotarget*, 2016, **7**, 41363-41379.

206. H. Petra, P. V. F.S., E. É. A., K. B. K., S. Gergely and K. C. R., *Antioxid. Redox signal.*, **0**, null.
207. D. S. Kalinowski, P. Quach and D. R. Richardson, *Future Med Chem*, 2009, **1**, 1143-1151.
208. S. Attia, J. Kolesar, M. R. Mahoney, H. C. Pitot, D. Laheru, J. Heun, W. Huang, J. Eickhoff, C. Erlichman and K. D. Holen, *Invest. New Drugs*, 2008, **26**, 369-379.
209. R. C. DeConti, B. R. Toftness, K. C. Agrawal, R. Tomchick, J. A. Mead, J. R. Bertino, A. C. Sartorelli and W. A. Creasey, *Cancer Res.*, 1972, **32**, 1455-1462.
210. L. Feun, M. Modiano, K. Lee, J. Mao, A. Marini, N. Savaraj, P. Plezia, B. Almassian, E. Colacino, J. Fischer and S. MacDonald, *Cancer Chemother. Pharmacol.*, 2002, **50**, 223-229.
211. I. H. Krakoff, E. Etcubanas, C. Tan, K. Mayer, V. Bethune and J. H. Burchenal, *Cancer Chemother. Rep.*, 1974, **58**, 207-212.
212. C. Neuberg and W. Neimann, *Eur. J. Inorg. Chem*, 1902, **35**, 2049-2056.
213. B. A. Gingras, R. L. Somorjai and C. H. Bayley, *Can. J. Chem.*, 1961, **39**, 973-985.
214. N. Bailey, S. Hull, C. Jones and J. McCleverty, *J. Chem. Soc. Chem. Comm.*, 1970, 124-126.
215. M. C. Rodriguez-Argüelles, M. B. Ferrari, G. G. Fava, C. Pelizzi, P. Tarasconi, R. Albertini, P. P. Dall'Aglio, P. Lunghi and S. Pinelli, *J. Inorg. Biochem.*, 1995, **58**, 157-175.
216. J. R. Dilworth and R. Hueting, *Inorganica Chim. Acta*, 2012, **389**, 3-15.
217. S. I. Pascu, P. A. Waghorn, B. W. C. Kennedy, R. L. Arrowsmith, S. R. Bayly, J. R. Dilworth, M. Christlieb, R. M. Tyrrell, J. Zhong, R. M. Kowalczyk, D. Collison, P. K. Aley, G. C. Churchill and F. I. Aigbirhio, *Chem. As. J.*, 2010, **5**, 506-519.
218. M. Christlieb, H. J. Claughton, A. R. Cowley, J. M. Heslop and J. R. Dilworth, *Transition Met. Chem.*, 2006, **31**, 88-92.
219. L. F. Clarke, F. O'Sullivan and A. F. Hegarty, *Perkin. Trans. 2*, 1991, 1649-1652.
220. B. T. Heaton, D. M. P. Mingos, J. R. Dilworth, C. D. Garner, G. Frenking, R. Richards, G. Gamlen, J. Lewis, D. Adams and J. Postgate, *Modern coordination chemistry: the legacy of Joseph Chatt*, Royal Society of Chemistry, 2007.

221. J. S. Casas, M. S. García-Tasende and J. Sordo, *Coord. Chem. Rev.*, 2000, **209**, 197-261.
222. B. A. Booth and A. C. Sartorelli, *Mol. Pharmacol.*, 1967, **3**, 290-302.
223. Q. Fu, Z.-Y. Gao, J. Zhang, H.-Y. Sun, C. Liu and J.-H. Ren, *Bangladesh J. Pharmacol.*, 2014, **9**, 466-473.
224. D. Palanimuthu, S. V. Shinde, K. Somasundaram and A. G. Samuelson, *J. Med. Chem.*, 2013, **56**, 722-734.
225. P. J. Crouch, L. W. Hung, P. A. Adlard, M. Cortes, V. Lal, G. Filiz, K. A. Perez, M. Nurjono, A. Caragounis, T. Du, K. Laughton, I. Volitakis, A. I. Bush, Q. X. Li, C. L. Masters, R. Cappai, R. A. Cherny, P. S. Donnelly, A. R. White and K. J. Barnham, *Proc. Natl. Acad. Sci. USA*, 2009, **106**, 381-386.
226. V. B. Kenche and K. J. Barnham, *Br. J. Pharmacol.*, 2011, **163**, 211-219.
227. P. S. Donnelly, A. Caragounis, T. Du, K. M. Laughton, I. Volitakis, R. A. Cherny, R. A. Sharples, A. F. Hill, Q. X. Li, C. L. Masters, K. J. Barnham and A. R. White, *J. Biol. Chem.*, 2008, **283**, 4568-4577.
228. R. I. Maurer, P. J. Blower, J. R. Dilworth, C. A. Reynolds, Y. Zheng and G. E. Mullen, *J. Med. Chem.*, 2002, **45**, 1420-1431.
229. J. L. Dearling, J. S. Lewis, G. E. Mullen, M. J. Welch and P. J. Blower, *J. Biol. Inorg. Chem.*, 2002, **7**, 249-259.
230. Z. Xiao, P. S. Donnelly, M. Zimmermann and A. G. Wedd, *Inorg. Chem.*, 2008, **47**, 4338-4347.
231. A. L. Vāvere and J. S. Lewis, *Dalton Trans.*, 2007, 4893-4902.
232. P. D. Bonnitcha, S. R. Bayly, M. B. M. Theobald, H. M. Betts, J. S. Lewis and J. R. Dilworth, *J. Inorg. Biochem.*, 2010, **104**, 126-135.
233. R. Hueting, V. Kersemans, B. Cornelissen, M. Tredwell, K. Hussien, M. Christlieb, A. D. Gee, J. Passchier, S. C. Smart, J. R. Dilworth, V. Gouverneur and R. J. Muschel, *J. Nucl. Med.*, 2014, **55**, 128-134.
234. R. Hueting, V. Kersemans, M. Tredwell, B. Cornelissen, M. Christlieb, A. D. Gee, J. Passchier, S. C. Smart, V. Gouverneur, R. J. Muschel and J. R. Dilworth, *Metallomics*, 2015, **7**, 795-804.

235. L. Carroll, R. Bejot, R. Hueting, R. King, P. Bonnitcha, S. Bayly, M. Christlieb, J. R. Dilworth, A. D. Gee and J. Declerck, *Chem. Commun.*, 2010, **46**, 4052-4054.

236. A. R. Cowley, J. Davis, J. R. Dilworth, P. S. Donnelly, R. Dobson, A. Nightingale, J. M. Peach, B. Shore, D. Kerr and L. Seymour, *Chem. Commun.*, 2005, **7**, 845-847.

237. M. E. Ostergaard and P. J. Hrdlicka, *Chem. Soc. Rev.*, 2011, **40**, 5771-5788.

238. C. L. Masters, R. Cappai, K. J. Barnham and V. L. Villemagne, *J. Neurochem.*, 2006, **97**, 1700-1725.

239. P. A. Waghorn, M. W. Jones, M. B. M. Theobald, R. L. Arrowsmith, S. I. Pascu, S. W. Botchway, S. Faulkner and J. R. Dilworth, *Chem. Sci.*, 2013, **4**, 1430-1441.

240. S. I. Pascu, P. A. Waghorn, T. D. Conry, H. M. Betts, J. R. Dilworth, G. C. Churchill, T. Pokrovska, M. Christlieb, F. I. Aigbirhio and J. E. Warren, *Dalton Trans.*, **43**, 2007, , 4988-4997.

241. H. M. Betts, P. J. Barnard, S. R. Bayly, J. R. Dilworth, A. D. Gee and J. P. Holland, *Angew. Chem. Int. Ed. Engl.*, 2008, **47**, 8416-8419.

242. J. R. Dilworth and S. I. Pascu, in *The Chemistry of Molecular Imaging*, John Wiley & Sons, Inc, 2014, ch6, pp. 137-164.

243. A. V. Rudnev, L. S. Foteeva, C. Kowol, R. Berger, M. A. Jakupec, V. B. Arion, A. R. Timerbaev and B. K. Keppler, *J. Inorg. Biochem.*, 2006, **100**, 1819-1826.

244. C. R. Kowol, R. Berger, R. Eichinger, A. Roller, M. A. Jakupec, P. P. Schmidt, V. B. Arion and B. K. Keppler, *J. Med. Chem.*, 2007, **50**, 1254-1265.

245. S. I. Pascu, P. A. Waghorn, B. W. Kennedy, R. L. Arrowsmith, S. R. Bayly, J. R. Dilworth, M. Christlieb, R. M. Tyrrell, J. Zhong, R. M. Kowalczyk, D. Collison, P. K. Aley, G. C. Churchill and F. I. Aigbirhio, *Chem. Asian J.*, 2010, **5**, 506-519.

246. I. S. Alam, R. L. Arrowsmith, F. Cortezon-Tamarit, F. Twyman, G. Kociok-Köhn, S. W. Botchway, J. R. Dilworth, L. Carroll, E. O. Aboagye and S. I. Pascu, *Dalton Trans.*, 2016, **45**, 144-155.

247. W. H. Perkin, *J. Chem. Soc.*, 1868, **21**, 53-63.

248. C. T. Supuran, *Nat. Rev. Drug Discov.*, 2008, **7**, 168-181.

249. C. Temperini, A. Innocenti, A. Scozzafava, S. Parkkila and C. T. Supuran, *J. Med. Chem.*, 2009, **53**, 850-854.

250. L. Dubois, S. Peeters, N. G. Lieuwes, N. Geusens, A. Thiry, S. Wigfield, F. Carta, A. McIntyre, A. Scozzafava, J.-M. Dogné, C. T. Supuran, A. L. Harris, B. Masereel and P. Lambin, *Radiother. Oncol.*, 2011, **99**, 424-431.
251. C. Wang, C. Wu, J. Zhu, R. H. Miller and Y. Wang, *J. Med. Chem.*, 2011, **54**, 2331-2340.
252. N. Touisni, A. Maresca, P. C. McDonald, Y. Lou, A. Scozzafava, S. Dedhar, J.-Y. Winum and C. T. Supuran, *J. Med. Chem.*, 2011, **54**, 8271-8277.
253. P. C. McDonald, J.-Y. Winum, C. T. Supuran and S. Dedhar, *Oncotarget*, 2012, **3**, 84-97.
254. P. McDonald and S. Dedhar, in *Carbonic Anhydrase: Mechanism, Regulation, Links to Disease, and Industrial Applications*, eds. S. C. Frost and R. McKenna, Springer Netherlands, 2014, vol. 75, ch. 13, pp. 255-269.
255. Y. Lou, P. C. McDonald, A. Oloumi, S. Chia, C. Ostlund, A. Ahmadi, A. Kyle, U. auf dem Keller, S. Leung, D. Huntsman, B. Clarke, B. W. Sutherland, D. Waterhouse, M. Bally, C. Roskelley, C. M. Overall, A. Minchinton, F. Pacchiano, F. Carta, A. Scozzafava, N. Touisni, J.-Y. Winum, C. T. Supuran and S. Dedhar, *Cancer Res.*, 2011, **71**, 3364-3376.
256. R. P. Feynman, *Engineering and science*, 1960, **23**, 22-36.
257. N. Taniguchi, *Proc. Int. Conf. Prod. Eng.* 1974.
258. M. K. Teli, S. Mutalik and G. K. Rajanikant, *Curr. Pharm. Des.*, 2010, **16**, 1882-1892.
259. J. Venugopal, M. P. Prabhakaran, S. Low, A. T. Choon, Y. Z. Zhang, G. Deepika and S. Ramakrishna, *Curr. Pharm. Des.*, 2008, **14**, 2184-2200.
260. M. Ferrari, *Nat. Rev. Cancer*, 2005, **5**, 161.
261. J. R. Heath and M. E. Davis, *Annu. Rev. Med.*, 2008, **59**, 251-265.
262. M. E. Davis and D. M. Shin, *Nat. Rev. Drug Discov.*, 2008, **7**, 771.
263. W. H. Gmeiner and S. Ghosh, *Nanotechnol. Rev.*, 2015, **3**, 111-122.
264. V. L. Silva and W. T. Al-Jamal, *J. Control. Release*, 2017, **253**, 82-96.
265. T. A. P. F. Doll, R. Dey and P. Burkhard, *J. Nanobiotechnol.*, 2015, **13**, 73.
266. D. R. Elias, A. Poloukhtine, V. Popik and A. Tsourkas, *Nanomedicine*, 2013, **9**, 194-201.

267. R. F. Minchin and D. J. Martin, *Endocrinology*, 2010, **151**, 474-481.
268. S. K. Nune, P. Gunda, P. K. Thallapally, Y.-Y. Lin, M. L. Forrest and C. J. Berkland, *Expert Opin. Drug Deliv.*, 2009, **6**, 1175-1194.
269. F. C. Cortezon-Tamarit, PhD thesis, University of Bath, Bath, 2016.
270. S. S. Malapure, S. Bhushan, R. Kumar and S. Bharati, *2018*, 2018, **5**, 10.
271. A. Polyak and T. L. Ross, *Curr Med Chem*, 2017, **24**, 1-24.
272. S. Guerrero, J. R. Herance, S. Rojas, J. F. Mena, J. D. Gispert, G. A. Acosta, F. Albericio and M. J. Kogan, *Bioconjugate Chem.*, 2012, **23**, 399-408.
273. R. Torres Martin de Rosales, R. Tavaré, R. L. Paul, M. Jauregui-Osoro, A. Protti, A. Glaria, G. Varma, I. Szanda and P. J. Blower, *Angew. Chem. Int. Ed. Engl.*, 2011, **50**, 5509-5513.
274. R. Torres Martin de Rosales, R. Tavaré, A. Glaria, G. Varma, A. Protti and P. J. Blower, *Bioconjugate Chem.*, 2011, **22**, 455-465.
275. D. L. J. Thorek, D. Ulmert, N.-F. M. Diop, M. E. Lupu, M. G. Doran, R. Huang, D. S. Abou, S. M. Larson and J. Grimm, *Nat. Commun.*, 2014, **5**, 3097.
276. M. Lledos, V. Mirabello, S. Sarpaki, H. Ge, H. J. Smugowski, L. Carroll, E. O. Aboagye, F. I. Aigbirhio, S. W. Botchway, J. R. Dilworth, D. G. Calatayud, P. K. Plucinski, G. J. Price and S. I. Pascu, *Chem. Nano. Mat.*, 2018, **4**, 361-372
277. C. Perez-Campana, V. Gomez-Vallejo, M. Puigivila, A. Martin, T. Calvo-Fernandez, S. E. Moya, R. F. Ziolo, T. Reese and J. Llop, *ACS Nano*, 2013, **7**, 3498-3505.
278. Z. Wu, S. Yang and W. Wu, *Nanoscale*, 2016, **8**, 1237-1259.
279. B. P. Burke, C. Cawthorne and S. J. Archibald, *Philos. Trans. A Maths, Phys Eng. Sci.*, 2017, **375**.
280. T. Tang, J. Garcia and A. Y. Louie, in *Design and Applications of Nanoparticles in Biomedical Imaging*, eds. J. W. M. Bulte and M. M. J. Modo, Springer International Publishing, Cham, 2017, ch10, pp. 205-228.
281. J. R. Lamb and J. P. Holland, *J Nucl Med*, 2017, DOI: 10.2967/jnumed.116.187419.
282. N. Lee, D. Yoo, D. Ling, M. H. Cho, T. Hyeon and J. Cheon, *Chemic.Rev.*, 2015, **115**, 10637-10689.
283. V. M. Blanco, Z. Chu, K. LaSance, B. D. Gray, K. Y. Pak, T. Rider, K. D. Greis and X. Qi, *Oncotarget*, 2016, **7**, 32866-32875.

284. D. W. Hwang, H. Y. Ko, J. H. Lee, H. Kang, S. H. Ryu, I. C. Song, D. S. Lee and S. Kim, *J. Nucl. Med.*, 2010, **51**, 98-105.
285. Y. Hancock, *J. Phys. D*, 2011, **44**, 473001.
286. G. Gonçalves, M. Vila, I. Bdikin, A. de Andrés, N. Emami, R. A. S. Ferreira, L. D. Carlos, J. Grácio and P. A. A. P. Marques, *Sci. Rep.*, 2014, **4**, 6735.
287. S. Goenka, V. Sant and S. Sant, *J. Control. Release*, 2014, **173**, 75-88.
288. K. S. Novoselov, A. K. Geim, S. V. Morozov, D. Jiang, Y. Zhang, S. V. Dubonos, I. V. Grigorieva and A. A. Firsov, *Science*, 2004, **306**, 666-669.
289. M. Rahman, S. Akhter, M. Z. Ahmad, J. Ahmad, R. T. Addo, F. J. Ahmad and C. Pichon, *Nanomedicine*, 2015, **10**, 2405-2422.
290. M. R. Karim and S. Hayami, in *Graphene Materials-Advanced Applications*, InTech, 2017.
291. X. Sun, Z. Liu, K. Welsher, J. T. Robinson, A. Goodwin, S. Zaric and H. Dai, *Nano Res.*, 2008, **1**, 203-212.
292. H. Bao, Y. Pan, Y. Ping, N. G. Sahoo, T. Wu, L. Li, J. Li and L. H. Gan, *Small*, 2011, **7**, 1569-1578.
293. L. Zhang, J. Xia, Q. Zhao, L. Liu and Z. Zhang, *Small*, 2010, **6**, 537-544.
294. M. Orecchioni, R. Cabizza, A. Bianco and L. G. Delogu, *Theranostics*, 2015, **5**, 710-723.
295. J. A. Tyson, D. G. Calatayud, V. Mirabello, B. Mao and S. I. Pascu, *Adv. Inorg. Chem.*, 2016, **68**, 397-440.
296. K. Yang, S. Zhang, G. Zhang, X. Sun, S.-T. Lee and Z. Liu, *Nano Lett.*, 2010, **10**, 3318-3323.
297. G. Gollavelli and Y. C. Ling, *Biomaterials*, 2012, **33**, 2532-2545.
298. X. Huang, S. Lee and X. Chen, *Am. J. Nucl. Med. Mol. Imaging*, 2011, **1**, 3-17.
299. Y. Zhou, X. Jing and Y. Chen, *J. Mater. Chem. B*, 2017, **5**, 6451-6470.
300. T. Jiao, R. Xing, L. Zhang and J. Zhou, in *Nano/Micro-Structured Materials for Energy and Biomedical Applications: Latest Developments, Challenges and Future Directions*, eds. B. Li and T. Jiao, Springer Singapore, Singapore, 2018, ch7, pp. 227-254.

301. G. Miao, H. Jie, D. Yibin, S. He, M. Yufei, Z. Mengxin, Z. Aijun, L. Yanli, H. He, W. Yangyun, Y. Xiangliang, Z. Zhijun and C. Huabing, *Adv. Funct. Mater.*, 2015, **25**, 58-58.

302. A. Deb and V. R, *Int. J. Biol. Macromol.*, 2018, **107**, 2320-2333.

303. Y. Zeng, Z. Yang, H. Li, Y. Hao, C. Liu, L. Zhu, J. Liu, B. Lu and R. Li, *Sci. Rep.*, 2017, **7**, 43506.

304. P. Yongzheng, B. Hongqian, S. N. Gopal, W. Tongfei and L. Lin, *Adv. Funct. Mater.*, 2011, **21**, 2754-2763.

305. T. Yan, H. Zhang, D. Huang, S. Feng, M. Fujita and X. D. Gao, *Nanomaterials (Basel)*, 2017, **7**.

306. A. B. Seabra, A. J. Paula, R. de Lima, O. L. Alves and N. Duran, *Chem. Res. Toxicol.*, 2014, **27**, 159-168.

307. M. Rahman, M. Z. Ahmad, I. Kazmi, S. Akhter, M. Afzal, G. Gupta, F. Jalees Ahmed and F. Anwar, *Expert. Opin. Drug Deliv.*, 2012, **9**, 367-381.

308. H. Golzar, F. Yazdian, M. Hashemi, M. Omidi, D. Mohammadrezaei, H. Rashedi, M. Farahani, N. Ghasemi, J. Shabani shayeh and L. Tayebi, *New Journal of Chemistry*, 2018, **42**, 13157-13168

309. M.-L. Chen, J.-W. Liu, B. Hu, M.-L. Chen and J.-H. Wang, *Analyst*, 2011, **136**, 4277-4283.

310. J. Ge, M. Lan, B. Zhou, W. Liu, L. Guo, H. Wang, Q. Jia, G. Niu, X. Huang, H. Zhou, X. Meng, P. Wang, C. S. Lee, W. Zhang and X. Han, *Nat. Commun.*, 2014, **5**, 4596.

311. C. Peng, W. Hu, Y. Zhou, C. Fan and Q. Huang, *Small*, 2010, **6**, 1686-1692.

312. K. Welsher, Z. Liu, S. P. Sherlock, J. T. Robinson, Z. Chen, D. Daranciang and H. Dai, *Nat. Nanotechnol.*, 2009, **4**, 773-780.

313. K. Yang, L. Feng, H. Hong, W. Cai and Z. Liu, *Nat. Protoc.*, 2013, **8**, 10.1038/nprot.2013.1146.

314. S. Shi, K. Yang, H. Hong, H. F. Valdovinos, T. R. Nayak, Y. Zhang, C. P. Theuer, T. E. Barnhart, Z. Liu and W. Cai, *Biomaterials*, 2013, **34**, 3002-3009.

315. G. Gollavelli and Y.-C. Ling, *Biomaterials*, 2014, **35**, 4499-4507.

316. S. H. Hu, Y. W. Chen, W. T. Hung, I. W. Chen and S. Y. Chen, *Adv. Mater.*, 2012, **24**, 1748-1754.

Chapter 2: New thiosemicarbazonato complexes rely on mono(substituted) ligands: design, synthesis and characterisation

2.1. Overview

In the late 1950's, E. Skipper and co-workers observed an antileukemic activity in a family of compounds known as thiosemicarbazones (TSC). Their studies introduced for the first time these compounds, along with their derivatives, as potential antitumoral therapeutics.[1] Since then, they have been studied and developed by a number of research groups, with a special interest in their ability to chelate a variety of transition metals (such as Cu(II), Fe(II/III), Zn(II), Ga(III)), where these materials have the potential of being exploited as antineoplastic drugs.[2-4] In the last decades, these chelators have been related not only with the formation of reactive oxygen species (ROS)[4-8], but also with the blockage of hypoxia through the stabilization of HIF-1α.[9-12] In this context, two different aspects concerning the chemistry and the biological properties of TSC acenaphthenequinone mono(substituted) ligands have been explored by the Pascu and Dilworth groups over the last 10 years. Studies have been also carried out for developing novel metal complexes with applications as diagnostic multimodal imaging agents of cancerous diseases.

While a variety of thiosemicarbazone substituents (alkyl, allyl, aryl) and metallic species (Cu(II), Zn(II), Ni(II), Ga(III)) have been explored for acenaphthenequinone-based compounds, their chemistry has been limited to the bis(substituted) derivatives and mainly to the symmetric ones. So, the aim of the work presented in this chapter was to develop a library of mono(substituted) ligands that could be later used in the chelation of asymmetric bis(thiosemicarbazonato) complexes. In addition, a synthetic strategy for the corresponding non-radiolabelled or radiolabelled metal coordinated derivatives was also developed and the complexes were evaluated for their *in vitro* properties.

2.2. Synthesis of thiosemicarbazonate mono(substituted) complexes

2.2.1. Synthesis of mono(substituted) ligands

The synthesis towards a variety of thiosemicarbazone mono(substituted) substituents has been extensively studied by the Pascu group. In this sense, a recent synthetic breakthrough was based on a microwave (μW) assisted reaction between a commercially available thiosemicarbazide compound and an acenaphthenequinone moiety under slightly acidic conditions (**Scheme 4**).[13, 14]

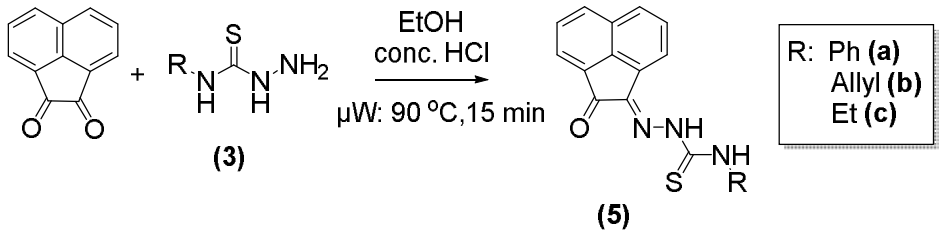

Scheme 4: Synthesis of mono(substituted) ligands with commercially available thiosemicarbazides.

In our case, the synthesis of non-commercial thiosemicarbazides was introduced. The aim was to synthesise a mono(substituted) ligand able to react under the conditions required for a "click" reaction. In order to obtain novel thiosemicarbazides, diethyl amines were converted into their corresponding methyl dithiocarbamates and subsequently transformed into thiosemicarbazides by hydrazinolysis (**Scheme 5**).

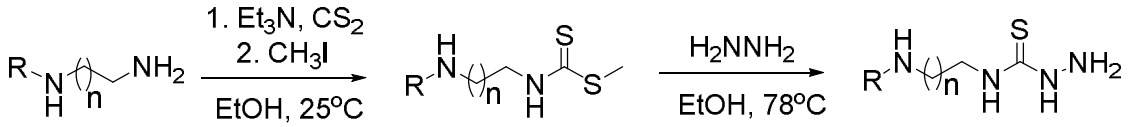

Scheme 5: Synthetic route for the synthesis of new thiosemicarbazides.

The synthesis of thiosemicarbazides with a pendant propargyl group was challenging since the triple bond tended to react with the sulphur group forming a cyclised by-product (**Scheme 6**) which was isolated during the attempted optimisation. Suitable crystals for single crystal X-ray were obtained from DMSO solution for the cyclic by-product and the molecular structure is presented below (**Figure 15**).

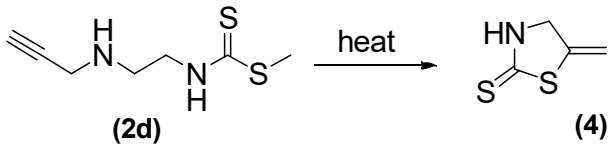

Scheme 6: Cyclisation reaction of methyl (2-(prop-2-yn-1-ylamino)ethyl)carbamodithioate (**2**) to 5-methylene-2-(l1-sulfanyl)thiazolidine (**4**).

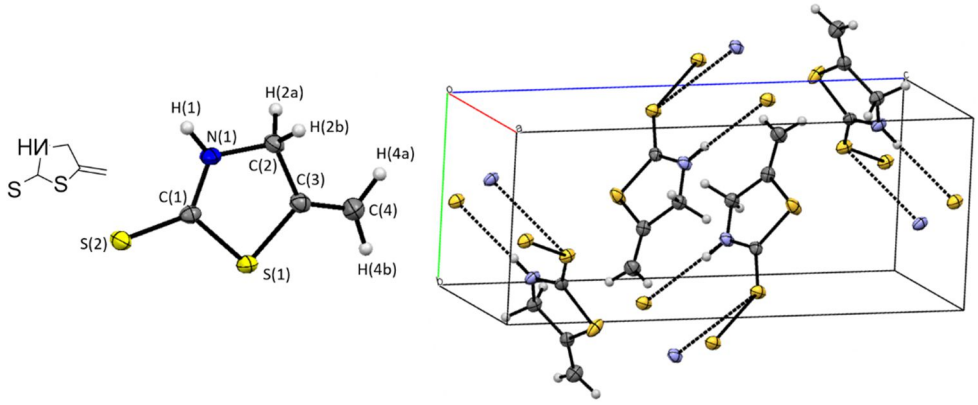

Figure 18: Molecular structures of 5-methylene-2-(l1-sulfanyl)thiazolidine (**4**). Thermal ellipsoids at 50% probability.

The structure revealed that a 5-exo-dig ring closure reaction had occurred. This type of reaction is favourable according to Baldwin's rules. More specifically, the cyclisation reaction between the propargyl group and the sulphur leads to the formation of a new bond (C1-S1) and a five-membered ring with an exocyclic C=C double bond. (**Figure 18**) A summary of bond lengths is presented in **Table 2**.

Table 2: Bond lengths for the 5-methylene-2-(l1-sulfanyl)thiazolidine (**4**).

Bond	Bond Length (Å)	Bond	Bond Length (Å)
S(2)-C(1)	1.6686(16)	**C(2)-C(3)**	1.511(2)
S(1)-C(1)	1.7499(16)	**C(2)-H(2Aa)**	0.9900
S(1)-C(3)	1.7735(16)	**C(2)-H(2b)**	0.9900
N(1)-C(1)	1.3252(19)	**C(3)-C(4)**	1.315(2)
N(1)-C(2)	1.452(2)	**C(4)-H(4a)**	0.9500
N(1)-H(1)	0.84(2)	**C(4)-H(4b)**	0.9500

To avoid the ring closure reaction, we attempted to couple the mono(substituted) ligand with 4-ethynylbenzaldehyde. However, the imine bond which is required for subsequent steps was unstable. The reduction of the imine bond was challenging because the structure of the mono(substituted) precursor contains other imine, hydrazine and thiocarbonyl bonds that might also be affected during the reaction (**Scheme 8**, compound **5**). To overcome all these difficulties, the use of different benzylamines was introduced for the synthesis of compounds such as thiosemicarbazides (**Scheme 7**). The phenyl ring could eliminate the side reaction of the triple bond with the sulphur group. In addition, the shorter acrylic chain as well as the absence of an amino group would prevent any internal cyclisation. Our attempts led us to a successful synthetic methodology for a new hydrazide series which were fully characterised by NMR spectroscopy and mass spectrometry. Some of them were additionally characterised by X-ray crystallography when suitable crystals were obtained. In **Figures 19** and **20,** the crystal structures of the formed products are presented as obtained on both steps of the synthesis (**2e** and **3e**).

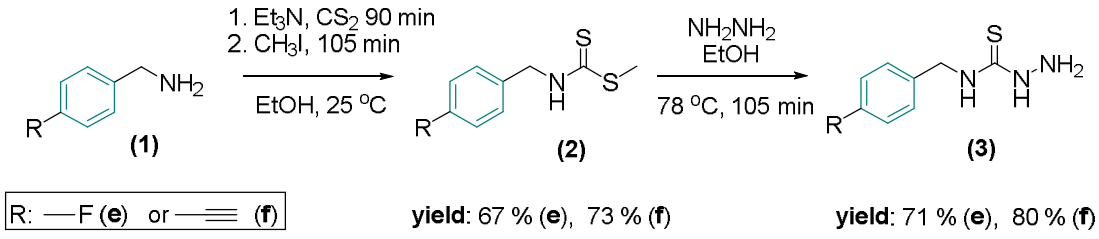

Scheme 7: Synthesis of new thiosemicarbazides containing a phenyl ring (blue) in their structure to avoid undesirable production of by-products.

In particular, suitable crystals for single crystal X-ray were obtained from the mother liquor for both compounds, **2e** and **3e**. Both compounds were crystallised in the triclinic system (Tables S3 and S5, Appendix) (all three axes and all three angles are unequal to each other). The crystal unit cell is formed by 2 molecules for compound **2e** and 4 molecules for compound **3e** (**Figures 19** and **20**). A summary regarding the lengths for both methyl thiocarbamate (**2e**) and thiosemicarbazide (**3e**) derivatives is presented in **Tables 3** and **4** respectively.

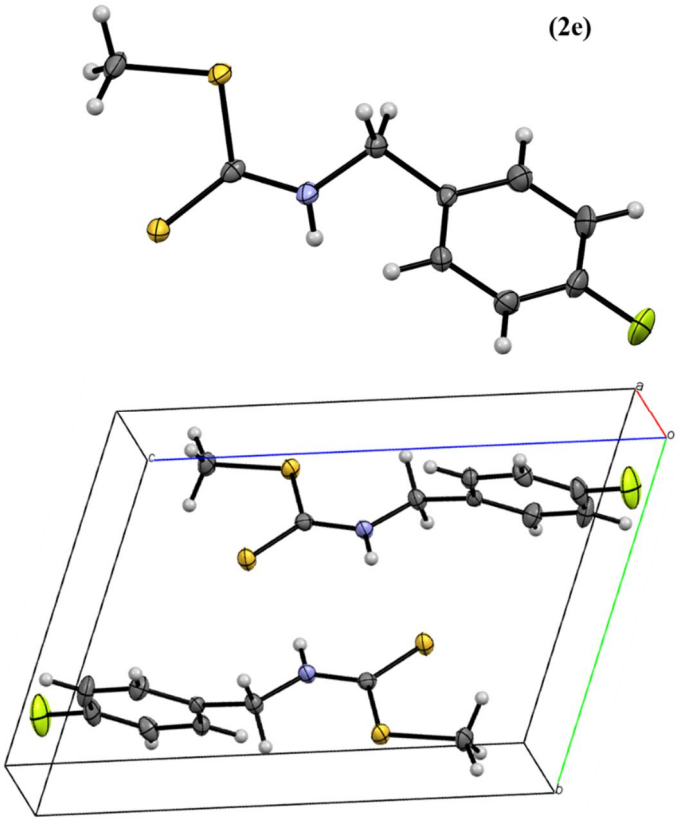

Figure 19: Molecular structure of methyl (4-fluorobenzyl)carbamodithioate (**2e**). Thermal ellipsoids at 50% probability.

Table 3: Selected bond lengths for the methyl (4-fluorobenzyl)carbamodithioate (**2e**).

Bond	Bond Length (Å)	Bond	Bond Length (Å)
S(1)-C(2)	1.763(2)	**C(4)-C(9)**	1.386(3)
S(1)-C(1)	1.793(2)	**C(4)-C(5)**	1.388(3)
S(2)-C(2)	1.673(2)	**C(5)-C(6)**	1.386(3)
N(1)-C(2)	1.328(3)	**C(6)-C(7)**	1.368(3)
N(1)-C(3)	1.462(3)	**C(7)-F**	1.358(2)
C(3)-C(4)	1.509(3)	**C(7)-C(8)**	1.371(4)

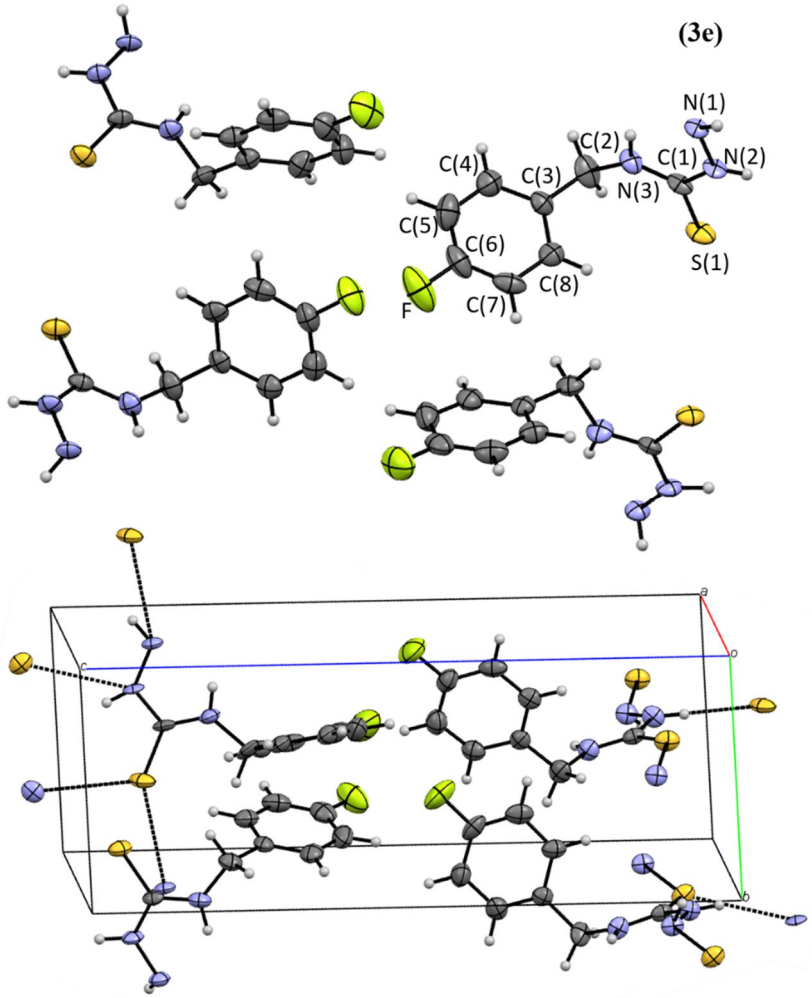

Figure 20: Molecular structures of N-(4-fluorobenzyl)hydrazinecarbothioamide (**3e**). Thermal ellipsoids at 50% probability.

Table 4: Selected bond lengths for the N-(4-fluorobenzyl)hydrazinecarbothioamide (**3e**).

Bond	Bond Length (Å)	Bond	Bond Length (Å)
C(1)-N(3)	1.319(9)	**C(4)-C(5)**	1.396(12)
C(1)-N(2)	1.354(8)	**C(5)-C(6)**	1.367(13)
C(1)-S(1)	1.697(7)	**C(6)-F(1)**	1.354(9)
C(2)-N(3)	1.471(8)	**C(6)-C(7)**	1.393(13)
C(3)-C(8)	1.371(11)	**C(7)-C(8)**	1.393(12)
C(3)-C(4)	1.388(10)		

In the next step the synthesis of the mono(substituted) ligands was achieved, as described previously. In an acidic environment, under microwave irradiation, a coupling reaction between the new thiosemicarbazides (**3e**, **3f**) and acenaphthenequinone took place at 90 °C for 20 minutes (**Scheme 8**). The crude product was then washed by *vacuum* filtration yielding a yellowish compound in both cases. To increase the purity of the product the EtOH/HCl solution was replaced by acidic acid. Both thiosemicarbazide derivatives (**3e** and **3f**) appeared to be more soluble in acidic acid as opposed to acidified ethanol. The crystal structures of the two new mono(substituted) ligands (**5e**, **5f**) are shown in the following figures (**Figures 21** and **22**).

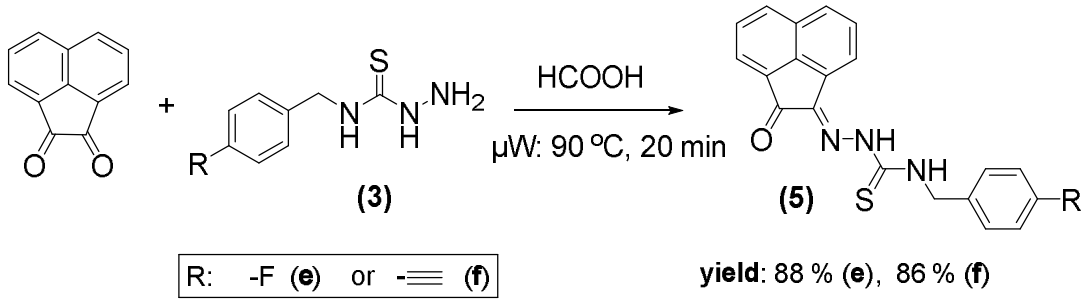

Scheme 8: Preparation of mono(substituted) ligands with the new synthesised thiosemicarbazides.

The structure revealed that a condensation reaction between the carbonyl group and the amine occurred forming an imine bond (C12-N1) (**Figure 21** and **22**). Suitable crystals for single crystal X-ray were obtained from DMSO solution for both compounds, **5e** and **5f**. Both compounds crystallise in the sphenoidal orthorhombic system (Tables S7 and S9, Appendix) (all three axes are unequal in length, all are perpendicular to each other) and the crystal cell unit is formed by 4 molecules (**Figures 21** and **22**). A summary of their bond lengths is presented in **Tables 5** and **6**.

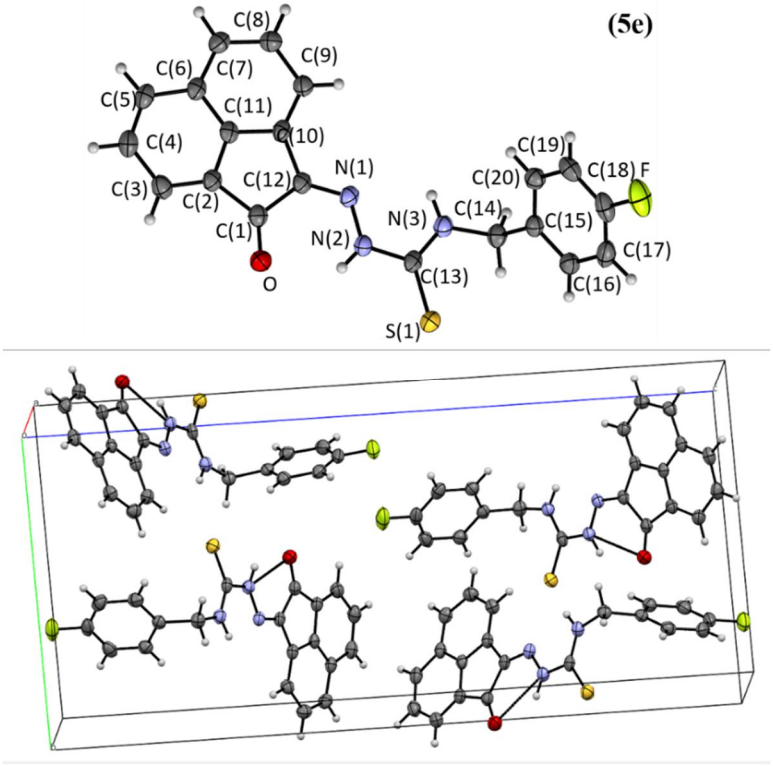

Figure 21: Molecular structure of 4-F-benzyl-3-thiosemicarbazone acenaphthenequinone (**5e**). Thermal ellipsoids at 50% probability.

Table 5: Selected bond lengths for the 4-F-benzyl-3-thiosemicarbazone acenaphthenequinone (**5e**).

Bond	Bond Length (Å)	Bond	Bond Length (Å)
C(1)-O	1.215(3)	**C(10)-C(12)**	1.466(3)
C(1)-C(2)	1.496(3)	**C(12)-N(1)**	1.294(3)
C(1)-C(12)	1.517(3)	**C(13)-N(3)**	1.333(3)
C(2)-C(3)	1.372(4)	**C(13)-N(2)**	1.378(3)
C(2)-C(11)	1.405(4)	**C(13)-S**	1.671(3)
C(3)-C(4)	1.420(4)	**C(14)-N(3)**	1.459(3)
C(4)-C(5)	1.364(4)	**C(14)-C(15)**	1.514(3)
C(5)-C(6)	1.424(4)	**C(15)-C(16)**	1.385(4)
C(6)-C(11)	1.402(3)	**C(15)-C(20)**	1.392(4)
C(6)-C(7)	1.412(4)	**C(17)-C(18)**	1.366(5)
C(7)-C(8)	1.378(4)	**C(18)-F**	1.369(3)
C(8)-C(9)	1.426(4)	**C(18)-C(19)**	1.374(5)
C(9)-C(10)	1.369(4)	**C(19)-C(20)**	1.389(4)
C(10)-C(11)	1.408(3)	**N(1)-N(2)**	1.352(3)

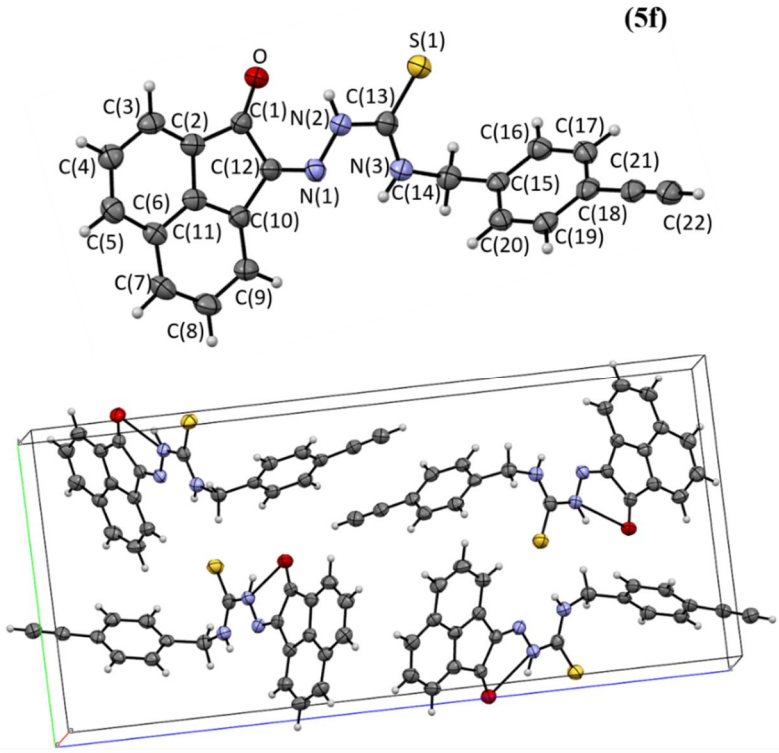

Figure 22: Molecular structure of 4-ethynylbenzyl-3-thiosemicarbazone acenaphthenequinone (**5f**). Thermal ellipsoids at 50% probability.

Table 6: Selected bond lengths for the 4-ethynylbenzyl-3-thiosemicarbazone acenaphthenequinone (**5f**).

Bond	Bond Length Å	Bond	Bond Length Å
S-C(13)	1.673(5)	**C(6)-C(7)**	1.411(6)
N(1)-C(12)	1.297(6)	**C(7)-C(8)**	1.370(7)
N(1)-N(2)	1.339(5)	**C(8)-C(9)**	1.412(7)
N(2)-C(13)	1.365(6)	**C(9)-C(10)**	1.370(6)
N(3)-C(13)	1.335(6)	**C(10)-C(11)**	1.406(7)
N(3)-C(14)	1.465(6)	**C(10)-C(12)**	1.464(6)
O-C(1)	1.217(6)	**C(14)-C(15)**	1.513(6)
C(1)-C(2)	1.483(7)	**C(15)-C(16)**	1.372(6)
C(1)-C(12)	1.514(6)	**C(15)-C(20)**	1.388(7)
C(2)-C(3)	1.370(7)	**C(16)-C(17)**	1.392(7)
C(2)-C(11)	1.408(6)	**C(17)-C(18)**	1.392(7)
C(3)-C(4)	1.409(7)	**C(18)-C(19)**	1.396(7)
C(4)-C(5)	1.366(7)	**C(18)-C(21)**	1.441(7)
C(5)-C(6)	1.407(7)	**C(19)-C(20)**	1.384(7)
C(6)-C(11)	1.402(6)	**C(21)-C(22)**	1.179(7)

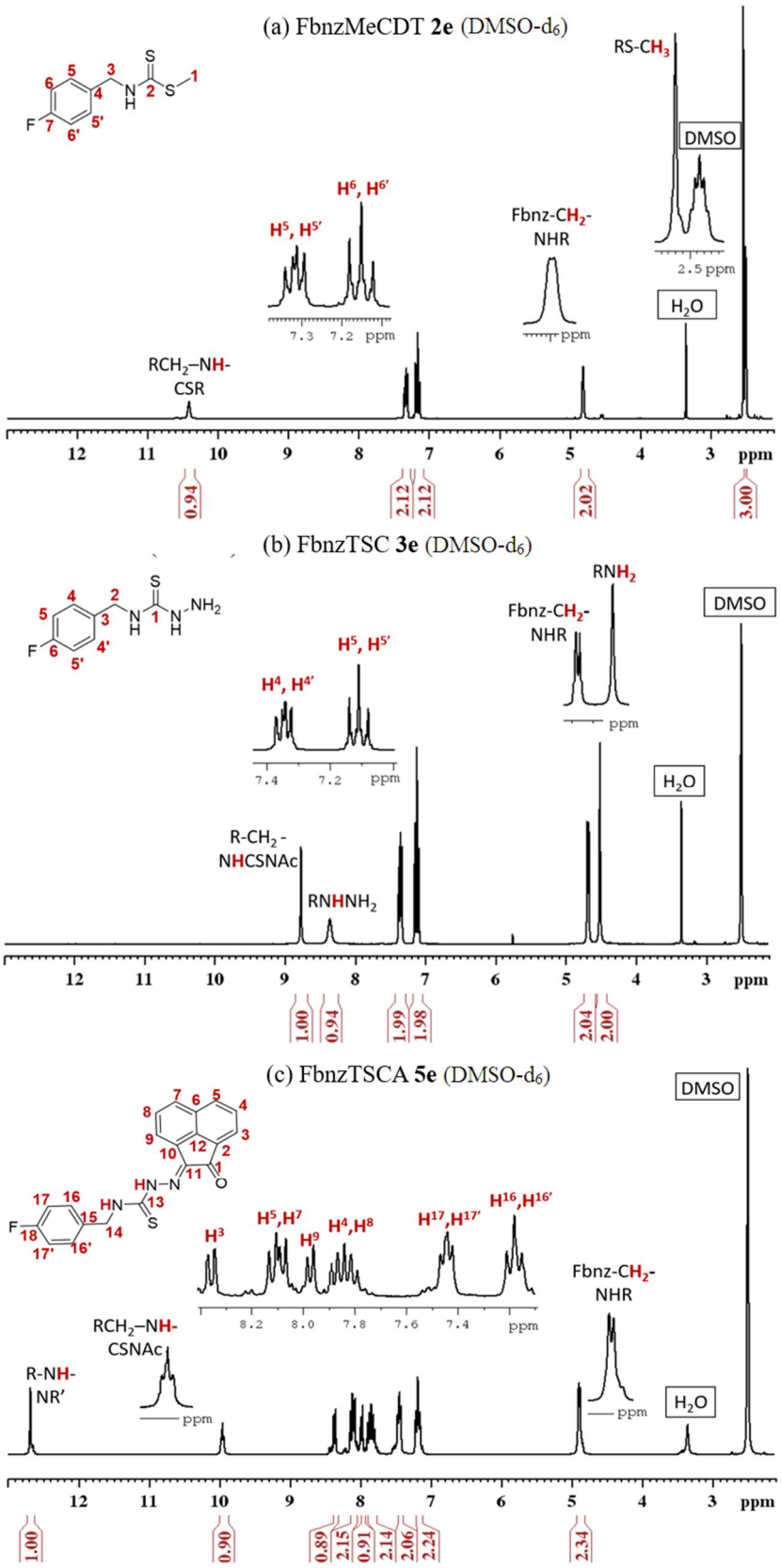

Figure 23: Comparative ^{1}H NMR spectrum (500 MHz, DMSO) of all the steps for the synthesis of mono(substituted) substituent **5e** (FbnzTSCA).

^{1}H NMR spectroscopy was applied in a step by step monitoring of the formation of the mono(substituted) (**5e**) ligand (**Figure 23**). The proton resonance at 10.40 ppm (**Figure 23 a**) corresponds to the secondary amine (RCH_2-*N**H***-CSR) of compound **2e** After the formation of the thiosemicarbazide derivative (**3e**), this resonance is shifted down-field around 2.05 ppm (**Figure 23 b**). In the next step of the synthetic strategy, after the coupling reaction with the acenaphthenequinone unit (**5e**) occurred, the proton resonance is shielded up-field by 1.61 ppm (**Figure 23 c**). Notably, there are characteristic resonances which are formed and disappeared during the synthesis. More specifically, the resonance at 2.5 ppm (**Figure 23 a**) corresponding to the protons of the methyl group from the methyl dithiocarbamate compound (**2e**) only exists in the top spectrum, while the resonance at 4.5 ppm is related to the primary amine (R*N**H**$_2$*) and it can be observed only in the spectrum of thiosemicarbazide derivative (**3e, Figure 23 b**). Finally, in the spectrum that depicts the mono(substituted) precursor **5e,** the aromatic resonances of the acenaphthenequinone moiety (-*C**H***-) are introduced in the region between 7 ppm and 8.5 ppm. All these results are in agreement with the proposed structures.

2.2.2. *Metal coordinated complexes*

The coordination of the mono(substituted) thiosemicarbazone ligands with different metals in methanolic environment under microwave radiation was investigated here. The reactions of the ligands to Zn(II) and Ga(III) were studied in order to form ML_2-type complexes. Each of the ligands acted as a tridentate O/N/S donor and the synthesised compounds present a distorted octahedral geometry. The coordination mode with Zn(II) and Cu(II) is known only for a couple of aliphatic thiosemicarbazone backbones. However, the species with aromatic ligand backbones have not been studied extensively. Different Zn(II) coordinated thiosemicarbazone species, which result from commercially available thiosemicarbazides were first reported by Rodriguez-Argüelles *et al.*.[15] Herein is introduced for the first time the novel synthesis of thiosemicarbazide compounds which were derived from mono(substituted) ligands. Finally, they were coordinated with Zn(II) as metal centre and employing as the heating source microwave-assisted radiation.

The coordination of the mono(substituted) ligands with either Ga(III) or Zn(II) was attempted. The Zn(II) coordination was carried out successfully in an alcoholic

environment under both conditional heating or microwave-assisted radiation with an excess of zinc acetate (**Scheme 9**). The crude products were purified *via* filtration and washed further with methanol, forming different variations of orange solids depending on the initial mono(substituted) ligand used.

The Ga(III) coordinated complex was not obtained regardless of the different conditions applied or when transmetallation from Zn(II) to Ga(III) was attempted. Even though under specific conditions gallium species were present at mass spectra, the results weren't conclusive since the theoretical and experimental isotopic pattern were not in agreement.

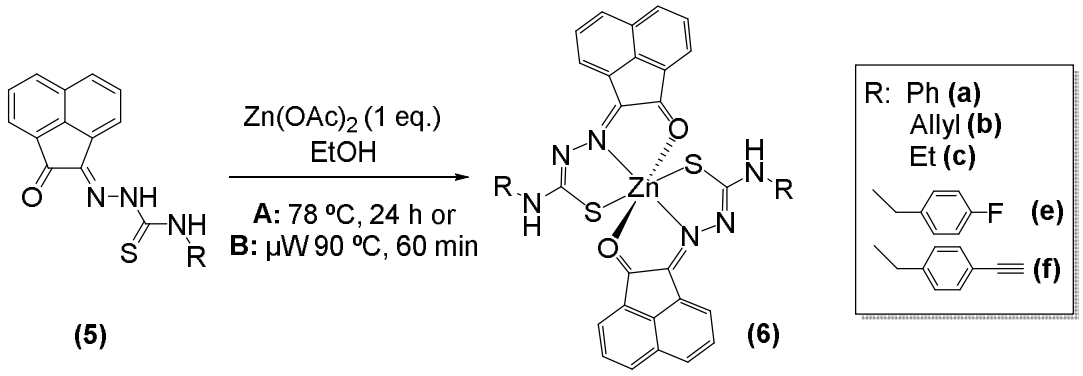

Scheme 9: Synthesis of the mono(substituted) complexes produced from amines.

Furthermore, the comparative NMR spectroscopy, which follows, depicts the formation of the Zn(II)-coordinated mono(substituted) complex from the mono(substituted) ligand, (**5e**) (**Figure 24** from a to the b). In the following NMR, the disappearance of the resonance at 12.62 ppm (**Figure 24 a**) provides strong evidence of a secondary amine (R-N***H***-NR'). This resonance corresponds to the amino function of the thiosemicarbazide group found in the mono(substituted) ligand **5e** (FbnzTSCA). When the mono(substituted) ligands are coordinated with the metal centre of Zn(II) (**6e**) the nitrogen loses its hydrogen so this resonance no longer appears. Additionally, it is shown that the secondary amine resonance related to the fluorobenzylamine (RCH_2-N***H***-CSNA) is duplicated in the **Figure 24 b** spectrum (**6e**) due to the presence of two mono(substituted) ligands (9.00-10.00 ppm). Similar effects can be observed also in the area between 7.00 and 8.60 ppm (**Figure 24**), where the resonances from aromatic hydrogens (***H***-Ar) are depicted, as well as at 4.89 ppm where the (Fbnz-C$\boldsymbol{H_2}$-NHR) unit appears. These results strongly suggest the coordination of two mono(substituted) ligands

in the coordination sphere of Zn(II) which was also confirmed by mass spectrometry (**Figure 25**).

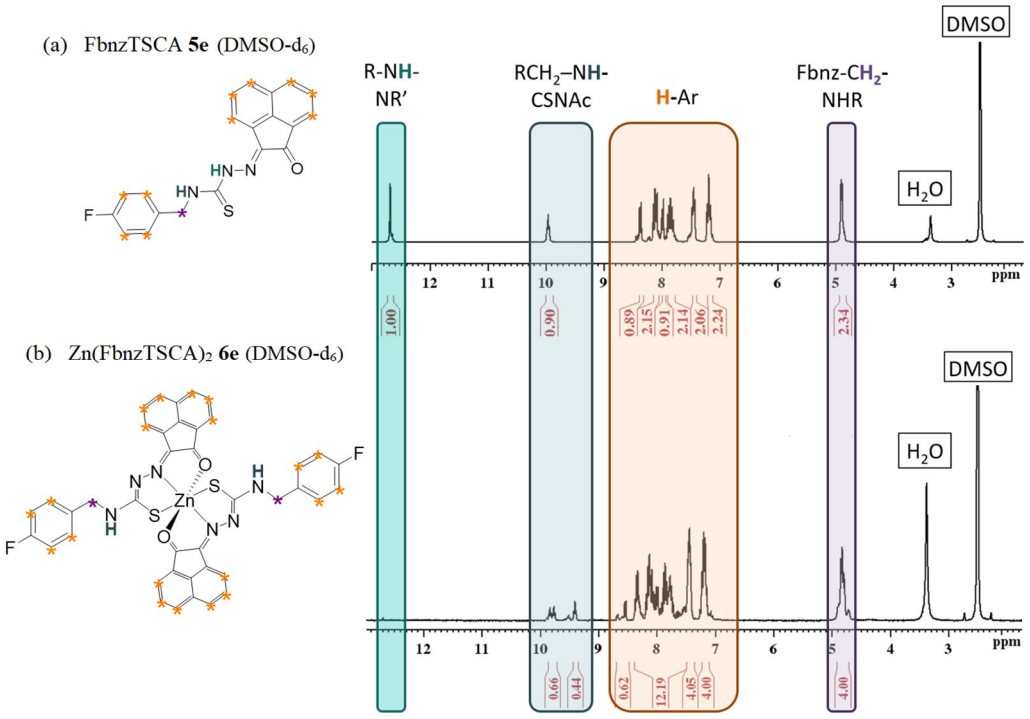

Figure 24: Comparative ^{1}H NMR spectrum (500 MHz, DMSO) of the monosubstituted ligand (FbnzTSCA-**5e**) (a) and its Zn derivative (Zn(FbnzTSCA)$_2$ -**6e**) (b).

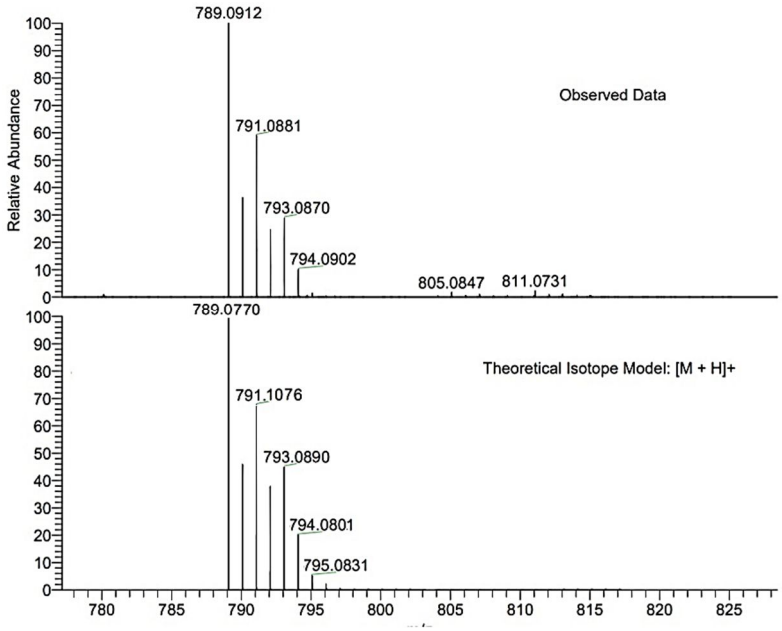

Figure 25: ESI mass spectrometry result for the Zinc(II) [mono (F-benzyl thiosemicarbazonate-acenaphthenequinone]$_2$ (**6e**).

2.3. Radiolabelling of mono(substituted) ligands.

2.3.1. Coordination of mono(substituted) ligands with [^{68}Ga]Ga(III).

The radiolabelling of the mono(substituted) thiosemicarbazone acenaphthenequinone molecules with gallium-68 has not been reported to date. Some examples of mono(substituted) thiosemicarbazone compounds coordinated with copper-64 were investigated by Dilworth's group, but only for aliphatic thiosemicarbazones and not analogues from the aromatic backbone family.[16, 17] In this work it is reported the coordination of the mono(substituted) precursors with gallium(III) for the first time. Even though this reaction was not achieved in a thermodynamic controlled environment (reactions with gallium), it was successful under the kinetic controlled environment that can be found in radiochemical reactions, with gallium-68. The radiolabelling is based on a coordination reaction between two mono(substituted) ligands and [^{68}Ga]Ga(III) (**Scheme 10**), where the ligands probably behave in a similar way than the previously mentioned Zn(II) complexes.

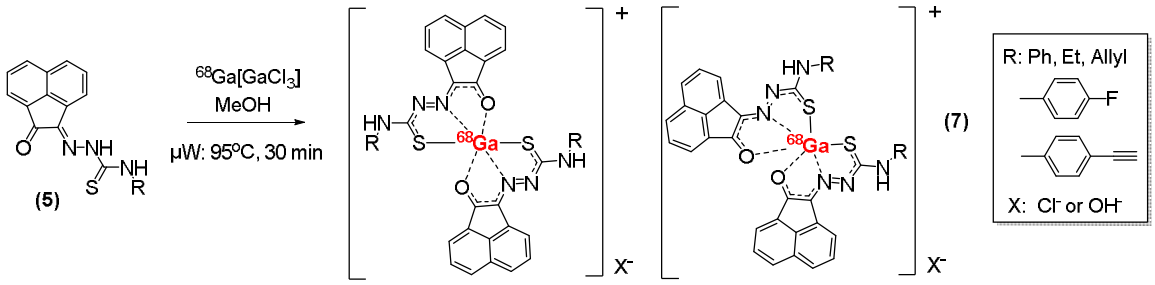

Scheme 10: Reaction regarding the coordination of the mono(substituted) ligands with gallium-68 in aqueous media.

Establishing a protocol in the field of radiolabelling regarding this family of molecules was challenging. Key points of the reaction seem to be the elution of the [^{68}Ga]GaCl$_3$ (aq), the drying procedure of [^{68}Ga]Ga(III), the pH of the reaction and the ratio between the precursor (mono(substituted) ligand) and the [^{68}Ga]GaCl$_3$. Three different eluents were used to optimise the reaction. Acetone/ 0.02M HCl (98%), THF/ 0.02M HCl (98%) was suggested from previous similar experiments[14] and celite/ 0.02M HCl (98%) was used in order to ameliorate the pH adjustment of the reaction. For the experiments carried out with the first two eluents, [^{68}Ga]GaCl$_3$ (aq) was first dried

under a stream of nitrogen at 110 °C for 15 minutes. Despite [^{68}Ga]$GaCl_3$ (aq) being carefully dried in both cases, the eluent of THF/ 0.02M HCl (98%) appeared to result in a much higher radiochemical incorporation (ROI) rather than the acetone elution. For the experiments carried out with celite/ 0.02M HCl (98%) both reactions in dry [^{68}Ga]$GaCl_3$ or in solution were attempted, however none of them were successful.

Table 7: Summary of the experiments carried out on the **5b** mono(substituted) ligand (EtTSCA) for optimisation of the radiolabelling reaction of the ligand with [^{68}Ga]$GaCl_3$ through different conditions. (Note: When a range of pH values are stated this indicates that more than one experiment was carried out at this pH range). All experiments were repeated more than two times.

Solvent	Concertation of 5b (mM)	Buffer NaOAC	Final pH	T (°C) (μW)	Time (min)	R.O.I.
EtOH	0.42	pH 4.5	4.5	95 °C	30-60	-
EtOH	0.42	pH 5.0	5.2-6.4	95 °C	30-60	-
EtOH	0.34	No buffer use	4.5-6.5	95 °C	30-60	-
MeOH	0.34	pH 4.5	4.8	95 °C	30-60	-
MeOH	0.34	pH 5.0	4.8-6.4	95 °C	30-60	-
MeOH	0.34	No buffer use	5.8	95 °C	30-60	✓
MeOH	0.34	No buffer use	~2	95 °C	30-60	-
MeOH	0.34	No buffer use	3.8-6.4	95 °C	30	55-65 %

The use of a buffer was also investigated, but it did not improve the radiochemical incorporation (ROI) of the reaction. **Table 7** shows all the different conditions applied to optimise the reaction using elution of [^{68}Ga]$GaCl_3$ with THF/ 0.02M HCl (98%) solution. Most of the conditions were used with each of the different eluants. The reaction was optimised using the **5b** (EtTSCA) mono(substituted) ligand (2 mg/mL in DMSO) and then attempted with the remaining mono(substituted) ligands.

In more detail, the radiolabelling of the mono(substituted) thiosemicarbazone acenaphthoquinone complexes was achieved as follows. The [^{68}Ga]$GaCl_3$ (aq) was eluted through the generator and trapped in a CXS4 cartridge. It was then washed with 20 mL of H_2O before being eluted with a THF/ 0.02M HCl (98%) solution. Additional washing of the cartridge with water was found to be crucial in order to keep the ROI high. The eluted [^{68}Ga]$GaCl_3$ (aq) was subsequently dried for 10-15 minutes under a nitrogen

stream at 95 °C. Pure methanol was then used to resuspend [^{68}Ga]$GaCl_3$ and the mono(substituted) ligand was added (2 mg/mL in DMSO). This was heated under microwave-assisted (μW) radiation at 95 °C for 30 minutes and injected into a radio-HPLC.

The ROI that is proposed through the radio-HPLC for each monosubstituted ligand is presented in the following table (**Table 8**). The greatest radiochemical incorporations were achieved with ligand **5e** (FbnzTSCA). Despite the various different conditions applied, some of which include adjusting the pH of the reaction or changing the ratio between the mono(substituted) ligand and the [^{68}Ga]$GaCl_3$, it was not possible to achieve as high a ROI for ligands **5a-d** and **5f** as it was for **5e**.

Table 8: Optimum percentage values of the radiochemical incorporation for all the mono(substituted) ligands with gallium-68 applying microwave radiation for 30 minutes at 95 °C. All the reactions were repeated a minimum of two times.

Precursors (mono(substituted) ligands)	Radiochemical incorporation (ROI)
PhTSCA (5a)	70 %
AllylTSCA (5b)	67 %
EtTSCA (5c)	75 %
FbnzTSCA (5e)	98 %
PropbnzTSCA (5f)	55 %

The reaction was also successfully carried out with conventional heating by allowing for a longer reaction time. The HPLC in both cases indicated that the conversion of the mono(substituted) ligand to the respective gallium-68 complex had occurred. However presence of [^{68}Ga]$GaCl_3$ signal was also found indicating that radiolabelling did not proceed to completion (**Figure 26**). As shown in the following figure (**Figure 26**), the reaction in which microwave radiation (red trace) was used had the greatest ROI as opposed to the reaction which underwent conditional heating (grey trace).

In addition the reaction was successfully carried out also with gallium-68 extracted by a cyclotron via the ^{68}Zn(p,n)^{68}Ga reaction in aqueous solution. The eluted [^{68}Ga]$GaCl_3$ (aq) was then trapped in a CXS4 cartridge and the procedure followed was

as stated earlier resulted in a radiolabelled complex with similar ROI as the one stated above.

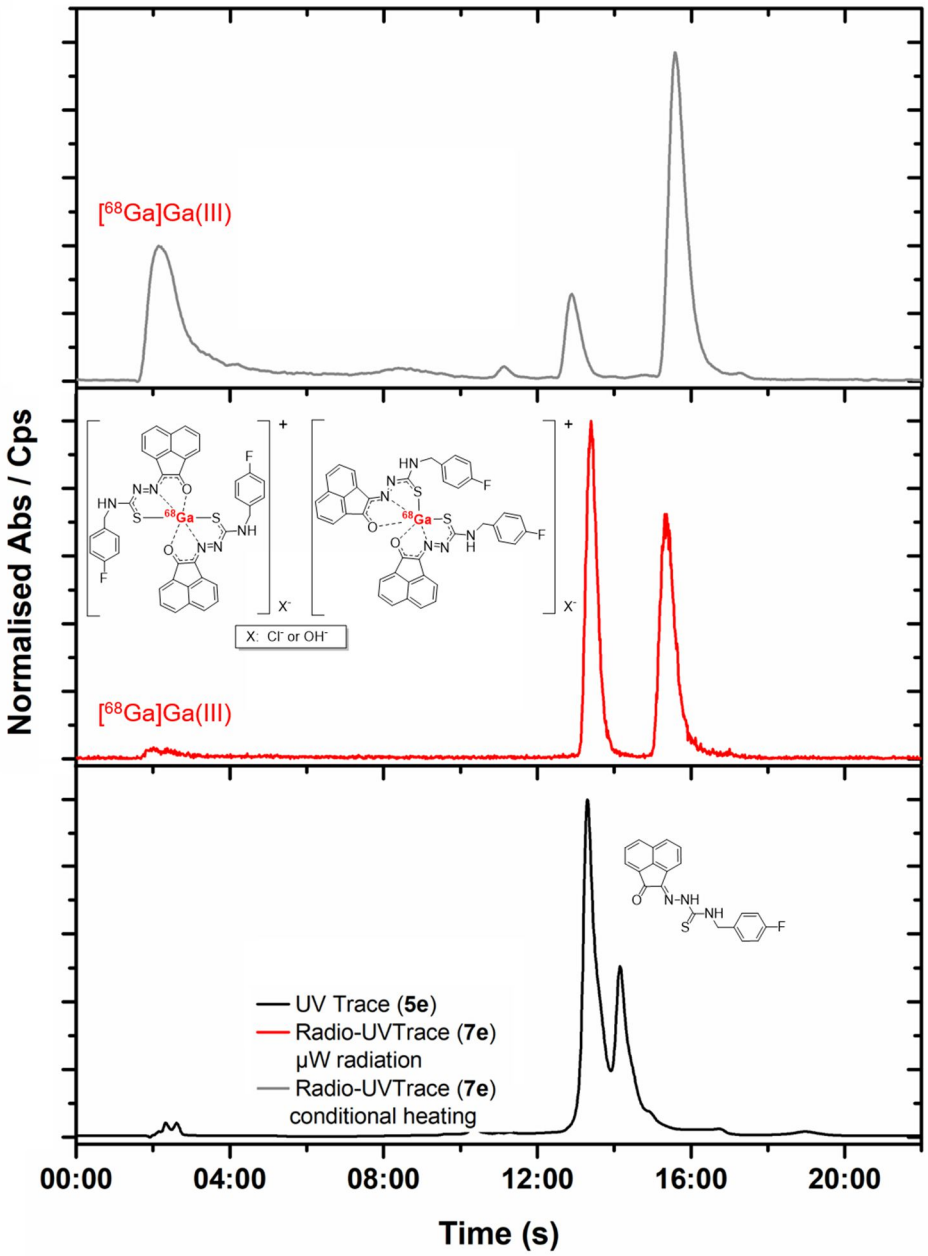

Figure 26: HPLC and radio-HPLC traces for radiolabelling of mono(substituted) ligand (**5e**, black) with aqueous [^{68}Ga]$GaCl_3$ through either microwave-assisted (µW) radiation or conditional heating. **[^{68}Ga]-7e** was formed (red and grey respectively) in both cases, but the radiochemical purity was higher (98 % over 55 %) at the microwave assisted reaction.

Moreover, it was noticed that the ROI was influenced by the ratio between mono(substituted) ligand and [^{68}Ga]$GaCl_3$. We were also interested in scaling up the reaction regarding the radioactivity used to proceed further to *in vitro* experiments.

However, treatment of the same amounts of mono(substituted) ligand with higher activity resulted in low or zero ROI. Thus, it was concluded that the most promising ratio between the mono(substituted) ligand used, the solvent and the [^{68}Ga]GaCl$_3$ was 75 µL of compound/ 1 mL of solvent for 37 MBq of activity.

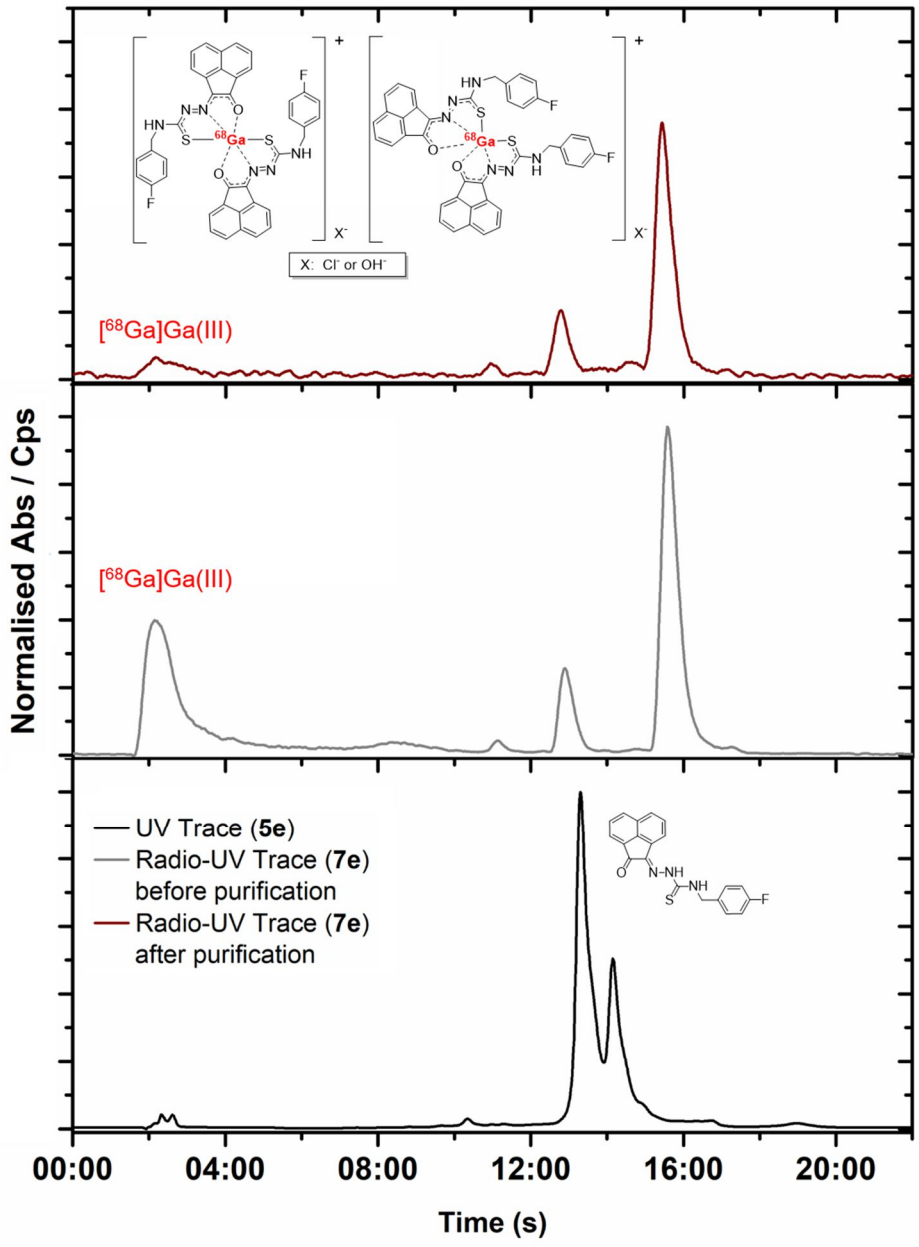

Figure 27: HPLC and radio-HPLC traces for radiolabelling of Fbnz-TSCA mono(substituted) ligand (**5e**, black) with [^{68}Ga]GaCl$_3$. **[^{68}Ga]-7e** was formed (grey) and was the purified (dark red).

A purification procedure was developed to extract only the radiolabelled compound Through the use of a tC18 cartridge. The cartridge was first activated with EtOH and then washed with H_2O before trapping the desired compound. It was further washed with H_2O, to elute all the unchelated [^{68}Ga]Ga(III) traces before it was eluted with a small amount of EtOH. The above figure (**Figure 27**) shows the radio-HPLC (red and grey) and HPLC traces (blue) for the radiolabelling of mono(substituted) ligand (**5e**) with [^{68}Ga]$GaCl_3$ and its purification.

2.3.2. Coupling reaction of the free NH_2-TSCA mono(substituted) ligands with [^{18}F]FBA.

Further to the radiolabelling of the monosubstituted ligands with [^{68}Ga]Ga(III), the possible radiolabelling of the mono(substituted) ligands with ^{18}F was investigated. Preliminary experiments were carried out for the radiolabelling of the free-amine TSCA mono(substituted) ligand (**5h**) with [^{18}F]fluorobenzaldehyde ([^{18}F]FBA). This labelling method is based on a carbonyl addition reaction between an aldehyde and a primary amine which results in the formation of an imine and the loss of the carbonyl oxygen. The same coupling reaction was also successfully carried out with non-radioactive fluorobenzaldehyde (FBA) (**Scheme 11**).

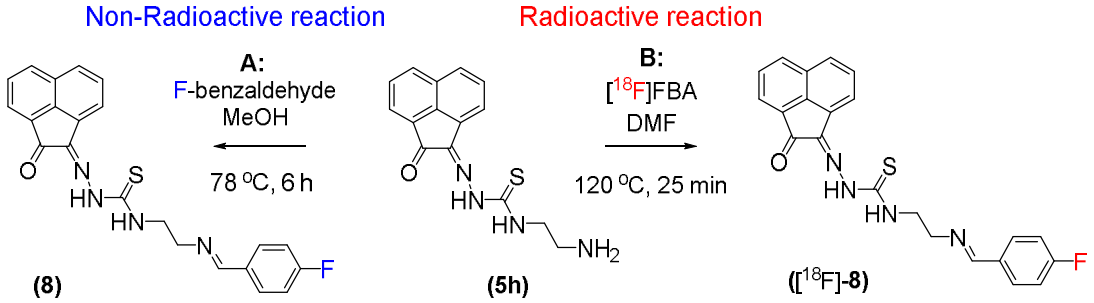

Scheme 11: Coupling reaction between the NH_2TSCA (**5h**) mono(substituted) ligand and either non-radioactive fluorobenzaldehyde (A) or radioactive [^{18}F]fluorobenzaldehyde (B).

Synthesis of [^{18}F]fluorobenzaldehyde was conducted, under the supervision of Chris Barnes at Imperial College London using the FASTlab^{TM} *via* an automated procedure. In the first step, the [^{18}F]fluoride was dried and then was trapped on a Sep-Pak

QMA-carbonate Light Cartridge before being eluted into the reactor using an eluent consisting of Kryptofix K_{222} and $KHCO_3$ in acetonitrile: water (4:1). The content of the reactor was evaporated at 120 ºC under vacuum and a low flow of nitrogen. The 'dried' fluoride was then dissolved with anhydrous acetonitrile and transferred to a vial. The fluorination step was then performed manually. Part of the dried fluoride was added by syringe to a v-bottom vial containing the precursor. The vial was then heated at 90 °C for 15 minutes resulting in consistently >98% radiochemical purity according to radio-HPLC, and then used for further labelling reactions.

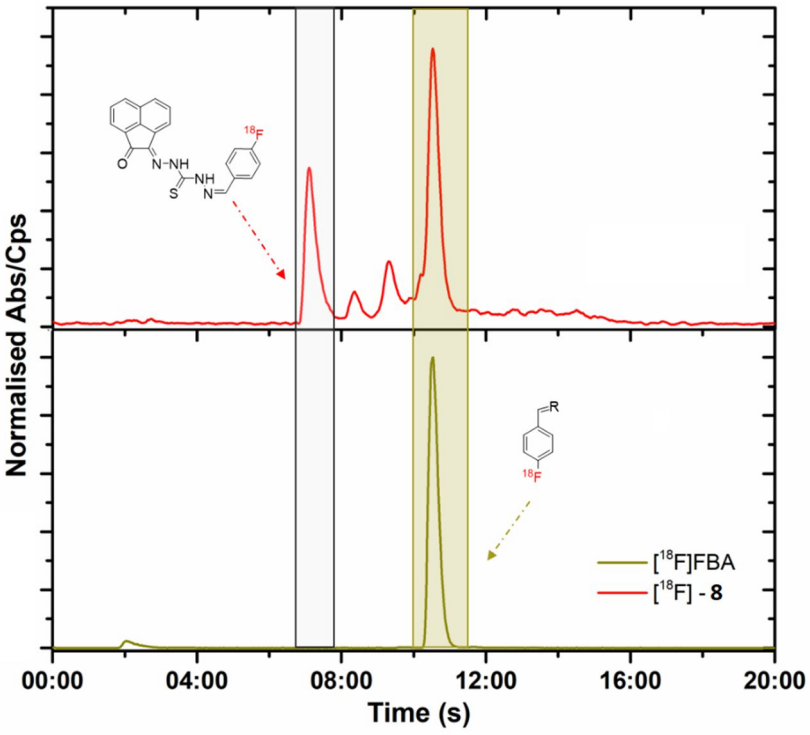

Figure 28: Radio-HPLC traces for radiolabelling of NH_2TSCA mono(substituted) ligand (**5h**) with [^{18}F]FBA. **[^{18}F]-8** was formed (red).

Additionally, in order to find the most efficient conditions for labelling the precursor **5h** (NH_2TSCA), a variety of experiments were conducted evaluating the temperature and the solvents used. The first experiment was carried out using MeOH at 90 °C, but the ROI was very low (3%). Then the temperature was increased at 120 °C and a small augmentation in the ROI followed. Thus, it was decided that a different solvent should be used, suitable for high temperature conditions, regardless the duration of the reaction. Therefore, DMF was employed as a solvent and the reaction was allowed to proceed at

120 °C for 25 minutes, resulting in a ROI of 30 % as shown in the trace below (**Figure 28**).

2.4. *In vitro* evaluation of mono(substituted) precursors and metal complexes

2.4.1. MTT assays

Prior to the application of the asymmetric complexes in biological experiments, preliminary cytotoxicity studies were considered to be necessary in order to determine the working concentration suitable for avoiding concomitant cell damage. A variety of techniques are used for the measurement of cell metabolic activity. The use of tetrazolium salts and more specifically the use of 2-(4,5-dimethyl-2-thiazolyl)-3,5-diphenyl-2H-tetrazolium bromide (MTT) has become a gold standard for the assessment of alterations in cell viability.[18-20] The exact mechanism for the action of MTT is not well understood, but the accepted mechanism suggests that the reduction of MTT dye is caused by nicotinamide species (i.e. NAD(P)H). These species can be found in the cytoplasm and mitochondria of the cells giving rise to the formation of formazan derivatives (**Scheme 12**). Consequently, a colorimetric method was applied which allows the viable cells to convert MTT to formazan species, forming a characteristic purple colour and a maximal absorbance at 570 nm. On the contrary, upon cell death the forementioned reduction can not proceed. This colour differentiation between viable and dead cells is used as a marker in these assays. More specifically, the concentration can be calculated from the absorbance and the number of viable cells in the presence of the compound of interest. It is important prior to absorbance measurement to solubilise the coloured formazan species which are not soluble in cellular media.

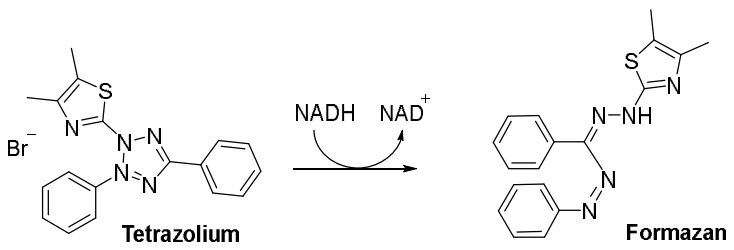

Scheme 12: Formation of the dye detected in MTT assays by biological reduction.

In this work, MTT assays were performed in a range of different concentrations in order to calculate the IC_{50} values for all the mono(substituted) ligands. The viability assays were carried out in both PC-3 and EMT-6 cell lines under normoxic and chemically induced hypoxic conditions ($CoCl_2 \cdot 6H_2O$). Cells were placed in 96-well plates and incubated with the selected compounds in serum medium (1% DMSO) and at 8 different concentrations for 48 hours at 37 ºC. In the following steps, cells were washed with PBS 1-3 times to remove compounds and then the MTT dye was added and incubated for 2 h. MTT reagents were removed and the insoluble formazan species that resulted from this procedure were then solubilised in DMSO prior to cell measurement with a plate reader. The detailed conditions can be found in Chapter 7.

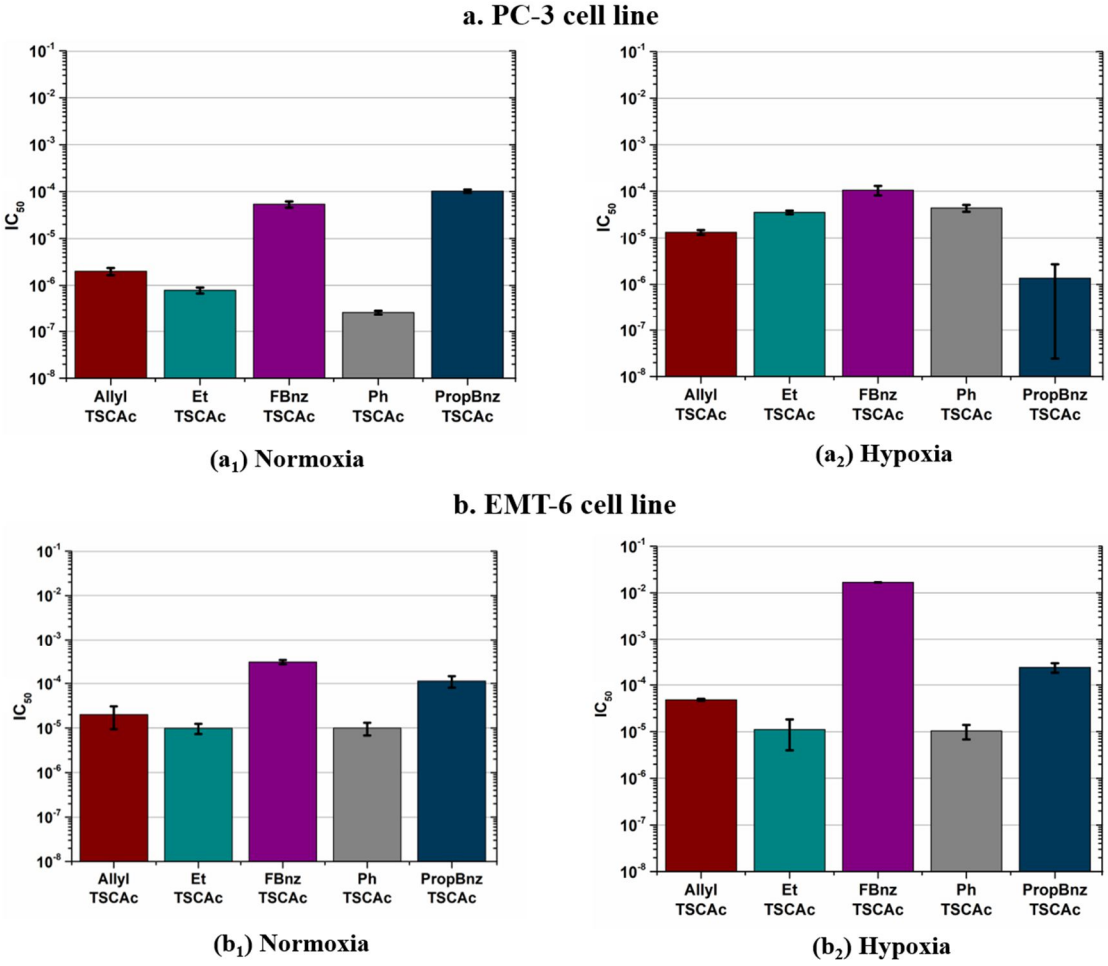

Figure 29: Estimation of IC_{50} values from MTT assays with PC-3 **(a)** and EMT-6 **(b)** cell lines under both normoxic **(a_1, b_1)** and hypoxic **(a_2, b_2)** conditions for a variety of mono(substituted) ligands (**5a-c**, **5e** and **5f)**. Error bar stands for standard error (±SE), calculated from six repeated measurements.

The IC_{50} values of the mono(substituted) ligands are shown in **Figure 29**. In the literature an IC_{50} value is referred to as the concentration of the compound tested where its response is reduced by 50%.[21] It can be noted that some of the mono(substituted) ligands present high cytotoxicity in the PC-3 cell line in normoxic conditions at 48 h. The only ligand that does not present a remarkable cytotoxicity for any of the conditions measured was **5e** (FbnzTSCA). Nevertheless, the response seems to be cell-dependant since there is a small variation in the cytotoxicity effects depending on the cell line used. The mono(substituted) ligand **5e** (FbnzTSCA) shows a considerable reduce of the cytotoxicity when it is incubated in EMT-6 hypoxia chemically induced cells compared to the rest of the conditions tested.

2.4.2. Fluorescence microscopy investigations

PC-3 (prostate carcinoma) cells were cultured using standard protocols, analogous with earlier investigations of the group[22] on fluorescent thiosemicarbazones. The viability of the cells was monitored by optical imaging prior and during the imaging studies. All the mono(substituted) ligands were imaged in normoxic conditions, cultured as described in the experimental section. The *in vitro* imaging was performed using epi-fluorescence and confocal fluorescence microscopy aiming to investigate the fluorescence distribution of the compounds in cells. In epifluorescence microscopy a mercury lamp was used as the light source whilst in confocal one photon excitation at 488 nm, was used, with the emission long pass filtered at 515 nm.

For the imaging studies, cells were incubated with 100 μM of compound in a DMSO:RPMI 0.5:99.5 cell medium solvent mix for 15 minutes at 37 °C. Whereby the final DMSO concentration on the imaging plate was lower than 1%. Then, the cells were carefully washed initially with pre-warmed PBS (37 °C) and then with FCS-free medium. The later was used to remove any remained non-internalised fluorescent dispersion before the fluorescence imaging takes place. All the imaging studies were carried out in the absence of serum. Absence of serum is required to avoid potential background fluorescence and to ensure the suitability of the compound. The necessity to use concentrations as high as 50 μM in these studies was a result of the rather weak fluorescence emissions (by comparison with organic, commercial dyes such as BODIPY, FITC).[23, 24]

Control experiments prior to incubation of cells with the compounds of interest were obtained by epi- and confocal fluorescence imaging (see Appendix for further details) to ensure that the cell morphology remained unaltered prior to the imaging experiments. No significant changes in cell morphology were observed by optical microscopy after 15 minutes incubation with respect to the control. The following figures (**Figure 30**) depict representative epi-fluorescence and confocal fluorescence microscopy images in PC-3 cell for the **5g** (free NH_2TSCA) mono(substituted) ligand which was the only mono(substituted) ligand that showed an intense fluorescence enhancement. It is evident, from the intense colour in the centre of the cells that **5h** (free NH_2TSCA) was most probably taken up into the cell nucleus.

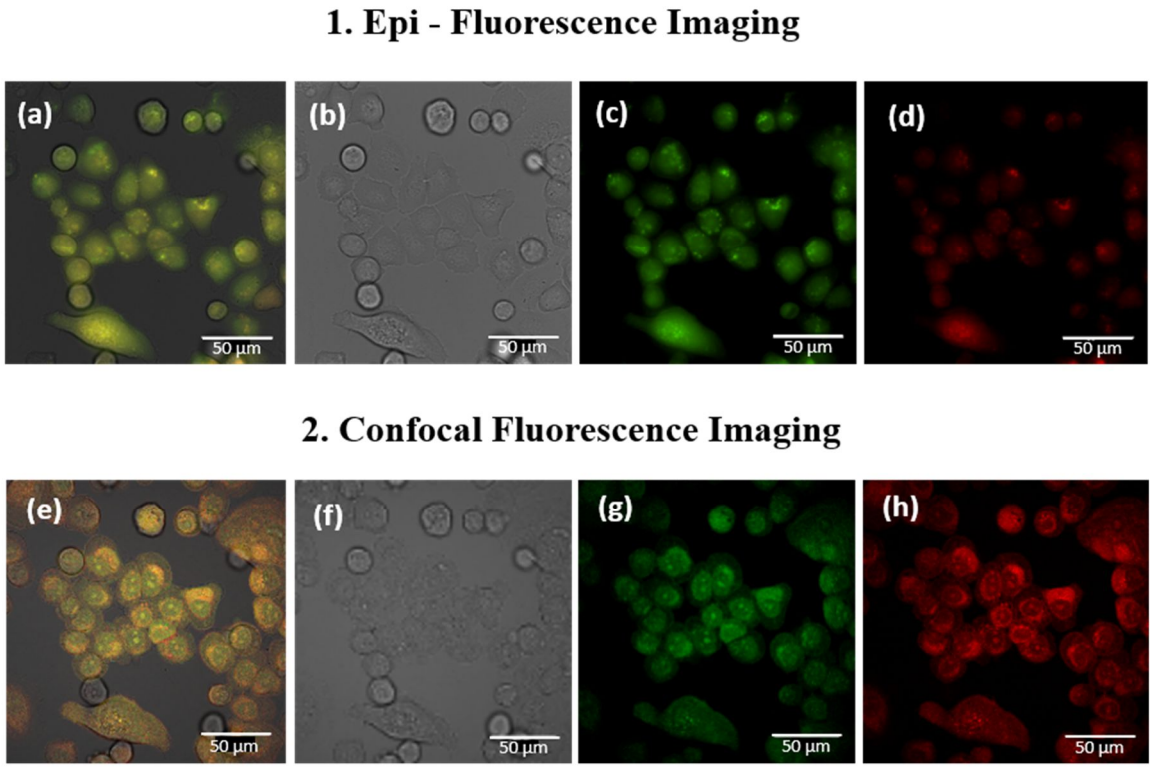

Figure 30: PC-3 cells incubated at 37 °C for 15 minutes with NH_2-free-TSCA (**5h**) (100 µM, in 5: 95 DMSO: serum-free medium). **1. a)** overlay of the green-red channels and DIC image **b)** DIC image **c)** green: λ_{ex} = 465-495 nm; λ_{em} = 515-555 nm. **d)** red: λ_{ex} = 530-560 nm; λ_{em} = 590-650 nm. **2. e)** overlay of the green-red channels and DIC image **f)** DIC image **g)** green: λ_{ex} = 405 nm; λ_{em} = 500-550 nm . **h)** red: λ_{ex} = 405 nm; λ_{em} = 570-750 nm. (scale bar 50 µm).

2.4.3. Cell uptake of the radiolabelled compound

The uptake of the [^{68}Ga]Ga(III)-coordinated mono(substituted) acenaphthenequinone thiosemicarbazonato complexes has been studied to observe the complexes inside human cancer cells using radiolabelling techniques. Intra-cellular tracking of the gallium (III) complexes by γ-ray counting is expected to provide information about their behaviour inside cells. Moreover, valuable information regarding their subsequent intracellular fate and processing could be obtained and potentially provide insights into the retention mechanism. Due to its greatest radiochemical purity immediately after the reaction, the compound tested was the **[^{68}Ga]-7e** ([^{68}Ga]Ga(FbnzTSCA)$_2$) complex. Different cell-lines were tested for both hypoxic and normoxic conditions in an attempt to measure the selectivity of gallium (III) complex under hypoxic conditions. The compound was further tested under different time frames ranging from 1 to 2 hours. A general protocol was developed for each condition. In the case of hypoxia, a protocol was developed using $CoCl_2$ to form an induced hypoxia environment (chemically induced hypoxia). In each case, a set of six-well plates were measured twice for each data point to estimate a level of response in preclinically quantitative measurements.

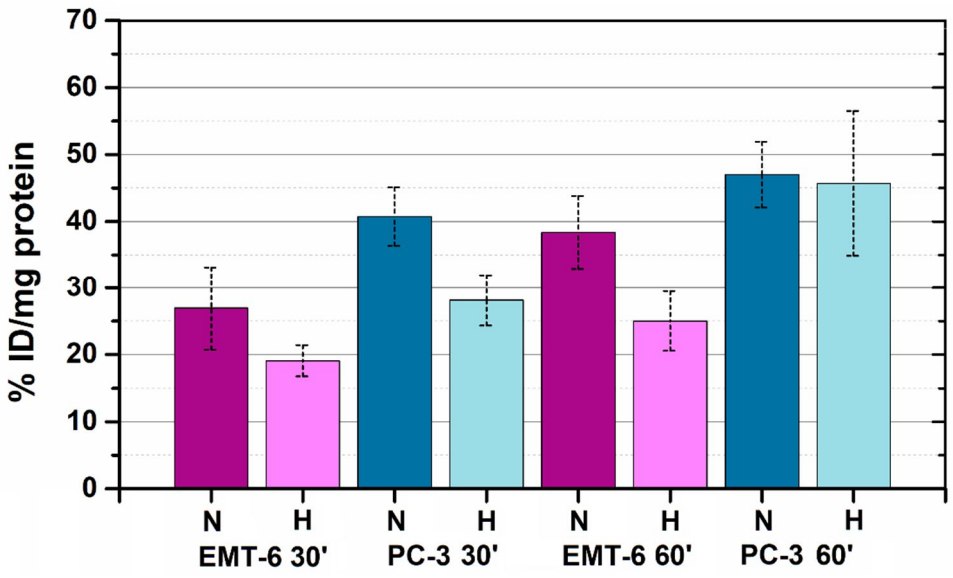

Figure 31: Estimation of **[^{68}Ga]-7e** ([^{68}Ga]Ga(FbnzTSCA)$_2$) uptake in normoxic and hypoxic (18 h treatment with $CoCl_2$) in PC-3 and EMT6 cells under serum-free conditions for 30 min and 60 min. n=1 technical repeats for each group. Difference in **[^{68}Ga]-7e** ([^{68}Ga]Ga(FbnzTSCA)$_2$) uptake at the two different cell lines were significant. Error bar stands for standard error (±SE), calculated from six repeated measurements.

As shown in the chart above (**Figure 31**) notable differences in cellular uptake and localisation can be seen between cell lines. However, a noticeable selectivity was not achieved under hypoxia. PC-3 (human prostatic small cell neuroendocrine carcinoma) cell line has not been reported to have a highly oxidative phenotype.[25] Therefore, treatment with the compound might trigger a metabolic transition phase (30 min) followed by an adjustment state (60 min). On the other hand, the EMT6 (mouse breast mammary adenocarcinoma) cell line has been shown to have an increased sensitivity upon exposure to hypoxic conditions,[26] which can be reflected in the reduced cellular uptake of this compound.

2.5. Conclusion to Chapter 2

New thiosemicarbazone mono(substituted) ligands were successfully synthesised and characterised by ESI-MS, NMR and single X-ray diffraction. All of the new mono(substituted) ligands (**5e** and **5f**) along with a variety of already published compounds (**5a**, **5b** and **5c**), have been coordinated with zinc and have been radiolabelled for the first time with gallium-68. The radiochemical protocol has been further tested with gallium-68 extracted by both a generator and a cyclotron and both of them produce the same result. They have been extensively tested *in vitro* with a variety of different techniques. Cytotoxicity assays have confirmed that some of the mono(substituted) ligands are more toxic for PC-3 and EMT-6 cell lines than others. More specifically, the new synthesised mono(substituted) ligands (**5e** and **5f**) appear to be less toxic rendering them as potential imaging agents. Their fluorescence properties were analysed showing enhanced biodistribution in normoxic cells. Furthermore, the cell uptake experiments performed on the radiolabelled molecules have revealed a variable localisation and aggressiveness, under various incubation periods within cell lines with different genetic background. However, their selectivity towards a hypoxic environment is not fully confirmed. Therefore, further optimisation of the cell uptake assay is needed regarding the incubation times, as well as the strategies exploited for inducing hypoxia. Use of a hypoxia chamber could be suggested as a potential environment to decipher how the redox chemistry might affect the cellular uptake. Lastly, conducting similar experiments including a wider panel of cancer cell lines is suggested. A diverse degree of sensitivity to hypoxia and metabolic response such as of the small lung cancer cell line H69 or the

breast cancer cell line MCF-7, has shown a higher sensitivity to drugs under hypoxia[27] and could provide more information regarding the compounds' utility in cells.

2.6. References to Chapter 2

1. R. W. Brockman, J. R. Thomson, M. J. Bell and H. E. Skipper, *Cancer Res*, 1956, **16**, 167-170.
2. Y. Yu, D. S. Kalinowski, Z. Kovacevic, A. R. Siafakas, P. J. Jansson, C. Stefani, D. B. Lovejoy, P. C. Sharpe, P. V. Bernhardt and D. R. Richardson, *J. Med. Chem.*, 2009, **52**, 5271-5294.
3. K. Agrawal and A. Sartorelli, *Prog. Med. Chem*, 1978, **15**, 321-356.
4. D. S. Kalinowski and D. R. Richardson, *Pharmacol. Rev.*, 2005, **57**, 547-583.
5. D. S. Kalinowski and D. R. Richardson, *Chem. Res. Toxicol.*, 2007, **20**, 715-720.
6. D. R. Richardson, P. C. Sharpe, D. B. Lovejoy, D. Senaratne, D. S. Kalinowski, M. Islam and P. V. Bernhardt, *J. Med. Chem.*, 2006, **49**, 6510-6521.
7. D. S. Kalinowski, Y. Yu, P. C. Sharpe, M. Islam, Y. T. Liao, D. B. Lovejoy, N. Kumar, P. V. Bernhardt and D. R. Richardson, *J Med Chem*, 2007, **50**, 3716-3729.
8. L. M. Bystrom, M. L. Guzman and S. Rivella, *Antioxid. Redox Signal*, 2014, **20**, 1917-1924.
9. K. Salnikow, T. Davidson, Q. Zhang, L. C. Chen, W. Su and M. Costa, *Cancer Res.*, 2003, **63**, 3524-3530.
10. F. Grasselli, G. Basini, S. Bussolati and F. Bianco, *Reprod. Fertil. Dev.*, 2005, **17**, 715-720.
11. F. Martin, T. Linden, D. M. Katschinski, F. Oehme, I. Flamme, C. K. Mukhopadhyay, K. Eckhardt, J. Troger, S. Barth, G. Camenisch and R. H. Wenger, *Blood*, 2005, **105**, 4613-4619.
12. Y. S. Chun, E. Choi, G. T. Kim, M. J. Lee, M. J. Lee, S. E. Lee, M. S. Kim and J. W. Park, *Biochem. Biophys. Res. Commun.*, 2000, **268**, 652-656.
13. I. S. Alam, R. L. Arrowsmith, F. Cortezon-Tamarit, F. Twyman, G. Kociok-Köhn, S. W. Botchway, J. R. Dilworth, L. Carroll, E. O. Aboagye and S. I. Pascu, *Dalton Trans.*, 2016, **45**, 144-155.
14. F. Cortezon-Tamarit, S. Sarpaki, D. G. Calatayud, V. Mirabello and S. I. Pascu, *Chem. Rec.*, 2016, **16**, 1380-1397.

15. M. C. Rodriguez-Argüelles, M. B. Ferrari, G. G. Fava, C. Pelizzi, G. Pelosi, R. Albertini, A. Bonati, P. P. Dall'Aglio, P. Lunghi and S. Pinelli, *J. Inorg. Biochem.*, 1997, **66**, 7-17.
16. A. R. Cowley, J. R. Dilworth, P. S. Donnelly and J. M. White, *Inorganic Chemistry*, 2006, **45**, 496-498.
17. J. R. Dilworth and R. Hueting, *Inorganica Chim. Acta*, 2012, **389**, 3-15.
18. M. V. Berridge and A. S. Tan, *Arch. Biochem. Biophys.*, 1993, **303**, 474-482.
19. F. M. Freimoser, C. A. Jakob, M. Aebi and U. Tuor, *Appl. Environ. Microbiol.*, 1999, **65**, 3727-3729.
20. J. Shi, Y. Wan and W. Di, *Oncol. Rep.*, 2008, **20**, 803-807.
21. G. W. Caldwell, Z. Yan, W. Lang and J. A. Masucci, *Curr. Top Med. Chem.*, 2012, **12**, 1282-1290.
22. H. Ge, PhD thesis, University of Bath, 2015.
23. L. de Abreu Costa and M. Henrique Fernandes Ottoni, 2017, **22**.
24. H. Ge, P. J. Riss, V. Mirabello, D. G. Calatayud, S. E. Flower, R. L. Arrowsmith, T. D. Fryer, Y. Hong, S. Sawiak, R. M. J. Jacobs, S. W. Botchway, R. M. Tyrrell, T. D. James, J. S. Fossey, J. R. Dilworth, F. I. Aigbirhio and S. I. Pascu, *Chem*, 2017, **3**, 437-460.
25. L. H. Higgins, H. G. Withers, A. Garbens, H. D. Love, L. Magnoni, S. W. Hayward and C. D. Moyes, *BBA-BIioenergetics*, 2009, **1787**, 1433-1443.
26. A. C. Sartorelli, M. F. Belcourt, W. F. Hodnick, S. R. Keyes, C. A. Pritsos and S. Rockwell, *Adv. Enzyme Regul.*, 1995, **35**, 117-130.
27. S. Strese, M. Fryknäs, R. Larsson and J. Gullbo, *BMC Cancer*, 2013, **13**, 331-331.

Chapter 3: Asymmetric bis(thiosemicarbazonato) metal complexes

3.1. Overview

Several different bis(thiosemicarbazones), based on acenaphthenequinone ligands, as well as their metal complexes with diverse metal centres (Zn(II), Ni(II), Cu(II), Ga(III)) have been explored through the years.[1, 2] However, the relevant chemistry has been limited to symmetric bis(substituted) derivatives, and the introduction of different amino functional groups has been little explored with no reports in the literature to date.

The discovery of hypoxia selectivity in Ga(III) acenaphthenequinone bis(thiosemicarbazonato) complexes under certain *in vitro* conditions, fuelled ongoing research for these derivatives.[3] The compounds of this family synthesised herein provide a readily available hypoxia-focused imaging probe, which can be easily functionalised. This can be achieved due to the asymmetric backbone of these complexes. Direct substitution reactions (SN) or "click" chemistry with specific targeting moieties could be applied on the -terminal groups of different arms and potentially lead to the development of promising imaging probes relevant to tumour hypoxia targeting approaches, applicable particularly in early detection and therapy of prostate cancer through molecular imaging.

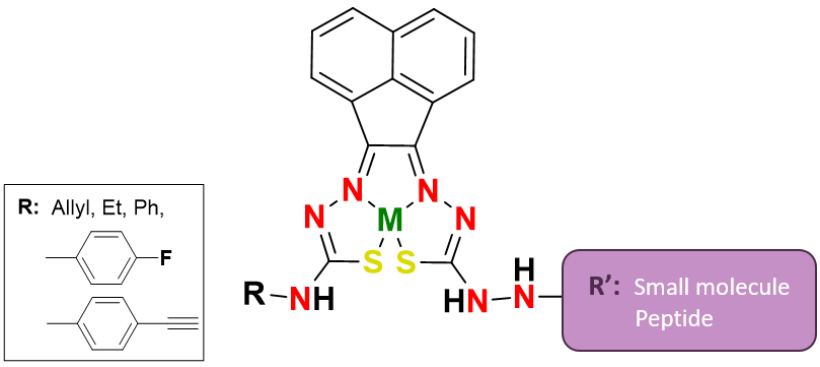

Figure 32: Proposed structure for a novel metal asymmetric bis(thiosemicarbazonato) complex with orthogonal functional groups.

Obtaining this asymmetry on the acenaphthenequinone derivatives is challenging, as the incorporation of different functional groups in a controlled way is hampered due to the

rigidity and planarity of this system. This prevents the free rotation around the C(O)-C(O) bond in the diketone precursor, a phenomenon absent in the aliphatic thiosemicarbazonato compounds, which are derived from 2,3-butanedione, glyoxal or pyruvaldehyde as starting materials.

The aim of the work presented in this chapter is to use the synthesised monosubstituted ligands described in Chapter 2, to develop metal asymmetric acenaphthenequinone bis(thiosemicarbazonates) able to be radiolabelled with gallium-68, whilst retaining their functional groups available to react with different targeting groups. In this work, a glycosyl coumarin (GC) unit has been developed and functionalised to allow coupling with asymmetric thiosemicarbazonato metal complexes. Furthermore, the potential radiolabelling of the asymmetric metal complexes using small molecules such as [^{18}F]4-fluorobenzaldehyde, is also investigated and discussed in this chapter.

3.2. Synthesis of novel metal complexes of asymmetric thiosemicarbazonate ligands

3.2.1. Zn(II) complexes

The synthesis of metal asymmetric thiosemicarbazonato acenaphthenequinone complexes has been previously attempted. However, there were scalability and purity limitations to their practical applications.[1] The synthesis of some asymmetric acenaphthenequinone thiosemicarbazonato complexes, containing a free NH_2 group, has been described by applying an one-pot template process which involves refluxing a mono(substituted) ligand with thiocarbohydrazide and zinc acetate leads to the formation of the desired complex.[4, 5]

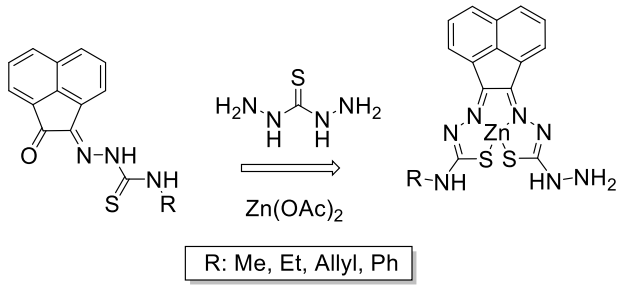

Scheme 13: Proposed reaction for the synthesis of zinc(II) coordinated asymmetric acenaphthenequinone thiosemicarbazonato complexes.

As there are different terminal groups in the mono-substituted ligands, one of the main challenges faced using the established procedure was that not all the different mono(substituted) ligands coordinate to Zn(II). This resulted in many cases in intractable mixtures of products, which were challenging to purify. For example, it is hypothesised that the electron density is reduced by delocalisation of electrons to the phenyl group at the mono(substituted) ligand **5a** (PhTSCA), resulting in a slower coordination opposed to the other monosubstituted ligands. Another limiting factor for obtaining the final product is that these reactions involve a long process since the reactions take 28-30 hours. Therefore, further optimisation was required in order to establish a microwave-assisted (μW) procedure, which would be less time-consuming and would lead to better coordination complexes due to dielectric heating treatment (**Scheme 13**). In addition, the strong binding with Zn was proven to be quite essential for the later transmetallation reaction with both aqueous non-radioactive gallium(III) (Section 3.2.2.) and radioactive gallium(III) (Section 3.3).

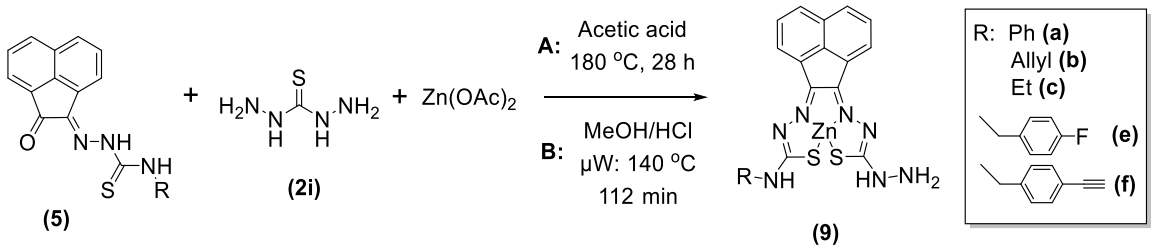

Scheme 14: Reactions relating to the synthesis of the asymmetric metal complexes; A: involves conventional heating whilst B: involves microwave assisted reaction.

In this respect, the proposed procedure for the synthesis of asymmetric acenaphthenequinone thiosemicarbazonato complexes of zinc(II) (**Scheme 14 A**) involved the initial reaction of the mono(substituted) ligand with an excess of zinc acetate (3 eq) in acetic acid. Then, an excess of thiocarbohydrazide (3 eq.) was added, and upon temperature increase to 120 °C, the obtained mixture was stirred under reflux for 28-30 h. When this procedure was carried out with the allyl derivative (**5b**) it was successful, which was confirmed by mass spectrometry analysis (**Figure 33**). However, when the same reaction was applied to the phenyl derivative (**5a**), limited incorporation of zinc was confirmed by mass spectrometry, indicating that this procedure is not suitable for this derivative (**Figure 34**). Therefore, a higher excess of zinc acetate was introduced (from 3 to 5 eq.),

resulting in a strongly orange-coloured compound with significant zinc incorporation (**Figure 33**).

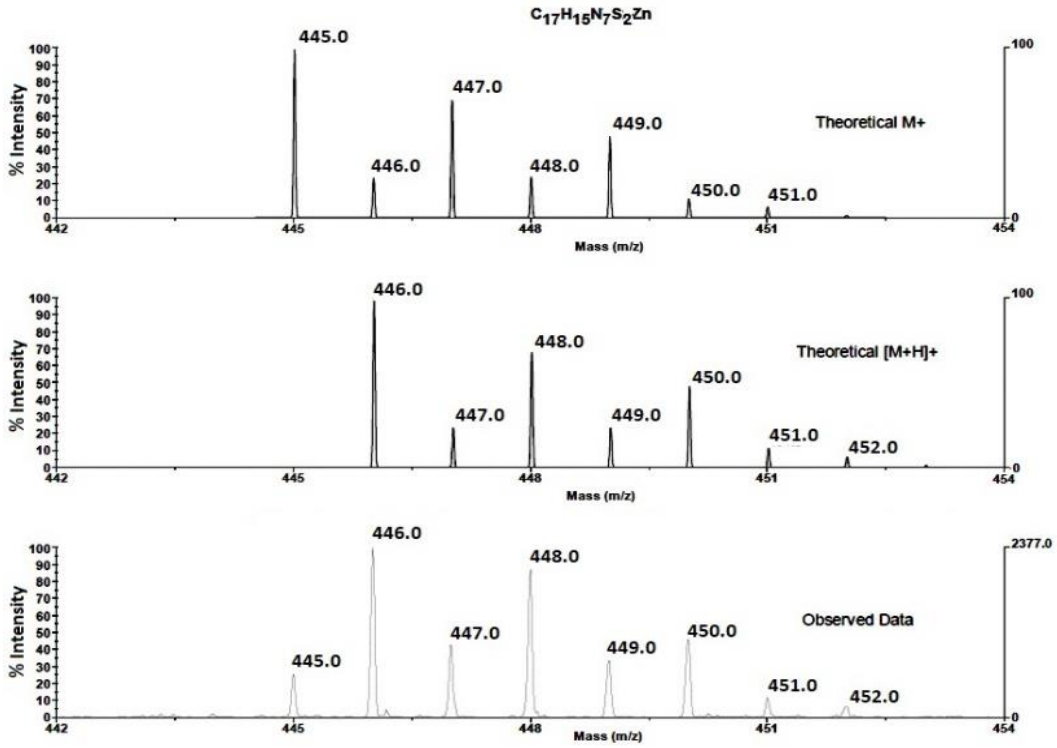

Figure 33: MALDI mass spectrometry result for the Zinc(II) 3-allyl-3-thiosemicarbazone-thiocarbohydrazide acenaphthenequinone (**9b**). The full spectrum can be found in the Appendix.

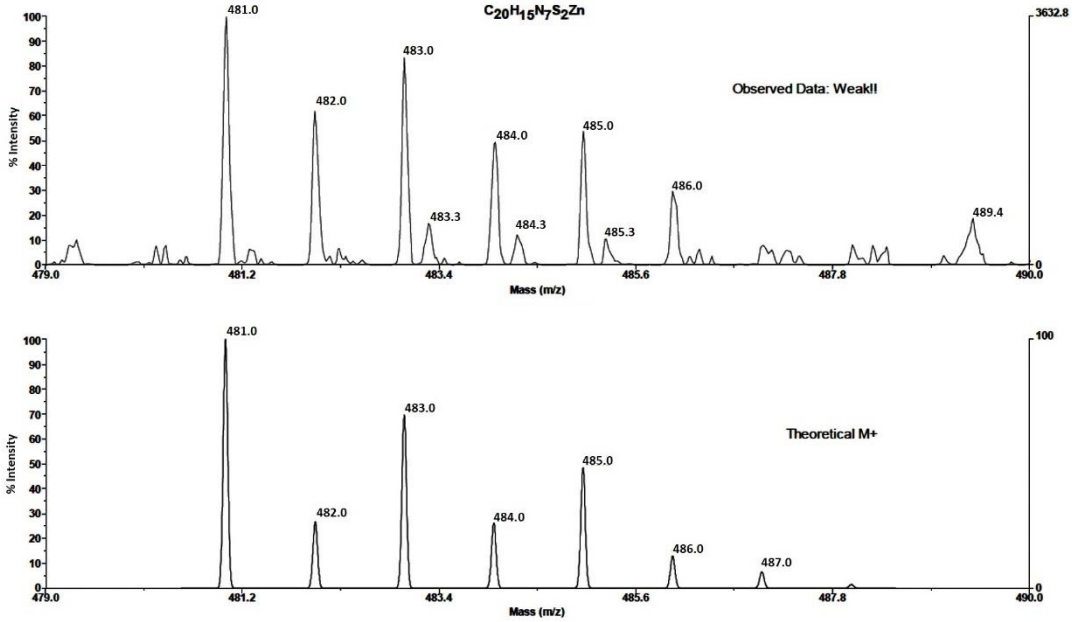

Figure 34: MALDI mass spectrometry result for the Zinc(II) 4-phenyl-3-thiosemicarbazone-thiocarbohydrazide acenaphthenequinone (**9a**).

In order to decrease the time of the reaction, microwave radiation was introduced as the energy source. The microwave-assisted reaction proved to be quite challenging, as a variety of different conditions (Table S16, Appendix) led to an impure final product. After optimising the working conditions, the reaction was successfully performed (**Scheme 14 B**) with most of the compounds being obtained pure and in high yields (**Table 9**). Among the relevant points for successful optimisation are: avoid temperatures higher than 140 °C, mix the mono(substituted) ligand with the zinc acetate prior to the addition of the thiocarbohydrazide in the reaction (as for conventional heating), and lastly, replacement of acetic acid by slightly acidic methanol (0.01% v/v HCl in methanol).

Table 9: Highest yields obtained for all the asymmetric zinc complexes.

Zn(II) Asymmetric Complex Abbreviation (Nº)	***Yield***
PhZnTSCA (9a)	99 %
AllylZnTSCA (9b)	92 %
EtZnTSCA (9c)	96 %
FbnzZnTSCA (9e)	97 %
PropbnzZnTSCA (9f)	73 %

More specifically, the reactions for the synthesis of metal asymmetric thiosemicarbazonates were carried out as follows: a microwave vial was filled with $Zn(OAc)_2$, in methanol, and heated (conventional heating) to 60 °C. Then, the monosubstituted ligand was added and the temperature was increased to 120 °C. When the reaction reached 120 °C, the thiocarbohydrazide was added along with a drop of HCl (37%). Following, the reaction was allowed to react at 140 °C (under microwave radiation) for 112 minutes. The crude product was then filtered and washed with cold methanol and diethyl ether in order to remove any remnants of the starting materials.

The ^{1}H NMR spectroscopy reflects the formation of the Zn complex (**9a**) from the mono(substituted ligand), **5a** (PhTSCA (**Figure 35**). The resonance at 11.01 ppm (**Figure 35 b**), corresponding to the secondary amine near the aromatic moiety (R-*N**H***-Ph) is shifted down-field after complex formation, while the ones at C3 and C9 at approximately 8.41 ppm and 8.15 ppm respectively are shifted up-field. It is noteworthy, in the spectrum of the complex (**Figure 35 a**) that the resonance of a primary amine group (R-*N**H**$_2$*) is observed at 6.78 ppm. These results suggest that the asymmetric complex was formed.

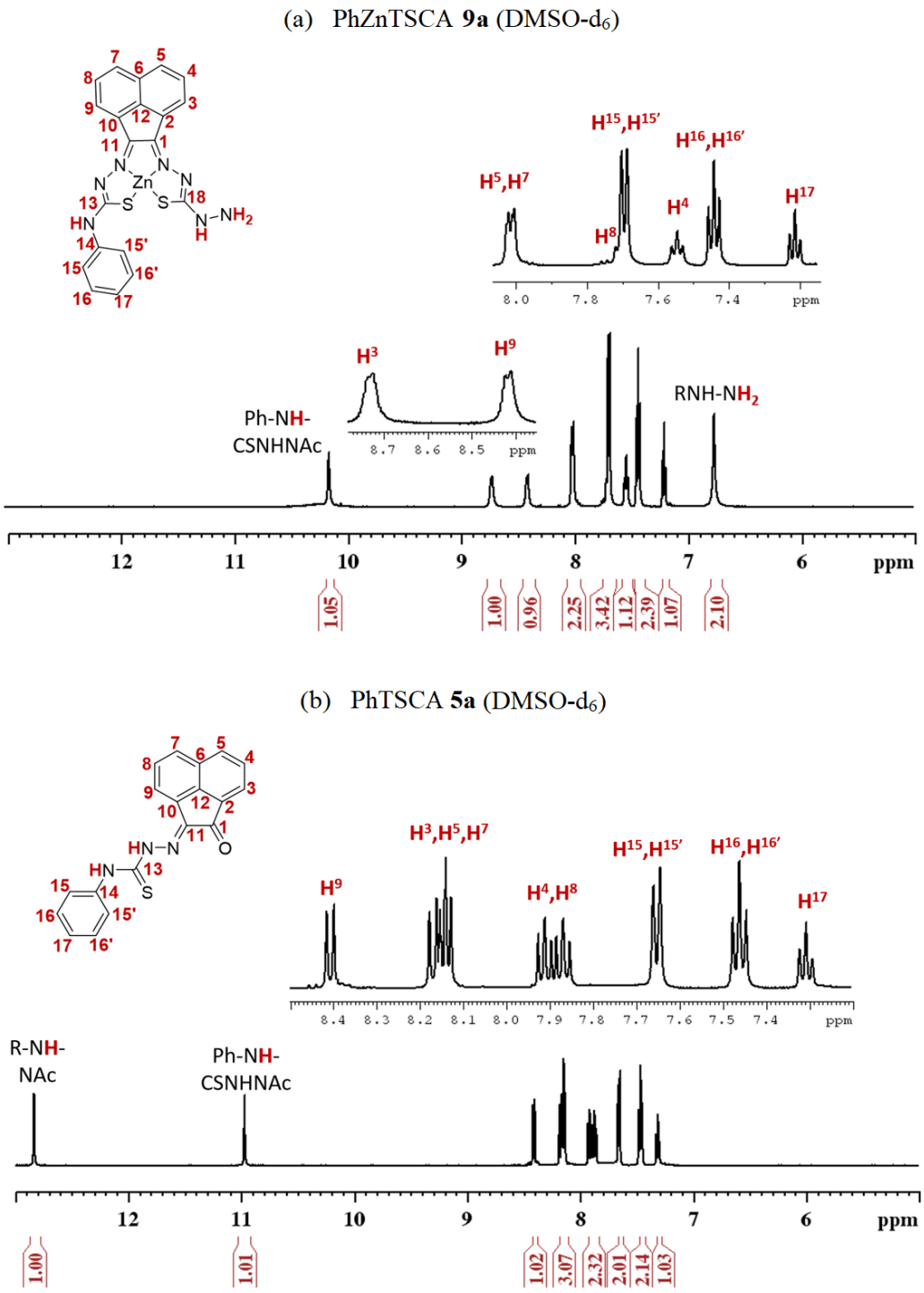

Figure 35: Comparative ^{1}H NMR spectra (500MHz, DMSO-d$_6$) of the mono (substituted) ligand **5a** (denoted PhTSCA) and the asymmetric complex **9a** (denoted PhZnTSCA).

FTIR spectra (**Figure 36**) show the absence of the stretching vibration band corresponding to the carbonyl group (C=O) of the acenaphthenequinone for compound **9a**, and changes in the bands between 3300-3500 cm^{-1}, corresponding to the N-H stretching vibrations for the two compounds (**5a** and **9a**). In particular, for compound **9a** the absorption bands at 3300-3500 cm^{-1} are broader compared to the one for compound **5a**,

which indicates the presence of a primary amino (NH_2) group. Lastly, a shift is observed in the CH_2 stretching, which usually appears around 2700-3000 cm^{-1}. These results are in agreement with the formation of the asymmetric complex **9a** (PhZnTSCA).

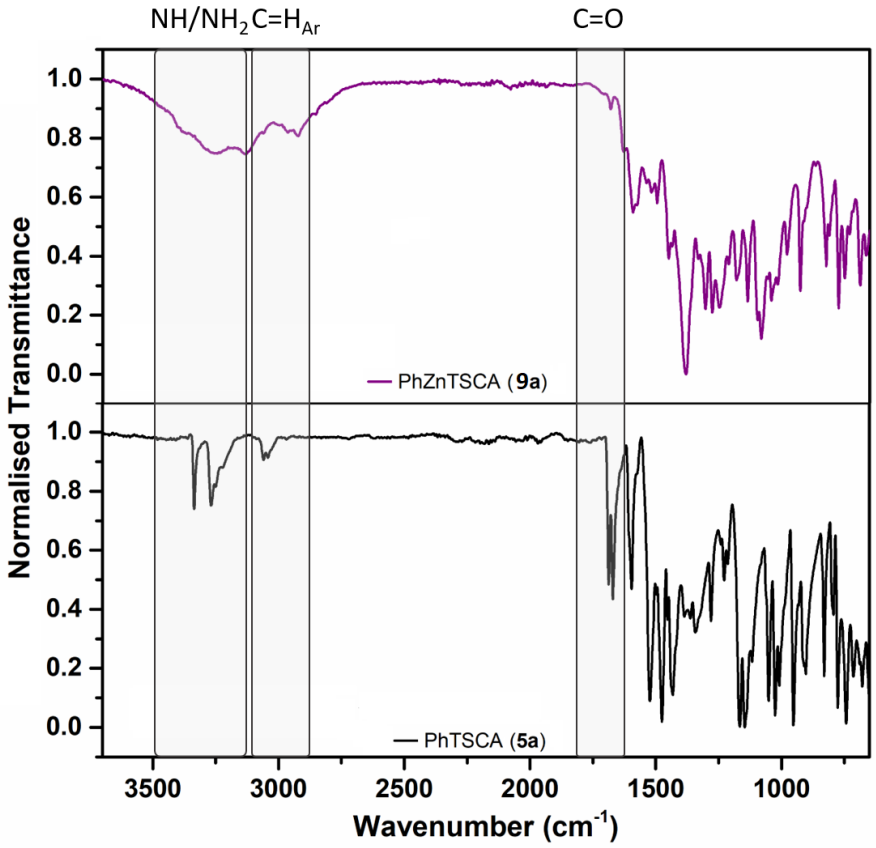

Figure 36: Comparative FTIR spectra for the mono (substituted) 3-phenyl-thiosemicarbazone acenaphthenequinone (**5e, black line**) and the Zn(II) 4-phenyl-3-thiosemicarbazone-thiocarbohydrazide acenaphthenequinone (**9a, violet line**).

3.2.2. Ga(III) complexes

The corresponding Ga(III) complexes were obtained by transmetallation reaction of the corresponding Zn(II) complexes using $GaCl_3$ and heating in methanol (**Scheme 15**). The synthesis of these non-radioactive Ga(III) complexes was dictated by their use as reference compounds for the radiolabelled molecules. The different derivatives demanded variable reaction times in order to obtain the completion of the transmetallation process. In the table below (**Table 10**), the yield of each transmetallation and the required time for each reaction is reported.

Table 10: Highest yields obtained, and the time required for complete reaction for all the asymmetric gallium(III) complexes.

Ga(III) Asymmetric Complex Abbreviation (Nº)	*Reaction length*	*Yield*
PhGaTSCA (10a)	6 h	74 %
AllylGaTSCA (10b)	16	44 %
EtGaTSCA (10c)	18	48 %
FbnzGaTSCA (10e)	14	62 %

Each of the reactions were carried out as described: excess gallium chloride was dissolved in methanol and then the corresponding zinc complex was added. Then, the mixture was allowed to react under reflux for 6-18 h depending on the zinc derivative. A colour change could be noticed to the formed gallium complexes and they were then precipitated with either diethyl ether or dichloromethane. They were further washed with diethyl ether and dried under reduced pressure. The optimisation of the reaction under microwave radiation was also attempted. However, despite variations applied in the temperature or the length of the reaction, a mixture of products always resulted which were difficult to purify.

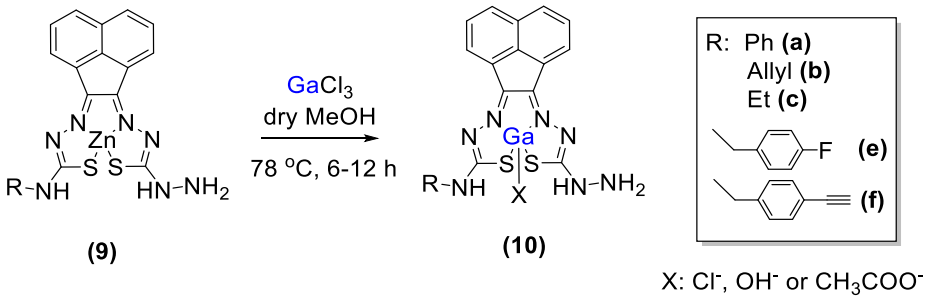

(9) (10)

Scheme 15: Transmetallation reaction for the synthesis of non-radiolabelled asymmetric thiosemicarbazonato complexes of Ga(III).

The comparative UV-Vis spectra (**Figure 37**) illustrates the formation of both the Zn complex from the mono (substituted ligand) and the Ga(III) complex from the transmetallation reaction. As shown in the spectra (**Figure 37**), the UV-Vis maximum absorption corresponds to the mono-substituted ligand, whilst the Ga complex UV-Vis absorption is significantly lower. A change can be also seen in the fluorescence spectra (**Figure 38**), where the emission peak is affected by the different forms of the molecule.

Here in contrast, the fluorescence of the Ga(III) complex is much higher than that of the other two compounds (**Figure 38**).

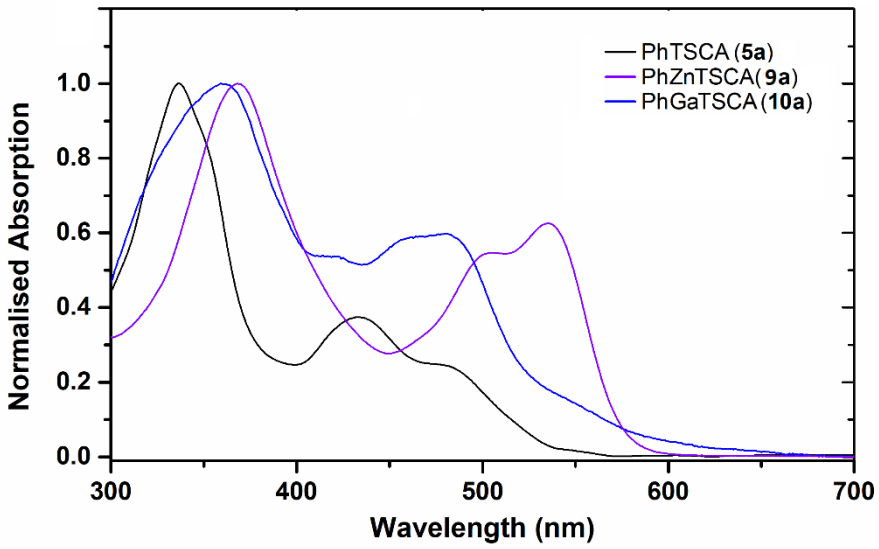

Figure 37: UV-Vis spectra for the mono (substituted) ligand **5a** (PhTSCA,0.002 mM, **black**), the asymmetric complex **9a** (PhZnTSCA,0.002 mM, **purple**) and the asymmetric complex **10a** (PhGaTSCA, 0.002 mM, **blue**).

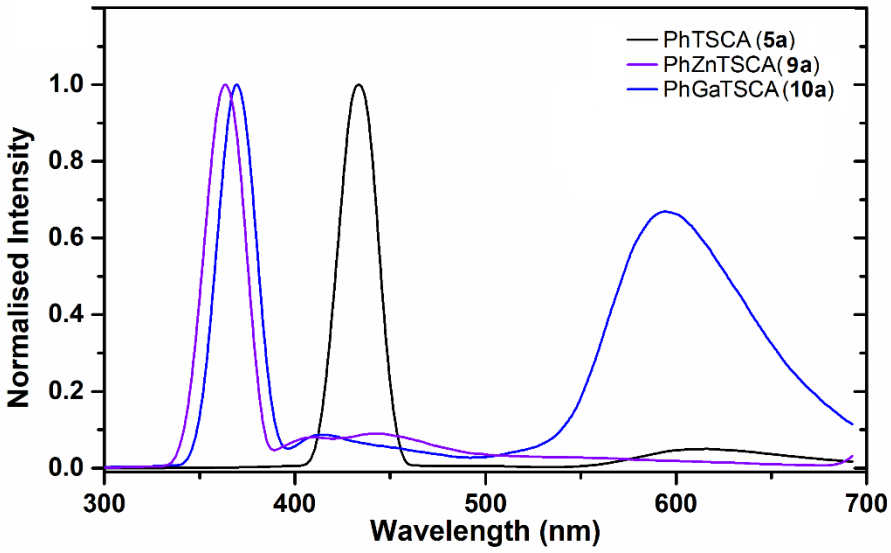

Figure 38: Fluorescence spectra of the mono (substituted) ligand **5a** (PhTSCA,0.002 mM, **black**), the asymmetric complex **9a** (PhZnTSCA,0.002 mM, **purple**) and the asymmetric complex **10a** (PhGaTSCA,0.002 mM, **blue**).

Unfortunately, suitable crystals for X-ray crystallography were not obtained. As a result, the structure of the complexes regarding the anionic species can only be originated from the rest of the obtained data and from what is published in literature. According to the

literature, the gallium(III) complexes featured a symmetrical acenaphthenoquinone bis(thiosemicarbazonate) present a square pyramidal configuration, where the metal ion is bend out of the plane tetradentate ligand and is coordinated and a Cl^- occupies the apex position.[1] Less often the position of the Cl^- is occupied by a another anionic species originated by the solvent. It suggested according to the IR spectroscopy (Appendix) that the counter ion of this complexes is not a OH^- since the stretching that corresponds to an OH group and appears usually at about 3500 cm^{-1} is missing.

3.3. Radiolabelling of asymmetric bis(thiosemicarbazonates) with different radionuclides

3.3.1. Coordination of asymmetric bis(thiosemicarbazonates) with gallium-68

Although the radiolabelling of asymmetric allyl bis(thiosemicarbazone) acenaphthenequinone with gallium-68 has been explored previously by Pascu's group, herewith, we focus on the radiolabelling of the Zn(II) asymmetric acenaphthenequinone thiosemicarbazonato complexes for the first time. The radiolabelling is based on a transmetallation reaction between and [^{68}Ga]Ga(III) as with the non-radioactive Ga(III) (**Scheme 16**). The established protocol for metal bis(thiosemicarbazone) acenaphthenequinone complexes was attempted for the asymmetric complexes without any success. Despite the anticipated absence of any alterations in the symmetry of the complexes during the radiolabelling procedure, similarly to the non-radioactive transmetallation reaction, the successful radiolabelling procedure eventually was different from the one for the symmetric allyl bis(thiosemicarbazone) acenaphthenequinone molecule reported earlier.[3]

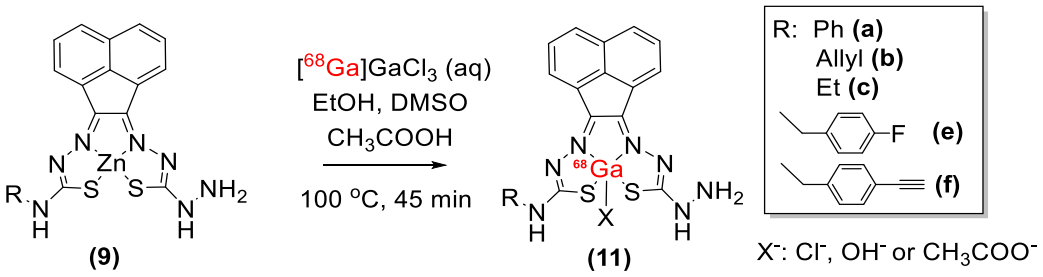

Scheme 16: Transmetallation reaction for the synthesis of radiolabelled asymmetric bis(thiosemicarbazonato) complexes with gallium-68.

In this sense, the key points for the reaction seem to be: the drying procedure of [^{68}Ga]Ga(III), maintaining the pH of the reaction between 4.5 and 6.5, the ratio between the precursor (zinc complex) and the [^{68}Ga]$GaCl_3$, as well as the strong binding of zinc(II) in the complexes. The presence of the latter is essential. Carrying out the reaction on complexes with limited Zn content, as suggested by mass spectrometry, resulted in failure. Lastly, a critical point for the success of the reaction could be considered the germanium-68 breakthrough from the generator. During the elution of gallium-68 from a ^{68}Ga/^{68}Ge generator, the parent radioisotope is usually trapped in the generator's column resulting in a pure gallium-68 solution. But through time, the sorbent materials of the generator's column cannot absorb the mother liquid as well so the germanium-68 contamination is gradually increases.[6, 7] This contamination of the eluted gallium-68 solution is interfering considerably in the transmetallation reaction. **Table 11** reports some of the different conditions attempted in order to optimise the reaction. As listed in the table, different solvents were used, but the radiolabelling only proceeded in EtOH. Additionally, the use of 0.5 M NaOAc buffer (pH 4.5-5.5) seems to improve the radiochemical incorporation. However, the amount of buffer used needed to be kept as low as possible since the thiosemicarbazone acenaphthenequinone complexes were found to be kinetically unstable in the presence of different buffers.[3] Moreover, changes in temperature or time did not seem to cause any difference in the labelling of the compounds.

In more detail, the radiolabelling of the Zn (II) acenaphthenequinone asymmetric thiosemicarbazonato complexes was achieved as follows. The [^{68}Ga]$GaCl_3$ was eluted through the generator in a 98% THF/HCl (0.02 M) solution. This was subsequently dried for 10-15 minutes under a nitrogen stream at 95 °C. Next, medical grade ethanol was used to resuspend [^{68}Ga]Ga(III) and a small amount of NaOAc buffer (pH=4.9) was used to stabilise the pH of the solution at 4.5. Then the corresponding Zn complex was added (2 mg/ mL in DMSO). The reaction solution was mixed for a few minutes by vortexing, then heated at 95 °C for 30 minutes and injected into a radio-HPLC.

The HPLC monitoring of this reaction indicated that the conversion of the zinc complex to the respective gallium-68 complex occurred, although the presence of the peak corresponding to the remaining [^{68}Ga]$GaCl_3$ indicated that radiolabelling had not gone to completion (**Figure 39**). The radiochemical incorporation indicated by the radio-HPLC is intermediate. However, the amount of the radioactivity injected into the HPLC was not in line with the result of the HPLC trace. TLCs were therefore carried out in order to evaluate the reaction and the radiochemical yield after half-life correction was calculated to be 75 %

(due to limitation of laboratory equipment, a γ ray counter was used and the table of these results can be found in the Appendix)

It is hypothesised that a possible interaction of the compound with the HPLC column might have resulted in distorted results. Use of different available columns was attempted along with the use of different solvent systems without a noticeable difference. The compound was further purified *via* solid phase extraction through C18 cartridges, resulting in a much-improved radio-HPLC trace.

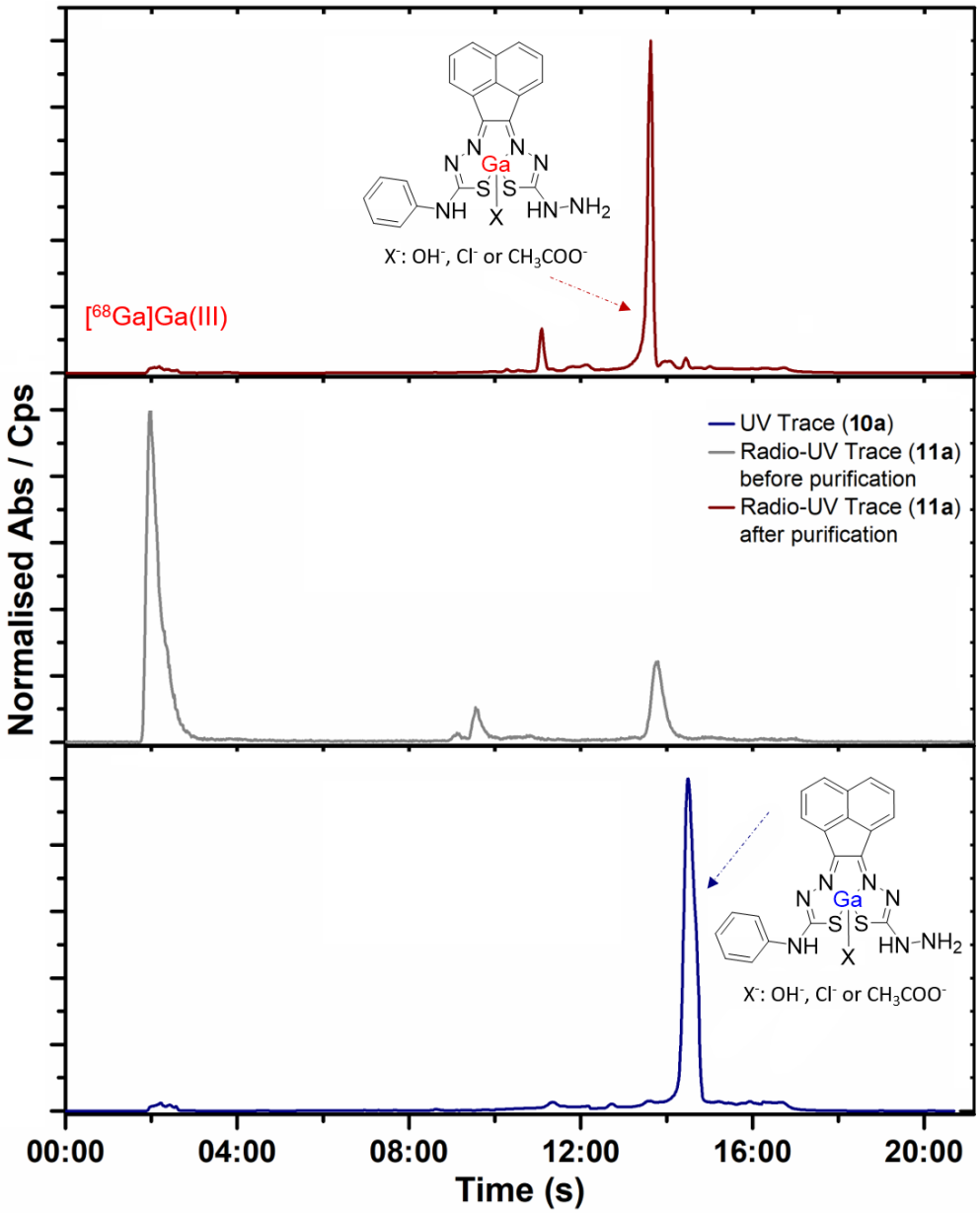

Figure 39: HPLC and radio-HPLC traces for the transmetallation of asymmetric complex **9a** (PhZnTSCA**, black**) with $^{68}Ga[GaCl_3]$. **[^{68}Ga]-11a** was formed (**grey**) and was then purified (**dark red**).

Table 11: Summary of the different conditions attempted under conventional heating for optimisation of the transmetallation reaction of the asymmetric thiosemicarbazonato complexes of Zn(II) with $^{68}Ga[GaCl_3]$ (compound **9a** was used during the optimisation process). The pH of the reactions was maintained between 4 and 6**.** All the attempted conditions were carried out at least two times.

Solvent	Concentration of the complex	Concentration (mM)	Solvent / Radioactivity	Buffer NaOAC (pH): Solvent	T (°C) heating	Time (min)	R.O.I.
EtOH	2 mg/mL in DMSO	4.2	1 ml / 44.4 MBq	No buffer use	95 °C	40 + 20	0
EtOH	2 mg/mL in DMSO	3.5	1 ml / 37 MBq	No buffer use	95 °C	45	small ROI, no significant difference between the two
MeOH	2 mg/mL in DMSO	4.2	1 ml / 37 MBq	No buffer use	95 °C	30	0
MeOH	2 mg/mL in DMSO	2.1	1 ml / 37 MBq	No buffer use	95 °C	45	0
EtOH	2 mg/mL in DMF	4.2	1 ml / 37 MBq	No buffer use	95 °C	30	0
EtOH	2 mg/mL in DMF	2.1	1 ml / 37 MBq	No buffer use	95 °C	30	0
MeOH	2 mg/mL in DMF	4.2	1 ml / 18.5 MBq	No buffer use	95 °C	30 + 30	0
NaCl/HCl	2 mg/mL in DMSO	1.7	1 ml / 37 MBq	1:1 (pH: 3.9)	95 °C	40	0
NaCl/HCl	2 mg/mL in DMSO	1.4	1 ml / 37 MBq	1:1.2 (pH: 3.9)	95 °C	40	0

EtOH	2 mg/mL in DMSO	2.8	1 ml / 37 MBq	No buffer use	95 °C	30	very small trace
EtOH	2 mg/mL in DMSO	2.8	1 ml / 37 MBq	No buffer use	110 °C	30	0
EtOH	2 mg/mL in DMSO	2.1	1 ml / 37 MBq	No buffer use	95 °C	30 + 30	small ROI, no significant change between the two
EtOH	2 mg/mL in DMSO	2.1	1 ml / 37 MBq	No buffer use	110 °C	30	0
EtOH	2 mg/mL in DMSO	5.2	1 ml / 37 MBq	No buffer use	95 °C	30	0
EtOH	2 mg/mL in DMSO	5.2	1 ml / 37 MBq	No buffer use	110 °C	30	0
EtOH	2 mg/mL in DMSO	5.2	1 ml / 37 MBq	1:3 (pH: 4.56)	95 °C	30	25 %
EtOH	2 mg/mL in DMSO	4.2	1 ml / 37 MBq	1:10 (pH: 4.56)	95 °C	30	46 %
EtOH	2 mg/mL in DMSO	4.2	1 ml / 29.6 MBq	1:10 (pH: 4.56)	95 °C	30	18 %
EtOH	2 mg/mL in DMSO	4.2	1 ml / 37 MBq	1:10 (pH: 3.9)	95 °C	30	29 %
EtOH	2 mg/mL in DMSO	4.2	1 ml / 29.6 MBq	1:17.5 (pH: 4.56)	95 °C	30	35 %

(continuation of Table 11)

Table 12: Summary of the different conditions attempted under microwave radiation (μW) con for optimisation of the transmetallation reaction of the asymmetric thiosemicarbazonato complexes of Zn(II) with $^{68}Ga[GaCl_3]$ (compound **9a** was used during the optimisation process). The pH of the reactions was maintained between 4 and 6**.** All the attempted conditions were carried out at least two times.

Solvent	Concentration of the complex	Concentration (mM)	Solvent / radioactivity	Buffer NaOAC (pH): Solvent	T (°C) μW	Time (min)	R.O.I.
EtOH	2 mg/mL in DMSO	3.5	1 ml / 37.0 MBq	No buffer use	95 °C h	45	small ROI, no significant difference between the two
MeOH	2 mg/mL in DMF	4.2	1 ml / 18.5 MBq	No buffer use	110 °C μW	25	0
					130 °C μW	+ 20	
DMF	2 mg/mL in DMF	4.2	1 ml / 22.2 MBq	No buffer use	110 °C μW	45	0
EtOH	2 mg/mL in DMSO	5.2	1 ml / 37.0 MBq	1:3 (pH: 4.56)	95 °C h	30	25 %
EtOH	2 mg/mL in DMSO	4.2	1 ml / 37.0 MBq	1:10 (pH: 4.56)	95 °C h	30	23 %
EtOH	2 mg/mL in DMSO	4.2	1 ml / 29.6 MBq	1:10 (pH: 4.56)	95 °C h	30	11 %
EtOH	2 mg/mL in DMSO	4.2	1 ml / 37.0 MBq	1:10 (pH: 3.9)	95 °C h	30	Very small trace

3.3.2. Functionalisation of asymmetric thiosemicarbazonate metal complexes with radioactive precursors

Numerous radiolabelled small molecules could have been used to be coupled with the asymmetric metal complexes.[8] In this case, the coupling reaction of complex **9a** (PhZnTSCA) with [^{18}F]4-fluorobenzaldehyde ([^{18}F]FBA) was carried out. This reaction was based on a carbonyl addition reaction between an aldehyde and a primary amine which results in the formation of an imine and the loss of the carbonyl oxygen.

The radiolabelling of asymmetric ATSM molecules with [^{18}F]FBA has previously been reported by Carroll *at al.*[9] but herein we explored for the first time the analogous radiolabelling of asymmetric thiosemicarbazone acenaphthenequinone metal complexes.

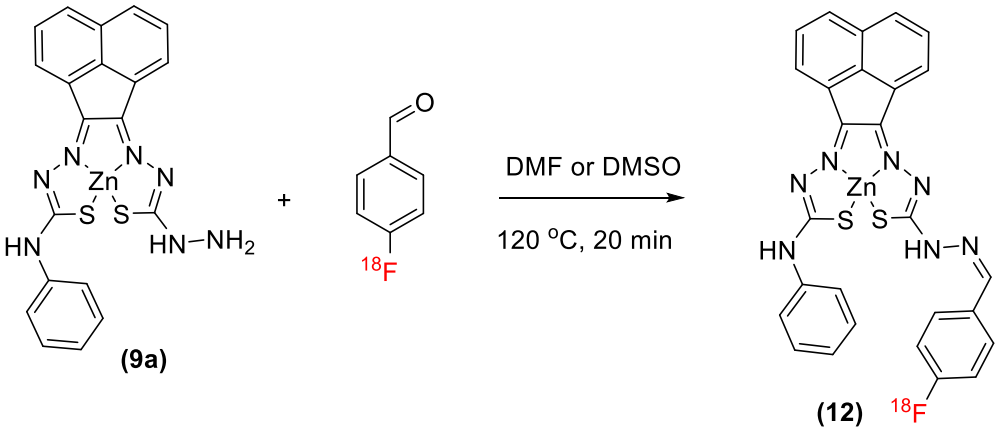

Scheme 17: Radiolabelling of complex **9a** (PhZnTSCA) with [^{18}F]FBA.

The preparation of [^{18}F]FBA precursor was performed, with assistance from Mr. Chris Barnes at Imperial College, London. In the first step, the [^{18}F]fluoride was dried by means of an automated process on the GE FASTlab synthesiser. The [^{18}F]fluoride was trapped on a Sep-Pak QMA-carbonate Light Cartridge before being eluted into the reactor using an eluent consisting of acetonitrile, water, Kryptofix K222 and $KHCO_3$. The contents of the reactor were evaporated at 120 °C under vacuum and a low flow of nitrogen. The 'dried' fluoride was then dissolved in anhydrous acetonitrile before being transferred to a vial. The fluorination step was then performed manually. The 'dried' [^{18}F]fluoride was mixed with the precursor and the vial was then heated at 90 °C for 15 minutes (**Scheme 18**) resulting in consistently >98% radiochemical incorporation.

The resulting [^{18}F]FBA was analysed by HPLC (rt. 10 min) to check radiochemical purity before being used in low volume portions for further labelling reactions as described.

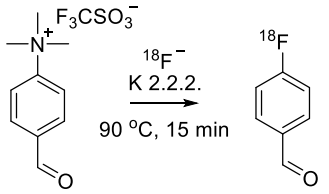

Scheme 18: Synthesis of 4-[^{18}F]fluorobenzaldehyde from dried [^{18}F]fluoride.

Additionally, in order to find the best possible conditions for labelling of the precursor (**9a**), a variety of experiments were conducted evaluating the temperature, the reaction time and the solvents used. Due to the instability of the thiosemicarbazonate complexes at high temperature, the first experiment was carried out using MeCN at 90 °C, but the reaction did not proceed. Thiosemicarbazonato complexes are very insoluble compounds in most organic solvents, except DMSO and DMF, and that was considered as a possible reason for the previous reaction failure. About 4.5 mg of the compound was then diluted in 500 μL of DSMO and mixed with 50 μL of [^{18}F]FBA solution. The mixture was left to react at 90 °C for 20 minutes resulting in a low ROI. Thus, another 20 minutes were allowed for the reaction without a significant change in the ROI as a result. The temperature was then increased to 120 °C and the reaction was left for 25 more minutes which resulted in a doubling of the ROI (10 %). This increase indicated the necessity of high temperature for this reaction, however, these conditions were already at the limit of the stability of the thiosemicarbazonato complexes.

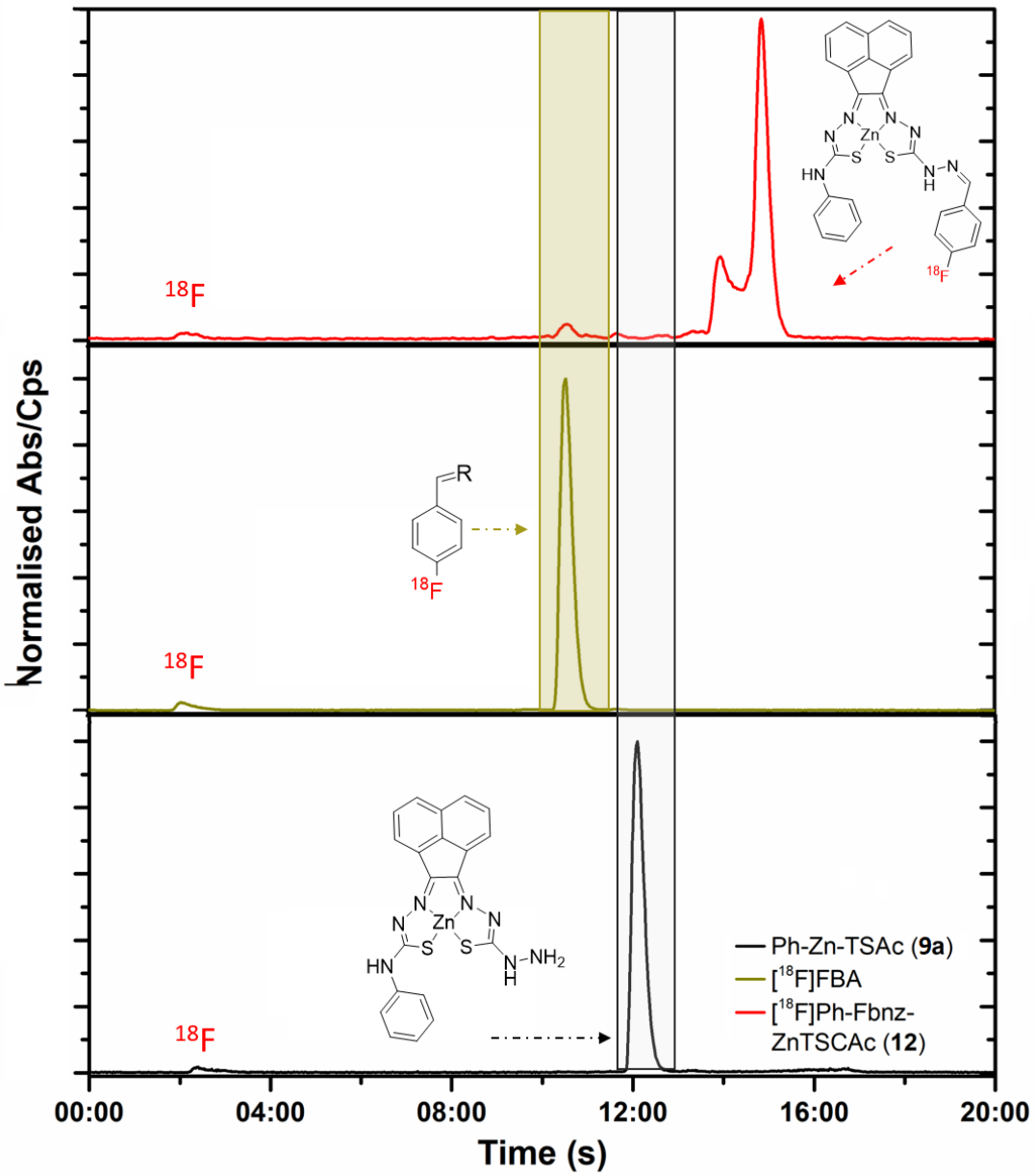

Figure 40: UV-Vis and radio-HPLC traces for radiolabelling of denoted PhZnTSCA **(9a)** (black) complex with ^{18}F[FBA] (green). Complex [^{18}F]-**12 (**denoted [^{18}F]-Ph-Fbnz-ZnTSCA) was formed (red).

A variety of further experiments were carried out regarding the ratio between the metal complex and the [^{18}F]FBA solution as well as different solvents . The experimental challenges were the highest possible ROI in the minimum possible reaction time, without exceeding a temperature of 120 °C. At last, the highest ROI was achieved as follows: 8.2 mg of PhZnTSCA complex (**9a**) was diluted in 0.2 mL of DMSO and mixed with 60 µL of [^{18}F]FBA (11.84 MBq). The temperature was then raised to 120 °C and the

mixture allowed to react for 20 minutes, resulting in a ROI of 94 % (**Figure 40**). This excellent ROI was considered sufficient to proceed with this compound for further biological experiments.

3.4. Functionalisation of asymmetric bis(thiosemicarbazonates) with a glycosyl coumarin derivative.

3.4.1. Synthesis of a glycosyl coumarin derivative

Supuran and colleagues[10] suggested that a selected deprotection of α-D-mannose pentaacetate with morpholine[11] leads to a tetraacetyl-D-mannopyranose (**13**). Treatment of the latter compound with trichloroacetonitrile affords the corresponding tetra-*O*-acetyl-D-mannopyranose trichloroacetamidate (**14**) (**Scheme 19**). Then, coupling of the obtained intermediate (**14**) with 4-methylumbelliferone gives a methylumbelliferyl-tetraacetyl-D-mannopyranose (**15**) and finally, hydrolysis of the acetyl groups results in the desired compound, methylumbelliferyl-D-mannopyranose (GC, **16**) (**Scheme 19**).

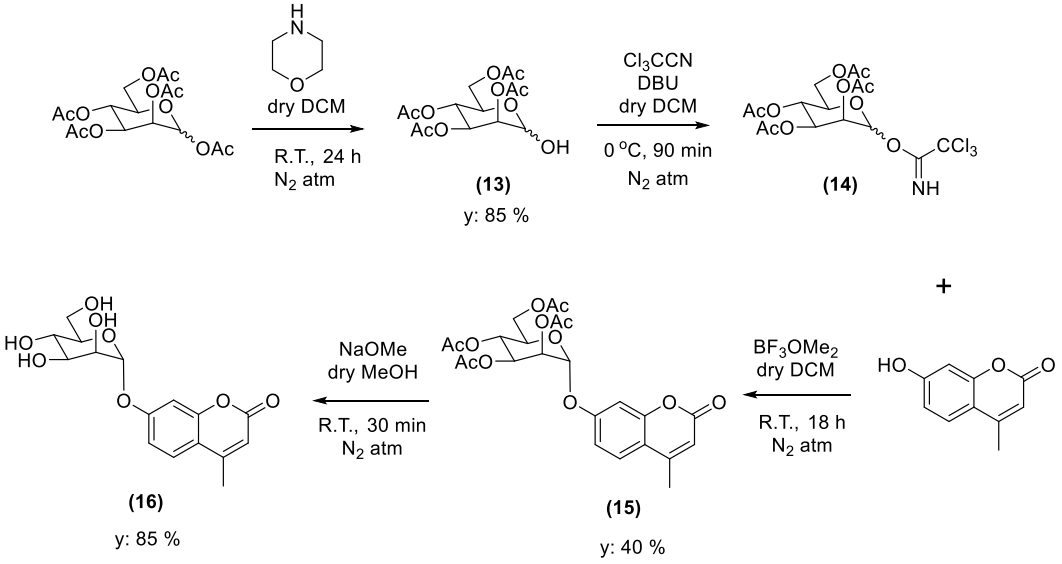

Scheme 19: Synthetic procedure for glycosyl coumarin GC-204 (**16**).[10]

The hydroxyl functionalities of carbohydrates can be protected with variety of groups with the acetyl group being one of the most commonly used. Considering the easy cleavage of acetyl groups by various common solvents, such as methanol and/or H_2O,

the protection reactions must often be carried out carefully under both anhydrous conditions and low temperature. Moreover, the hemiacetal nature of the anomeric alcohol group of the sugar makes its selective deprotection easier if the glucoside is acetyl-protected rather than when it is protected with other known protecting groups. Following the procedure of Supuran *et al.*, α-D-mannose pentaacetate was treated with morpholine in dry dichloromethane at room temperature overnight. This effected the deprotection of the anomeric group affording the corresponding tetraacetyl-D-mannopyranose (**13**) with a high yield of 85 %. Then, conversion of the alcohol to the trichloracetimidate was carried out in dry dichloromethane at 0 °C for 90 minutes. This reaction was carried out with a catalytic amount of DBU, an amidine base which is commonly used as a catalyst for numerous base-mediated organic transformations (**Scheme 19**).

The intermediate (**14**) was subsequently coupled with 4-methylumbulliferone in dry dichloromethane at room temperature for 16 hours in the presence of a small amount of boron trifluoride dimethyl etherate, which was used to initiate the oxygen's activation as a Lewis acid. This coupling produce methylumbelliferyl-tetraacetyl-D-mannopyranose (AcGC, **15**) in high purity after crystallisation (**Figure 41**) with a moderate yield (40 %). Finally, the hydrolysis of methylumbelliferyl-tetraacetyl-D-mannopyranose (AcGC, **15**) was carried out, to deprotect the sugar moiety, using methanol and sodium methoxide at room temperature for 30 minutes. The target compound (**16**) was afforded with an overall yield of 30 %.

Suitable crystals for single crystal X-ray were obtained from the mother liquor for both compounds, **15** and **16,** confirming that the desired products had been obtained. The X-ray structures are shown in **Figures 41** and **42**. The compound methylumbelliferyl-tetraacetyl-D-mannopyranose (AcGC, **15**) crystallises in the orthorhombic system (Tables and crystallography data are included in Appendix) (all three axes are unequal in length; all are perpendicular to each other) where a crystal with $P2_12_12$ space group resulted due to a network of hydrogen bonds that provides intermolecular bonding (**Figure 41**).

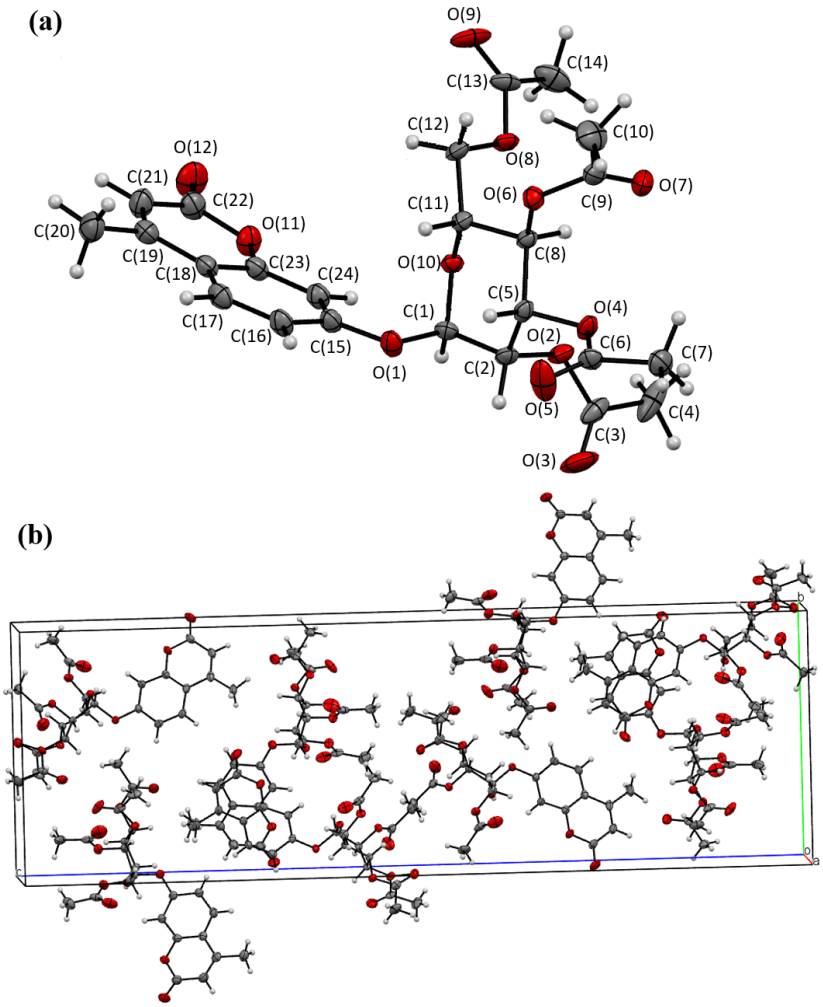

Figure 41: (a) Molecular structure of 4-methylumbelliferyl-7-yl-2,3,4,6-tetra-O-acetyl- α-D-mannopyranose (**15**). Only one of the molecules of the asymmetric unit is shown for clarity. **(b)** 3D X-ray packing showing the unit cell. Thermal ellipsoids at 50% probability.

On the other hand, 4-methylumbelliferyl-7-yl-α-D-mannopyranose (GC, **16**) crystallises in the triclinic system (Tables and crystallography data are included in Appendix) where a crystal with P1 space group was determined. The crystal cell unit is composed of 2 molecules (z=2, **Figure 42**). In both crystal structures, the asymmetric unit is formed by two unsymmetrically equivalent molecules linked together through π-π interactions (~3.8 Å) between the coumarin groups and the pyranose ring retains the "chair" configuration.

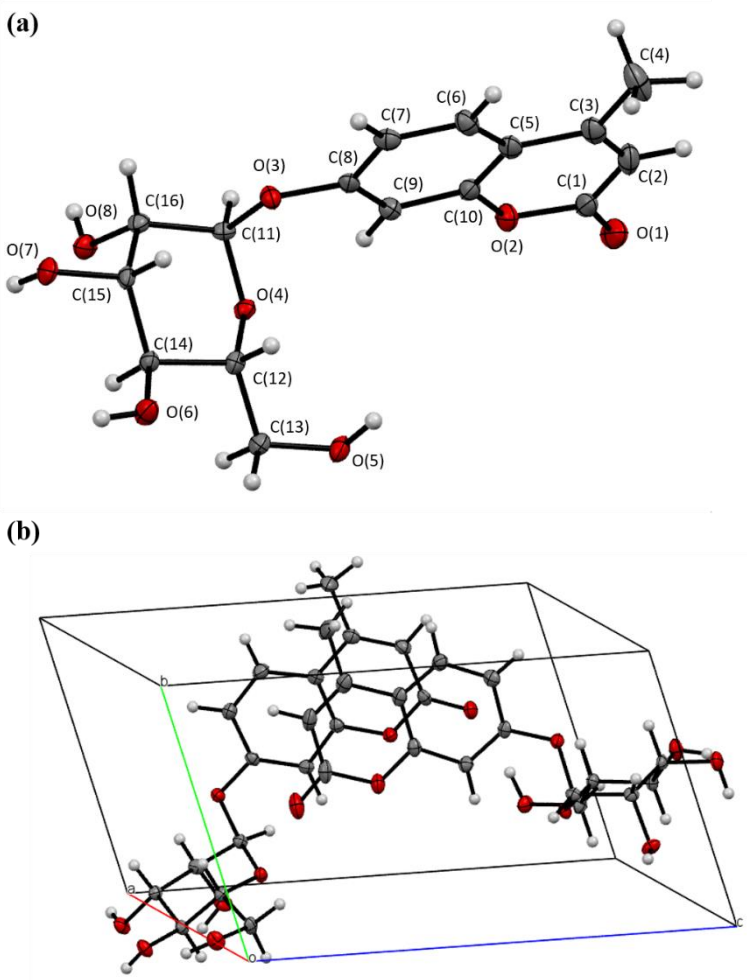

Figure 42: (a) Molecular structure of 4-methylumbelliferyl-7-yl-α-D-mannopyranose **(GC, 16).** Only one of the molecules of the asymmetric unit is shown for clarity**. (b)** 3D X-ray packing showing the unit cell. Thermal ellipsoids at 50% probability.

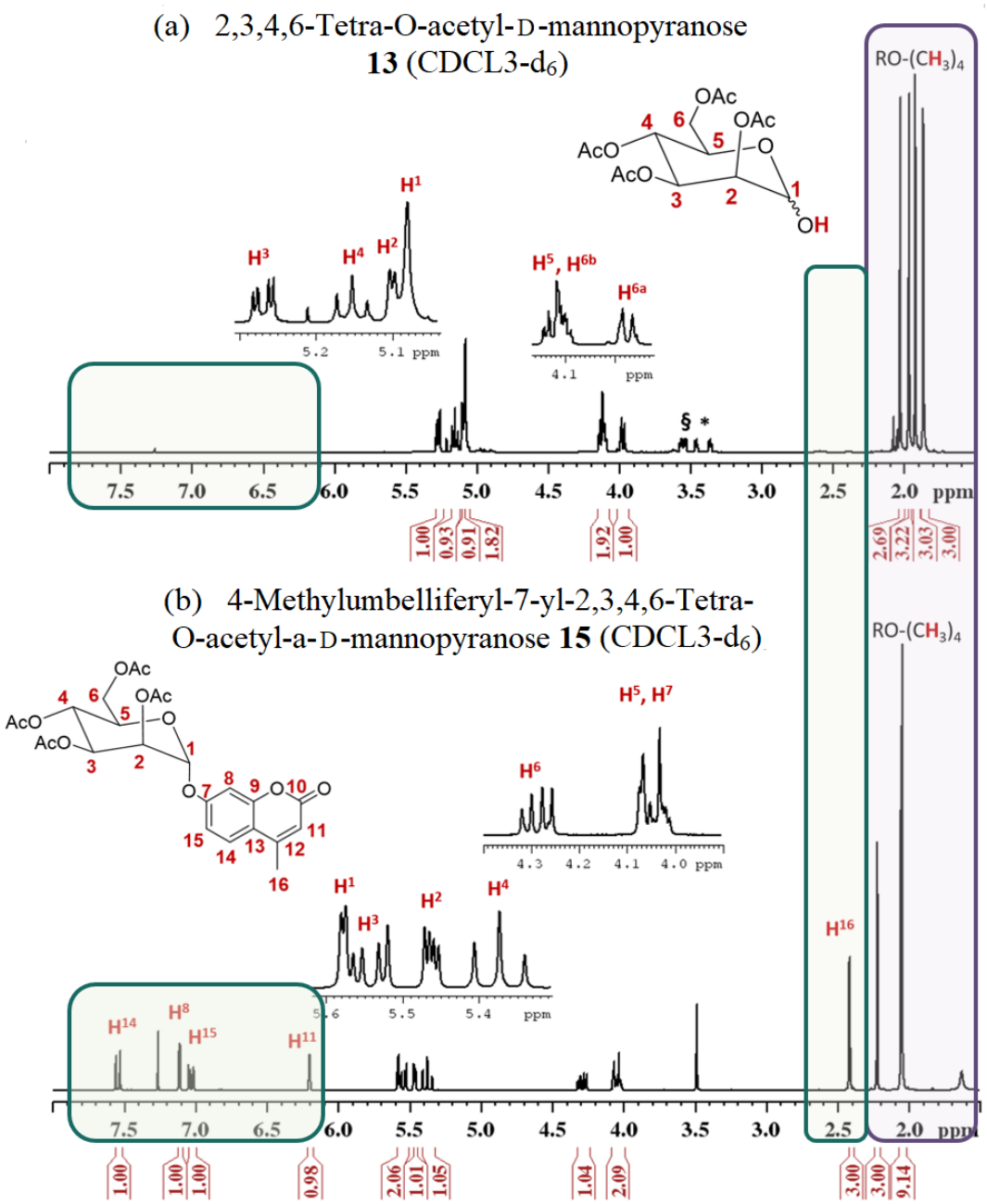

Figure 43: Comparative ^{1}H NMR (500MHz, $CDCl_3$) spectra of the obtained product from 2 different steps (step 1; a, step 3; b) of the synthesis of 4-methylumbelliferyl-7-yl-2,3,4,6-tetra-O-acetyl-α-D-mannopyranose **(15)**. The highlighted in purple area where the acetyl groups are observed and in green the area where the coumarin unit characteristic resonances can be found.

A comparison between the ^{1}H-NMR spectra of the corresponding obtained products for two of the steps in the formation of compound **15** (AcGC) (from the bottom to the top) is presented in **Figure 43**. The resonances at 1.80-2.10 ppm (**Figure 43 a)** which corresponds to the acetyl groups of the glycosyl moiety are shifted up-field (**Figure 43 b**) due to the coupling with the coumarin moiety. In more detail, the resonance at 2.05 ppm

of the acetyl group at C2 is shifted up-field about δ= 0.15 ppm after the coupling reaction. In addition, the resonances between 6.90 and 7.60 ppm which can be identified in the bottom spectrum (**Figure 43 b**) were observed after the coupling of the tetracetyl glycosyl derivative (**14**) with the 4-methylumbelliferone and corresponds to its aromatic hydrogens. Lastly, as with the aromatic resonances, the resonance at 2.44 ppm corresponding to the methyl group of position 16 is only observed after the coupling of the coumarin moiety (**Figure 43 b**).

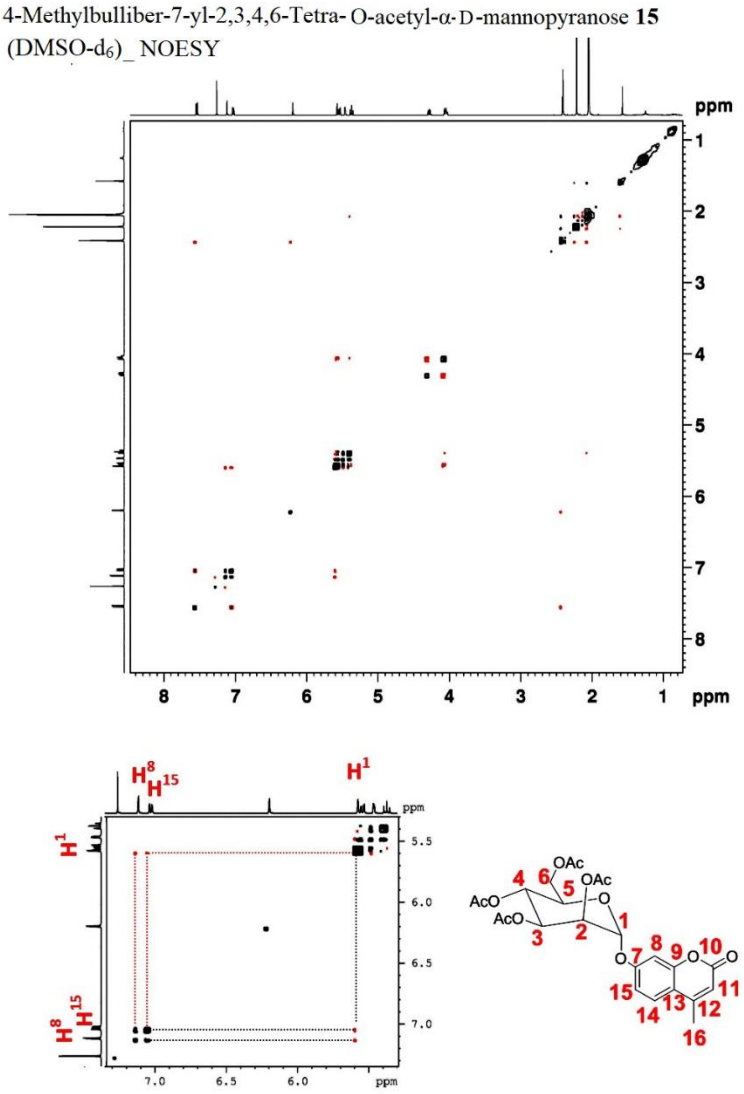

Figure 44: ^{1}H-^{1}H NOESY NMR spectrum, NOE resonances of 4- Methylumbelliferyl-7-yl-2,3,4,6-Tetra-O-acetyl- α -D-mannopyranose **(15)** proves that coupling between 4- methylumbelliferylone with tetracetyl- α -D-mannopyranose **(14)** occurred.

To ensure that the coupling reaction had been achieved a NOESY NMR experiment was carried out. By NOESY NMR, the NOE cross resonances between the protons in the anomeric position and the ones in the ortho position of the coumarin should be visible if the coupling was successful (**Figure 44**). Indeed, NOE cross resonances between H^1- H^8 (at δ=5.59 ppm and 7.15 ppm) and H^1- H^{15} resonances were found (at δ=5.59 ppm and 7.03 ppm) confirming the coupling between the two compounds.

Moreover, the success of the deprotection at the final step of the synthesis (denoted GC,**16**) was confirmed by both IR and NMR spectroscopy. In the following figure (the absence of all resonances between 1.80 and 2.45 ppm (**Figure 45**, purple area) suggests the absence of acetyl groups and as a consequence the deprotection of the methylumbelliferyl-tetraacetyl-D-mannopyranose (denoted AcGC, **15**) to form the glycosyl coumarin compound (**16**).

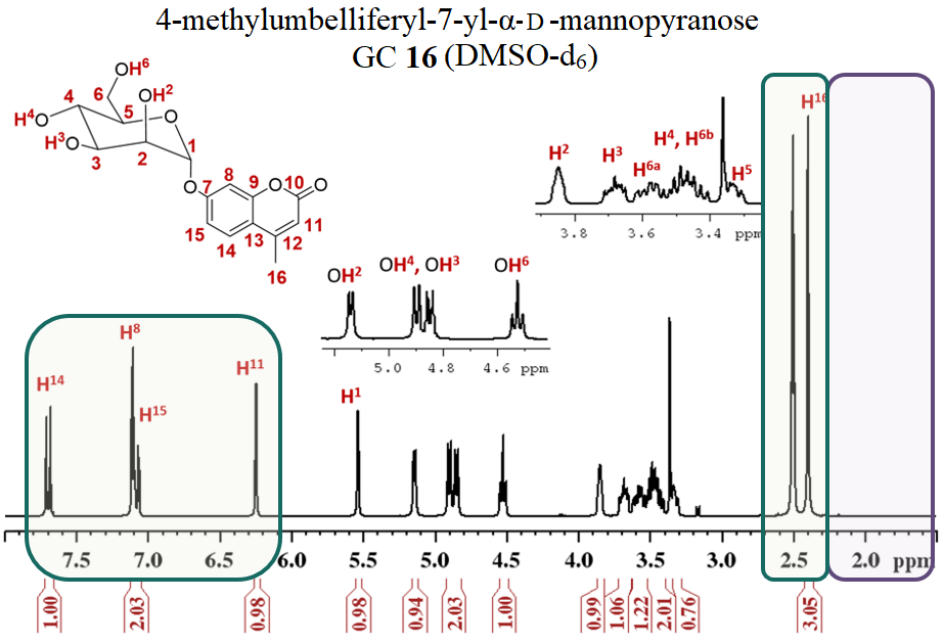

Figure 45: ^{1}H NMR (500MHz, DMSO-d_6) spectra of 4-methylumbelliferyl-7-yl-α-D-mannopyranose **(**GC, **16)**. The area where the acetyl groups are usually observed is highlighted in purple and the area where the coumarin characteristic peaks can be found is shown in green.

Additionally, IR spectroscopy in the solid state was carried out to establish whether the deprotection had occurred. The absorption band at 1600-1700 cm^{-1} which corresponds to the stretching vibration of the C=O group decreases corresponding to the loss of acetyl groups to reveal the hydroxyl functions. The appearance of a new broad band around

3120-4000 cm^{-1} due to the O-H stretching vibration provides further evidence for the successful deprotection of the glycosyl moiety (**Figure 46**).

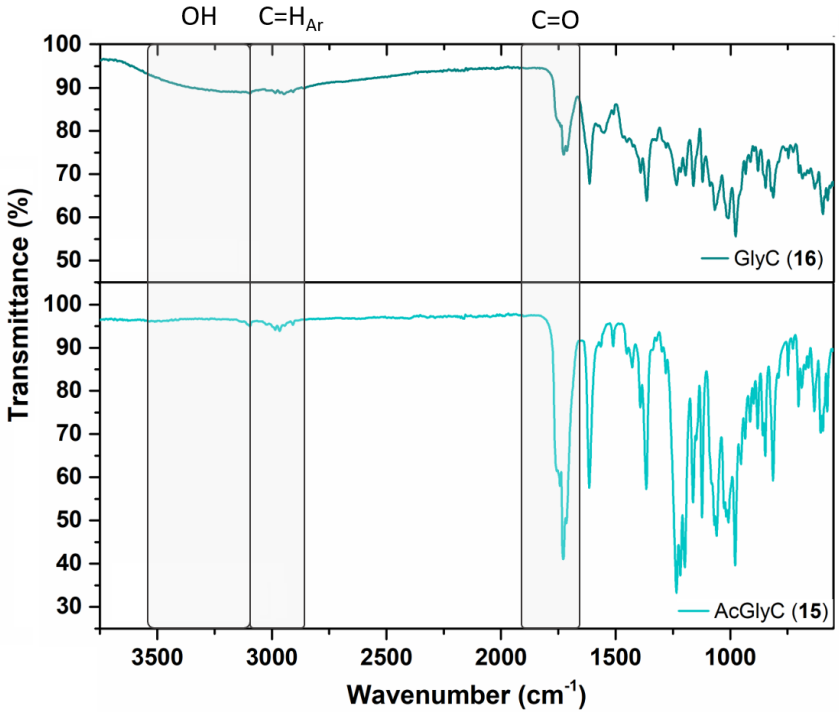

Figure 46: Comparative IR spectra for the tetracetyl-glycosyl coumarin (denoted **AcGC, 15**) (bottom) and glycosyl coumarin (denoted **GC, 16**) (top).

3.4.2. Coupling of glycosyl coumarin with the asymmetric thiosemicarbazonate metal complexes.

Having achieved the synthesis of GC, the following step was the coupling with complex **9a** (PhZnTSCA) to form an aminoglycosidic bond. It is known that the formation of this linkage can be achieved under mildly acidic conditions through the reaction of carbonyl group of the anomeric C-atom (position 1) of the sugar in the open-chain form with an amino group (Maillard reaction)[12]. A straightforward coupling was attempted (**Scheme 20**), dissolving both molecules in slightly acidic methanol and carrying out the reaction under reflux overnight (18-20 h), the reaction was monitored by HPLC. These conditions were established taking into account a variety of other coupling experiments that were previously carried out for complex **9a** (PhZnTSCA)[6] and the fact that acenaphthenequinone thiosemicarbazonato complexes were found to be unstable at high temperature in previous studies.[13]

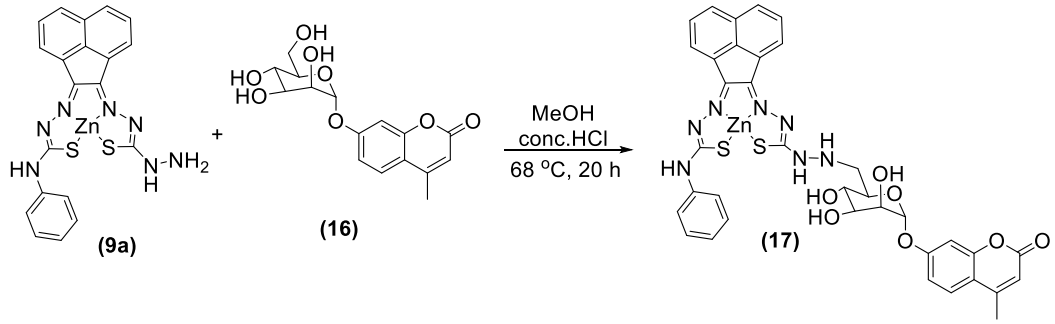

Scheme 20: Coupling reaction of the denoted PhZnTSCA (**9a**) precursor complex with the GC (**16**).

NMR spectroscopy results indicate the presence of the starting materials however mass spectrometry data (**Figure 47**) are consistent with the formation of the asymmetrical complex **17** (Ph-GC-ZnTSCA). Further increase of temperature was not recommended and a metal-catalysed coupling reaction is not a desirable option due to the possible Zn transmetallation, so further optimisation of the coupling above was not carried out.

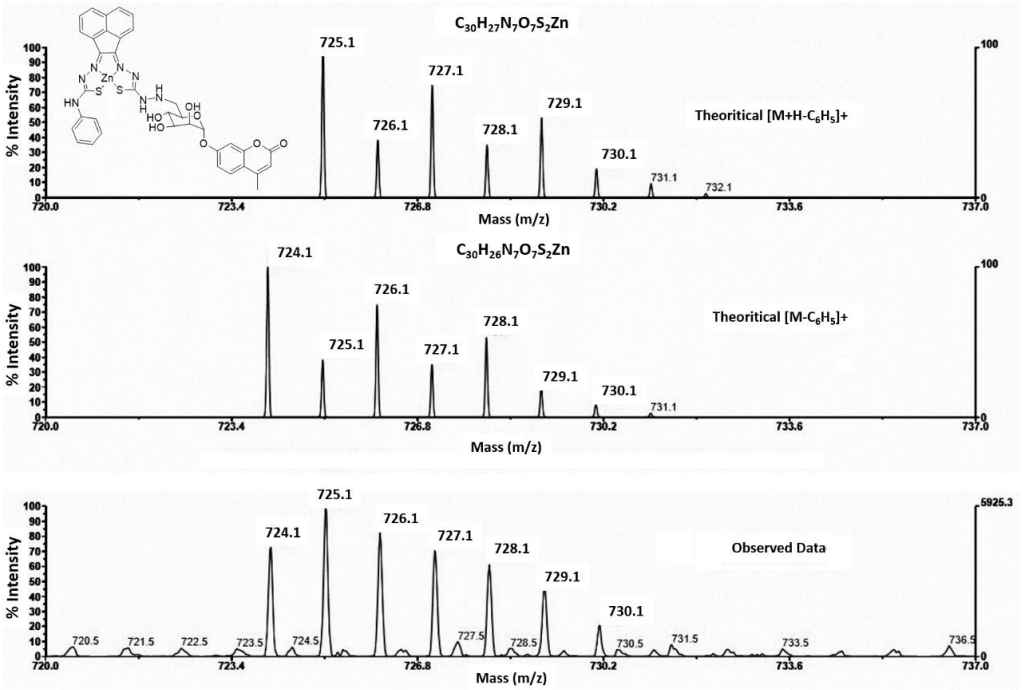

Figure 47: Atmospheric-pressure chemical ionization (APCI) analysis mass spectrometry result for the complex **17** (denoted Ph-GC-ZnTSCA) (Full spectrum can be found in appendix).

As an alternative strategy, the selective activation of the primary carbohydrate alcohol group (position 6 in the sugar moiety) was explored, through its conversion to an aldehyde. Thus, the selective oxidation of the 6-OH group of **16** (GC) was attempted as reported by Angelin and colleagues.[14] According to these authors, a selective oxidation of the primary carbohydrate hydroxyl group to an aldehyde is possible by a TEMPO (2,2,6,6-Tetramethylpiperidine 1-oxyl) catalysed reaction using TCC (3,4,4` trichlorocarbanilide) as a secondary oxidant and $NaHCO_3$ as a base, at low temperature under anhydrous conditions. Unfortunately, in this case, the reaction did not progress (**Scheme 21**). Optimisation of the reaction conditions was attempted, such as slight increase of temperature (15 °C), addition of higher equivalents of both TEMPO and TCC, as well as prolonging the reaction time; however, the reaction did not appear to take place according to HPLC monitoring. The lack of success of this reaction can possibly be explained due to steric hindrance caused by the aromatic ring of the coumarin. Another route targeting the selective functionalization therefore needed to be explored.

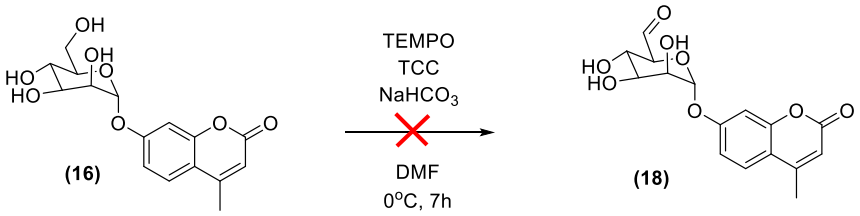

Scheme 21: Oxidation reaction of the carbohydrate hydroxyl group of denoted GC (**16**) to afford the corresponding dialdo-GC (**18**).

Similarly, other reactions and synthetic pathways were tried in an attempt to selectively activate the primary carbohydrate hydroxyl group, but disappointingly most of them were unsuccessful. Finally, the activation was carried out following the Appel reaction where an alcohol is converted to the corresponding alkyl halide via activation by triphenylphosphine and the S_N2 displacement of a halide ion from a tetrahalomethane.

Even though this reaction usually takes place under mild condition and affords a high yield, in this case, the reaction was carried out overnight, monitored by HPLC, and the yield of the halogenated product was low (7.1%). More specifically the reaction was carried out as follows (**Scheme 22**). Compound **16** (GC) was dissolved in dry pyridine and triphenylphosphine was added at 0 °C. The mixture was allowed to react for half an hour then tetrabromoethane was added slowly. Then, the resultant mixture was heated to

reflux and reacted for 16 hours. Mass spectrometry results confirmed the formation of the corresponding halogenated glycosyl coumarin (denoted BrGC, **19**) as the theoretical isotopic pattern and the observed one were found to be a good match for this compound (**Figure 48**).

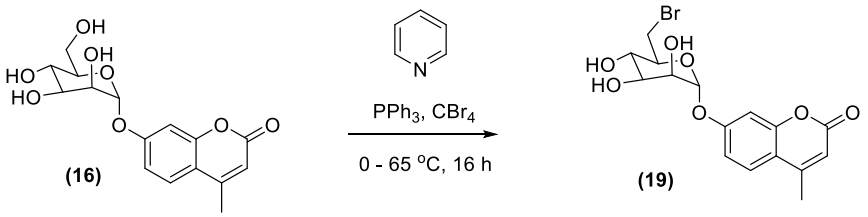

Scheme 22: Conversion of the primary carbohydrate hydroxyl group of GC (**16**) to an alkyl bromide (**18**).

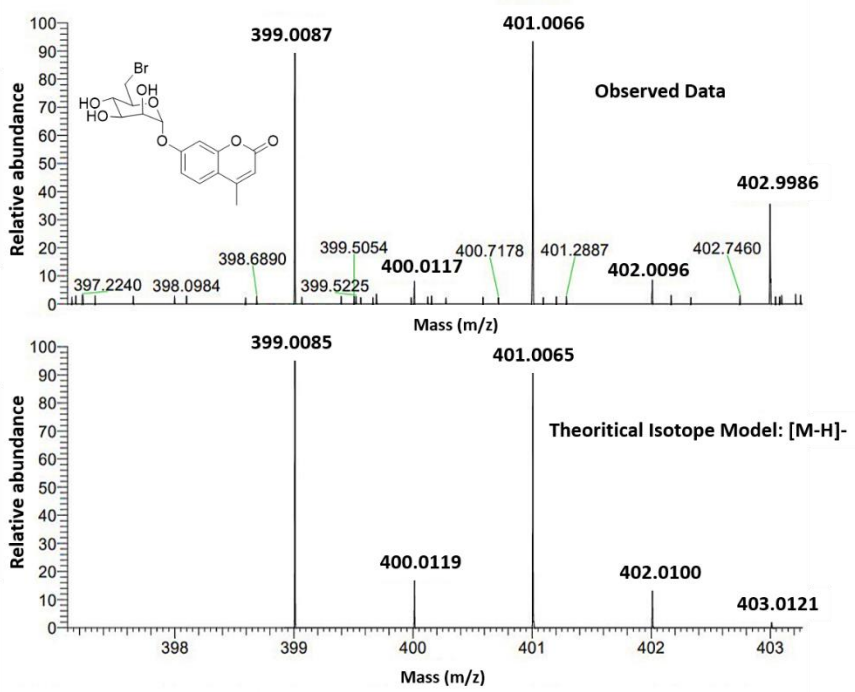

Figure 48: Nano-electrospray ionisation (nano-ESI) mass spectrometry result for BrGC **(19)**.

This bromination step was crucial since bromide constitutes a good leaving group and can be subsequently displaced under relatively mild conditions. Consequently, further functionalisation of the group attached to the carbohydrate group of the sugar would now be possible. The conversion to an azido group is considered a good option to follow aiming to apply "click" chemistry in the resulting compound.

3.5. Evaluation of asymmetric complexes *in vitro*

3.5.1. Investigation by crystal violet assays

Preliminary cytotoxicity studies prior to the application of the asymmetric complexes in biological experiments have been considered to be essential for the determination of the optimal working concentration in order to avoid cellular damage. The crystal violet assay is a simple method facilitating the detection of cellular adhesion and integrity. The aim is to target proteins and DNA, but upon induction of cell death, cell detachment results in a different pattern of the stained cellular population which allows for later quantification.[15]

In this work, all the monosubstituted ligands were tested in crystal violet assays in a range of different concentrations in order to calculate the IC_{50} values. The viability assays were carried out in PC-3 and EMT-6 cell lines under normoxic and chemically induced hypoxic conditions ($CoCl_2$). Incubation was performed in 96-well plates with the selected compounds in serum medium (1% DMSO), at different concentrations, for 48 h at 37 ºC. Then serum media was removed, and cells were washed with PBS three times. Fixing of cells with a methanol/water solution (1:1) and a methanol (100%) solution was followed. Afterwards, 0.5 % crystal violet solution was added and incubated for 20 min at room temperature. Crystal violet was then removed, plate was rinsed an indirect flow of tap water. Then the plate was inverted and leave to dry on the bench at room temperature. Moreover, methanol was added to the plates and incubated for a further 20 min at room temperature prior to absorbance measurement through a plate reader. The detailed conditions are listed in Chapter 7.

In the following chart (**Figure 49**) the results of the aforementioned experiments are presented. As the chart shows, both complexes present a noticeable toxicity at 48 h, especially in normoxic conditions. For the Ga(III) complex (PhGaTSCA, **10a**) toxicity was much higher than for the corresponding Zn(II) complex (PhZnTSCA, **9a**) in both cell lines. Thus, cell viability, time-dependence experiments were carried out to examine the toxicity of both complexes as a function of time (**Figure 50**).

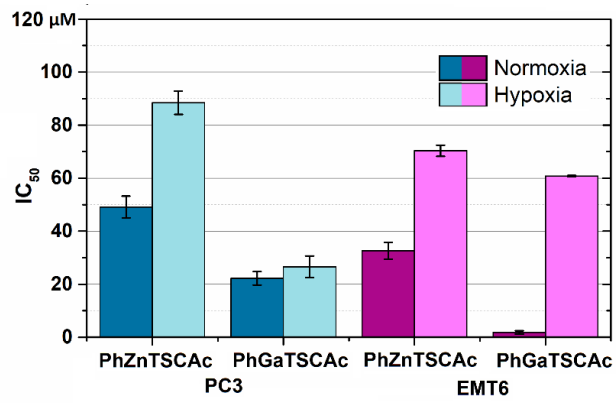

Figure 49: Estimate of IC_{50} values from crystal violet assays with PC3 (**blue**) and EMT6 (**purple**) cell lines under both normoxic (**dark**) and chemically induced hypoxic (**light**) conditions after 48 h incubation of compounds **9a** (denoted PhZnTSCA) and **10a** (denoted PhGaTSCA) complexes. Error bar stands for standard error (±SE), calculated from six repeated measurements.

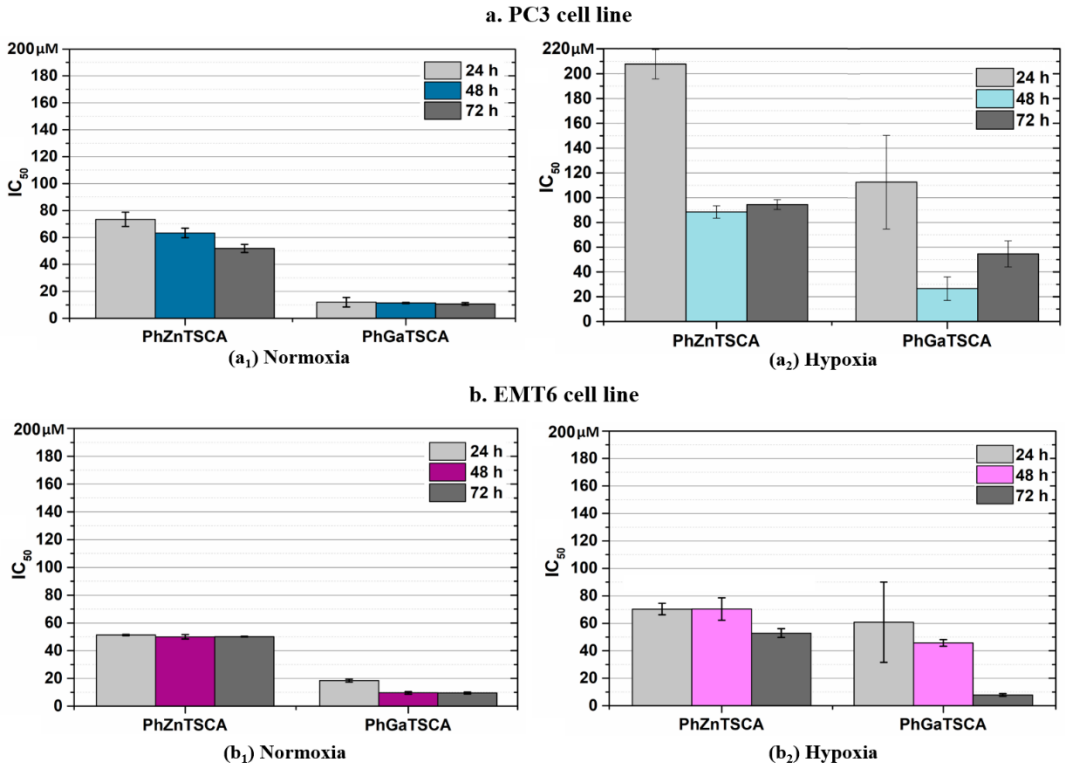

Figure 50: Estimation of IC_{50} values from crystal violet assays for PC3 (**a**) and EMT6 (**b**) cell lines under both normoxic (**1**) and chemically induced hypoxic (**2**) conditions after 24 h (**light grey**), 48 h (**blue,purple**) and 72 h (**dark grey**) of **9a** (denoted PhZnTSCA) and **10a** (denoted PhGaTSCA) complexes incubation. Error bar stands for standard error (±SE), calculated from six repeated measurements.

In fact, the compounds were tested at 24 h, 48 h and 72 h, being in agreement with the previously mentioned results (**Figures 49** and **50** conditions stated with identical colours). Moreover, these results imply that the complex **9a** (PhZnTSCA) was not detrimental for the cells at the 24 h time point, regardless of the cell line. The IC_{50} values for the subsequent points increase gradually. On the other hand, the complex **10a** (PhGaTSCA) is much more toxic to the cells after the first 24 h of incubation. Notably, the compounds seem to be more toxic against normoxic cells rather than chemically induced hypoxic cells. This might be associated with the experimental conditions used to induce hypoxia in the cell culture, since $CoCl_2$ induced hypoxia assays could mimic the hypoxic environment, but perhaps introduce limitations regarding the redox chemistry behind it. In order to decipher the effect of the compound on hypoxic cells, further experiments under a hypoxia chamber environment are required.

*3.5.2. Fluorescence microscopy of compound denoted PhGaTSCA (**10a**) in cancer cells*

Fluorescence microscopy was carried out to determine the uptake of the compounds by PC-3 cells. For these assays, cells were cultured using standard protocols, analogous with earlier investigations on fluorescent thiosemicarbazonates. Cell viability assessments were tested prior to fluorescence experiments and over the course of the experiments cell morphology was observed by optical imaging. The uptake of the complexes **9a** (PhZnTSCA) and **10a** (PhGaTSCA) was imaged in the PC-3 (prostate carcinoma) cell line under both normoxic and hypoxic conditions (cultured as described in the Experimental section, Chapter 7) by confocal fluorescence microscopy using one photon excitation at 488 nm and emission in all the different colour channels; blue: λ_{em} = 417-477 nm; c) green: λ_{em} = 515-555 nm. c) red: λ_{em} 570-750.

The imaging studies were performed as previously described in Chapter 2. Control experiments were obtained by fluorescence imaging, prior to incubation of cells with the compounds of interest, to assess the original cellular morphology before any treatment. No significant changes in cellular shape were observed by optical microscopy after 15 minutes incubation with respect to the control. The previous figures depict representative confocal fluorescence microscopy images in PC-3 cells for the complex **10a** (PhGaTSCA) which showed an intense fluorescence enhancement and some hypoxia selectivity (**Figure 51**).

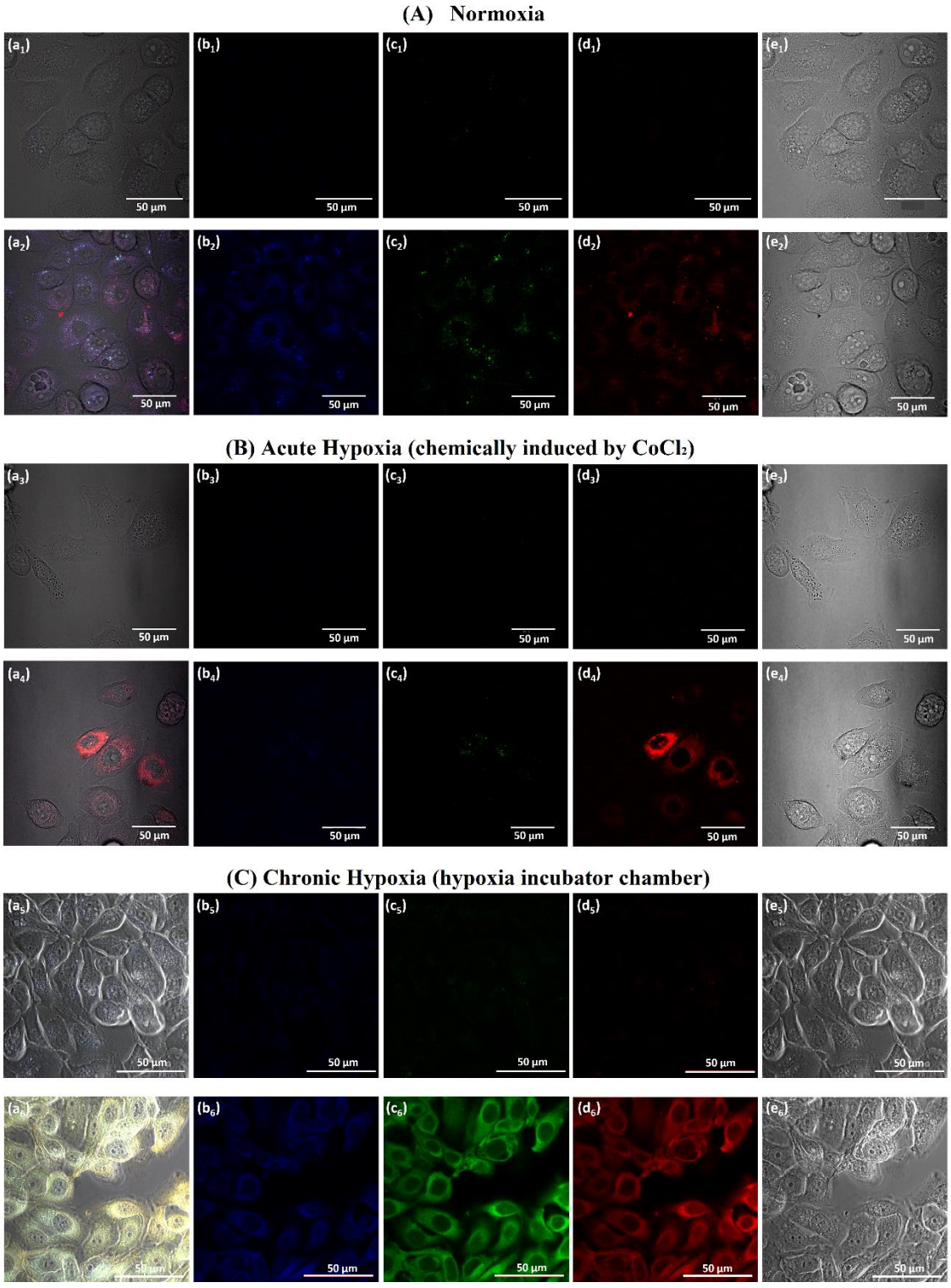

Figure 51: Confocal cellular imaging of PC-3 cells grown under different conditions were incubated at 37 °C for 15 minutes with **10a** (100 µM, in 5: 95 DMSO : serum-free medium). Laser was excited at 405 nm. a) overlay of the green-red channels and DIC image b) blue: λ_{em} = 417-477 nm; c) green: λ_{em} = 515-555 nm. c) red: λ_{em} 570-750 nm; d) DIC image; 1,3,5: control. 2,4,6: compound (scale bar 50µm). (A larger image of these cells and can be found in the Appendix)

Cells were acquired after a 15 minutes incubation and their profiles are presented above. The observation of fluorescence in these images suggests that under normoxic conditions, a substantial amount of these complexes remain intact intracellularly. Despite that, frames under hypoxic conditions (cells treated with $CoCl_2$ or cultured inside a hypoxia chamber) depict a widespread distribution of the gallium complex within the cell cytoplasm (**Figure 51**). It must be noted that the compound was not evident in any image in the blue and green channels under reduced hypoxic conditions, whilst it was detected in all the different colour channels in hypoxic environment caused by the hypoxic chamber (**Figure 51 B,C**). One of the reasons that this might happening is due to the redox chemistry taking place under these hypoxic conditions having some differences from that caused by chemically induced hypoxia.

The intracellular distribution of the compound is substantial in the hypoxic environment induced in the chamber and it seems that the compound does not precipitate at all (**Figure 51 C**). This observation was made for the reduced hypoxic environment (**Figure 51 B**) and was even more evident for the normoxic environment (**Figure 51 A**). It should be noted here that the images acquired for the cells cultured in the hypoxic chamber have been collected from a different fluorescence microscopy device than the rest of the samples, which results in higher resolution images (**Figure 51**; a_5-e_5 and a_6-e_6).

*3.5.3. Multiphoton fluorescence lifetime evaluation of compound denoted PhGaTSCA (**10a**) in PC-3 cells*

Two-photon excitation experiments were performed at the Rutherford Appleton Laboratory following the methodology described in Pascu *et al.* 2011[16] with the assistance of Prof. S Botchway and his group.

In order to be able to quantify the compound's fluorescence, the background autofluorescence of cells had to be assessed beforehand. The background fluorescence can be attributable to biological fluorophores; at 910 nm (two photon excitation) this includes flavin adenine dinucleotide (FAD) and lipoamide dehydrogenase (LipDH),[17] which also absorb at 810 nm. Biological molecules such as reduced nicotinamide adenine dinucleotide (NADH) and nicotinamide adenine dinucleotide phosphate (NADPH) absorb 810 nm light, but not 910 nm, therefore contributing to the difference in autofluorescence intensity observed at the respective wavelengths.[17]

The fluorescence lifetime of the compound was obtained from both Time-Correlated Single Photon Counting (TCSPC) and the fluorescence life-time imaging microscopy (FLIM) distribution curve in solution and PC3 cancer cells respectively. When compound **10a** (PhGaTSCA) was tested by TCSPC, two fluorescence lifetime components (**Figure 52 a**) could be determined in DMSO at 10 mM, with the τ_1 accounting for at least 93%. The minor component (τ_2) of the fluorescence lifetime of the ligand precursors in DMSO at 10 mM was found to be 861.5 ps. These numbers, however, are to be taken with caution as the errors are much larger than for τ_1 due to the weakness of this second component (< 5%) (see table in **Figure 52 a**).

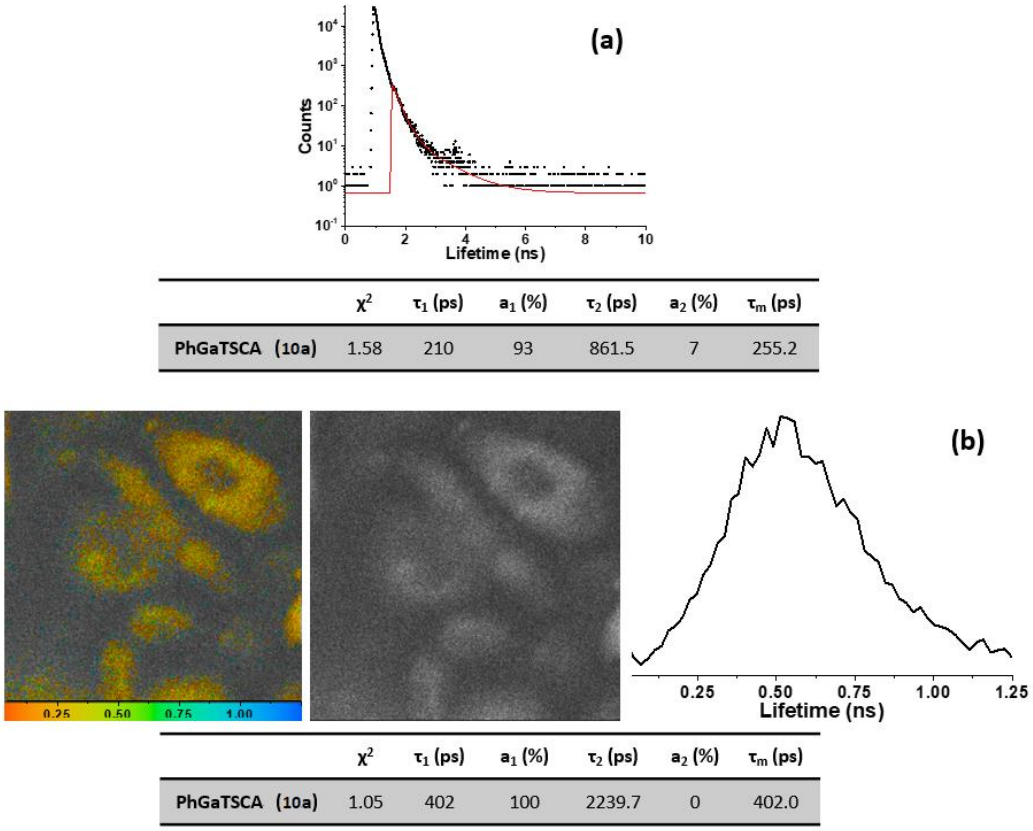

	χ^2	τ_1 (ps)	a_1 (%)	τ_2 (ps)	a_2 (%)	τ_m (ps)
PhGaTSCA (10a)	1.58	210	93	861.5	7	255.2

	χ^2	τ_1 (ps)	a_1 (%)	τ_2 (ps)	a_2 (%)	τ_m (ps)
PhGaTSCA (10a)	1.05	402	100	2239.7	0	402.0

Figure 52: FLIM map in PC-3 cell line in normoxic conditions with lifetime distribution and 2P fluorescence spectra for **10a** (PhGaTSCA) complex in DMSO (100 μM).

Moreover, compound **10a** (PhGaTSCA) was tested by FLIM. The conditions used were 100 μM **10a** (1% DMSO), with an incubation time of 20 minutes. The FLIM data were measured in the range 0.52±0.24 ns, which represents the life-time distribution of the compound *in vitro*. As it is shown in the table of **Figure 52 b**, for example when a

random chosen spot is measured, a two-life time component with an average life-time (τ_m) of 0.4 ns is calculated.

The major components could be related with the compound being inside the cell, whilst the minor components could be correlated with different aspects, possibly a different orientation of the molecule. Interestingly, although consistency of data was observed in cells, the respective short component is slightly shorter (ca. 0.2 ns) than the overall fluorescence life time in cells, suggesting that the complexity of the cellular environment does have impact on the lifetime.

3.6. Conclusion to Chapter 3

Metal asymmetric thiosemicarbazonato complexes were successfully synthesised and characterised by ESI-MS and NMR spectroscopy. They were also radiolabelled for the first time through a transmetallation reaction with gallium-68 and tested *in vitro* for cytotoxicity, optical imaging (confocal and two-photon FLIM) and cellular uptake assays. Their fluorescence properties were analysed, denoting a weak distribution in normoxic cells, but enhanced distribution in both acute hypoxic environment (chemically induced by $CoCl_2$) and chronic hypoxic environments (cells grown in hypoxia chamber) Furthermore, the fluorescence lifetime components of these compounds determined both in solution and in cells have distinct characteristic data that proved different from cellular autofluorescence. This sufficient discrimination between the fluorescent lifetime components in the cytoplasm suggests the uptake of the compound by the cells. The cell viability assays for these complexes suggest a decreased number of viable cells at 48 hours post-incubation, therefore time-dependent experiments were conducted, confirming that the zinc(II) derivatives present low toxicity at 24 h under all the different conditions attempted. However, the gallium(III) derivative is more toxic than the zinc(II) derivatives, especially in normoxic cells. Having obtained and analysed these results, it is clear that further toxicity assays are required using a hypoxia chamber, to decipher how the redox chemistry might affect the viability of the cells. Lastly, since the radiolabelling protocol is now established, the next step is to study the stability of the compounds under different biological environments, and also to carry out cell uptake experiments.

More over the functionalisation of asymmetric thiosemicarbazonato metal complexes with a couple of small molecules was attempted herein for the first time. The success of these attempts was rather variable - this is most likely due to the aromatic backbone of the metal complexes which makes the hydrazino moiety of these molecules less active than the one in traditional ATSM complexes. Nevertheless, here it is presented for the first time the radiolabelling of an asymmetric thiosemicarbazonato complex with a prosthetic group ([^{18}F]4-fluorobenzaldehyde) in a new and promising radiochemical incorporation protocol. Further optimisation of the purification would lead to a high purity radiolabelled compound which could potentially be tested not only *in vitro* for cell uptake but also *in vivo* on mouse or rat models. Finally, the coupling of a hypoxia-targeting small molecule with an asymmetric metal complex was achieved and significant steps were made for the optimisation of this coupling by selective modification of the primary carbohydrate hydroxyl group of the glucosyl moiety of compound **16** (GC). Even though the functionalisation of the primary carbohydrate hydroxyl group is often reported, these strategies are usually applied to monosaccharides with the anomeric hydroxyl group protected as a methyl ether rather than in the presence of an aromatic aglycone moieties, such as a coumarin. But the selective bromination that was now carried out will possibly allow further activation of this specific group through different routes.

3.7. References to Chapter 3

1. F. Cortezon-Tamarit, S. Sarpaki, D. G. Calatayud, V. Mirabello and S. I. Pascu, *Chem. Rec.*, 2016, **16**, 1380-1397.
2. J. R. Dilworth and R. Hueting, *Inorganica Chim. Acta*, 2012, **389**, 3-15.
3. I. S. Alam, R. L. Arrowsmith, F. Cortezon-Tamarit, F. Twyman, G. Kociok-Köhn, S. W. Botchway, J. R. Dilworth, L. Carroll, E. O. Aboagye and S. I. Pascu, *Dalton Trans.*, 2016, **45**, 144-155.
4. R. L. Arrowsmith, PhD thesis, University of Bath, 2013.
5. F. C. Cortezon-Tamarit, PhD thesis, University of Bath, 2016.
6. D. Hanahan and R. A. Weinberg, *Cell*, 2011, **144**, 646-674.
7. D. Hanahan and R. A. Weinberg, *Cell*, 2000, **100**, 57-70.

8. R. Schirrmacher, B. Wängler, J. Bailey, V. Bernard-Gauthier, E. Schirrmacher and C. Wängler, *Semin. Nucl. Med.*, 2017, **47**, 474-492.
9. L. Carroll, R. Bejot, R. Hueting, R. King, P. Bonnitcha, S. Bayly, M. Christlieb, J. R. Dilworth, A. D. Gee and J. Declerck, *Chem. Commun.*, 2010, **46**, 4052-4054.
10. N. Touisni, A. Maresca, P. C. McDonald, Y. Lou, A. Scozzafava, S. Dedhar, J.-Y. Winum and C. T. Supuran, *J. Med. Chem.*, 2011, **54**, 8271-8277.
11. B. Sandhofer, M. Meckel, J. M. Delgado-Lopez, T. Patricio, A. Tampieri, F. Rosch and M. Iafisco, *ACS Appl. Mater. Interfaces*, 2015, **7**, 10623-10633.
12. G. P. Ellis, *Adv. Carbohyd. Chem.*, ed. M. L. Wolfrom, Academic Press, 1959, **14**, 63-134.
13. R. L. Arrowsmith, PhD thesis Doctor of Philosophy, University of Bath, 2013.
14. M. Angelin, M. Hermansson, H. Dong and O. Ramström, *Eur. J. Org. Chem.*, 2006, **2006**, 4323-4326.
15. M. Feoktistova, P. Geserick and M. Leverkus, *Cold Spring Harb. Protoc.*, 2016, **2016**, pdb.prot087379.
16. R. L. Arrowsmith, P. A. Waghorn, M. W. Jones, A. Bauman, S. K. Brayshaw, Z. Hu, G. Kociok-Kohn, T. L. Mindt, R. M. Tyrrell, S. W. Botchway, J. R. Dilworth and S. I. Pascu, *Dalton Trans.*, 2011, **40**, 6238-6252.
17. S. Huang, A. A. Heikal and W. W. Webb, *Biophys. J.*, 2002, **82**, 2811-2825.

Chapter 4: Use of graphene oxide as nanocarrier to chosen molecules

4.1. Overview

Nanotechnology has advanced over the past 20 years as a research field because of the unique physicochemical properties of nanostructures, which allows interesting technical applications in different scientific areas. The interest for nanotechnology in nanomedicine, also called the application of nanotechnology in healthcare and medicine is called, has grown rapidly in the last decade because of the higher specificity of a nano-dimensional drug, compared to a molecular drug, against a precise disease target. Graphene presents relevant opportunities for the development of a broad range of biomedical applications.[1] Due to graphene oxide's lower toxicity and to its superior biocompatibility in comparison with other nanoparticles (e.q. metallic NPs), its use has started to be explored as nanocarrier for drug/ gene delivery[2-6] or as probe for molecular imaging (**Figure 53**).[5-9]

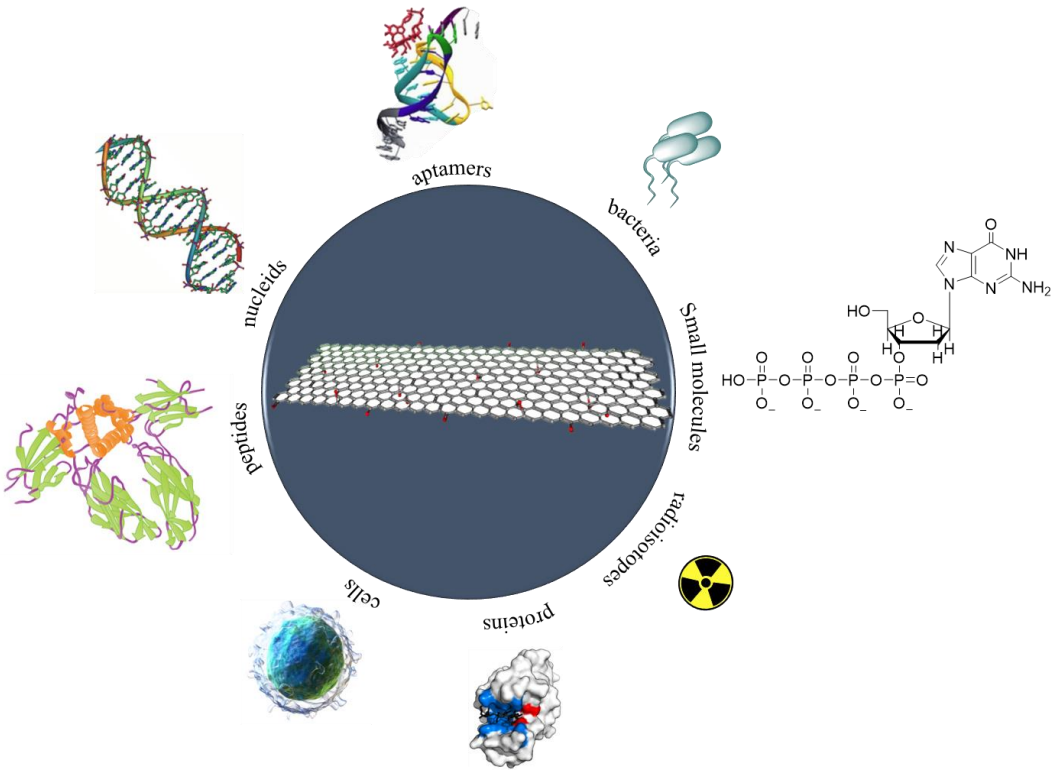

Figure 53: Possible imaging and sensing modalities including the use of GO nanosheets as supports.

Recently, graphene and its derivatives were tested as potential nanoplatforms for a variety of imaging techniques, such as magnetic resonance imaging (MRI),[7, 10-12] fluorescence[7, 13-15] or positron emission tomography (PET) imaging and photoacoustic imaging.[7, 16-18] Furthermore, the combination of different imaging techniques on the same nanocomposite has been tested.[7, 19, 20] Several research studies have showed that graphene oxide (GO) nanocomposites can be conjugated with polyethylene glycol (PEG) or small chelating molecules (e.g. 1,4,7-triazacyclononane-1,4,7-tris acetic acid; NOTA) and, in turn, radiolabelled with various radioisotopes (e.g. iodine-131, gallium-68, copper-64), through chelator radiolabelling.[7] It was not only until recently that Cai's research group suggested that the chelator- free labelling of GO nanocomposites with copper-64 is also possible, allowing the synthesis of radio-nanocomposites with high kinetic stability.[21]

The large surface area of graphene with its sp^2 hybridisation, allows the functionalisation of the sp^2 honeycomb sheet *via* either π-π- interactions and/or van der Waals forces. In this study, graphene oxide nanocomposites were employed as nanocarriers for chelator-free [^{68}Ga]Ga(III)-radiolabelling towards PET imaging and simultaneously as potential carriers of the new unsymmetric thiosemicarbazone complexes and/or glycosyl coumarin compound developed in this work.

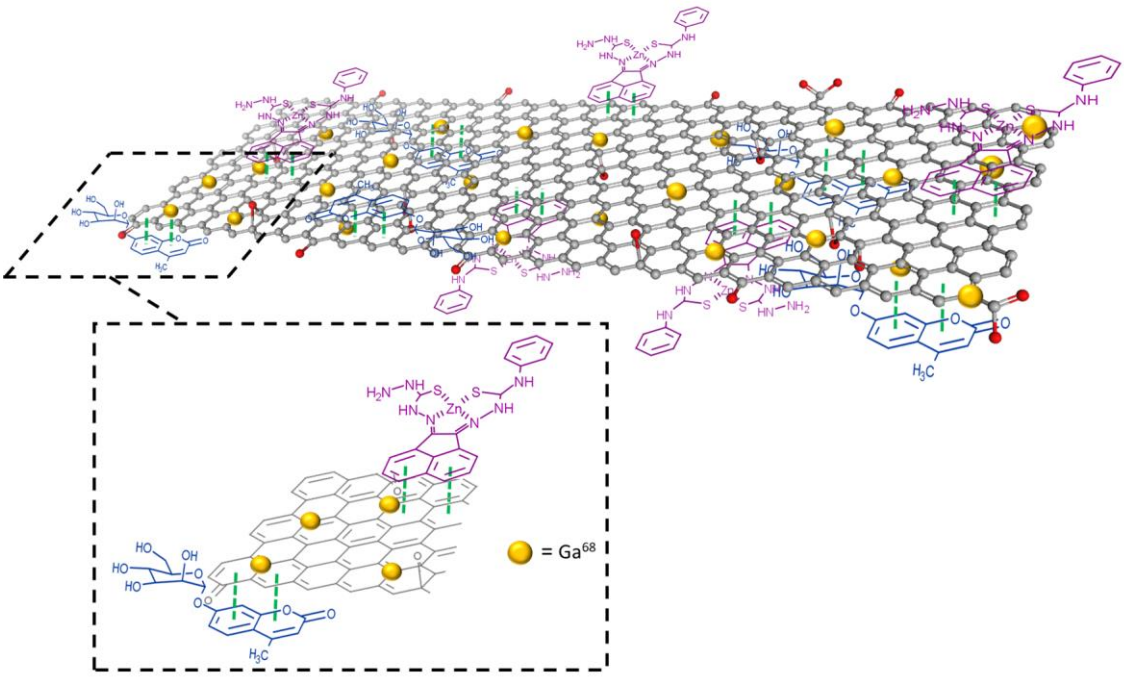

Figure 54: Schematic illustration of a possible complexation of the desired GO nanocarrier.

4.2. Synthesis and functionalisation of graphene oxide nanocomposites.

4.2.1. Synthesis of novel graphene oxide nanocomposites

The GO nanocomposites that were used at this study, have been synthesised together with Danielle Divall and Simone Giuseppe Giuffrida, at the University of Bath. They have been synthesised following a modification of Hummer's method, a process widely used to produce graphene oxide from graphene flakes.[7] The synthesised nanocomposites have been fully characterised by both Raman spectroscopy and transmission electron microscopy (TEM).[22]

*4.2.2. Evaluation of the possible use of GO nanocomposites as carriers for glycosyl coumarin (**16**).*

The extensive domains of sp^2-bonded carbon atoms of GO nanocomposites offer the opportunity to functionalise the sp^2 sheets *via* π-π interactions. It was hypothesised that glycosyl coumarin (GC, **16**) may also be non-covalently attached to the graphene sheets by using the π conjugation within its structure, given its flat and aromatic structure. This could occur by alignment of the aromatic components of the coumarin unit in a parallel conformation along the planar graphitic surface. To achieve this, a suspension of GO nanocomposites diluted in DMSO was mixed for a five minutes with a GC (**16**) solution in DMSO to afford the desired nanocomposite (**20**, **Scheme 23**).

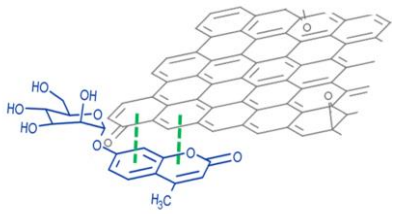

Scheme 23: Schematic representation of nanocomposite **20** (**GC@GO**) showing that compound **16** denoted GC (denoted GC) is non-covalently attached to the GO nanosheet.

The chemical composition of GC (**16**) consists exclusively of C, O, and N atoms, so the use of analytical techniques such as TEM and EDX, which are commonly applied for

the analysis of GO nanocomposites (which also incorporate C/O), is not suitable to detect this species. Therefore, spectroscopic investigation in solution was applied to demonstrate if there was a possible binding between GO and GC (**16**). In this sense, continuous variation method, as Job's method is also known, is one of the most popular methods to determine the stoichiometry of a binding event using common spectroscopic methods.

Usually, the method involves the preparation of equimolar "host" and "guest" solutions which are mixed at a variable volume ratio. The sum of the molar concentration of these solutions remains constant whilst the relative proportions of host and guest solutions alter resulting in a series of samples with different molar fraction.[23, 24] The concentration of the resulting complex is plotted against the molar fraction, resulting in a maximum value which could be considered as the preferable host-guest complex's stoichiometry.[23] Job's method was initially applied to organometallic chemistry but it has proved to be a very useful tool for more complicated complexation where the concentration of the bound ligand is not determined.[7, 25]

The field of GO species has long been investigated in different aspects, but their structural and molecular analysis are aspects that still need to be understood.[7] The molecular weight of GO is unknown, so determination of binding stoichiometry is not possible to state in a precise way, but Job's method can be used in a similar manner as a tool to evidence the differentiation in the emission intensity due to the possible quenching of the fluorescence emission upon titration experiments.

It is known that GO and related species can be directly coated on sugars through their hydroxyl groups *via* hydrogen bonds[26]. To explore whether there is a π-π interaction between GC (**16**) and GO's surface the initial titration experiment was carried out using AcGC (**15**) where the hydroxyl groups are protected, in addition to GC (**16**). This control experiment was chosen to determine the fluorescence emission that corresponds to coumarin unit using different fluorescence excitations. In this context, it is important to take on consideration that previous studies have suggested that the presence of hydroxyl groups in a coumarin moiety could be a deciding factor of its fluorescence efficiency and total absorption.[27] For instance, the fluorescence emission of coumarin can be detected at 376 nm when excited at 310 nm, however when a hydroxyl group is present, the fluorescence emission is observed at 460 nm instead. These explains the diversity within

fluorescence maxima of glycosyl coumarin which is observed in the following titration experiments.

Fluorescent titration of a GO dispersion with acetyl glycosyl coumarin (15) solution

In a typical titration experiment, aliquots of a specific amount of guest solution was added gradually to a host solution keeping the overall concentration constant and the fluorescence emission was measured on a photo counting steady state using a fluorescence spectrophotometer. More specifically, a solution of compound **15** (AcGC) (1 mM) and a stock dispersion of GO nanocomposite (1 mg/mL) were prepared in DMSO. Then the solution of compound **15** (AcGC) was excited at 310 nm and the emission spectrum was measured in a 330-600 nm range. The dispersion of GO nanocomposite (1 mg/mL) (guest) was added gradually (50 μL) into 1.2 mL of compound **15** (AcGC) solution (host) and the total concentration of {GO + [**15**]} for each fluorescence measurement was kept constant (**Figure 55**) to examine whether GO was able to quench the fluorescence of compound **15** (AcGC). The resulting saturated suspensions were well-mixed before and after addition of an aliquot of guest and excess GO was allowed to settle before each measurement for up to 5 minutes.

As shown in **Figure 55**, the fluorescence intensity that corresponds to compound **15** (AcGC) is reduced upon addition of GO suspension. This reduction could be a result of the static and dynamic quenching due to the complex aggregation of the two molecules resulting in strong π-π interactions[28] (**Scheme 24**).

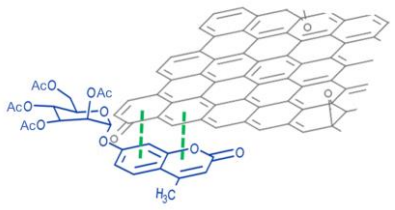

Scheme 24: Schematic representation of nanocomposite **21** (**15**@GO) showing that compound **15** (denoted AcGC) is non-covalently attached to the GO nanosheet.

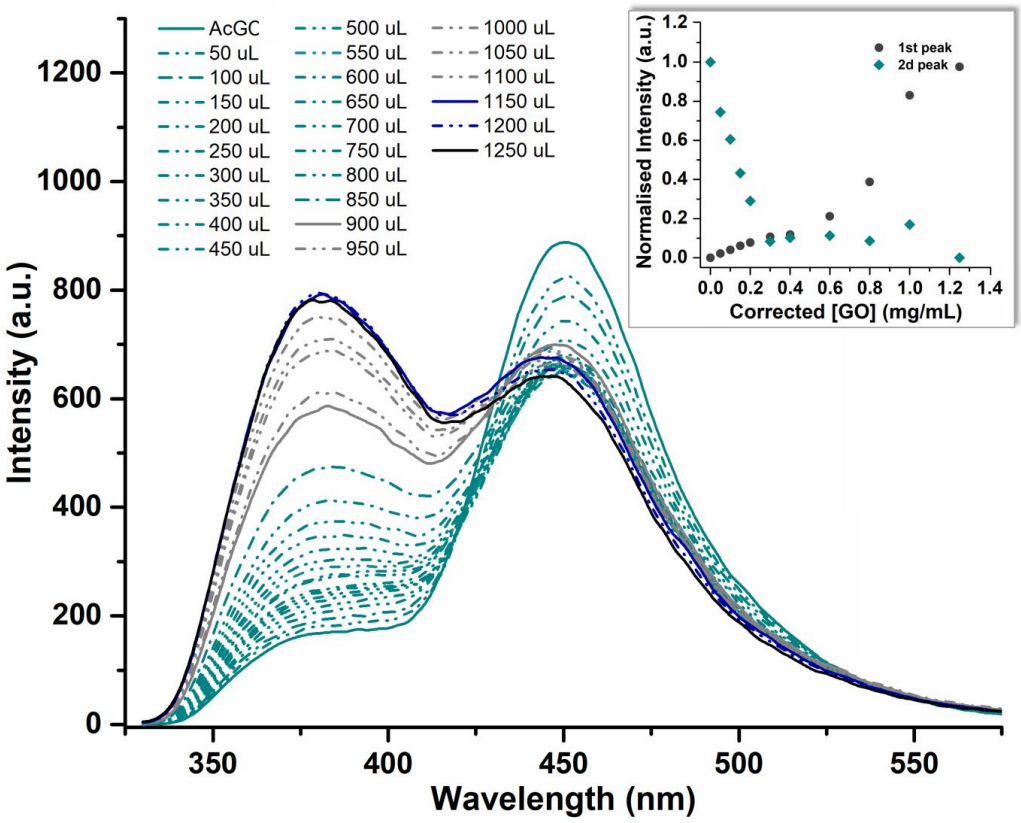

Figure 55: Fluorescence emission quenching in a solution of compound **15** (AcGC) (0.3 mM) during titration of graphene oxide (GO) nanocomposite (mg/mL) in DMSO. The inset shows the normalised fluorescence emission intensity of the two highest peaks at the relevant GO concentration.

A model of a variety of arrangements likely to happen within two different species has been reported by Jabbari-Farouji and colleagues[29]. These authors have described spontaneous self-assembled systems whereby two species could "recognise" each other and bind in disputed phase. **Figure 55** (inset graph) suggests that the complexation of the two molecules is more complicated than the idealised molecule presented in Scheme 27. These complicated aggregation events might occur in a concerted way and result in the partial increase of the intensity to the peak corresponding to denoted AcGC and in a decrease of absorption of the formed complex (blue and black lines from **Figure 55**). It is likely that other GO nanocomposites will stack on the top or on the bottom of the already formed complex resulting in a sandwich-like complex, with either GO or AcGC (**15**) being in the middle or a complex of AcGC (**15**) and GO with dimer-like species. In the following figure (**Figure 56**) some of the possible species that could be formed are represented due to non-covalent binding between, GO and AcGC (**15**).

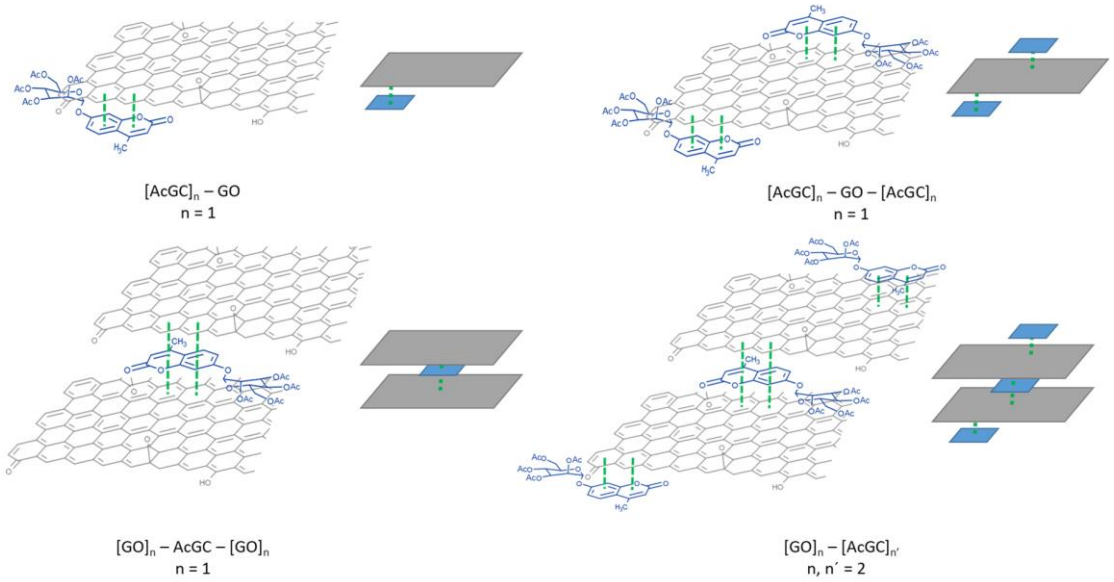

Figure 56: Schematic illustration of the different species that could result from the complexation of GO with compound **15 (**AcGC). In this figure, the simplest version of these species is illustrated, thus n=1 or 2.

Estimation of the binding stoichiometry between GC (16) and coronene

In the present work, since the binding stoichiometry could not be determined for GO nanocomposites, to examine the possible binding a theoretical model was used. Coronene was chosen for this purpose ($C_{24}H_{12}$, **Scheme 25**). Coronene is a planar molecule consisting of seven fused benzene rings, being a member of the polycyclic aromatic hydrocarbon (PAH) family. In the solid state, it is a yellow crystallised material and it is mainly soluble in benzene or toluene, and sparingly in other organic solvents.[1, 4] This system, has long been used by different research groups as theoretical model to study either graphene's oxidative process or aromatic interactions with graphene.[1, 30, 31] The structure and the molecular weight of coronene are known allowing kinetic and thermodynamic studies of the supramolecular association between graphene nanosheets and chromophores to be carried out. A better understanding of the strength of such interactions in solution has been sought by employing this is as a model titration investigation.

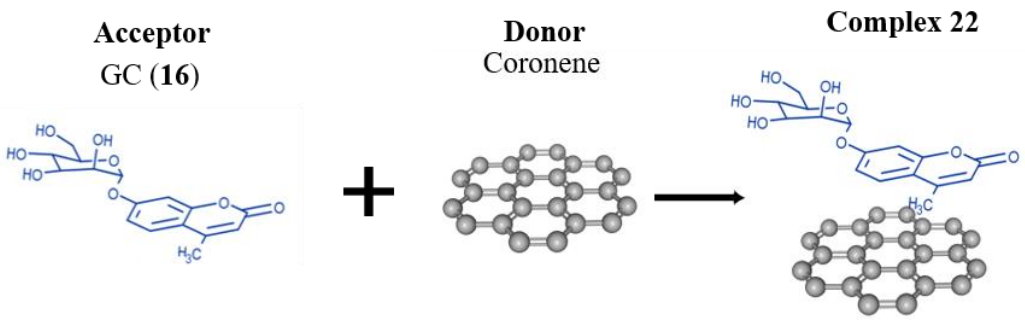

Scheme 25: Schematic representation of the formation of compound **16** (GC) – coronene planar system complex (**22**).

More specifically a fluorescence titration of coronene was carried out on an equimolar mixture of compound **16** (GC) to estimate the possible binding process between them. The solution of compound **16** (0.125 mM) was excited at 310 nm and the emission spectrum was measured from 330 nm to 600 nm. Gradual addition of the guest solution (0.125 mM of coronene) to the host solution (GC,**16**) then followed, as described in the experimental section, till the ratio of GO to compound **16** (GC) was slightly more than 1:1. The resulting saturated suspension was well-mixed before and after addition of each guest aliquot (**Figure 57**).

As the graph of **Figure 57** suggests, the intrinsic fluorescence of compound **16** (GC) is quenched upon addition of coronene suspension and a shift in emission maxima is noticed which is later quenched as the titration progresses. The reduction of **16** fluorescence indicates the possible complexation of the two molecules and the quenching of the new fluorescence band suggests that the coronene molecule is likely to be bound with the initially formed complex resulting in a sandwich-like complex, with either coronene or **16** (GC) being in the middle or a complex with dimer-like species (complex **22**). As it was suggested by Farouji and colleagues,[29] it is then very difficult to predict all these possible arrangements, for purposes of simplicity the discussion is limited to the association constant for the 1:1 complexes. However, we attempted to model the titration data according to 2:1 system also.

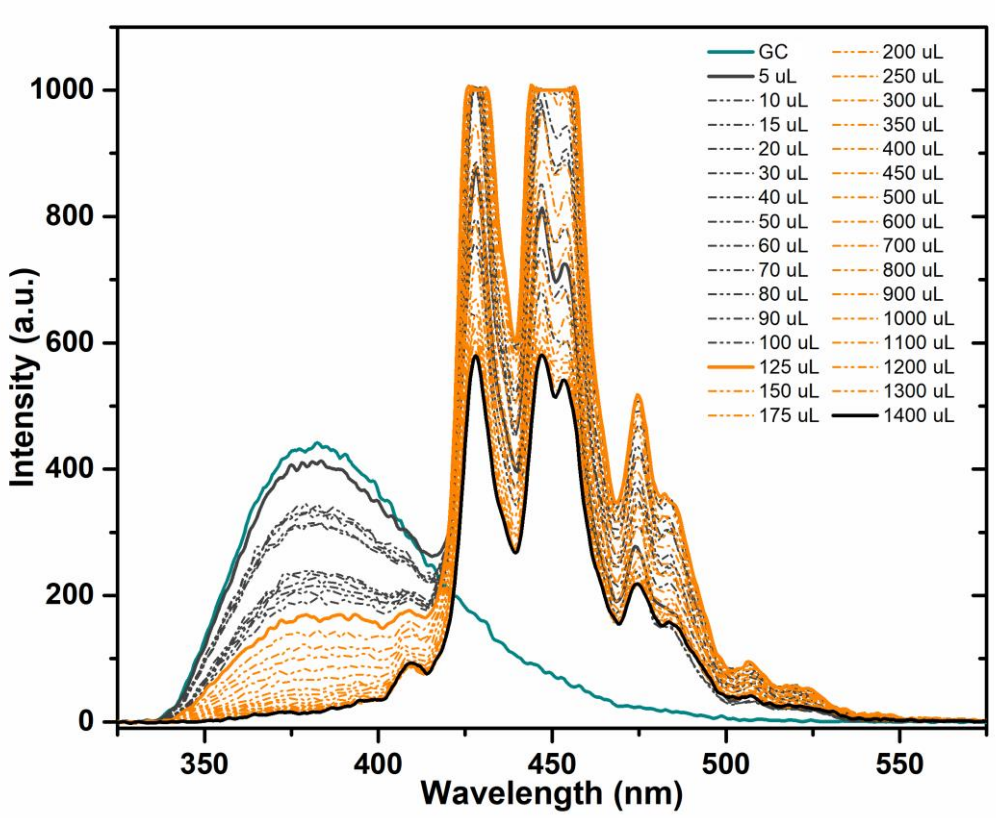

Figure 57: Fluorescence emission quenching in a solution of compound **16** (GC) (0.125 mM) during titration with coronene (0.125 mM) in DMSO.

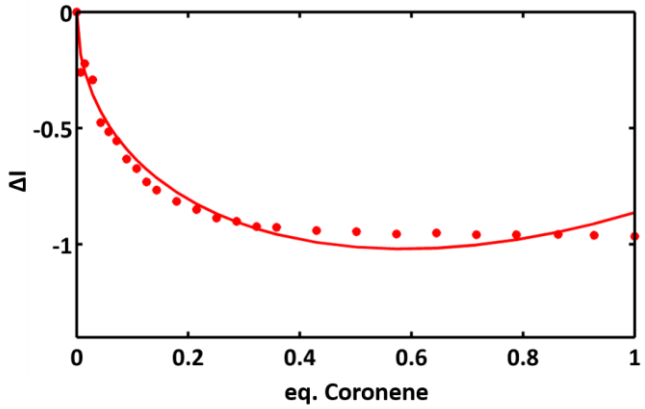

Figure 58: Experimental data (markers) and fitting curve (line) of a 2:1 isotherm binding model at the relative **16**: coronene ratio.

Table 12: Table presenting the binding constant $K_a^{2:1}$ (M^{-1}), the standard error of estimated data (SE) and the covariance of fit (Cov_f) calculated according to MATLAB m-files.[32]

	$K_a^{2:1}$	SE_y	Cov_f
GC (16)	$1.18594*10^{12}$ M^{-1}	0.051025667	0.028747143

The decrease of fluorescence absorption of compound **16** (GC) was monitored and a new emission maxima resulted upon the progressive increase of coronene's concentration. The data were collected, analysed by MATLAB m-files[32] and fitted for 1:1, 1:2, 2:1 $C_{24}H_{12}$:GC binding isotherms. This software resulted in Ka (eq.1) and statistical parameters such as standard error of estimated data (SEy) and covariance of fitting (Covf).

$$K_a = \frac{[H\,G]}{[H][G]} \quad \text{(eq. 1)}$$

Binding constants and statistical parameters for compound **16** (GC) are reported in **Table 12**. Here, binding constants are described as Km:n where m and n are integers. A complex where m or n is greater than 1 describes a system where either the host or guest possesses more than one binding site. Despite repeated attempts to adjust modelling parameters, to 1:1 and 1:2 $C_{24}H_{12}$: **16** simulations gave physically non-sensible results suggesting that these models are not favoured systems for the $C_{24}H_{12}$: GC complexes, and 2:1 is more likely to be happening. The 2:1 $C_{24}H_{12}$: **16** isotherm fitting reveals much lower values of $Ka_1^{2:1}$ for GC in comparison to $Ka_2^{2:1}$ ($Ka_2^{2:1} = 1.18594*10^{12}$ M^{-1}) These values suggest that during the second binding event more complicated species are assembled (see **Figure 58**, the values between 0.4 and 0.8). All the different equilibriums that may be formed due to such interactions are very difficult to predict.[33]

Use Graphene Oxide Nanocomposites as carriers for glycosyl coumarin (16) and 9a (PhZnTSCA).

Based on the previous results and the fact that the asymmetric metal complexes can be attached to the GO nanocomposites, we examined the possibility of the non-covalent binding of **16** (GC) and **9a** (PhZnTSCA) on the graphitic surface. This was tested in a similar manner as the conjugation of **15** (AcGC) on the GO nanocomposites. More specifically **9a**@GO complex (**23**) (donor) was incorporated and effectively bound with the solubilised **16** (GC) molecules (acceptor) (**Scheme 26**).

In more detail, a solution of **16** (GC) (1 mM in DMSO) was excited at 310 nm and the emission spectrum was measured from 330 nm to 800 nm. Then a suspension of nanocomposite **24** (1 mg/mL in DMSO) was added gradually into the **16** (GC) solution

(host) and fluorescence spectra were measured (**Figure 59**) to examine whether complex **23** was able to quench the fluorescence of compound **16** (GC).

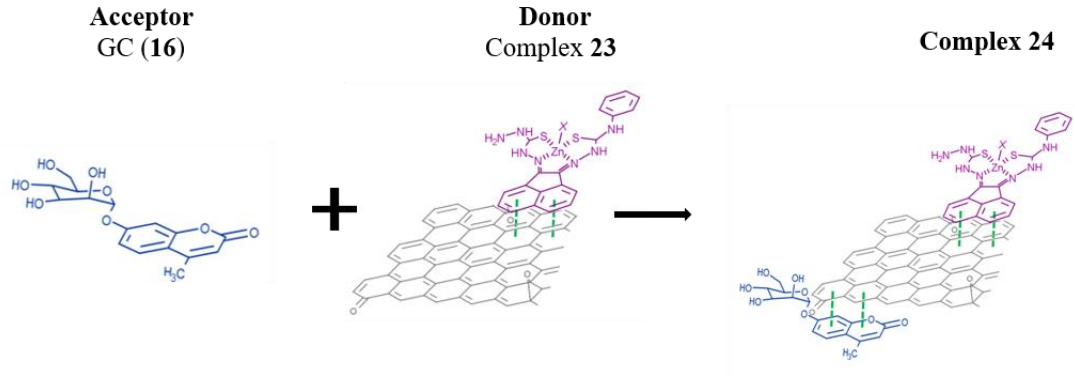

Scheme 26: Schematic representation of the formation of complex **24**; where the compound **16** (GC) and the **9a** (PhZnTSCA) asymmetric complex are non-covalently attached to the planar graphitic surface of the nanocomposite.

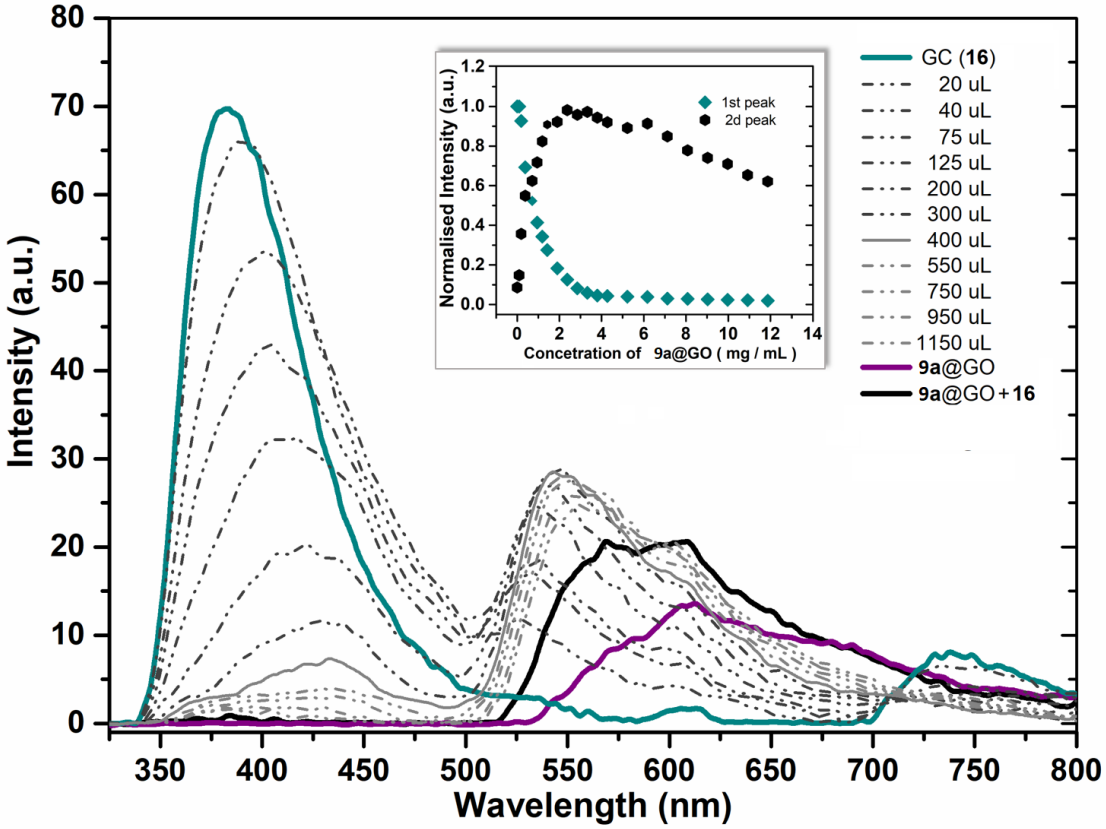

Figure 59: Fluorescence emission quenching in a solution of GC (**16**) (0.3 mM) during titration of PhZnTSCAc@GO (**23**) nanocomposite (mg/mL) in DMSO. The inset shows the normalised fluorescence emission intensity of the two highest peaks at the relevant concentration of **23**.

As it is proposed from **Figure 59**, the emission intensity that corresponds to compound **16** (GC) (blue line) is reduced upon addition of the complex **23** (**9a**@GO) suspension and a new fluorescence maximum is observed. The maximum fluorescence intensity of this emission band (dark grey line) does not emit at the same wavelength as the complex **23** (**9a**@GO) which could suggest the complexation of the two molecules is forming different species (**Scheme 26**). It is important to note that as the titration proceeds, this new emission band is quenched, suggesting a rearrangement of the formed complex (**29**). The inset graph of **Figure 59** depicts the normalised intensity of both emission bands at the relevant complex **23** (**9a**@GO) concentration and implies a relation between the increasing fluorescence intensity of the one emission band and the decreasing fluorescence intensity of the other.

Additionally, **Figure 60** confirms this hypothesis. The graph presents the normalised ratio between the initial fluorescence absorption of each peak to the partial intensity of it at the relevant complex **23** (**9a**@GO) concentration and it clearly shows that the second emission band only increases its fluorescence intensity after the quenching of the first one. These results suggest that the formed hybrid has a more complex supramolecular structure than the one suggested in **Scheme 26**. **Figure 61** shows some of the proposed possible arrangements of possible species formed due to the non-covalent binding between complex **23** (**9a**@GO) and compound **16** (GC).

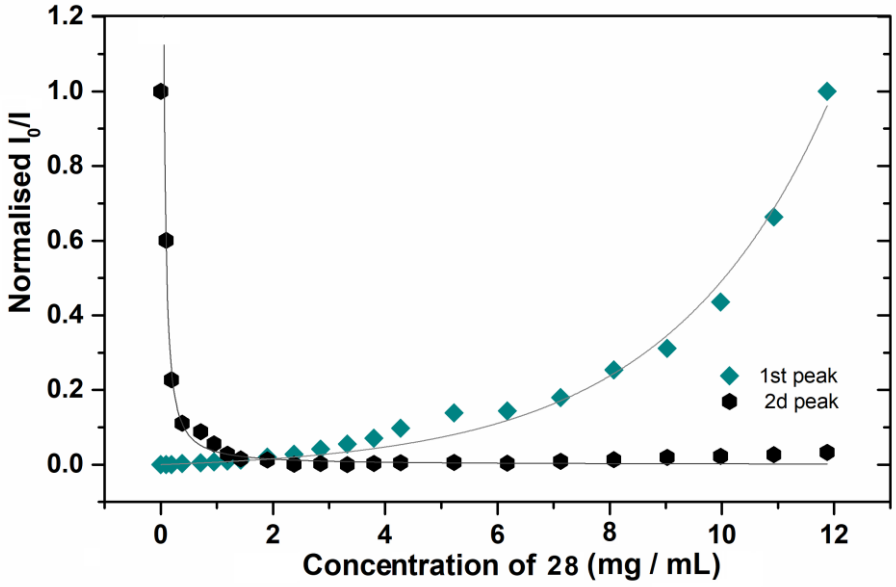

Figure 60: Normalised ratio of the initial emission intensity to the partial intensity for the two fluorescence maxima at the relevant complex **23** (**9a**@GO) concentration.

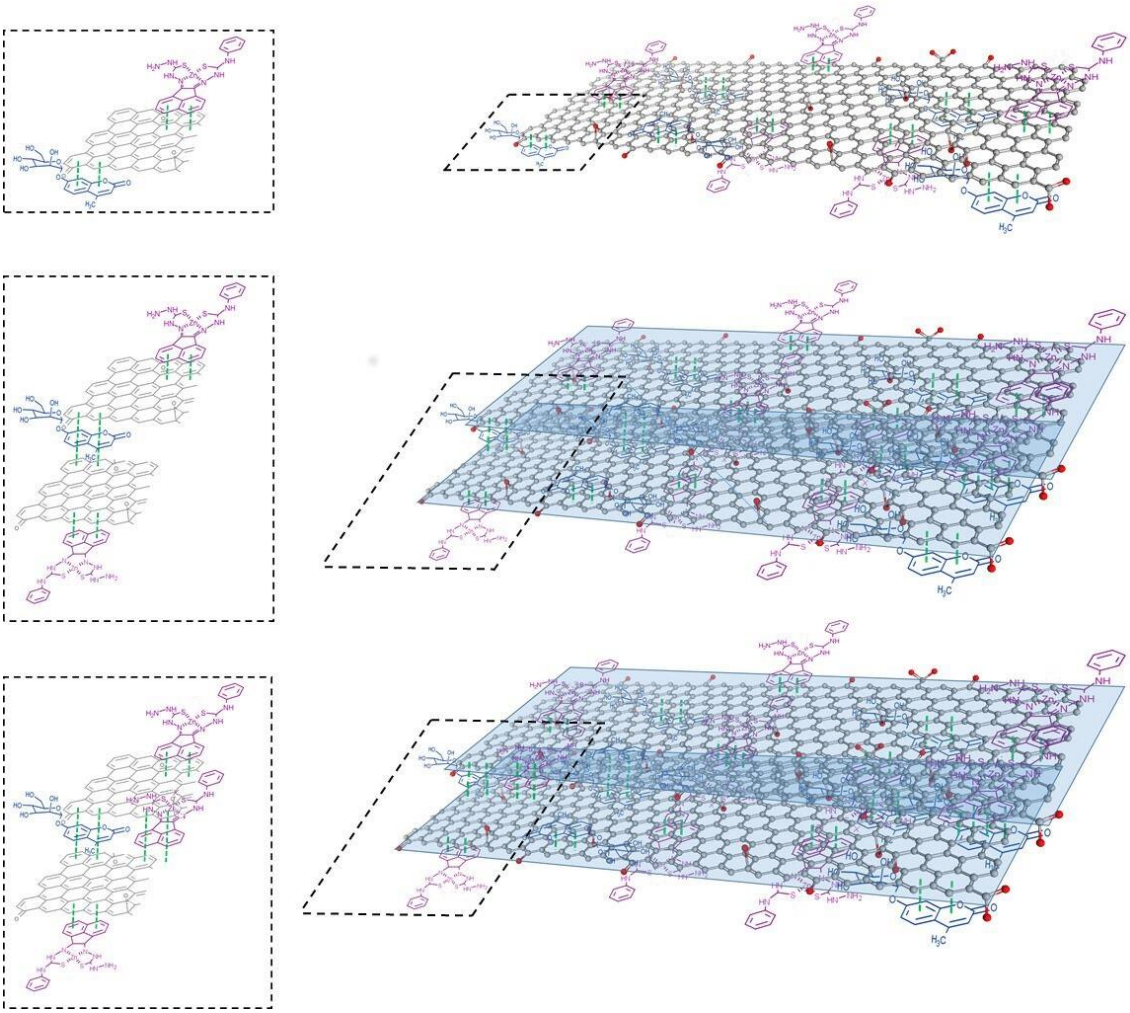

Figure 61: Schematic illustration of the different species of complex **24** (**16**+**9a**@GO)**.** In this figure the simplest version of those species is illustrated, thus n=1 or 2.

4.3. Radiolabelling of GO nanocomposites.

4.3.1. Radiolabelling of GO nanocomposites with gallium-68.

The non-covalent labelling of a number of GO nanocomposites with [^{68}Ga]$GaCl_3$ was attempted herein. More specifically, it was hypothesised that the chelator-free labelling of GO nanocomposites with gallium-68 could be possible due to transition metal-π electron interactions based on the electron transfer between Ga(III) cations and π electron density on the surface of GO. Theoretically, [^{68}Ga]Ga^{3+} ($3d^{10}$) has three free

p-orbitals in its outermost sub-shell which could be used with the π electron density of the GO nanostructures to form a stable electron configuration. The [^{68}Ga]-labelling was successfully carried out by simple mixing of a GO nanocomposite suspension (2 mg/ DMSO mL) with dry [^{68}Ga]$GaCl_3$ in a 4:1 methanol: sodium acetate buffer solution (pH = 4.5) for 30 minutes at 95 °C. The origin of the [^{68}Ga]$GaCl_3$ (aq) did implied to play a crucial role as the labelling was succesful with both gallium-68 extracted by a cyclotron via the ^{68}Zn(p,n)^{68}Ga reaction in aqueous solution and eluted through a [^{68}Ge]/[^{68}Ga] generator.

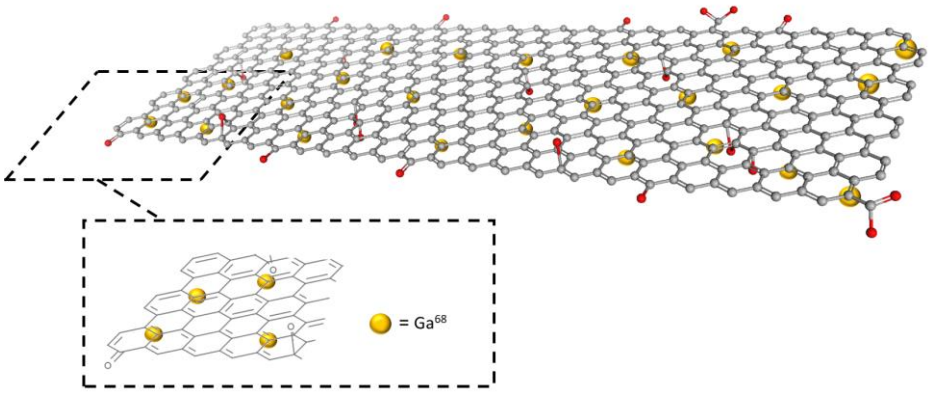

Figure 62: Schematic illustration of the suggested species of **[^{68}Ga]-25** complexation ([^{68}Ga]Ga @GO), where the gallium-68 binds non-covalently to the GO nanostructure.

The radiolabelling of GO nanocomposites was also achieved with the GO complexes **23** and **24**. The radiochemical yield of crude [^{68}Ga]Ga@GO nanocomposites varied between the different nanocomposites used from 98 ± 4.6 % to 99.7 ± 0.74 %, providing all of them as a single radioactive species, based on the amount of activity detected by paper chromatography (Whatman 3MM) as reported in **Figure 65**. All the suggested species are presented in **Figures 62-64.**

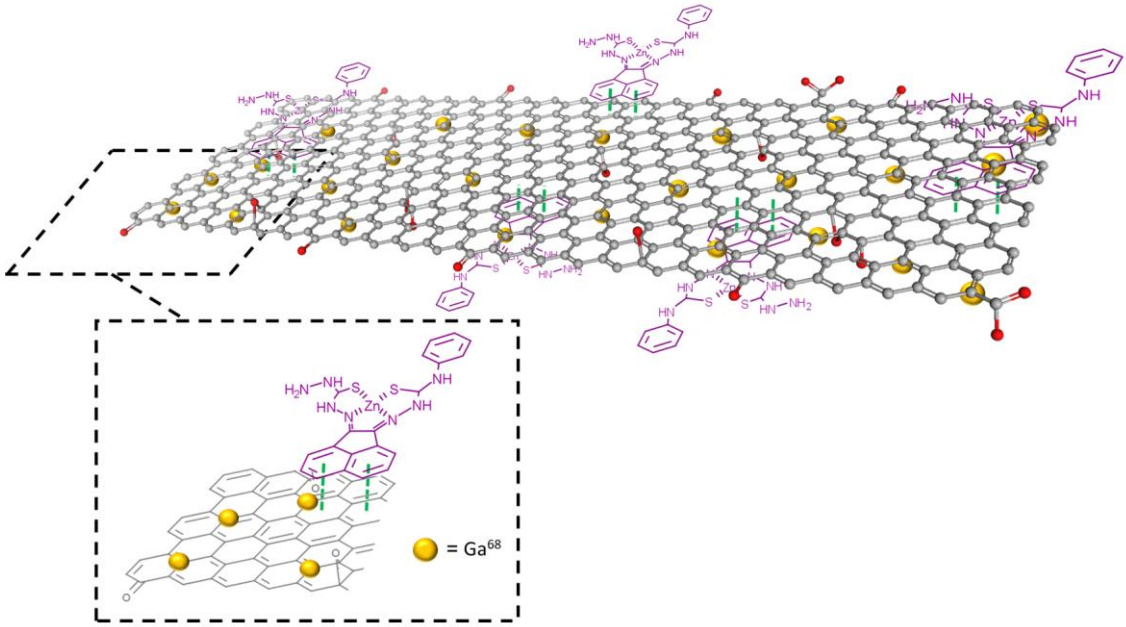

Figure 63: Schematic illustration of the suggested species of **[^{68}Ga]-26** complexation ([^{68}Ga]Ga+**9a@**GO), where the gallium-68 binds non- covalently to the complex **23**.

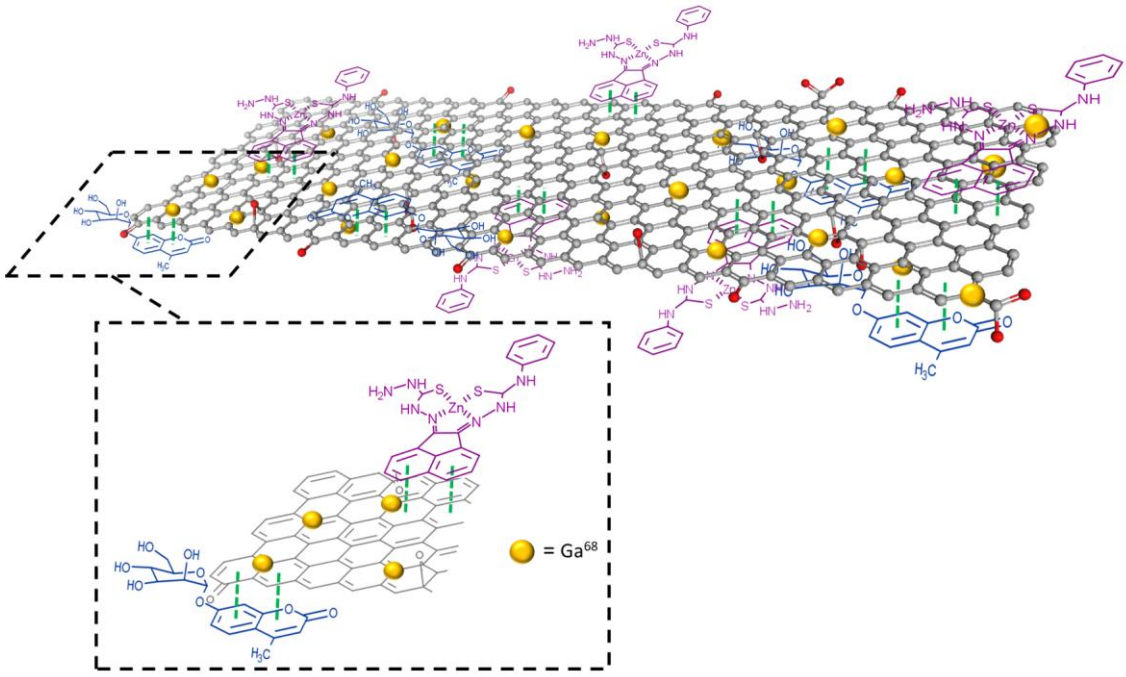

Figure 64: Schematic illustration of the suggested species of **[^{68}Ga]-27** complexation ([^{68}Ga]Ga+**16**+**9a**@GO), where the gallium-68 binds non- covalently to the complex **24**.

.

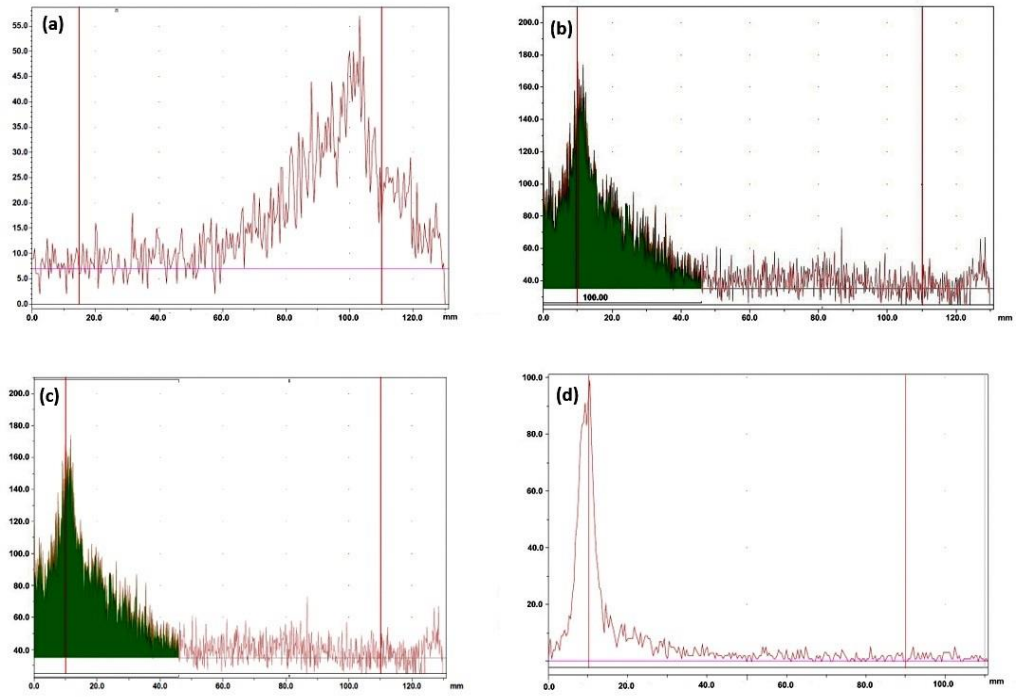

Figure 65: Radio TLC of (a) [^{68}Ga]$GaCl_3$, (b) crude **[^{68}Ga]-25**, (c) crude **[^{68}Ga]-26** and d) crude **[^{68}Ga]-27** developed on Whatman 3MM with 0.35M ethylenediaminetetraacetic acid (EDTA) as the mobile phase. The radio-TLC are shown zero to minimal amount of free [^{68}Ga]$GaCl_3$.

4.3.2. Radiolabelling of GO nanocomposites with ^{89}Zr(IV).

Further, ^{89}Zr-labelling was attempted as a control experiment aiming to validate the hypothesis of specific radiolabelling due to p-electron interactions. [^{89}Zr]Zr^{+4} ($4p^6$) does not have p-electrons in the outermost atomic orbital and subsequently could not interact with the π electron density on the surface of GO. As it was expected, the reaction did not proceed regardless of the time or the pH conditions employed in the reactions.

More specifically the experiment was carried out under different pH (3.5, 5.5, 7.0 and 8.5) in an attempt to optimise the radiolabelling protocol and the incorporation of the radioisotope to the GO nanocomposites. This was examined by radio-TLC after 1 h, 2 h and 16 h. The temperature was kept at 23 °C during the reaction time. All the results showed zero to a minimum labelling (2-3%). Further experiments were carried out to investigate a potential radiolabelling of zirconium-89 in the presence of a chelator which could possibly be used as a π donor (**Scheme 27**). A commercially available desferrioxamine (DFO) chelator was used in order to chelate zirconium-89

(**Figures S50**). The radiolabelled compound was then reacted with the GO nanocomposites overnight at 60 °C. A 70% incorporation was suggested after purifying the radiolabelled nanocomposites. This labelling could be caused either by non-covalent binding between GO nanocomposites and DFO or from the coupling of the amide group of the DFO with the oxide groups of the GO nanocomposite (**Scheme 27**).

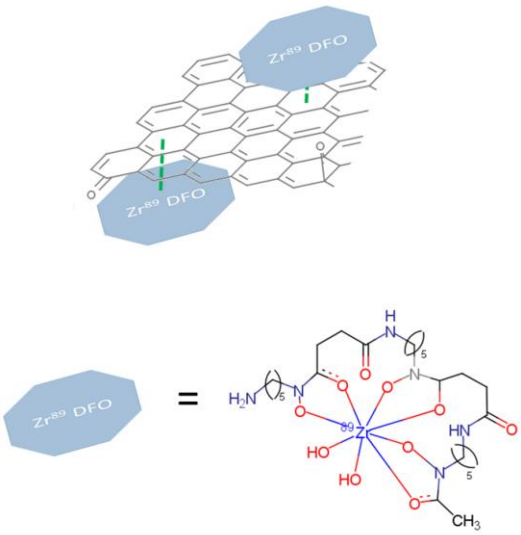

Scheme 27: Schematic representation of the [^{89}Zr]ZrDFO and non-covalent attachment to the planar graphitic surface of the nanocomposite.

4.4. Kinetic stability evaluation of GO nanocomposites in aqueous environment

4.4.1. Kinetic stability tests of the non-radiolabelled GO nanocomposites

The kinetic stability of the nanocomposites was estimated under various incubation conditions. Ga(III) was attached non-covalently to GO nanocomposite and complex **23** resulting in non-radioactive complexes **25** and **26**. Those complexes were incubated under various conditions to optimise the stability of the complexes in media likely to be encountered in a cell biology experiment. In more details, this investigation employed UV-visible absorption using a 2 mg/mL concentration of the assay agent (complex **25** or **26**) in DMSO.

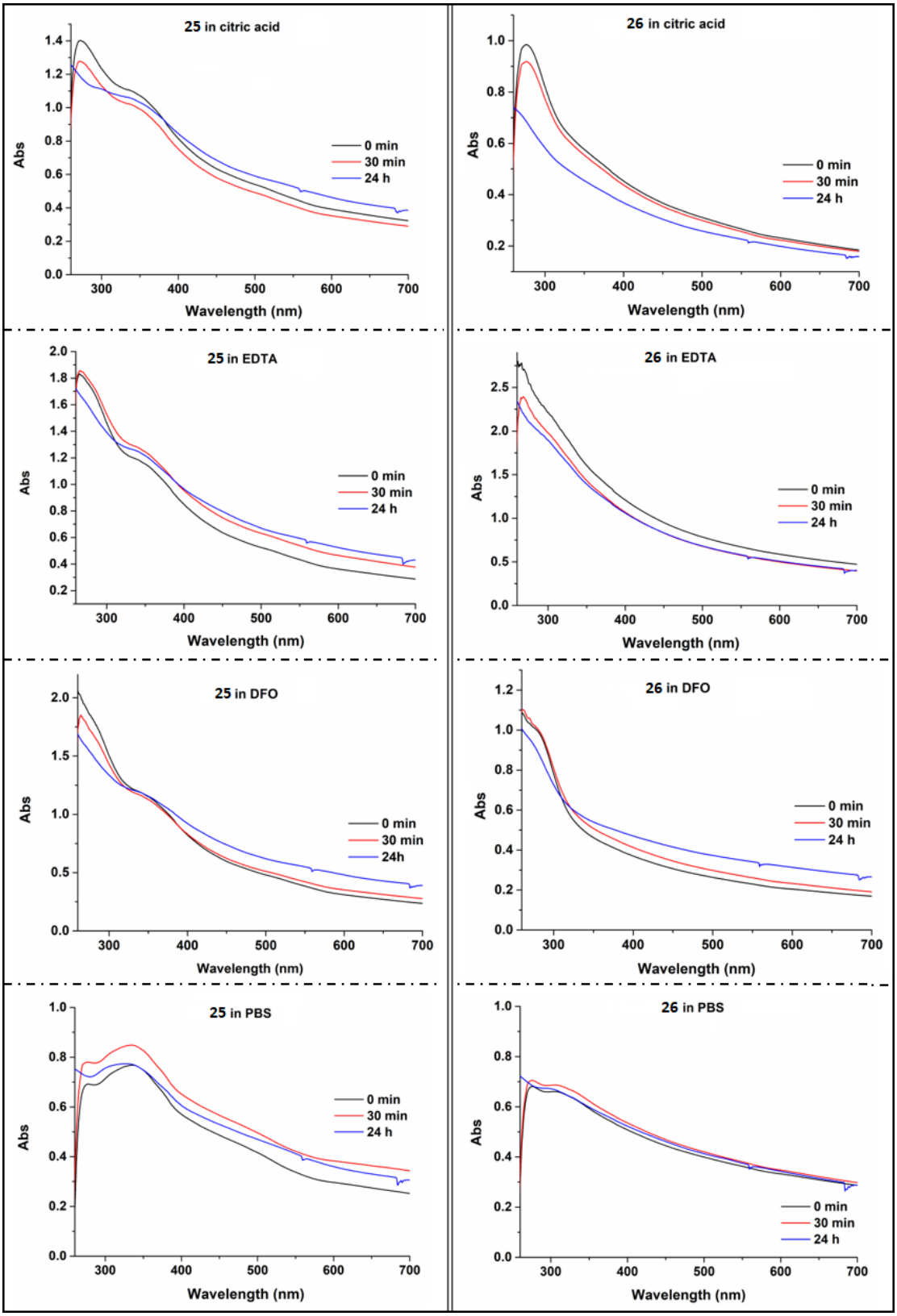

Figure 66: Uv-Vis spectroscopy probing the potential *in vitro* stability of the Ga@GO (**25**) and Ga+PhZnTSCA@GO (**Ga+9a@GO; 26**) nanocomposites at two time points post-preparation (p.p.) under various incubation conditions (citric acid, EDTA, PBS and DFO).

Solutions of 1:1 DMSO[assay agent]: H_2O were formed, and assays were carried out by incubating the samples at 37 °C using citric acid, PBS, EDTA and DFO. Both complexes were found to be sufficiently stable in the timescale of an imaging experiment with respect to decomposition in a mixture of DMSO and several aqueous buffers which are of relevance to standard cellular imaging assays (**Figure 66**). Whilst there were no changes observed in the UV/Vis spectra after 30 minutes of incubation, some slight changes were observed for the gallium complex Ga(III) over an incubation of 24 h (**Figure 66**).

4.4.2. Kinetic stability optimisation of the radiolabelled GO nanocomposites

The stability of the radiolabelled compounds used for PET and SPECT imaging is considered a parameter of high importance. Detachment of the radioisotope from the molecule of interest will lead to false positive or false negative results. Consequently, the stability of the radiolabelled complexes (**[^{68}Ga]-25**, **[^{68}Ga]-26** and **[^{68}Ga]-27**) was investigated. Due to the short half-life ($t_{1/2}$) of [^{68}Ga]Ga(III) (68 minutes), the kinetic stability of the radiolabelled compounds was tested after incubation in a number of agents at 37 °C at 60 and 120 minutes.

The stability profile of the radiolabelled complex was high (>98 %) during incubation in biological media (e.g. PBS, mouse plasma) at a volume ratio of 1:1 of the radiolabelled GO nanocomposites remaining intact up to 2 h post-preparation. On the other hand, the stability in EDTA was not as good as in biological media (>65 %) which might be caused by the strong ability of EDTA to bind gallium (III).[34, 35] **Figures 67-69** show a bar graph representation of the stability optimisation results for **[^{68}Ga]-25** ([^{68}Ga]Ga@GO) nanocomposites. All the analysis can be found in the tables presented in the Appendix.

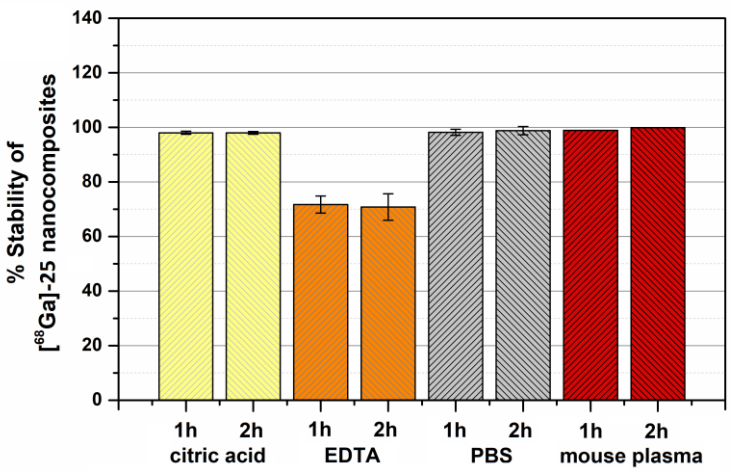

Figure 67: Graph presenting the results acquired from the kinetic stability tests of the **[^{68}Ga]-25** ([^{68}Ga]Ga@GO) nanocomposites up to two hours post preparation (p.p.) under various incubation conditions (citric acid, EDTA, PBS, fresh mouse plasma).

The kinetic stability results of the radiolabeled GO nanocomposites denote very good performance under biological media challenges, rendering the radiolabelled complexes appropriate candidates for later *in vitro* or *in vivo* studies.

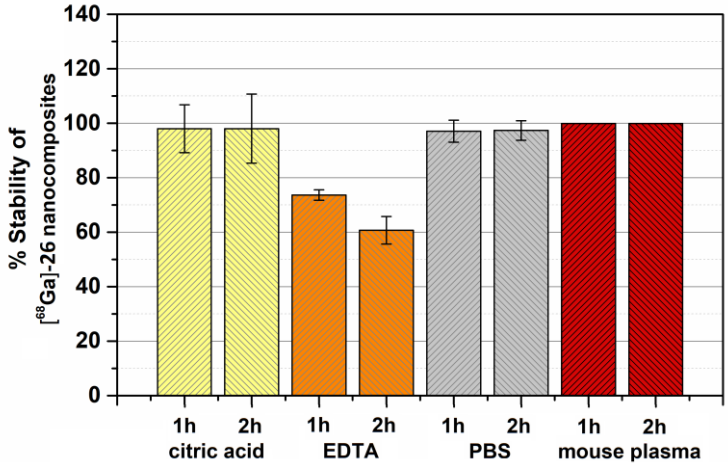

Figure 68: Graph presenting the results acquired from the kinetic stability tests of the **[^{68}Ga]-26 (**[^{68}Ga]Ga+**9a**@GO) nanocomposites at two time points post preparation (p.p.) under various incubation conditions (citric acid, EDTA, PBS, fresh mouse plasma).

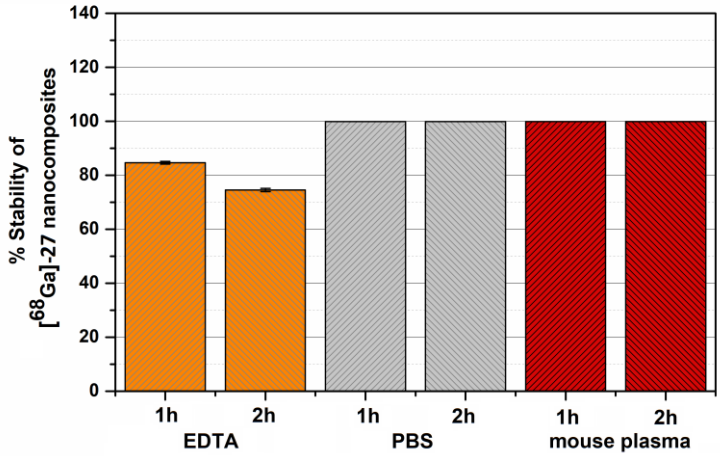

Figure 69: Graph presenting the results acquired from the kinetic stability tests of the **[^{68}Ga]-27** ([^{68}Ga]Ga+**9a**+**16**@GO) nanocomposites at two time points post preparation (p.p.) under various incubation conditions (EDTA, PBS, fresh mouse plasma).

4.4.3. Cell viability assays of non-radiolabelled GO nanocomposites

Preliminary cytotoxicity studies prior to the application of the GO nanocomposites in biological experiments was considered to be necessary. The purpose of our compounds is to be used as imaging agents. Typically, the preparation of a radioactive material, the precursor is used in large molar excess over the radioisotope and then the sample is used without further purification of the precursor. Which means that it is necessary to determine the maximum possible concentration of the precursor which is safe to be used without causing any damage to cells.[36] Similarly to previous chapters, herein the crystal violet assay was used as a simple method to assess the activity of a variety functionalised GO nanocomposites in cancer cells under both normoxic and chemically induced hypoxic conditions.

More specifically, crystal violet assays were performed in a range of concentrations to calculate the IC_{50} values of 4 different types of GO nanocomposites (GO and complexes **20**, **23, 24** and **27**). The viability assays were carried out in the PC-3 cell line under normoxic and chemically induced hypoxic conditions ($CoCl_2$) as previously described. The detailed conditions can be found in Chapter 7.

Most cells survived from the highest concentration to the lowest concentration over the experimental period (from the dose-response curve), so all those compounds show low to minimum toxicity (dose response curves presented in Appendix).

*4.4.4. Cell Uptake assays of **[^{68}Ga]-27**.*

The uptake of the **[^{68}Ga]-27** nanocomposite (**Figure 75**) was exploited to observe the complexes inside human cancer cells using radiolabelling techniques. Intra-cellular tracking of the gallium-68 complexes by γ-ray counting is expected to provide information about the analogous gallium (III) complexes, and their intracellular fate and processing, and potentially provide insights into the retention mechanism. After the reaction (Chapter 5.3.1), the **[^{68}Ga]-27** nanocomposite was washed with methanol and water by centrifugation and tested in PC3 cells under both normoxic and hypoxic (reduce hypoxia) conditions. Similar general protocols to the one used with the [^{68}Ga]-**7e** complex ([^{68}Ga]Ga(FbnzTSCAc)$_2$) (Chapter 2) was developed. As previously, $CoCl_2$ was used to chemically induced hypoxic environment.

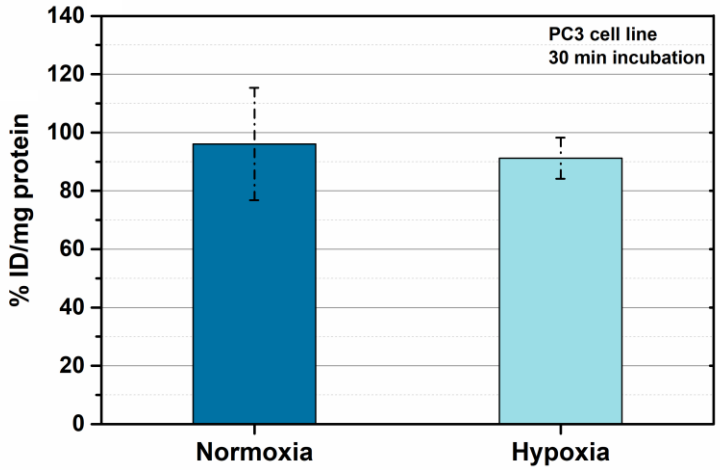

Figure 70: Preliminary *in vitro* cell uptake results of **[^{68}Ga]-27** ([^{68}Ga]Ga+**16**+**9a**@GO) under normoxic and chemically induced hypoxic conditions ($CoCl_2$) at a 30 min incubation time point. The data were expressed as % injected dose (ID)/mg of protein present in each well with p values ≤0.05 considered statistically significant (n = 6).

The complex **[^{68}Ga]-27** was incubated in PC3 cell line at 37 °C for 30 minutes, and then the complex was washed off prior to radioactivity measurement through a gamma ray counter At the same time control experiments were also performed using [^{68}Ga]$GaCl_3$ (as extracted from the generator) to eliminate any possible measurements associated with ligand-free aqueous ^{68}Gallium(III) active species. Protein quantification assays (BCA) were then carried out on the cells to calculate the actual percentage of the radioactive

nanocomposites taken up by the cells. The detailed experimental conditions can be found in Chapter 7.

There was no significant difference in gallium-68 retention under hypoxia compared to normoxia, with a difference of only 7% for this period of time (**Figure 70**). Further experiments need to be carried out for longer time points as well as in different cell lines to have a clearer view of the uptake of the compound from cancerous cells.

4.5. Conclusions to Chapter 4

For the first time, GO nanocomposites were successfully radiolabelled with [^{68}Ga]$GaCl_3$ through a non-covalent binding and no use of any chelator. The non-covalent binding of the small molecules such as either the Zn complexes or GC points to potential medical applications of the radiolabelled GO molecules. Crystal violet assays were carried out on the non-radiolabelled complexes indicating high cell viability, rendering them appropriate candidates as imaging agents. Moreover, the stability of both radiolabelled and non-radiolabelled nanocomposites was also tested *in vitro* with different solutions indicating an adequate stability towards EDTA and citric acid, whereas they proved to be very stable in relevant biological media. Further, the cell uptake of **[^{68}Ga]-27** was examined, suggesting very high uptake in PC3 cells but without any specificity under normoxic or hypoxic conditions.

4.6. References to Chapter 4

1. J. A. Tyson, V. Mirabello, D. G. Calatayud, H. Ge, G. Kociok-Köhn, S. W. Botchway, G. Dan Pantoş and S. I. Pascu, *Adv. Funct. Mater.*, 2016, **26**, 5641-5657.
2. X. Sun, Z. Liu, K. Welsher, J. T. Robinson, A. Goodwin, S. Zaric and H. Dai, *Nano Res.*, 2008, **1**, 203-212.
3. H. Bao, Y. Pan, Y. Ping, N. G. Sahoo, T. Wu, L. Li, J. Li and L. H. Gan, *Small*, 2011, **7**, 1569-1578.
4. L. Zhang, J. Xia, Q. Zhao, L. Liu and Z. Zhang, *Small*, 2010, **6**, 537-544.

5. M. Orecchioni, R. Cabizza, A. Bianco and L. G. Delogu, *Theranostics*, 2015, **5**, 710-723.
6. K. Yang, S. Zhang, G. Zhang, X. Sun, S.-T. Lee and Z. Liu, *Nano Lett.*, 2010, **10**, 3318-3323.
7. J. A. Tyson, D. G. Calatayud, V. Mirabello, B. Mao and S. I. Pascu, *Adv. Inorg. Chem.*, 2016, **68**, 397-440.
8. G. Gollavelli and Y. C. Ling, *Biomaterials*, 2012, **33**, 2532-2545.
9. X. Huang, S. Lee and X. Chen, *Am. J. Nucl. Med. Mol. Imaging*, 2011, **1**, 3-17.
10. L. Chen, L. Zhang, J. Bao, J. Zhang, C. Li, Y. Xia, X. Huang and J. Wang, *Gut*, 2013, **62**, 1520-1521.
11. S. Wang, Q. Zhang, X. F. Luo, J. Li, H. He, F. Yang, Y. Di, C. Jin, X. G. Jiang, S. Shen and D. L. Fu, *Biomaterials*, 2014, **35**, 9473-9483.
12. W. Chen, P. Yi, Y. Zhang, L. Zhang, Z. Deng and Z. Zhang, *ACS Appl. Mater. Interfaces*, 2011, **3**, 4085-4091.
13. M.-L. Chen, J.-W. Liu, B. Hu, M.-L. Chen and J.-H. Wang, *Analyst*, 2011, **136**, 4277-4283.
14. P. S. Wate, S. S. Banerjee, A. Jalota-Badhwar, R. R. Mascarenhas, K. R. Zope, J. Khandare and R. D. K. Misra, *Nanotechnology*, 2012, **23**, 415101.
15. J. Ge, M. Lan, B. Zhou, W. Liu, L. Guo, H. Wang, Q. Jia, G. Niu, X. Huang, H. Zhou, X. Meng, P. Wang, C. S. Lee, W. Zhang and X. Han, *Nat. Commun.*, 2014, **5**, 4596.
16. H. Hong, K. Yang, Y. Zhang, J. W. Engle, L. Feng, Y. Yang, T. R. Nayak, S. Goel, J. Bean, C. P. Theuer, T. E. Barnhart, Z. Liu and W. Cai, *ACS Nano*, 2012, **6**, 2361-2370.
17. K. Yang, L. Feng, H. Hong, W. Cai and Z. Liu, *Nat. Protoc.*, 2013, **8**, 10.1038/nprot.2013.1146.
18. S. Shi, K. Yang, H. Hong, H. F. Valdovinos, T. R. Nayak, Y. Zhang, C. P. Theuer, T. E. Barnhart, Z. Liu and W. Cai, *Biomaterials*, 2013, **34**, 3002-3009.
19. G. Gollavelli and Y.-C. Ling, *Biomaterials*, 2014, **35**, 4499-4507.
20. S. H. Hu, Y. W. Chen, W. T. Hung, I. W. Chen and S. Y. Chen, *Adv. Mater.*, 2012, **24**, 1748-1754.
21. S. Shi, C. Xu, K. Yang, S. Goel, H. F. Valdovinos, H. Luo, E. B. Ehlerding, C. G. England, L. Cheng, F. Chen, R. J. Nickles, Z. Liu and W. Cai, *Angew. Chem. Int. Ed.*, 2017, **56**, 2889-2892.

22. D. N. Divall, Master in Chemistry, University of Bath, 2017.
23. K. C. Ingham, *Anal. Biochem.*, 1975, **68**, 660-663.
24. J. S. Renny, L. L. Tomasevich, E. H. Tallmadge and D. B. Collum, *Angew.Chem. Int.*, 2013, **52**, 11998-12013.
25. W. Likussar and D. F. Boltz, *Anal. Chem.*, 1971, **43**, 1265-1272.
26. M. Li, Z. Liu, S. Wang, D. G. Calatayud, W.-H. Zhu, T. D. James, L. Wang, B. Mao and H.-N. Xiao, *Chem. Commun.*, 2018, **54**, 184-187.
27. B. N. Mattoo, *J. Chem. Soc. Faraday Trans.*, 1956, **52**, 1184-1194.
28. G. v. Bünau, *Ber. der Bunsenges. Phy. Chem.*, 1970, **74**, 1294-1295.
29. S. Jabbari-Farouji and P. van der Schoot, *J. Chem. Phys.*, 2012, **137**, 064906.
30. B. Mao, D. G. Calatayud, V. Mirabello, B. J. Hodges, J. A. R. Martins, S. W. Botchway, J. M. Mitchels and S. I. Pascu, *Adv. Funct. Mater.*, 2016, **26**, 687-697.
31. B. Mao, D. G. Calatayud, V. Mirabello, N. Kuganathan, H. Ge, R. M. J. Jacobs, A. M. Shepherd, J. A. Ribeiro Martins, J. Bernardino De La Serna, B. J. Hodges, S. W. Botchway and S. I. Pascu, *Chem. Eur. J.*, 2017, **23**, 9772-9789.
32. P. Thordarson, *Chem. Soc. Rev.*, 2011, **40**, 1305-1323.
33. C. A. Hunter and H. L. Anderson, *Angew. Chem. Int. Ed.*, 2009, **48**, 7488-7499.
34. D. J. Hnatowich, *J. Nucl. Med.*, 1975, **16**, 764-768.
35. A. R. Jalilian, *Iran J. Nucl. Med.*, 2016, **24**, 1-10.
36. J. Koziorowski, M. Behe, C. Decristoforo, J. Ballinger, P. Elsinga, V. Ferrari, P. Kolenc Peitl, S. Todde and T. L. Mindt, *EJNMMI Radiophar. Chem.*, 2016, **1**, 1.

Chapter 5: Summary and Outlook

New thiosemicarbazone monosubstituted ligands were successfully synthesised and characterised extensively by NMR, IR, UV-Vis spectroscopy, mass spectrometry and, when suitable crystals were obtained, by single crystal X-ray crystallography. Coordination with zinc(II) has been achieved for both monosubstituted precursors, as well as for asymmetric thiosemicarbazone ligands. These asymmetric complexes served their purpose as metallated precursors, in order to be transmetallated and obtain their designed gallium(III) derivatives. The selectivity of these complexes under hypoxic conditions[1] was evaluated. In addition, the conjugation of the asymmetric thiosemicarbazonato metal complexes has been performed with several small molecules or peptides.

The hydrazine moiety of the new complexes is characterised by a relative loss of reactivity compared to the traditional ATSM complexes, probably due to its aromatic backbone.[2] This loss of reactivity was reflected in the reactions of this moiety with potential targeting molecules. Nevertheless, significant progress has been made towards the coupling of a hypoxia-targeting small molecule with novel asymmetric metal complexes. More specifically, the selective conversion of the primary carbohydrate hydroxyl group of the glucosyl moiety of GC (**16**) was performed through Appel's reaction, rendering the carbohydrate moiety more accessible for further modification. Although the functionalisation of the primary carbohydrate hydroxyl group is often reported, these strategies are usually applied to sugars with the anomeric hydroxyl group protected as a methoxy either rather than in the presence of an aromatic aglycone moieties, such as a coumarin. In addition, coupling of a peptide format, bombesin (7-13) to the asymmetric complex has been attempted *via* hydrazine conjugation. However, optimisation of the reaction conditions is required in order to achieve the coupling, for instance a microwave radiated reaction might give better results. The potential benefits of bombesin and related peptides in targeting prostate cancer cells have been studied extensively, underlining the importance to establish a protocol in terms of a successful coupling.

Lastly, GO nanocomposites were introduced as carriers of the selected molecules. These were added to the GOs through non-covalent binding, most likely due to π-π interactions. These nanocomposites were attached either to Zn(II) complexes or GC giving rise to the formation of new synthetic precursors. These hybrid materials have great potential to contribute to the application of radiolabelled GO systems as theranostic agents.

Radiolabelling with gallium-68 and fluorine-18 was conducted for the first time with both mono(substituted) thiosemicarbazone ligands and asymmetric bis(thiosemicarbanozonato) complexes. All the mono(substituted) TSCs were successfully radiolabelled with a good radiochemical incorporation. More particularly FbnzTSCA (**5e**) presented an outstanding labelling and an adequate stability over time, showing that the radiolabelled complex has potential for further *in vitro* and *in vivo* examination. The transmetallation of the asymmetric PhZnTSCA (**9a**) complex with [^{68}Ga]Ga(III) was also tested. The application of the initial protocol, that was based on previous reports for the [^{68}Ga]Ga(III) labelling of symmetric bis(thiosemicarbazonato) complexes[1] was not successful. As a result, the design of a new protocol was required. Indeed, a new strategy for the radiolabelling of asymmetric bis(thiosemicarbazonato) metal complexes was applied, which led to the efficient synthesis of these compounds. Stability tests of the compounds under different biological environments needs to be performed before proceeding to *in vitro* assays and further optimisation is suggested, in order to increase the radiochemical incorporation and to optimise the purification conditions of the labelled complex. Furthermore, the orthogonal ^{18}F labelling of the mono(substituted) ligands and the asymmetric bis(thiosemicarbazonato) metal complex *via* their hydrasine moieties was achieved with the prosthetic group [^{18}F]FBA. The radiochemical incorporation of PhZnTSCA (**9a**) was very promising (~97%) and in order to finally obtain a radiolabelled substance in the highest possible purity, further optimisation of the purification step is now recommended before it will be applied to *in vitro* cell up-take experiments or *in vivo* imaging to mouse or rat models. Besides the radiolabelling of the small molecules, labelling of GO nanocomposites with [^{68}Ga]$GaCl_3$ was successfully achieved with a chelator-free labelling method through non-covalent binding. The radiochemical incorporation that was observed through radio-TLC was excellent (≤100 %) and the kinetic stability of both radiolabelled and non-radiolabelled nanocomposites was tested *in vitro* with different assays.

The new nano-materials present an adequate stability in EDTA and citric acid, whereas they show to be very stable in biological media rendering them as appropriate candidates for further biological assays. It is important to note that the validity of the radiolabelling protocol for the majority of the radiolabelled complexes was confirmed to be successful when [^{68}Ga]$GaCl_3$ (aq) was eluted either from a cyclotron through the ^{68}Zn(p,n)^{68}Ga reaction or from a ^{68}Ga/^{68}Ge generator where the contamination of germanium-68 is limited.

Many of the synthesised compounds have been extensively tested *in vitro* with a variety of different techniques. Cytotoxicity assays were performed under normoxic and induced hypoxic conditions ($CoCl_2$) at 48 hours post incubation using PC-3 and EMT-6 cells. When these assays were performed for the mono(substituted) TSCA a range of cell viabilities was observed. Among them, the FbnzTSCA (**5e**) ligand presented the lowest toxicity and was found to be a promising imaging agent. Moreover, the cell viability assays employing the asymmetric metal complexes present a notable variation on the results of the zinc(II) and gallium(III) derivatives (**9a** and **10a** respectively). At 48 hours post incubation, zinc(II) derivatives showed an increased number of viable cells at this time point in contrast with the gallium(III) derivatives, which appeared to be much more toxic. Time-dependent experiments were conducted, aiming to establish the potential value of these compounds as imaging agents. As expected, these experiments confirmed the low toxicity of zinc(II) derivatives at 24 h, under various conditions, but gallium(III) derivatives showed an increased toxicity, especially in normoxic cells. Moreover, the cytotoxicity of loaded and non-loaded GO nanocomposites was tested *via* crystal violet assays, which indicated high cell viability, thus supporting our aim to use them for imaging applications. Although the protocol followed for the cytotoxicity assays was previously established by Dr.Haobo Ge based on several classes of anticancer reagents and compounds with similar structures to those studied in this thesis, such compounds were not re-examined here.[3] Further cytotoxicity assays including these molecules previously used to validate the assays would therefore be critical to provide a direct comparison between the cytotoxicities of all the compounds.

The fluorescence optical imaging properties were analysed for several different new mono(substituted) ligands and bis(thiosemicarbazonato) metal complexes. The

mono(substituted) ligands revealed an enhanced biodistribution in normoxic cells. On the other hand, the fluorescence properties of Ga(III) bis(thiosemicarbazonato) complexes showed a weak distribution in normoxic cells and enhanced distribution in an hypoxic environment. The hypoxia experiments in this case were conducted upon induction of either acute hypoxia (chemically induced hypoxia with $CoCl_2$) or chronic hypoxia (cells cultured in a hypoxia chamber). Furthermore, study of the fluorescence lifetime components of the PhGaTSCA (**10a**) complex were determined both in solution and PC3 cells. Auto-fluorescence experiments were conducted confirming the decomposition of the complex in the cells by deconvoluting, due to the sufficient discrimination between the results of the two life time fluorescence components, the various fluorescence lifetime components.

Finally, uptake studies were performed on radiolabelled molecules with the highest radiochemical incorporation (ROI) and purity. The cell uptake experiments conducted on the **[^{68}Ga]-7e** ([^{68}Ga]Ga(FbnzTSCA)$_2$), demonstrated a variable localisation and toxicity of the compound that depends on the genetic background of the different cell lines and the incubation time periods applied. Nevertheless, no hypoxia selectivity was confirmed. Similar results were suggested by cell uptake experiments for **[^{68}Ga]-27** nanocomposite. Although high uptake in the PC3 cell line was suggested from the results, no specificity within normoxic or hypoxic conditions was noticed. Since the protocol for the labelling of the asymmetric bis(thiosemicarbazonate) complexes with gallium-68 is now established, *in vitro* uptake experiments under radiochemistry techniques should be performed, as this compound is holds great promise due to its distinct hypoxia selectivity.

Given the biological results obtained up to now, the scaffold of the compounds seems to require further optimisation in order to increase their hypoxia selectivity. Currently, the anionic species of the non-radiolabelled complexes is considered to be Cl^- based on previously obtained crystal structures,[4] however detection of gallium speciation in cells could help in the understanding of the mechanism of action of the complexes in biological systems.[5, 6] This characterisation could be carried out through inductively coupled plasma mass spectrometry (ICP-MS), a mass spectrometry technique which is able to detect metals and non-metals at very low concentrations.[5] Moreover, optimisation of the *in vitro* studies is required with respect to the incubation times, alongside the strategies exploited in order to

induce hypoxia. The protocol used for inducing hypoxia has been applied previously,[6] but in the current work no independent quantification of the amount of hypoxia was carried out. Moreover deciphering the response of the compounds in redox chemistry conditions and its influence on cell uptake would be a topic to be further studied. Use of a hypoxia chamber for *in vitro* assays could be a promising choice for future detailed experiments, even though the study of cell uptake *in vitro* with radiochemistry techniques is challenging under these circumstances. Lastly, similar experiments including a wider panel of cancer cell lines that are known to display diverse degrees of sensitivity to hypoxia and metabolic response thereafter could be executed. There are multiple cell lines reported to have increased sensitivity to drugs under hypoxia[7] compared to anoxia or normoxia; such as the small lung cancer cell line, H69 or the breast cancer cell line, MCF-7. The use of a wider spectrum of cell lines with similar genetic backgrounds might facilitate a more thorough understanding of the utilisation of these compounds in cells.

5.1. References to Chapter 5

1. I. S. Alam, R. L. Arrowsmith, F. Cortezon-Tamarit, F. Twyman, G. Kociok-Köhn, S. W. Botchway, J. R. Dilworth, L. Carroll, E. O. Aboagye and S. I. Pascu, *Dalton Trans.*, 2016, **45**, 144-155.
2. L. Carroll, PhD thesis, New College, Oxford, Trinity, 2010
3. H. Ge, PhD thesis, University of Bath, Bath, 2015.
4. F. Cortezon-Tamarit, S. Sarpaki, D. G. Calatayud, V. Mirabello and S. I. Pascu, *Chem. Rec.*, 2016, **16**, 1380-1397.
5. J. Koziorowski, M. Behe, C. Decristoforo, J. Ballinger, P. Elsinga, V. Ferrari, P. Kolenc Peitl, S. Todde and T. L. Mindt, *EJNMMI Radiopharm. Chem.*, 2016, **1**, 1.
6. Y. Li, MPhil, Imperial College London, London, 2016.
7. S. Strese, M. Fryknäs, R. Larsson and J. Gullbo, *BMC Cancer*, 2013, **13**, 331-331.

Chapter 6: Experimental Section

6.1. Instrumentation and General Information

6.1.1. Chemistry

All reactions involving air- or moisture-sensitive reagents or intermediates were carried out under nitrogen atmosphere and anhydrous conditions, unless otherwise stated, using standard Schlenk techniques. All reagents and solvents were obtained from Aldrich Chemical Co. (Gillingham, UK), Fluoro Chem (Hadfield, UK) and Fisher (Acros; Geel Belgium) and used without further purification, unless otherwise stated. Solvents with high purity or HPLC grade were obtained from Aldrich Chemical Co. (Gillingham, UK) and/or VWR (Radnor, PA, USA). Milli-Q water was obtained from a Millipore Milli-Q purification system and anhydrous solvents from a PS-400-7 Innovative technologies SPS system.

Microwave reaction were conducted in a Biotage (Uppsala, Sweden) Initiator 2.5 reactor (o-450 depending on T) in stirred capped vials. The reaction mixtures were pre-stirred for 30 s and heated to the desired temperature by applying maximum power of 400W that was reduced and kept constant once the final temperature was reached.

Thin layer chromatography (TLC) was carried out on Merck silica gel 60 F254 analytical plates (Matrix silica gel with aluminium support and fluorescent indicator 254 nm, 0.2 mm thickness) and visualized by ultraviolet (UV) fluorescence (λ= 254, 366 nm) both: by charring with 10% $KMnO_4$ in 1 M H_2SO_4 or by charring with 5% Na_2SO_4 in EtOH. The elution conditions for TLC were varied and are quoted for each compound.

NMR spectrometry was performed using 300 MHz, 500 MHz Bruker (Banner Lane, UK) Advance NMR spectrometer and/or a 500 MHz Agilent automated system. Bruker and Agilent 500 Spectra were acquired at 500 MHz for ^{1}H NMR, at 125 MHz for ^{13}C NMR and at 470 MHz for ^{19}F NMR. ^{1}H and ^{13}C chemical shifts are referenced to tetramethylsilane (TMS), as internal reference whilst ^{19}F to TFA. All spectra were acquired at 298 K, unless otherwise stated. All spectra are referenced to residual solvent and coupling constants (*J*) are reported in Hertz (Hz) with a possible discrepancy ≥ 0.2 Hz.

Chemical shifts δ are reported in ppm. Chemical shifts of solvent residues were identified as follows: $CDCl_3$-d_6: ^1H, $\delta = 7.26$, ^{13}C, $\delta = 77.0$; DMSO-d_6: ^1H, $\delta = 2.50$; ^{13}C, $\delta = 39.5$; D_2O: ^1H, $\delta = 4.79$). Peak multiplicities are referred as follows: s, singlet; d, doublet; t, triplet; q, quartett; m, multiplet; appd, apparent doublet, appt, apparent triplet, appq, apparent quartet, br, broad.

Accurate Mass Spectrometry was carried out at the EPSRC National Mass Spectrometry Centre of Swansea University, UK, using different techniques, such as MALDI, ESI and EI.

Analytical phase/reverse-phase was performed either on a Dionex Ultimate 3000 series HPLC system (Sunnyvale, California.) or on an Agilent 1100 series HPLC system (Agilent Technologies, Stockport, UK). The Dionex system was equipped with a UV-Vis diode array detector (measuring at eight wavelengths from 200-800 nm), using a Phenomenex Gemini (Macclesfield, UK) water C18 column (250 mm × 4.6 mm, 110 A) at a flow rate of 0.8 mL/min. The gradient elution was 0.1% trifluoroacetic acid (TFA) in milli-Q water as solvent A and 0.1% TFA in MeCN as solvent B. A reverse gradient was applied starting with A at 95%, going to 5% of A at 7.5 minutes, then an isocratic step until 15 minutes and a gradient until 95% A, then keep for 18 minutes (**Method A**). In addition, for the synthesis of Bombesin, a Phenomenex Gemini (Macclesfield, UK) water C18 column (150 mm × 4.6 mm, 110 A) at a flow rate of 1 mL/min. The gradient elution was 0.1% trifluoroacetic acid (TFA) in milli-Q water as solvent A and 0.1% TFA in MeCN as solvent B. A reverse gradient was applied starting with A at 95%, going to 5% of A at 10 minutes, then an isocratic step until 15 minutes and a gradient until 95% A, then keep for 18 minutes (**Method B**). The Agilent 1100 series HPLC system (Agilent Technologies, Stockport, UK) is equipped with a UV detector (254 nm) and a Lab-Logic Flow-count radio-detector, using a Phenomenex Gemini (Macclesfield, UK) water C18 column (250 mm × 4.6 mm, 110 A) and a Laura 3 software (LabLogic, Sheffield, UK) at a flow rate of 1mL/min. The gradient elution was 0.1% TFA in milli-Q water as solvent A and 0.1% TFA in MeCN as solvent B. A reverse gradient was applied starting with A at 95% for 2 minutes, going up to 5% A at 12 minutes, then an isocratic step until 14 minutes and gradient until 95% A at 16 minutes, then hold to 25 minutes (**Method C)**.

IR Spectroscopy was carried out on a Perkin Elmer (Waltham, Massachusetts) Frontier FTIR machine in ATR mode.

X-ray crystallography data were acquired by Gabriele Kociok-Köhn, at the University of Bath. Intensity data were collected at 150(2) K on an Agilent (Santa Clara, California, U.S.) SuperNova Dual Diffractometer Cu at zero, EosS2, using monochromated Cu-Kα radiation λ = 1.547184 Å. All the structures were solved with SHELXT and refined by a full-matrix least-squares procedure based on F^2 (Shelxl-2014/7).[1] All non-hydrogen atoms were refined anisotropically. Hydrogen atoms were placed onto calculated position and refined using a riding model except for the OH hydrogen atoms which have been located in the difference Fourier map and were refined with bond lengths restraints.

UV-Vis spectroscopy was performed in 1 cm quartz cuvettes on a Perkin Elmer (Waltham, Massachusetts) Lambda 35 UV-Vis spectrometer controlled by UV-Winlab software.

Fluorescence spectroscopy was performed in 1 cm quartz cuvettes on a Perkin Elmer (Waltham, Massachusetts) LS55 luminescence spectrometer controlled by FL-Winlab 4.0 software.

6.1.2. Radiochemistry methods

Radio-HPLC was performed either on an Agilent 1100 series HPLC system (Agilent Technologies, Stockport, UK) equipped with a γ-RAM Model 3 gamma-detector (IN/US Systems Inc, Florida, USA) and a Laura 3 software (LabLogic, Sheffield, UK). The gradient elution was 0.1% TFA in milli-Q water as solvent A and 0.1% TFA in MeCN as solvent B. A reverse gradient was applied starting with A at 95% for 2 minutes, going up to 5% A at 12 minutes, isocratic level until 14 minutes and gradient until 95% A at 16 minutes, then hold to 25 minutes (**Method C)**. Or on an Agilent 1100 series HPLC system (Agilent Technologies, Stockport, UK) equipped with a γ-RAM Model 3 gamma-detector (IN/US Systems Inc, Florida, USA) and a Laura 3 software (LabLogic, Sheffield, UK). The gradient elution was 0.1% TFA in milli-Q water as solvent A and 0.1% TFA in MeCN as solvent B. A reverse gradient was applied starting with A at 95% for 2 minutes, going up to 5% A at 12 minutes, isocratic level until 14 minutes and gradient until 95% A at 16 minuets, then hold to 25 minutes (**Method D)**.

Radio-TLC was performed on a LabLogic PET/SPECT radio-TLC Scanner system (LabLogic, Sheffield, UK) and a Laura software (LabLogic, Sheffield, UK). The

radio-TLC was developed on Whatman 3MM with 0.35 M ethylenediaminetetraacetic acid (EDTA) as the mobile phase.

The positron emitting radiotracer gallium-68 was extracted either from a SnO_2-based column matrix $^{68}Ge/^{68}Ga$ generator (Department of Surgery and Cancer of Imperial College in London) using a 0.6 M HCl solution or produced through a cyclotron (PETIC, Cardiff, UK) using a 0.1 M HCl solution. The eluted $^{68}Ga(III)$ was purified as follows; the activity was trapped in a SCX cartridge, which was already activated with 1 mL of HCl solution 0.1M and washed with 10 mL of water. Then the $^{68}GaCl_3$ was eluted from the cartridge with 0.8 mL of a THF/HCl (0.02 M) solution (98%) or acetone/HCl (0.02 M) solution (98%) and was further dried under nitrogen atmosphere.

The positron emitting radiotracer zirconium-89 was produced through a cyclotron (PETIC, Cardiff, UK) through the methods of Dabkowski *et al*.[2] and purified *via* the methods of Walther and collaborators.[3] A remote handling rig from an Eckert & Ziegler was developed with 6 valve dispensing cassette and syringes allowing the decrease of radiation exposure to all steps of the yttrium-89 target dissolution and zirconium-89 purification. In addition, this also allowed to decrease considerably the elution times by the application of compressed air pressure to the zirconium-89 separation column without reducing separation efficiencies. The zirconium-89 was extracted in 3 x 1 mL fractions of 1 M oxalic acid, with the middle fraction to contain routinely 1 GBq of purified [^{89}Zr]Zr(IV) in 76% yield.

The positron emitting radiotracer [^{18}F]fluoride was produced through a cyclotron (Imanova, London, UK). Synthesis of [^{18}F]fluorobenzaldehyde was performed, by Chris Barnes at Imperial College London, on the FASTlab™ *via* an automated procedure. The [^{18}F]fluoride was first dried and then was trapped on a Sep-Pak QMA-carbonate Light Cartridge. Then it was eluted into the reactor using an eluent consisting of Kryptofix K_{222} and $KHCO_3$ in acetonitrile: water (4:1). The content of the reactor was evaporated at 120 ºC under vacuum and a low flow of nitrogen. The "dried" fluoride was then dissolved with 600µl of anhydrous acetonitrile before being transferred to a Wheaton vial. The fluorination step was then performed manually. 400 µL of the "dried" fluoride was added by syringe to a v-bottom vial containing 3 mg of the precursor. The vial was then heated at 90 °C for 15 minutes resulting in consistently >98% radiochemical purity according to radio-HPLC, and it was then used to further labelling reactions.

Microwave reactions were conducted in a Biotage (Uppsala, Sweden) Initiator 2.5 reactor (0-450 depending on T) in stirred capped vials. The reaction mixtures were pre-stirred for 30 s and heated to the desired temperature by applying maximum power of 400 W that was reduced and kept constant once the target temperature was reached.

All the radiolabelling experiments stated in this thesis were repeated minimum twice.

6.1.3. In vitro experiments

Cell Culturing and Cell Preparation

Cells were cultured by Dr. Haobo Ge (University of Bath), at 37 °C in a humidified atmosphere in air and harvested once >70% confluence had been reached. Both PC3 (prostate cancer cells) and EMT6 (breast cancer cells) were cultured in RPMI (Roswell Park Memorial Institute) in 1640 serum medium. The media contained 10% foetal calf serum (FCS), 0.5% penicillin/streptomycin (10,000 IU mL-1/10,000 mg mL-1) and 1% 200 mM L-Glutamine. All steps were performed in the absence of phenol red.

Supernatant containing dead cell matter and excess protein was aspirated. The live adherent cells were then washed with 10 mL of phosphate buffer saline (PBS) solution twice to remove any remaining media containing FCS. Cells were incubated in 3 mL of trypsin solution (0.25% trypsin) for 5 to 7 minutes at 37 °C. After trypsinisation, 6 mL of medium containing 10% serum was added to inactivate the trypsin and the solution was centrifuged for 5 minutes (1000 rpm, 25 ºC) to precipitate cells. The supernatant liquid was aspirated and 5 mL of serum medium (10% FCS) was added to the cell matter left behind. Cells were counted using a haemocytometer and then seeded as appropriate.

Acute Hypoxia Cell Culturing Protocol (chemically induced by $CoCl_2$)

A stock solution of $CoCl_2$ was prepared prior to each assay. 4.76 mg of $COCl_2 \cdot 6H_2O$ (237.9 g/mol) was dissolved in 1 mL of Milli-Q water to make a 20 mM $CoCl_2$ stock solution.

Cytotoxicity assays: Cells were prepared in a similar manner as previously described. After cell sub-culturing, cells were divided in aliquots (7000 cells per well), seeded in a 96-well plate and cultured at 37 °C for 24 hours in a conventional incubator (37 °C; 5% CO_2) prior

to the addition of $COCl_2$ stock solution (1μL). The cells were incubated for further 24 hours. Then the compounds were loaded, and the cells were continuously cultured at 37 °C for a time period relative to each experiment (24, 48 or 72 hours).

Fluorescence assays: Cells were prepared in a similar manner as previously described. After cell sub-culturing, cells were divided in aliquots ($0.15 \cdot 10^6$ cells per glass bottom dish), seeded on a glass bottom seed and cultured at 37 °C for 48 hours in a conventional incubator (37 °C; 5% CO_2) prior to the addition of $COCl_2$ stock solution (10 μL/dish). The cells were incubated for further 24 hours and then cells were treated as described in the fluorescence assay protocol.

Chronic Hypoxia Cell Culturing (Hypoxia Chamber)

Cells were prepared in a similar manner as previously described. After cell sub-culturing, cells were divided in aliquots ($0.15 \cdot 10^6$ cells per dish), seeded on a glass bottom seed and moved to a Baker Ruskinn (Maine. USA) UM-025 SCI-tive Dual Asymmetric hypoxia chamber (1% O_2, 5% CO_2, 70% humidity and 37 °C) where incubated for 24 hours. Then cells were treated as described in the fluorescence assay protocol and images were captured inside hypoxia chamber with a mounted fluorescence microscopy.

Cell viability assays

Cell viability assays (MTT, crystal violet) were performed culturing cells in 96-well plates (ca. $5 \cdot 10^4$ cells/mL). The protocols for these assays were previously established by Dr Haobe Ge for several classes of anticancer reagents and compounds with similar structures to those studied in this thesis.[4] For the compounds with a known molecular weight, the concentration used ranged between 250 μM (1% DMSO, 99% RPMI-1640 (10% FCS, or 15 % FCS as per cell line) and 1 nM as they were shown in **Tables 13**. The concentrations used for GO nanocomposites (the molecular weight is not known) were 10 μg/mL to 0.5ng/mL as they were shown in **Tables 14**. Data were calculated from at least six consistent results per experiment and in some cases, when state, the experiments were repeated at least twice. The IC_{50} values calculated from a fitting plot obtained using Origin 9.0 program. The standard error reported corresponds to the error of the mean. Cell viability studies were carried out by Dr Haobo Ge following previously validated protocols.[5, 6]

Table 13: Concentrations of different samples in the cytotoxicity/cell viability assays.

ctrl	Ctrl (DMSO)	Sample 1 (μM)		Sample 2 (μM)		Sample 3 (μM)		Sample 4 (μM)		Sample 5 (μM)	
		250	1	250	1	250	1	250	1	250	1
		250	1	250	1	250	1	250	1	250	1
		100	0.5	100	0.5	100	0.5	100	0.5	100	0.5
		100	0.5	100	0.5	100	0.5	100	0.5	100	0.5
		50	0.01	50	0.01	50	0.01	50	0.01	50	0.01
		50	0.01	50	0.01	50	0.01	50	0.01	50	0.01
		10	0.001	10	0.001	10	0.001	10	0.001	10	0.001
		10	0.001	10	0.001	10	0.001	10	0.001	10	0.001

Table 14: Concentrations of different samples in the cytotoxicity/cell viability assays for GO nanocomposites.

Ctrl	Ctrl (DMSO)	Sample 1 (μg/mL)		Sample 2 (μg/mL)		Sample 3 (μg/mL)		Sample 4 (μg/mL)		Sample 5 (μg/mL)	
		1	0.01	1	0.01	1	0.01	1	0.01	1	0.01
		1	0.01	1	0.01	1	0.01	1	0.01	1	0.01
		0.5	0.005	0.5	0.005	0.5	$5x10^{-3}$	0.5	0.005	0.5	0.005
		0.5	0.005	0.5	0.005	0.5	$5x10^{-3}$	0.5	0.005	0.5	0.005
		0.1	0.001	0.1	0.001	0.1	0.001	0.1	0.001	0.1	0.001
		0.1	0.001	0.1	0.001	0.1	0.001	0.1	0.001	0.1	0.001
		0.05	0.0005	0.05	0.0005	0.05	0.0005	0.05	0.0005	0.05	0.0005
		0.05	0.0005	0.05	0.0005	0.05	0.0005	0.05	0.0005	0.05	0.0005

Fluorescence experiments

All the *in vitro* fluorescence were conducted under the supervision of Dr. Haobo Ge, Dr. Vincenzo Mirabello and/or Dr. Fernando Cortezon Tamarit, at University of Bath

Epi-fluorescence microscopy images were acquired in a Nikon (Surrey, UK) Eclipse Ti instrument equipped with a mercury lamp (Nikon HG-100W, Tokyo, Japan) as the excitation source, and a high-definition cooled colour digital camera (DXM 1200C, with 12.6-mega output pixels). Fluorescence images were captured at four different channels, including, DAPI (blue) channel: λ_{ex} = 340-380 nm, λ_{em} = 435-485 nm. GFP-L (green) channel: λ_{ex} = 460-500 nm, λ_{em} = 510 nm long pass. CY5 HYQ (red) channel: λ_{ex} = 590-650 nm, λ_{em} = 663-738 nm. The images obtained were processed using the Nikon NIS elements-AR Analysis 4.30.02 software.

Confocal microscopy images were acquired in a Nikon (Surrey, UK) Eclipse Ti instrument equipped with 405 nm / 488 nm / 561 nm excitation lasers. The images obtained were processed using the Nikon NIS elements-AR Analysis 4.30.02 software. In addition, some further confocal microscopy images were acquired in a Zeiss (Oberkochen, Germany) LSM 880 instrument equipped with 405 nm / 488 nm / 594 nm excitation lasers. The images obtained were processed using the ZEN software platform. In all cases wells were fixed with 4% paraformaldehyde pH=7. The working distance of a 60x objective lens is 0.17 mm (40x = 0.2 mm); therefore, cells were seeded onto single well plates where the coverslip was the bottom of the well.

Fluorescence lifetimes and FLIM measurements were conducted at the Rutherford Appleton Laboratory (Central Lasers Facility, Research Complex at Harwell) with the assistance of Lifetime calculations were processed using SPCImage software.

Cell uptake assays

The intracellular radioactivity at the uptake assays of the mono(substituted) coordinated complexes was counted in a LKB Wallac 1282 Compugamma Laboratory gamma counter (PerkinElmer, USA) whilst for GO nanocomposites was calculated at a Wizard^2 2480 1-Detector gamma counter (PerkinElmer, USA). On BCA assays the cells were counted at a Sunrise absorbance reader (Tecan Trading AG, Switzerland). All the obtained results

were analysed through the scientific 2D graphing and statistics software GraphPad Prism (GraphPad Software, California).

6.2. Experimental Details for Chapter Two

6.2.1. Synthesis thiosemicarbazonate molecules; from starting materials to Zn complexes

Synthesis of starting materials

Methyl-N-(2-tert-butoxycarbonylaminoethyl)dithiocarbamate (1d)

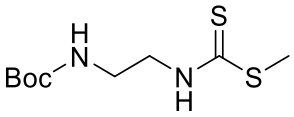

To a solution of N-Boc-ethylenediamine (1.72 mL, 11mmol) and triethylamine (1.65 mL, 12 mmol) in EtOH (20 mL), carbon disulphide (0.72 mL, 12 mmol) was added dropwise under stirring. The formed slurry was allowed to react for 1.5 h at 25 °C. Then iodomethane (0.8508 g, 6.0 mmol) was added into the mixture and stirred for 1.45 h. Afterwards, the excess of solvent was removed under *vacuum*. The resulting residue was re-suspended in EtOAc and washed with 1M HCl (50 mL), saturated $NaHCO_3$ solution (50 mL) and distilled H_2O (50 mL). The organic phase was then dried over $MgSO_4$ and the excess of solvent was removed under reduced pressure to afford 1.6312 g of methyl-N-(2-tert-butoxycarbonylaminoethyl) dithiocarbamate (**1d**) as a yellowish solid (61%).

^{1}H NMR (300 MHz, CDCl3-d_6) δ_H: 8.41 (brs, 1H, N***H***-CS), 5.01 (brs, 1H, N***H***-Boc), 3.79 (appq, 2H, C***H***$_2$-NHCS), 3.42 (appq, 2H, C***H***$_2$-NHBoc), 2.59 (s, 3H, S-C***H***$_3$), 1.44 (s, 9H, O(C***H***$_3$)$_3$) ppm.

Mass Spectrometry: (ASAP) for $C_9H_{18}N_2O_2S_2$, calcd for ($[M]^+$) 250.0804 found 250.0801; ($[M+H]^+$) 251.0882 found 251.0879.

Methyl (4-fluorobenzyl)carbamodithioate (1e)

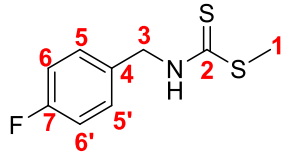

Carbon disulphide (3.2 mL, 52.56 mmol) was added dropwise to a solution of fluorobenzylamine (5 mL, 43.75 mmol) and triethylamine (7.4 mL, 52.56 mmol) in EtOH (60 mL) under stirring. The obtained slurry was allowed to react for 1.5 h at 25 °C, then iodomethane (3.3 mL, 52.56 mmol) was added into the mixture and stirred for 1.45 h. Afterwards, the excess of solvent was removed under *vacuum*. The resulting residue was re-suspended in EtAc and washed with 1M HCl (100 mL), saturated $NaHCO_3$ solution (200 mL) and distilled H_2O (300 mL). The organic phase was then dried over $MgSO_4$ and the excess of solvent was removed under reduced pressure to afford 6.2706 g of methyl-N-(2-tert-butoxycarbonylaminoethyl) dithiocarbamate (**1e**) as a yellowish solid (67%).

^{1}H NMR (500 MHz, DMSO-d_6, 298 K) δ_H: 10.40 (s, R-N***H***CSR') 7.31 (m, 2H, ***H^5 H$^{5'}$***), 7.15 (appt, 2H, ^3J= 8.9 Hz, ***H^6 H$^{6'}$***), 4.79 (d, 2H, ^3J= 3.3 Hz, ***H^3***), 4.53 (bs, 1H, R-N***H***$_2$-CSR'), 2.51 (s, 3H, RS-C***H***$_3$)

^{13}C NMR (75 MHz, d^6-DMSO) δ_C : 17.8 (RS-***C***H_3), 49.1(R-***C***H_2-bnz), 115.3 (***C^3***), 115.5 (d, $J_{C\text{-}F}$= 20.6 Hz, ***C^6 C$^{6'}$***), 130.6 (d, $J_{C\text{-}F}$= 8.1 Hz, ***C^5 C$^{5'}$***), 134.1 (d, $J_{C\text{-}F}$= 2.9 Hz, ***C***F), 160.1, 163.3 (***C^4***), 198.3 (***C***S) ppm

^{19}F NMR (470 MHz, DMSO-d_6) δ_C: -118.05.

Mass Spectrometry: ASAP for $C_9H_{10}FNS_2$, calcd for ($[M+H]^+$) 216.0311 found 216.0312;

X-Ray Structure (Appendix)

Methyl (4-ethynylbenzyl)carbamodithioate (1f)

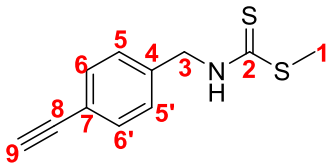

To a solution of ethynyl phenyl methenamine (0.6000 g, 4.56 mmol) and triethylamine (0.76 mL, 5.46 mmol) in EtOH (10 mL) carbon disulphide (0.33 mL, 5.46 mmol) was added dropwise under stirring. The obtained slurry was allowed to react for 1.5 h at 25 °C. Then iodomethane (0.34 mL, 5.46 mmol) was added into the mixture and stirred for 1.45 h. Afterwards, the excess of solvent was removed under *vacuum*. The resulting residue was re-suspended in EtAc and washed with 1M HCl (50 mL), saturated $NaHCO_3$ solution (50 mL) and distilled H_2O (100 mL). The organic phase was then dried over $MgSO_4$ and the excess of solvent was removed under reduced pressure to afford 0.7404 g of methyl (4-ethynyl benzyl)carbamodithioate (**1f**) as a yellowish solid (73%).

^{1}H NMR (300 MHz, DMSO-d$_6$) δ_H: 10.42 (s, 1H, R-N***H***$_2$-CSR') 7.43 (d, 2H, ^{3}J= 8.2 Hz, ***H^{5} H$^{5'}$***), 7.26 (d, 2H, ^{3}J= 8.4 Hz, ***H^{6} H$^{6'}$***), 4.84 (d, 2H, ^{3}J= 4.8 Hz, ***H^{3}***), 4.16 (s, 1H, RCC***H***), 2.53 (s, 3H, S-C***H***) ppm.

^{13}C NMR (125 MHz, DMSO-d$_6$) δ_C : 198.3 (***C***S), 137.8 (***C^{4}***), 133.2 (***C^{6} C$^{6'}$***), 127.6 (***C^{5} C$^{5'}$***), 121.1 (***C^{3}***), 85.4 (R-***C***CH$_3$), 80.2 (RC-***C***H$_3$), 52.0 (R-***C***H$_2$-bnz), 18.1 (RS-***C***H$_3$) ppm

Mass Spectrometry: ASAP for $C_{11}H_{11}NS_2$, calcd for ([M+H]$^+$) 222.0406 found 222.040.

N-(4-fluorobenzyl)hydrazinecarbothioamide (2e):

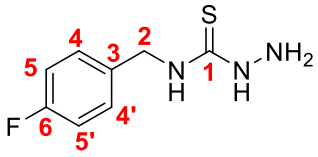

To a solution of methyl (4-fluorobenzyl)carbamodithioate (**1e**) (6.2700 g, 29.12 mmol) in EtOH (60 mL), hydrazine monohydrate (1.8 mL, 36.45 mmol) was added dropwise, under stirring. The obtained slurry was allowed to react for 5 h under reflux (78 °C). Then, the excess of solvent was removed under reduced pressure and the resulting residue was re-suspended in chloroform. It was further purified by recrystallisation from MeOH to afford 4.12 g of 4-N-(2-tert- N-(4-fluorobenzyl)hydrazinecarbothioamide (**vd**) as white crystals (71%).

^{1}H NMR (300 MHz, DMSO-d^6) δ_H: 8.76 (s, 1H, RN***H***-NH$_2$), 8.35 (brs, 1H, RN***H***-CSR'), 7.35 (m, 2H, ***H^{4} H$^{4'}$***), 7.11 (m, 2H, ***H^{5} H$^{5'}$***), 4.67 (d, 2H, ^{3}J= 6.1 Hz, ***H^{8}***), 4.49 (appq, 2H, RNH-N***H***$_2$);

^{13}C NMR (75 MHz, DMSO-d$_6$) δ_C: 45.68 (***C^{2}***), 115.09 (d, $J_{C\text{-}F}$= 20.6 Hz, ***C^{5} C$^{5'}$***), 129.72 (d, $J_{C\text{-}F}$= 7.8 Hz, ***C^{4} C$^{4'}$***), 136.49 (d, $J_{C\text{-}F}$= 2.9 Hz, ***C***F), 163.05 (***C^{3}***), 181.77 (***C***S) ppm.

^{19}F NMR (470 MHz, DMSO-d$_6$) δ_C: -113.85

Mass Spectrometry: ASAP for $C_8H_{10}FN_3S$, calcd for ([M+H]$^+$) 200.0652 found 200.0650.

X-Ray Structure (Appendix)

N-(4-ethynyl benzyl)hydrazinecarbothioamide (2f):

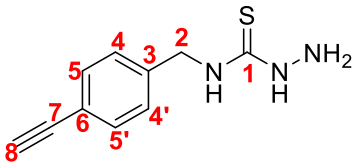

Hydrazine monohydrate (0.21 mL, 4.16 mmol) was added dropwise to a solution of methyl (4-ethynyl benzyl)carbamodithioate (**1f**) (0.7400 g, 3.32 mmol) in EtOH (20 mL) under stirring. The obtained slurry was allowed to react for 5 h under reflux (78 °C). Then, the excess of solvent was removed under reduced pressure and the resulting residue was re-suspended in chloroform. It was further purified using a silica plug, washing with $CHCl_3$ (50 mL) and MeOH (100 mL) and the methanolic fraction was concentrated under *vacuum*. The compound was crashed out in MeOH to afford 0.5452 g of N-(4-ethynyl benzyl)hydrazinecarbothioamide (**2f**) as an off-white solid (80%).

^{1}H NMR (300 MHz, MeOH-d_6) δ_H :8.81 (s, 1H, RN***H***-NH_2), 8.41 (brs, 1H, RN***H***-CSR'), 7.42 (appd, 2H, ^3J= 8.1 Hz ***H^4 H$^{4'}$***), 7.30 (appd, 2H, ^3J= 8.1 Hz, ***H^5 H$^{5'}$***), 4.72 (d, 2H, ^3J= 6.0 Hz, ***H^2***), 4.53 (bs, 2H, RNH-N***H***$_2$), 4.14 (s, 3H, S-C***H***) ppm.

^{13}C NMR (75 MHz, MeOH-d_6) δ_C: 181.9 (***C***S), 141.6 (***C^3***), 127.9(***C^5 C$^{5'}$***), 126.2 (***C^4 C$^{4'}$***), 120.2, (***C^6***), 83.9 (R-***C***CH_3), 80.9 (RC-***C***H_3), 46.2 (R-***C***H_2-bnz) ppm

Mass Spectrometry: ASAP for $C_{10}H_{11}N_3S$, calcd for ($[M+H]^+$) 206.0752 found 206.0749.

4-N-(2-tert-butoxycarbonylaminoethyl)-3-dithiocarbamate (2g):

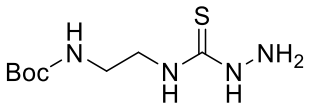

Hydrazine monohydrate (0.39 mL, 8.09 mmol) was added dropwise to a solution of methyl-N-(2-tert-butoxycarbonylaminoethyl) dithiocarbamate (**1d**) (1.6206 g, 6.47 mmol) in EtOH (15 mL) under stirring. The obtained slurry was allowed to react for 2.5 h under reflux (78 ºC). Then, the excess of solvent was removed under reduced pressure and the resulting residue was re-suspended in chloroform. It was further purified using a silica plug, washing with $CHCl_3$ (50 mL) and MeOH (100 mL) and the methanolic fraction was concentrated under *vacuum*. Further purification was needed and a flash column chromatography was carried out using $CHCl_3$/MeOH solution (1% to 10%) to afford 1.0312 g of 4-N-(2-tert-butoxycarbonylaminoethyl)-3-dithiocarbamate (**2δ**) as an off-white solid (68%).

^{1}H NMR (500 MHz, DMSO-d_6) δ_H :8.68 (brs, 1H, R-N***H***-NH_2), 7.94 (brs, 1H, R-N***H***-Boc), 4.99 (brs, 1H, R-N***H***-$CSNHNH_2$), 4.44 (s, 2H, R-N***H*****$_2$**), 3.49 (appq, 2H, ^{3}J =6.0 Hz, R-C***H***$_2$-NHBoc), 3.38 (appq, 2H, ^{3}J =5.9 Hz, R-C***H***$_2$-$NHCSNHNH_2$), 1.38 (s, 9H, ROC-(CH_3)$_3$);

^{13}C NMR (125 MHz, DMSO-d_6) δ_C: 197.9 (RNH-***C***S-$NHNH_2$), 156.1 (RNH-***C***O-$OC(CH_3)_3$), 78.2 (RNHCO-O***C***$(CH_3)_3$), 46.4 (R-***C***H_2-$NHCSNHNH_2$), 38.5 (R-***C***H_2-NHBoc), 28.6 (ROC-(CH_3)$_3$) ppm.

Mass Spectrometry: ASAP for $C_8H_{18}N_4O_2S$, calcd for ($[M+H]^+$) 235.1221 found 235.1223.

Synthesis of mono(substituted) ligands

Mono (substituted) 4-phenyl-3-thiosemicarbazone acenaphthenequinone (5a):

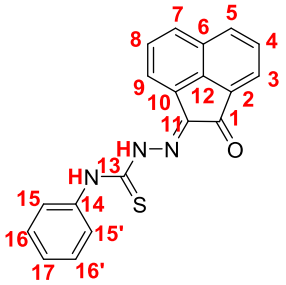

A microwave tube was filled with acenaphthenoquinone (0.2500 g, 1.37 mmol), 4-phenylthiosemicarbazid (0.2210 g, 1.37 mmol), 10 mL of EtOH and 2 drops of concentrated HCl. The mixture was reacted at 90 °C in the microwave for 10 minutes, under stirring. The resulting mixture was then allowed to cool, filtrated and washed with Et_2O. The precipitate was collected to afford the desired compound (**5a**) as an orange solid (58%). No further purification was necessary.

^{1}H NMR (500 MHz, DMSO-d_6) δ_H: 12.85 (s, 1H, N-N***H***); 11.01 (s, 1H, N***H***-Ph); 8.42 (d, 1H, ^{3}J= 8.3 Hz, ***H*****^{9}**); 8.16 (m, 3H, ***H*****^{7}**, ***H*****^{5}**, ***H*****^{3}**); 7.89 (m, 2H, ***H*****^{8}**, ***H*****^{4}**), 7.65 (appd, 2H, ^{3}J= 7.7 Hz, ***H*****^{15}** ***H*****$^{15'}$**), 7.47 (appt, 2H, ^{3}J= 7.6 Hz, ***H*****^{16}** ***H*****$^{16'}$**), 7.31 (t, 1H, ^{3}J= 7.6 Hz, ***H*****^{17}**) ppm.

^{13}C NMR (125 MHz, DMSO-d_6) δ_C: 188.6 (***C***=O); 176.6 (NHR-***C***S-NHPh); 139.4 (***C***=N-R); 138.5 (***C*****^{14}**); 137.7 (***C*****^{12}**); 132.8 (***C*****^{9}**); 130.4 (***C*****^{2}**); 129.9 (***C*****^{6}**); 129.8 (***C*****^{12}**); 128.9 (***C*****^{4}**); 128.6 (***C*****^{8}**); 128.4 (***C*****^{16}**); 127.2 (***C*****^{5}**); 126.2 (***C*****^{17}**); 125.7 (***C*****^{15}**); 122.5 (***C*****^{7}**); 118.8 (***C*****^{3}**) ppm.

Mass Spectrometry: ASAP for $C_{19}H_{13}N_3OS$, calcd for ($[M-H]^+$) 330.0696 found 330.0699.

IR (solid): ν (cm^{-1}) 3296, 3265, 3058, 1684, 1595, 1540, 1472, 1046, 1023 cm^{-1}

HPLC (Method C): R_f = 11.41 min

X-ray diffraction were obtained in DMSO after 2 days at room temperature.

Mono (substituted) 3-allyl-4-thiosemicarbazone acenaphthenequinone (5b):

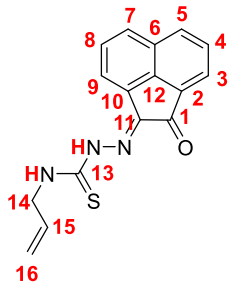

A microwave tube was filled with acenaphthenoquinone (0.5000 g, 2.74 mmol), 4-phenylthiosemicarbazid (0.3595 g, 2.74 mmol), 15 mL of EtOH and 0.1mL of concentrated HCl. The mixture was reacted at 90 °C in the microwave for 10 min. The slurry was then allowed to cool, filtrated and washed with Et_2O. The precipitate was collected to afford the desired compound (**5b**) as an orange solid (58%). No further purification was necessary.

^{1}H NMR (300 MHz, DMSO-d_6) δ_H: 12.63 (s, 1H, N-N*H*); 9.59 (t, 1H, ^3J= 5.7 Hz, N**H**-Allyl); 8.36 (d, 1H, ^3J= 8.0 Hz, ***H*^{9}**); 8.11 (overlapping d, 1H, ^3J= 14.7 Hz, ***H*^{7}**); 8.08 (overlapping d, 1H, ^3J= 13.4 Hz, ***H*^{5}**); 7.99 (d, 1H, ^3J= 7.0 Hz, ***H*^{3}**); 7.84 (m, 2H, ***H*^{4}, *H*^{8}**), 5.96 (m, 1H, R-C***H***-CH_2), 5.22 (overlapping d, 1H, ^3J= 23.5 Hz, RCH-C***H*$_2^a$**); 5.16 (overlapping d, 1H, ^3J= 16.7 Hz, RCH-C***H*$_2^b$**); 4.30 (t, 1H, ^3J= 4.9 Hz, NHC*H*$_2$-**C**H-CH_2) ppm

^{13}C NMR (125 MHz, DMSO-d_6) δ_C: 188.5 (***C***=O); 177.5 (NHR-***C***S-NHAllyl); 139.15 (***C*^{11}**); 137.3 (***C*^{12}**); 134.0 (R-***C***H-CH_2); 132.8 (***C*^{9}**); 130.5 (***C*^{6}**); 130.1 (***C*^{2}**); 129.9 (***C***=N-R); 128.9 (***C*^{4}**); 128.6 (***C*^{8}**); 127.1 (***C*^{7}**); 122.5 (***C*^{5}**); 118.4 (***C*^{3}**); 116.3 (RCH-***C***H_2); 46.5 (NH-***C***H_2-R) ppm.

Mass Spectrometry: ASAP for $C_{16}H_{13}N_3OS$, calcd for ($[M-H]^+$) 294.0691 found 294.0696.

IR (solid): ν (cm^{-1}) 3296, 3265, 2951, 1685, 1597, 1533, 1477, 1051, 1027 cm^{-1}

HPLC (Method C): R_f = 10.82 min

X-ray diffraction were obtained in DMSO after 2 days at room temperature.

Mono (substituted) 3-ethyl-4-thiosemicarbazone acenaphthenequinone (5c):

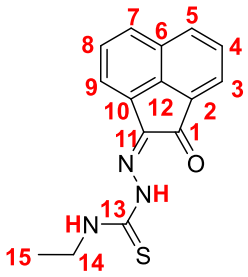

A microwave tube was filled with acenaphthenoquinone (0.5000 g, 2.74 mmol), 4-ethylthiosemicarbazide (0.3259 g, 2.74 mmol), 15 mL of EtOH and 0.1mL of concentrated HCl. The mixture was reacted at 90 °C in the microwave for 10 min. The slurry was then allowed to cool, filtrated and washed with Et_2O. The precipitate was collected to afford the desired compound (**7c**) as an orange solid (84%). No further purification was necessary.

^{1}H NMR (300 MHz, DMSO-d_6) δ_H: 12.59 (s, 1H, N-N***H***); 9.44 (t, 1H, ^3J= 5.44 Hz, N***H***-Et); 8.36 (d, 1H, ^3J= 8.27 Hz, ***H^9***); 8.12 (overlapping d, 1H, ^3J= 13.7 Hz, ***H^5***), 8.08 (overlapping d, 1H, ^3J= 12.1 Hz, ***H^7***); 7.99 (d, 1H, ^3J=7.0 Hz, ***H^3***); 7.84 (m, 2H, ***H^8,H^4***); 3.66 (q, 2H, NH-C***H$_2$***-CH_3); 1.20 (t, H, ^3J= 6.9 Hz, R-C***H$_3$***).

^{13}C NMR (75 MHz, DMSO-d_6) δ_C: 188.9 (***C***=O); 177.2 (NHR-***C***S-NHEt); 139.4 (***C***=N-R); 137.53 (***C^{12}***); (***C^2***); 133.1 (***C^9***); 130.9 (***C^6***); 130.5 (***C^2***); 130.3 (***C^{10}***); 129.3 (***C^4***); 129.0 (***C^8***); 127.41 (***C^7***); 122.84 (***C^5***); 118.63 (***C^3***); 14.4 (RCH_2-***C***H_3); ppm.

Mass Spectrometry: ASAP for $C_{15}H_{13}N_3OS$, calcd for ($[M+H]^+$) 284.0858 found 284.0855.

IR (solid): ν (cm^{-1}) 3298, 3278, 2976, 1682, 1605, 1533, 1471, 1056, 1027 cm^{-1}

HPLC (Method C): R_f = 10.71 min

X-ray diffraction were obtained in DMSO after 2 days at room temperature.

Mono (substituted) 4-F-benzyl-3-thiosemicarbazone acenaphthenequinone (5e):

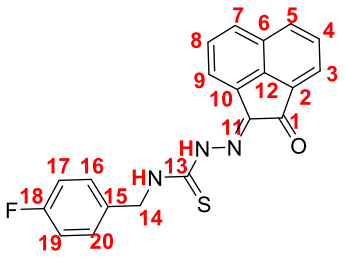

A microwave tube was filled with acenaphthenoquinone (0.5000 g, 2.74 mmol), 4-F-benzylamine thiosemicarbazide (0.5450 g, 2.74 mmol), 15 mL of acetic acid. The mixture was reacted at 90 °C in the microwave for 20 min. The slurry was then allowed to cool,

filtrated and washed with Et_2O. The precipitate was collected to afford 0.9564 g of the desired compound as a yellow solid (88%). No further purification was necessary.

^{1}H NMR (500 MHz, DMSO-d_6) δ : 12.62 (s, 1H, N-N***H***); 9.96 (t, 1H, ^3J= 6.10 Hz, N***H***-bnzF); 8.37 (d, 1H, ^3J= 8.2 Hz, ***H^3***); 8.12 (overlapping d, 1H, ^3J= 12.4 Hz, ***H^5***); 8.08 (overlapping d, 1H, ^3J= 11.0 Hz ***H^7***); 7.99 (d, 1H, ^3J= 6.9 Hz, ***H^9***); 7.84 (m, 2H, ***H^4 H^8***); 7.45 (appt, 2H, ^3J= 6.6 Hz, ***H^{16} H^{20}***); 7.18 (appt, 2H, ^3J= 8.8 Hz, ***H^{17} H^{19}***); 4.89 (appd, 2H, ^3J= 5.8 Hz, ***H^{14}***),

^{13}C NMR (125 MHz, DMSO-d_6) δ: 189.0 (***C***=O); 178.4 (NHR-***C***S-NHR) 161.8 (d, $J_{C\text{-}C}$ = 242.5 Hz, ***C^{18}***); 139,7 (***C^{11}***); 138.0 (***C^{12}***); 134.9 (***C^3***); 133.1 (***C^6***); 130.8 (***C^2***); 129.9 (d, $J_{C\text{-}C}$= 8.4 Hz ***C^{16}***); 129.7 (d, $J_{C\text{-}C}$= 8.4 Hz ***C^{20}***); 129.3 (***C^4***); 129.1 (***C^8***); 127.6 (***C^5***); 122.9 (***C^7***); 128.9 (***C^{10}***); 118.9 (***C^9***); 115.3 ((d, $J_{C\text{-}C}$= 21.4 Hz ***C^{17} C^{19}***); 47.1 (***C^{14}***) ppm.

^{19}F NMR (470 MHz, ΔMΣO) δ_F : -115.74

Mass Spectrometry: ASAP for $C_{20}H_{14}FN_3OS$, calcd for ($[M+H]^+$) 364.0920 found 364.0915.

IR (solid): ν (cm^{-1}) 3321, 3269, 1691, 1604, 1525, 1453, 1082, 1025, 853, 772 cm^{-1}

HPLC (Method C): R_f = 11.33 min

X-ray diffraction were obtained in DMSO after 2 days at room temperature.

Mono (substituted) 4-ethynylbenzyl-3-thiosemicarbazone acenaphthenequinone (5f):

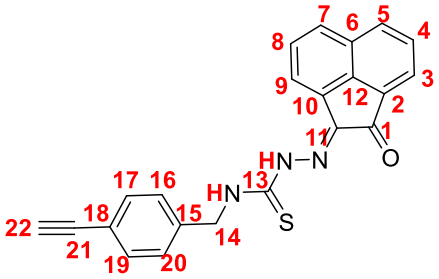

A microwave tube was filled with acenaphthenoquinone (0.2500 g, 1.37 mmol), 4-ethynyl-benzylamine thiosemicarbazide (0.2802 g, 1.37 mmol), 10 mL of acetic acid. The mixture was reacted at 90 °C in the microwave for 20 min. The slurry was then allowed to cool, filtrated and washed with Et_2O. The precipitate was collected to afford 0.9468 g of the desired compound as a yellow solid (86%). No further purification was necessary.

^{1}H NMR (300 MHz, DMSO-d^6) δ : 12.69 (s, 1H, N-N***H***); 9.97 (t, 1H, ^3J= 5.8 Hz, N***H***-bnzprop); 8.35 (d, 1H, ^3J= 8.1 Hz, ***H^9***); 8.12 (overlapping d, 1H, ^3J= 12.9 Hz, ***H^5***); 8.08 (overlapping d, 1H, ^3J= 11.3 Hz ***H^7***); 7.97 (d, 1H, ^3J= 6.9 Hz, ***H^3***); 7.84 (m, 2H,

H*[4] *H*[8]**); 7.43 (dd, 4H, ^{3}J= 7.7, 16.1 Hz, ***H*[16] *H*[17] *H*[19] *H*[20]**); 4.91 (t, 2H, ^{3}J= 5.6 Hz, ***H*[14]**); 4.16 (s, 1H, RCH***) ppm.

^{13}C NMR (125 MHz, DMSO-d^{6}) δ: 188.9 (***C***=O); 178.4 (NHR-***C***S-NHR); 152.4 (***C*[11]**); 139.6 (***C*[12]**); 138.0 (***C*[15]**); 133.1 (***C*[5] *C*[7]**); 132.1 (***C*[16] *C*[20]**); 130.8 (***C*[6]**); 130.4 (***C*[9]**); 130.2 (***C*[3]**); 129.2 (***C*[4]**); 128.9 (***C*[8]**); 127.9 (***C*[17] *C*[19]**); 127.5 (***C*[2]**); 122.9 (***C*[10]**); 120.7 (***C*[18]**); 83.8 (***C*[21]**); 81.1 (***C*[22]**); 47.7 (***C*[14]**) ppm.

Mass Spectrometry: ASAP for $C_{22}H_{15}N_3OS$, calcd for ($[M+H]^+$) 507.1497 found 507.1483.

IR (solid): ν (cm^{-1}), 3259, 3236, 2950, 1684, 1527, 1452, 1082, 1026 cm^{-1}

HPLC (Method C): R_f = 11.37 min

X-ray diffraction were obtained in DMSO after 2 days at room temperature.

Mono (substituted) 4-Boc-diethylamine-3-thiosemicarbazone acenaphthenequinone (5g):

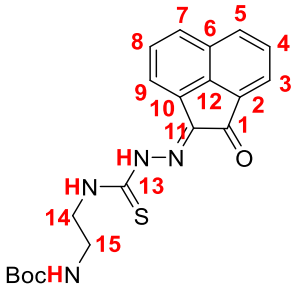

A microwave tube was filled with acenaphthenoquinone (0.5000 g, 2.74 mmol), 4-Boc-diethylamine thiosemicarbazide (0.640 g, 2.74 mmol), 15 mL of acetic acid. The mixture was reacted at 90 °C in the microwave for 20 min. The slurry was then allowed to cool, filtered and washed with Et_2O. The precipitate was collected to afford 0.9564 g of the desired compound as a yellow solid (88%). No further purification was necessary.

^{1}H NMR (300 MHz, DMSO-d$_6$) δ : 12.62 (s, 1H, N-N***H***); 9.45 (t, 1H, ^{3}J= 5.3 Hz, N***H***-Boc); 8.38 (d, 1H, ^{3}J= 8.2 Hz, ***H*[9]**); 8.13 (overlapping d, ^{3}J= 16.3 Hz 1H, ***H*[5]**); 8.11 (overlapping d, 1H, ^{3}J= 14.1 Hz ***H*[8]**); 8.01 (d, 1H, ^{3}J= 7.1 Hz, ***H*[3]**); 7.86 (overlapping t, 2H, ***H*[4] *H*[8]**), 7.11 (t, 1H, ^{3}J= 5.5 Hz, N***H***-CS), 3.66 (q , 2H, ^{3}J= 6.2 Hz, C***H*$_2$**-NHBoc); 3.66 (q, 2H, ^{3}J= 5.8 Hz, C***H*$_2$**-CS); 1.39 (s, 8H, O(C***H*$_3$**)$_3$) ppm.

^{13}C NMR (125 MHz, DMSO-d$_6$) δ: 188.6 (***C***=O); 177.6 (NHR-***C***S-NHR); 156.2 ((CH$_3$)O-***C***=O); 139.2 (R-***C***H$_2$-NHBoc); 137.3 (***C*[12]**); 132.9 (***C*[2]**); 130.5 (***C*[9]**); 130.1 (***C*[10]**); 130.0 (***C*[6]**); 128.88 (***C*[Boc]**); 128.7 (***C*[4]**); 127.2 (***C*[8]**); 122.6 (***C*[7]**); 118.7 (***C*[5]**); 78.1 (***C*[3]**); 78.0 (R-***C***H$_2$-NHCSR); 28.2 (O(***C***H$_3$)$_3$) ppm.

Mass Spectrometry: ASAP for $C_{20}H_{22}N_4O_3S$, calcd for ($[M+H]^+$) 399.1485 found 399.1483.

IR (solid): ν (cm^{-1}) 3383, 3326, 2946, 1669, 1509, 1482, 1246, 1067, 1026 cm^{-1}

HPLC (Method C): R_f = 11.80 min

X-ray diffraction were obtained in DMSO after 2 days at room temperature.

Synthesis of zinc(II) complexes

Zn(II) [mono (phenyl thiosemicarbazonate) acenaphthenequinone]$_2$ (6a):

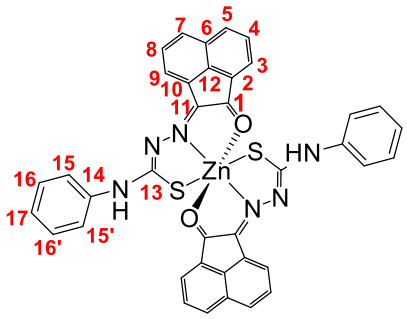

Mono (substituted) 3-phenyl-4-thiosemicarbazone acenaphthenequinone (**5a**) (0.5000 g, 2.74 mmol) and anhydrous zinc acetate (0.5450 g, 2.74 mmol) were suspended in 5 mL of EtOH. The mixture was reacted at 90 °C under microwave irradiation for 60 min. The slurry was then filtrated and washed with Et_2O. The precipitate was collected to afford 0.9564 g of the desired compound as a yellow solid (88%). No further purification was necessary.

^{1}H NMR (500 MHz, DMSO-d^6) δ_H : 10.9 (s, 2H, N***H***-Ph); 8.37 (appd, 2H, ^3J= 8.1 Hz, ***H^9***); 8.19 (appd, 4H, ^3J= 8.2 Hz, ***H^5 H^7***); 8.19 (appd, 2H, ^3J= 8.1 Hz, ***H^3***); 7.83 (appd, 4H, ^3J= 8.1 Hz, ***H^8***, ***H^4***), 7.78 (overlapping d, 2H, ^3J= 7.0 Hz, ***H^{15} H$^{15'}$***), 7.47 (t, 2H, ^3J= 6.6 Hz, ***H^{16} H$^{16'}$***), 7.31 (appt, 1H, ^3J= 6.0 Hz, ***H^{17}***) ppm.

^{13}C NMR (125 MHz, DMSO-d^6) δ_C: 189.9 (***C***=O); 177.1 (NHR-***C***S-NHPh); 139.9 (***C***=N-R); 138.2 (***C^{12}***); 137.4 (***C^2***); 133.6 (***C^9***); 130.9 (***C^{14}***); 130.4 (***C^3***); 130.4 (***C^6***); 129.4 (***C^8***); 129.1 (***C^4***); 128.9 (***C^{16}***); 127.7 (***C^3***); 126.6 (***C^{17}***); 126.2 (***C^{15}***); 123.0 (***C^7***); 119.3 (***C^5***).

Mass Spectrometry: ASAP for $C_{19}H_{13}N_3OS$, calcd for ($[M-H]^+$) 330.0696 found 330.0699.

IR (solid): ν (cm^{-1}) 3294, 1684, 1593, 1540, 1376, 1042, 1025 cm^{-1}

HPLC (Method C): R_f = 11.55, 12.13 min

Zn(II) [mono (allyl thiosemicarbazonate) acenaphthenequinone]$_2$ (6b):

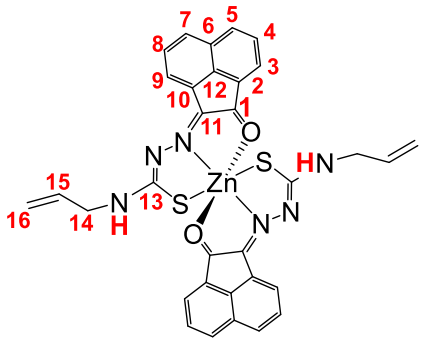

Mono (substituted) 3-allyl-4-thiosemicarbazone acenaphthenequinone (**5b**) (0.1000 g, 0.34 mmol) and anhydrous zinc acetate (0.1242 g, 0.68 mmol) were suspended in 10 mL of EtOH. The mixture was reacted at 90 °C under microwave irradiation for 60 min. The slurry was then filtrated and washed with Et_2O. The precipitate was collected to afford 0.1160 g of the desired compound as an orange solid (53%). No further purification was necessary.

^{1}H NMR (500 MHz, DMSO-d_6) δ_H: 9.51 (t, 2H, ^3J= 5.4 Hz, N***H***-Et); 8.56 (d, 2H, ^3J= 6.8 Hz, ***H^3***); 8.47 (d, ^3J= 6.8 Hz, 2H, ***H^9***); 8.34 (m, 4H, ***H^7 H^5***), 7.83 (m, 4H, ***H^4, H^8***), 6.0 (m, 4H, NH-C***H$_2$***-CHCH_2), 5.17 (overlapping dd, 4H, ^3J= 17.2, 17.5 Hz, RCH-C***H$_2$***); 4.28 (appt, 2H, ^3J= 5.6 Hz, NHC***H$_2$***-**C**H-CH_2) ppm.

^{13}C NMR (125 MHz, DMSO-d_6) δ_C: 188.6 (***C***=O); 177.6 (NHR-***C***S-NHAllyl); 139.2 (***C^{12}***); 137.6 (***C^2***); 134.6 (R-***C***H-CH_2); 133.2 (***C^7***); 130.46 (***C^{10}***); 130.06 (***C***=N-R); 129.9 (***C^6***); 128.6 (***C^{11}***); 127.9 (***C^4***); 127.2 (***C^8***); 124.3 (***C^9***); 124.1 (***C^5***); 123.8 (***C^3***); 116.7 (RCH-***C***H_2); 46.1 (NH-***C***H_2-R) ppm.

Mass Spectrometry: ASAP for $C_{32}H_{24}N_6O_2S_2Zn$, calcd for ([M+H]$^+$) 653.0772 found 653.0764.

IR (solid): ν (cm^{-1}) 3295, 3055, 1685, 1594, 1536, 1048, 1023 cm^{-1}

HPLC (Method C): R_f = 13.11 min

Zn(II) [mono (ethyl thiosemicarbazonate) acenaphthenequinone]$_2$ (6c):

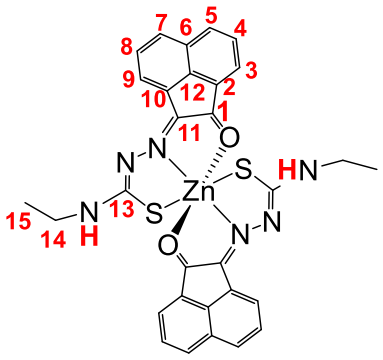

Mono (substituted) 3-ethyl-4-thiosemicarbazone acenaphthenequinone (**5c**) (0.1844 g, 0.65 mmol) and anhydrous zinc acetate (0.1195 g, 0.65 mmol) were suspended in 10 mL of EtOH. The mixture was reacted at 90 °C under microwave irradiation for 60 min. The slurry was then filtrated and washed with Et_2O. The precipitate was collected to afford 0.1508 g of the desired compound as an orange solid (37%). No further purification was necessary.

^{1}H NMR (500 MHz, DMSO-d_6) δ_H: 9.52 (appq, 2H, ^3J= 6.5, 8.5 Hz, N**H**-Allyl); 8.47 (overlapping d, 2H, ^3J= 7.1 Hz, ***H*^{9}**); 8.32 (overlapping d, 2H, ^3J= 8.4 Hz, ***H*^{5}**), 8.08 (overlapping d, 1H, ^3J= 8.4 Hz, ***H*^{7}**), 7.84 (m, 4H, ***H*^{4}, *H*^{8}**), 3.76 (appt, 4H, 2H, ^3J= 8.4 Hz, NH-C***H*$_2$**-CH_3), 1.35 (t, 6H, ^3J= 7.1 Hz, RCH_2-C***H*$_3$**)

^{13}C NMR (125 MHz, DMSO-d^6) δ_C: 188.91 (***C***=O); 177.21 (NHR-***C***S-NHEt); 139.44 (***C*^{12}**); 137.53 (***C*^{2}**); 133.2 (***C*^{7}**); 130.8 (***C*^{10}**); 130.5 (***C***=N-R); 130.3 (***C*^{6}**); 129.3 (***C*^{11}**); 127.9 (***C*^{3}**); 124.2 (***C*^{9}**); 123.4 (***C*^{4}**, ***C*^{8}**); 39.1 (R-**C**H_2-*C*H_3); 14.9 (RCH_2-**C**H_3) ppm.

Mass Spectrometry: ASAP for $C_{30}H_{24}N_6O_2S_2Zn$, calcd for ($[M+H]^+$) 629.0772 found 629.0765.

IR (solid): ν (cm^{-1}) 3281, 2918, 1683, 1574, 1442,1394 1078, 1022 cm^{-1}

HPLC (Method C): R_f = 13.01, 13.55 min

Zn(II) [mono (F-benzyl thiosemicarbazonate) acenaphthenequinone]$_2$ (6e):

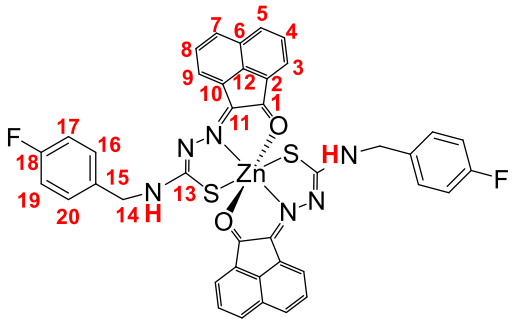

Mono (substituted) 4-F-benzyl-3-thiosemicarbazone acenaphthenequinone (**5e**) (0.2000 g, 0.55 mmol) and anhydrous zinc acetate (0.2020 g, 1.10 mmol) were suspended in 5 mL of EtOH. The mixture was reacted at 90 °C under microwave irradiation for 60 min. The slurry was then filtrated and washed with Et_2O. The precipitate was collected to afford 0.9564 g of the desired compound as an orange solid (88%). No further purification was necessary.

^{1}H NMR (500 MHz, DMSO-d^6) δ : 8.96 (appd, 2H, ^3J= 5.4 Hz, N***H***-bnzF); 8.56 (appt, 2H, ^3J= 7.5 Hz, ***H^9***); 8.34 (appt, 2H, ^3J= 7.9 Hz, ***H^3***); 8.12 (appt, 4H, ^3J= 7.3 Hz, ***H^5 H^7***); 7.89 (appt, 4H, ^3J= 6.6 Hz, ***H^4 H^8***); 7.77 (m, 8H, ***H^{16} H^{17} H^{19} H^{20}***); 4.89 (t, 4H, ^3J= 5.46 Hz, ***H^{14}***) ppm.

^{13}C NMR (125 MHz, DMSO) δ: 189.9 (***C***=O); 178.2 (NHR-***C***S-NHR) 163.3 (***C^{18}***); 160.1 (***C^{11}***); 139.6 (***C^{12}***); 134.9 (***C^3***); 133.1 (***C^6***); 130.8 (***C^2***); 130.3 (d, $J_{C\text{-}C}$= 8.4 Hz ***C^{16}***); 129.8 (d, $J_{C\text{-}C}$= 8.4 Hz ***C^{20}***); 129.7 (***C^4***); 129.2 (***C^8***); 127.6 (***C^5***); 122.9 (***C^7***); 128.9 (***C^{10}***); 118.9 (***C^9***); 115.3 (***C^{17} C^{19}***); 47.5 (***C^{14}***) ppm.

^{19}F NMR (470 MHz, DMSO-d$_6$) δ_F : -116.44 ppm.

Mass Spectrometry: ASAP for $C_{40}H_{26}F_2N_6O_2S_2Zn$, calcd for ($[M+H]^+$) 789.0896 found 789.0912 .

IR (solid): ν (cm^{-1}) 3243, 2936, 1538, 1449, 1392, 1081, 1022, 773 cm^{-1}

HPLC (Method C): R_f = 11.43, 14.47 min

6.2.2. Radiolabelling of mono(substituted) ligands

Coordination of monosubstituted ligands with [^{68}Ga]Ga(III).

A SnO_2-based column matrix $^{68}Ge/^{68}Ga$ generator was used to elute 10 mL of 0.6 M HCl, ca. 178 MBq of gallium-68, which was trapped on a Strata x-c 33 µm Polymeric Strong Cation Cartridge from Phenomenex and eluted with 700 µL of 0.02M HCl (98% THF). This was subsequently dried for 7-10 min under a nitrogen stream at 95 °C. Next 30 µL of the monosubstituted compound in dry DMSO (2mg/mL) was added along with 0.6 mL of injectable MeOH. This was heated under microwave radiation at 95 °C for 30 min. Analysis by reverse-phase HPLC (**Method C**) gave two different retention times for each compound which in comparison with the HPLC trace of the precursors suggest that this could be isomers of the compound**.** Remains of $[^{68}Ga]GaCl_3$ were indicate that radiolabelling of the mono(substituted) ligands had not gone to completion.

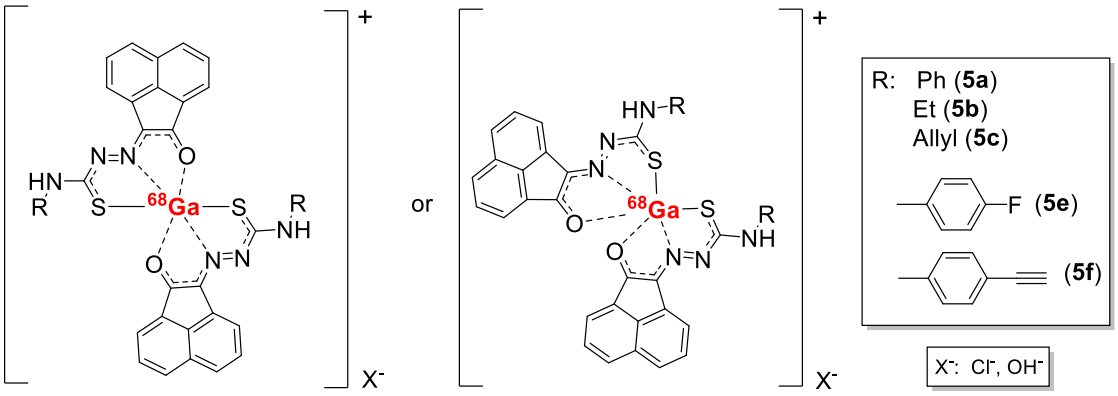

Scheme 28: Schematic illustration of the proposed structures of the radiolabelled mono(substituted) ligands with [^{68}Ga]Ga(III).

Table 15: Percentage of the optimal radiochemical incorporation for all the mono(substituted) ligands with [^{68}Ga]Ga(III) applying microwave radiation.

MONOSUBSTITUTED LIGAND ABBREVIATION	PROPOSED STRUCTURE NO	RETENTION TIME	ROI %
PHTSCA	**5a**	13.42 16.41	70 %
ALLYLTSCA	**5b**	12.37 15.17	67 %
ETTSCA	**5c**	12.13 15.05	75 %
FBNZTSCA	**5e**	13.25 15.24	98 %
PROPBNZTSCA	**5f**	13.41 15.36	55 %

Coupling of the NH_2-free TSCA monosubstituted ligands with [^{18}F]FBA.

In a sealed reaction vial, NH_2-free TSCA (**5h**) (1.20 mg, 0.0042 mmols) was diluted in 0.5 mL of DMF and mixed with 25 μL of the SPE purified solution of compound [^{18}F]-FBA in MeCN (5.44 MBq). The slurry was heated to 120 °C for 25 min. Analysis by reverse-phase HPLC (Method D) gave a retention time of 7.08 min which in comparison with the reference HPLC trace suggested to confirm the synthesis of **[^{18}F]-8**. The extent of conversion to the product was measured as 30 %.

6.2.3. In vitro experiments to mono(monosubstituted) TSCA ligands

MTT assays

Cells (5-7×10^3 cells per well) were seeded on a sterile 96-well plate and incubated for 48 h to adhere. All the monosubstituted ligands were subsequently loaded at different concentration (as mentioned earlier, section 7.1.3) into wells and cultured for another 48 h. Subsequently, cells were washed three times with PBS and 3-(4, 5-dimethylthiazol-2-yl)-2, 5-diphenyltetrazolium bromide (MTT) was added (0.5 mg/ mL, 90% serum-free medium (SFM)) + 10% PBS followed by a two-hour incubation. After aspiration, 100 μL of DMSO was added and the 96-well plates were read by an ELISA plate reader, Molecular Devices

Versa Max (BN02877). The absorption wavelength was at 570 nm and 630 nm wavelength was used as a reference. For establishing the correct protocols, a library of known compounds with similar solubility and which also carries the N/S motifs were analysed.

Fluorescence microscopy

PC3 cells were cultured in normoxia environment as previously described (p.160). Cells were then seeded in a single well plate at least 48 h prior to the microscopy experiment (10,000 cell per well plate) where they washed twice with PBS and incubated at 37 ºC. Control fluorescence images were recorded before the addition of compound. For both confocal and epi-fluorescence microscopy, NH_2-free TSCA mono(substituted) ligand in a DMSO: RPMI 0.5:99.5 solution mixture (100 μM), was loaded into the wells and cells were allowed to incubate for 15 min, at 37 °C. They were then carefully washed with Phosphate Buffered Saline (PBS) pre-warmed to 37 °C and then it was replaced by FCS-free medium to remove the non-internalised fluorescent dispersion prior to fluorescence imaging.

Cell uptake of the radiolabelled compound

PC3 and EMT6 cells ($3 \cdot 10^3$ cells) were seeded in 6-well plates and incubated in normoxia and hypoxia environments as described before (p.160). After treatments, plates were aspirated and washed twice with warm PBS buffer. Each well plate was then loaded with 1000 μL of [^{68}Ga]Ga(FbnzTSCA)$_2$ (**[^{68}Ga]-7e**) in DMSO:PBS solution mixture (0.5:95.5) (3 MBq/ mL) and incubated for 1 h. Posterior incubation, the reaction was stopped by washing wells with ice-cold PBS buffer twice, followed by addition of 1 mL of ice-cold, 0.1 % Triton X-100 and 0.1 M NaOH Lysates. A homogenous mixture was obtained by blending the components with up/down pipetting. 800 μL of each dissolved cell was then transferred and capped into counting tubes for gamma counting. The stock [^{68}Ga]Ga(FbnzTSCA)$_2$ (**[^{68}Ga]-7e**) solution was aliquoted in 3 of 10μL dose and placed to the counting tubes as standards. The intracellular radioactivity was immediately counted using an LKB Wallac 1282 Compugamma Laboratory gamma counter (PerkinElmer, USA). Lastly, protein concentration determination by BCA was carried out. This normalisation of decay-corrected radioactivity counts per minute (CPM) to protein concentration, was required in order to give a measure of radiotracer uptake as % ID/mg of protein= CPM in 1 mL/ (standard in mL · protein concentration in mg) · 100 %.

6.3. Experimental Details for Chapter Three

6.3.1. Synthesis of asymmetric thiosemicarbazone metal complexes

Synthesis of Zn(II) coordinated complexes

Zinc(II) 4-phenyl-3-thiosemicarbazone-thiocarbohydrazide acenaphthenoquinone (9a):

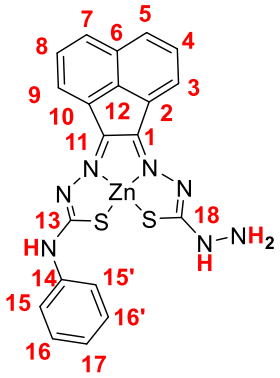

In a μW vial 3 mL of EtOH were added and heated to 60 °C. At that moment zinc acetate (0.3521 g, 1.92 mmol) was added along with 4-phenyl-3-thiosemicarbazone acenophthenoquinone (**5a**) (0.2120 g, 0.64 mmol), then the reaction was heated further to 120 °C and thiocarbohydrazide (0.3395 g, 3.20 mmol) was added together with 2 mL of EtOH and several drops of conc. HCl. The reaction mixture was heated under μW radiation at 150 °C for 106 min, then it was filtered hot, re-suspended in Et_2O (100 mL), stirred for another 15 min and filtered under vacuum. The resulting precipitate was further washed with Et_2O (200 mL) and Zinc (II) 4-phenyl-3-thiosemicarbazone-thiocarbohydrazide acenaphthenoquinone (**10a**) was isolated as an orange solid (91 %).

^{1}H NMR (500 MHz, DMSO-d_6) δ_H : 10.15 (s, 1H, N***H***-Ph); 8.71 (appd, 1H, ^3J=5.8 Hz, ***H^9***); 8.40 (appd, 1H, ^3J=6.5 Hz, ***H^3***); 7.99 (dd, 2H, ^3J=3.4, 4.6 Hz, ***H^5***, ***H^7***); 7.72 (overlapping t, 1H ^3J=7.9 Hz, ***H^8***); 7.67 (overlapping d, 1H ^3J=7.5 Hz, ***H^{15}*** ***H$^{15'}$***); 7.52 (t, 1H, ^3J=7.7 Hz, ***H^4***); 7.48 (t, 2H, ^3J=8.1 Hz, ***H^{16}*** ***H$^{16'}$***), 7.18 (appt, 2H, ^3J=7.4 Hz, ***H^{17}***); 6.75 (s, 2H, N***H$_2$***).

^{13}C NMR (125 MHz, DMSO-d_6) δ_C: 176.4 (RN=***C***S-NHPh); 147.4 (RN=***C***S-NHNH$_2$); 140.7 (***C^{11}***); 140.5 (***C^1***); 135.4 (***C^{12}***); 132.9 (***C^{14}***); 130.6 (***C^6***); 129.9 (***C^{10}***); 129.0 (***C^{16}***); 128.9 ***C^2***); 128.5 (***C^4***); 128.3 (***C^5***); 128.0(***C^8***); 127.8 (***C^7***); 126.6 (***C^9***); 124.5 (***C^{17}***); 123.7 (***C^{15}***); 120.9 (***C^3***);

Mass Spectrometry: MALDI-MS for $C_{20}H_{15}N_7S_2Zn$, calcd for ($[M]^+$) 481 found 481.

IR (solid): ν 3296, 2966, 1682, 1593, 1376, 1278, 1135 cm^{-1}

HPLC (Method C): R_f = 13.44 min

Zinc(II) 3-allyl-3-thiosemicarbazone-thiocarbohydrazide acenaphthenoquinone (9b):

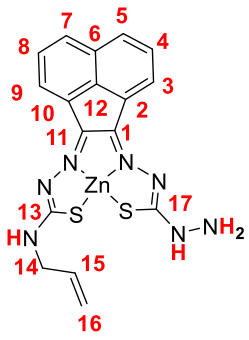

In a μW vial 3 mL of EtOH were added and heated to 60 °C. At that moment zinc acetate (0.3106 g, 1.69 mmol) was added along with 3-allyl-3-thiosemicarbazone acenophthenoquinone (**5b**) (0.1000 g, 0.35 mmol) Then the reaction was heated further to 120 °C and thiocarbohydrazide (0.1091 g, 1.06 mmols) was added together with 2 mL of EtOH and a couple of drops of HCl. The reaction mixture was heated under μW radiation at 150 °C for 106 min. Then it was filtrated hot, re-suspended in Et_2O (100 mL), stirred for another 15 min and filtrated under vacuum. Resulting precipitate was further washed with Et_2O (200 mL) and Zinc (II) 3-allyl-3-thiosemicarbazone-thiocarbohydrazide acenaphthenoquinone (**10b**) was isolated as an orange colour solid (92 %).

^{1}H NMR (500 MHz, DMSO-d_6) δ: 10.03(bs, 1H, N***H***-Allyl); 8.59 (bs, 1H, ***H^9***); 8.38 (bs, 1H, ***H^3***); 7.94 (overlapping, 2H, ***H^5***, ***H^7***), 7.67 (overlapping, 2H, ***H^4***,***H^8***); 6.65 (bs, 2H,N***H***$_2$); 6.05 (m, 1H, NHC***H***$_2$-CHCH$_2$); 5.29 (d, 1H, ^{3}J= 16.8 Hz, NHCH$_2$CH=C***H***$_2$); 5.16 (d, 1H, ^{3}J= 10.0 Hz, NHCH$_2$-C***H***=CH$_2$); ppm.

^{13}C NMR (125 MHz, DMSO-d_6) δ_C: 177.9 (RN=***C***S-NHPh); 175.4 (RN=***C***S-NHNH$_2$); 150.1 (***C^{11}***); 146.5 (***C^1***); 135.3 (***C^{12}***); 130.2 (***C^6***); 129.9 (***C^{10}***); 128.7 (***C^2***); 127.4 (***C^9***); 128.7 (***C^4***,***C^8***); 127.8 (***C^5***,***C^7***); 126.4 (***C^3***); 116.1 (NHCH$_2$-***C***H=CH$_2$); 116.0 (NHCH$_2$CH=***C***H$_2$); 45.7 (NH***C***H$_2$-CHCH$_2$)

Mass Spectrometry: MALDI-MS for $C_{17}H_{15}N_7S_2Zn$, calcd for ($[M]^+$) 445 found 445 and for ($[M+H]^+$) 446 found 446.

IR (solid): ν 3296, 3055, 1596, 1383, 1277, 1138 cm^{-1}

HPLC (Method C): R_f = 11.35 min

Zinc(II) 3-ethyl-3-thiosemicarbazone-thiocarbohydrazide acenaphthenoquinone (9c):

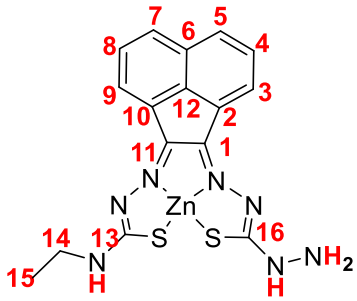

In a μW vial 3 mL of EtOH were added and heated to 60 °C. At that moment zinc acetate (0.3241 g, 1.77 mmol) was added along with 4-ethyl-3-thiosemicarbazone acenopthenoquinone (**5c**) (0.1000 g, 0.35 mmol) Then the reaction was heated further to 120 °C and thiosemicarbohydrazide (0.1125 g, 1.06 mmols) was added together with 2 mL of EtOH and a couple of drops of HCl. The reaction mixture was heated under μW radiation at 150 °C for 106 min. Then it was filtrated hot, re-suspended in Et_2O (100 mL), stirred for another 15 min and filtrated under vacuum. The resulting deposit was further washed with Et_2O (200 mL) and Zinc (II) 3-allyl-3-thiosemicarbazone-thiocarbohydrazide acenaphthenoquinone (**10c**) was isolated as an orange colour solid (86 %).

^{1}H NMR (500 MHz, DMSO-d_6) δ: 8.98 (bs, 1H, N***H***-Ethyl); 8.22 (bs, 1H, N***H***-NH_2); 8.62 (overlapping, 2H, ***H^3***, ***H^9***); 7.96 (overlapping, 2H, ***H^5*, *H^7***), 7.68 (overlapping, 2H, ***H^4*, *H^8***); 6.58 (bs, 2H, N***H***$_2$); 3.58 (bs, 2H, R-C***H***$_2$-CH_3); 1.56 (appt, 3H, ^{3}J= 7.1 Hz, RCH_2-C***H$_3$***) ppm.

^{13}C NMR (125 MHz, DMSO-d_6) δ_C: 176.7 (RN=***C***S-NHbnzF); 176.4 (RN=***C***S-$NHNH_2$); 146.5 (***C^{11}***); 138.1 (***C^1***); 135.5 (***C^{12}***); 135.3 (***C^6***); 131.3 (***C^{10}***); 130.0 (***C^2***); 128.7 (***C^8***) 128.2 (***C^4***); 127.6 (***C^{5}C^7***); 126.1 (***C^9***); 24.1 (***C^{14}***) 14.3 (***C^{15}***) ppm,

Mass Spectrometry: MALDI-MS for $C_{16}H_{15}N_7S_2Zn$, calcd for ($[M]^+$) 433 found 433.

IR (solid): ν (cm^{-1}) 3277, 2939, 1687, 1577, 1395, 1245, 1169 cm^{-1}

HPLC (Method C): R_f = 11.23 min

Zinc(II) 4-fluorobenzyl-3-thiosemicarbazone-thiocarbohydrazide acenaphthenoquinone (9e):

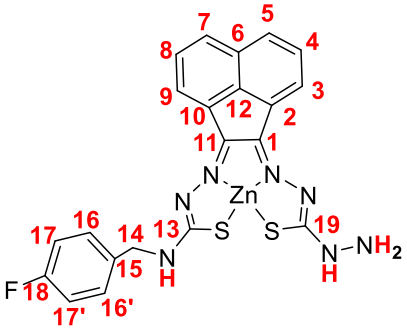

In a μW vial 3 mL of EtOH were added and heated to 60 °C. At that moment zinc acetate (0.2527 g, 1.38 mmol) was added along with 4-fluorobenzyl-3-thiosemicarbazone acenopthenoquinone (**5e**) (0.1000 g, 0.28 mmol) Then the reaction was heated further to 120 °C and thiosemicarbohydrazide (0.0881 g, 0.83 mmols) was added together with 2 mL of EtOH and couple of drops of HCl. The reaction mixture was heated under μW radiation at 150 °C for 106 min. Then was filtrated hot, re-suspended in Et_2O (100 mL), stirred for another 15 min and filtrated under vacuum. Resulting deposit was further washed with Et_2O (200 mL) and Zinc (II) 4-phenyl-3-thiosemicarbazone-thiocarbohydrazide acenaphthenoquinone (**10e**) was isolated as an orange colour solid (97 %).

^{1}H NMR (500MHz, DMSO-d_6) δ_H : 8.57 (bs, 1H, N***H***-bnzF); 8.33 (s, 1H, ***H^9***); 8.39 (s, 1H, ***H^9***); 7.91 (overlapping, 2H, ***H^5***, ***H^7***), 7.63 (overlapping, 1H, ***H^3***); 7.56 (overlapping, 2H, ***H^8***, ***H^4***); 7.44 (appt, 2H, ^3J= 6.2 Hz, ***H^{16} H$^{16'}$***); 7.16 (appt, 2H, ^3J= 8.0 Hz, ***H^{17} H$^{17'}$***); 6.42 (bs, 2H, N***H$_2$***); 4.72 (bs, 2H, ***H^{14}***) ppm.

^{13}C NMR (125MHz, DMSO-d_6) δ_C: 177.8 (RN=***C***S-NHbnzF); 176.6 (RN=***C***S-NHNH$_2$); 162.7 (***C^{11}***); 160.6 (***C^1***); 146.98 (***C^{15}***); 136.2 (***C^{12}***); 135.3 (***C^{16}***); 130.0 (***C^{10}***); 129.9 (***C^2***); 129.2 (***C^{16}***); 128.5 (***C^3***); 128.3 (***C^8***, ***C^4***); 127.8 (***C^7***); 126.7 (***C^5***); 126.3 (***C^9***); 115.4 (d, $J_{C\text{-}C}$= 21.5 Hz ***C^{17}***); 45.8 (***C^{14}***) ppm,

^{19}F NMR (470 MHz, DMSO-d_6) δ_F : -115.22

Mass Spectrometry: MALDI-MS for $C_{21}H_{16}FN_7S_2Zn$, calcd for ($[M]^+$) 513 found 513.

IR (solid): ν 3275, 3131, 2919, 1541, 1394, 1243, 1174, 772 cm^{-1}

HPLC (Method C): R_f = 12.34 min

Synthesis of Ga (III) complexes

Gallium (III) 4-phenyl-3-thiosemicarbazone-thiocarbohydrazide acenaphthenoquinone (10a):

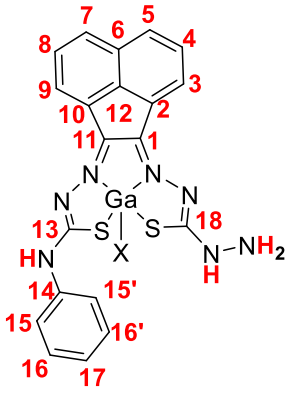

Zinc(II) 4-phenyl-3-thiosemicarbazone- thiocarbohydrazide acenaphthenoquinone (**9a**) (0.1000 g, 0.21 mmol) was added to a solution of gallium(III) chloride (0.3644 g, 2.07 mmol) in dry MeOH (60 mL) and the reaction mixture heated to 68 ºC for 6 h. The majority of the solvent was removed under vacuum and Et_2O was added dropwise to the residue until a precipitate is formed. The precipitate was then filtered off and the filtrate was concentrated under vacuum. The product was isolated as a red solid (74%).

^{1}H NMR (500 MHz, DMSO-d_6) δ_H : 10.38 (d, 1H, ^3J = 7.03 Hz, *N**H**N*H_2); 8.66 (d, 1H, *N**H**C*H_2); 8.62 (d, 1H, ^3J = 7.1 Hz, ***H*^{5}**); 8.15 (d, 1H, ^3J = 8.3 Hz, ***H*^{3}**); 7.99 (d, ^3J = 8.2 Hz, 1H, ***H*^{9}**); 7.86 (d, 1H, ^3J = 6.9 Hz, ***H*^{7}**); 7.82 (t, 1H, ^3J = 7.8 Hz, ***H*^{4}**); 7.76 (t, ^3J = 7.6 Hz, 1H, ***H*^{8}**); 7.59 (s, 2H, N***H***$_2$); 5.96 (m, 1H, ***H*^{15}**); 5.33 (d, 1H, $^3J_{trans}$ = 17.3 Hz, ***H*^{16}**); 5.19 (d, 1H, $^3J_{cis}$= 10.4 Hz, ***H*^{16}**); 4.22 (s, 2H, ***H*^{14}**) ppm.

Mass Spectrometry: TOF-MS for $C_{26}H_{17}N_6S_2Ga$, calcd for ([M+$HOOCH_3$]$^+$) 547.0290 found 547.0295.

HPLC (method C) R_f = 14.33

Gallium(III) 3-allyl-3-thiosemicarbazone-thiocarbohydrazide acenaphthenoquinone (10b):

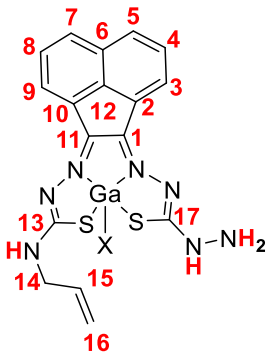

Zinc(II) 4-phenyl -3- thiosemicarbazone- thiocarbohydrazide acenaphthenoquinone (**9b**) (0.100 g, 0.23 mmol) was added to a solution of gallium(III) chloride (0.3941 g, 2.24 mmol) in dry MeOH (30 mL) and the reaction mixture heated to 68 ºC for 6 h. The majority of the solvent was removed under vacuum and Et_2O added dropwise to the residue until a precipitate appeared. The precipitate was then filtered off and the filtrate was concentrated under vacuum. The product was obtained as a red solid (94%)

^{1}H NMR (500 MHz, DMSO-d_6) δ_H : 10.23 (s, 1H, *N**H**N*H_2); 8.75 (s, 1H, *N**H**C*H_2); 8.62 (d, 1H, ^3J = 7.1 Hz, ***H*^{5}**); 8.15 (d, 1H, ^3J = 8.3 Hz, ***H*^{3}**); 7.99 (d, ^3J = 8.2 Hz, 1H, ***H*^{9}**); 7.86 (d, 1H, ^3J = 6.9 Hz, ***H*^{7}**); 7.82 (t, 1H, ^3J = 7.8 Hz, ***H*^{4}**); 7.76 (t, ^3J = 7.6 Hz, 1H, ***H*^{8}**); 7.59 (s, 2H, N***H***$_2$); 5.96 (m, 1H, ***H*^{15}**); 5.33 (d, 1H, $^3J_{trans}$ = 17.3 Hz, ***H*^{16}**); 5.19 (d, 1H, $^3J_{cis}$= 10.4 Hz, ***H*^{16}**); 4.22 (s, 2H, ***H*^{14}**).

Mass spectrum: nanoESI-MS calc. for $C_{17}H_{15}GaN_7NaS_2$ [M]+: 450.0086 found: 450.0074.

IR (solid): ν (cm-1) 3202, 2997, 1607, 1508, 1412, 1140, 1107.

HPLC (Method C): Rt (min) 15.23.

Gallium(III) 3-ethyl-3-thiosemicarbazone-thiocarbohydrazide acenaphthenequinone (10c):

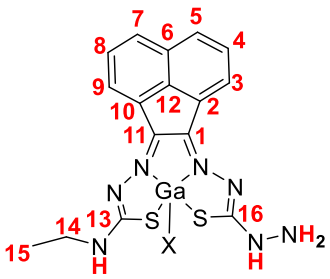

Zinc(II) 3-ethyl-3-thiosemicarbazone-thiocarbohydrazide acenaphthenequinone (**9c**) (0.075 g, 0.17 mmol) was added to a solution of gallium(III) chloride (0.3036 g, 1.73 mmol) in dry MeOH (30 mL) and the reaction mixture heated to 68 ºC for 6 h. The majority of the solvent was removed under vacuum and Et_2O added dropwise to the residue until a precipitate appeared. The precipitate was filtered off and the filtrate was concentrated under vacuum. The product was obtained as a red solid (95%).

^{1}H NMR (500 MHz, DMSO-d_6) δ: 9.50 (s, 1H, N***H***-Ethyl); 8.94 (s, 1H, N***H***-NH_2); 8.71 (appd, 1H, ^{3}J= 7.9 Hz, ***H*^{9}**); 8.62 (appd, 1H, ^{3}J= 7.1 Hz, ***H*^{3}**); 8.24 (m, 2H, ***H*^{5}, *H*^{7}**), 7.92 (m 2H, ***H*^{4}, *H*$^{'}$**); 7.85 (m, 2H, N***H***$_2$); 3.64 (t, 1H, ^{3}J= 5.6 Hz, ***H*^{14}**); 1.28 (m, 3H, ***H*^{15}**) ppm.

Mass Spectrometry: MALDI-MS for $C_{16}H_{15}N_7GaS_2$, calcd for ([M+$HOOCH_3$]$^+$) 495.01 found 495.05

HPLC (Method C): R_f = 15.14 min

Gallium(III) 4-fluorobenzyl-3-thiosemicarbazone-thiocarbohydrazide acenaphthenequinone (10e):

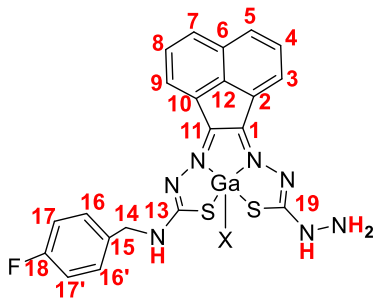

Zinc(II) 4-fluorobenzyl-3-thiosemicarbazone-thiocarbohydrazide acenaphthenequinone (**9e**) (0.1000 g, 0.19 mmol) was added to a solution of gallium(III) chloride (0.3419 g, 1.94 mmol) in dry MeOH (50 mL) and the reaction mixture heated to 68 ºC for 6 h. The majority of the solvent was removed under vacuum and Et_2O added dropwise to the residue until a precipitate appeared. The precipitate was filtered off and the filtrate was concentrated under vacuum. The product was obtained as a red solid (58 %).

^{1}H NMR (500MHz, DMSO-d_6) δ_H : 9.93 (bs, 1H, N***H***-bnzF); 9.39 (s, 1H, R-N***H***-NH_2); 8.53 (d, 1H, ^3J= 7.6 Hz, ***H^9***); 8.44 (s, 1H, ^3J= 6.4 Hz, ***H^3***); 8.22 (overlapping, 2H, ***H^5***, ***H^7***), 7.82 (overlapping, 2H, ***H^8***, ***H^4***); 7.48 (m, 2H, ***H^{16} H$^{16'}$***); 7.20 (m, 2H, ***H^{17} H$^{17'}$***); 4.86 (appt, 2H, ^3J= 28.97 Hz, ***H^{14}***).

^{19}F NMR (470 MHz, DMSO-d_6) δ_F : -115.53

HPLC (Method C): R_f = 12.19, 16.04 min

6.3.2. Radiolabelling of asymmetric complexes with different radionuclides

Synthesis of [^{68}Ga] Gallium(III) R-3-thiosemicarbazone-thiocarbohydrazide acenaphthenequinone (11):

A SnO_2-based column matrix ^{68}Ge/^{68}Ga generator was used to elute 10 mL of 0.6 M HCl, ca. 148 MBq of gallium-68, which was trapped on a strata x-c 33 µm Polymeric Strong Cation Cartridge from Phenomenex and eluted with 700 µL of 0.02 M HCl (98% THF). This was subsequently dried for 7-10 min under a nitrogen stream at 95 °C. Next, 25 µL of the Zinc complex in dry DMSO (2 mg/mL) was added along with 0.4 mL of injectable MeOH and 0.1 mL of buffer. This mixture was heated at 95 °C for 45 min. Analysis by reverse-phase HPLC (Method C) gave a retention time of 12:10 min which by comparison with the reference HPLC trace seemed to confirm the synthesis of **[^{68}Ga]-11**, however with remaining [^{68}Ga]$GaCl_3$ indicating that radiolabelling had not gone to completion. The conversion to the product was measured as 30 %.

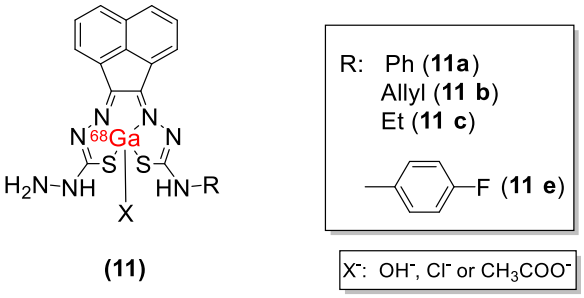

Scheme 29: Schematic illustration of the proposed structures of the radiolabelled mono(substituted) ligands with gallium-68.

Table 16: Table summarising the results of the radiolabelling of all the asymmetric bis(thiosemicarbazonato) complexes with gallium-68.

ASSYMETRIC COMPLEXES ABBREVIATION	PROPOSED STRUCTURE NO	RETENTION TIME	ROI %
PHZNTSCA	11 a	17.15	46
FBNZZNTSCA	11 e	17.02	12

Synthesis of [^{18}F] (4-phenyl-3-thiosemicarbazonato)-3-(4-N-amino-(4-fluorobenzilidene)- 3-thiosemicarbazonato) Zinc(II) complex (24)

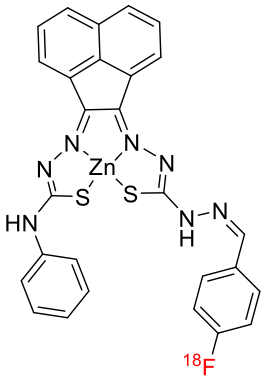

In a sealed reaction vial, PhZnTSCA complex (**10a**) (8.2 mg, 0.017 mmols) was diluted in 0.2 mL of DMSO and mixed with 60 µL of the SPE purified solution of compound [^{18}F]-FBA in MeCN (11.84 MBq). The mixture was heated to 120 °C for 20 min. Analysis by reverse-phase HPLC (Method D) gave a retention time of 13:57 and 14:49 min which by comparison with the precursor HPLC trace suggested the successful synthesis of **[^{18}F]-24**. The conversion to the product was measured as 94 %.

6.3.3. Functionalisation of asymmetric bis(thiosemicarbazonates) with a glycosyl coumarin derivative

Synthesis of glycosyl coumarin derivative

The synthesis was carried out using an adapted method from that was previously described by Supuran *et al.* [7].

Synthesis of 2,3,4,6-Tetra-O-acetyl-D-mannopyranose (13):

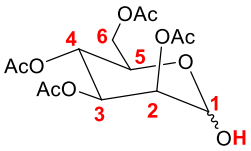

α-D-mannose pentaacetate (d) (3.0001 g, 7.69 mmol) was dissolved in dry DCM (30 mL). Morpholine (2.68 mL, 30.75 mmol) was then added and the reaction mixture was allowed under N_2 at room temperature, overnight. The slurry was first washed with HCl solution (1 N) (2·30 mL), then with distilled water (3·30 mL) and finally dried over magnesium sulphate. The excess solvent was removed under reduced pressure to afford 2,3,4,6-Tetra-O-acetyl-D-mannopyranose (**13**) as a light-yellow oil at room temperature, which was used without any further purification. (2.1602 g, 71 %).

^{1}H NMR (500MHz, $CDCl_3$-d_6) δ_H: 5.26 (dd, 1H, ^3J =10.1, 3.3 Hz, ***H*^{4}**); 5.15 (t, 1H, ^3J = 9.9 Hz, ***H*^{5}**); 5.10 (d, 1H, ^3J =3.5 Hz, ***H*^{3}**); 5.08 (s, 1H, ***H*^{2}**); 4.12 (appdd, 1H, ***H*^{8}**); 4.09 (appd, 1H, ***H*^{6b}**); 3.97 (appd, 1H, ***H*^{6a}**); 2.04 (s, 3H, C***H*$_3$**Ac); 1.98 (d, 3H, J^3=3.3 Hz, C***H*$_3$**Ac); 1.94 (s, 3H, C***H*$_3$**Ac); 1.88 (d, 3H, ^3J =5.0Hz, C***H*$_3$**Ac) ppm

^{13}C NMR (125 MHz, $CDCl_3$-d_6) δ_C: 170.9 (***C***=O); 170.3 (***C***=O); 170.1 (***C***=O); 169.9 (***C***=O); 91.9 (***C***-OH); 70.2 (***C*^{2}**); 68.9 (*C*^{3}); 68.0 (***C*^{5}**); 66.1 (***C*^{4}**); 62.5 (***C*^{6}**); 20.7 (***C***H_3OOR) ppm.

Mass Spectrometry: ESI-MS calcd for $C_{14}H_{20}O_{10}$, ($[M+Na]^+$) calcd for 371.10 found 371.1039

Synthesis of 2,3,4,6-Tetra-O-acetyl-D-mannopyranose trichloroacetamidate (14):

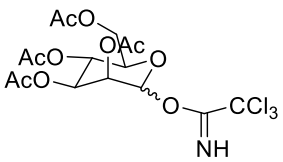

2,3,4,6-Tetra-O-acetyl-D-mannopyranose (2.1502 g, 6.17 mmol) and trichloroacetonitrile (2.19 mL, 6.17 mmol) were dissolved in dry DCM (30 mL) and the reaction mixture was allowed under N_2 at 0 °C for 1 h. then a catalytic amount of DBU (0.19 mL, 1.23 mmols) was added and slurry was stirred for further 30 min under N_2 at 0 °C. The excess solvent was removed under reduced pressure to afford a crude compound of 2,3,4,6-

Tetra-O-acetyl-D-mannopyranose trichloroacetamidate (**14**) as a yellow oil at room temperature, which was used without any further purification.

Synthesis of 4- Methylumbelliferyl-7-yl-2,3,4,6-Tetra-O-acetyl- α -D-mannopyranose (15):

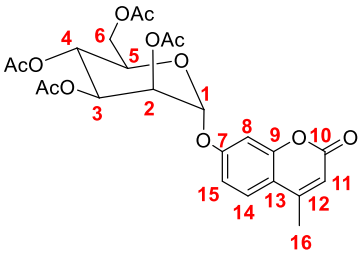

The crude 2,3,4,6-Tetra-O-acetyl-D-mannopyranose-trichloro-acetamidate) (**14**) was dissolved in dry DCM (40 mL). 4-Methylumbelliferylone (**15**) (2.2805 g, 6.17 mmols) was added to the mixture along with boron trifluoride metharate (0.11 mL, 1.21 mmol) and the reaction mixture was allowed under N_2 at 23 °C over nigh. The slurry was first diluted with 10 mL of DCM, then washed with HCl solution (1N) (2·20 mL) and distilled water (3·20 mL) and dried over magnesium sulphate. The excess solvent was removed under reduced pressure. The crude product was then purified by crystallisation with MeOH to afford 4- Methylumbelliferyl-7-yl-2,3,4,6-Tetra-O-acetyl- α -D-mannopyranose (**15**) as a white solid (2.4712 g, 40 %).

^{1}H NMR (500MHz, $CDCl_3$-d_6) δ_H: 7.53 (d, 1H, ^3J =9.0 Hz, ***H*^{14}**); 7.12 (d, 1H, ^3J =2.4 Hz, ***H*^{8}**); 7.03 (dd, 1H, ^3J = 8.8, 2.7 Hz, ***H*^{15}**); 6.20 (d, 1H, ^3J =1.2 Hz, ***H*^{11}**); 5.58 (d, 1H, ^3J =1.8 Hz, ***H*^{1}**); 5.55 (dd, 1H, ^3J = 10.04, 3.5 Hz, ***H*^{3}**); 5.47 (appq, ^3J =1.8, 3.5Hz, 1H, ***H*^{2}**); 5.37 (t, 1H, ^3J =10.1 Hz, ***H*^{4}**); 4.29 (dd, 1H, ^3J =12.4, 5.7 Hz, ***H*^{6}**); 4.05 (m, 2H, ***H*^{5}, *H*^{7}**); 2.41 (d, 3H, ^3J =1.1 Hz, C***H***$_3$Ac); 2.21 (s, 3H, C***H***$_3$Ac); 2.05 (d, 9H, ^3J =4.8 Hz, C***H***$_3$Ac);

^{13}C NMR (125 MHz, $CDCl_3$-d_6) δ_C: 170.5 (***C***=O); 170.0 (***C***=O); 169.9 (***C***=O); 169.6 (***C***=O); 160.8 (***C*^{7}**); 158.2 (***C*^{10}**); 154.9 (***C*^{9}**); 152.1 (***C*^{12}**); 125.8 (***C*^{14}**); 115.5 (***C*^{13}**); 113.4 (***C*^{15}**); 113.3 (***C*^{11}**); 104.4 (***C*^{16}**); 95.9 (***C*^{1}**); 69.6 (***C*^{2}**); 69.1 (***C*^{3}**); 68.7 (***C*^{5}**); 65.8 (***C*^{4}**); 62.0 (***C*^{6}**); 20.9 (***C***H_3OOR); 20.7 (***C***H_3OOR); 20.6 (***C***H_3OOR); 20.6 (***C***H_3OOR); 18.7 (***C***H_3OOR).

Mass Spectrometry: ESI-MS for $C_{24}H_{26}O_{12}$, calcd for ($[M+Na]^+$) 529.13 found 529.14.

X-ray diffraction were obtained in MeOH after 16 h at room temperature.

4-methylumbelliferyl-7-yl-α-D-mannopyranose (16):

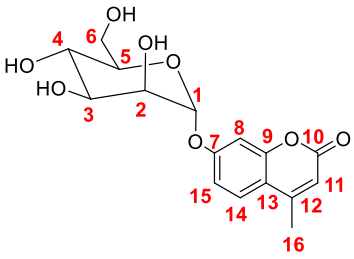

4- Methylumbelliferyl-7-yl-2,3,4,6-Tetra-O-acetyl- α -D-mannopyranose (**15**) (0.3202 g, 0.64 mmol) was added in a solution of sodium methoxide (0.0611 g, 0.96 mmol) in dry MeOH (7 mL). The reaction mixture was stirred under N_2 at room temperature for 30 min. The crude product was purified by crystallisation with MeOH. The solid was removed by filtration and the excess solvent of filtrate was removed by reduced pressure to afford the desired compound (**16**) as an off-white oil (0.2015 g, 93%).

^{1}H NMR (300MHz, D_2O) δ_H : 6.85 (d, 1H, ^3J = 8.2 Hz, ***H*^{14}**); 6.36 (d, 1H, ^3J = 2.3 Hz, ***H*^{8}**); 6.28 (dd, 1H, ^3J = 8.2, 2.3 Hz, ***H*^{15}**); 5.88 (s, 1H); 5.54 (s, 1H, ***H*^{11}**); 4.14 (d, 1H, ^3J =1.52 Hz, ***H*^{1}**); 4.03 (dd, ^3J =3.4, 8.8 Hz, 1H, ***H*^{2}**); 3.79 (m, 4H, ***H*^{4}**, ***H*^{5}** ,***H*^{6}**, ***H*^{7}**).

^{13}C NMR (125MHz, D_2O) δ_C: 177.5 (***C*^{7}**); 165.0 (***C*^{10}**); 156.6 (***C*^{9}**); 147.3 (***C*^{12}**); 129.8 (***C*^{14}**); 128.2 (***C*^{13}**); 124.1 (***C*^{11}**); 108.1 (***C*^{8}**); 103.1 (***C*^{15}**); 98.7 (***C*^{1}**); 73.7 (***C*^{5}**); 70.8 (***C*^{2}**); 70.7 (***C*^{3}**); 67.1 (***C*^{4}**); 61.1 (***C*^{6}**); 24.3 (***C*^{16}**) ppm.

Mass Spectrometry: ES^+ $C_{16}H_{18}O_8$, calcd for ($[M+H]^+$) 339.1074 found 339.1079.

X-ray diffraction were obtained in MeOH after 16 h at room temperature.

7-(((2R,3S,4S,5S,6S)-6-(bromomethyl)-3,4,5-trihydroxytetrahydro-2H-pyran-2-yl)oxy)-4-methyl-2H-chromen-2-one (19):

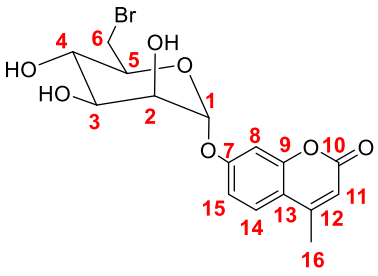

To a stirred solution of 4-methylumbelliferyl-7-yl-α-D-manopyranose (**13**) (0.2000 g, 0.59 mmol) in anhydrous pyridine (4 mL) at 0 °C were added triphenylphosphine (0.3101 g, 1.18 mmol) and carbon tetrabromide (0.2941 g, 8.87 mmol). The resulting mixture was protected from moisture and stirred at 0 °C for 10 min. It was then allowed to warm to 65 °C and was stirred for an additional 4 h. MeOH (10 mL) was added to decompose any excess reagent. The solvent was removed by reduced pressure and was further purified by a silica filtration with DCM followed by DCM/MeOH 20:1 and MeOH.

^{1}H NMR (300 MHz, CD_3OD) δ_H : 8.84 (d, 1H, ^{3}J = 5.8 Hz, ***H*^{14}**); 7.88 (t, 1H, ^3J = 7.1 Hz, ***H*^{15}**); 7.80 (m, 1H, ***H*^{8}**); 6.26 (d, 1H, ^{3}J = 1.0 Hz, ***H*^{11}**); 5.55 (d, 1H, ^3J =4.6 Hz, ***H*^{1}**); 5.38 (d, 1H, ^{3}J = 4.6 Hz, O***H*^{2}**); 5.18 (d, 1H, ^{3}J = 5.8 Hz, O***H*^{4}**); 4.89 (m, 1H, O***H*^{3}**); 4.68 (m, 1H, ***H*^{3}**); 4.42 (s, 1H, O***H*^{2}**); 3.86 (t, 1H, ^{3}J = 4.5 Hz, ***H*^{2}**) 3.15 (d, 2H, ^3J =5.1Hz, ***H*^{6}**); 3.69 (m, 4H, ***H*^{4}**, ***H*^{5}**), 2.38 (s, 3H, ***H*^{16}**).

^{13}C NMR (125 MHz, CD_3OD) δ_C: 160.25 (***C*^{10}**); 157.69 (***C*^{7}**); 154.18 (***C*^{9}**); 153.51 (***C*^{12}**); 145.65 (***C*^{14}**); 128.06 (***C*^{13}**); 127.68 (***C*^{15}**); 126.64 (***C*^{8}**); 112.34 (***C*^{11}**); 98.08 (***C*^{1}**); 72.88 (***C*^{5}**); 70.70 (***C*^{3}**); 68.87 (***C*^{4}**); 68.05 (***C*^{2}**); 48.96 (***C*^{6}**); 18.59 (***C*^{16}**) ppm.

Mass Spectrometry: ESI-MS $C_{16}H_{17}BrO_7$ calcd for ($[M-H]^+$) 399.0085 found 399.0087

6.3.4. Evaluation of asymmetric complexes in vitro

Crystal Violet assays

PC3 and EMT6 cells (5-7·10^3 cells per well) were seeded in a 96-well plate and incubated for 48 h to adhere. They were loaded with different concentrations of the metal complex (see Table 7-1) and left to incubate for another 24, 48 or 72 h, depending the experiment. Subsequently, cells were washed with PBS and fixed by MeOH. Crystal violet staining solution (100 µL of 0.5%) was added to each well and incubated for 20 min at room temperature. Then, plates were washed four times in an indirect stream of tap water and the plate allowed to air-dry at room temperature. Subsequently, each well was loaded with MeOH, and incubated for 20 min at room temperature on a bench rocker with a frequency of 20 oscillations per minute. The optical density was measured at 570 nm (OD570) for each well plate with a plate reader (BN02877 ELISA plate reader, Molecular Devices Versa Max).

Confocal fluorescence microscopy

PC3 cells were cultured as previously (p.160-161) described in normoxia, acute hypoxia (reduced by $CoCl_2$) and chronic hypoxia environments. Cells from all the three different environments were seeded in different wells at least 48 h prior to the microscopy experiment cells (10,000 cell per dish), washed twice with PBS and refill with SFM incubated at 37 ºC. Control fluorescence images were obtained before the addition of compound. Subsequently, PhGaTSCA complex (**10a**) in DMSO: RPMI 0.5:99.5 solution mixture (100 µM), was loaded to each well and the cells allowed to incubate for 15 min, at 37 °C. They were then carefully washed with Phosphate Buffered Saline (PBS) pre-warmed to 37 °C, which was replaced by FCS-free medium to remove the non-internalised fluorescent dispersion prior to fluorescence imaging. In the case of chronic

hypoxia experiments, the fluorescence microscopy was carried out under normoxia due to limitations of the current equipment.

Multiphoton fluorescence lifetime evaluation

Cell uptake studies were performed using, PC-3 cells. PC3 cells were seeded on glass petri dishes and incubate for 24 h at 37 °C. Control FLIM were recorded before the addition of compound. Plates were then mounted on the microscope stage and kept at 37 °C. Cells were then loaded with PhZnTSCA (**9a**) complex in DMSO: RPMI 0.5:99.5 solution mixture (10 μM) and incubated for 15 min prior to confocal imaging, FLIM was carried out immediately after the confocal imaging with the same area as the confocal imaging. The fluorescence decay curve is well fitted to a multiexponential function as:

$$I(t) = \sum_i a_i \exp(\frac{-t}{\tau_1})$$

6.4. Experimental Details for Chapter Four

6.4.1. Functionalisation of graphene oxide nanocomposites.

Synthesis of Ga coordinated graphene oxide nanocomposites (Ga@GO, 30).

In a typical coordination experiment of Ga(III) with GO nanocomposites, 20 mg of $GaCl_3$ diluted in 1 mL of EtOH and 20 mg of GO nanocomposites diluted in 1 mL of DMSO. A 1:1 reaction mixture was then formed and diluted down further with 2 mL of EtOH and 1 mL of $NaHCO_3$ buffer in order to adjust the pH to 5.5. The mixture was allowed to react at 100 °C for 2.5 h, when it was allowed to cool down, centrifuged, washed with EtOH and H_2O and allowed to freeze dry overnight.

Synthesis of Ga coordinated graphene oxide nanocomposites enriched with Zn(II) thiosemicarbazide complexes (Ga+PhZnTSCA@GO, 31)

The Ga(III) coordination of the PhZnTSCA@GO was performed in a similar way, only this time a 1:1 solution mixture of PhZnTSCA (20 mg/ DMSO mL) with GO (20 mg/ DMSO mL) was used before being mixed with $GaCl_3$.

SEM indicated some level of aggregation of the $GaCl_3$ and $GaCl_3$-PhZnTSCA on the GO flakes. **EDX** mapping showed a high affinity of binding of the Ga on the GO flakes, however; the low-intensity signal of Zn and S does not allow a conclusion to be made as to whether the Ga has been adsorbed alone or as the transmetallated complex.

6.4.2. Fluorescence titration experiments.

Fluorescent titration of a GO dispersion with a Acetyl Glycosyl Coumarin solution

A 1 mM solution of AcGC (**15**) was prepared. To this solution was added a saturating quantity of GO (1 mg/mL). The resulting saturated suspensions were then sonicated until the mixtures became homogeneous. The excess of coronene was allowed to settle. The resulting suspension supernatant was titrated against another 1 mM solution of AcGC (**15**) in DMSO. Excitation wavelength was set at 310 nm for all experiments. An emission range 330-600 nm was scanned at 500 nm cm^{-1} for all experiments. Titrations were conducted in a 1.2 mL cuvette. Suspension containing AcGC (**15**) at 1 mM concentration in DMSO was added to the cuvette and the emission spectrum scanned. Subsequent scans were conducted with 50 μL aliquots removed from cuvette and replaced with 50 μL aliquots of 1 mM AcGC (**15**) suspension saturated with GO in order to maintain constant AcCG (**15**) concentration throughout the experiments. The resulting saturated suspension was well mixed before and after the addition of the saturated suspension of GC and GO. GO excess allowed to settle before each measurement for 5 min.

Determination of likely binding stoichiometry between glycosyl coumarin and coronene

To a 0.125 mM solution of GC (**16**) coronene was added until the maximum concentration was reached in which the suspension was stable (0.125 mM). The resulting concentrated suspensions were then sonicated until the mixtures became homogeneous. The excess of coronene was allowed to settle. The resulting suspension supernatant was titrated against another 0.125 mM solution of GC (**16**) in DMSO. Excitation wavelength was set at 310 nm for all experiments. An emission range of 330-600 nm was scanned at 100 nm min^{-1} for all experiments. Titrations were conducted in a 1.4 mL cuvette. A suspension containing GC (**16**) at 0.125 mM concentration in DMSO was added to the cuvette and the emission spectrum scanned. Subsequent scans were conducted with 5 μL to 100 μL aliquots removed from the cuvette and replaced with according corresponding aliquot of 0.125 mM GC (**16**) suspension saturated with coronene in order to maintain constant CG (**16**) concentration

throughout the experiments. The resulting saturated suspension was well mixed before and after the addition of the saturated suspension of GC and coronene.

Use of Graphene Oxide Nanocomposites as carriers to Glycosyl Coumarin and asymmetric Zn thiosemicarbazone acenaphthenequinone complexes.

A 1 mM solution of GC (**16**) was prepared. To this solution was added a saturating quantity of complex **23** (**9a**@GO) (1mg/mL). The resulting saturated suspensions were then sonicated until the mixtures became homogeneous. The excess coronene was allowed to settle. The resulting suspension supernatant was titrated against another 1 mM solution of GC (**16**) in DMSO. Excitation wavelength was set at 310 nm for all experiments. An emission range of 330-800 nm was scanned at 500 nm min^{-1} for all experiments. Titrations were conducted in a 1.2 mL cuvette. A suspension containing GC (**16**) at 1 mM concentration in DMSO was added to the cuvette and the emission spectrum was scanned. Subsequent scans were conducted with 20 μL to 200 μL aliquots removed from cuvette and replaced with a corresponding aliquot of 1 mM GC (**16**) suspension saturated with complex **23** in order to maintain constant CG (**16**) concentration throughout the experiments. The resulting saturated suspension was well mixed before and after the addition of the saturated suspension of GC and **c**omplex **23**. GO excess allowed to settle for 2-3 min before each measurement.

6.4.3. Radiolabelling of GO nanocomposites.

Radiolabelling of GO nanocomposites with [^{68}Ga]Ga(III).

A SnO_2-based column matrix ^{68}Ge/^{68}Ga generator was used to elute 10 mL of 0.6 M HCl, ca. 4 mCi of ^{68}Ga, which was trapped on a strata x-c 33 μμ Polymeric Strong Cation Catridge from Phenomenex and eluted with 700 μL of 0.02 M HCl (98% THF). This was subsequently dried for 7-10 min under a nitrogen stream at 95 °C.

Radiolabelling of graphene oxide nanocomposites with [^{68}Ga]Ga(III) ([^{68}Ga]Ga@GO, [^{68}Ga]-25).

In a typical non-covalent radiolabeling experiment 400 μl [^{68}Ga]Ga(III) of a 150 MBq (in 800 μl) stock solution were added to a Wheaton vial before drying. 0.40 μL of GO nanocomposites solution (2 mg/ DMSO mL) was then added to the same vial along with

0.4 mL of ethanol and 0.1 mL of buffer solution (pH 4.5) in order to adjust the pH approximately to 5.5. The mixture was allowed to react at 95 °C for 45 min and it was then allowed to cool down. Radio thin layer chromatography (radio-TLC) was used directly after the reaction to measure the radiochemical incorporation.

Radiolabelling of zinc(II) 4-phenyl-3-thiosemicarbazone-thiocarbohydrazide acenaphthenequinone at graphene oxide with [^{68}Ga]Ga(III) ([^{68}Ga]Ga^{+3} + PhZnTSCA@GO, [^{68}Ga]-26).

The [^{68}Ga]Ga(III) labelling of the PhZnTSCA@GO was performed in a similar way, only this time a 1:1 solution mixture of PhZnTSCA (**9a**) (2 mg/ DMSO mL) was used with GO (2 mg/ DMSO mL) before mixing with [^{68}Ga]$GaCl_3$.

Radiolabelling of zinc(II) 4-phenyl-3-thiosemicarbazone-thiocarbohydrazide acenaphthenequinone and glycosyl coumarin at graphene oxide with [^{68}Ga]Ga(III) ([^{68}Ga]Ga^{+3} +GC + PhZnTSCA@GO, [^{68}Ga]-27).

The [^{68}Ga]Ga(III) labelling of the PhZnTSCA@GO was performed in a similar way, only this time a 1:1 solution mixture of GlyC (**16**) (2 mg/ DMSO mL) PhZnTSCA (**9a**) @ GO (2 mg/ DMSO mL) was used before mixing with [^{68}Ga]$GaCl_3$.

6.4.4. Kinetic stability evaluation of GO nanocomposites

Kinetic stability evaluation of the non-radiolabelled GO nanocomposites

This investigation utilised UV-visible absorption using a 2 mg/mL concentration of the assay agent in DMSO. Solutions of 1:1 DMSO[assay agent]:H_2O were prepared. UV-Visible spectras were acquired at 15 min and 24 h. The assays were carried out by incubating the samples at 37 °C using citric acid, PBS, EDTA and DFO and this enabled complex stability to be evaluated in media likely to be encountered in a cell biology experiment. Whilst there were no changes observed in the UV/Vis spectra after 30 min of incubation, some slight changes were observed for the gallium complex Ga(III) over an incubation of 24 h (**Figure 66**).

Kinetic stability evaluation of the radiolabelled GO nanocomposites

For this investigation the labelled ^{68}Ga-GO, PhZnTSCA@^{68}Ga-GO were incubated in EDTA, citric acid, PBS and mouse plasma at 37 °C for 1 h or 2 h. The mixtures were filtered through 300 kDa MWCO filter in a centrifuge at 13.000 r/min. The radioactivity that remained on the filter was measured after discarding the filtrate from the wastes. In the tables (Appendix) below the results are presented for these experiments and in the following graph (Appendix fig.12) the radiotrace from the radio-HPLC is presented for the wastes using EDTA solution for stability testing.

6.4.5. In Vitro evaluation of GO nanocomposites

Crystal Violet assays of the non-radiolabelled GO nanocomposites

PC3 and EMT6 cells (5-7×10^3 cells per well) were seeded in a 96-well plate and incubated for 48 h to adhere. Then the wells were loaded with different concentrations of the metal complex (see Table 7-1) and left to incubate for another 24, 48 or 72 h, depending upon the experiment. Subsequently, cells were washed with PBS and fixed by MeOH. Crystal violet staining solution (100 μL of 0.5%) was added to each well and incubated for 20 min at room temperature. The plates were then washed four times in an indirect stream of tap water and the plate allowed to air-dry at room temperature. Subsequently, each well was loaded with MeOH and incubated for 20 min at room temperature on a bench rocker with a frequency of 20 oscillations per minute. The optical density was measured at 570 nm (OD570) for each well plate with a plate reader (BN02877 ELISA plate reader, Molecular Devices Versa Max).

Cell Uptake assays of the radiolabelled GO nanocomposites [^{68}Ga]-27

PC3 cells (3 x 103 cells) were seeded in 6-well plates and incubated in normoxia and hypoxia environments as described earlier. After treatments, plates were aspirated and washed twice with warm PBS buffer. Each well plate was then loaded with 1000 μL of **[^{68}Ga]-27** in DMSO: PBS solution mixture (0.5:95.5) (3 MBq/ mL) and incubated for 1 h. After incubation, the reaction was stopped by washing wells with ice-cold PBS buffer twice, followed by addition of 1 mL of ice-cold, 0.1 % Triton X-100 and 0.1 M NaOH Lysates. A homogenous mixture was acquired by blending the components with up/down

pipetting. 800 μL of each dissolved cell was then transferred and capped into counting tubes for gamma counting. The stock **[^{68}Ga]-27** solution was aliquoted in 10μL doses, three times and placed to the counting tubes as standards. The intracellular radioactivity was immediately counted using an LKB Wallac 1282 Compu gamma Laboratory gamma counter (PerkinElmer, USA). Lastly, protein concentration determination by BCA was carried out. This normalisation of decay-corrected radioactivity counts per minute (CPM) to protein concentration, was required in order to give a measure of radiotracer uptake as % ID/mg of protein= CPM in 1 mL/ (standard in mL x protein concentration in mg) x 100%.

6.5. References to Chapter 6

1. B. Mao, D. G. Calatayud, V. Mirabello, B. J. Hodges, J. A. R. Martins, S. W. Botchway, J. M. Mitchels and S. I. Pascu, *Adv. Funct. Mater.*, 2016, **26**, 687-697.
2. A. Dabkowski, S. Paisey, M. Talboys and C. Marshall, *Acta Phys. Pol. A*, 2015, **127**, 1479-1482.
3. M. Walther, P. Gebhardt, P. Grosse-Gehling, L. Wurbach, I. Irmler, S. Preusche, M. Khalid, T. Opfermann, T. Kamradt, J. Steinbach and H. P. Saluz, *Appl. Radiat. Isot.*, 2011, **69**, 852-857.
4. H. Ge, PhD thesis, University of Bath, Bath, 2015.
5. I. S. Alam, R. L. Arrowsmith, F. Cortezon-Tamarit, F. Twyman, G. Kociok-Köhn, S. W. Botchway, J. R. Dilworth, L. Carroll, E. O. Aboagye and S. I. Pascu, *Dalton Trans.*, 2016, **45**, 144-155.
6. F. Cortezon-Tamarit, S. Sarpaki, D. G. Calatayud, V. Mirabello and S. I. Pascu, *Chem. Rec.*, 2016, **16**, 1380-1397.
7. N. Touisni, A. Maresca, P. C. McDonald, Y. Lou, A. Scozzafava, S. Dedhar, J.-Y. Winum and C. T. Supuran, *J. Med. Chem.*, 2011, **54**, 8271-8277.

APPENDIX

Table of Contents for Appendix

APPENDIX 1: X-RAY Crystallographic Data

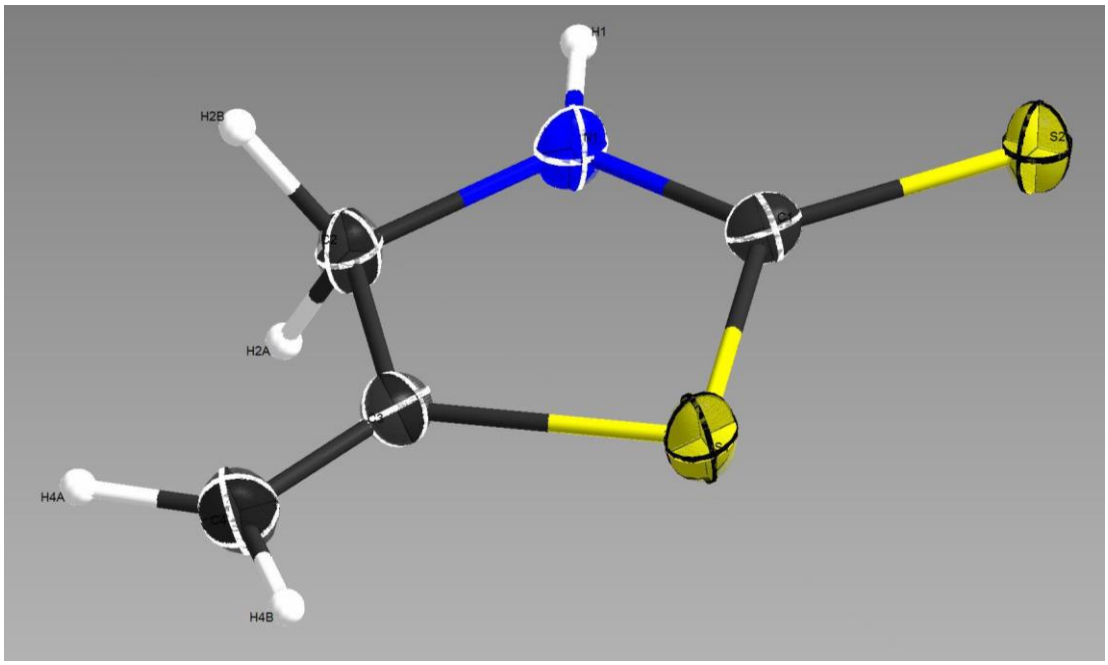

Figure S1: Chrystal structure 5-methylene-2-(l1-sulfanyl)thiazolidine (**4**). Thermal ellipsoids at 50% probability.

Table S1: Crystal data and structure refinement for 5-methylene-2-(l1-sulfanyl)thiazolidine (**4**).

IDENTIFICATION CODE	**E16SIP12**	
EMPIRICAL FORMULA	C4 H5 N S2	
FORMULA WEIGHT	131.21	
TEMPERATURE	150.0(4) K	
WAVELENGTH	0.71073 Å	
CRYSTAL SYSTEM	Monoclinic	
SPACE GROUP	$P2_1/n$	
UNIT CELL DIMENSIONS	a = 6.1770(3) Å	α= 90°.
	b = 6.0691(3) Å	β= 91.868(4)°.
	c = 15.2900(8) Å	γ = 90°.
VOLUME	572.90(5) $Å^3$	
Z	4	
DENSITY (CALCULATED)	1.521 Mg/m^3	
ABSORPTION COEFFICIENT	0.791 mm^{-1}	
F(000)	272	
CRYSTAL SIZE	0.400 x 0.350 x 0.180 mm^3	
THETA RANGE FOR DATA COLLECTION	3.519 to 30.065°.	
INDEX RANGES	-8<=h<=8, -8<=k<=8, -21<=l<=20	

REFLECTIONS COLLECTED	4880
INDEPENDENT REFLECTIONS	1525 [R(int) = 0.0302]
COMPLETENESS TO THETA = 25.242°	99.9 %
ABSORPTION CORRECTION	Semi-empirical from equivalents
MAX. AND MIN. TRANSMISSION	1.00000 and 0.96866
REFINEMENT METHOD	Full-matrix least-squares on F^2
DATA / RESTRAINTS / PARAMETERS	1525 / 0 / 68
GOODNESS-OF-FIT ON F^2	1.059
FINAL R INDICES [I>2SIGMA(I)]	R1 = 0.0307, wR2 = 0.0692
R INDICES (ALL DATA)	R1 = 0.0381, wR2 = 0.0726
EXTINCTION COEFFICIENT	n/a
LARGEST DIFF. PEAK AND HOLE	0.317 and -0.245 e.Å^{-3}

Table S2: Bond lengths [Å] and angles [°] for 5-methylene-2-(l1-sulfanyl)thiazolidine (**4**).

S(2)-C(1)	1.6686(16)	C(2)-N(1)-H(1)	121.3(13)
S(1)-C(1)	1.7499(16)	N(1)-C(1)-S(2)	127.39(13)
S(1)-C(3)	1.7735(16)	N(1)-C(1)-S(1)	110.95(12)
N(1)-C(1)	1.3252(19)	S(2)-C(1)-S(1)	121.65(9)
N(1)-C(2)	1.452(2)	N(1)-C(2)-C(3)	106.98(12)
N(1)-H(1)	0.84(2)	N(1)-C(2)-H(2A)	110.3
C(2)-C(3)	1.511(2)	C(3)-C(2)-H(2A)	110.3
C(2)-H(2A)	0.9900	N(1)-C(2)-H(2B)	110.3
C(2)-H(2B)	0.9900	C(3)-C(2)-H(2B)	110.3
C(3)-C(4)	1.315(2)	H(2A)-C(2)-H(2B)	108.6
C(4)-H(4A)	0.9500	C(4)-C(3)-C(2)	126.33(14)
C(4)-H(4B)	0.9500	C(4)-C(3)-S(1)	124.53(13)
C(1)-S(1)-C(3)	93.11(7)	C(2)-C(3)-S(1)	109.14(11)
C(1)-N(1)-C(2)	118.94(14)	C(3)-C(4)-H(4AorB)	120.0
C(1)-N(1)-H(1)	119.7(13)	H(4A)-C(4)-H(4B)	120.0

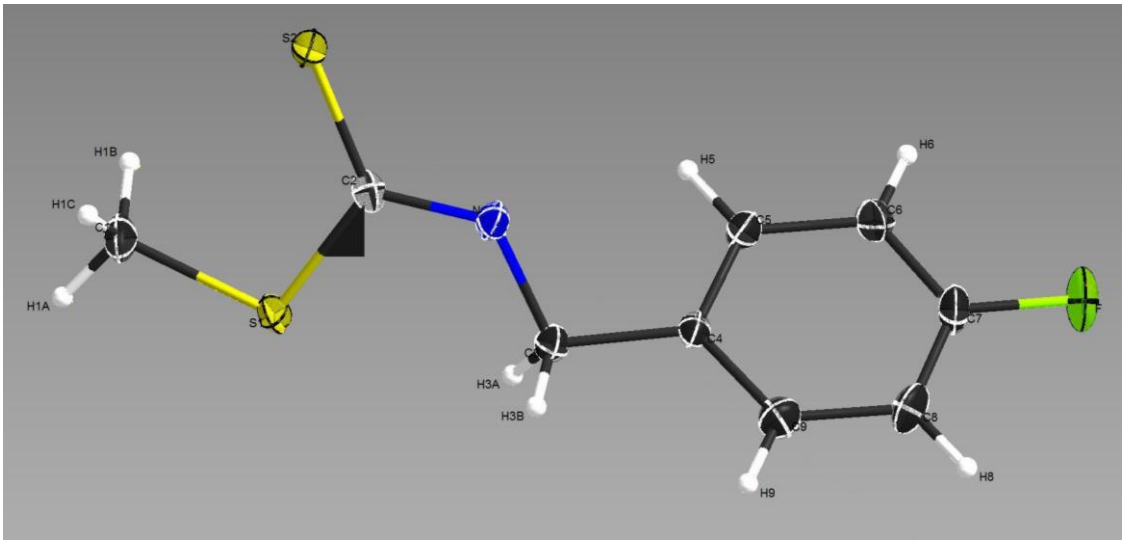

Figure S2: Molecular structure of methyl (4-fluorobenzyl)carbamodithioate Fbnz-MeCDT (**2e**). Thermal ellipsoids at 50% probability.

Table S3: Crystal data and structure refinement for Fbnz-MeCDT (**2e**).

IDENTIFICATION CODE	**E16SIP13**	
EMPIRICAL FORMULA	C9 H10 F N S2	
FORMULA WEIGHT	215.30	
TEMPERATURE	150.0(4) K	
WAVELENGTH	0.71073 Å	
CRYSTAL SYSTEM	Triclinic	
SPACE GROUP	P-1	
UNIT CELL DIMENSIONS	a = 5.8689(5) Å	α= 70.418(8)°.
	b = 8.0985(7) Å	β= 84.161(7)°.
	c = 11.1040(9) Å	γ = 87.618(7)°.
VOLUME	494.65(8) $Å^3$	
Z	2	
DENSITY (CALCULATED)	1.446 Mg/m^3	
ABSORPTION COEFFICIENT	0.503 mm^{-1}	
F(000)	224	
CRYSTAL SIZE	0.400 x 0.350 x 0.100 mm^3	
THETA RANGE FOR DATA COLLECTION	3.490 to 30.136°.	
INDEX RANGES	-7<=h<=7, -10<=k<=10, -15<=l<=15	
REFLECTIONS COLLECTED	4239	
INDEPENDENT REFLECTIONS	2496 [R(int) = 0.0247]	
COMPLETENESS TO THETA = 25.242°	99.8 %	
ABSORPTION CORRECTION	Semi-empirical from equivalents	
MAX. AND MIN. TRANSMISSION	1.00000 and 0.96032	
REFINEMENT METHOD	Full-matrix least-squares on F^2	

DATA / RESTRAINTS / PARAMETERS	2496 / 0 / 123
GOODNESS-OF-FIT ON F^2	1.065
FINAL R INDICES [I>2SIGMA(I)]	R1 = 0.0475, wR2 = 0.0883
R INDICES (ALL DATA)	R1 = 0.0608, wR2 = 0.0936
EXTINCTION COEFFICIENT	n/a
LARGEST DIFF. PEAK AND HOLE	0.423 and -0.294 e.$Å^{-3}$

Table S4: Bond lengths [Å] and angles [°] for Fbnz-MeCDT (**2e**).

S(1)-C(2)	1.763(2)	C(8)-C(9)	1.383(3)	C(4)-C(3)-H(3B)	109.3
S(1)-C(1)	1.793(2)	C(8)-H(8)	0.9500	H(3A)-C(3)-H(3B)	108.0
S(2)-C(2)	1.673(2)	C(9)-H(9)	0.9500	C(9)-C(4)-C(5)	118.90(19)
N(1)-C(2)	1.328(3)	C(2)-S(1)-C(1)	103.09(10)	C(9)-C(4)-C(3)	120.3(2)
N(1)-C(3)	1.462(3)	C(2)-N(1)-C(3)	126.18(18)	C(5)-C(4)-C(3)	120.77(19)
N(1)-H(1)	0.85(2)	C(2)-N(1)-H(1)	114.6(15)	C(6)-C(5)-C(4)	120.9(2)
C(1)-H(1A)	0.9800	C(3)-N(1)-H(1)	118.8(15)	C(6)-C(5)-H(5)	119.6
C(1)-H(1B)	0.9800	S(1)-C(1)-H(1A)	109.5	C(4)-C(5)-H(5)	119.6
C(1)-H(1C)	0.9800	S(1)-C(1)-H(1B)	109.5	C(7)-C(6)-C(5)	118.3(2)
C(3)-C(4)	1.509(3)	H(1A)-C(1)-H(1B)	109.5	C(7)-C(6)-H(6)	120.9
C(3)-H(3A)	0.9900	S(1)-C(1)-H(1C)	109.5	C(5)-C(6)-H(6)	120.9
C(3)-H(3B)	0.9900	H(1A)-C(1)-H(1C)	109.5	F-C(7)-C(6)	118.3(2)
C(4)-C(9)	1.386(3)	H(1B)-C(1)-H(1C)	109.5	F-C(7)-C(8)	119.0(2)
C(4)-C(5)	1.388(3)	N(1)-C(2)-S(2)	122.46(16)	C(6)-C(7)-C(8)	122.7(2)
C(5)-C(6)	1.386(3)	N(1)-C(2)-S(1)	114.28(16)	C(7)-C(8)-C(9)	118.3(2)
C(5)-H(5)	0.9500	S(2)-C(2)-S(1)	123.26(12)	C(9)-C(8)-H(8)	120.8
C(6)-C(7)	1.368(3)	N(1)-C(3)-C(4)	111.58(17)	C(8)-C(9)-C(4)	120.9(2)
C(6)-H(6)	0.9500	N(1)-C(3)-H(3A)	109.3	C(8)-C(9)-H(9)	119.6
C(7)-F	1.358(2)	C(4)-C(3)-H(3A)	109.3	C(4)-C(9)-H(9)	119.6
C(7)-C(8)	1.371(4)	N(1)-C(3)-H(3B)	109.3		

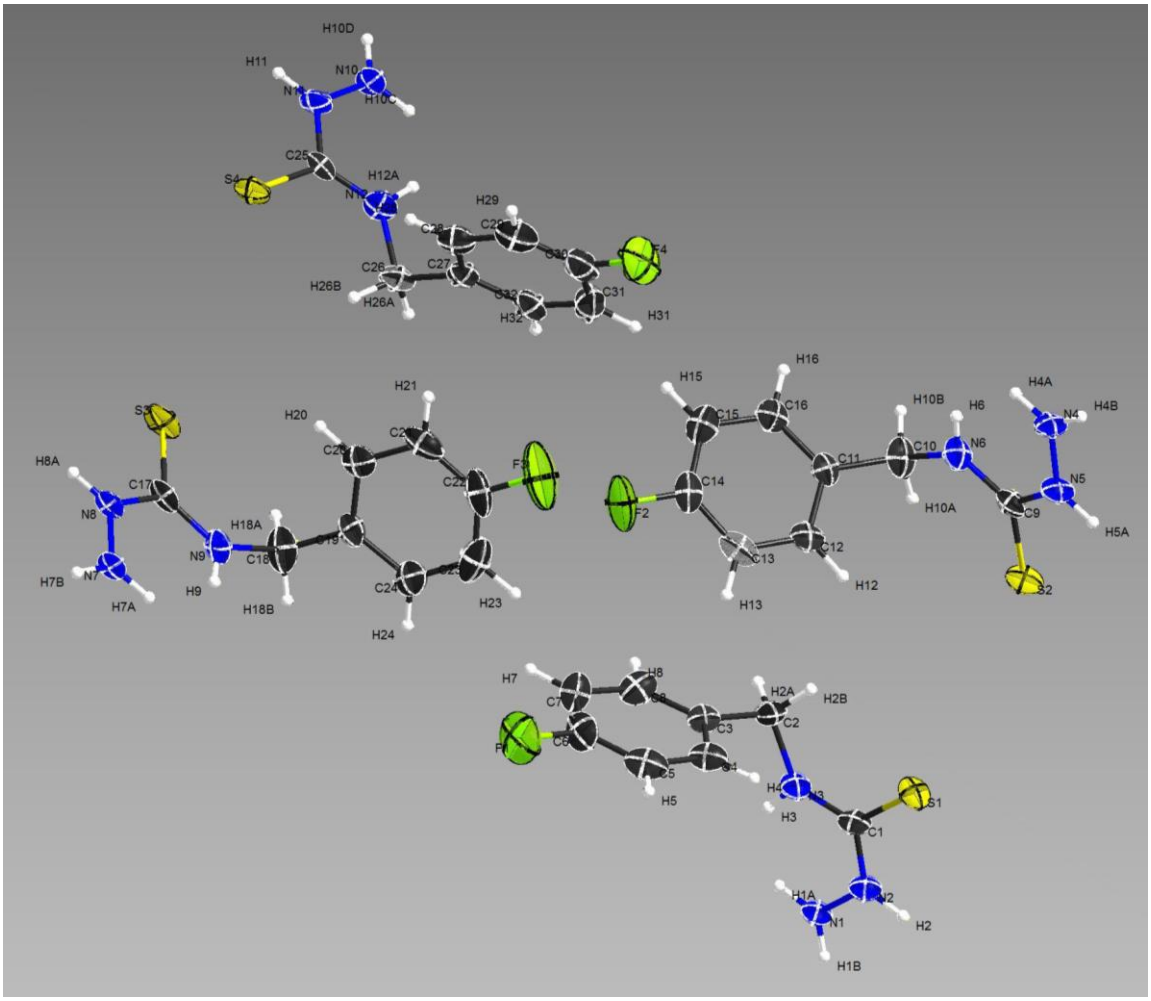

Figure S3: Molecular structures of N-(4-fluorobenzyl)hydrazinecarbothioamide Fbnz-TSC (**3e**). Thermal ellipsoids at 50% probability.

Table S5: Crystal data and structure refinement for Fbnz-TSC (**3e**).

IDENTIFICATION CODE	**S16SIP5**	
EMPIRICAL FORMULA	C8 H9 F N3 S	
FORMULA WEIGHT	198.24	
TEMPERATURE	150(2) K	
WAVELENGTH	1.54184 Å	
CRYSTAL SYSTEM	Triclinic	
SPACE GROUP	P1	
UNIT CELL DIMENSIONS	a = 7.0643(3) Å	α= 94.160(4)°.
	b = 7.0809(3) Å	β= 94.390(4)°.
	c = 18.6832(12) Å	γ = 91.891(3)°.
VOLUME	928.67(8) $Å^3$	
Z	4	
DENSITY (CALCULATED)	1.418 Mg/m^3	
ABSORPTION COEFFICIENT	2.891 mm^{-1}	

F(000)	412
CRYSTAL SIZE	0.600 x 0.400 x 0.050 mm^3
THETA RANGE FOR DATA COLLECTION	4.761 to 73.415°.
INDEX RANGES	-8<=h<=5, -6<=k<=8, -23<=l<=22
REFLECTIONS COLLECTED	6570
INDEPENDENT REFLECTIONS	4097 [R(int) = 0.0398]
COMPLETENESS TO THETA = 67.684°	99.8 %
REFINEMENT METHOD	Full-matrix least-squares on F^2
DATA / RESTRAINTS / PARAMETERS	4097 / 13 / 517
GOODNESS-OF-FIT ON F^2	1.095
FINAL R INDICES [I>2SIGMA(I)]	R1 = 0.0662, wR2 = 0.1677
R INDICES (ALL DATA)	R1 = 0.0681, wR2 = 0.1698
ABSOLUTE STRUCTURE PARAMETER	0.05(3)
EXTINCTION COEFFICIENT	n/a
LARGEST DIFF. PEAK AND HOLE	0.938 and -0.457 e.$Å^{-3}$

Table S6: Bond lengths [Å] and angles [°] for Fbnz-TSC (**3e**).

C(1)-N(3)	1.319(9)	**N(8)-H(8)**	0.88(2)	**C(24)-C(23)-H(23)**	120.3
C(1)-N(2)	1.354(8)	**N(9)-H(9)**	0.87(2)	**C(22)-C(23)-H(23)**	120.3
C(1)-S(1)	1.697(7)	**N(10)-N(11)**	1.410(8)	**C(23)-C(24)-C(19)**	121.2(9)
C(2)-N(3)	1.471(8)	**N(10)-H(10)**	0.87(2)	**C(23)-C(24)-H(24)**	119.4
C(2)-C(3)	1.513(11)	**N(11)-H(11)**	0.96(9)	**C(19)-C(24)-H(24)**	119.4
C(2)-H(2A)	0.9900	**N(12)-H(12)**	0.90(8)	**N(12)-C(25)-N(11)**	115.2(6)
C(2)-H(2B)	0.9900	**N(3)-C(1)-N(2)**	115.8(6)	**N(12)-C(25)-S(4)**	125.2(5)
C(3)-C(8)	1.371(11)	**N(3)-C(1)-S(1)**	124.7(5)	**N(11)-C(25)-S(4)**	119.6(5)
C(3)-C(4)	1.388(10)	**N(2)-C(1)-S(1)**	119.5(5)	**N(12)-C(26)-C(27)**	110.8(6)
C(4)-C(5)	1.396(12)	**N(3)-C(2)-C(3)**	112.3(6)	**N(12)-C(26)-H(26A)**	109.5
C(4)-H(4A)	0.9500	**N(3)-C(2)-H(2A)**	109.2	**C(27)-C(26)-H(26A)**	109.5
C(5)-C(6)	1.367(13)	**C(3)-C(2)-H(2A)**	109.2	**N(12)-C(26)-H(26B)**	109.5
C(5)-H(5A)	0.9500	**N(3)-C(2)-H(2B)**	109.2	**C(27)-C(26)-H(26B)**	109.5
C(6)-F(1)	1.354(9)	**C(3)-C(2)-H(2B)**	109.2	**H(26A)-C(26)-H(26B)**	108.1
C(6)-C(7)	1.393(13)	**H(2A)-C(2)-H(2B)**	107.9	**C(28)-C(27)-C(32)**	118.3(8)
C(7)-C(8)	1.393(12)	**C(8)-C(3)-C(4)**	119.6(8)	**C(28)-C(27)-C(26)**	120.2(7)
C(7)-H(7A)	0.9500	**C(8)-C(3)-C(2)**	120.4(7)	**C(32)-C(27)-C(26)**	121.5(7)
C(8)-H(8A)	0.9500	**C(4)-C(3)-C(2)**	120.0(7)	**C(27)-C(28)-C(29)**	120.6(8)
C(9)-N(6)	1.335(10)	**C(3)-C(4)-C(5)**	119.9(8)	**C(27)-C(28)-H(28)**	119.7
C(9)-N(5)	1.338(9)	**C(3)-C(4)-H(4A)**	120.1	**C(29)-C(28)-H(28)**	119.7
C(9)-S(2)	1.701(7)	**C(5)-C(4)-H(4A)**	120.1	**C(30)-C(29)-C(28)**	119.6(9)

C(10)-N(6)	1.464(9)	**C(6)-C(5)-C(4)**	118.7(8)	**C(30)-C(29)-H(29)**	120.2
C(10)-C(11)	1.503(11)	**C(6)-C(5)-H(5A)**	120.7	**C(28)-C(29)-H(29)**	120.2
C(10)-H(10A)	0.9900	**C(4)-C(5)-H(5A)**	120.7	**C(29)-C(30)-F(4)**	120.0(10)
C(10)-H(10B)	0.9900	**F(1)-C(6)-C(5)**	120.2(9)	**C(29)-C(30)-C(31)**	121.9(9)
C(11)-C(16)	1.377(11)	**F(1)-C(6)-C(7)**	116.5(8)	**F(4)-C(30)-C(31)**	118.1(9)
C(11)-C(12)	1.389(11)	**C(5)-C(6)-C(7)**	123.3(8)	**C(32)-C(31)-C(30)**	117.7(8)
C(12)-C(13)	1.400(12)	**C(6)-C(7)-C(8)**	116.2(7)	**C(32)-C(31)-H(31)**	121.2
C(12)-H(12A)	0.9500	**C(6)-C(7)-H(7A)**	121.9	**C(30)-C(31)-H(31)**	121.2
C(13)-C(14)	1.372(12)	**C(8)-C(7)-H(7A)**	121.9	**C(31)-C(32)-C(27)**	121.8(9)
C(13)-H(13)	0.9500	**C(3)-C(8)-C(7)**	122.4(8)	**C(31)-C(32)-H(32)**	119.1
C(14)-F(2)	1.355(9)	**C(3)-C(8)-H(8A)**	118.8	**C(27)-C(32)-H(32)**	119.1
C(14)-C(15)	1.376(13)	**C(7)-C(8)-H(8A)**	118.8	**N(2)-N(1)-H(1)**	102(5)
C(15)-C(16)	1.366(12)	**N(6)-C(9)-N(5)**	115.9(6)	**C(1)-N(2)-N(1)**	119.8(6)
C(15)-H(15)	0.9500	**N(6)-C(9)-S(2)**	125.6(5)	**C(1)-N(2)-H(2)**	111(4)
C(16)-H(16)	0.9500	**N(5)-C(9)-S(2)**	118.6(5)	**N(1)-N(2)-H(2)**	127(4)
C(17)-N(9)	1.329(10)	**N(6)-C(10)-C(11)**	112.0(6)	**C(1)-N(3)-C(2)**	127.3(6)
C(17)-N(8)	1.351(8)	**N(6)-C(10)-H(10A)**	109.2	**C(1)-N(3)-H(3)**	117(5)
C(17)-S(3)	1.706(7)	**C(11)-C(10)-H(10A)**	109.2	**C(2)-N(3)-H(3)**	116(5)
C(18)-N(9)	1.453(9)	**N(6)-C(10)-H(10B)**	109.2	**N(5)-N(4)-H(4)**	113(5)
C(18)-C(19)	1.503(11)	**C(11)-C(10)-H(10B)**	109.2	**C(9)-N(5)-N(4)**	119.8(6)
C(18)-H(18A)	0.9900	**H(10A)-C(10)-H(10B)**	107.9	**C(9)-N(5)-H(5)**	125(5)
C(18)-H(18B)	0.9900	**C(16)-C(11)-C(12)**	117.8(7)	**N(4)-N(5)-H(5)**	111(5)
C(19)-C(24)	1.389(11)	**C(16)-C(11)-C(10)**	122.3(7)	**C(9)-N(6)-C(10)**	125.0(7)
C(19)-C(20)	1.397(11)	**C(12)-C(11)-C(10)**	119.9(7)	**C(9)-N(6)-H(6)**	117(6)
C(20)-C(21)	1.396(12)	**C(11)-C(12)-C(13)**	120.8(7)	**C(10)-N(6)-H(6)**	118(6)
C(20)-H(20)	0.9500	**C(11)-C(12)-H(12A)**	119.6	**N(8)-N(7)-H(7)**	113(6)
C(21)-C(22)	1.352(14)	**C(13)-C(12)-H(12A)**	119.6	**C(17)-N(8)-N(7)**	117.6(6)
C(21)-H(21)	0.9500	**C(14)-C(13)-C(12)**	118.0(7)	**C(17)-N(8)-H(8)**	104(10)
C(22)-F(3)	1.348(10)	**C(14)-C(13)-H(13)**	121.0	**F(4)-C(30)-C(31)**	118.1(9)
C(22)-C(23)	1.377(15)	**C(12)-C(13)-H(13)**	121.0	**C(32)-C(31)-C(30)**	117.7(8)
C(23)-C(24)	1.373(14)	**F(2)-C(14)-C(13)**	118.0(8)	**C(32)-C(31)-H(31)**	121.2
C(23)-H(23)	0.9500	**F(2)-C(14)-C(15)**	119.3(8)	**C(30)-C(31)-H(31)**	121.2
C(24)-H(24)	0.9500	**C(13)-C(14)-C(15)**	122.7(8)	**C(31)-C(32)-C(27)**	121.8(9)
C(25)-N(12)	1.317(10)	**C(16)-C(15)-C(14)**	117.4(8)	**C(31)-C(32)-H(32)**	119.1
C(25)-N(11)	1.345(8)	**C(16)-C(15)-H(15)**	121.3	**C(27)-C(32)-H(32)**	119.1
C(25)-S(4)	1.697(6)	**C(14)-C(15)-H(15)**	121.3	**N(2)-N(1)-H(1)**	102(5)
C(26)-N(12)	1.479(9)	**C(15)-C(16)-C(11)**	123.2(8)	**C(1)-N(2)-N(1)**	119.8(6)
C(26)-C(27)	1.523(11)	**C(15)-C(16)-H(16)**	118.4	**C(1)-N(3)-C(2)**	127.3(6)
C(26)-H(26A)	0.9900	**C(11)-C(16)-H(16)**	118.4	**C(1)-N(3)-H(3)**	117(5)
C(26)-H(26B)	0.9900	**N(9)-C(17)-N(8)**	117.3(6)	**C(2)-N(3)-H(3)**	116(5)

C(27)-C(28)	1.377(11)	**N(9)-C(17)-S(3)**	124.4(5)	**N(5)-N(4)-H(4)**	113(5)
C(27)-C(32)	1.382(11)	**N(8)-C(17)-S(3)**	118.3(5)	**C(9)-N(5)-N(4)**	119.8(6)
C(28)-C(29)	1.388(12)	**N(9)-C(18)-C(19)**	111.5(6)	**C(9)-N(5)-H(5)**	125(5)
C(28)-H(28)	0.9500	**N(9)-C(18)-H(18A)**	109.3	**N(4)-N(5)-H(5)**	111(5)
C(29)-C(30)	1.346(14)	**C(19)-C(18)-H(18A)**	109.3	**C(9)-N(6)-C(10)**	125.0(7)
C(29)-H(29)	0.9500	**N(9)-C(18)-H(18B)**	109.3	**C(9)-N(6)-H(6)**	117(6)
C(30)-F(4)	1.348(11)	**C(19)-C(18)-H(18B)**	109.3	**C(10)-N(6)-H(6)**	118(6)
C(30)-C(31)	1.384(15)	**H(18A)-C(18)-H(18B)**	108.0	**N(8)-N(7)-H(7)**	113(6)
C(31)-C(32)	1.380(13)	**C(24)-C(19)-C(20)**	117.9(7)	**C(17)-N(8)-N(7)**	117.6(6)
C(31)-H(31)	0.9500	**C(24)-C(19)-C(18)**	121.3(8)	**C(17)-N(8)-H(8)**	104(10)
C(32)-H(32)	0.9500	**C(20)-C(19)-C(18)**	120.9(7)	**N(7)-N(8)-H(8)**	131(10)
N(1)-N(2)	1.407(8)	**C(21)-C(20)-C(19)**	120.7(7)	**C(17)-N(9)-C(18)**	127.3(6)
N(1)-H(1)	0.86(2)	**C(21)-C(20)-H(20)**	119.6	**C(17)-N(9)-H(9)**	109(6)
N(2)-H(2)	0.87(2)	**C(19)-C(20)-H(20)**	119.6	**C(18)-N(9)-H(9)**	123(6)
N(3)-H(3)	0.87(2)	**C(22)-C(21)-C(20)**	119.2(8)	**N(11)-N(10)-H(10)**	101(5)
N(4)-N(5)	1.421(8)	**C(22)-C(21)-H(21)**	120.4	**C(25)-N(11)-N(10)**	120.6(6)
N(4)-H(4)	0.86(2)	**C(20)-C(21)-H(21)**	120.4	**C(25)-N(11)-H(11)**	113(5)
N(5)-H(5)	0.89(2)	**F(3)-C(22)-C(21)**	118.9(10)	**N(10)-N(11)-H(11)**	121(5)
N(6)-H(6)	0.87(2)	**F(3)-C(22)-C(23)**	119.5(9)	**C(25)-N(12)-C(26)**	125.7(6)
N(7)-N(8)	1.416(8)	**C(21)-C(22)-C(23)**	121.6(8)	**C(25)-N(12)-H(12)**	106(5)
N(7)-H(7)	0.87(2)	**C(24)-C(23)-C(22)**	119.4(9)	**C(26)-N(12)-H(12)**	128(5)

Symmetry transformations used to generate equivalent atoms

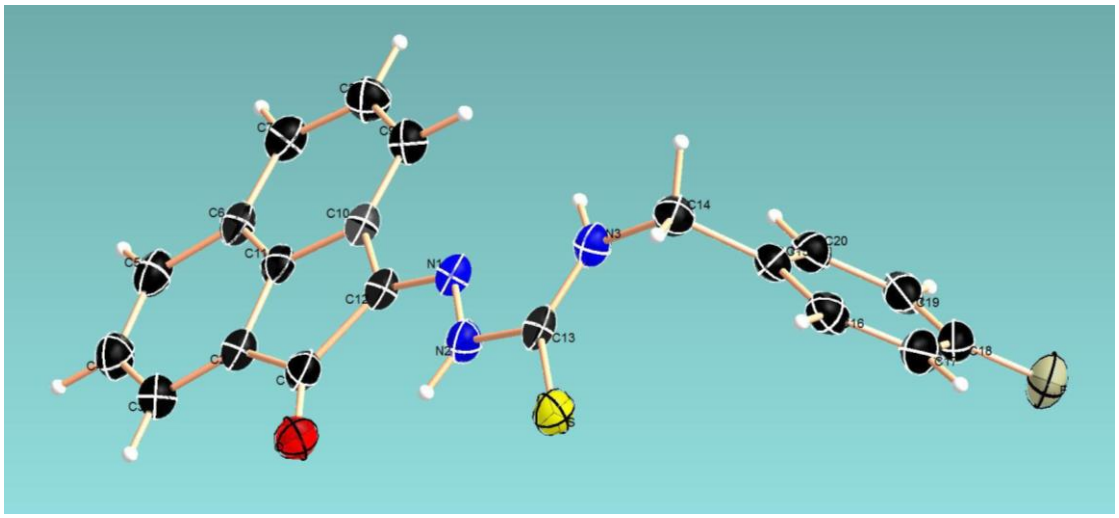

Figure S4: Molecular structures 4-F-benzyl-3-thiosemicarbazone acenaphthenequinone Fbnz-TSCAc (**5e**). Thermal ellipsoids at 50% probability.

Table S7: Crystal data and structure refinement for Fbnz-TSCAc (**5e**).

IDENTIFICATION CODE	**S16SIP7**	
EMPIRICAL FORMULA	C20 H14 F N3 O S	
FORMULA WEIGHT	363.40	
TEMPERATURE	150.00(10) K	
WAVELENGTH	1.54184 Å	
CRYSTAL SYSTEM	Orthorhombic	
SPACE GROUP	$P2_12_12_1$	
UNIT CELL DIMENSIONS	a = 5.11830(10) Å	α= 90°.
	b = 12.2027(2) Å	β= 90°.
	c = 26.4044(3) Å	γ= 90°.
VOLUME	1649.14(5) $Å^3$	
Z	4	
DENSITY (CALCULATED)	1.464 Mg/m^3	
ABSORPTION COEFFICIENT	1.964 mm^{-1}	
F(000)	752	
CRYSTAL SIZE	0.450 x 0.060 x 0.030 mm^3	
THETA RANGE FOR DATA COLLECTION	3.348 to 73.029°.	
INDEX RANGES	-6<=h<=4, -15<=k<=14, -32<=l<=30	
REFLECTIONS COLLECTED	19380	
INDEPENDENT REFLECTIONS	3297 [R(int) = 0.0543]	
COMPLETENESS TO THETA = 67.684°	100.0 %	
ABSORPTION CORRECTION	Semi-empirical from equivalents	
MAX. AND MIN. TRANSMISSION	1.00000 and 0.42048	
REFINEMENT METHOD	Full-matrix least-squares on F^2	
DATA / RESTRAINTS / PARAMETERS	3297 / 0 / 243	
GOODNESS-OF-FIT ON F^2	1.041	
FINAL R INDICES [I>2SIGMA(I)]	R1 = 0.0337, wR2 = 0.0867	
R INDICES (ALL DATA)	R1 = 0.0350, wR2 = 0.0879	
ABSOLUTE STRUCTURE PARAMETER	0.008(11)	
EXTINCTION COEFFICIENT	n/a	
LARGEST DIFF. PEAK AND HOLE	0.272 and -0.186 $e.Å^{-3}$	

Table S8: Bond lengths [Å] and angles [°] for Fbnz-TSCAc (**5e**).

C(1)-O	1.215(3)	**C(5)-C(6)**	1.424(4)	**C(8)-C(7)-C(6)**	120.2(2)
C(1)-C(2)	1.496(3)	**C(5)-H(5)**	0.9500	**C(8)-C(7)-H(7)**	119.9
C(1)-C(12)	1.517(3)	**C(6)-C(11)**	1.402(3)	**C(6)-C(7)-H(7)**	119.9
C(2)-C(3)	1.372(4)	**C(6)-C(7)**	1.412(4)	**C(7)-C(8)-C(9)**	122.5(3)
C(2)-C(11)	1.405(4)	**C(7)-C(8)**	1.378(4)	**C(7)-C(8)-H(8)**	118.7
C(3)-C(4)	1.420(4)	**C(7)-H(7)**	0.9500	**C(9)-C(8)-H(8)**	118.7
C(3)-H(3)	0.9500	**C(8)-C(9)**	1.426(4)	**C(10)-C(9)-C(8)**	117.8(2)
C(4)-C(5)	1.364(4)	**C(8)-H(8)**	0.9500	**C(10)-C(9)-H(9)**	121.1
C(4)-H(4)	0.9500	**C(9)-C(10)**	1.369(4)	**C(8)-C(9)-H(9)**	121.1
C(5)-C(6)	1.424(4)	**C(9)-H(9)**	0.9500	**C(9)-C(10)-C(11)**	119.7(2)
C(5)-H(5)	0.9500	**C(10)-C(11)**	1.408(3)	**C(9)-C(10)-C(12)**	133.9(2)
C(6)-C(11)	1.402(3)	**C(10)-C(12)**	1.466(3)	**C(11)-C(10)-C(12)**	106.3(2)
C(6)-C(7)	1.412(4)	**C(12)-N(1)**	1.294(3)	**C(6)-C(11)-C(2)**	122.9(2)
C(7)-C(8)	1.378(4)	**C(13)-N(3)**	1.333(3)	**C(6)-C(11)-C(10)**	123.2(2)
C(7)-H(7)	0.9500	**C(13)-N(2)**	1.378(3)	**C(2)-C(11)-C(10)**	113.9(2)
C(8)-C(9)	1.426(4)	**C(13)-S**	1.671(3)	**N(1)-C(12)-C(10)**	123.9(2)
C(8)-H(8)	0.9500	**C(14)-N(3)**	1.459(3)	**N(1)-C(12)-C(1)**	128.3(2)
C(9)-C(10)	1.369(4)	**C(14)-C(15)**	1.514(3)	**C(10)-C(12)-C(1)**	107.8(2)
C(9)-H(9)	0.9500	**C(14)-H(14A)**	0.9900	**N(3)-C(13)-N(2)**	115.0(2)
C(10)-C(11)	1.408(3)	**C(14)-H(14B)**	0.9900	**N(3)-C(13)-S**	126.04(19)
C(10)-C(12)	1.466(3)	**C(15)-C(16)**	1.385(4)	**N(2)-C(13)-S**	119.0(2)
C(12)-N(1)	1.294(3)	**C(15)-C(20)**	1.392(4)	**N(3)-C(14)-C(15)**	113.5(2)
C(13)-N(3)	1.333(3)	**C(16)-C(17)**	1.393(4)	**N(3)-C(14)-H(14A)**	108.9
C(13)-N(2)	1.378(3)	**C(16)-H(16)**	0.9500	**C(15)-C(14)-H(14A)**	108.9
C(13)-S	1.671(3)	**C(17)-C(18)**	1.366(5)	**N(3)-C(14)-H(14B)**	108.9
C(14)-N(3)	1.459(3)	**C(17)-H(17)**	0.9500	**C(15)-C(14)-H(14B)**	108.9
C(14)-C(15)	1.514(3)	**C(18)-F**	1.369(3)	**H(14A)-C(14)-H(14B)**	107.7
C(14)-H(14A)	0.9900	**C(18)-C(19)**	1.374(5)	**C(16)-C(15)-C(20)**	119.3(2)
C(14)-H(14B)	0.9900	**C(19)-C(20)**	1.389(4)	**C(16)-C(15)-C(14)**	120.0(2)
C(15)-C(16)	1.385(4)	**C(19)-H(19)**	0.9500	**C(20)-C(15)-C(14)**	120.7(2)
C(15)-C(20)	1.392(4)	**C(20)-H(20)**	0.9500	**C(15)-C(16)-C(17)**	120.5(3)
C(16)-C(17)	1.393(4)	**N(1)-N(2)**	1.352(3)	**C(15)-C(16)-H(16)**	119.8
C(16)-H(16)	0.9500	**N(2)-H(2A)**	0.86(4)	**C(17)-C(16)-H(16)**	119.8
C(17)-C(18)	1.366(5)	**N(3)-H(3A)**	0.88(4)	**C(18)-C(17)-C(16)**	118.4(3)
C(17)-H(17)	0.9500	**O-C(1)-C(2)**	129.0(2)	**C(18)-C(17)-H(17)**	120.8
C(18)-F	1.369(3)	**O-C(1)-C(12)**	125.9(2)	**C(16)-C(17)-H(17)**	120.8

C(18)-C(19)	1.374(5)	**C(2)-C(1)-C(12)**	105.1(2)	**C(17)-C(18)-F**	118.6(3)
C(19)-C(20)	1.389(4)	**C(3)-C(2)-C(11)**	120.0(2)	**C(17)-C(18)-C(19)**	123.0(3)
C(19)-H(19)	0.9500	**C(3)-C(2)-C(1)**	133.2(2)	**F-C(18)-C(19)**	118.3(3)
C(20)-H(20)	0.9500	**C(11)-C(2)-C(1)**	106.8(2)	**C(18)-C(19)-C(20)**	118.0(3)
N(1)-N(2)	1.352(3)	**C(2)-C(3)-C(4)**	117.8(3)	**C(18)-C(19)-H(19)**	121.0
N(2)-H(2A)	0.86(4)	**C(2)-C(3)-H(3)**	121.1	**C(20)-C(19)-H(19)**	121.0
N(3)-H(3A)	0.88(4)	**C(4)-C(3)-H(3)**	121.1	**C(19)-C(20)-C(15)**	120.7(3)
C(1)-O	1.215(3)	**C(5)-C(4)-C(3)**	122.5(3)	**C(19)-C(20)-H(20)**	119.6
C(1)-C(2)	1.496(3)	**C(5)-C(4)-H(4)**	118.8	**C(15)-C(20)-H(20)**	119.6
C(1)-C(12)	1.517(3)	**C(3)-C(4)-H(4)**	118.8	**C(12)-N(1)-N(2)**	117.8(2)
C(2)-C(3)	1.372(4)	**C(4)-C(5)-C(6)**	120.7(3)	**N(1)-N(2)-C(13)**	119.4(2)
C(2)-C(11)	1.405(4)	**C(4)-C(5)-H(5)**	119.7	**N(1)-N(2)-H(2A)**	123(2)
C(3)-C(4)	1.420(4)	**C(6)-C(5)-H(5)**	119.7	**C(13)-N(2)-H(2A)**	118(2)
C(3)-H(3)	0.9500	**C(11)-C(6)-C(7)**	116.6(2)	**C(13)-N(3)-C(14)**	123.6(2)
C(4)-C(5)	1.364(4)	**C(11)-C(6)-C(5)**	116.1(2)	**C(13)-N(3)-H(3A)**	122(2)
C(4)-H(4)	0.9500	**C(7)-C(6)-C(5)**	127.3(2)	**C(14)-N(3)-H(3A)**	114(2)

Symmetry transformations used to generate equivalent atoms:

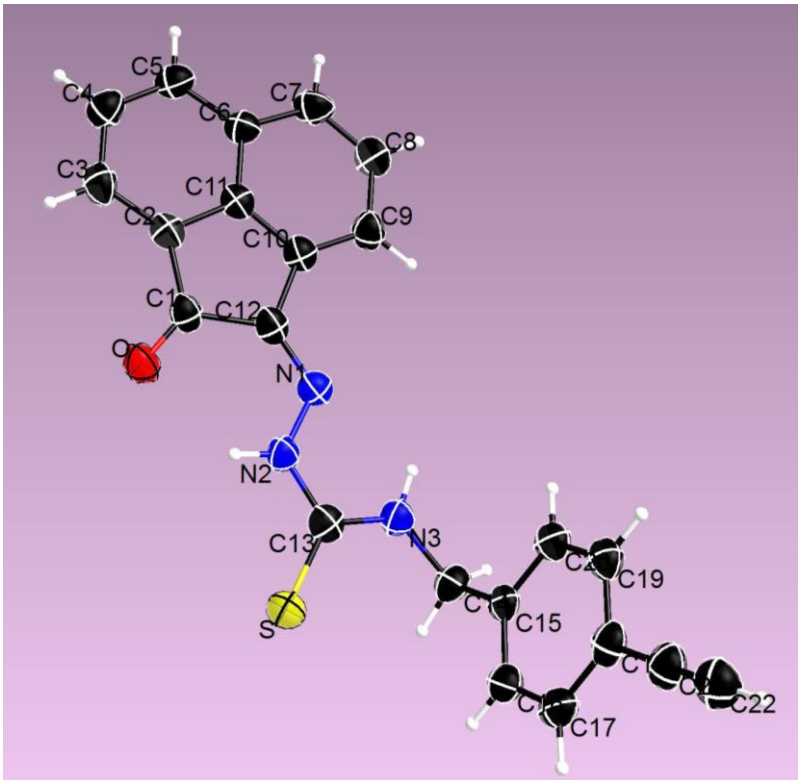

Figure S5: Molecular structures 4-ethynylbenzyl-3-thiosemicarbazone acenaphthenequinone propbnz-TSCAc (**5f**). Thermal ellipsoids at 50% probability.

Table S9: Crystal data and structure refinement for propbnz-TSCAc (**5f**).

IDENTIFICATION CODE	**S17SIP2**	
EMPIRICAL FORMULA	C22 H15 N3 O S	
FORMULA WEIGHT	369.43	
TEMPERATURE	150.00(10) K	
WAVELENGTH	1.54184 Å	
CRYSTAL SYSTEM	Orthorhombic	
SPACE GROUP	$P2_12_12_1$	
UNIT CELL DIMENSIONS	a = 5.3336(3) Å	α= 90°.
	b = 12.1295(5) Å	β= 90°.
	c = 27.1119(16) Å	γ = 90°.
VOLUME	1753.97(16) $Å^3$	
Z	4	
DENSITY (CALCULATED)	1.399 Mg/m^3	
ABSORPTION COEFFICIENT	1.774 mm^{-1}	
F(000)	768	
CRYSTAL SIZE	0.050 x 0.050 x 0.020 mm^3	
THETA RANGE FOR DATA COLLECTION	3.260 to 73.334°.	
INDEX RANGES	-6<=h<=6, -12<=k<=14, -33<=l<=31	
REFLECTIONS COLLECTED	10236	
INDEPENDENT REFLECTIONS	3461 [R(int) = 0.0590]	
COMPLETENESS TO THETA = 67.684°	100.0 %	
ABSORPTION CORRECTION	Semi-empirical from equivalents	
MAX. AND MIN. TRANSMISSION	1.00000 and 0.72088	
REFINEMENT METHOD	Full-matrix least-squares on F^2	
DATA / RESTRAINTS / PARAMETERS	3461 / 0 / 252	
GOODNESS-OF-FIT ON F^2	1.070	
FINAL R INDICES [I>2SIGMA(I)]	R1 = 0.0536, wR2 = 0.1228	
R INDICES (ALL DATA)	R1 = 0.0685, wR2 = 0.1311	
ABSOLUTE STRUCTURE PARAMETER	0.01(3)	
EXTINCTION COEFFICIENT	n/a	
LARGEST DIFF. PEAK AND HOLE	0.258 and -0.168 $e.Å^{-3}$	

Table S10: Bond lengths [Å] and angles [°] for propbnz-TSCAc (**5f**).

S-C(13)	1.673(5)	C(18)-C(21)	1.441(7)	C(8)-C(9)-H(9)	121.0
N(1)-C(12)	1.297(6)	C(19)-C(20)	1.384(7)	C(9)-C(10)-C(11)	119.2(5)
N(1)-N(2)	1.339(5)	C(19)-H(19)	0.9500	C(9)-C(10)-C(12)	134.5(5)

N(2)-C(13)	1.365(6)	C(20)-H(20)	0.9500	C(11)-C(10)-C(12)	106.3(4)
N(2)-H(2A)	0.87(6)	C(21)-C(22)	1.179(7)	C(6)-C(11)-C(10)	123.6(4)
N(3)-C(13)	1.335(6)	C(22)-H(22)	0.9500	C(6)-C(11)-C(2)	122.6(5)
N(3)-C(14)	1.465(6)	C(12)-N(1)-N(2)	118.1(4)	C(10)-C(11)-C(2)	113.8(4)
N(3)-H(3A)	0.87(6)	N(1)-N(2)-C(13)	119.6(4)	N(1)-C(12)-C(10)	123.7(4)
O-C(1)	1.217(6)	N(1)-N(2)-H(2A)	122(4)	N(1)-C(12)-C(1)	128.7(4)
C(1)-C(2)	1.483(7)	C(13)-N(2)-H(2A)	118(4)	C(10)-C(12)-C(1)	107.6(4)
C(1)-C(12)	1.514(6)	C(13)-N(3)-C(14)	124.4(4)	N(3)-C(13)-N(2)	115.2(4)
C(2)-C(3)	1.370(7)	C(13)-N(3)-H(3A)	116(4)	N(3)-C(13)-S	125.3(4)
C(2)-C(11)	1.408(6)	C(14)-N(3)-H(3A)	119(4)	N(2)-C(13)-S	119.5(4)
C(3)-C(4)	1.409(7)	O-C(1)-C(2)	129.5(5)	N(3)-C(14)-C(15)	112.3(4)
C(3)-H(3)	0.9500	O-C(1)-C(12)	124.8(5)	N(3)-C(14)-H(14A)	109.1
C(4)-C(5)	1.366(7)	C(2)-C(1)-C(12)	105.7(4)	C(15)-C(14)-H(14A)	109.1
C(4)-H(4)	0.9500	C(3)-C(2)-C(11)	119.6(5)	N(3)-C(14)-H(14B)	109.1
C(5)-C(6)	1.407(7)	C(3)-C(2)-C(1)	133.8(4)	C(15)-C(14)-H(14B)	109.1
C(5)-H(5)	0.9500	C(11)-C(2)-C(1)	106.6(4)	H(14A)-C(14)-H(14B)	107.9
C(6)-C(11)	1.402(6)	C(2)-C(3)-C(4)	118.4(4)	C(16)-C(15)-C(20)	120.0(5)
C(6)-C(7)	1.411(6)	C(2)-C(3)-H(3)	120.8	C(16)-C(15)-C(14)	119.7(4)
C(7)-C(8)	1.370(7)	C(4)-C(3)-H(3)	120.8	C(20)-C(15)-C(14)	120.2(4)
C(7)-H(7)	0.9500	C(5)-C(4)-C(3)	122.0(5)	C(15)-C(16)-C(17)	120.7(5)
C(8)-C(9)	1.412(7)	C(5)-C(4)-H(4)	119.0	C(15)-C(16)-H(16)	119.7
C(8)-H(8)	0.9500	C(3)-C(4)-H(4)	119.0	C(17)-C(16)-H(16)	119.7
C(9)-C(10)	1.370(6)	C(4)-C(5)-C(6)	121.1(5)	C(18)-C(17)-C(16)	119.6(5)
C(9)-H(9)	0.9500	C(4)-C(5)-H(5)	119.4	C(18)-C(17)-H(17)	120.2
C(10)-C(11)	1.406(7)	C(6)-C(5)-H(5)	119.4	C(16)-C(17)-H(17)	120.2
C(10)-C(12)	1.464(6)	C(11)-C(6)-C(5)	116.3(4)	C(17)-C(18)-C(19)	119.4(5)
C(14)-C(15)	1.513(6)	C(11)-C(6)-C(7)	116.0(4)	C(17)-C(18)-C(21)	120.7(5)
C(14)-H(14A)	0.9900	C(5)-C(6)-C(7)	127.7(5)	C(19)-C(18)-C(21)	119.9(5)
C(14)-H(14B)	0.9900	C(8)-C(7)-C(6)	120.3(5)	C(20)-C(19)-C(18)	120.2(5)
C(15)-C(16)	1.372(6)	C(8)-C(7)-H(7)	119.8	C(20)-C(19)-H(19)	119.9
C(15)-C(20)	1.388(7)	C(6)-C(7)-H(7)	119.8	C(18)-C(19)-H(19)	119.9
C(16)-C(17)	1.392(7)	C(7)-C(8)-C(9)	122.9(5)	C(19)-C(20)-C(15)	120.0(5)
C(16)-H(16)	0.9500	C(7)-C(8)-H(8)	118.5	C(19)-C(20)-H(20)	120.0
C(17)-C(18)	1.392(7)	C(9)-C(8)-H(8)	118.5	C(15)-C(20)-H(20)	120.0
C(17)-H(17)	0.9500	C(10)-C(9)-C(8)	118.0(5)	C(22)-C(21)-C(18)	178.5(6)
C(18)-C(19)	1.396(7)	C(10)-C(9)-H(9)	121.0	C(21)-C(22)-H(22)	180.0

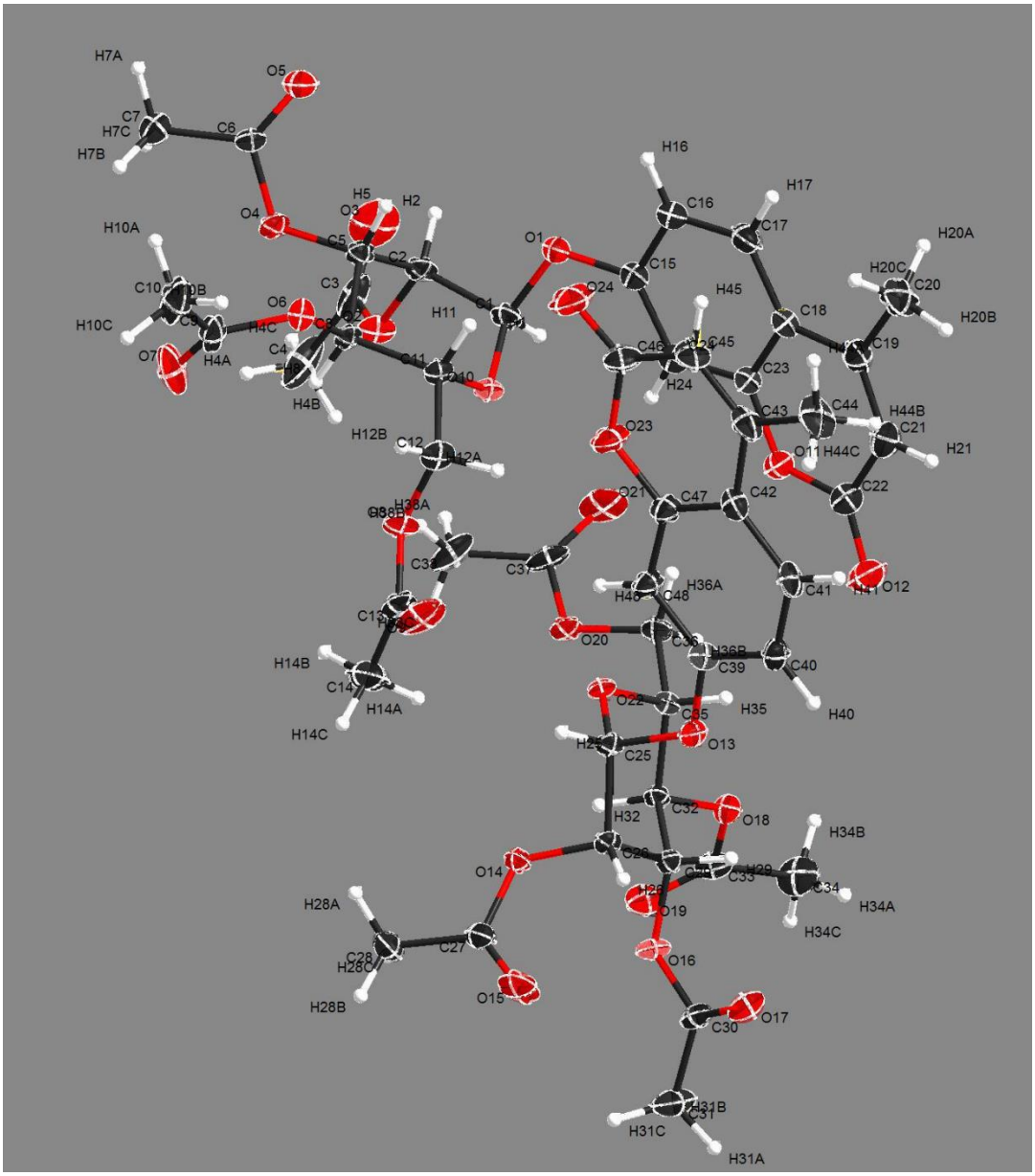

Figure S6: Chrystal structure of AcGC (**15**).

Table S11: Crystal data and structure refinement for AcGC (**15**).

IDENTIFICATION CODE	**S15SIP4**	
EMPIRICAL FORMULA	C24 H26 O12	
FORMULA WEIGHT	506.45	
TEMPERATURE	150(2) K	
WAVELENGTH	1.54184 Å	
CRYSTAL SYSTEM	Orthorhombic	
SPACE GROUP	$P2_12_12_1$	
UNIT CELL DIMENSIONS	a = 8.45570(10) Å	α= 90°.
	b = 13.6108(2) Å	β= 90°.
	c = 42.3604(6) Å	γ = 90°.

VOLUME	4875.21(11) $Å^3$
Z	8
DENSITY (CALCULATED)	1.380 Mg/m^3
ABSORPTION COEFFICIENT	0.955 mm^{-1}
F(000)	2128
CRYSTAL SIZE	0.320 x 0.150 x 0.100 mm^3
THETA RANGE FOR DATA COLLECTION	4.512 to 71.987°.
INDEX RANGES	-6<=h<=10, -16<=k<=16, -45<=l<=52
REFLECTIONS COLLECTED	42452
INDEPENDENT REFLECTIONS	9541 [R(int) = 0.0602]
COMPLETENESS TO THETA = 67.684°	99.9 %
ABSORPTION CORRECTION	Semi-empirical from equivalents
MAX. AND MIN. TRANSMISSION	1.00000 and 0.78152
REFINEMENT METHOD	Full-matrix least-squares on F^2
DATA / RESTRAINTS / PARAMETERS	9541 / 0 / 660
GOODNESS-OF-FIT ON F^2	1.026
FINAL R INDICES [I>2SIGMA(I)]	R1 = 0.0439, wR2 = 0.1129
R INDICES (ALL DATA)	R1 = 0.0473, wR2 = 0.1163
ABSOLUTE STRUCTURE PARAMETER	0.09(7)
EXTINCTION COEFFICIENT	n/a
LARGEST DIFF. PEAK AND HOLE	0.665 and -0.282 $e.Å^{-3}$

Table S12: Bond lengths [Å] and angles [°] for AcGC (**15**).

C(1)-O(10)	1.396(3)	**C(44)-H(44B)**	0.9800	**C(29)-C(26)-C(25)**	111.4(2)
C(1)-O(1)	1.431(4)	**C(44)-H(44C)**	0.9800	**O(14)-C(26)-H(26)**	110.1
C(1)-C(2)	1.529(4)	**C(45)-C(46)**	1.445(5)	**C(29)-C(26)-H(26)**	110.1
C(1)-H(1)	1.0000	**C(45)-H(45)**	0.9500	**C(25)-C(26)-H(26)**	110.1
C(2)-O(2)	1.437(3)	**C(46)-O(24)**	1.211(5)	**O(15)-C(27)-O(14)**	123.6(3)
C(2)-C(5)	1.523(4)	**C(46)-O(23)**	1.375(4)	**O(15)-C(27)-C(28)**	125.6(3)
C(2)-H(2)	1.0000	**C(47)-O(23)**	1.370(4)	**O(14)-C(27)-C(28)**	110.8(3)
C(3)-O(3)	1.199(5)	**C(47)-C(48)**	1.387(4)	**C(27)-C(28)-H(28A)**	109.5
C(3)-O(2)	1.351(4)	**C(48)-H(48)**	0.9500	**C(27)-C(28)-H(28B)**	109.5
C(3)-C(4)	1.485(5)	**C(4)-H(4A)**	0.9800	**H(28A)-C(28)-H(28B)**	109.5
C(5)-O(4)	1.430(3)	**C(4)-H(4B)**	0.9800	**C(27)-C(28)-H(28C)**	109.5
C(5)-C(8)	1.517(4)	**C(4)-H(4C)**	0.9800	**H(28A)-C(28)-H(28C)**	109.5
C(5)-H(5)	1.0000	**O(10)-C(1)-O(1)**	112.3(2)	**H(28B)-C(28)-H(28C)**	109.5
C(6)-O(5)	1.195(4)	**O(10)-C(1)-C(2)**	111.7(2)	**O(16)-C(29)-C(32)**	107.6(2)
C(6)-O(4)	1.348(4)	**O(1)-C(1)-C(2)**	105.0(2)	**O(16)-C(29)-C(26)**	110.1(2)

C(6)-C(7)	1.492(4)	**O(10)-C(1)-H(1)**	109.3	**C(32)-C(29)-C(26)**	112.0(2)
C(7)-H(7A)	0.9800	**O(1)-C(1)-H(1)**	109.3	**O(16)-C(29)-H(29)**	109.0
C(7)-H(7B)	0.9800	**C(2)-C(1)-H(1)**	109.3	**C(32)-C(29)-H(29)**	109.0
C(7)-H(7C)	0.9800	**O(2)-C(2)-C(5)**	107.5(2)	**C(26)-C(29)-H(29)**	109.0
C(8)-O(6)	1.436(3)	**O(2)-C(2)-C(1)**	106.2(2)	**O(17)-C(30)-O(16)**	123.6(3)
C(8)-C(11)	1.520(4)	**C(5)-C(2)-C(1)**	111.3(2)	**O(17)-C(30)-C(31)**	126.4(3)
C(8)-H(8)	1.0000	**O(2)-C(2)-H(2)**	110.6	**O(16)-C(30)-C(31)**	110.1(3)
C(9)-O(7)	1.191(5)	**C(5)-C(2)-H(2)**	110.6	**C(30)-C(31)-H(31A)**	109.5
C(9)-O(6)	1.367(4)	**C(1)-C(2)-H(2)**	110.6	**C(30)-C(31)-H(31B)**	109.5
C(9)-C(10)	1.491(5)	**O(3)-C(3)-O(2)**	123.8(3)	**H(31A)-C(31)-H(31B)**	109.5
C(10)-H(10A)	0.9800	**O(3)-C(3)-C(4)**	126.0(3)	**C(30)-C(31)-H(31C)**	109.5
C(10)-H(10B)	0.9800	**O(2)-C(3)-C(4)**	110.2(3)	**H(31A)-C(31)-H(31C)**	109.5
C(10)-H(10C)	0.9800	**O(4)-C(5)-C(8)**	107.2(2)	**H(31B)-C(31)-H(31C)**	109.5
C(11)-O(10)	1.433(3)	**O(4)-C(5)-C(2)**	110.1(2)	**O(18)-C(32)-C(29)**	108.7(2)
C(11)-C(12)	1.509(4)	**C(8)-C(5)-C(2)**	111.2(2)	**O(18)-C(32)-C(35)**	106.6(2)
C(11)-H(11)	1.0000	**O(4)-C(5)-H(5)**	109.4	**C(29)-C(32)-C(35)**	108.2(2)
C(12)-O(8)	1.439(4)	**C(8)-C(5)-H(5)**	109.4	**O(18)-C(32)-H(32)**	111.1
C(12)-H(12A)	0.9900	**C(2)-C(5)-H(5)**	109.4	**C(29)-C(32)-H(32)**	111.1
C(12)-H(12B)	0.9900	**O(5)-C(6)-O(4)**	123.1(3)	**C(35)-C(32)-H(32)**	111.1
C(13)-O(9)	1.199(5)	**O(5)-C(6)-C(7)**	126.5(3)	**O(19)-C(33)-O(18)**	124.5(3)
C(13)-O(8)	1.343(4)	**O(4)-C(6)-C(7)**	110.3(3)	**O(19)-C(33)-C(34)**	126.4(3)
C(13)-C(14)	1.490(5)	**C(6)-C(7)-H(7A)**	109.5	**O(18)-C(33)-C(34)**	109.2(3)
C(14)-H(14A)	0.9800	**C(6)-C(7)-H(7B)**	109.5	**C(33)-C(34)-H(34A)**	109.5
C(14)-H(14B)	0.9800	**H(7A)-C(7)-H(7B)**	109.5	**C(33)-C(34)-H(34B)**	109.5
C(14)-H(14C)	0.9800	**C(6)-C(7)-H(7C)**	109.5	**H(34A)-C(34)-H(34B)**	109.5
C(15)-O(1)	1.374(4)	**H(7A)-C(7)-H(7C)**	109.5	**H(34B)-C(34)-H(34C)**	109.5
C(15)-C(24)	1.387(4)	**H(7B)-C(7)-H(7C)**	109.5	**O(22)-C(35)-C(36)**	107.2(2)
C(15)-C(16)	1.397(4)	**O(6)-C(8)-C(5)**	108.7(2)	**O(22)-C(35)-C(32)**	109.3(2)
C(16)-C(17)	1.377(5)	**O(6)-C(8)-C(11)**	107.4(2)	**C(36)-C(35)-C(32)**	115.0(2)
C(16)-H(16)	0.9500	**C(5)-C(8)-C(11)**	108.7(2)	**O(22)-C(35)-H(35)**	108.4
C(17)-C(18)	1.409(4)	**O(6)-C(8)-H(8)**	110.7	**C(36)-C(35)-H(35)**	108.4
C(17)-H(17)	0.9500	**C(5)-C(8)-H(8)**	110.7	**C(32)-C(35)-H(35)**	108.4
C(18)-C(23)	1.399(4)	**C(11)-C(8)-H(8)**	110.7	**O(20)-C(36)-C(35)**	108.9(2)
C(18)-C(19)	1.443(4)	**O(7)-C(9)-O(6)**	123.8(3)	**O(20)-C(36)-H(36A)**	109.9
C(19)-C(21)	1.343(5)	**O(7)-C(9)-C(10)**	126.5(3)	**C(35)-C(36)-H(36A)**	109.9
C(19)-C(20)	1.502(5)	**O(6)-C(9)-C(10)**	109.7(3)	**O(20)-C(36)-H(36B)**	109.9
C(20)-H(20A)	0.9800	**C(9)-C(10)-H(10A)**	109.5	**C(35)-C(36)-H(36B)**	109.9
C(20)-H(20B)	0.9800	**C(9)-C(10)-H(10B)**	109.5	**H(36A)-C(36)-H(36B)**	108.3
C(20)-H(20C)	0.9800	**H(10A)-C(10)-H(10B)**	109.5	**O(21)-C(37)-O(20)**	122.5(3)
C(21)-C(22)	1.449(5)	**H(10B)-C(10)-H(10C)**	109.5	**O(21)-C(37)-C(38)**	125.1(3)

C(21)-H(21)	0.9500	**O(10)-C(11)-C(12)**	107.1(2)	**O(20)-C(37)-C(38)**	112.4(3)
C(22)-O(12)	1.211(4)	**C(12)-C(11)-H(11)**	108.6	**C(37)-C(38)-H(38A)**	109.5
C(22)-O(11)	1.378(4)	**C(8)-C(11)-H(11)**	108.6	**C(37)-C(38)-H(38B)**	109.5
C(23)-O(11)	1.369(4)	**O(8)-C(12)-C(11)**	108.0(2)	**H(38A)-C(38)-H(38B)**	109.5
C(23)-C(24)	1.388(4)	**O(8)-C(12)-H(12A)**	110.1	**C(37)-C(38)-H(38C)**	109.5
C(24)-H(24)	0.9500	**C(11)-C(12)-H(12A)**	110.1	**H(38A)-C(38)-H(38C)**	109.5
C(25)-O(22)	1.403(3)	**O(8)-C(12)-H(12B)**	110.1	**H(38B)-C(38)-H(38C)**	109.5
C(25)-O(13)	1.424(3)	**C(11)-C(12)-H(12B)**	110.1	**O(13)-C(39)-C(48)**	122.7(3)
C(25)-C(26)	1.521(4)	**H(12A)-C(12)-H(12B)**	108.4	**O(13)-C(39)-C(40)**	116.3(3)
C(25)-H(25)	1.0000	**O(9)-C(13)-O(8)**	123.0(3)	**C(48)-C(39)-C(40)**	121.0(3)
C(26)-O(14)	1.441(3)	**O(9)-C(13)-C(14)**	125.1(3)	**C(41)-C(40)-C(39)**	119.5(3)
C(26)-C(29)	1.521(4)	**O(8)-C(13)-C(14)**	111.9(3)	**C(41)-C(40)-H(40)**	120.2
C(26)-H(26)	1.0000	**C(13)-C(14)-H(14A)**	109.5	**C(39)-C(40)-H(40)**	120.2
C(27)-O(15)	1.194(4)	**C(13)-C(14)-H(14B)**	109.5	**C(40)-C(41)-C(42)**	121.0(3)
C(27)-O(14)	1.357(3)	**H(14A)-C(14)-H(14B)**	109.5	**C(40)-C(41)-H(41)**	119.5
C(27)-C(28)	1.490(4)	**C(13)-C(14)-H(14C)**	109.5	**C(42)-C(41)-H(41)**	119.5
C(28)-H(28A)	0.9800	**H(14A)-C(14)-H(14C)**	109.5	**C(47)-C(42)-C(41)**	117.3(3)
C(28)-H(28B)	0.9800	**H(14B)-C(14)-H(14C)**	109.5	**C(47)-C(42)-C(43)**	118.3(3)
C(28)-H(28C)	0.9800	**O(1)-C(15)-C(24)**	123.5(3)	**C(41)-C(42)-C(43)**	124.4(3)
C(29)-O(16)	1.435(3)	**O(1)-C(15)-C(16)**	115.4(3)	**C(45)-C(43)-C(42)**	118.4(3)
C(29)-C(32)	1.513(3)	**C(24)-C(15)-C(16)**	121.0(3)	**C(45)-C(43)-C(44)**	121.5(3)
C(29)-H(29)	1.0000	**C(17)-C(16)-C(15)**	119.6(3)	**C(42)-C(43)-C(44)**	120.2(3)
C(30)-O(17)	1.204(4)	**C(17)-C(16)-H(16)**	120.2	**C(43)-C(44)-H(44A)**	109.5
C(30)-O(16)	1.345(3)	**C(15)-C(16)-H(16)**	120.2	**C(43)-C(44)-H(44B)**	109.5
C(30)-C(31)	1.500(4)	**C(16)-C(17)-C(18)**	121.3(3)	**H(44A)-C(44)-H(44B)**	109.5
C(31)-H(31A)	0.9800	**C(16)-C(17)-H(17)**	119.3	**C(43)-C(44)-H(44C)**	109.5
C(31)-H(31B)	0.9800	**C(18)-C(17)-H(17)**	119.3	**H(44A)-C(44)-H(44C)**	109.5
C(31)-H(31C)	0.9800	**C(23)-C(18)-C(17)**	116.9(3)	**H(44B)-C(44)-H(44C)**	109.5
C(32)-O(18)	1.432(3)	**C(23)-C(18)-C(19)**	118.1(3)	**C(43)-C(45)-C(46)**	123.2(3)
C(32)-C(35)	1.524(4)	**C(17)-C(18)-C(19)**	125.1(3)	**C(43)-C(45)-H(45)**	118.4
C(32)-H(32)	1.0000	**C(21)-C(19)-C(18)**	118.8(3)	**C(46)-C(45)-H(45)**	118.4
C(33)-O(18)	1.358(4)	**C(21)-C(19)-C(20)**	121.0(3)	**O(24)-C(46)-O(23)**	116.7(3)
C(33)-C(34)	1.499(4)	**C(18)-C(19)-C(20)**	120.2(3)	**O(24)-C(46)-C(45)**	126.8(3)
C(34)-H(34A)	0.9800	**C(19)-C(20)-H(20A)**	109.5	**O(23)-C(46)-C(45)**	116.5(3)
C(34)-H(34B)	0.9800	**C(19)-C(20)-H(20B)**	109.5	**O(23)-C(47)-C(42)**	121.8(3)
C(34)-H(34C)	0.9800	**H(20A)-C(20)-H(20B)**	109.5	**O(23)-C(47)-C(48)**	115.1(3)
C(35)-O(22)	1.429(3)	**C(19)-C(20)-H(20C)**	109.5	**C(42)-C(47)-C(48)**	123.1(3)
C(35)-C(36)	1.508(4)	**H(20A)-C(20)-H(20C)**	109.5	**C(39)-C(48)-C(47)**	118.0(3)
C(35)-H(35)	1.0000	**H(20B)-C(20)-H(20C)**	109.5	**C(39)-C(48)-H(48)**	121.0
C(36)-O(20)	1.443(4)	**C(19)-C(21)-C(22)**	123.2(3)	**C(47)-C(48)-H(48)**	121.0

C(36)-H(36A)	0.9900	**C(19)-C(21)-H(21)**	118.4	**C(15)-O(1)-C(1)**	117.3(2)
C(36)-H(36B)	0.9900	**C(22)-C(21)-H(21)**	118.4	**C(3)-O(2)-C(2)**	116.0(2)
C(37)-O(21)	1.208(5)	**O(12)-C(22)-O(11)**	117.2(3)	**C(6)-O(4)-C(5)**	118.7(2)
C(37)-O(20)	1.346(3)	**O(12)-C(22)-C(21)**	126.4(3)	**C(3)-C(4)-H(4A)**	109.5
C(37)-C(38)	1.493(5)	**O(11)-C(22)-C(21)**	116.4(3)	**C(3)-C(4)-H(4B)**	109.5
C(38)-H(38A)	0.9800	**O(11)-C(23)-C(24)**	115.2(3)	**H(4A)-C(4)-H(4B)**	109.5
C(38)-H(38B)	0.9800	**O(11)-C(23)-C(18)**	121.7(3	**C(3)-C(4)-H(4C)**	109.5
C(38)-H(38C)	0.9800	**C(19)-C(21)-C(22)**	123.2(3)	**H(4A)-C(4)-H(4C)**	109.5
C(39)-O(13)	1.374(3)	**C(24)-C(23)-C(18)**	123.0(3)	**H(4B)-C(4)-H(4C)**	109.5
C(39)-C(48)	1.383(4)	**C(15)-C(24)-C(23)**	117.9(3)	**C(9)-O(6)-C(8)**	118.2(2)
C(39)-C(40)	1.395(4)	**C(15)-C(24)-H(24)**	121.0	**C(13)-O(8)-C(12)**	114.4(2)
C(40)-C(41)	1.380(4)	**C(23)-C(24)-H(24)**	121.0	**C(1)-O(10)-C(11)**	114.7(2)
C(40)-H(40)	0.9500	**O(22)-C(25)-O(13)**	112.4(2)	**C(23)-O(11)-C(22)**	121.8(3)
C(41)-C(42)	1.408(4)	**O(22)-C(25)-C(26)**	112.0(2)	**C(39)-O(13)-C(25)**	117.0(2)
C(41)-H(41)	0.9500	**O(13)-C(25)-C(26)**	104.8(2)	**C(27)-O(14)-C(26)**	116.4(2)
C(42)-C(47)	1.384(4)	**O(22)-C(25)-H(25)**	109.2	**C(30)-O(16)-C(29)**	116.8(2)
C(42)-C(43)	1.447(4)	**O(13)-C(25)-H(25)**	109.2	**C(33)-O(18)-C(32)**	118.0(2)
C(43)-C(45)	1.343(5)	**C(26)-C(25)-H(25)**	109.2	**C(37)-O(20)-C(36)**	113.1(2)
C(43)-C(44)	1.497(5)	**O(14)-C(26)-C(29)**	109.0(2)	**C(25)-O(22)-C(35)**	114.4(2)
C(44)-H(44A)	0.9800	**O(14)-C(26)-C(25)**	106.2(2)	**C(47)-O(23)-C(46)**	121.7(3)

Symmetry transformations used to generate equivalent atoms

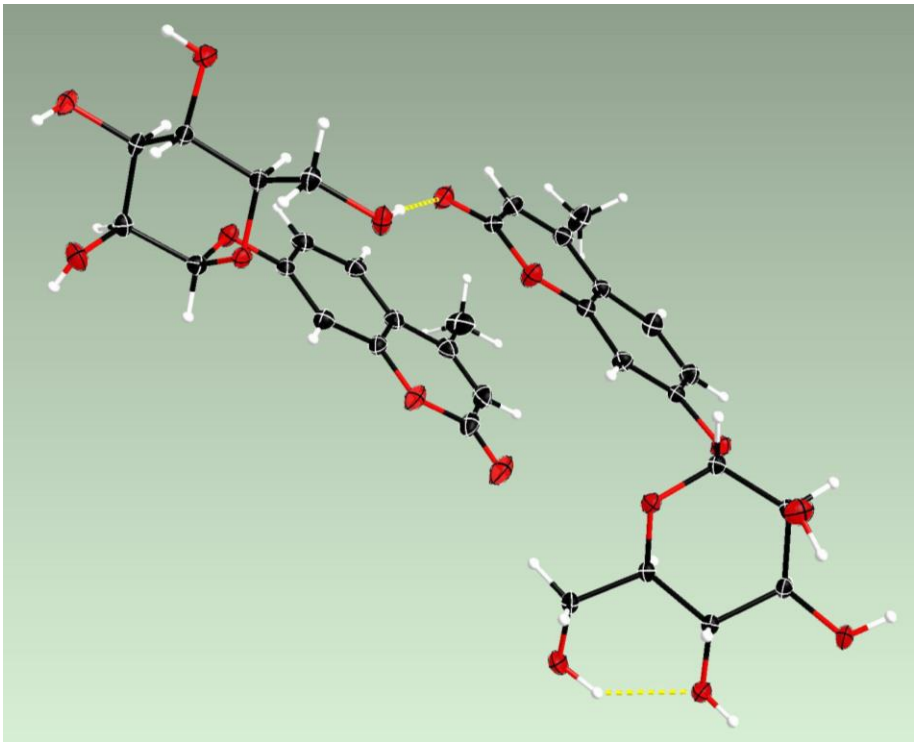

Figure S7: Crystal Structure of GC (16).

Table S13: Crystal data and structure refinement for GC (**16**).

IDENTIFICATION CODE	**S17SIP7**	
EMPIRICAL FORMULA	C16 H18 O8	
FORMULA WEIGHT	338.30	
TEMPERATURE	150.01(10) K	
WAVELENGTH	1.54184 Å	
CRYSTAL SYSTEM	Triclinic	
SPACE GROUP	P1	
UNIT CELL DIMENSIONS	a = 7.9134(3) Å	α= 105.567(4)°.
	b = 7.9212(4) Å	β= 104.160(4)°.
	c = 12.5663(6) Å	γ = 91.397(3)°.
VOLUME	732.32(6) $Å^3$	
Z	2	
DENSITY (CALCULATED)	1.534 Mg/m^3	
ABSORPTION COEFFICIENT	1.060 mm^{-1}	
F(000)	356	
CRYSTAL SIZE	0.150 x 0.090 x 0.020 mm^3	
THETA RANGE FOR DATA COLLECTION	3.782 to 73.044°.	
INDEX RANGES	-9<=h<=8, -9<=k<=9, -15<=l<=13	
REFLECTIONS COLLECTED	4688	
INDEPENDENT REFLECTIONS	3355 [R(int) = 0.0226]	
COMPLETENESS TO THETA = 67.684°	99.8 %	
ABSORPTION CORRECTION	Semi-empirical from equivalents	
MAX. AND MIN. TRANSMISSION	1.00000 and 0.82567	
REFINEMENT METHOD	Full-matrix least-squares on F^2	
DATA / RESTRAINTS / PARAMETERS	3355 / 3 / 467	
GOODNESS-OF-FIT ON F^2	1.034	
FINAL R INDICES [I>2SIGMA(I)]	R1 = 0.0296, wR2 = 0.0769	
R INDICES (ALL DATA)	R1 = 0.0307, wR2 = 0.0781	
ABSOLUTE STRUCTURE PARAMETER	-0.03(12)	
EXTINCTION COEFFICIENT	n/a	
LARGEST DIFF. PEAK AND HOLE	0.220 and -0.193 $e.Å^{-3}$	

Table S14: Bond lengths [Å] for GC (**16**).

O(1)-C(1)	1.213(4)	**C(8)-C(9)**	1.390(3)	**O(16)-H(16A)**	0.84(4)
O(2)-C(1)	1.376(3)	**C(9)-C(10)**	1.383(3)	**C(17)-C(18)**	1.447(3)
O(2)-C(10)	1.378(3)	**C(9)-H(9)**	0.9500	**C(18)-C(19)**	1.342(3)
O(3)-C(8)	1.368(3)	**C(11)-C(16)**	1.525(3)	**C(18)-H(18)**	0.9500
O(3)-C(11)	1.433(3)	**C(11)-H(11)**	1.0000	**C(19)-C(21)**	1.447(3)
O(4)-C(11)	1.398(3)	**C(12)-C(13)**	1.512(3)	**C(19)-C(20)**	1.499(3)
O(4)-C(12)	1.444(3)	**C(12)-C(14)**	1.532(3)	**C(20)-H(20A)**	0.9800
O(5)-C(13)	1.433(3)	**C(12)-H(12)**	1.0000	**C(20)-H(20B)**	0.9800
O(5)-H(5A)	0.93(4)	**C(13)-H(13A)**	0.9900	**C(20)-H(20C)**	0.9800
O(6)-C(14)	1.421(3)	**C(13)-H(13B)**	0.9900	**C(21)-C(26)**	1.393(3)
O(6)-H(6A)	0.80(4)	**C(14)-C(15)**	1.521(3)	**C(21)-C(22)**	1.404(3)
O(7)-C(15)	1.429(3)	**C(14)-H(14)**	1.0000	**C(22)-C(23)**	1.373(3)
O(7)-H(7A)	0.87(5)	**C(15)-C(16)**	1.518(3)	**C(22)-H(22)**	0.9500
O(8)-C(16)	1.428(3)	**C(15)-H(15)**	1.0000	**C(23)-C(24)**	1.396(3)
O(8)-H(8A)	0.74(4)	**C(16)-H(16)**	1.0000	**C(23)-H(23)**	0.9500
C(1)-C(2)	1.448(4)	**O(9)-C(17)**	1.223(3)	**C(24)-C(25)**	1.387(3)
C(2)-C(3)	1.347(4)	**O(10)-C(17)**	1.364(3)	**C(25)-C(26)**	1.390(3)
C(2)-H(2)	0.9500	**O(10)-C(26)**	1.379(3)	**C(25)-H(25)**	0.9500
C(3)-C(5)	1.447(3)	**O(11)-C(24)**	1.374(3)	**C(27)-C(32)**	1.531(3)
C(3)-C(4)	1.506(4)	**O(11)-C(27)**	1.423(3)	**C(27)-H(27)**	1.0000
C(4)-H(4A)	0.9800	**O(12)-C(27)**	1.401(3)	**C(28)-C(29)**	1.523(3)
C(4)-H(4B)	0.9800	**O(12)-C(28)**	1.441(3)	**C(28)-C(30)**	1.531(3)
C(4)-H(4C)	0.9800	**O(13)-C(29)**	1.428(3)	**C(28)-H(28)**	1.0000
C(5)-C(10)	1.394(3)	**O(13)-H(13)**	0.90(5)	**C(29)-H(29A)**	0.9900
C(5)-C(6)	1.405(4)	**O(14)-C(30)**	1.426(3)	**C(29)-H(29B)**	0.9900
C(6)-C(7)	1.378(3)	**O(14)-H(14A)**	0.80(4)	**C(30)-C(31)**	1.522(3)
C(6)-H(6)	0.9500	**O(15)-C(31)**	1.419(3)	**C(30)-H(30)**	1.0000
C(7)-C(8)	1.403(3)	**O(15)-H(15A)**	0.88(5)	**C(31)-C(32)**	1.532(3)
C(7)-H(7)	0.9500	**O(16)-C(32)**	1.414(3)	**C(31)-H(31)**	1.0000

Table S15: Bond angles [°] for GC (**16**)

C(1)-O(2)-C(10)	121.2(2)	**C(30)-O(14)-H(14A)**	107(3)
C(8)-O(3)-C(11)	118.79(18)	**C(31)-O(15)-H(15A)**	115(3)
C(11)-O(4)-C(12)	114.12(16)	**C(32)-O(16)-H(16A)**	108(2)
C(13)-O(5)-H(5A)	111(2)	**O(9)-C(17)-O(10)**	116.6(2)

C(14)-O(6)-H(6A)	108(2)	**O(9)-C(17)-C(18)**	125.7(2)
C(15)-O(7)-H(7A)	108(3)	**O(10)-C(17)-C(18)**	117.8(2)
C(16)-O(8)-H(8A)	110(3)	**C(19)-C(18)-C(17)**	122.0(2)
O(1)-C(1)-O(2)	116.1(2)	**C(19)-C(18)-H(18)**	119.0
O(1)-C(1)-C(2)	126.7(3)	**C(17)-C(18)-H(18)**	119.0
O(2)-C(1)-C(2)	117.2(2)	**C(18)-C(19)-C(21)**	119.4(2)
C(3)-C(2)-C(1)	122.8(2)	**C(18)-C(19)-C(20)**	121.9(2)
C(3)-C(2)-H(2)	118.6	**C(21)-C(19)-C(20)**	118.8(2)
C(1)-C(2)-H(2)	118.6	**C(19)-C(20)-H(20A)**	109.5
C(2)-C(3)-C(5)	118.6(2)	**C(19)-C(20)-H(20B)**	109.5
C(2)-C(3)-C(4)	122.4(2)	**H(20A)-C(20)-H(20B)**	109.5
C(5)-C(3)-C(4)	119.0(3)	**C(19)-C(20)-H(20C)**	109.5
C(3)-C(4)-H(4A)	109.5	**H(20A)-C(20)-H(20C)**	109.5
C(3)-C(4)-H(4B)	109.5	**C(26)-C(21)-C(22)**	117.4(2)
H(4A)-C(4)-H(4B)	109.5	**C(26)-C(21)-C(19)**	118.0(2)
C(3)-C(4)-H(4C)	109.5	**C(22)-C(21)-C(19)**	124.6(2)
H(4A)-C(4)-H(4C)	109.5	**C(23)-C(22)-C(21)**	121.1(2)
H(4B)-C(4)-H(4C)	109.5	**C(23)-C(22)-H(22)**	119.4
C(10)-C(5)-C(6)	117.1(2)	**C(21)-C(22)-H(22)**	119.4
C(10)-C(5)-C(3)	118.4(2)	**C(22)-C(23)-C(24)**	119.7(2)
C(6)-C(5)-C(3)	124.5(2)	**C(22)-C(23)-H(23)**	120.1
C(7)-C(6)-C(5)	121.3(2)	**C(24)-C(23)-H(23)**	120.1
C(7)-C(6)-H(6)	119.3	**C(26)-C(21)-C(22)**	117.4(2)
C(5)-C(6)-H(6)	119.3	**O(11)-C(24)-C(25)**	124.2(2)
C(6)-C(7)-C(8)	119.4(2)	**O(11)-C(24)-C(23)**	114.7(2)
C(6)-C(7)-H(7)	120.3	**C(25)-C(24)-C(23)**	121.1(2)
C(8)-C(7)-H(7)	120.3	**C(24)-C(25)-C(26)**	117.8(2)
O(3)-C(8)-C(9)	124.2(2)	**C(24)-C(25)-H(25)**	121.1
O(3)-C(8)-C(7)	114.9(2)	**C(26)-C(25)-H(25)**	121.1
C(9)-C(8)-C(7)	121.0(2)	**O(10)-C(26)-C(25)**	115.7(2)
C(10)-C(9)-C(8)	117.8(2)	**O(10)-C(26)-C(21)**	121.5(2)
C(10)-C(9)-H(9)	121.1	**C(25)-C(26)-C(21)**	122.8(2)
C(8)-C(9)-H(9)	121.1	**O(12)-C(27)-O(11)**	111.81(17)
O(2)-C(10)-C(9)	115.0(2)	**O(12)-C(27)-C(32)**	113.44(18)
O(2)-C(10)-C(5)	121.7(2)	**O(11)-C(27)-C(32)**	106.33(17)
C(9)-C(10)-C(5)	123.3(2)	**O(12)-C(27)-H(27)**	108.4
O(4)-C(11)-O(3)	112.52(18)	**O(11)-C(27)-H(27)**	108.4
O(4)-C(11)-C(16)	112.85(18)	**C(32)-C(27)-H(27)**	108.4
O(3)-C(11)-C(16)	104.25(17)	**O(12)-C(28)-C(29)**	105.89(17)
O(4)-C(11)-H(11)	109.0	**O(12)-C(28)-C(30)**	108.45(17)

O(3)-C(11)-H(11)	109.0	**C(29)-C(28)-C(30)**	113.01(17)
C(16)-C(11)-H(11)	109.0	**O(12)-C(28)-H(28)**	109.8
O(4)-C(12)-C(13)	107.32(17)	**C(29)-C(28)-H(28)**	109.8
O(4)-C(12)-C(14)	110.58(16)	**C(30)-C(28)-H(28)**	109.8
C(13)-C(12)-C(14)	111.36(18)	**O(13)-C(29)-C(28)**	110.51(18)
O(4)-C(12)-H(12)	109.2	**O(13)-C(29)-H(29A)**	109.5
C(13)-C(12)-H(12)	109.2	**C(28)-C(29)-H(29A)**	109.5
C(14)-C(12)-H(12)	109.2	**O(13)-C(29)-H(29B)**	109.5
O(5)-C(13)-C(12)	114.07(18)	**C(28)-C(29)-H(29B)**	109.5
O(5)-C(13)-H(13A)	108.7	**H(29A)-C(29)-H(29B)**	108.1
C(12)-C(13)-H(13A)	108.7	**O(14)-C(30)-C(31)**	111.47(17)
O(5)-C(13)-H(13B)	108.7	**O(14)-C(30)-C(28)**	107.50(17)
O(5)-C(13)-C(12)	114.07(18)	**C(31)-C(30)-C(28)**	108.98(17)
C(12)-C(13)-H(13B)	108.7	**O(14)-C(30)-H(30)**	109.6
H(13A)-C(13)-H(13B)	107.6	**C(31)-C(30)-H(30)**	109.6
O(6)-C(14)-C(15)	111.62(18)	**C(28)-C(30)-H(30)**	109.6
O(6)-C(14)-C(12)	106.71(17)	**O(15)-C(31)-C(30)**	107.10(17)
C(15)-C(14)-C(12)	108.79(17)	**O(15)-C(31)-C(32)**	110.86(18)
O(6)-C(14)-H(14)	109.9	**C(30)-C(31)-C(32)**	110.20(18)
C(15)-C(14)-H(14)	109.9	**O(15)-C(31)-H(31)**	109.5
C(12)-C(14)-H(14)	109.9	**C(30)-C(31)-H(31)**	109.5
O(7)-C(15)-C(16)	110.97(17)	**C(32)-C(31)-H(31)**	109.5
O(7)-C(15)-C(14)	112.62(18)	**O(16)-C(32)-C(27)**	105.23(19)
C(16)-C(15)-C(14)	110.82(18)	**O(16)-C(32)-C(31)**	112.70(18)
O(7)-C(15)-H(15)	107.4	**C(27)-C(32)-C(31)**	110.93(17)
C(16)-C(15)-H(15)	107.4	**O(16)-C(32)-H(32)**	109.3
C(14)-C(15)-H(15)	107.4	**C(27)-C(32)-H(32)**	109.3
O(8)-C(16)-C(15)	108.14(18)	**C(31)-C(32)-H(32)**	109.3
O(8)-C(16)-C(11)	109.74(18)	**O(14)-C(30)-H(30)**	109.6
C(15)-C(16)-C(11)	108.98(17)	**C(31)-C(30)-H(30)**	109.6
O(8)-C(16)-H(16)	110.0	**C(28)-C(30)-H(30)**	109.6
C(15)-C(16)-H(16)	110.0	**O(15)-C(31)-C(30)**	107.10(17)
C(11)-C(16)-H(16)	110.0	**O(15)-C(31)-C(32)**	110.86(18)
C(17)-O(10)-C(26)	121.38(18)	**C(30)-C(31)-C(32)**	110.20(18)
C(24)-O(11)-C(27)	116.60(17)	**O(15)-C(31)-H(31)**	109.5
C(27)-O(12)-C(28)	112.83(16)	**C(30)-C(31)-H(31)**	109.5
C(29)-O(13)-H(13)	109(3)	**C(32)-C(31)-H(31)**	109.5

APPENDIX 2: Spectroscopic analysis for selected compounds

NMR Spectroscopy

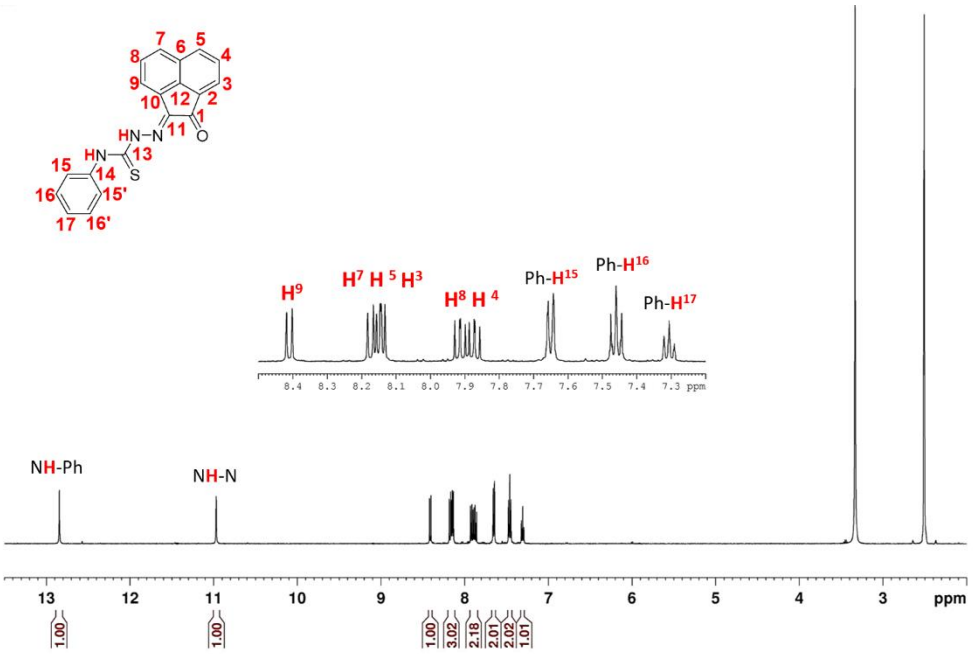

Figure S8: ^{1}H NMR spectrum (500 MHz, DMSO-d_6) presented the monosubstituted ligand PhTSCA (**5a**).

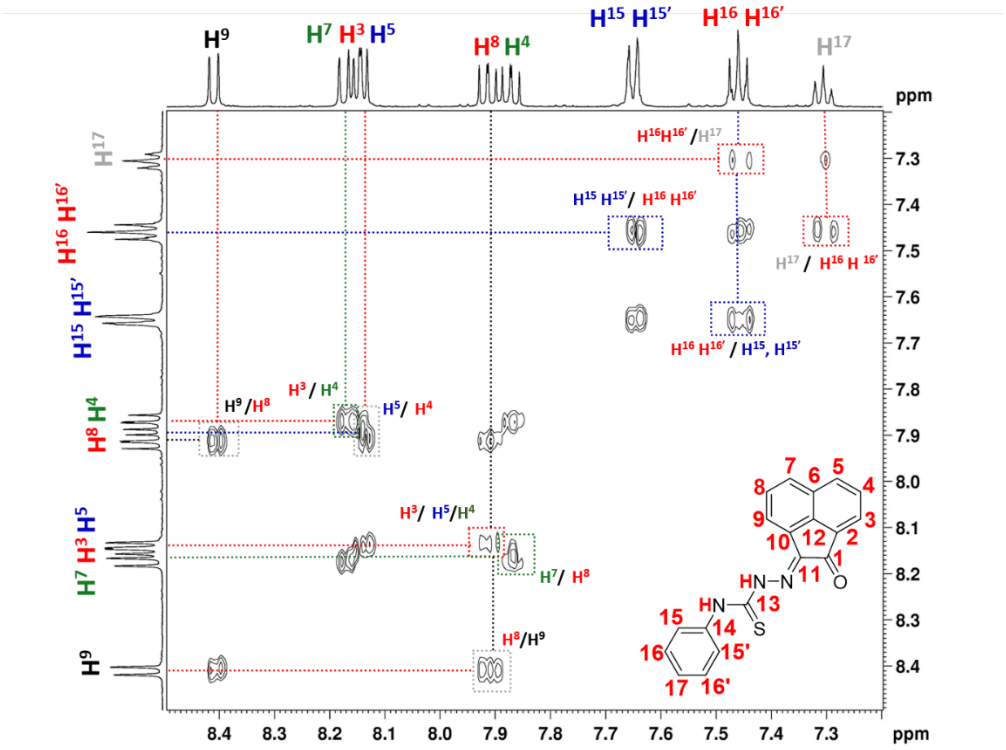

Figure S9: ^{1}H COSY NMR spectrum (500 MHz, DMSO-d_6) presented the monosubstituted ligand PhTSCA (**5a**).

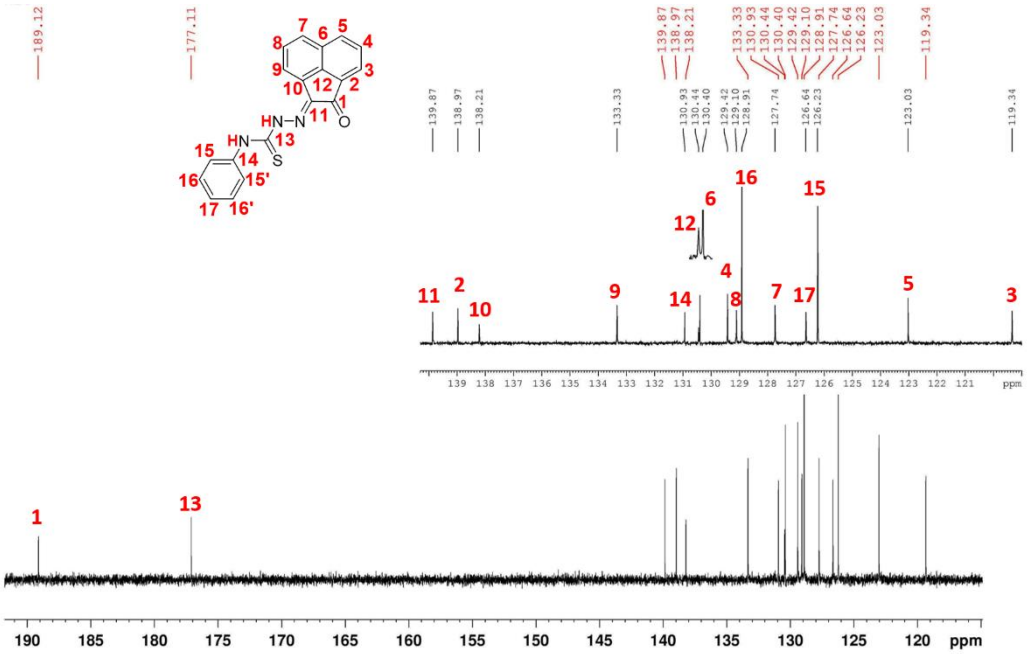

Figure S10: ^{13}C NMR spectrum (500 MHz, DMSO-d_6) presented the monosubstituted ligand PhTSCA (**5a**).

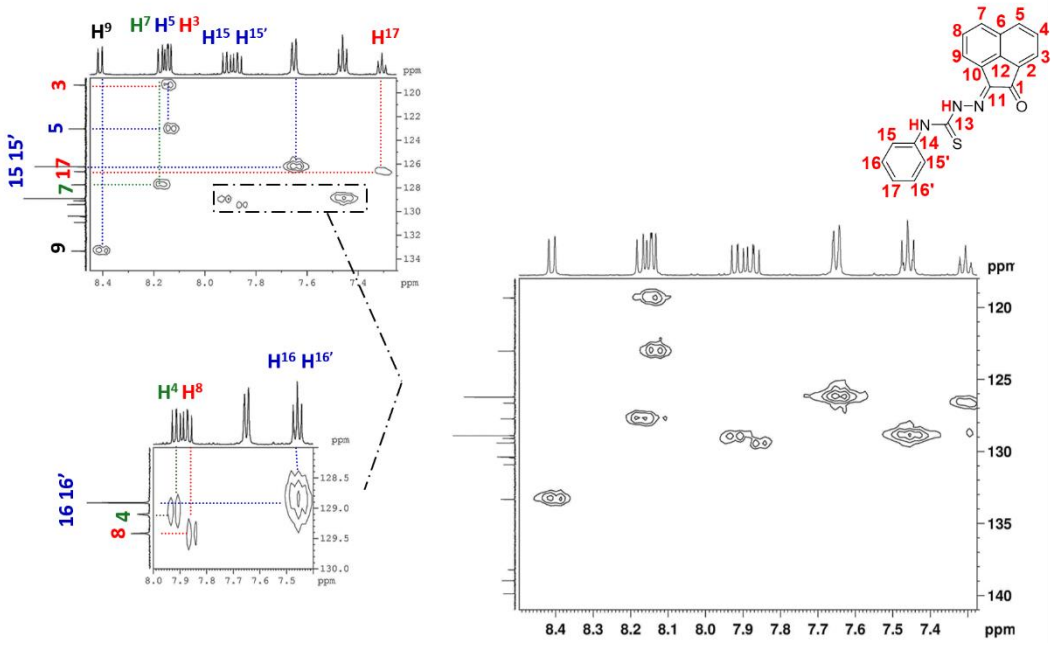

Figure S11: ^{1}H-^{13}C HSQC NMR spectrum (500 MHz, DMSO-d_6) presented the monosubstituted ligand PhTSCA (**5a**).

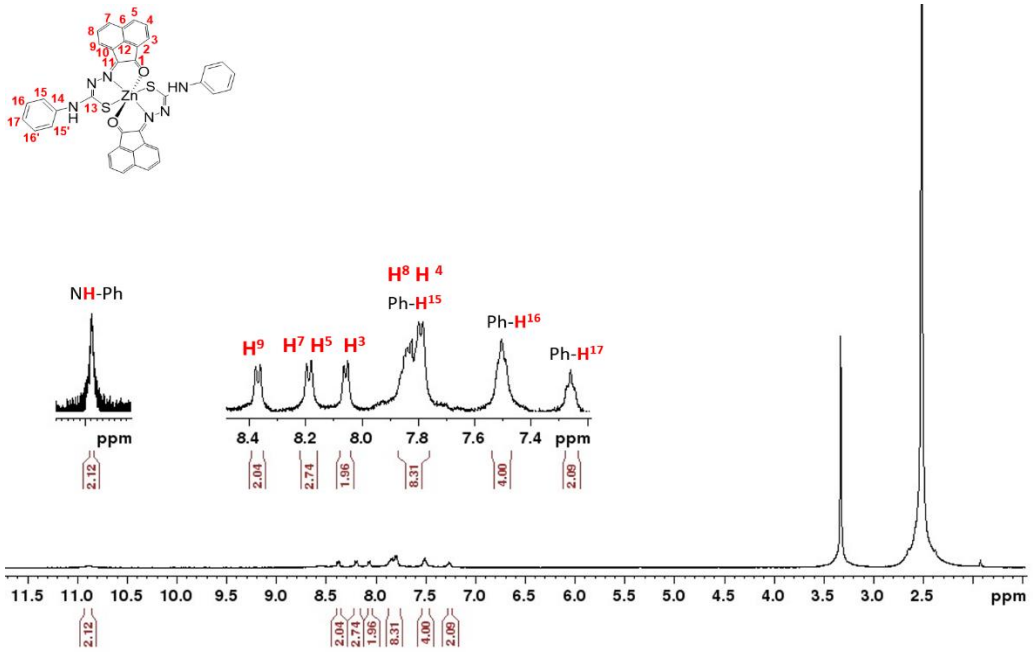

Figure S12: ^{1}H NMR spectrum (500 MHz, DMSO-d_6) presented the Zn(II) coordinated monosubstituted ligand Zn(PhTSCA)$_2$ (**6a**).

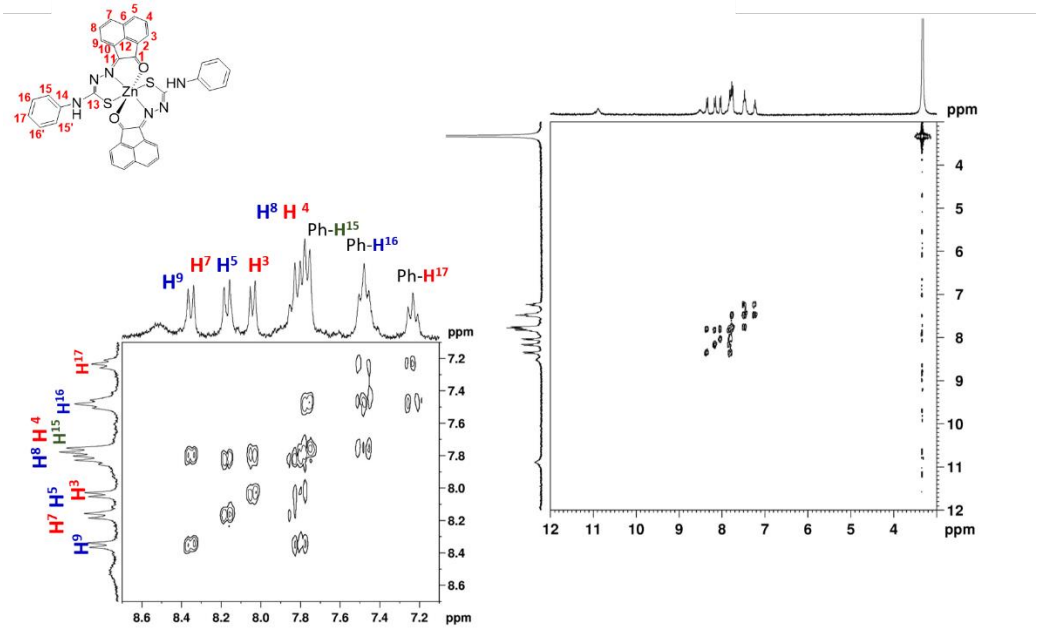

Figure S13: ^{1}H COSY NMR spectrum (500 MHz, DMSO-d_6) presented the Zn(II) coordinated monosubstituted ligand Zn(PhTSCA)$_2$ (**6a**).

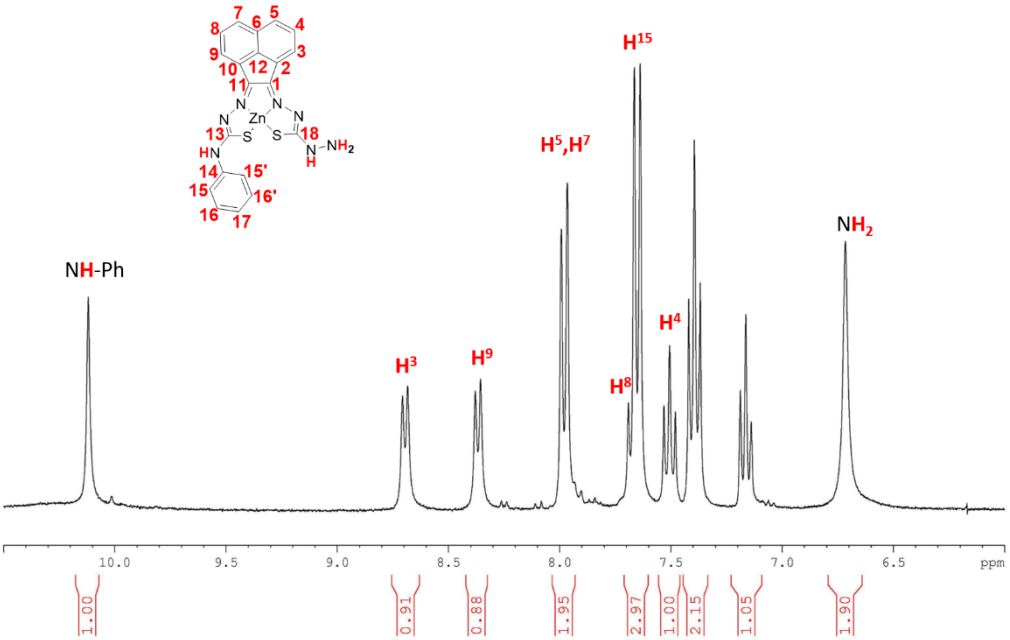

Figure S14: ^{1}H NMR spectrum (500 MHz, DMSO-d_6) of presented the asymmetric PhZnTSCA complex (**9a**).

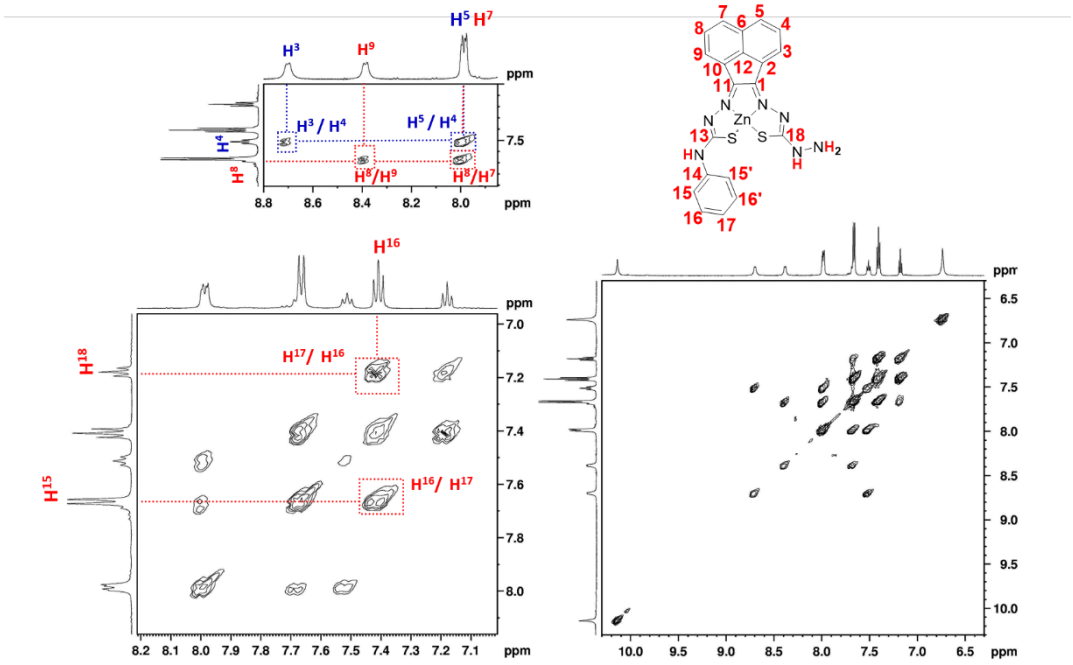

Figure S15: ^{1}H COSY NMR spectrum (500 MHz, DMSO-d_6) presented the asymmetric PhZnTSCA complex (**9a**).

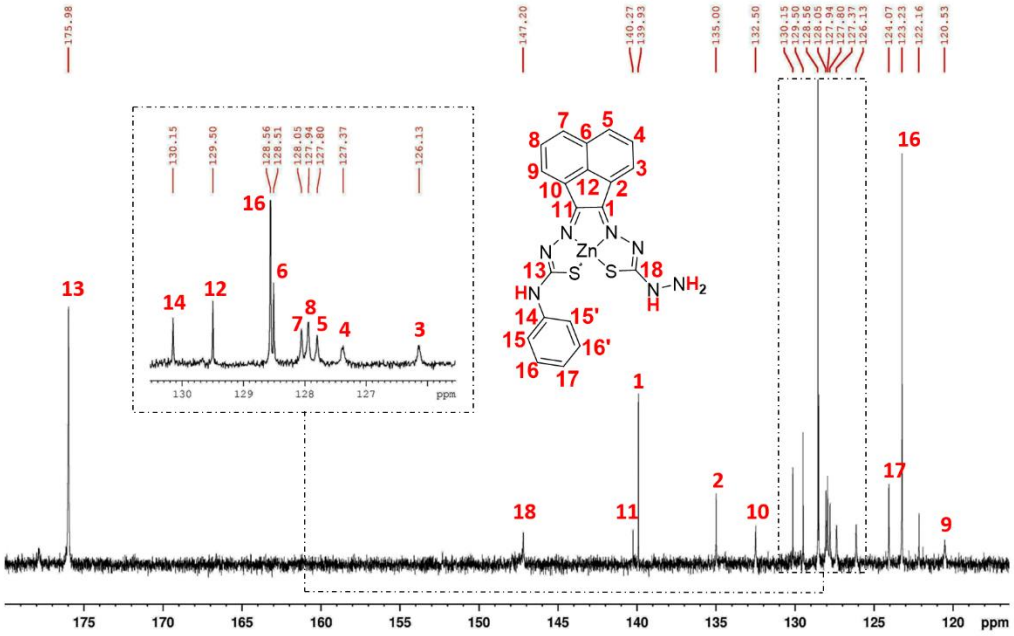

Figure S16: ^{13}C NMR spectrum (500 MHz, DMSO-d_6) presented the asymmetric PhZnTSCA complex (**9a**).

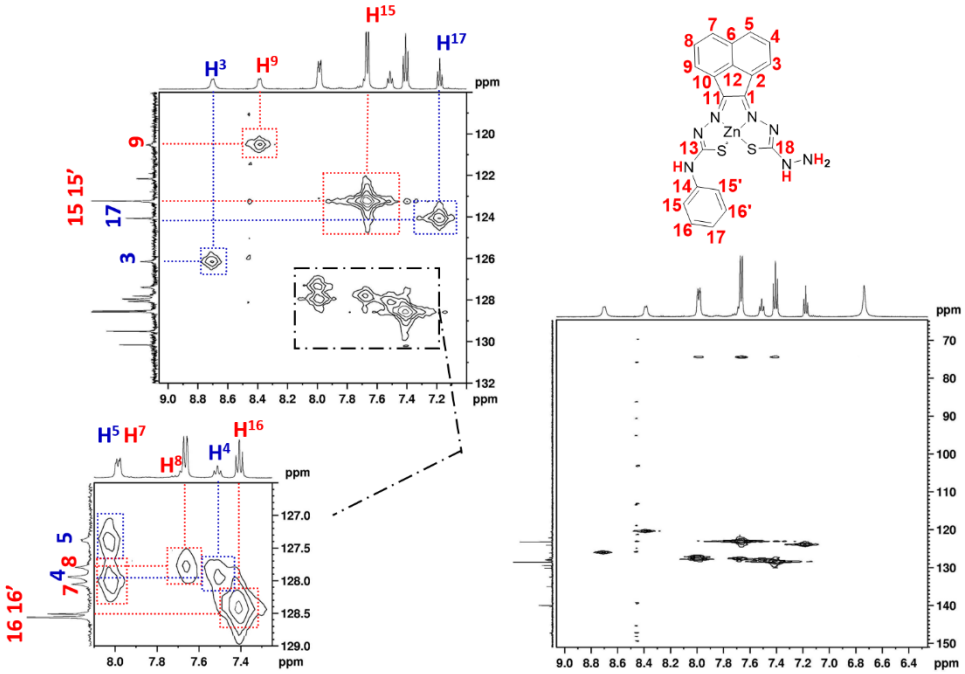

Figure S17: ^{1}H-^{13}C HSQC NMR spectrum (500MHz, DMSO-d_6) presented the asymmetric PhZnTSCA complex (**9a**).

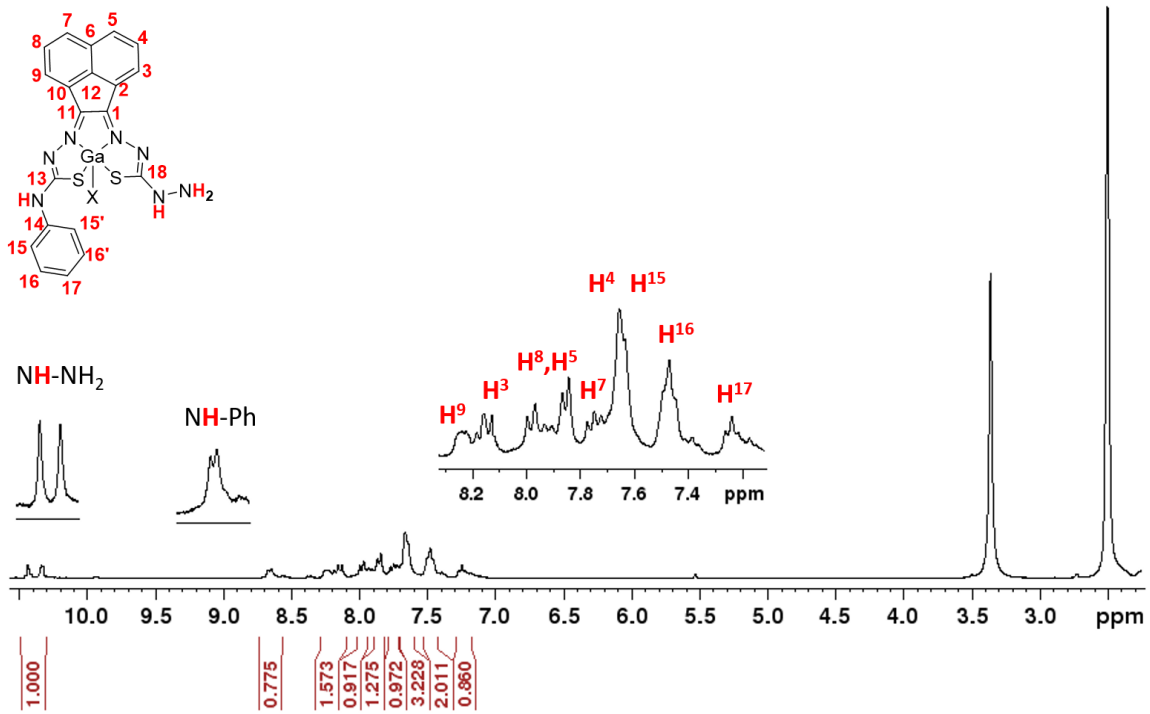

Figure S18: ^{1}H NMR spectrum (300 MHz, DMSO-d_6) of presented the asymmetric PhGaTSCA complex (**10a**).

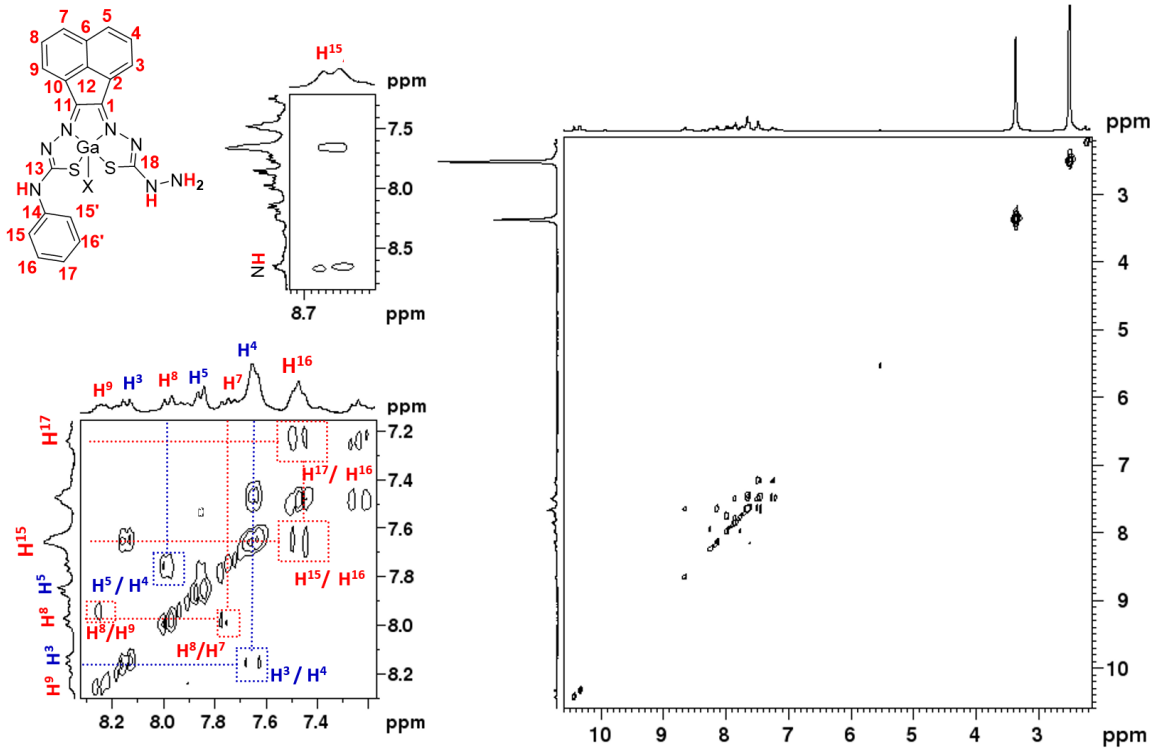

Figure S19: ^{1}H COSY NMR spectrum (300 MHz, DMSO-d_6) presented the asymmetric PhGaTSCA complex (**10a**).

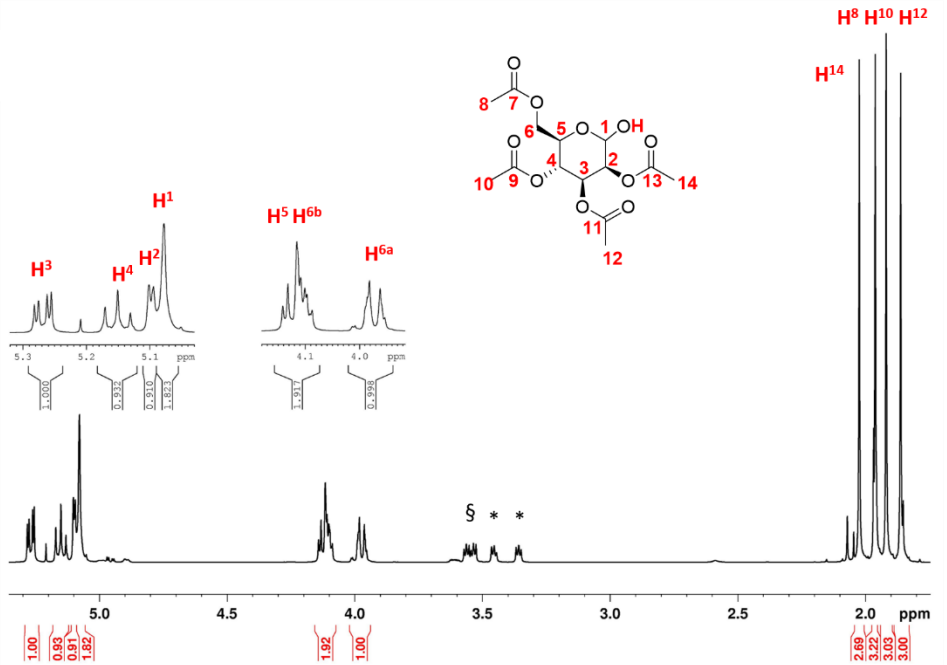

Figure S20: ^{1}H NMR spectra (500 MHz, $CDCl_3$-d_6) presenting the 2,3,4,6-Tetra-O-acetyl-D-mannopyranose (**13**).

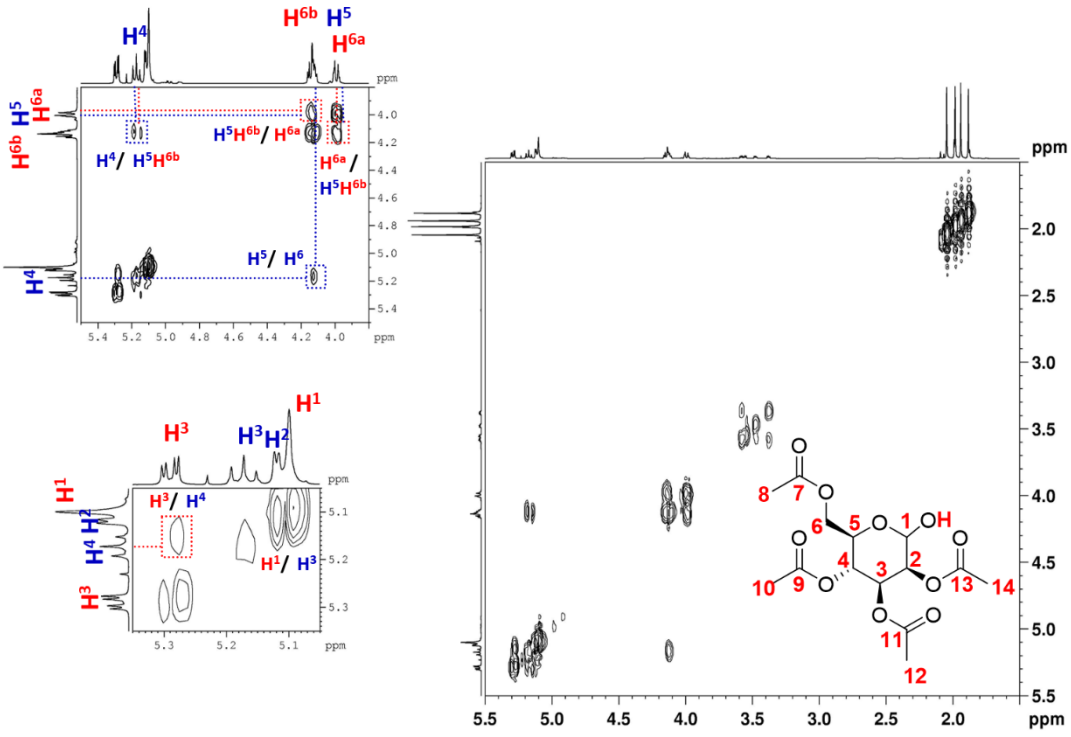

Figure S21: ^{1}H COSY NMR spectra (500 MHz, $CDCl_3$-d_6) presenting the 2,3,4,6-Tetra-O-acetyl-D-mannopyranose (**13**).

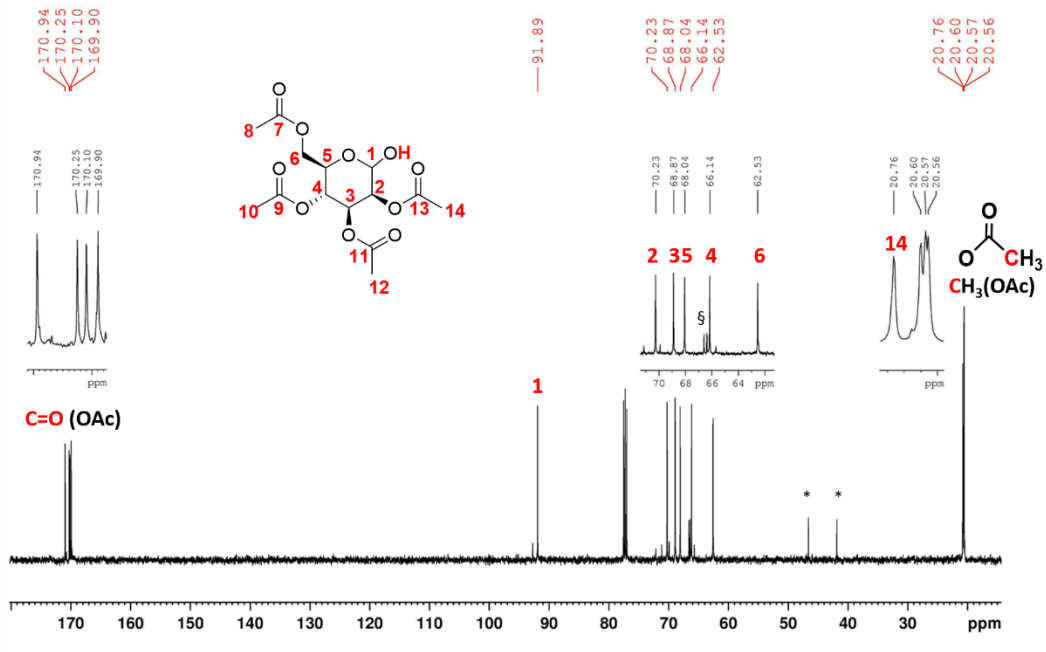

Figure S22: ^{13}C NMR spectra (500 MHz, $CDCl_3$-d_6) presenting the 2,3,4,6-Tetra-O-acetyl-D-mannopyranose (**13**).

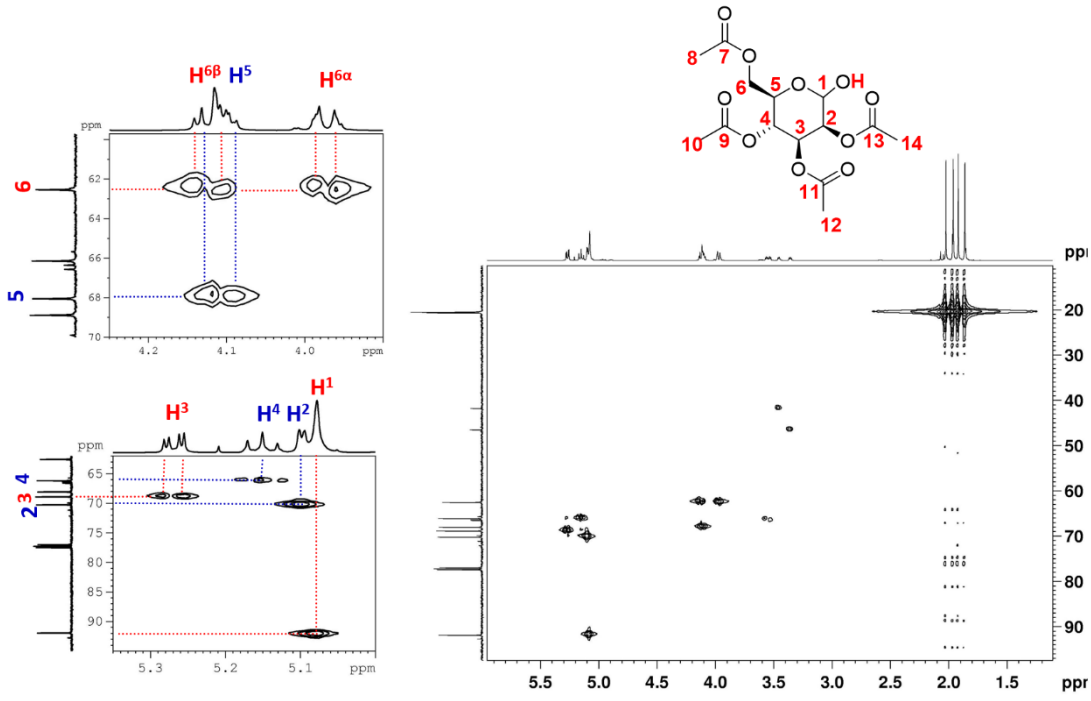

Figure S23: ^{1}H-^{13}C HSQC NMR spectra (500 MHz, $CDCl_3$-d_6) presenting the 2,3,4,6-Tetra-O-acetyl-D-mannopyranose (**13**).

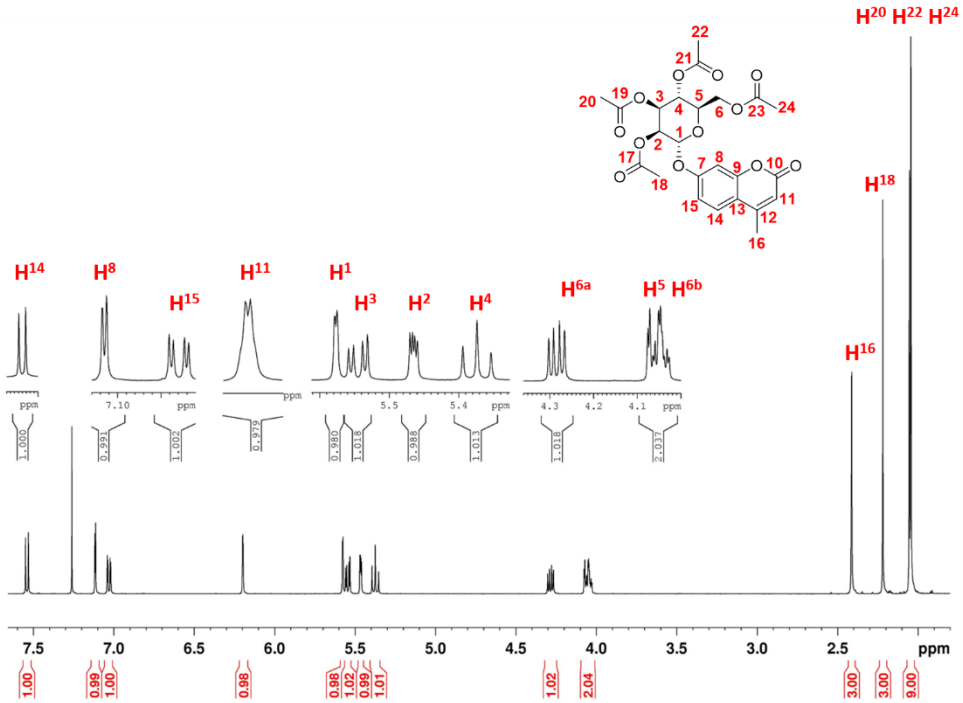

Figure S24: ^{1}H NMR spectra (500 MHz, $CDCl_3$-d_6) presenting the 4- Methylumbelliferyl-7-yl-2,3,4,6-Tetra-O-acetyl- α -D-mannopyranose (AcGC, **15**).

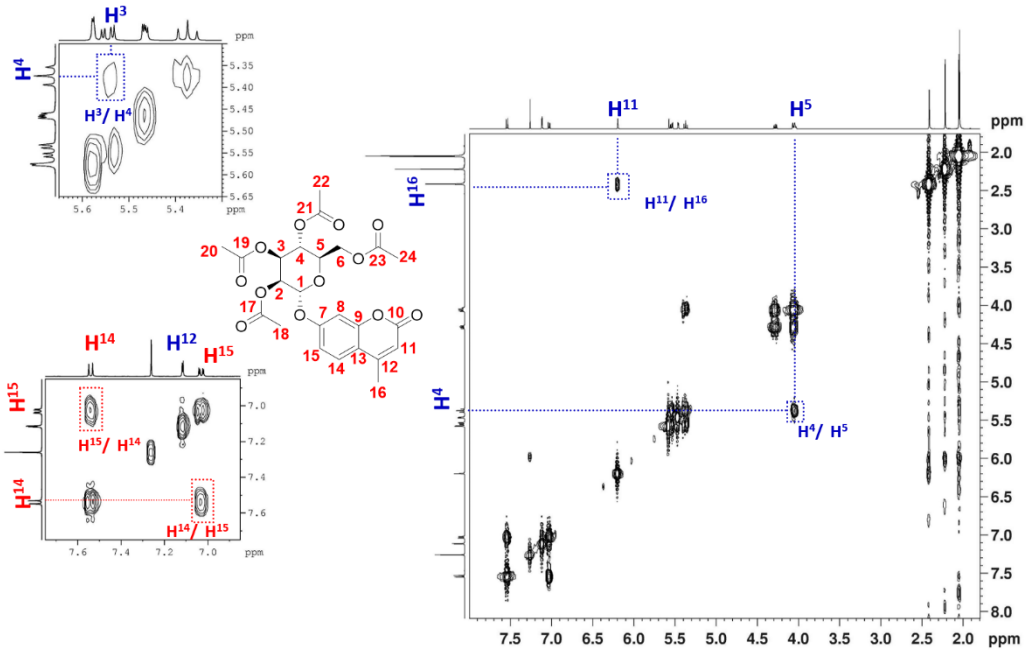

Figure S25: ^{1}H COSY NMR spectra (500 MHz, $CDCl_3$-d_6) presenting the 4- Methylumbelliferyl-7-yl-2,3,4,6-Tetra-O-acetyl- α -D-mannopyranose (AcGC, **15**).

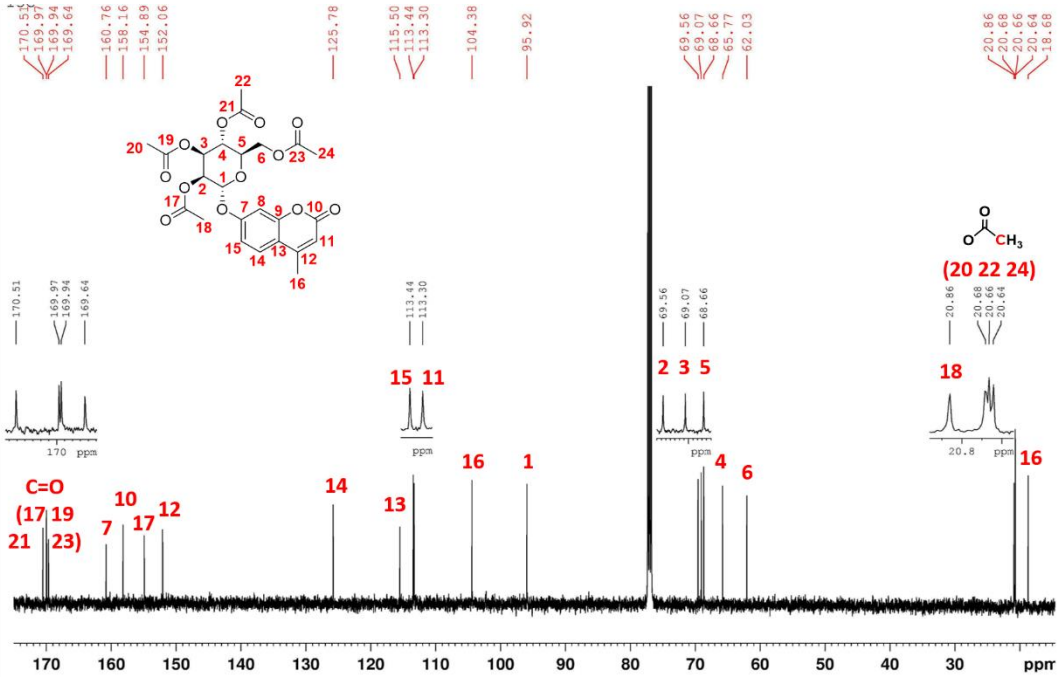

Figure S26: ^{13}C NMR spectra (500 MHz, $CDCl_3$-d_6) presenting the 4- Methylumbelliferyl-7-yl-2,3,4,6-Tetra-O-acetyl- α -D-mannopyranose (AcGC, **15**).

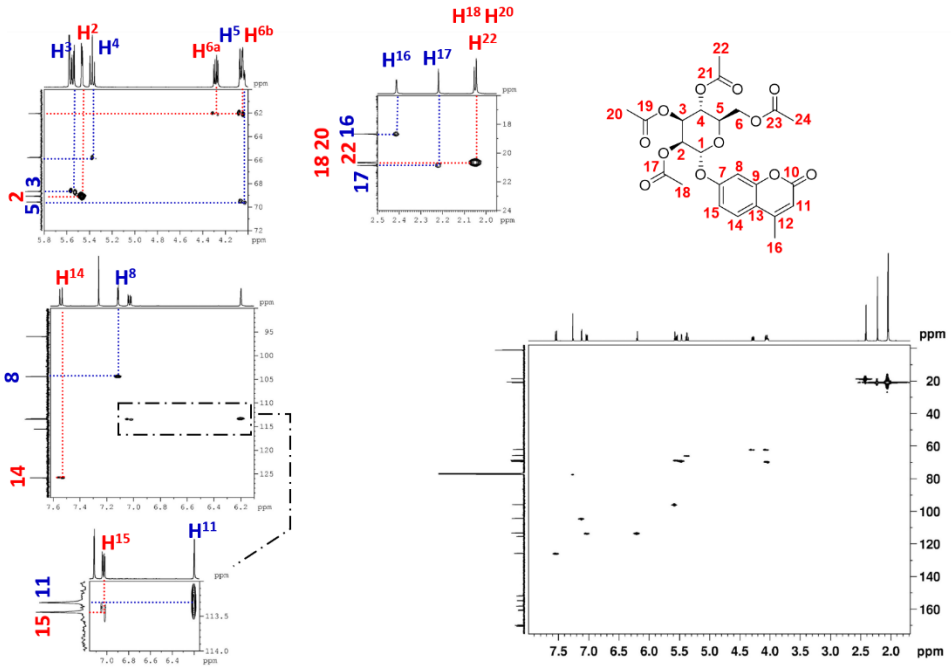

Figure S27: ^{1}H-^{13}C HSQC NMR spectra (500 MHz, $CDCl_3$-d_6) presenting the 4-Methylumbelliferyl-7-yl-2,3,4,6-Tetra-O-acetyl- α -D-mannopyranose (AcGC, **15**).

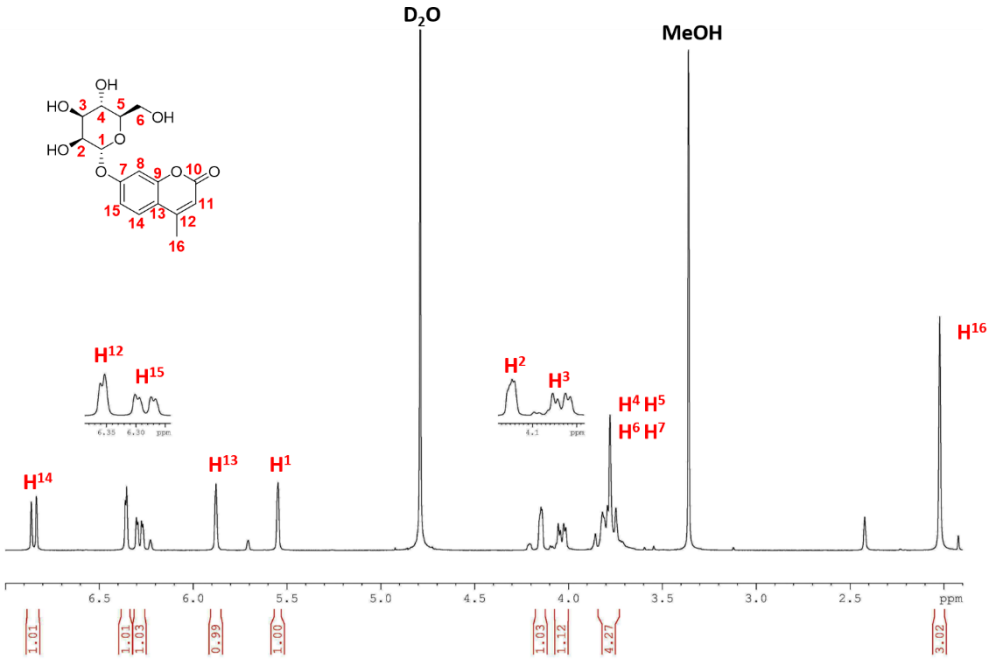

Figure S28: ^{1}H NMR spectra (500 MHz, MeOD-d_6) presenting the 4- Methylumbelliferyl-7-yl - α -D-mannopyranose (GC, **16**).

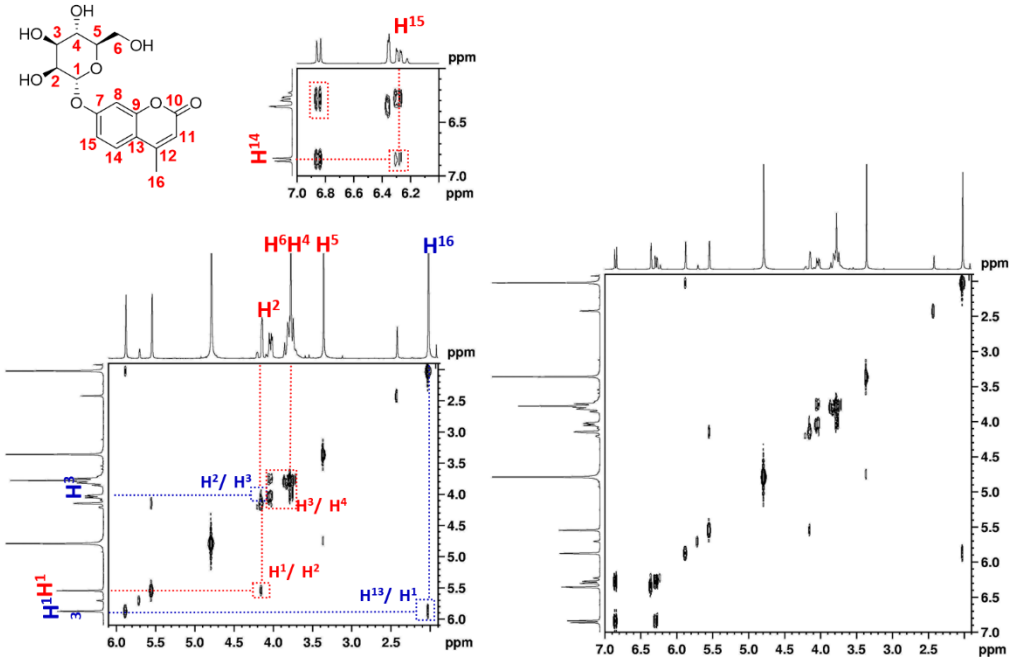

Figure S29: ^{1}H COSY NMR spectra (500 MHz, MeOD-d_6) presenting the 4- Methylumbelliferyl-7-yl - α -D-mannopyranose (GC, **16**).

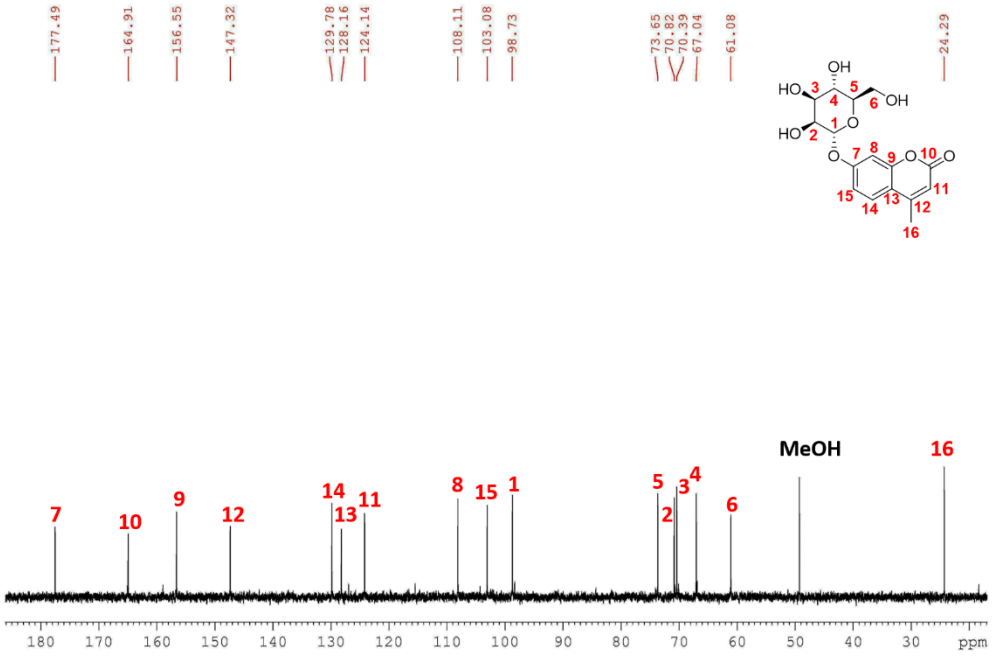

Figure S30: ^{13}C NMR spectra (500 MHz, MeOD-d_6) presenting the 4- Methylumbelliferyl-7-yl - α -D-mannopyranose (GC, **16**).

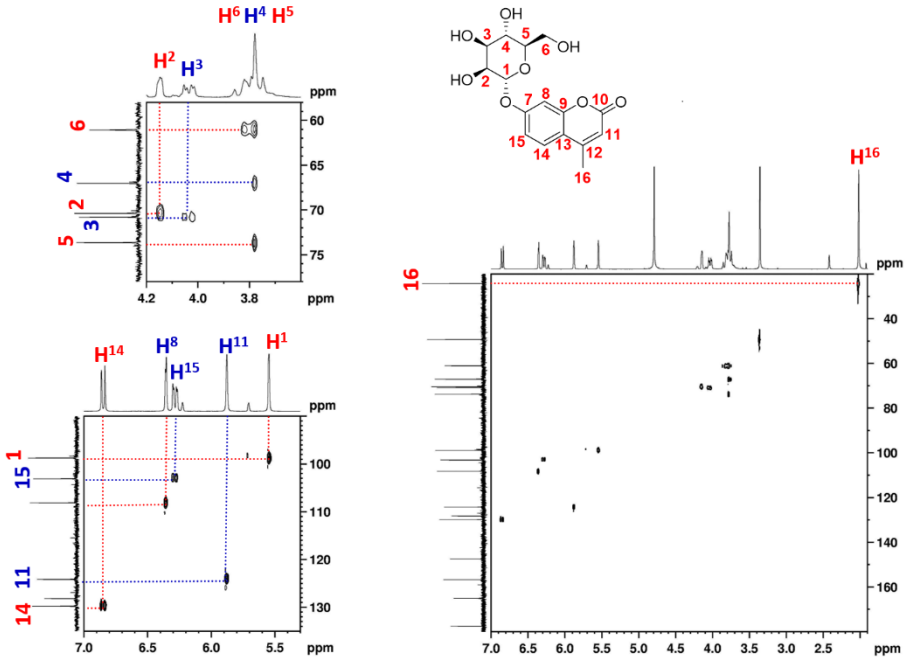

Figure S31: ^{1}H-^{13}C HSQC NMR spectra (500 MHz, MeOD-d_6) presenting the 4- Methylumbelliferyl-7-yl - α -D-mannopyranose (GC, **16**).

Mass spectrometry

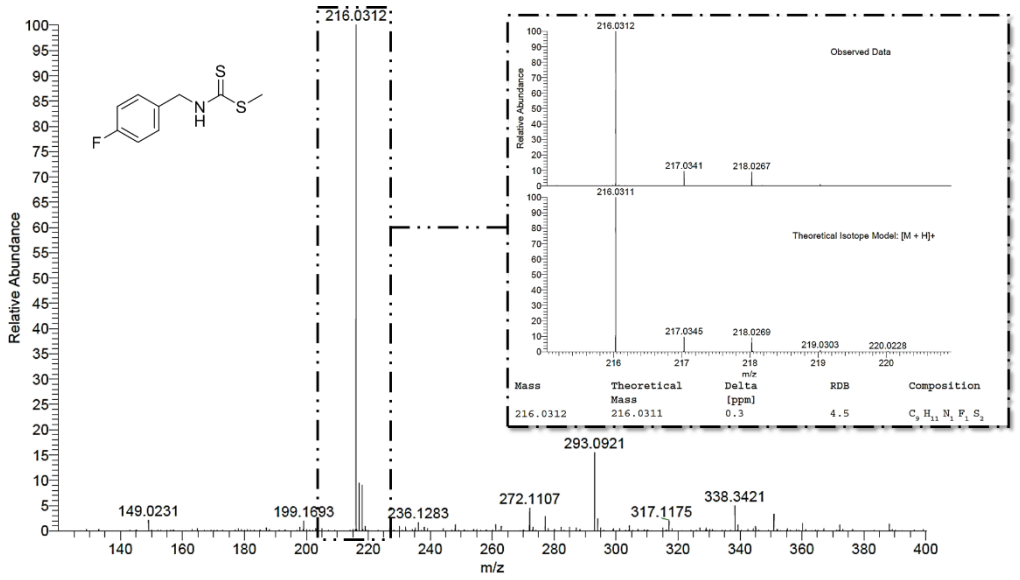

Figure S32: ESI-MS analysis mass spectrometry results for methyl (4-fluorobenzyl)carbamodithioate (FbnzMeCDT, **2e**).

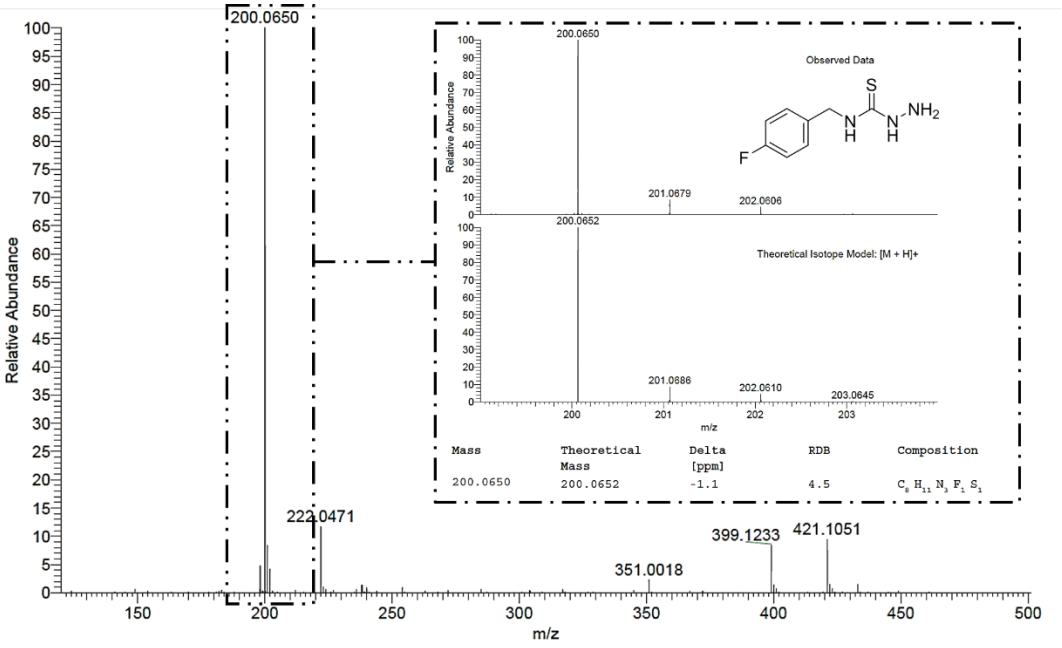

Figure S33: ESI-MS analysis mass spectrometry results for N-(4-fluorobenzyl)hydrazinecarbothioamide (Fbnz-TSC, **3e**).

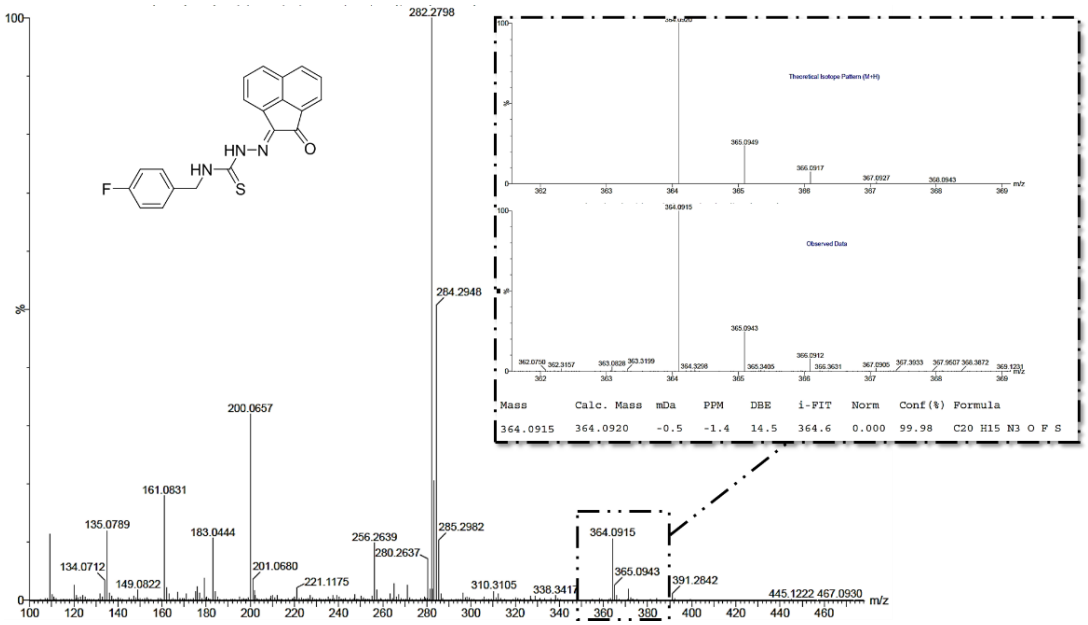

Figure S34: ESI-MS analysis mass spectrometry results for 4-F-benzyl-3-thiosemicarbazone acenaphthenequinone (FbnzTSCA, **5e**)

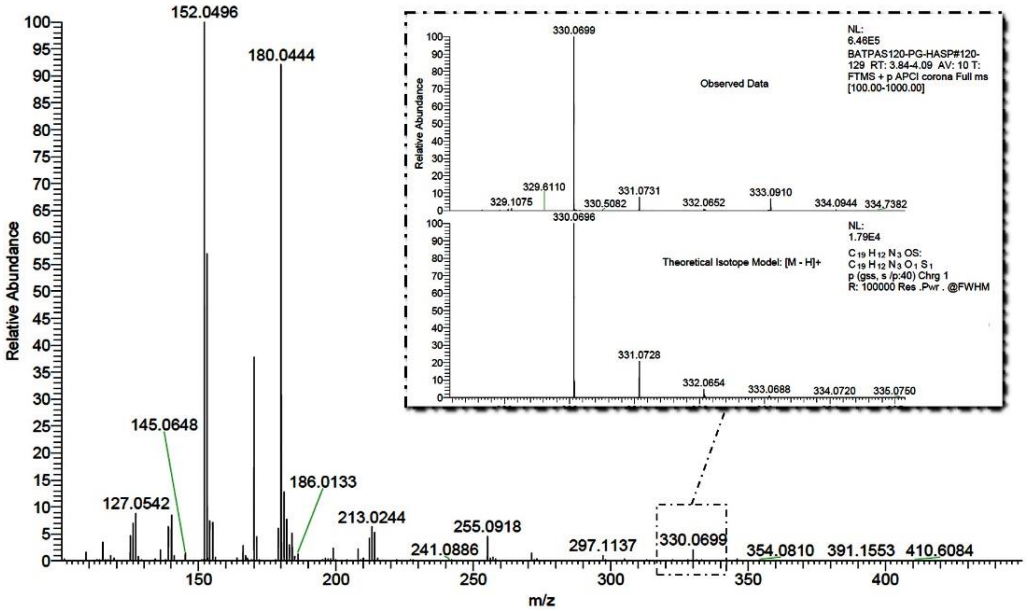

Figure S35: ESI-MS analysis mass spectrometry results for 4-phenyl-3-thiosemicarbazone acenaphthenequinone (PhTSCA, **5a**).

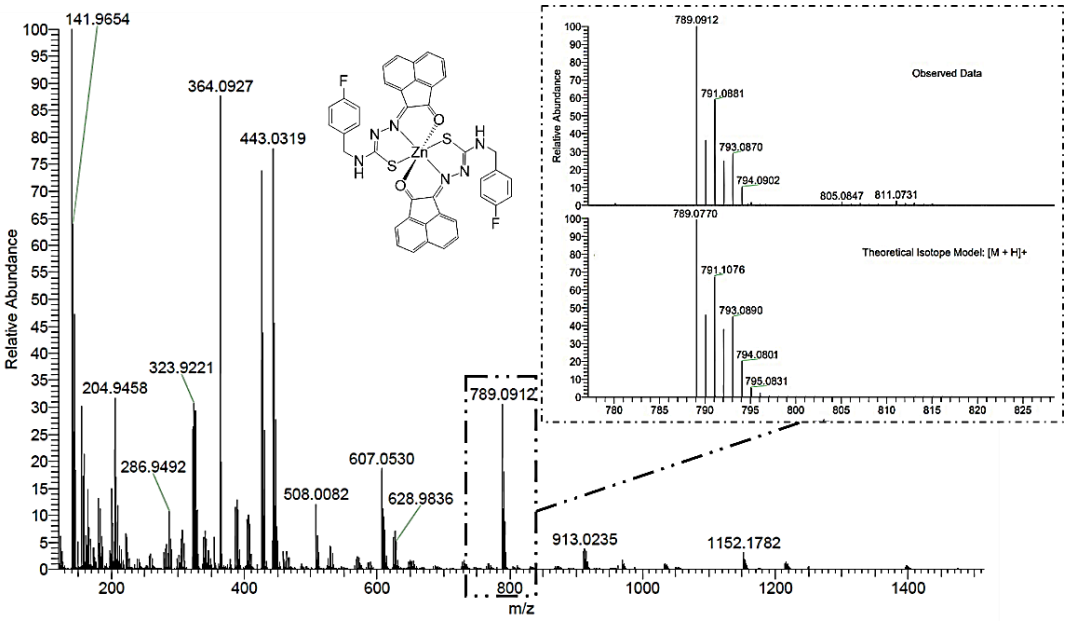

Figure S36: ESI-MS analysis mass spectrometry result for the Zinc(II) [mono (F-benzyl thiosemicarbazonate- acenaphthenequinone]$_2$ (**6e**). (Full spectrum of figure 25 – Chapter 2).

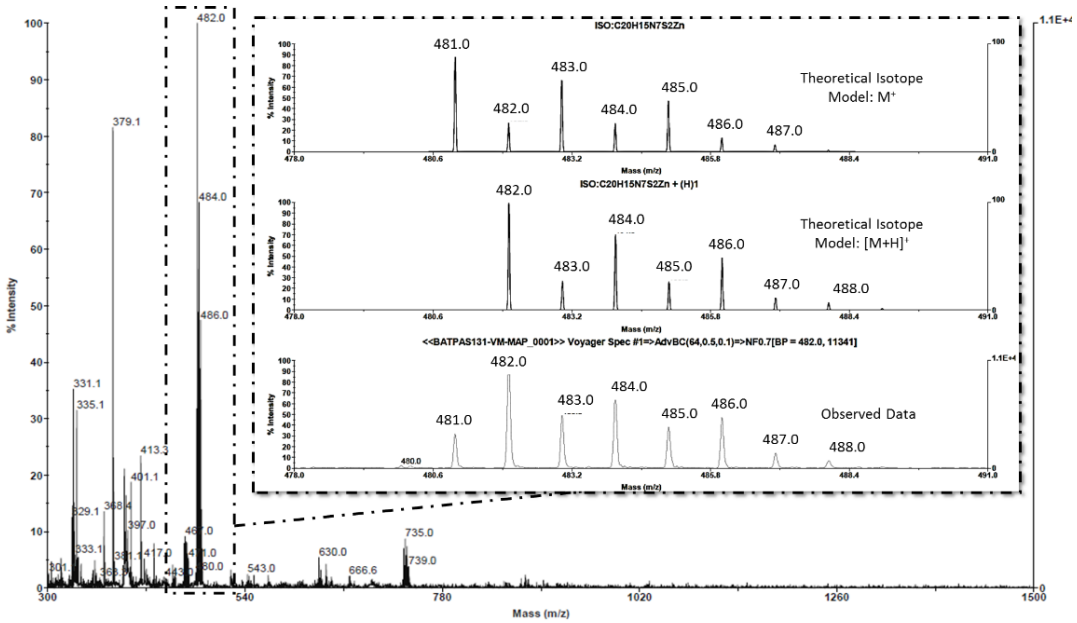

Figure S37: MALDI analysis mass spectrometry result for the Zinc(II) 4-phenyl-3-thiosemicarbazone-thiocarbohydrazide acenaphthenequinone (**9a**). (Full spectrum of figure 34 -Chapter 3).

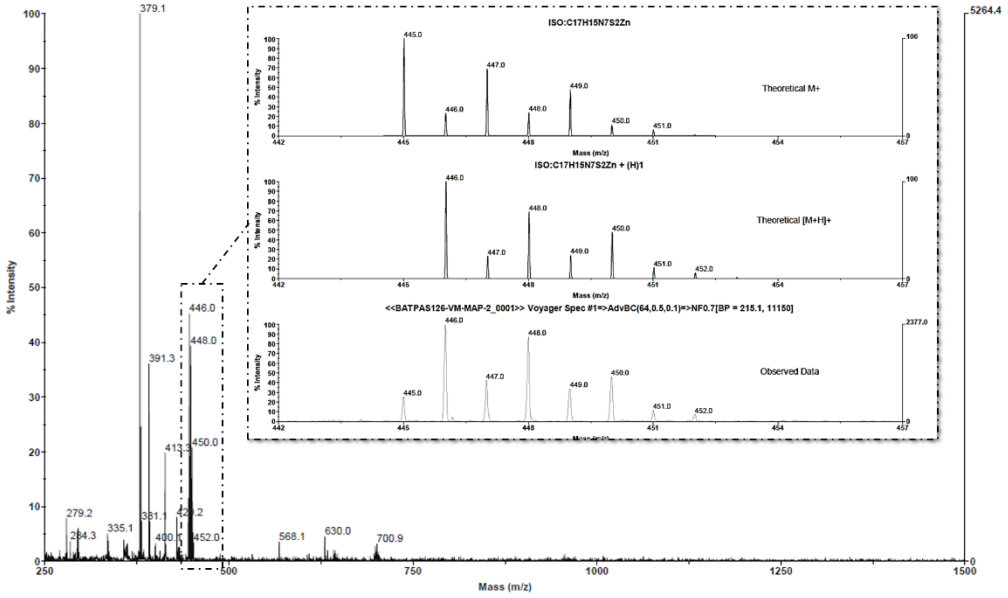

Figure S38: MALDI analysis mass spectrometry result for the Zinc(II) 3-allyl-3-thiosemicarbazone-thiocarbohydrazide acenaphthenequinone (**9b**). (Full spectrum of figure 33 - Chapter 3).

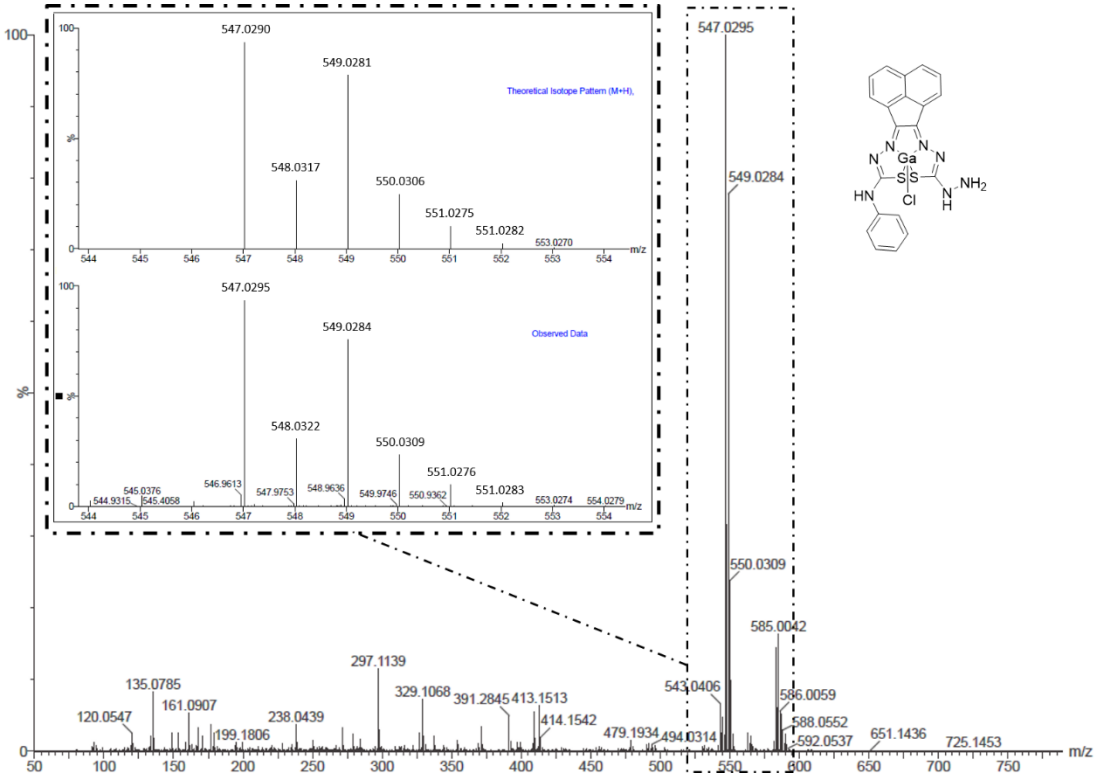

Figure S39: TOF-MS analysis mass spectrometry result for the Ga(III) 4-phenyl-3-thiosemicarbazone-thiocarbohydrazide acenaphthenequinone (**10a**).

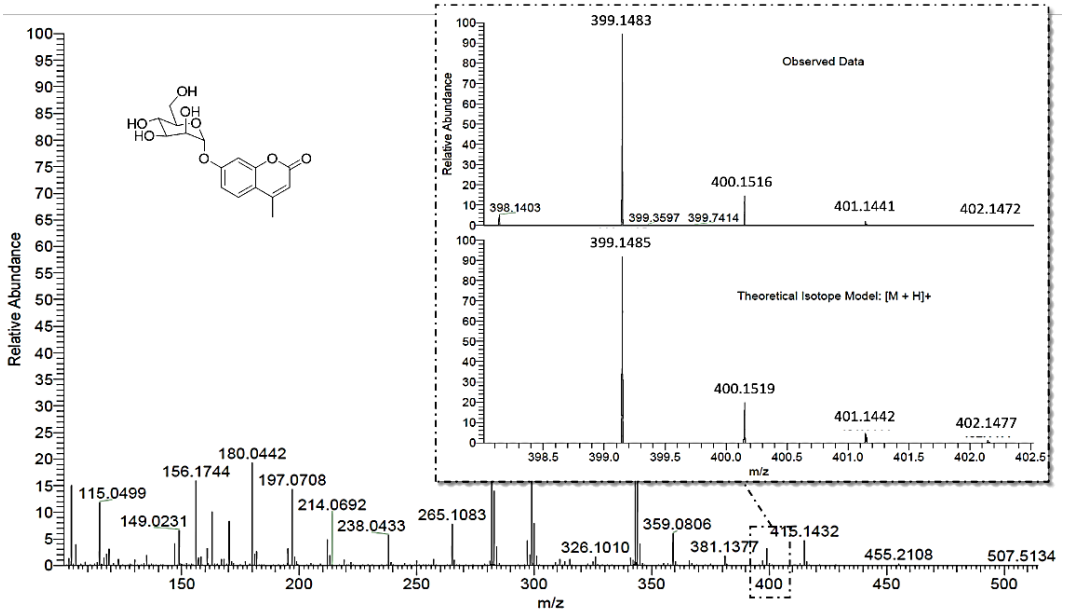

Figure S40: nano-ESI analysis mass spectrometry result for GC (**16**).

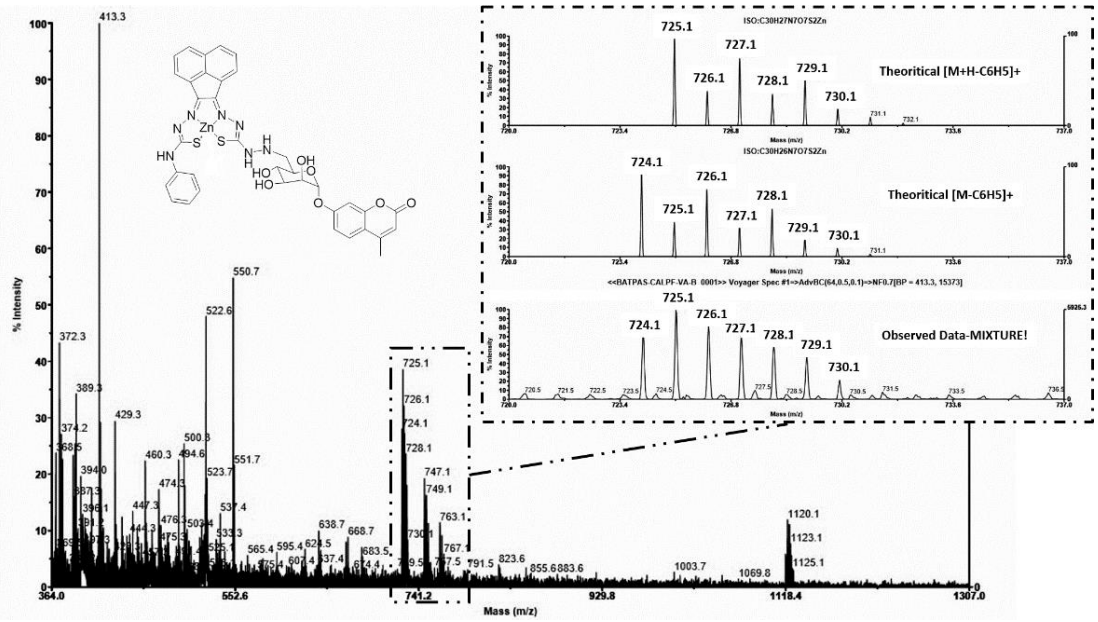

Figure S41: Atmospheric-pressure chemical ionization (APCI) analysis mass spectrometry result for the complex **17** (Ph-GC-ZnTSCA). (Full spectrum of figure 47 – Chapter 3).

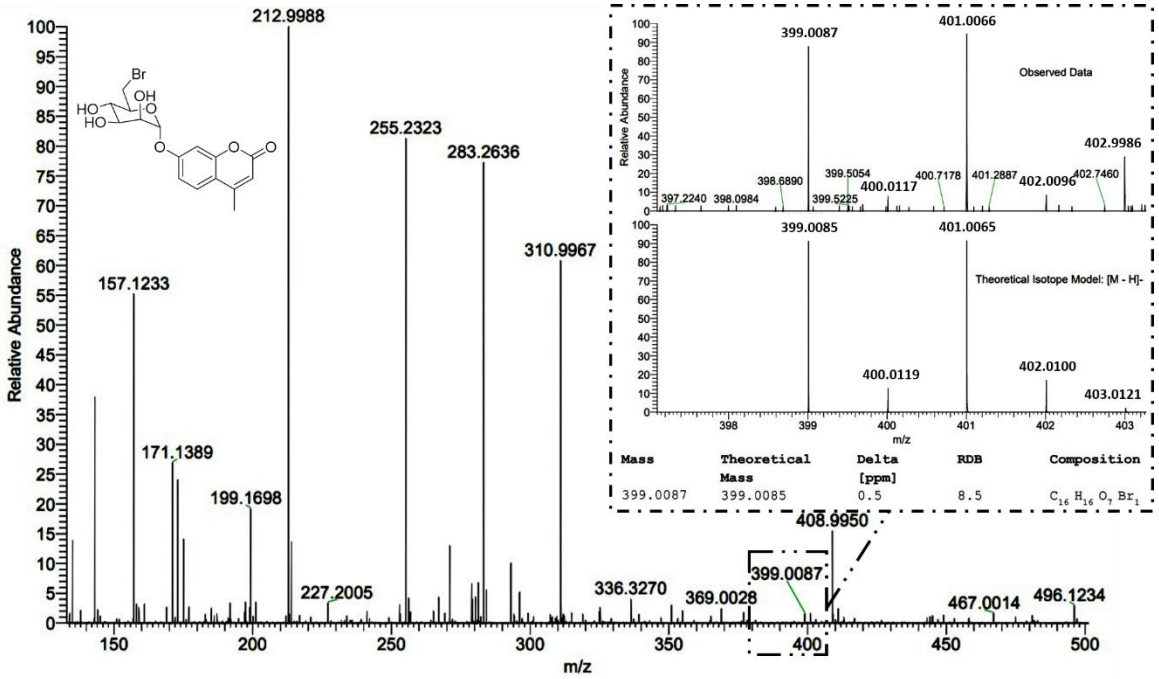

Figure S42: nano-ESI analysis mass spectrometry result for BrGC (**19**). (Full spectrum of figure 48 – Chapter 3).

IR Spectroscopy

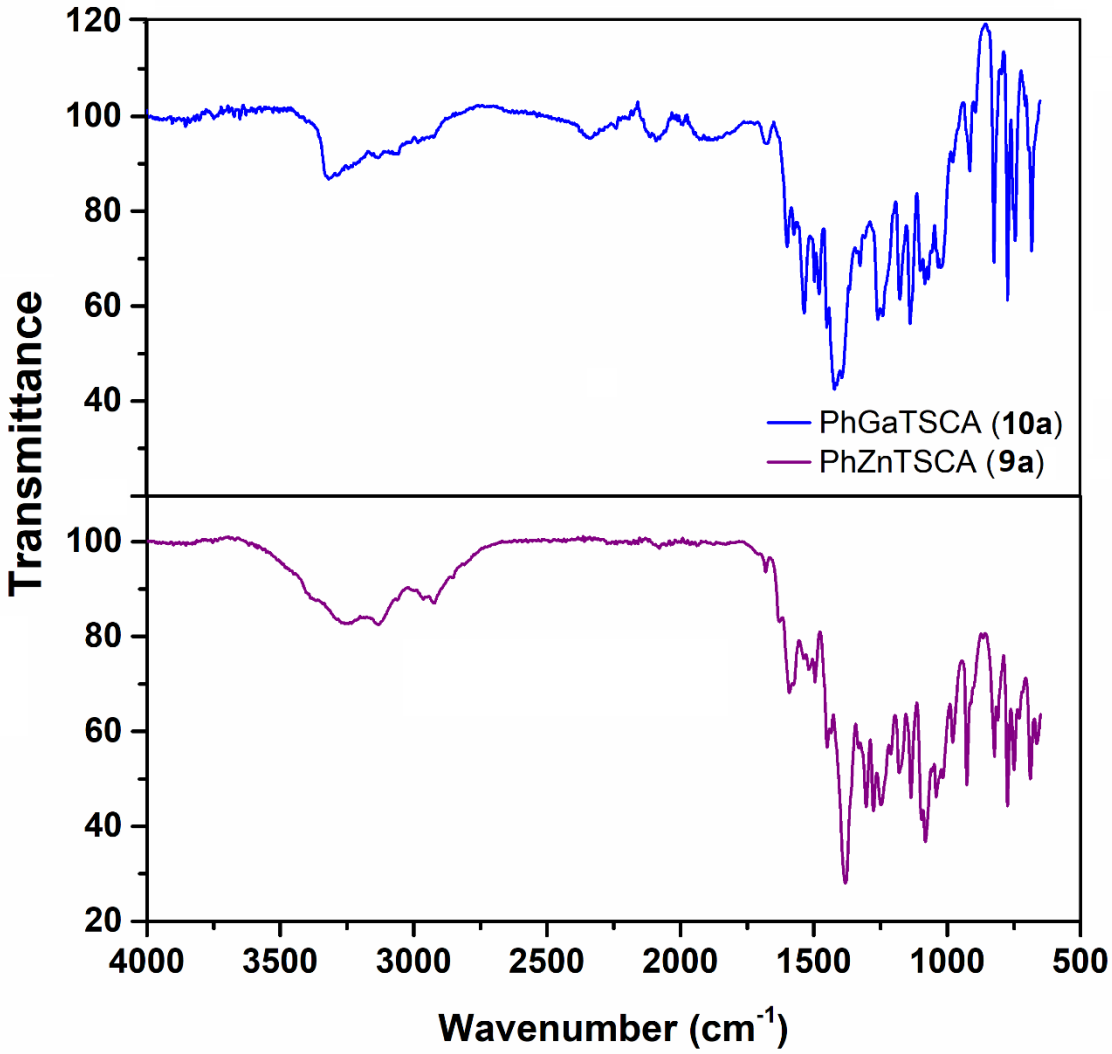

Figure S43: Comparative FTIR spectra for the Zn(II) 4-phenyl-3-thiosemicarbazone-thiocarbohydrazide acenaphthenequinone (**9a**, violet) and the Ga(III) 4-phenyl-3-thiosemicarbazone-thiocarbohydrazide acenaphthenequinone (**10a**, blue).

APPENDIX 3: Radiochemical experiments

Table S16: Summary of the different conditions at the experiments attempted for optimisation of the transmetallation reaction of the asymmetric thiosemicarbazonato complexes of Zn(II) with $^{68}Ga[GaCl_3]$. The pH of the reactions was always between 4 and 6.

Solvent	Solvent in which complex was diluted	Complex: Solvent	Solvent / Activity	Buffer NaOAC (pH): Solvent	T (°C)	Time (min)	R.O.I.
EtOH	2 mg/mL in DMSO	1:10	1 ml / 1.2 mCi	-	95 °C h	40 + 20	X
EtOH	2 mg/mL in DMSO	1:12	1 ml / 37 MBq	-	95 °C h	45	3.5 %
EtOH	2 mg/mL in DMSO	1:12	1 ml / 37 MBq		95 °C μW	45	3.2 %
MeOH	2 mg/mL in DMSO	1:10	1 ml / 37 MBq	-	95 °C h	30	X
MeOH	2 mg/mL in DMSO	1:20	1 ml / 37 MBq	-	95 °C h	45	X
EtOH	2 mg/mL in DMF	1:10	1 ml / 37 MBq	-	95 °C h	30	X
EtOH	2 mg/mL in DMF	1:20	1 ml / 37 MBq	-	95 °C h	30	X
MeOH	2 mg/mL in DMF	1:10	1 ml / 0.5 mCi	-	95 °C h	30	X

						+ 30	
MeOH	2 mg/mL in DMF	1:10	1 ml / 17.5 MBq	-	110 °C µW	25	X
				-	130 °C µW	+ 20	
DMF	2 mg/mL in DMF	1:10	1 ml / 22.2 MBq	-	110 °C µW	45	X
NaCl/HCl	2 mg/mL in DMSO	1:25	1 ml / 37 MBq	1:1 (pH: 3.9)	95 °C h	40	X
NaCl/HCl	2 mg/mL in DMSO	1:30	1 ml / 37 MBq	1:1.2 (pH: 3.9)	95 °C h	40	X
EtOH	2 mg/mL in DMSO	1:15	1 ml / 37 MBq	-	95 °C h	30	-
EtOH	2 mg/mL in DMSO	1:15	1 ml / 37 MBq	-	110 °C h	30	X
EtOH	2 mg/mL in DMSO	1:20	1 ml / 37 MBq	-	95 °C h	30	2.5 %
EtOH	2 mg/mL in DMSO	1:20	1 ml / 37 MBq	-	95 °C h	60	2.8 %
EtOH	2 mg/mL in DMSO	1:20	1 ml / 37 MBq	-	110 °C h	30	X
EtOH	2 mg/mL in DMSO	1:8	1 ml / 37 MBq	-	95 °C h	30	X
EtOH	2 mg/mL in DMSO	1:8	1 ml / 37 MBq	-	110 °C h	30	X
EtOH	2 mg/mL in DMSO	1:8	1 ml / 37 MBq	1:3 (pH: 4.56)	95 °C h	30	25 %
EtOH	2 mg/mL in DMSO	1:8	1 ml / 37 MBq	1:3 (pH: 4.56)	95 °C µW	30	25 %
EtOH	2 mg/mL in DMSO	1:10	1 ml / 37 MBq	1:10 (pH: 4.56)	95 °C h	30	46 %
EtOH	2 mg/mL in DMSO	1:10	1 ml / 37 MBq	1:10 (pH: 4.56)	95 °C µW	30	23 %

EtOH	2 mg/mL in DMSO	1:10	1 ml / 29.6 MBq	1:10 (pH: 4.56)	95 °C h	30	18 %
EtOH	2 mg/mL in DMSO	1:10	1 ml / 29.6 MBq	1:10 (pH: 4.56)	95 °C μW	30	11 %
EtOH	2 mg/mL in DMSO	1:10	1 ml / 37 MBq	1:10 (pH: 3.9)	95 °C h	30	29 %
EtOH	2 mg/mL in DMSO	1:10	1 ml / 37 MBq	1:10 (pH: 3.9)	95 °C μW	30	Very low ROI
EtOH	2 mg/mL in DMSO	1:10	1 ml / 29.6 MBq	1:17.5 (pH: 4.56)	95 °C h	30	35 %

Radio Thin Layer Chromatography:

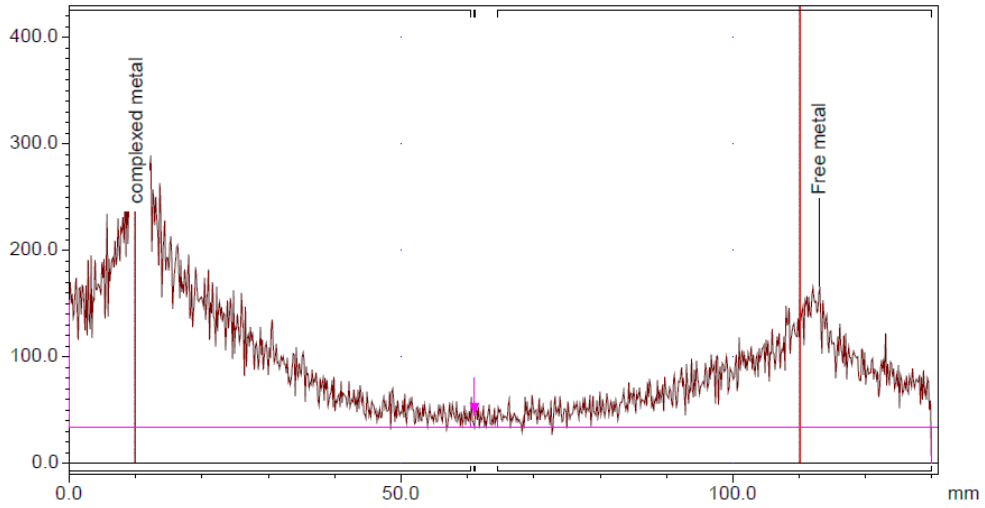

Name	Start (mm)	End (mm)	Retention (RF)	Area (Counts)	%ROI (%)	%Total (%)
complexed metal	0.0	60.5	0.003	34182.0	63.88	63.68
BP 1	61.1	61.2	0.511			
Free metal	64.5	129.9	1.030	19325.0	36.12	36.00
2 Peaks				53507.0	100.00	99.68

Total Area: 53681.0 Counts
Average Background: 34.0 Counts

Figure S44: Radio TLC of crude **[^{68}Ga]-7e** ([^{68}Ga]Ga(FbnzTSCA)$_2$), developed on Whatman 3 MM with 0.35 M ethylenediaminetetraacetic acid (EDTA) as the mobile phase. The radio-TLC shows 36 % of free [^{68}Ga]GaCl$_3$. This TLC was ontained after a conventional heating reaction.

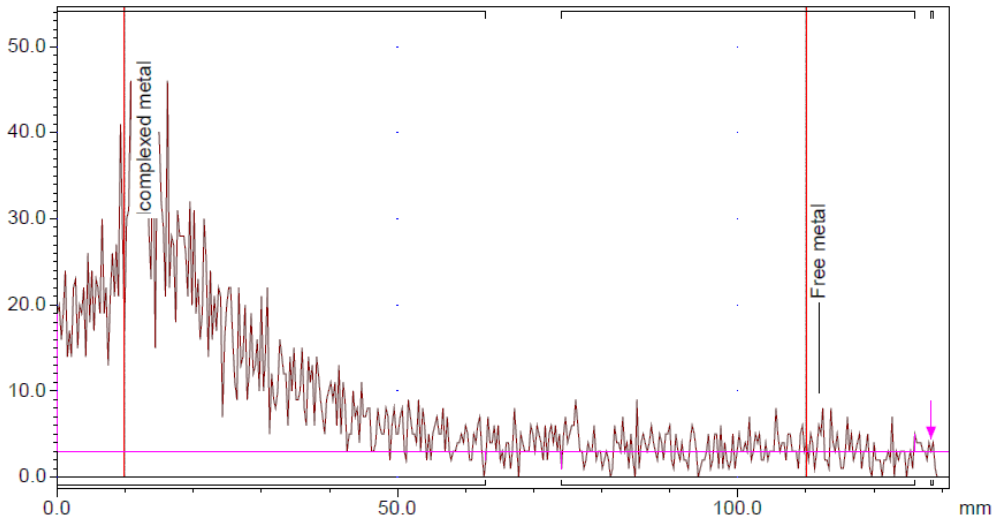

Name	Start (mm)	End (mm)	Retention (RF)	Area (Counts)	%ROI (%)	%Total (%)
complexed metal	0.0	63.0	0.030	2535.0	97.80	96.61
Free metal	74.1	126.0	0.707	57.0	2.20	2.17
BP 1	128.4	128.7	1.183			
2 Peaks				2592.0	100.00	98.78

Total Area: 2624.0 Counts
Average Background: 3.0 Counts

Figure S45: Radio TLC of crude **[^{68}Ga]-25**, developed on Whatman 3 MM with 0.35 M ethylenediaminetetraacetic acid (EDTA) as the mobile phase. The radio-TLC shows minimum amount of free [^{68}Ga]GaCl$_3$ (Figure 65b – Chapter 4).

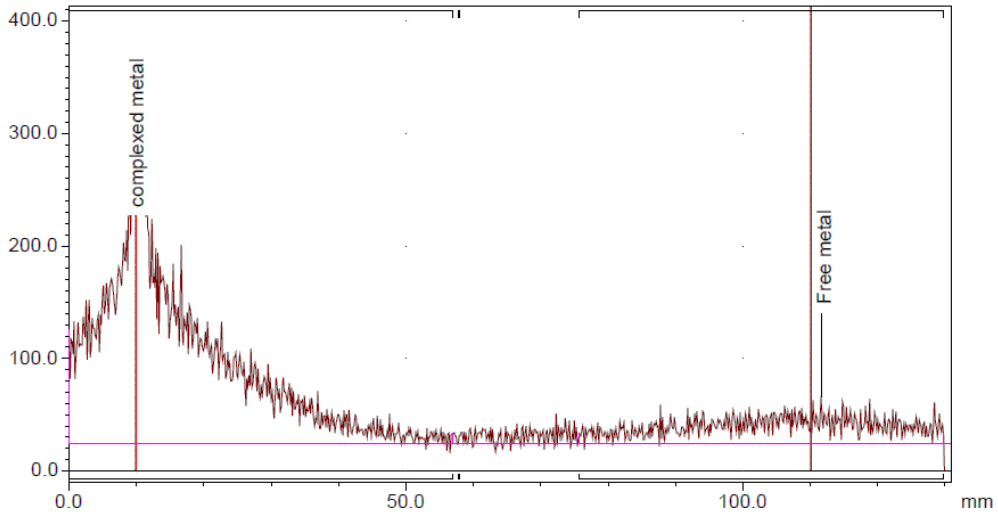

Name	Start (mm)	End (mm)	Retention (RF)	Area (Counts)	%ROI (%)	%Total (%)
complexed metal	0.0	57.0	0.003	26416.0	81.73	79.54
BP 1	57.8	57.9	0.478			
Free metal	75.8	129.8	1.015	5906.0	18.27	17.78
2 Peaks				32322.0	100.00	97.33

Total Area: 33209.0 Counts
Average Background: 24.0 Counts

Figure S46: Radio TLC of crude **[^{68}Ga]-26**, developed on Whatman 3 MM with 0.35M ethylenediaminetetraacetic acid (EDTA) as the mobile phase. The radio-TLC shows minimum amount of free [^{68}Ga]$GaCl_3$ (Figure 65c – Chapter 4).

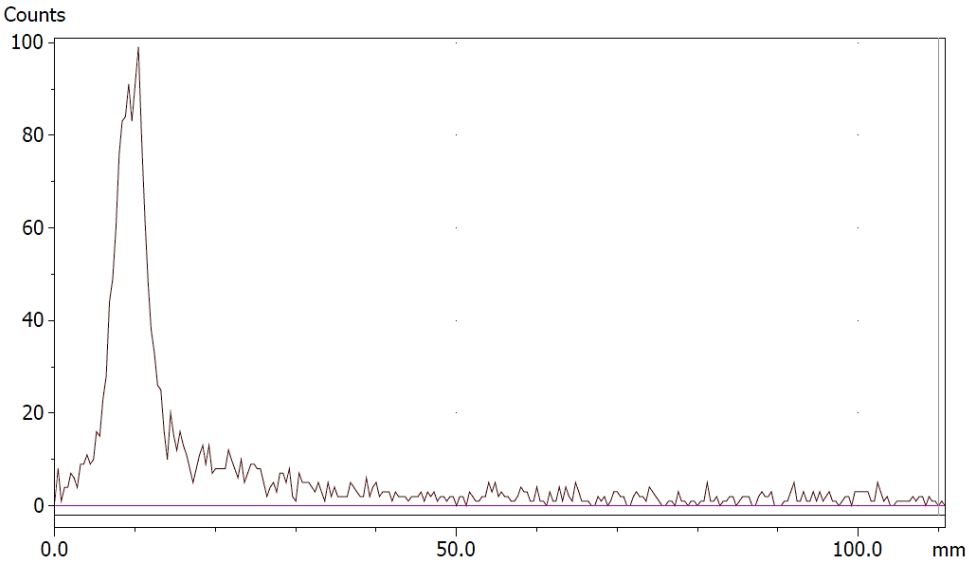

Name	Start (mm)	End (mm)	Retention (RF)	Area (Counts)	%ROI (%)	%Total (%)
No ROIs allocated.						
0 Peaks				0	100.00	0.00

Total Area: 1989 Counts
Average Background: 0 Counts

Figure S47: Radio TLC of crude **[^{68}Ga]-27**, developed on Whatman 3MM with 0.35M ethylenediaminetetraacetic acid (EDTA) as the mobile phase. The radio-TLC was shown no amount of free [^{68}Ga]$GaCl_3$ (Figure 65d – Chapter 4).

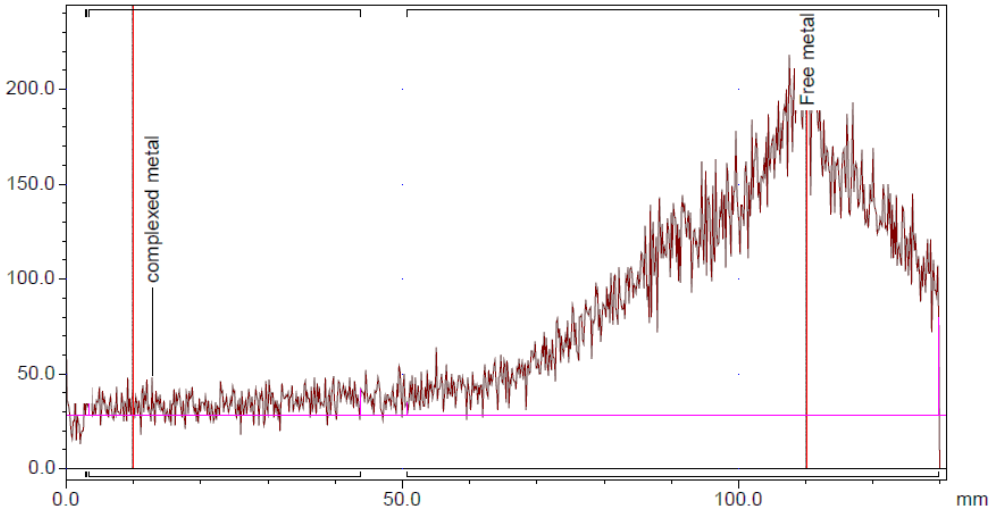

Name	Start (mm)	End (mm)	Retention (RF)	Area (Counts)	%ROI (%)	%Total (%)
BP 1	2.9	3.0	-0.070			
complexed metal	3.5	43.8	0.298	1760.0	4.12	4.08
Free metal	50.7	129.8	1.003	40920.0	95.88	94.76
2 Peaks				42680.0	100.00	98.84

Total Area: 43183.0 Counts
Average Background: 28.0 Counts

Figure S48: Radio TLC of the slurry obtained from the reaction between GO and $[^{89}Zr]Zr^{+4}$, developed on Whatman 3 MM with 0.35 M ethylenediaminetetraacetic acid (EDTA) as the mobile phase. The radio-TLC was shown almost only free $[^{89}Zr]Zr^{+4}$.

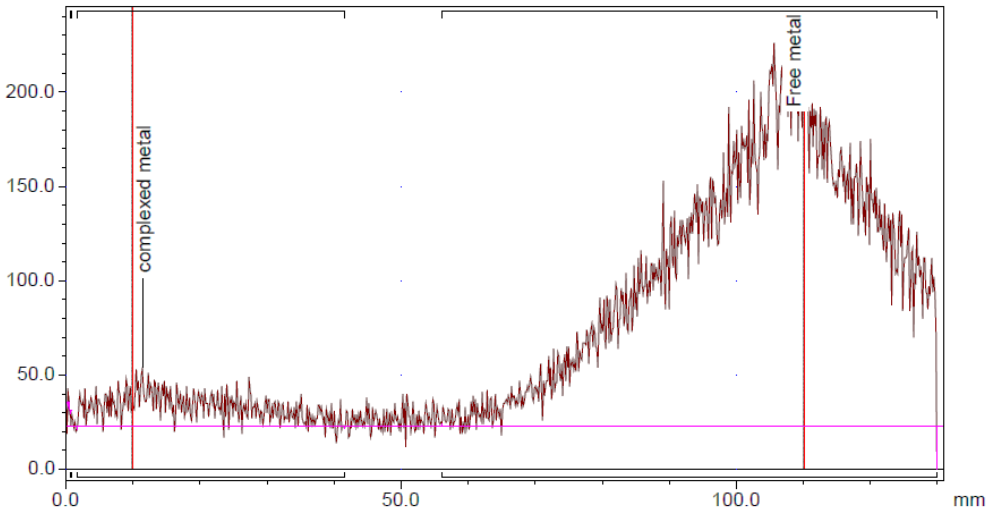

Name	Start (mm)	End (mm)	Retention (RF)	Area (Counts)	%ROI (%)	%Total (%)
BP 1	0.8	0.9	-0.091			
complexed metal	1.7	41.6	0.015	2730.0	6.15	6.10
Free metal	56.1	129.9	0.987	41627.0	93.85	93.08
2 Peaks				44357.0	100.00	99.18

Total Area: 44723.0 Counts
Average Background: 23.0 Counts

Figure S49: Radio TLC of the slurry obtained from the reaction between nanocomposite **23** (PhZnTSC@GO) and $[^{89}Zr]Zr^{+4}$, developed on Whatman 3 MM with 0.35 M ethylenediaminetetraacetic acid (EDTA) as the mobile phase. The radio-TLC shows almost only free $[^{89}Zr]Zr^{+4}$.

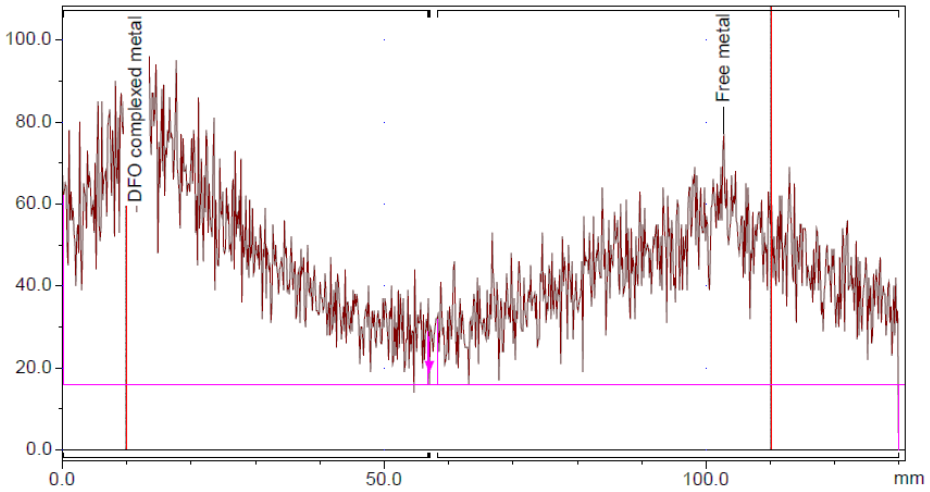

Name	Start (mm)	End (mm)	Retention (RF)	Area (Counts)	%ROI (%)	%Total (%)
DFO complexed metal	0.2	56.7	0.015	13550.0	50.82	50.52
BP 1	57.0	57.2	0.470			
Free metal	58.2	129.9	0.927	13112.0	49.18	48.89
2 Peaks				26662.0	100.00	99.41

Total Area:	26820.0 Counts
Average Background:	16.0 Counts

Figure S50: Radio TLC [^{89}Zr]ZrDFO, developed on Whatman 3 MM with 0.35 M ethylenediaminetetraacetic acid (EDTA) as the mobile phase. The radio-TLC shows 49 % of free [^{89}Zr]Zr^{+4}.

Kinetic stability assays of radiolabelled GO nanocomposites:

Table S17: Results acquired from the kinetic stability tests of the **[^{68}Ga]-25**) nanocomposites up to two hours post preparation (p.p.) under various incubation conditions (EDTA, PBS, fresh mouse plasma).

Time	**[^{68}Ga]-25 in PBS**				**[^{68}Ga]-25 in EDTA**				**[^{68}Ga]-25 in mouse plasma**			
	1	*2*	*MO*	*STDEV*	*1*	*2*	*MO*	*STDEV*	*1*	*2*	*MO*	*STDEV*
1 h	99.0	97.4	98.2	1.1314	73.9	69.5	71.7	3.1113	98.9	98.9	98.9	0.0000
2 h	99.9	97.7	98.8	1.5556	74.2	67.4	70.8	4.8083	99.9	99.9	99.9	0.0000

Table S18: Results acquired from the kinetic stability tests of the **[^{68}Ga]-26** nanocomposites up to two hours post preparation (p.p.) under various incubation conditions (EDTA, PBS, fresh mouse plasma).

Time	**[^{68}Ga]-26 in PBS**				**[^{68}Ga]-26 in EDTA**				**[^{68}Ga]-26 in mouse plasma**			
	1	*2*	*MO*	*STDEV*	*1*	*2*	*MO*	*STDEV*	*1*	*2*	*MO*	*STDEV*
1 h	99.9	94.2	97.05	4.0305	75	72.3	73.65	1.9091	99.9	99.9	99.9	0.0000
2 h	99.9	94.8	97.35	3.6062	57.1	64.3	60.7	5.0911	99.9	99.9	99.9	0.0000

Table S19: Results acquired from the kinetic stability tests of the **[^{68}Ga]-27** nanocomposites up to two hours post preparation (p.p.) under various incubation conditions (EDTA, PBS, fresh mouse plasma).

Time	**[^{68}Ga]-27 in PBS**				**[^{68}Ga]-27 in EDTA**				**[^{68}Ga]-27 in mouse plasma**			
	1	*2*	*MO*	*STDEV*	*1*	*2*	*MO*	*STDEV*	*1*	*2*	*MO*	*STDEV*
1 h	99.9	99.9	99.9	0.0000	85	84.3	84.65	0.49497	99.9	99.9	99.9	0.0000
2 h	99.9	99.9	99.9	0.0000	75	74.1	74.55	0.6364	99.9	99.9	99.9	0.0000

APPENDIX 4: In vitro evaluation

Cell viability assays:

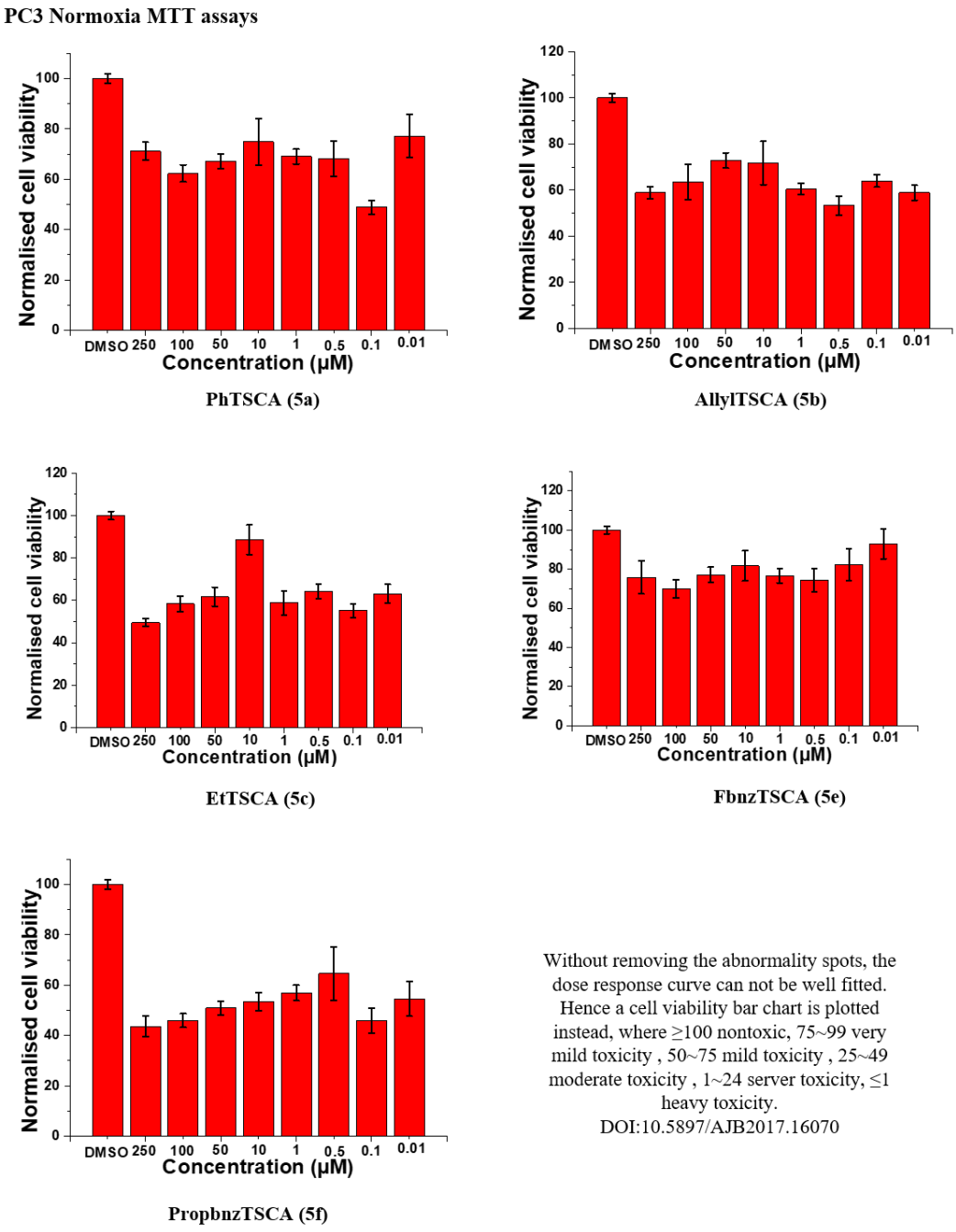

Figure S51: Cell viability bar chart calculated for a variety of mono(substituted) precursors in PC3cells, incubated for 48 hours to normoxic cells.

PC3 Hypoxia MTT assays

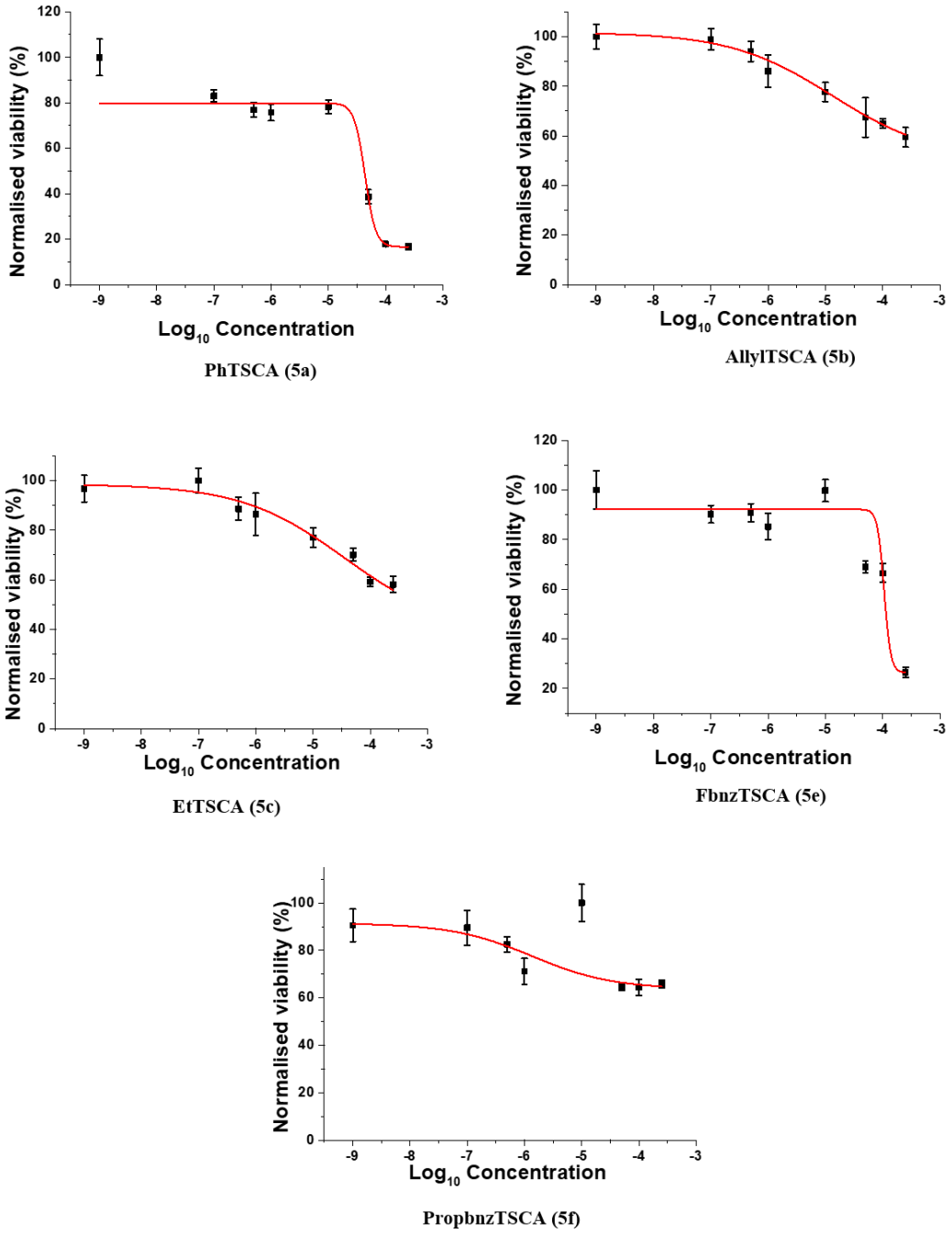

Figure S52: Dose response curves and calculated EC50 of a variety of mono(substituted) precursors in PC3 cells, incubated for 48 hours to induced (by $CoCl_2$) hypoxic cells.

EMT6 Normoxia MTT assays

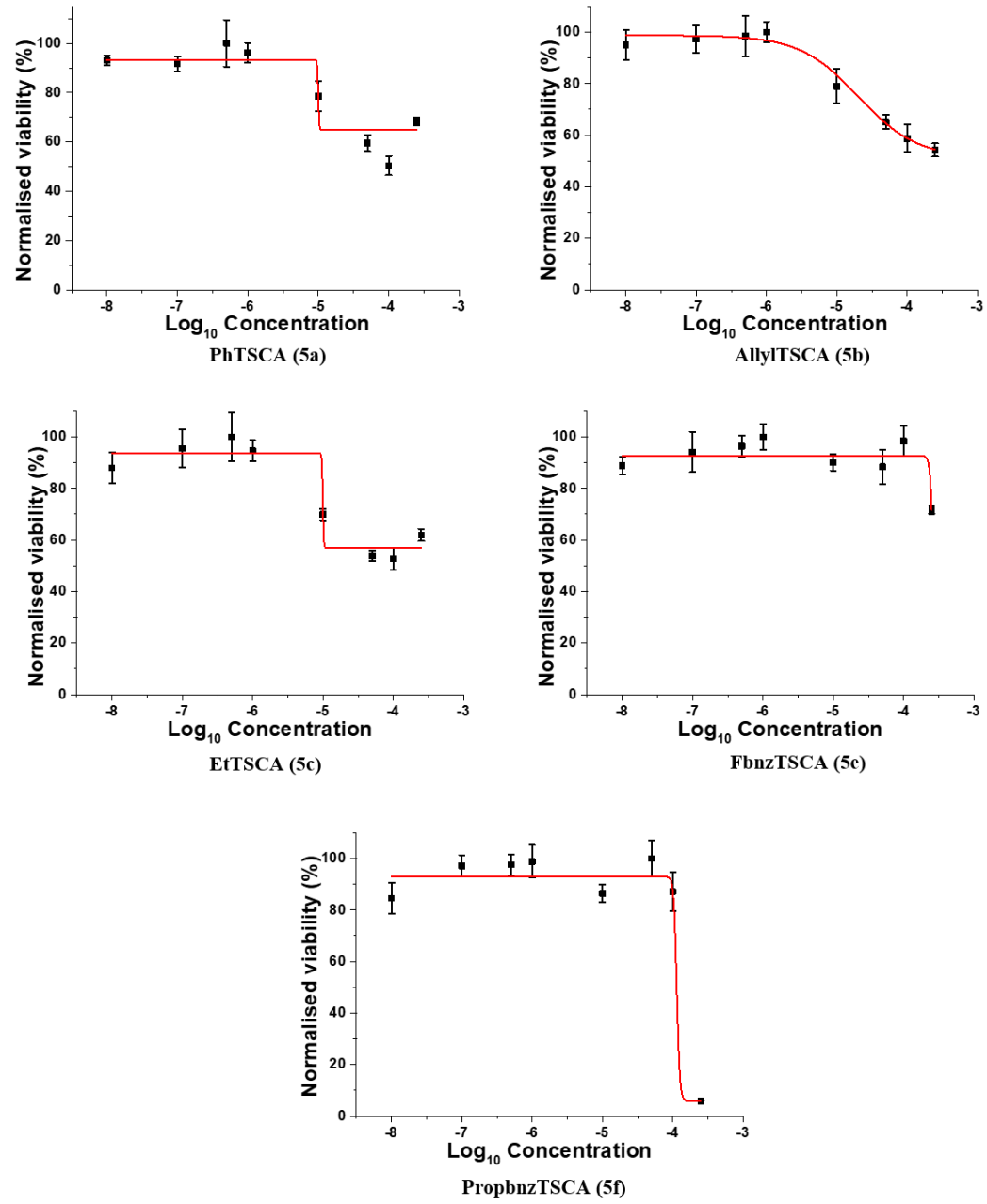

Figure S53: Dose response curves and calculated EC50 of a variety of mono(substituted) precursors in EMT6 cells, incubated for 48 hours to induced (by $CoCl_2$) normoxic cells.

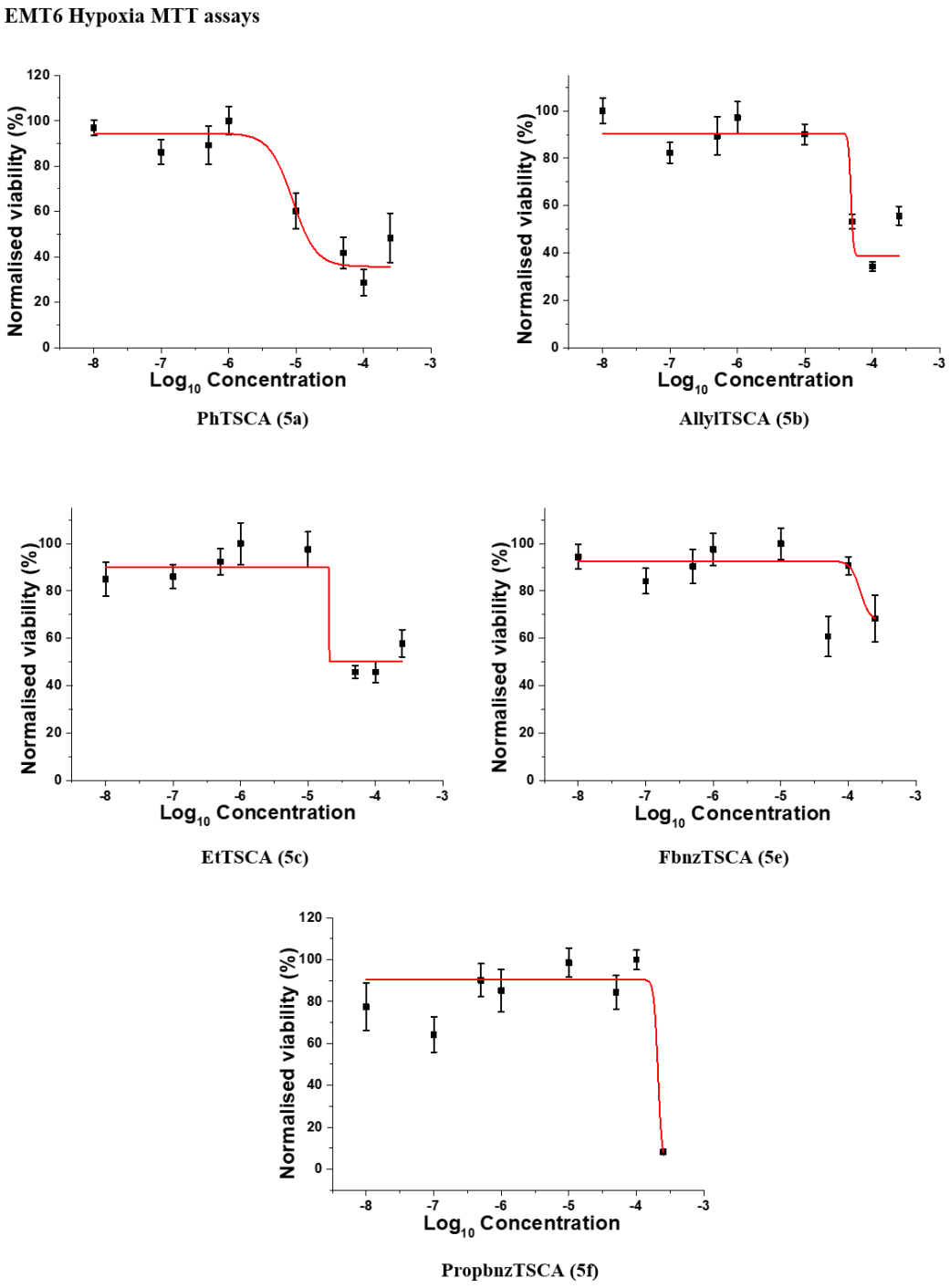

Figure S54: Dose response curves and calculated EC50 of a variety of mono(substituted) precursors in EMT6 cells, incubated for 48 hours to induced (by $CoCl_2$) hypoxic cells.

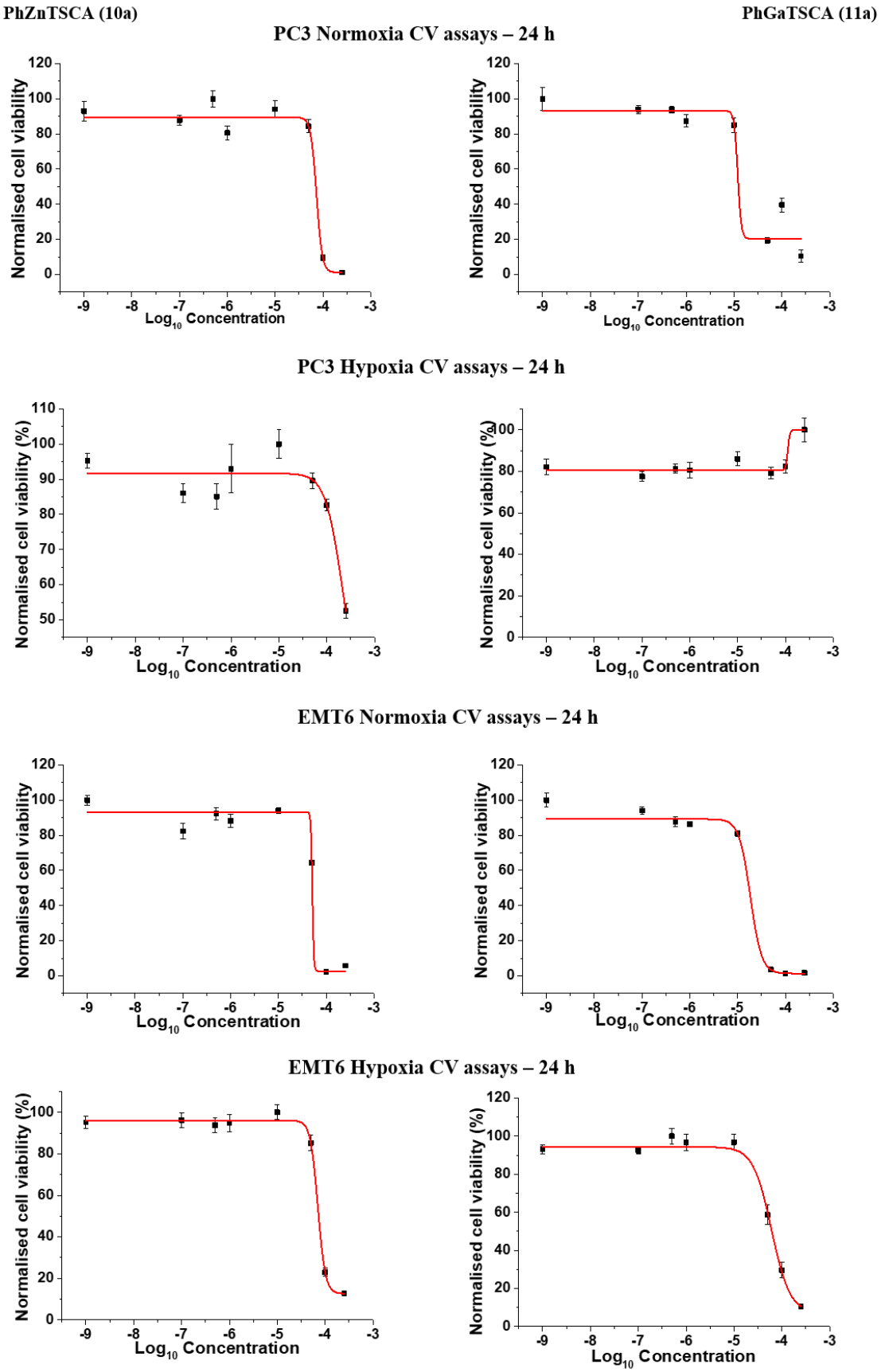

Figure S55: Dose response curves and calculated EC50 of asymmetric **9a** and **10a** complexes in PC3 and EMT6 cells, incubated for 24 hours in both normoxic and induced (by $CoCl_2$) hypoxic cells.

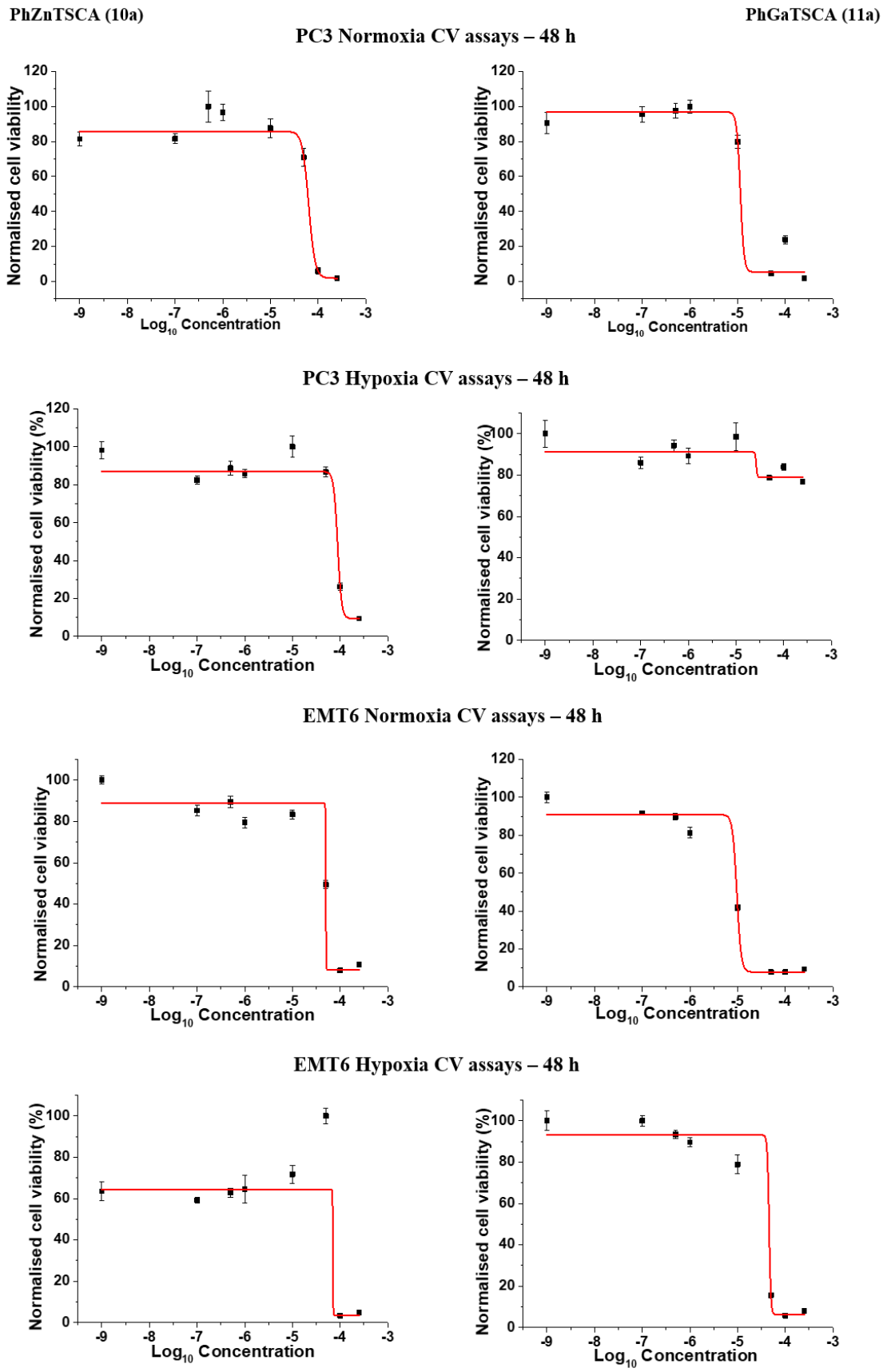

Figure S56: Dose response curves and calculated EC50 of asymmetric **9a** and **10a** complexes in PC3 and EMT6 cells, incubated for 48 hours in both normoxic and induced (by $CoCl_2$) hypoxic cells.

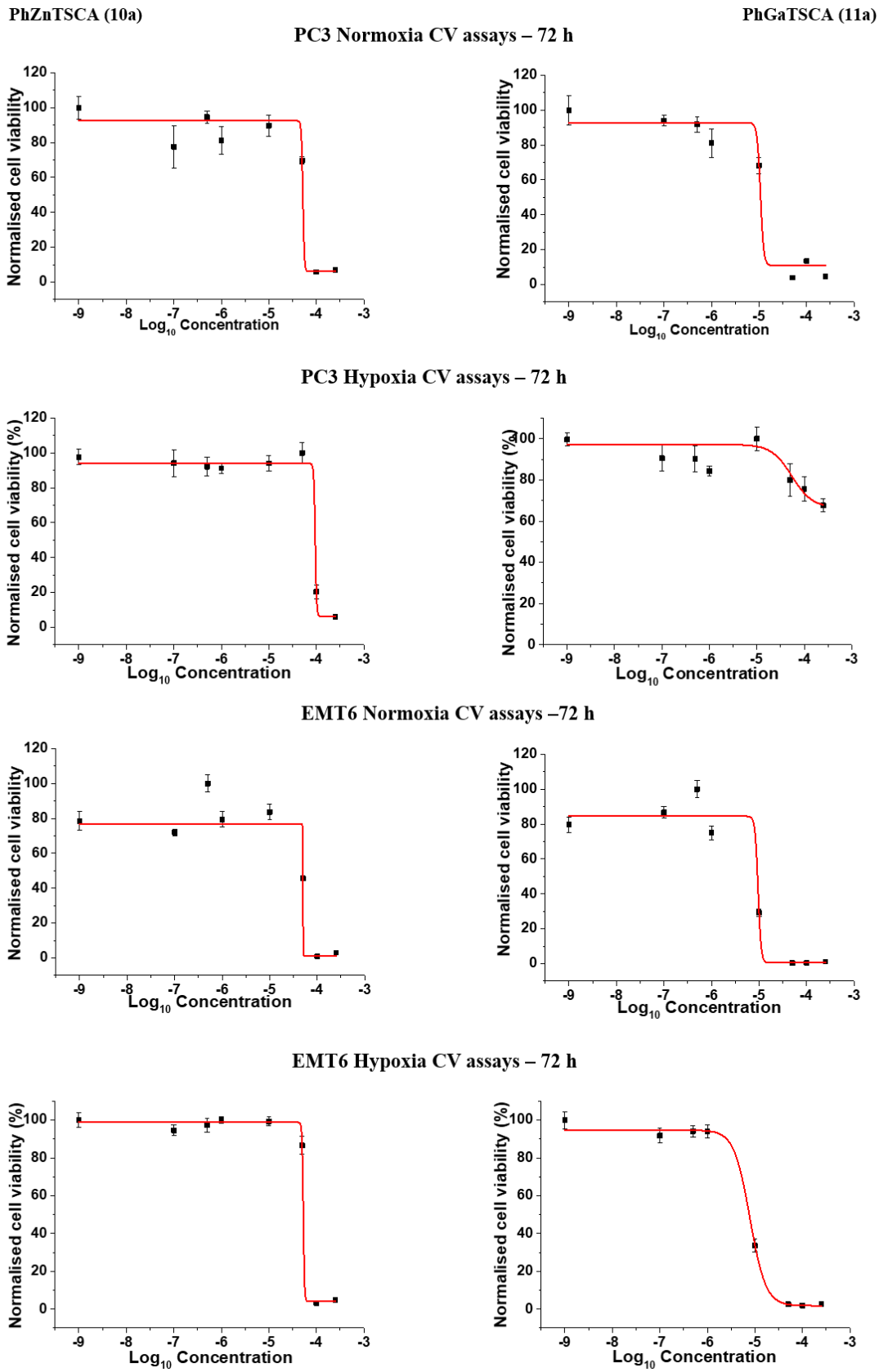

Figure S57: Dose response curves and calculated EC50 of asymmetric **9a** and **10a** complexes in PC3 and EMT6 cells, incubated for 72 hours in both normoxic and induced (by $CoCl_2$) hypoxic cells.

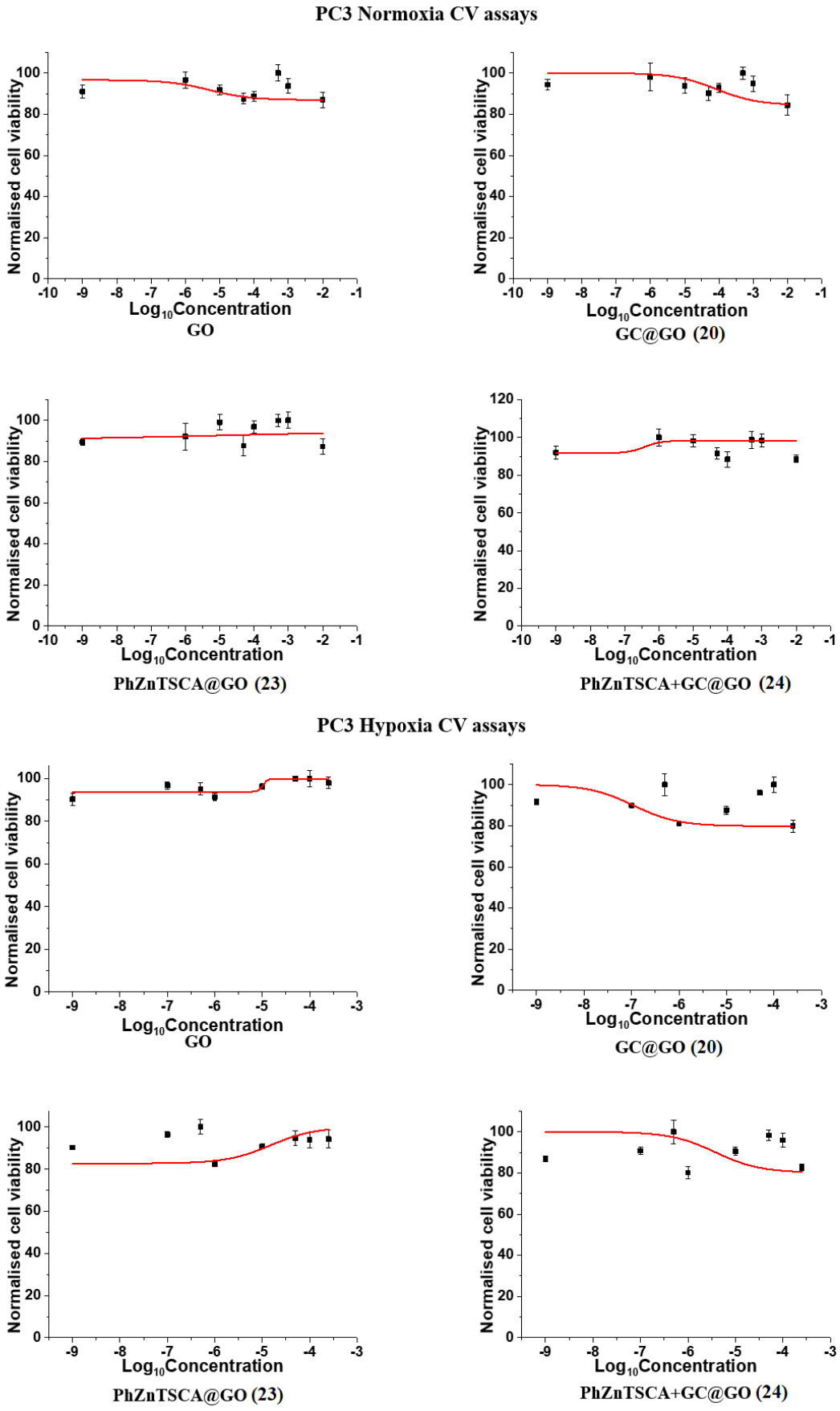

Figure S58: Dose response curves and calculated EC50 of different GO nanocomposites in PC3 cells, incubated for 48 hours in both normoxic and induced (by $CoCl_2$) hypoxic cells.

In vitro fluorescence imaging

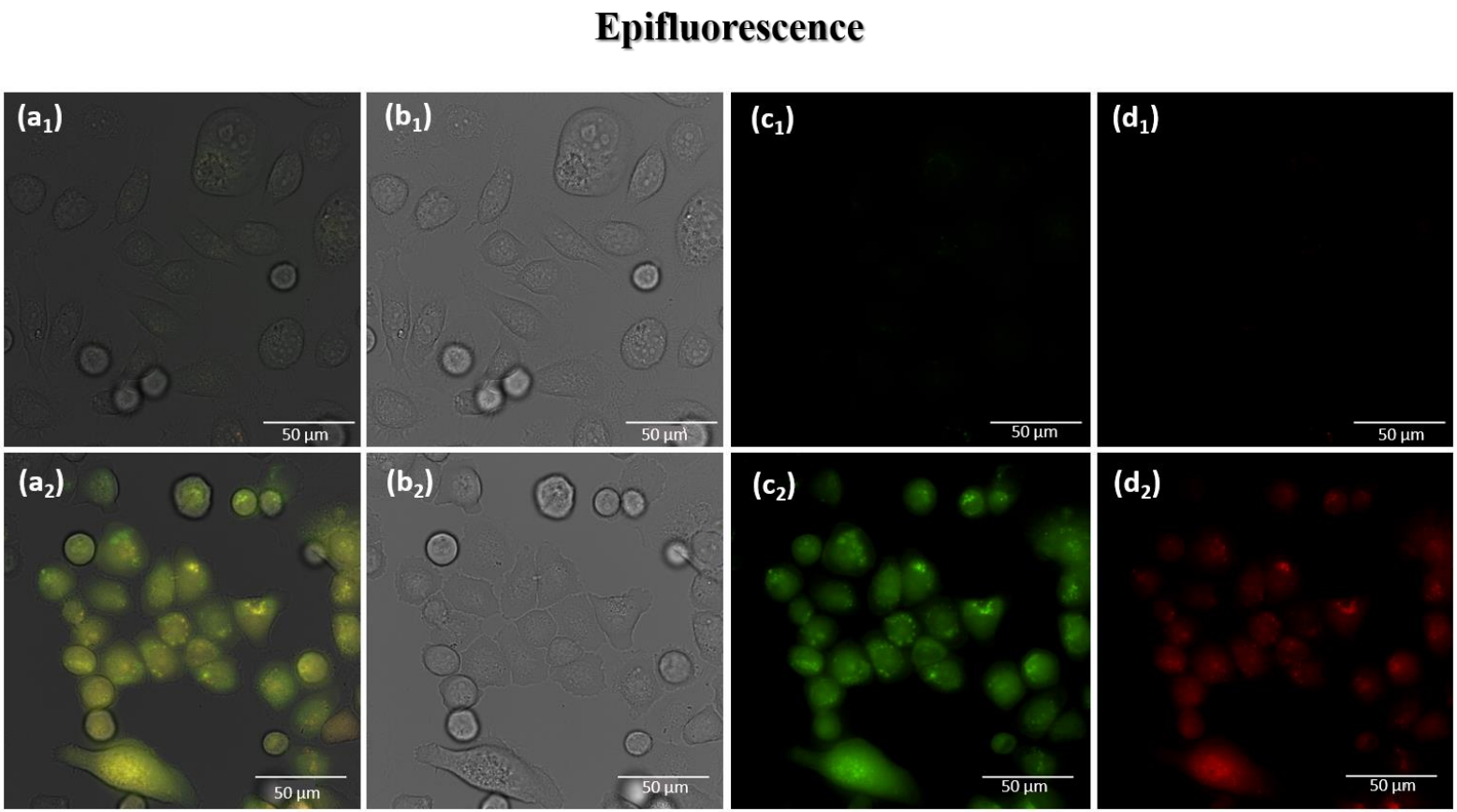

Figure S59: PC-3 cells grown under different conditions were incubated at 37 °C for 15 minutes with **5h** monosubstituted precursor (100 µM, in 5: 95 DMSO : serum-free medium). a) overlay of the green-red channels and DIC image, b) DIC image, c) green: λ_{ex} = 465-495 nm; λ_{em} = 515-555 nm, d) red: λ_{ex} = 530-560 nm; λ_{em} = 590-650 nm. 1: control. 2: compound (scale bar 50µm). (Figure 30.1 - Chapter 2).

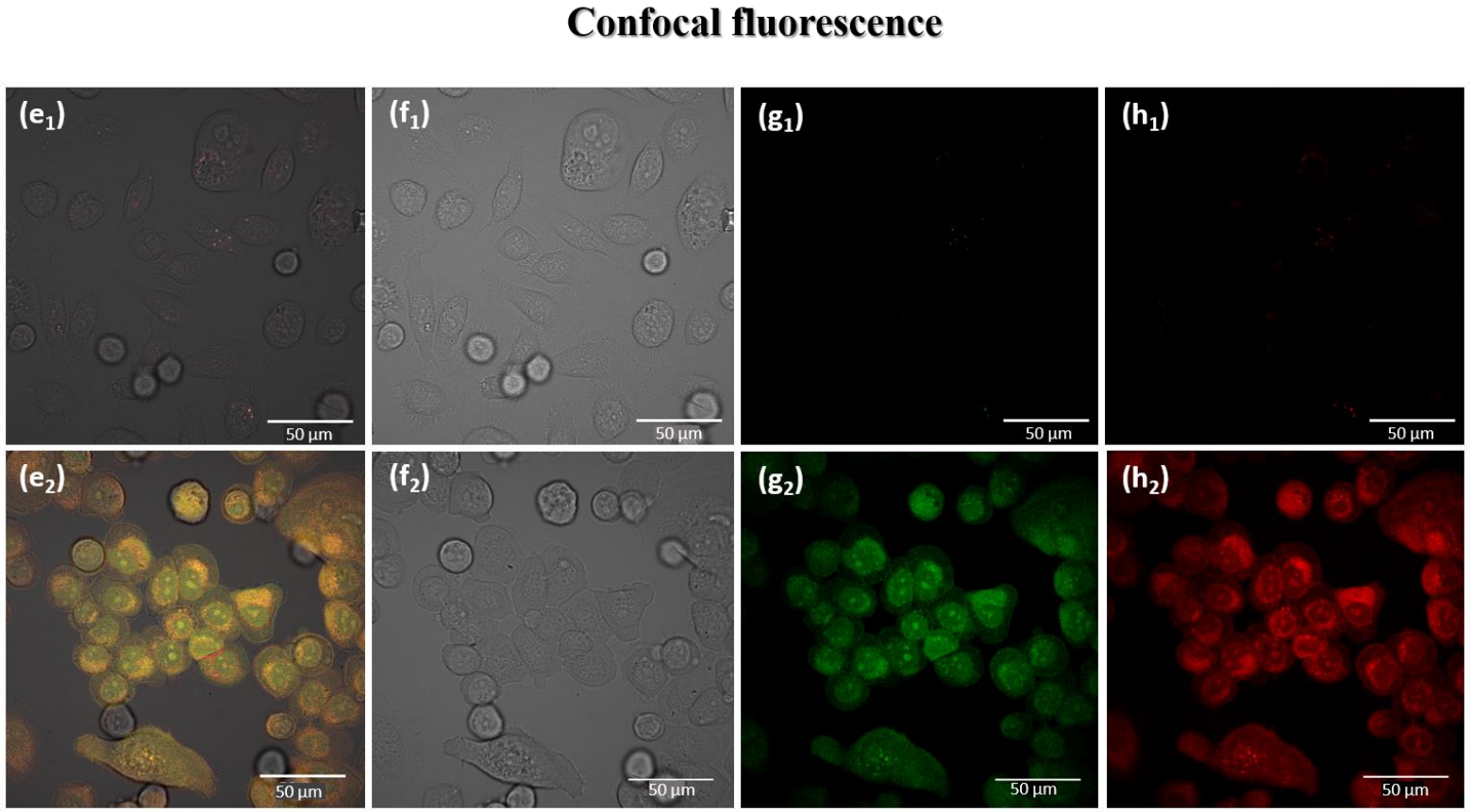

Figure S60: PC-3 cells grown under different conditions were incubated at 37 °C for 15 minutes with **5h** monosubstituted precursor (100 µM, in 5: 95 DMSO : serum-free medium). e) overlay of the green-red channels and DIC image, f) DIC image, g) green: λ_{ex} = 500-550 nm; λ_{em} = 515-555 nm, h) red: λ_{ex} 570-750 nm; 1: control. 2: compound (scale bar 50µm). (Figure 30.2 - Chapter 2).

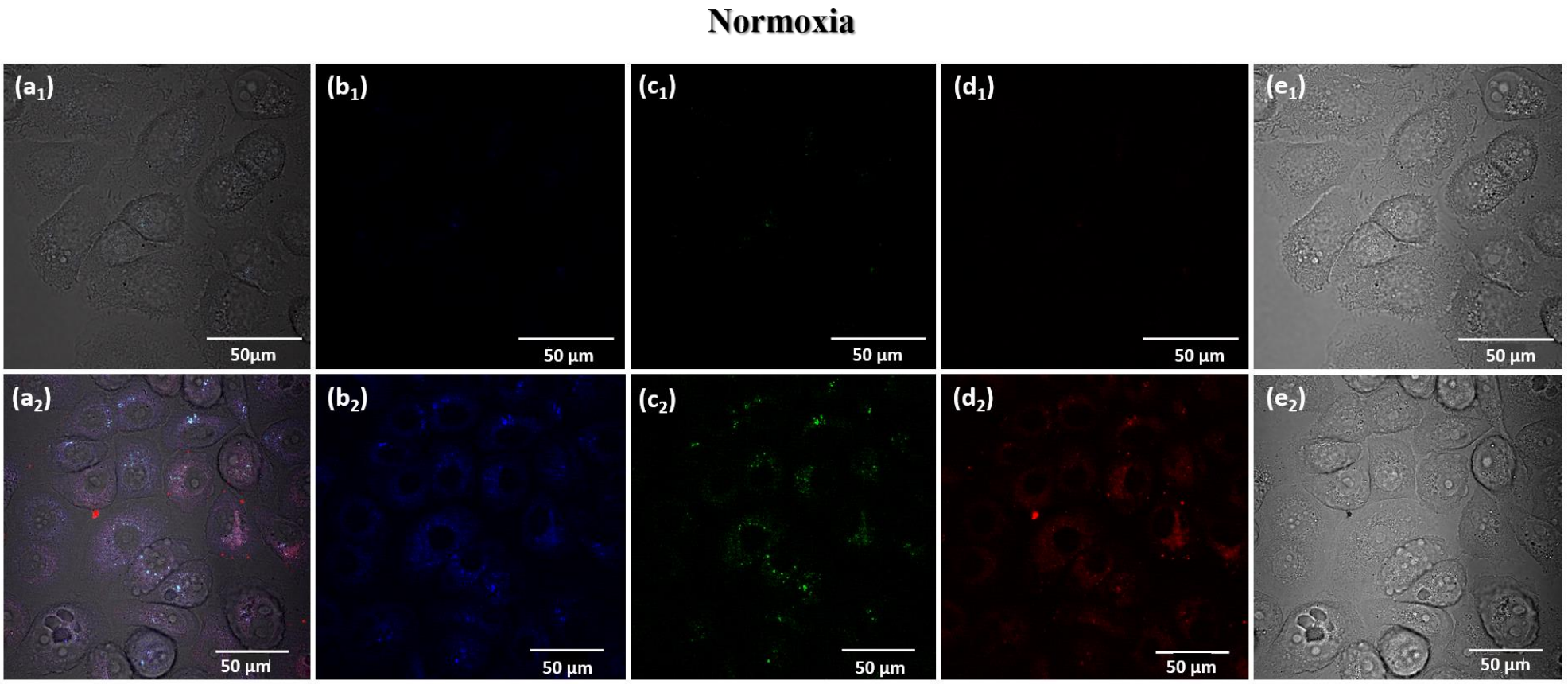

Figure S61: PC-3 cells grown under different conditions were incubated at 37 °C for 15 minutes with **10a** complex (100 µM, in 5: 95 DMSO : serum-free medium). a) overlay of the green-red channels and DIC image, b) blue: λ_{ex} = 417-477 nm, c) green: λ_{ex} = 500-550 nm, c) red: λ_{ex} 570-750 nm, d) DIC image 1: control. 2: compound (scale bar 50 µm). (Figure 51 - Chapter 3).

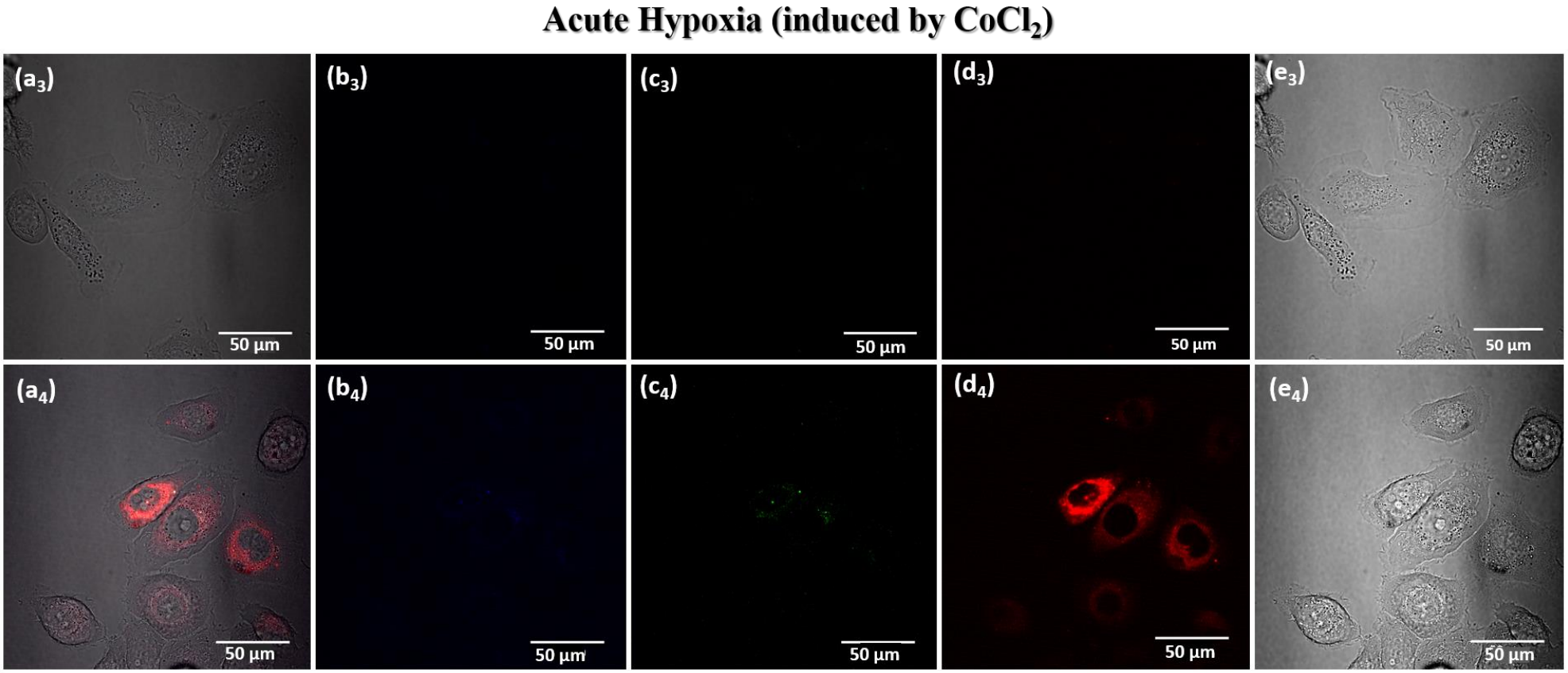

Figure S62: PC-3 cells grown under different conditions were incubated at 37 °C for 15 minutes with **10a** complex (100 µM, in 5: 95 DMSO : serum-free medium). a) overlay of the green-red channels and DIC image, b) blue: λ_{ex} = 417-477 nm, c) green: λ_{ex} = 500-550 nm, c) red: λ_{ex} 570-750 nm, d) DIC image. 3: control. 4: compound (scale bar 50 µm). (Figure 51 - Chapter 3).

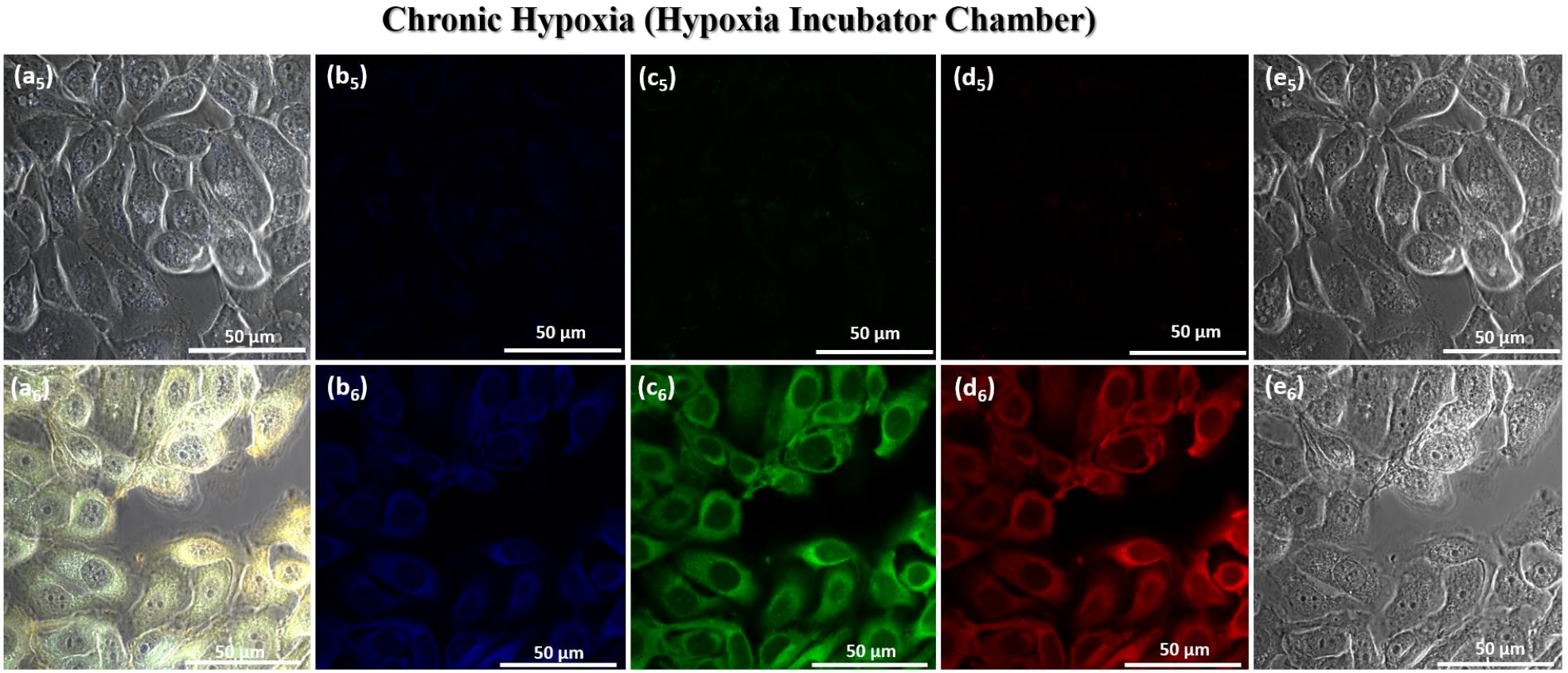

Figure S63: PC-3 cells grown under different conditions were incubated at 37 °C for 15 minutes with **10a** complex (100 µM, in 5: 95 DMSO : serum-free medium). a) overlay of the green-red channels and DIC image, b) blue: λ_{ex} = 417-477 nm, c) green: λ_{ex} = 500-550 nm, c) red: λ_{ex} 570-750 nm, d) DIC image 5: control. 6: compound (scale bar 50µm). (Figure 51 - Chapter 3).

APPENDIX 5: Attempt of functionalisation of asymmetric bis(thiosemicarbazonato) metal complexes with a fragment of bombesin

5.1 Synthesis of a bombesin peptide fragment.

Bombesin is a peptide which has shown potential pharmacologic effects since it was first discovered[1] and it was soon found that it was related with gastrin release[2] and cancer biology.[3, 4] Bombesin consists of 14 amino acids of which only 7 of them are proposed as essential for its targeting role.[5, 6] Thus, typical targeting peptide sequences are the [6-14] or the [7-13] fragments, and they have been widely used for cancer imaging and targeted therapy.[5-10] In this work, the [7-13] fragment was chosen to be prepared (**Figure S64**) due to its simpler synthesis and its application in several studies which suggest that the gastrin-related properties of the original peptide can be preserved.[8, 11, 12]

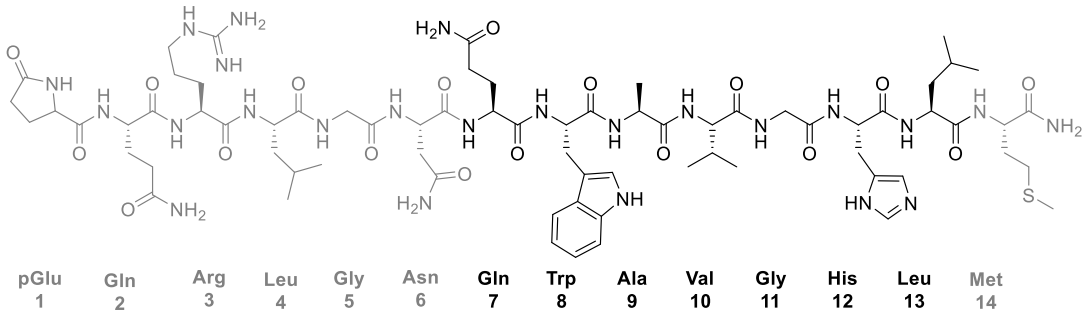

Figure S64: Schematic illustration of bombesin (14 amino acids). The [7-13] fragment which was synthesised in this work is highlighted.

Solid-phase peptide synthesis (SPPS) was used herein to prepare the desired fragment. SPPS is currently the main tool for peptide synthesis and is characterised by the step-wise construction of a polypeptide through sequential coupling reactions between N^{α} and side-chain protected amino acids, in a *C*→*N* direction, attached to a solid resin support.[13-15] In a typical SPPS procedure (**Figure S65**), the *C*-terminal amino acid is initially attached to a solid support then the N^{α}-protecting group is removed selectively without removing the protecting groups of the side chain.[13-15] Another coupling reaction is then initiated and this procedure is repeated until the completion of the desired sequence. Finally, the solid support is removed along with the side-chain protecting groups.[14]

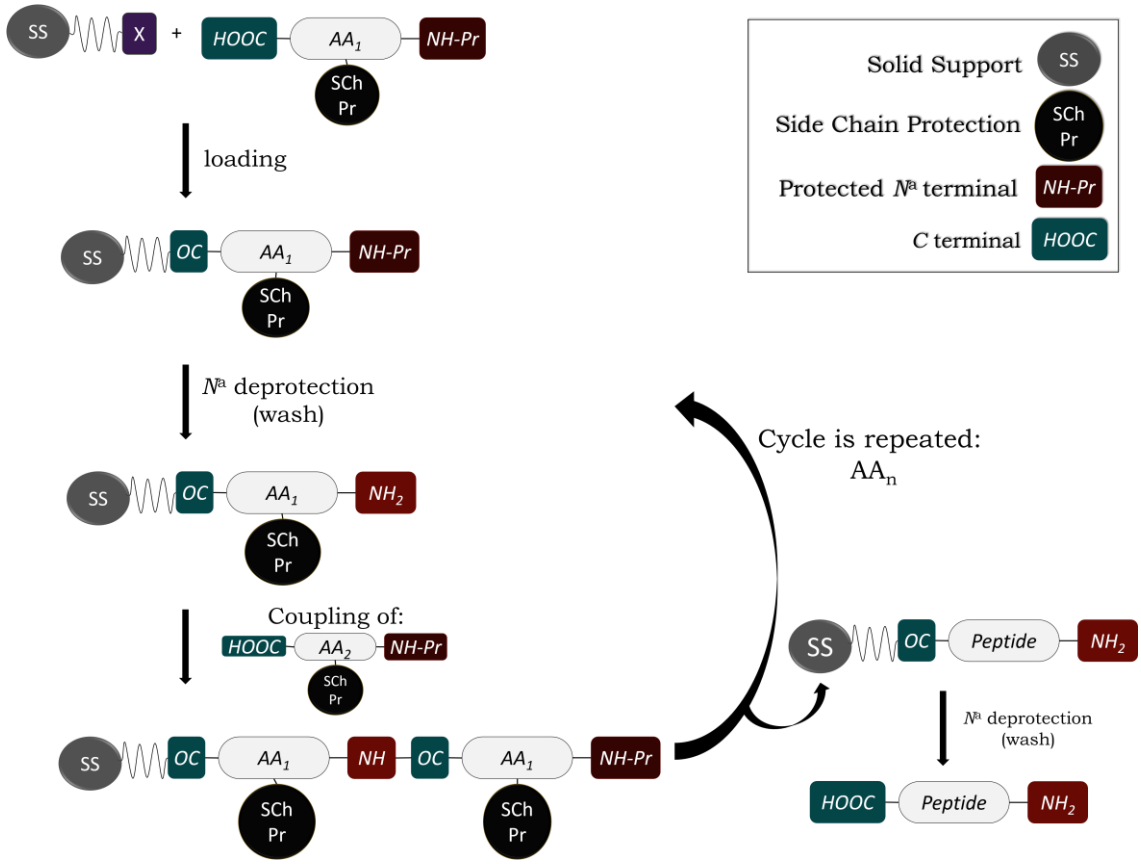

Figure S65: SPPS principle; AA: amino acid.[13]

In recent years, reactions of SPPS have been increasingly carried out either with microwave irradiation, or under conventional heating. This can significantly decrease the reaction time required for both couplings and deprotections, as well as increasing the efficiency of coupling reactions in cases where room temperature reactions are not effective, which would otherwise lead to low purity products, or even failure sequences.[13, 16, 17]

Bombesin (7-13) was prepared by automated SPPS using conventional heating (Scheme 22). Rink amide resin was used as solid support and couplings were carried out with benzo-1-yl-oxytripyrrolidinophosphonium hexafluorophosphate (PyBOP) to activate the carboxyl function of the amino acid derivatives, with *N*,*N*-diisopropylethylamine as base. The first amino acid was coupled manually to the Rink amide resin at room temperature, then the resin was transferred to the synthesiser and subsequent coupling steps were carried out with heating. The coupling reactions were carried out at 60 °C for 35 minutes. Removal of the fluorenylmethyloxycarbonyl (Fmoc) protecting groups was carried out with 25% piperidine in DMF at room temperature.

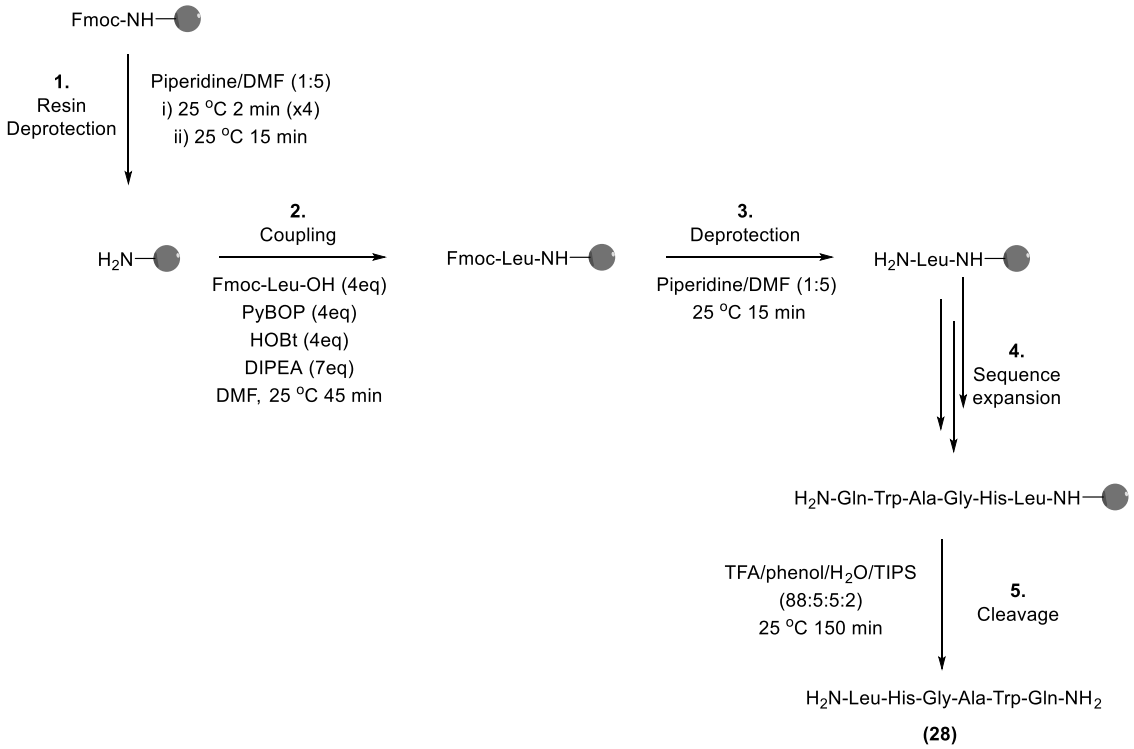

Scheme S1: Synthetic pathway for the production of bombesin (fragment [7-13]).

The full synthetic methodology can be divided into 5 steps, depicted in **Scheme S1**:

- First, the resin was swollen in "solvent" and then its deprotection followed upon addition of a piperidine/DMF (1:5 v/v) solution for two minutes at room temperature. Then, the resin was washed with DMF and the procedure was repeated four times (2 minutes of reaction) before it was left to react for a further 15 minutes (**Scheme S1**, step 1).
- After deprotection, the resin was washed thoroughly with CH_2Cl_2 and the deprotection was confirmed by a Kaiser test. The Kaiser test is a quantitative test which is based on the fact that when primary amines react with ninhydrin, a deep blue colour results.[18] The coupling of the first amino acid (**Scheme S1**, step 2) was then carried out.
- A mixture of the amino acid and the coupling reagents (PyBOP and HOBt) in DMF and DIPEA in a 1:1:1 stoichiometry, were shaken for two minutes before being added to the resin and reacted for a further 45 minutes. The deprotection of the resin-bound amino acid then followed (**Scheme S1**, step 3) as previously and a Kaiser test was repeated to ensure the success of the deprotection.
- The amino acid sequence was consequently elongated (**Scheme S1**, step 4) using an automated SPPS, where the rest of the amino acids where added to the

sequence in a similar manner.

- The final step of this synthetic process was the cleavage of the peptide from the resin (**Scheme S1**, step 5). A cocktail was prepared for this purpose, with trifluoroacetic acid, phenol, water and triisopropylsilane (88:5:5:2) and reacted with the peptide for 2.5 hours at room temperature.

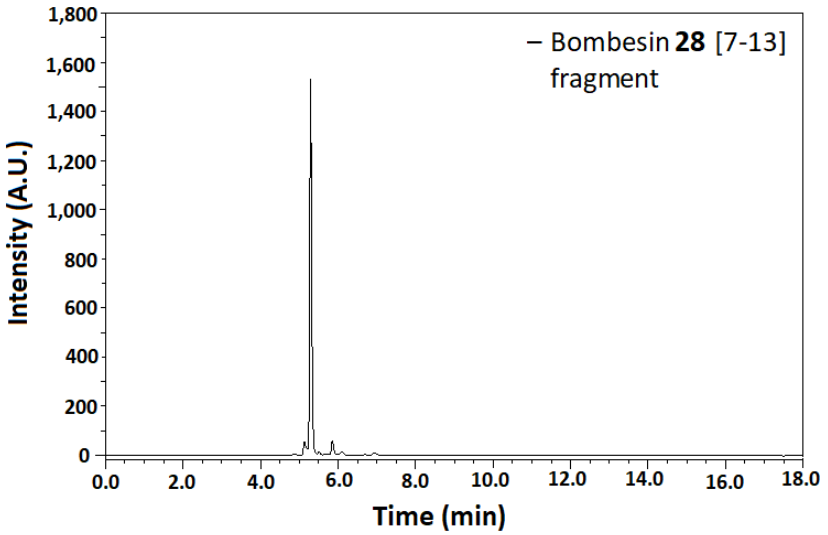

Figure S66: HPLC trace of bombesin fragment [7-13] (28) using the UV-Vis detection at 280 nm.

The peptide was then isolated as a white solid by precipitation in cold ether and following centrifugation. The purity of the synthesised peptide was determined to be about 98 % by HPLC (**Figure S66**), so no further purification was needed. The mass spectrometry results agreed with the formation of the above-mentioned peptide since the observed isotopic pattern matched with the theoretical one (**Figure S67**).

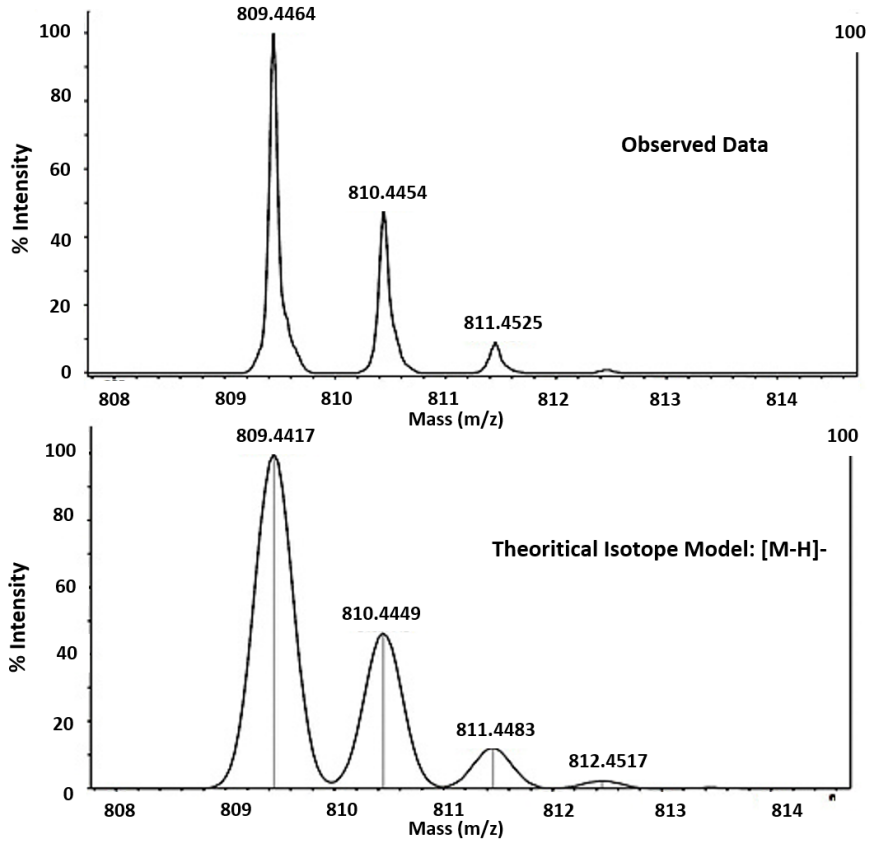

Figure S67: ESI-TOF mass spectrometry results for the bombesin fragment [7-13] (28).

5.2. Coupling of bombesin with asymmetric thiosemicarbazonate metal complexes.

In order for the bombesin fragment to be coupled with the hydrazine moiety of the asymmetric metal complexes, a modification of its amino-terminus was necessary to introduce a carbonyl function.[19] Thus, pyruvic acid was coupled at the N-terminus of the bombesin analogue before its later reaction with complex **9a** (PhZnTSCA) (**Scheme S2**). More specifically, pyruvic acid was added in a DMF solution of the coupling agents of 1-ethyl-3- 3-dimethyl aminopropyl carbodiimide hydrochloride (EDC) and HOBt on ice and left to react for 45 minutes. The peptide was then added and the pH of the mixture was adjusted to 8 and reacted for two more hours. Mass spectrometry results confirmed the synthesis of the derivatised bombesin **29** (**Figure S68**).

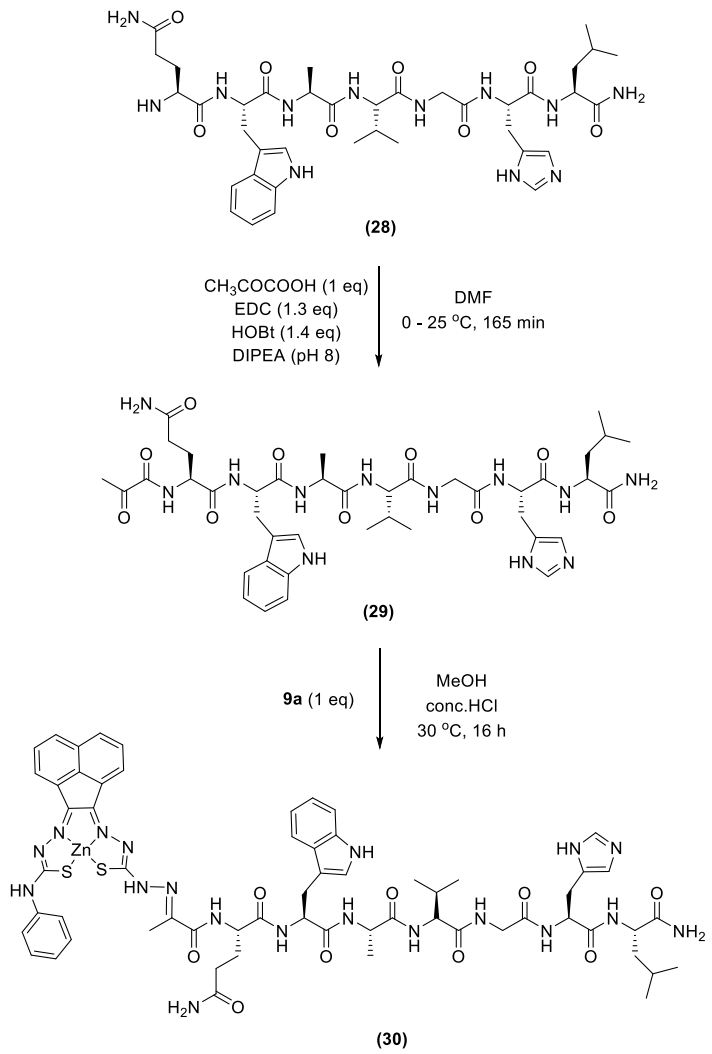

Scheme S2: Functionalisation of bombesin fragment (28) with pyruvic acid and attempted coupling of the corresponding molecule (29) with PhZnTSCA (9a) complex.

Following this, the derivatised bombesin analogue was reacted with complex **9a** (PhZnTSCA) (solubilised in DMSO), in slightly acidic methanol (drops of conc. HCl), resulting in an instant colour change from dark orange to yellow. The mixture was then left to react at 30 °C for 16 hours and the solution became pale red (**Scheme S2**). Next, it was freeze-dried and re-suspended in methanol and washed with diethyl ether under vacuum filtration. Although the HPLC trace suggested the formation of a new product, along with unchanged starting material, mass spectrometry results did not confirm the successful coupling of the two compounds (Appendix) which suggested that further optimisation of the reaction is needed.

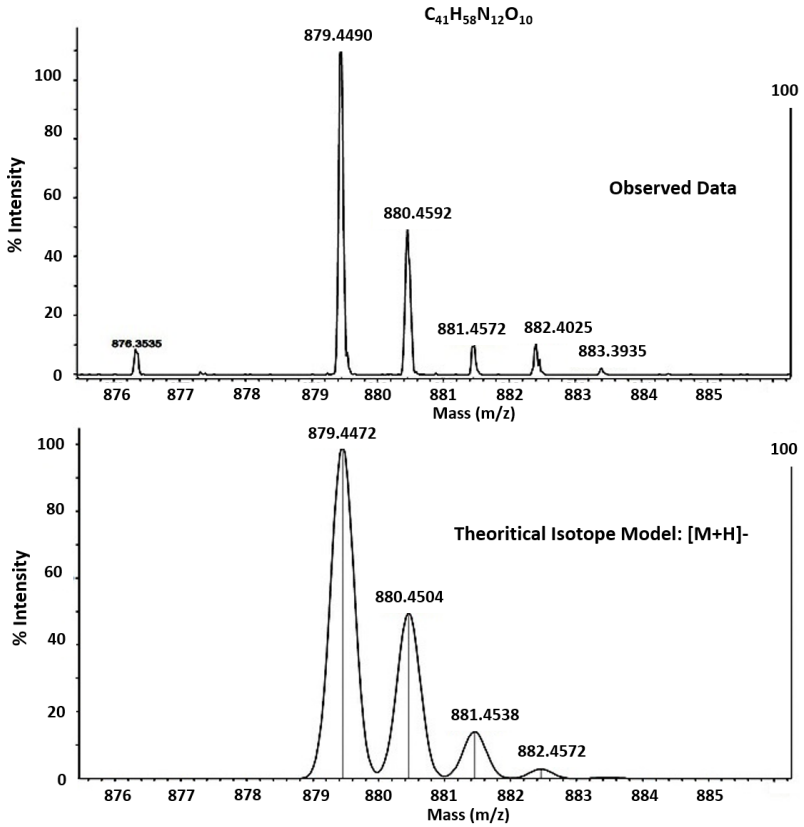

Figure S68: ESI-TOF mass spectrometry results for the functionalised bombesin (29).

5.3. References for Appendix 5

1. V. Erspamer, G. F. Erspamer and M. Inselvini, *J. Pharm. Pharmacol.*, 1970, **22**, 875-876.
2. M. E. Sunday, L. M. Kaplan, E. Motoyama, W. W. Chin and E. R. Spindel, *Lab. Invest.*, 1988, **59**, 5-24.
3. N. Minamino, K. Kangawa and H. Matsuo, *Biochem. Biophys. Res. Commun.*, 1984, **119**, 14-20.
4. N. S. Track and E. Cutz, *Life Sci.*, 1982, **30**, 1553-1556.
5. S. R. Preston, G. V. Miller and J. N. Primrose, *Crit. Rev. Oncol. Hematol.*, **23**, 225-238.
6. N. Gonzalez, T. W. Moody, H. Igarashi, T. Ito and R. T. Jensen, *Curr. Opin. Endocrinol. Diabetes Obes.*, 2008, **15**, 58-64.
7. I. Ramos-Alvarez, P. Moreno, S. A. Mantey, T. Nakamura, B. Nuche-Berenguer, T. W. Moody, D. H. Coy and R. T. Jensen, *Peptides*, 2015, **72**, 128-144.
8. A. Safavy, K. P. Raisch, M. B. Khazaeli, D. J. Buchsbaum and J. A. Bonner, *J. Med. Chem.*, 1999, **42**, 4919-4924.

9. G. Schwartsmann, L. P. DiLeone, M. Horowitz, D. Schunemann, A. Cancella, A. S. Pereira, M. Richter, F. Souza, A. B. da Rocha, F. H. Souza, P. Pohlmann and G. De Nucci, *Invest. New Drugs.*, 2006, **24**, 403-412.
10. R. Mansi, K. Abiraj, X. Wang, M. L. Tamma, E. Gourni, R. Cescato, S. Berndt, J. C. Reubi and H. R. Maecke, *J. Med. Chem.*, 2015, **58**, 682-691.
11. B. E. Rogers, M. E. Rosenfeld, M. B. Khazaeli, G. Mikheeva, M. A. Stackhouse, T. Liu, D. T. Curiel and D. J. Buchsbaum, *J. Nucl. Med.*, 1997, **38**, 1221-1229.
12. R. Markwalder and J. C. Reubi, *Cancer Res.*, 1999, **59**, 1152-1159.
13. S. L. Pedersen, A. P. Tofteng, L. Malik and K. J. Jensen, *Chem. Soc. Rev.*, 2012, **41**, 1826-1844.
14. R. B. Merrifield, *J. Am. Chem. Soc.*, 1963, **85**, 2149-2154.
15. D. Hanahan and R. A. Weinberg, *Cell*, 2000, **100**, 57-70.
16. K. Barlos, D. Papaioannou, S. Patrianakou and T. Tsegenidis, *Liebigs Ann. Chem.*, 1986, **1986**, 1950-1955.
17. R. Schirrmacher, B. Wängler, J. Bailey, V. Bernard-Gauthier, E. Schirrmacher and C. Wängler, *Semin. Nucl. Med.*, 2017, **47**, 474-492.
18. E. Kaiser, R. L. Colescott, C. D. Bossinger and P. I. Cook, *Anal. Biochem.*, 1970, **34**, 595-598.
19. D. Hanahan and R. A. Weinberg, *Cell*, 2011, **144**, 646-674.